The Magmatic, Thermal and Exhumation History of the Nanga Parbat-Haramosh Massif, Western Himalaya

Thesis

The Magmatic, Thermal and Exhumation History of the Nanga Parbat-Haramosh Massif, Western Himalaya

A thesis submitted for the degree of

Doctor of Philosophy

MARK T. GEORGE

BSc. (Hons.) *Durham.* 1989

Department of Earth Sciences,

The Open University.

September 1993

Date of submission: 28 September 1993
Date of award: 15 February 1994

ProQuest LLC.
789 East Eisenhower Parkway
P.O. Box 1346
Ann Arbor, MI 48106 – 1346

Abstract

This study presents important new constraints on the geological evolution of a structurally-anomalous basement massif in the western Himalaya. In northern Pakistan, Indian continental crust of the Nanga Parbat-Haramosh massif (NPHM) has been recently exhumed from beneath the Kohistan-Ladakh island arc. Integrated structural, metamorphic, geochronological and geochemical techniques have provided valuable evidence for the thermal, magmatic and denudation history of the NPHM and adjacent parts of the Kohistan arc.

The northern part of the Kohistan arc is composed of a range of intrusive igneous rocks and associated metasediments, whilst the adjacent NPHM is characterised by orthogneiss with subsidiary intercalations of pelitic gneiss and calcsilicate. The contact zone between the western margin of the NPHM and the Kohistan arc is characterised by a steeply-inclined, high-grade shear zone, along which there has been a significant variation in movement sense. In the south of the area, the rocks of the NPHM have been thrust north-westwards over Kohistan, resulting in the active exhumation of Indian continental crust. In contrast, in the north of the area, the uplift of the NPHM has been accommodated within the shear zone by dextral transtension.

The metamorphic rocks of the NPHM have mostly equilibrated under 600-750 °C and 7-10 kbar, whilst those from adjacent lithologies in the Kohistan arc have equilibrated under 550-700°C and 6-8 kbar (as determined by rim compositions). The change in estimated peak metamorphic grade across the region is gradual, and major metamorphic breaks are absent. The majority of samples from both the NPHM and Kohistan record retrogressive P-T pathways, which is thought to reflect the extended exhumation history of the region. The variable results of Gibbs modelling are interpreted as indicating lithological control on garnet growth, resulting in the preservation of different segments of the same PT path. The most recent equilibration of metamorphic assemblages occurred at > 30 Ma in Kohistan and < 25 Ma in the NPHM, suggesting that contrasting structural levels can be exhumed without preserving substantial metamorphic discontinuities.

$^{40}Ar/^{39}Ar$ and Rb-Sr mica ages mostly lie in the ranges 1-8 Ma and 17-26 Ma for the NPHM and the Kohistan arc, respectively, and are considered to be exhumation-related cooling ages. The interpretation of such cooling ages in terms of cooling rates and exhumation rates is dependant on the reliable estimation of mineral closure temperatures and palaeogeotherms. However, in general the ages indicate that cooling through the relevant closure temperatures has occurred more recently and more rapidly for the NPHM compared with the Kohistan arc, confirming the recent differential exhumation of the NPHM relative to Kohistan. Cooling ages for deformed samples collected from the shear zone are highly variable, which

is probably a reflection of variable closure temperatures or variable degrees of isotopic resetting of rocks characterised by contrasting strain-states, lithologies and fluid-contents. The observed variation in mineral ages may also partly be a result of the late-stage juxtaposition of different structural levels by shearing and/or open system behaviour.

The variable geochemistry of Himalayan-age granite magmatism in the region is a reflection of contrasting source compositions. In Kohistan, undeformed 26-50 Ma granitoid sheets are characterised by relatively primitive initial Sr and Nd isotopic compositions ($^{87}Sr/^{86}Sr_i$=0.7045-0.7054; $\varepsilon_{Nd(T)}$=0.1-2.7), indicating that locally, underthrusting of relatively evolved Indian continental crust beneath Kohistan had not occurred before 30 Ma. The majority of the granites were generated by the fluid-absent breakdown of biotite in an isotopically juvenile, LILE and LREE-enriched source. Proximal to the NPHM, the isotopic and trace element compositions of deformed granites have been significantly affected by both the assimilation of Indian continental crust and sub-solidus fluid mobility.

The tourmaline leucogranites of the NPHM display a wide range of geochemically and isotopically evolved compositions ($^{87}Sr/^{86}Sr_i$=0.72-0.97; $\varepsilon_{Nd(T)}$=-24 to -26), and have been generated by the fluid-absent melting of mature pelitic rocks within the NPHM. The leucogranites are low melt fractions that probably result from the decompression melting of Indian crustal material with unusually high heat productivity during rapid tectonic exhumation.

Frontispiece. Climbing out of the Indus gorge near Sassi : the route to Darchan.

The supply road between Astor and Gilgit :

The march was the worst on the whole road.... It was impossible to exaggerate the vileness of this portion of the road; it plunged down over a thousand feet of tumbled rocks, in steps from six inches to two feet deep; then for a mile it ran ankle-deep in loose sand filled with sharp-edged stones; it passed by a shelf six inches wide across the face of a precipice; in fact it concentrated into those five short miles every horror which would be possible to conceive of a road in the worst nightmare....The next three marches to Gilgit were through a howling wilderness; for nearly 20 miles there was not a drop of water, except where the road dipped right down to the bank of the Gilgit river, and that was running thick and slab like gritty cocoa. Up and down over spurs of hills, into gaping ravines, now at the level of the river, now a thousand feet up, along cliffs glaring and blazing in the sun, the miserable path ran on.

Col. Algernon Durand, British Agent in Gilgit, 1889-1894.
'The Making of a Frontier' (1901)

Acknowledgements

I would first like to thank may supervisors Nigel Harris and Rob Butler, for guidance and support throughout the duration of this project, and for constructive criticism of earlier drafts of this thesis.

The logistical support and hospitality given by Prof. Shams, Munir Ghazanfar, Nawaz Chaudhary and students, of the Institute of Geology, Punjab University, is gratefully acknowledged. Thanks must also go to numerous guides, porters, camp-followers and hangers-on, who provided assistance and company in the northern areas, and to the Hunza Inn for being such a welcome haven.

At the Open University, thanks to Kay Chambers and Brian Ellis for making polished and thin sections, and especially for preparing numerous 'final samples'. Thanks also to Andy Tindle for providing Mac and microprobe advice, Pete Webb and John Watson for XRF facilities, and John Taylor and Andy Lloyd for cartographic support. Thanks to Dentinho for advice in all matters, but especially on how to get the best results out of an old microprobe, for making Macdraw Pro. seem user-friendly, and for initiating me into the delights of *thermocalc*.

I would like to acknowledge the help given by Chris Hawkesworth and everybody in the isotope lab. Special thanks go to Peter van Calsteren and Mabs Johnston for numerous lab. parties, abundant 'column gossip', and for helping me to overcome the tries and tribulations of running mica samples. Thanks to Steve Reddy for running samples in the argon lab., and for commenting on various paper drafts.

For making life at the OU so enjoyable, thanks to everybody in the Dept. Earth Sciences. In particular, thanks must go to past house-mates (I hope I wasn't too stressed), office mates, and all enthusiasts of football, 6-a-side cricket, hockey, squash and tennis. Cheers to the people whom I worked on the bar with, and to others at the sailing club for some great racing. Finally, special thanks must go to my whole family for support during my time at the OU.

Contents

Chapter 3 : The Structure and Origin of the Nanga Parbat-Haramosh Massif

Chapter 4 : Mineral Chemistry and Metamorphism of the Nanga Parbat-Haramosh Massif - Kohistan Region

List of Figures

Chapter 1 : Introduction and Previous Work

Chapter 2 : Field Relations and Petrography

Chapter 3 : Structure and Origin of the NPHM

Chapter 4 : Mineral Chemistry and Metamorphism

Chapter 5 : Cooling History

Chapter 6 : Geochemistry of Granite Intrusions

Chapter 7 : Isotope Geology

Chapter 8 : Summary

List of Tables

Chapter 2

Chapter 4

Chapter 5

Chapter 6

Chapter 7

List of Plates

N.B. : The field of view in all photomicrographs is 3.5 mm unless otherwise stated. PPL = plane-polarised light; XPL = cross-polarised light.

Chapter 2

Chapter 3

Chapter 1
Introduction and Previous Work

1.1. The Nanga Parbat-Haramosh Massif

In northern Pakistan, the mountain ranges of the Himalaya, Hindu Kush, Karakoram and Pamir meet in a broad region known as the Roof of the World or Pamir Knot, containing ten of the world's thirty highest peaks. The region is bound to the west by Afghanistan, to the north by the Chinese province of Sinkiang and to the east by Indian held Kashmir. Much of the area is remote, isolated and largely uninhabited.

The western end of the 2500 km-long Himalayan chain is terminated by the sixth highest mountain in the world, Nanga Parbat (8125 m) (Fig. 1.1), which surmounts a broad massif. This massif is cut by the antecedent Indus river which flows west from a source in SW Tibet, before turning southwest towards the plains of the subcontinent. At a distance of 55 km to the northwest of Nanga Parbat, the Indus river lies at only 1200 metres, resulting in some of the highest relief on earth. To the north of the Indus, topographic continuity between the Himalaya and the more northerly Karakoram is maintained by the Haramosh range, capped by Haramosh peak (7409 m).

The Nanga Parbat-Haramosh massif (NPHM) is the most northerly exposure of Indian continental crust in the Himalayan orogen (Figs. 1.2 & 1.3). The NPHM has been exhumed from beneath a relict island arc complex (the Kohistan-Ladakh arc) which was sutured to the southern margin of Eurasia before the continental collision between Eurasia and continental India. The southern margin of the Kohistan arc is a steeply inclined shear zone called the Main Mantle Thrust (MMT), which can be traced north-eastwards to define the western margin of the NPHM (Tahirkheli et al. 1979; Chamberlain et al. 1991) (Fig. 1.2). Similarly, the Indus-Tsangpo suture, which borders the southern margin of the Ladakh portion of the island arc, can be traced north-westwards to define the eastern boundary of the massif (Tahirkheli et al. 1979). The northern contact between the NPHM and the Kohistan

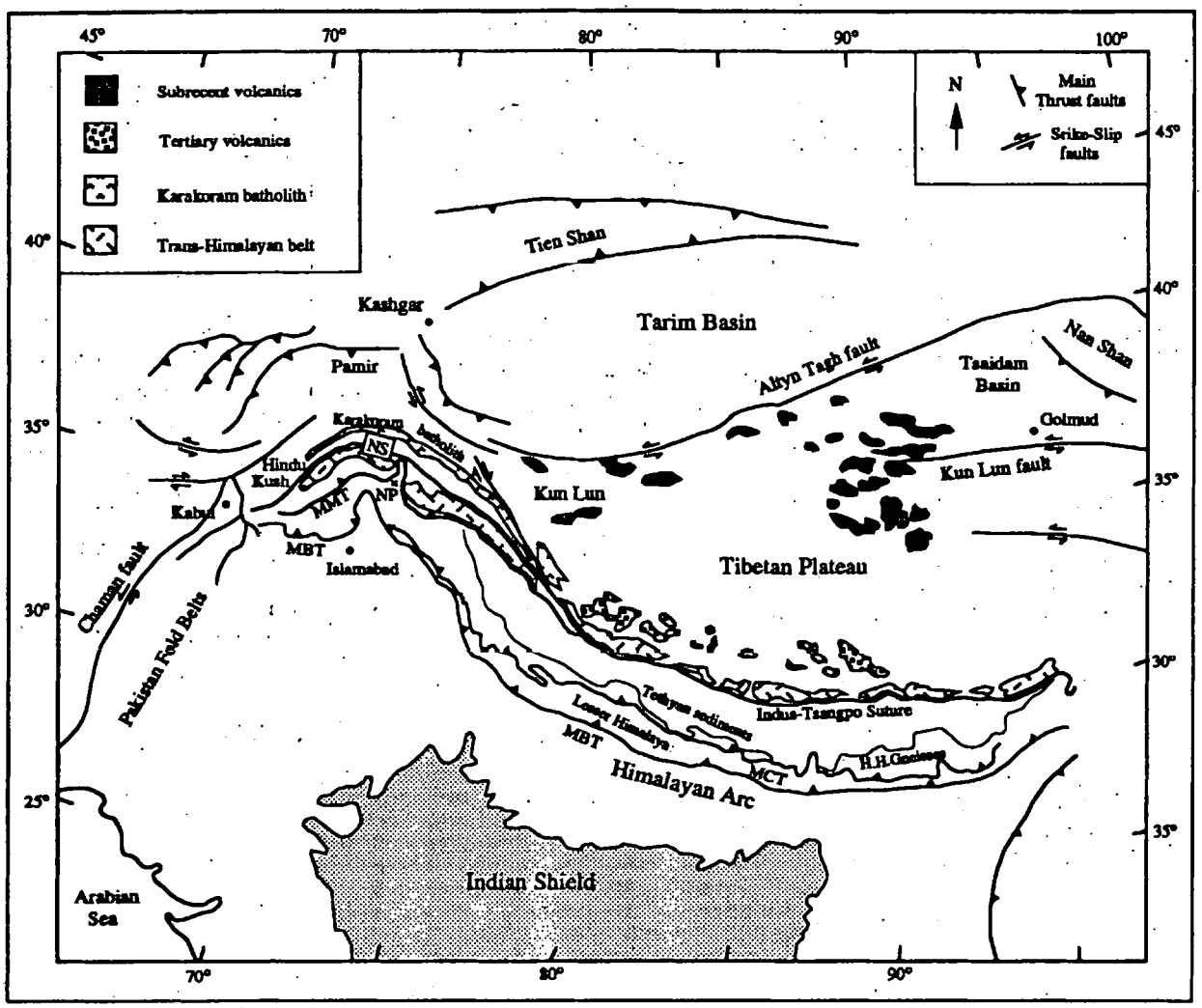

Fig. 1.1 Simplified tectonic sketch map of Tibet and the Himalaya, after Harrison et al. (1992) and Ni and Barazangi (1984). NP = Nanga Parbat; NS = Northern suture; MMT = Main Mantle Thrust; MCT = Main Central Thrust; MBT = Main Boundary thrust; HH Gneisses = High Himalayan gneisses (crystalline).

terrane has recently been identified (Butler et al. 1992), thus linking the map traces of the MMT with the Indus-Tsangpo suture.

The NPHM is the result of a somewhat anomalous structural and thermal evolution in late Himalayan times, which modern geological studies have sought to resolve. The massif has the form of a crustal-scale antiform, about which the MMT has been folded, and within which the main, south-verging L-S fabrics developed during early, southwards thrusting of Kohistan over India (Coward 1985; Coward et al. 1986; Treloar et al. 1992). The MMT bordering the NPHM has had a complex structural history, and there is evidence for both early amphibolite-grade deformation (Butler and Prior 1988a), and later, post-

metamorphic deformation (Lawrence and Ghauri 1983a; Verplanck et al. 1985; Butler and Prior 1988b; Butler et al. 1989; Madin et al. 1989). The late deformation is a reflection of the rapid exhumation of the NPHM within the last 10 Ma, as initially suggested by young K-Ar and fission track cooling ages (Zeitler et al. 1982; Zeitler 1985; Coward et al. 1986), and subsequently confirmed by more detailed ^{40}Ar-^{39}Ar and K-Ar mica and hornblende chronology (Treloar et al. 1989a; 1991; Zeitler et al. 1989). The exhumation was accommodated by a combination of folding within the massif and recent faulting on the margins (*op. cit.*) (Treloar et al. 1991; 1992).

Recent geochronological studies by Zeitler and co-workers have utilised a scanning high-resolution ion-microprobe (SHRIMP) in dating both metamorphic zircons and igneous zircons contained in post-tectonic leucogranite dykes. The metamorphic zircons yield U-Pb ages of about 1.9 Ga and 400-500 Ma for the gneisses of the NPHM (Zeitler et al. 1989), whilst the magmatic zircons indicate an intrusion age of < 12 Ma for the leucogranite dykes (Zeitler and Chamberlain 1991). Interestingly, the metamorphic zircons are characterised by very young (< 12 Ma) overgrowths, whilst U-Pb monazite ages for the gneisses lie in the range 4-11 Ma, suggesting that the rocks presently exposed in the NPHM may have experienced a very young metamorphic event (Smith et al. 1992; Zeitler et al. 1993).

1.2. Location of Field Area

The study area is centred on the Indus gorge where it bends through the Nanga Parbat-Haramosh massif (NPHM), before being joined by the Gilgit river, 35 km east of Gilgit town (Fig. 1.3). The region is part of the Northern Areas, a semi-autonomous province in northern Pakistan, formerly a part of Kashmir, which resisted annexation to India in 1948. The area has become relatively accessible since the construction of the Karakoram highway, built as a result of a Sino-Pak agreement in 1966 and opened in the late-1970s. This road winds through the mountains for 883 km, linking Pakistan with China, and in places following the course of the ancient Silk Route. The construction of the

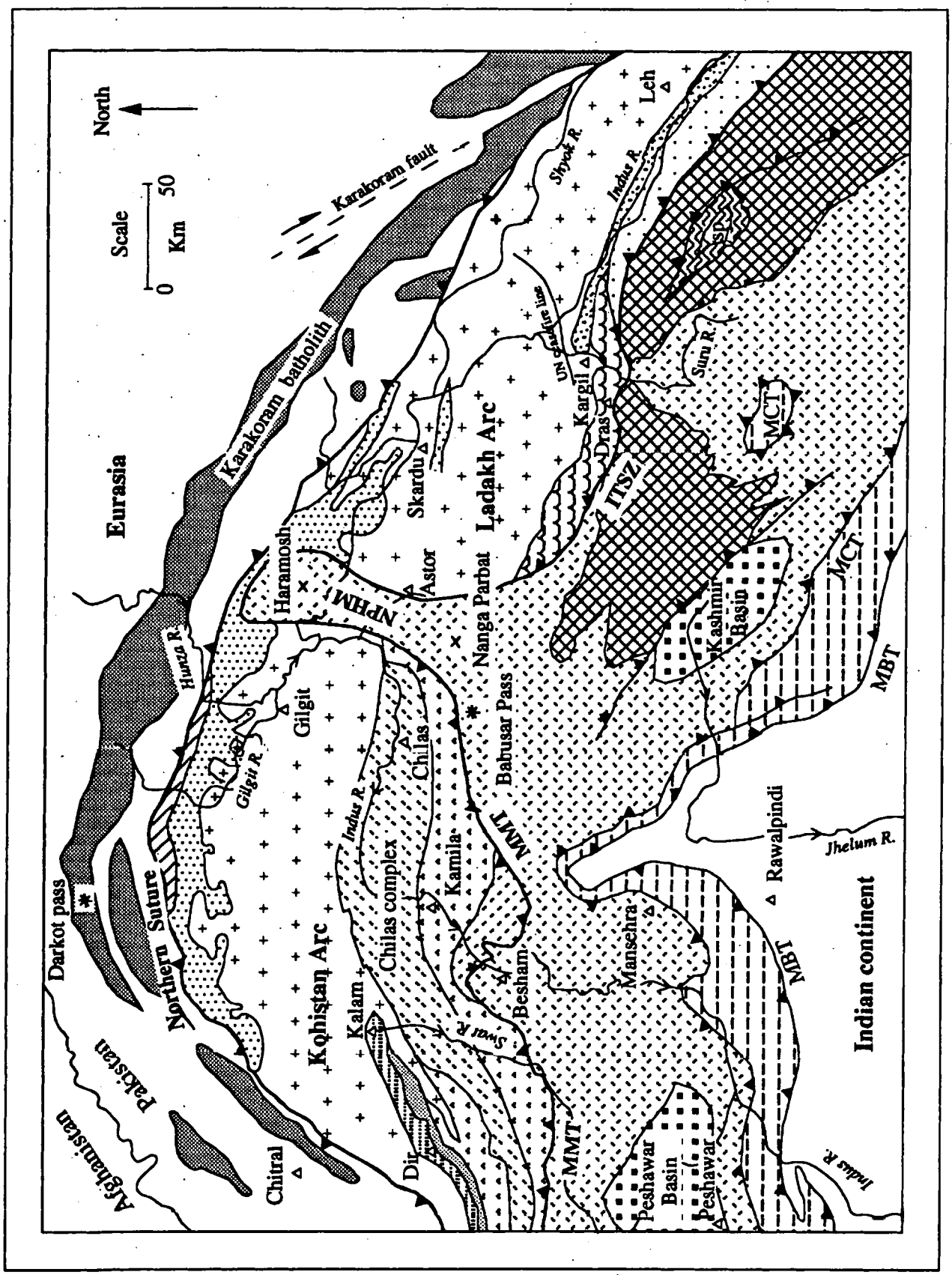

Fig. 1.2. Geological sketch map of the western Himalaya and Karakoram, after Searle et al. (1989) and Coward et al. (1986).

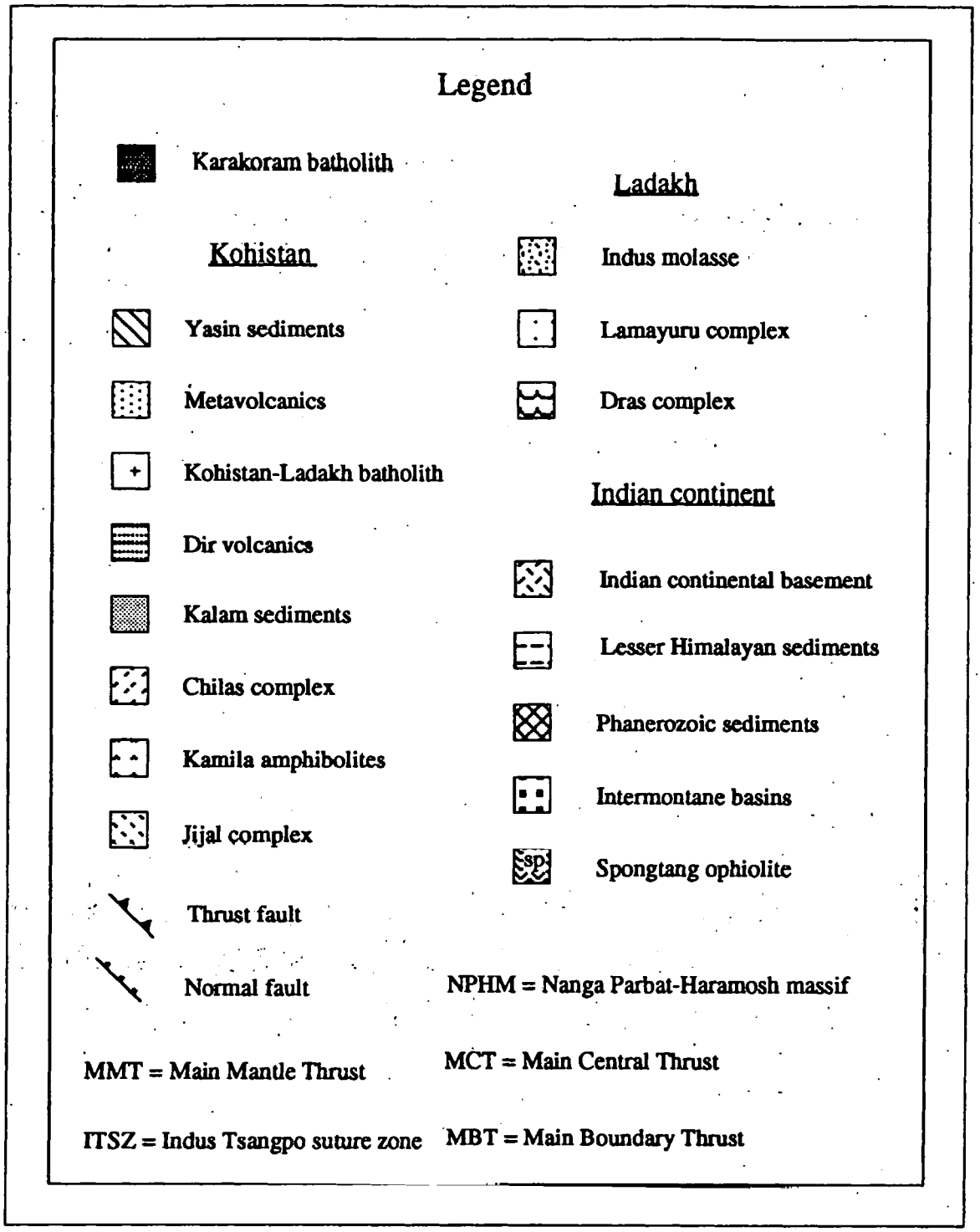

Fig. 1.2.(cont.)

Karakoram highway and other roads has provided readily accessible geological exposure which complements the natural exposure.

Detailed fieldwork was concentrated along road exposures in the Indus valley, in the remote Haramosh valleys lying to the north of the Indus, and in the Tato and Liachar valleys

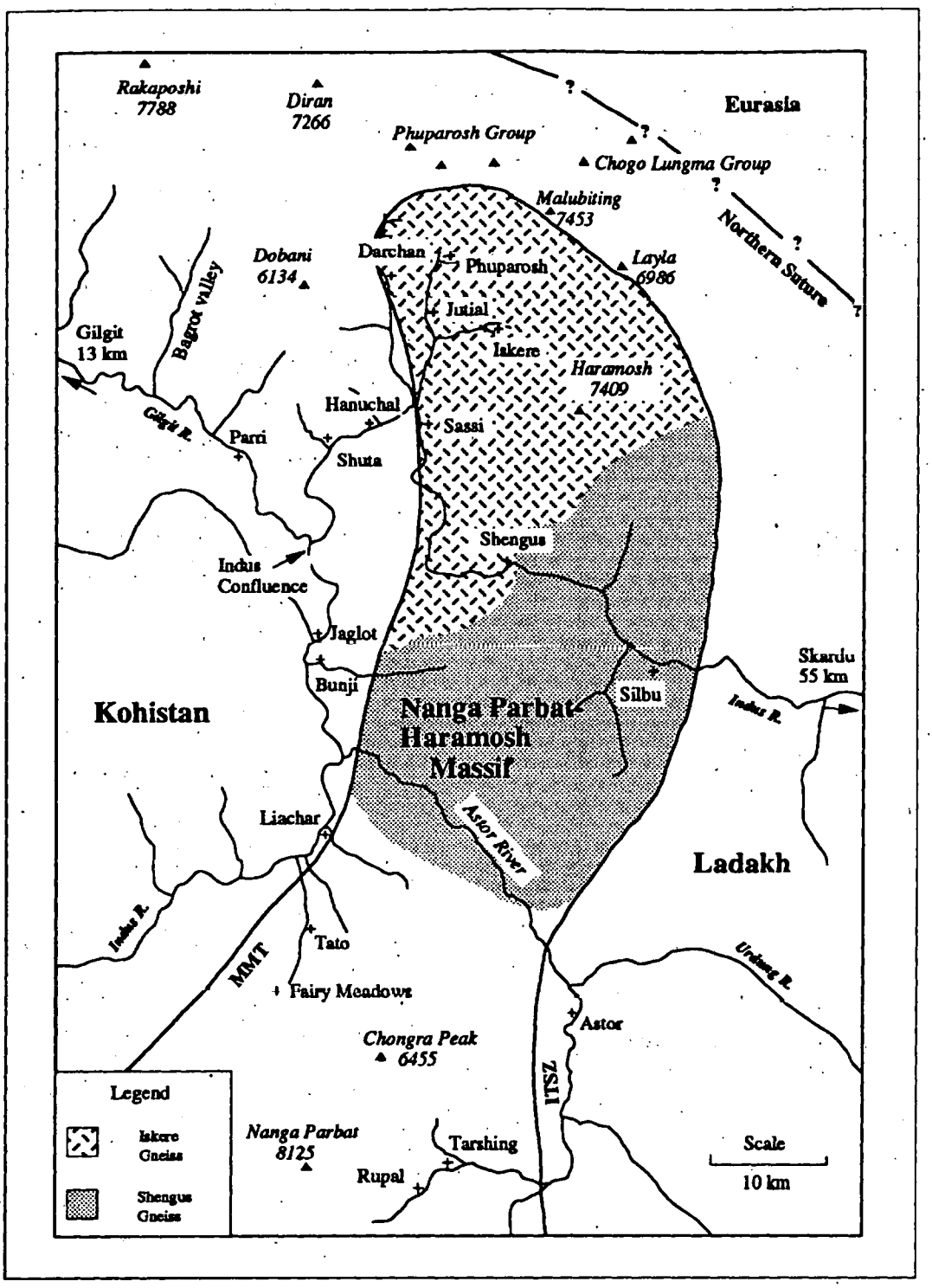

Fig. 1.3 Sketch Map of the Nanga Parbat-Haramosh Massif. Location of Iskere and Shengus gneisses after Madin et al. (1989). MMT = Main Mantle Thrust; ITSZ = Indus Tsangpo suture zone.

in the south of the region. Reconnaissance work was undertaken in the Astor valley and in the Tarshing-Rupal area (Fig. 1.3). The fieldwork was carried out on two separate visits in Febuary-March and September-November 1990. The first of these visits coincided with a period of political unrest in northern Kohistan, which resulted in the closure of the field area for part of the visit.

1.3. Objectives

This thesis is based on a detailed geological study carried out across the recently-active, regional-scale shear zone that separates the NPHM from the adjoining Kohistan island arc. The study has involved the use of integrated structural, metamorphic, geochemical and geochronological techniques. The prime objective is an understanding of the magmatic, metamorphic and cooling history of the NPHM region, and of the relationship between metamorphic and magmatic processes and both the structural evolution and the exhumation history of the NPHM. With this objective in mind, the study has involved the following :

(i) Characterisation of the structural setting of the shear zone separating the two contrasting terranes, and analysis of the temporal relationships between igneous intrusion and deformation.

(ii) Identification of the source regions, petrogenesis and timing of the granite magmatism in both the Kohistan arc and the NPHM.

(iii) Evaluation of the geochemical and isotopic effects of deformation and/or sub-solidus fluid flow observed in granites intruded into the suture zone.

(iv) Characterisation of the conditions of peak metamorphism and the metamorphic history (P-T path(s)), together with an evaluation of the timing of metamorphism in the region.

(v) Deduction of the cooling history of the suture zone and of the adjacent regions, and subsequently of the relationship between the structural and exhumation history of the region.

1.4. Tectonics of the Central Himalaya and Tibet

The Himalayan mountain belt and the Tibetan plateau together form a vast uplifted region of thickened continental crust and approximate north-south shortening (Fig. 1.1). Whilst the origin of the Tibetan plateau is still disputed, the Himalayan belt is directly the result of the Tertiary collision between the Indian continental plate and Eurasia. This continental collision is the latest in a series of collisions between the Eurasian continent and range of autochthonous blocks, accreted to the southern margin of Eurasia since about 200 Ma (Chang and Cheng 1973; Allègre et al. 1984; Dewey et al. 1988).

The Himalayan collision occurred along the Indus-Tsangpo suture zone (ITSZ) (Fig. 1.1), a complex belt of dismembered ophiolitic material, flysch and melange (Gansser 1964, 1980; Dewey et al. 1988). The timing of the collision can be deduced from the sea floor spreading histories of the Indian and Atlantic oceans. From sea-floor magnetic stripes, Molnar and Tapponnier (1975) suggested that collision occurred at 40 Ma (anomaly 20), since this time corresponded to a dramatic slowing down in the northwards movement of the Indian plate. Other workers have correlated continental collision with a decrease in the spreading rate at the East Indian ridge at 50 Ma (anomaly 22) (Johnson et al. 1976). More recently, comprehensive studies of the magnetic anomalies in the Indian ocean have suggested that collision occurred at 45-50 Ma, when the movement of the Indian plate slowed down and changed in direction from being northeasterly to being more northerly (Patriat and Achache 1984; Dewey et al. 1989) (Fig. 1.4).

An age of about 50 Ma for India-Eurasia collision is supported by a number of independent observations. From land-based palaeomagnetic data, Besse et al. (1984) and Klootwijk et al. (1979) suggested that collision occurred at 47-53 Ma. In the western Himalaya, an abrupt change from marine to continental sedimentation occurred at the end of the lower Eocene (Le Fort 1989), whilst the youngest, subduction-related granodiorites in the Trans-Himalayan belt have been dated at 41 Ma (Scharer et al. 1984a).

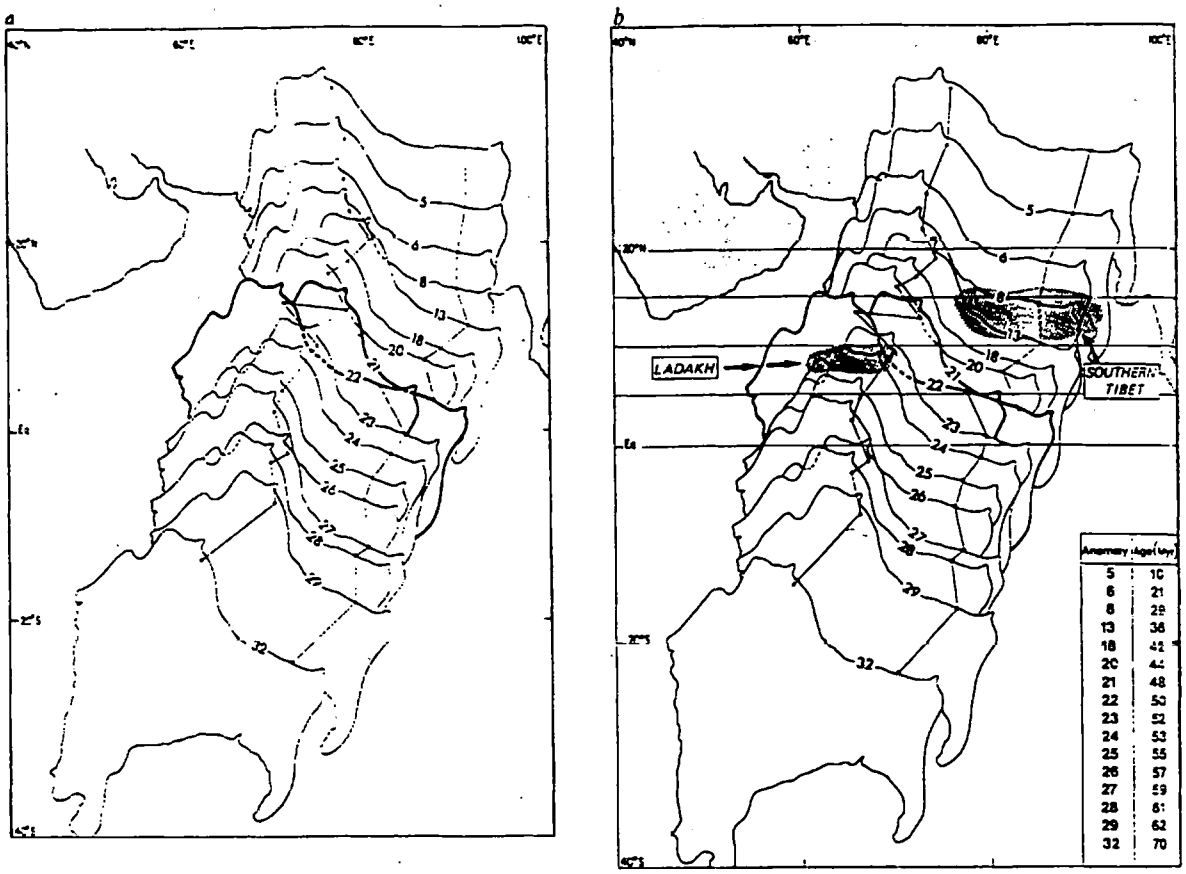

Fig. 1.4. Cenozoic northwards drift of India, from Patriat and Achache (1984). The position of India at the time of India-Eurasia collision (anomalies 22 & 21) is emphasised by the bold line; also plotted is the motion of two points lying near the northern margin of India. A. Relative motion of India with respect to Eurasia, kept arbitrarily fixed in its present position. B. Absolute motion of India in the hotspot frame of reference. The positions of southern Tibet and Ladakh before collision, deduced from palaeomagnetic data, are also indicated.

Prior to the final closure of Tethys in the Eocene, subduction of oceanic crust beneath the southern margin of Eurasia led to the generation of a linear belt of subalkaline to calc-alkaline intrusives with associated volcanics (Fig. 1.1) (Powell and Conaghan 1973; Molnar and Tapponnier 1975; Gansser 1980; Allègre et al. 1984; Powell 1986; Harris et al. 1988a). In Tibet, this belt is called the Gangdese belt or the Trans-Himalayan batholith, and was intruded at 110-40 Ma (Maluski et al. 1982; Scharer et al. 1984a, Xu et al. 1985). The close proximity between the ITSZ and the Trans-Himalayan batholith led Molnar and Tapponnier (1975) to infer that oceanic subduction had occurred at a relatively steep angle, but a more likely explanation is that after initial collision, most of the forearc was underthrusted beneath the southern margin of the Lhasa block (Harrison et al. 1992). Sm-

Nd and U-Pb isotopic systematics indicate a magma petrogenesis involving variable degrees of crustal contamination/assimilation of mantle-derived melts, confirming that the batholith was emplaced into sialic crust at a continental margin (Allègre et al. 1984; Scharer et al. 1984a; Gariepy et al. 1985; Xu et al. 1985; Harris et al. 1988b).

Palaeomagnetic data indicate that since the collision, continental India has continued to move northwards relative to Eurasia by about 1800 km in the west and 2700 km in the east (Dewey et al. 1988, 1989), but the mode of accommodation of this convergence has been the subject of considerable controversy. The accommodation has probably occurred by a combination of underthrusting of continental crust beneath Eurasia (Powell and Conaghan 1973, Bird 1978; Klootwijk et al. 1985; Powell 1986), crustal shortening within the Himalaya (Coward and Butler 1985; Searle 1986), north-south shortening and thickening of the Eurasian lithosphere (Dewey and Burke 1973; England and Houseman 1986; Mercier et al. 1987; Dewey et al. 1989) and strike-slip faulting in Tibet (Molnar and Tapponnier 1975, Tapponnier and Molnar 1976; Tapponnier et al. 1982). The relative contribution of each of these components has been assessed by an evaluation of the amount, style and timing of deformation and exhumation that has occurred in Tibet and the Himalaya, combined with palaeomagnetic and seismic studies. Many of the more recent tectonic models have incorporated the apparently young uplift of the Tibetan plateau (Zhao and Morgan 1985; Mercier et al. 1987; Dewey et al. 1988, 1989; Harrison et al. 1992), although the timing of this uplift is the subject of considerable uncertainty (Molnar and England 1990).

1.5. Crustal shortening and Thermal Evolution of the Himalaya

The Himalaya are essentially a pile of north-dipping thrust sheets present on the northern margin of Indian continental lithosphere (Gansser 1964). In the central Himalaya, immediately south of the ITSZ is a zone of low-grade Phanerozoic metasediments (Tethyan or Tibetan series), deposited on a thinned continental margin, which overlies the Precambrian High Himalayan crystalline (basement). In Nepal, the upper boundary of the basement cross-cuts the Tethyan stratigraphy and the division between the two is based on

metamorphic grade (Le Fort 1989). In northern Pakistan, the internal zones of the Indian continent are characterised by a Precambrian basement which is dominantly composed of metapelitic and metapsammitic gneisses and orthognesisses. The orthogneisses are thought to represent deformed Cambrian granites, which may be a continuation of the Lesser Himalayan cordierite granite belt of the central Himalaya (Le Fort et al. 1980; Coward et al. 1982). Unconformably overlying the basement is a high-grade Phanerozoic cover sequence of generally more calcareous metasediments (Treloar et al. 1989b & c), which may have been actively underthrusted early in the Himalayan orogeny (Barnicoat and Treloar 1988).

South of the High Himalaya, the Lesser Himalaya consist of generally unfossiliferous, low-grade sediments deposited in intracratonic, shallow marine conditions (Gansser 1964). In Pakistan, the internal zones are separated from the low-grade rocks of the Lesser-Himalaya to the south by the Mansehra and Panjal thrusts, which are structurally equivalent to the Main Central Thrust (MCT) of the central Himalaya (Coward et al. 1988). Further thrusts carry the Lesser Himalayan sequences over the molasse deposits of the sub-Himalaya, and are equivalent to the Main Boundary Thrust (MBT) of the central Himalaya (Le Fort 1975).

Following collision along the ITSZ at about 50 Ma, deformation migrated southwards (Le Fort 1975), possibly as a consequence of northwards-spreading deformation in Asia meeting more resistance. In the central Himalaya, thrusting probably began near the ITSZ during the late Eocene-Oligocene, with principle uplift on the MCT, 150 km south of the ITSZ, occurring in the early Miocene (Le Fort 1975; Maluski and Matte 1984). Movement occurred on the MBT from Pliocene to recent, with additional thrusts developing further south in the late Pliocene-Pleistocene (Le Fort 1989; Ni and Rawazangi 1984). Crustal imbrication in the Himalaya may have been confined to Indian upper crust above an intra-crustal detachment, with the inherent underthrusting of middle and lower Indian crust northwards beneath Eurasia (Fig. 1.5) (Coward and Butler 1985; Butler and Coward 1989). Alternatively, crustal shortening may have involved the whole-scale imbrication of the Indian continental crust south of the ITSZ, accompanied by the

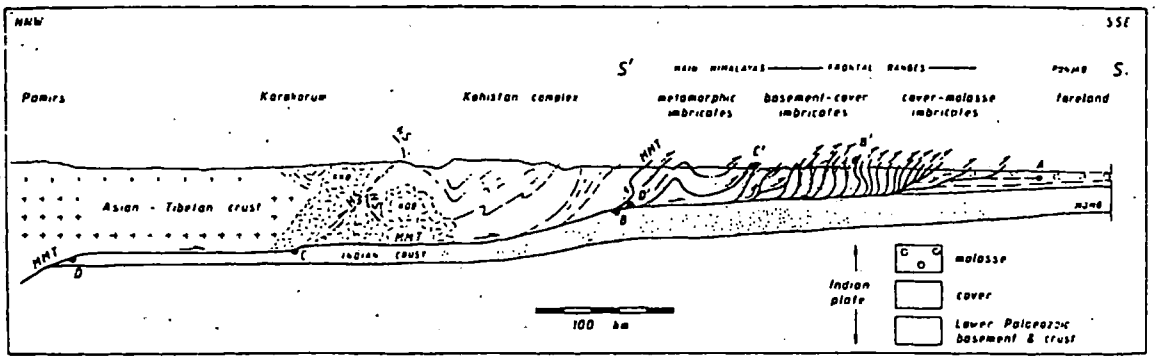

Fig. 1.5. Model for crustal thickening in the western Himalaya involving the imbrication of the upper crust only, based on balanced cross-sections in Pakistan. From Butler & Coward (1989). A = thrust front; B = Ramp across Hazara slates; C = ramp across crystalline basement; D = ramp across Indian lower crust. MMT = Main Mantle thrust; KOB = Kohistan batholith; KKB = Karakoram batholith; NS = Northern Suture.

underthrusting of Indian lithospheric mantle northwards below Eurasia (Fig. 1.6) (Mattauer 1986).

In India and Nepal, a major characteristic of the MCT zone is an associated, high-grade metamorphism, which is often inverted, and may have been superimposed on an earlier Barrovian metamorphism (Hodges and Silverberg 1988; Searle and Rex 1989). The timing and origin of the MCT-related metamorphism has been much debated, and seems to vary along the strike of the mountain belt. In Nepal, Le Fort (1975) observed that the metamorphism was syn-post MCT movement, and that the MCT and the isograds were parallel, and therefore proposed that the inversion was due to a combination of bending of isotherms and downwards heating during underthrusting along the MCT. Retrogression occurred during on-going thrusting, with a drop in temperature at the base of the slab due to downwards conduction, and a drop in pressure at higher levels due to unroofing (Le Fort

1989). In contrast, in the Zanskar Himalaya, Searle and Rex (1989) proposed that the inverted metamorphism was due to the large scale recumbant folding of the metamorphic isograds.

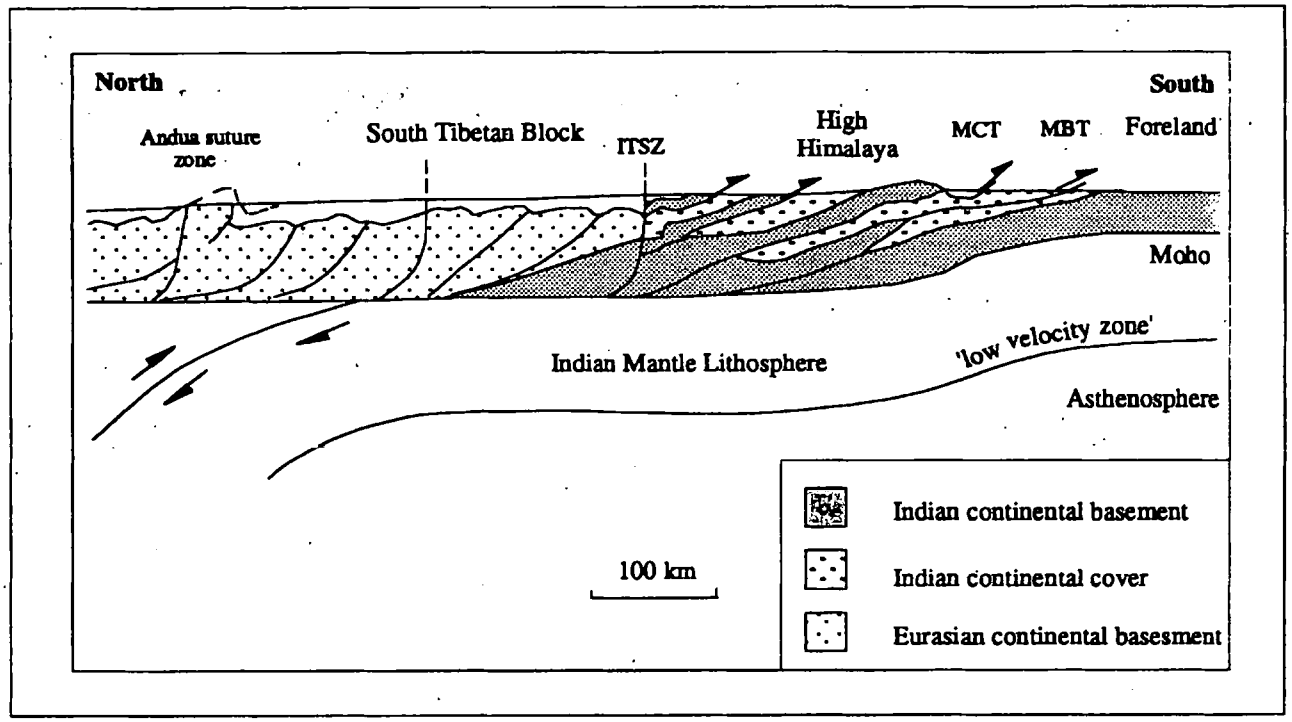

Fig. 1.6. Simplified tectonic section across the central Himalaya, showing the imbrication of the Indian continental crust and the underthrusting of the Indian sub-continental mantle lithosphere below Eurasia, after Mattauer (1986). ITSZ = Indus Tsangpo suture zone; MCT = Main Central thrust; MBT = Main Boundary thrust.

In the internal zones of Pakistan, both cover and basement suffered a Himalayan-age Barrovian metamorphism, although locally, basement rocks were thermally unaffected by Himalayan-age events (Williams et al. 1988). The grade of the metamorphism and the intensity of deformation both increase towards the Main Mantle Thrust (described below) (Coward et al. 1982). According to Maluski and Matte (1984) and Treloar et al. (1989b), this metamorphism was largely synkinematic to early, south-directed thrusting which generated the dominant foliation and north-south stretching lineation in the region. However, Lawrence et al. (1985) and DiPietro (1991) recognised pre-metamorphic nappe structures in Swat, which they interpreted as representing early collisional deformation of the leading edge of the Indian shield, with subsequent Himalayan-age metamorphism occurring by static recrystallisation, after the main phases of MMT-related deformation.

The post-metamorphic structural and cooling history of the internal zones of Pakistan has been described in detail by Treloar et al. (1989b & c) and Treloar and Rex (1990a & b). Hornblende ^{40}Ar-^{39}Ar cooling ages for the northern edge of the Indian continent lie in the range 35-40 Ma, suggesting that the metamorphism occurred soon after continental collision, and was closely followed by cooling through ~ 500 °C. The metamorphic stack was imbricated by continuing SSE-directed thrusting in the period 35-24 Ma, which caused the deformation of the peak metamorphic assemblages. These younger thrusts operated at temperatures no lower than mid greenschist-facies, and become more brittle southwards, reflecting progradation into higher structural levels. As a consequence, the internal zones consists of a series of crustal-scale nappes, each having its own lithostratigraphy and metamorphic history, and each showing metamorphic inversion. For example, in the Besham nappe, the metamorphism was accompanied by a marked pressure-increase, probably caused by underthrusting beneath the Kohistan arc. In this area, peak metamorphism reached 550-650 °C and 8-12 kb, and was terminated relatively early, probably by the subsequent rapid uplift (Treloar et al. 1989b). In contrast, in the Hazara nappe, peak metamorphism reached 650-700°C and 5-9 kb, and continued later than in the Besham nappe, thus having more of the characteristics of metamorphism following long-lived thermal relaxation (Treloar et al. 1989c).

The unroofing of the internal zone of Pakistan occurred most rapidly in the period 25-15 Ma, corresponding to the deposition of early Miocene molasse further south (Treloar and Rex 1990b). The exhumation was probably brought about by a combination of erosion together with high level back-thrusting, back-folding and normal faulting (Treloar et al. 1989c; Chamberlain et al. 1991).

Intrusive into the Tibetan slab are the High Himalayan Leucogranites, occurring as abundant sheets and larger plutons, and dated at about 14-25 Ma (Scharer et al. 1986). Initial Sr and Nd-isotope compositions are extremely variable but strongly evolved, and generally indicate a mature continental source such as the proximal High Himalayan gneisses. Stable isotope studies suggest that the variability of the radiogenic isotope compositions reflect

intrusion of the leucogranites as a succession of isotopically distinct magma batches (France-Lanord and Le Fort 1988). Le Fort et al. (1987) have proposed that the genesis of the High Himalayan granites was related to hot over cold thrusting along the MCT, with dehydration of footwall sediments causing anatexis in the structurally higher Tibetan slab. Alternatively, the genesis of the High Himalayan leucogranites may have involved the thermal insulation of High Himalayan gneisses by thick Tibetan sediments with low thermal conductivities (Jaupart and Provost 1985). Crustal melting may have been aided by the high radiogenic heat production of the gneisses (Pinet and Jaupart 1987).

In northern Pakistan, the northern margin of the Indian continent has also been intruded by post-tectonic leucogranites, which may be equivalent to the High Himalayan leucogranites of the central Himalaya (Coward et al. 1988). Two such leucogranite dykes have yielded U-Pb zircon ages of ~35 and ~50 Ma (Zeitler and Chamberlain 1991).

Recent studies have indicated the presence of large normal faults in some sections of the Himalaya, trending parallel to the mountain axis (Burg et al. 1984; Herren 1987). These faults are usually situated between the High Himalaya and the Tethyan sediments, and are related to either loading or thickening and subsequent gravitational collapse (Burchfield and Royden 1985). The normal faulting postdated or was synkinematic with respect to the intrusion of Miocene leucogranites, and often occurred synchronously with thrusting on the MCT (Searle 1986; Le Fort 1989).

1.6. The Kohistan-Ladakh-Karakoram Region

In the western Himalaya, the ITSZ bifurcates around the Kohistan-Ladakh terrane (Figs. 1.1 & 1.2) (Desio 1979; Gansser 1964, 1980). The NPHM separates the Kohistan and Ladakh portions of this terrane, whilst the Karakoram terrane lies immediately to the north. The NPHM is thus the pivotal point of three tectonically-contrasting areas described separately below.

1.6.1. The Kohistan Arc

In Kohistan, the southern branch of the ITSZ has been called the Main Mantle Thrust, so-called because of the ultramafic rocks and high pressure granulites that occur sporadically along the hanging-wall (Tahirkheli et al. 1979). In the Indus valley, the MMT is a north-dipping, 10-15 km wide shear zone, whilst in the Swat valley, the MMT appears to be a complex zone containing tectonic wedges of melange and blueschists (Shams 1972; Kazmi et al. 1984). Lawrence and Ghauri (1983b) and Treloar et al. (1989c) found evidence for a prolongued history of deformation in the MMT zone in the Hazara area, as shown by rapid changes in the ductility and temperature of formation of deformation fabrics across the shear zone, and the truncation of the youngest, SSE-directed shears in the foot-wall by the MMT fabrics. The youngest movements along the MMT may have been characterised by northwards extension, with a down-to-north movement sense, possibly contemporaneously with southwards movement on the Panjal thrust to the south (Treloar et al. 1992). Such extensional faulting would also account for the rapid cooling by unroofing of the Indian crust (Chamberlain et al. 1991; Treloar et al. 1989c). However, as noted by Zeitler et al. (1982), the similarity in apatite fission track ages on either side of the MMT in the Swat region indicates that any young faulting along the zone had probably ceased by 15 Ma.

In Kohistan, the northern branch of the ITSZ has been called the Northern suture (Coward et al. 1986) or Main Karakoram Thrust (Tahirkheli et al. 1979). This suture zone separates the Kohistan and the Karakoram terranes, and is a 150 metre-4 km wide belt containing a melange of volcanic, sedimentary and serpentinite blocks, whilst blueschists are conspicuous by their absence (Coward et al. 1982; Pudsey 1986).

The Kohistan terrane extends from the Nanga Parbat-Haramosh massif (NPHM) westwards to the Afghanistan border, and consists of a range of ultrabasic, basic and calc-alkaline intrusives, volcanics, volcaniclastics and metasediments, with the deepest arc rocks exposed in the south (Fig. 1.7) (Tahirkheli 1979a; Coward et al. 1982, 1988). This sequence has been interpreted to be a relict island arc, generated during the subduction of

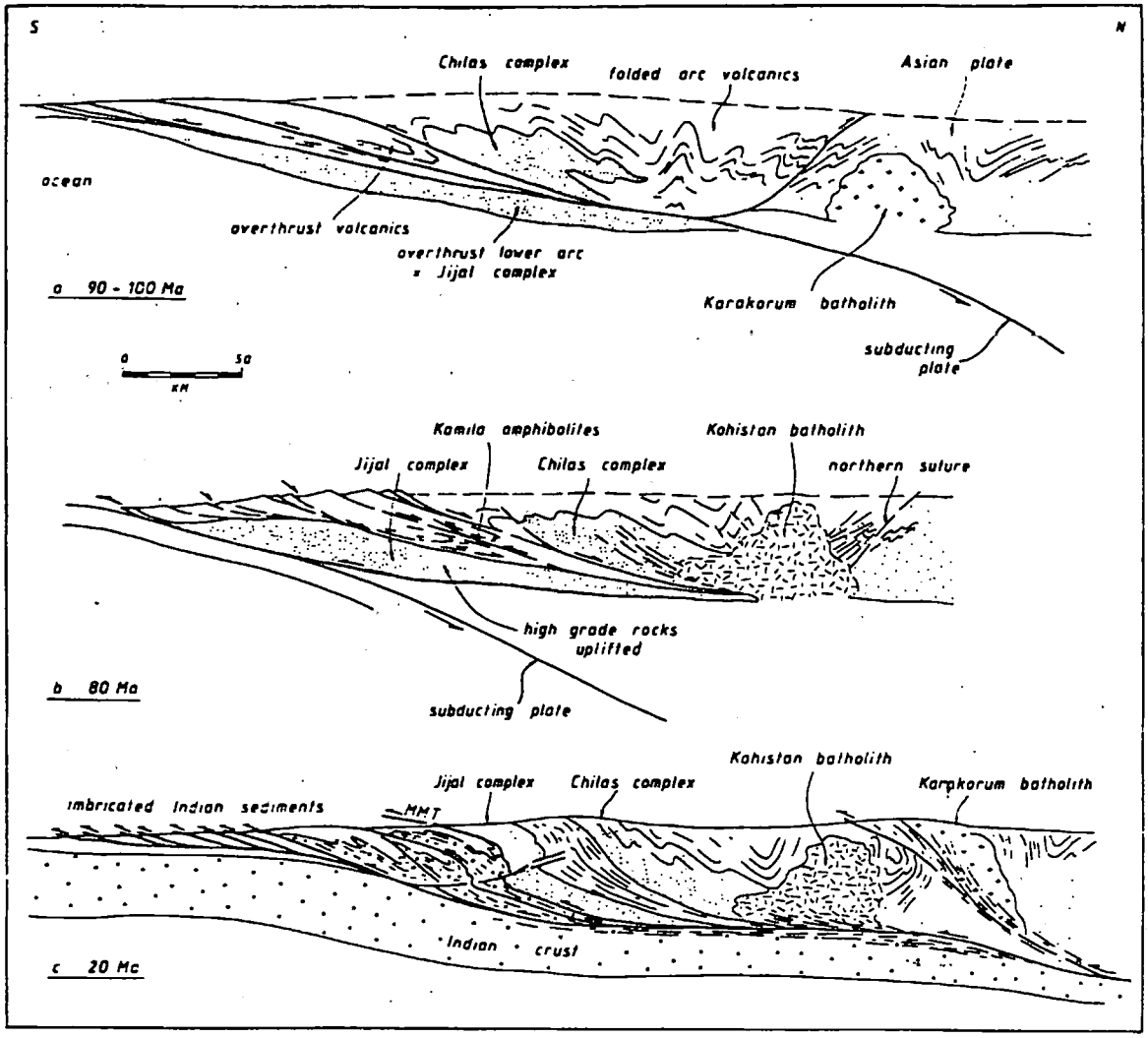

Fig. 1.7. Schematic structural evolution of the Kohistan arc, from Coward et al. (1987). a = during closure along the northern suture; b = during development of the Kohistan batholith; c = during collision between the Kohistan arc-batholith and continental India.

Tethyan oceanic crust (Tahirkheli 1979a), and later overthrust southwards onto the Indian continental margin along the MMT by at least 100 km (Butler and Coward 1989). From south to north, the generalised sequence in Kohistan is as follows (Fig. 1.2) :

(i) In the Indus valley, the Jijal complex occurs in the hanging-wall of the MMT, and consists of high-pressure garnet granulites and ultramafics. The granulites have a meta-igneous origin, and probably either differentiated from a tholeiitic magma, or crystallised from an island arc calc-alkaline magma (Jan and Howie 1981). Geothermobarometry of rim compositions indicates that the granulites were metamorphosed at 700-900 °C and 10-16 kbar (Jan and Howie 1981; Yamomoto 1993). The granulites followed an extended

anticlockwise P-T path, reaching maximum pressures of about 17 kbar at 950 °C (Yamomoto 1993). The ultramafics suffered a metamorphism at 800-850 °C and 8-12 kbar, probably independently of the granulites (Jan and Howie 1981). Granulite-facies metamorphism has been dated using Sm-Nd methods at about 104 Ma (Coward et al. 1982), and may reflect either crustal thickening by magmatic underplating during evolution of the arc, or tectonic thickening of crust that had been previously heated during the formation of a back-arc basin (Yamomoto 1993).

(ii) In tectonic contact with the Jijal complex is the Kamila belt which contains a range of highly deformed amphibolites, hornblendites, clinopyroxenites, anorthosites and tonalites. Rare garnet granulites within the Kamila belt were metamorphosed at 600-720 °C and 6-8 kbar (Yamomoto 1993). Tahirkheli (1979b) and Bard et al. (1980) proposed that the Kamila belt represented relict oceanic crust, whilst Coward et al. (1986) suggested that the belt was probably a highly deformed sequence of arc volcanics, possibly equivalent to the weakly deformed Dras volcanics of Ladakh (see below). Subsequent workers have proposed that the amphibolites are, at least partly, the retrograde product of the Chilas-type granulites (Treloar et al. 1990). The southern part of the Kamila belt is a high strain zone which may be a relict suture formed by the southward thrusting of the Kohistan arc over a forearc region (the Jutial complex) (Coward et al. 1987; Treloar et al. 1990).

(iii) To the north, the Kamila belt grades into the Chilas complex (Treloar et al. 1989c). This is a 300 km-long, stratiform cumulate body of gabbros, dunites, norites and harzburgites at granulite-grade, metamorphosed at 750-850 °C and 7-8 kbar (Jan and Howie 1980). The Chilas complex often shows phase banding with slump folds and syn-sedimentation faults, and forms the base of the arc (Bard et al. 1980). The geochemistry of the gabbro-norites suggests a generation by melting of a hornblende-bearing mantle source (Khan et al. 1989). Cooling of both the Kamila belt and Chilas complex occurred through 500 °C at about 80 Ma (Treloar et al. 1989a).

(iv) The Dir and Kalam groups are exposed in western Kohistan. These consist of calc-alkaline volcanics, including andesites, rhyolites, agglomerates and ignimbrite tuffs, interbedded with sediments that contain lower Eocene marine microfossils. The volcanics unconformably overlie some plutons of the calc-alkaline batholith (see below) and have been intruded by others, and thus may be the remnants of an early cover to the batholith (Bard et al. 1980).

(v) Northern Kohistan is dominated by the greenstone complex of Tahirkheli (1979b) (partly the Chalt volcanics of Coward et al. 1982 and Petterson and Windley 1985, 1991), which consists of generally low-grade volcanics with occasional pillows, together with volcaniclastics and metasediments. Tahirkheli (1979b) correlated this group with similar volcanics exposed in the Shigar valley of Baltistan (NW Ladakh), where they are interbedded with limestones containing Cretaceous fossils. Geochemically the volcanics are high-Mg tholeiites and calc-alkaline andesites, thought to have been generated by melting of a depleted mantle source and metasomatised mantle wedge source, respectively (Petterson and Windley 1991). Exposed sporadically along the Northern suture and interbedded with upper volcanics of the greenstone complex, occurs the Yasin group. This is a thin sequence of sediments containing Aptian and Albian fossils, probably deposited in a back-arc environment (Pudsey et al. 1986). There appears to be no equivalent of the Yasin group in Baltistan.

(vi) Intruding the northern part of the Kohistan Arc is a calc-alkaline Batholith, which has been considered by earlier workers to be a continuation of the Trans-Himalayan batholith of Tibet (Petterson and Windley 1985). The early magmatism, related to growth of the island arc, has been dated at 110-90 Ma, and is characterised by a range of deformed plutons of gabbro, diorite and tonalite at greenschist to lower-amphibolite grade (Petterson 1984; Petterson and Windley 1991). Younger, post-kinematic calc-alkaline magmas were intruded at 85-30 Ma, and range from gabbros to leucogranites with a general basic-acid temporal trend. Although Bard (1983) suggested that these magmas were derived by crustal anatexis during intracontinental thrusting, subsequent geochemical studies have demonstrated that

they were generated at an Andean-type continental margin (Petterson and Windley 1985; Debon et al. 1987). Initial Sr isotope compositions for both intrusive phases lie in the range 0.7039-0.7052, whilst $\varepsilon_{Nd}(T)$ lie in the range +6.9 to +2.0. The geochemical and isotope data suggest an origin by both fractionation of mantle-derived melts and melting of juvenile arc material (Petterson and Windley 1991; Petterson et al. 1993; Chapters 6 & 7).

Whereas the stratigraphic thickness of the Kohistan arc is about 30-40 km (Bard et al. 1980), gravity modelling indicates that the arc is now only 8-10 km thick, probably reflecting tectonic removal (Malinconico 1986). The lower part of the Kohistan arc has been affected by two phases of upright folding, attributed to the Eocene continental collision by Windley et al. (1986). However, geochronological work shows that most of the arc deformation pre-dates this collision (Coward et al. 1982, 1986, 1987; Treloar et al. 1989a). The earliest phase of deformation in the lower arc folded the Chilas complex and pre-dated the granulite-facies metamorphism. This phase of deformation probably occurred during early arc formation, or during the closure of the Northern suture. The later phase deformed the whole arc crust on east-west trending folds, and was accompanied by the late Cretaceous granulite-facies metamorphism of the Chilas complex (Coward et al. 1982).

1.6.2. The Ladakh Terrane

The Ladakh region provides a continuation of the island arc and batholith for about 400 km to the southeast of the NPHM (Fig. 1.2). According to Brookfield (1981), the greater proportion of volcanics and molasse in Ladakh compared with Kohistan suggests that higher crustal levels are exposed. Interestingly, remnants of continental crust such as migmatitic gneisses, quartzites, platform carbonates and metapelites are also present (Raz and Honegger 1989), suggesting that Ladakh may represent a transitional region between the Kohistan island arc to the west and the Andean-type margin of the Lhasa block to the east.

The branch of the Indus Tsangpo suture zone (ITSZ) which borders the southern margin of the Ladakh terrane is a structurally complex melange zone with remnants of

glaucophane schist, slices of Mesozoic flysch and basaltic relicts of Jurassic-Cretaceous ocean floor (Frank et al. 1977; Honegger et al. 1982; 1985). The majority of the present tectonic contacts in this zone are north-directed backthrusts (Searle 1986). The preservation of fossiliferous sediments in the suture contrasts with the MMT section where such sediments are absent, possibly due to the relatively high uplift rates in Kohistan (Zeitler et al. 1982). Associated with the flysch are alkaline volcanics interpreted to have been generated at a Triassic rifted continental margin (Honegger et al. 1982). The branch of the ITSZ that borders the northern margin of Ladakh (Shyok suture of previous workers) consists of a steep belt of volcanics, melange and flysch with Upper Cretaceous-Eocene fossils, which cross-cuts amphibolite-grade metamorphic isograds (Hanson 1989). The lithological units are bounded by thrust contacts which often cause tectonic repetition (Srimal 1986).

In southern Ladakh, the Dras volcanics are a belt of deformed island arc tholeiites at zeolite to lower greenschist-grade (Dietrich et al. 1983; Searle 1983). The volcanics are bounded by tectonic contacts, and occur as irregular flows or, more rarely, pillows or dykes. They contain imbricates of ophiolitic melange, intercalated radiolarian cherts and inclusions of Upper Cretaceous orbitulina limestones, suggesting an Upper Jurassic-mid Cretaceous age (Honegger et al. 1982; Dietrich et al. 1983). The Dras volcanics are locally underlain by cumulate olivine gabbros, gabbros, anorthosites and norites. The cumulates have similar geochemical and Sr isotopic compositions to the volcanics, and have been interpreted as representing relict magma chambers (Honegger et al. 1982; Dietrich et al. 1983), possibly comparable to the Chilas complex of Kohistan (Searle 1983). The volcanics pass laterally into shallow water, Upper Cretaceous volcaniclastics, interpreted to represent a back-arc flysch apron (Honegger et al. 1982). Trace element and Sr isotopic compositions for the Dras volcanics suggest a source in the upper mantle with a contribution from subducted oceanic crust (Honegger et al. 1982; Dietrich et al. 1983; Scharer et al. 1984b).

In northern Ladakh, the Ladakh batholith consists of a calc-alkaline suite of diorites, granodiorites and granites forming the Ladakh range (Honegger et al. 1982). Some of the Ladakh plutons have suffered a low-grade metamorphism, whilst others are post-kinematic

(Scharer et al. 1984b; Hanson 1989), a similar situation as that observed in the Kohistan batholith. Locally, plutons intrude and thermally metamorphose parts of the Dras unit, whilst other plutons are transgressed by the Indus molasse which contains an Eocene-Miocene non-marine fauna (Shah et al. 1976). Within the Indus molasse, clasts are present that have been derived from the underlying plutons, suggesting uplift and erosion of the batholith prior to the Eocene (Frank et al. 1977). Clasts of high-k calc-alkaline volcanics are also present within the molasse. These are similar to volcanics occurring in both northern and southern branches of the ITSZ, and may have once formed a cover to the Ladakh plutons (Honegger et al. 1982; Thakur and Misra 1984). Widely-spaced granitoids from the Ladakh batholith have yielded U-Pb zircon and Rb-Sr whole-rock ages in the range 60-100 Ma (Honegger et al. 1982; Scharer et al. 1984b). Mica cooling ages from the Ladakh plutons lie in the range 36-78 Ma (Desio et al. 1964; Saxena and Miller 1972; Brookfield and Reynolds 1981; Honegger et al. 1982), and give only a broad indication of the regional cooling path.

Initial strontium isotopic ratios for the Ladakh plutons are poorly constrained due to strontium isotopic heterogeneities; however, present day ratios for samples characterised by Rb/Sr < 1 lie in the range 0.704-0.707 (Honegger et al. 1982; Scharer et al. 1984b). The isotopic heterogeneities may reflect pulses of magmatism or rapid melting of a heterogeneous source (Honegger et al. 1982; Scharer et al. 1984b). There has been considerable debate over the nature of this source. From Sr and limited Pb isotopic evidence, Honegger et al. (1982) suggested that crustal contamination was insignificant and that large scale melting occurred in the upper mantle with some involvement of oceanic crust. However, the presence of inherited zircons in a granite at Leh (Scharer et al. 1984b), and the lead isotopic compositions of feldspars from two plutons (Gariepy et al. 1985), suggests the involvement of at least some continental material in the genesis of the Ladakh batholith. This conclusion is supported by limited Nd model ages from Ladakh intrusives, which lie in the range 600-800 Ma (Allègre and Ben Othman 1980), and the slight enrichment observed in δO^{18} by Blattner et al. (1983). The crustal isotopic signatures may reflect the subduction of continent-derived sediments during the evolution of the magmatic belt, crustal contamination during

intrusion of magmas in a mature arc, or the presence of ancient continental material in the source region.

1.6.3. The Karakoram Block

The Karakoram is a poorly defined, elevated region lying to the north of the Kohistan-Ladakh belt, extending northwards to the Pamir/Kun Lun, westwards into the Hindu Kush and eastwards into western Tibet (Lhasa block). According to Pudsey et al. (1985), Upper Palaeozoic sediments in the southern Karakoram locally contain Eurasian-type faunas, suggesting that the Karakoram was never a part of Gondwanaland, in contrast to the Lhasa block. However, the Karakoram block has suffered a Tertiary orogenesis, and therefore the geodynamic evolution of the block in Tertiary times is described briefly below.

The central Karakoram is broadly divided into three units, which from south to north are the Karakoram metamorphic complex, the Karakoram batholith occupying the axial region, and the northern Karakoram zone (Desio 1979; Searle and Tirrul 1991). The metamorphic complex to the south of the batholith consists of high-grade rocks which have locally suffered a low pressure metamorphic event (M1) which occurred before 208 Ma (Rex et al. 1988). However, the dominant metamorphism in the metamorphic complex is a high-grade, Barrovian event (M2) with a lower age limit of 37-40 Ma but a poorly constrained upper age limit (Treloar et al. 1989a; Searle and Tirrul 1991). This metamorphism may be related to crustal thickening, either associated with the India-Eurasia collision (Rex et al. 1988; Searle and Tirrul 1991) or with the closure of the Northern suture (Le Fort 1989).

The northern Karakoram zone consists of weakly metamorphosed Palaeozoic to Late Cretaceous platform sediments (Desio 1979; Searle et al. 1986, 1989), which contrast strongly with the generally high-grade rocks of the metamorphic complex, and may be the unmetamorphosed equivalents of these high-grade rocks (Rex et al. 1988).

The Karakoram batholith occurs as a 600 km long, discontinuous belt of plutons and complexes forming the backbone of the Karakoram mountains, and recording magmatism on the southern margin of Eurasia from Jurassic through to the Miocene. Plutons can be broadly divided into early, subduction related plutons that possess penetrative deformation fabrics, and younger, undeformed bodies related to crustal thickening (Reynolds et al. 1983; Debon et al. 1987; Searle et al. 1989). The early plutons include a range of calcalkaline granodiorites and tonalites that have yielded U-Pb zircon and Rb-Sr whole-rock ages in the range 95-120 Ma (Le Fort et al. 1983; Debon et al. 1987; Rex et al. 1988; Searle et al. 1989, 1990; Crawford and Searle 1992). These plutons are often characterised by heterogeneous Sr isotope systematics. Initial Sr-isotope ratios lie in the range 0.7044-0.7146, whilst $\varepsilon_{Nd}(T)$ mostly lie in the range -7.5 to -11.3 (Le Fort et al. 1983; Debon et al. 1987; Crawford and Searle 1992). These isotopic data, together with trace element abundances and evidence for crustal inheritance seen in zircons, led Crawford and Searle (1992) to suggest a petrogenesis involving crustal contamination of mantle-derived melts.

Scattered, undeformed leucogranites intruding the Karakoram batholith and cross-cutting the metamorphic complex, have yielded U-Pb zircon and Rb-Sr whole-rock ages in the range 14-43 Ma (Debon et al. 1987; R. Parrish, *in* Searle and Tirrul 1991). The Baltoro Plutonic Unit (BPU) is a larger suite of monzogranites and leucogranites that have yielded U-Pb zircon ages in the range 21-25 Ma (Parrish and Tirrul 1989; Scharer et al. 1990). Initial strontium isotopic ratios for the BPU lie in the range 0.7070-0.7183, whilst $\varepsilon_{Nd}(T)$ lie in the range -6.6 to -11.0 (Rex et al. 1988; Scharer et al. 1990; Searle et al. 1989, 1992). These isotope systematics, together with both trace element abundances and the presence of inherited components in zircons, suggest a crustal source for the BPU (Rex et al. 1988). The trace element abundances of the BPU indicate the large scale, vapour-absent melting of a crustal source with low Rb/Sr, which may have been enriched in LILE by a mantle derived melt (Rex et al. 1988). Searle et al. (1992) proposed that the source was composed of immature metapelites present in the thickened Karakoram crust. Melting may have been induced by fluids or material derived from a dehydrating mantle wedge being displaced

downwards by crustal thickening, a theory supported by the scattered occurrence of mantle-derived lamprophyres adjacent to the BPU (Crawford and Windley 1990).

Comparison between U-Pb zircon and monazite ages and younger cooling ages suggests that the BPU was intruded into warm country rocks, and stayed at relatively high temperatures for a considerable time (Parrish and Tirrul 1989; Scharer et al. 1990). Initial cooling may have been have inhibited by the downfaulting to the north of a slab of low conductivity sediments, which were subsequently thermally metamorphosed (Rex et al. 1988). Such an extensional stress regime in the upper crust would have also accommodated the rising magma (Searle et al. 1992). To the south of the BPU, field relations are complex, with some evidence for thermal overprinting of the high-grade gneisses by the intrusion of the BPU. Micas from the BPU and from the surrounding metasediments have yielded Miocene K-Ar and Rb-Sr cooling ages (Desio et al. 1964; Searle et al. 1989), and indicate that a rapid acceleration in the cooling rate occurred during the late Miocene. Searle et al. (1989, 1990) related this cooling to uplift controlled by widespread, south-directed thrusting in the southern part of the Karakoram.

1.6.4. Tectonic Evolution of the Kohistan-Ladakh-Karakoram Region

A large number of alternative tectonic models have been proposed for the region, based on a limited amount of geological data. There is general agreement that the Dras volcanics and Kohistan sequence represent late Cretaceous island arc(s) related to the northwards subduction of the Tethyan oceanic crust (Frank et al. 1977; Tahirkheli et al. 1979; Brookfield and Reynolds 1981). Field relations and radiometric dating suggest that this arc evolved into an Andean type continental margin along which a belt of calc-alkaline plutons was emplaced (Honegger et al. 1982; Petterson and Windley 1985).

The Cretaceous-Palaeogene, subduction-related magmatism of the Kohistan-Ladakh batholith is contemporaneous with similar magmatism in the Karakoram dated at about 100 Ma, as shown in Fig. 1.8. The two magmatic belts were probably either generated at a

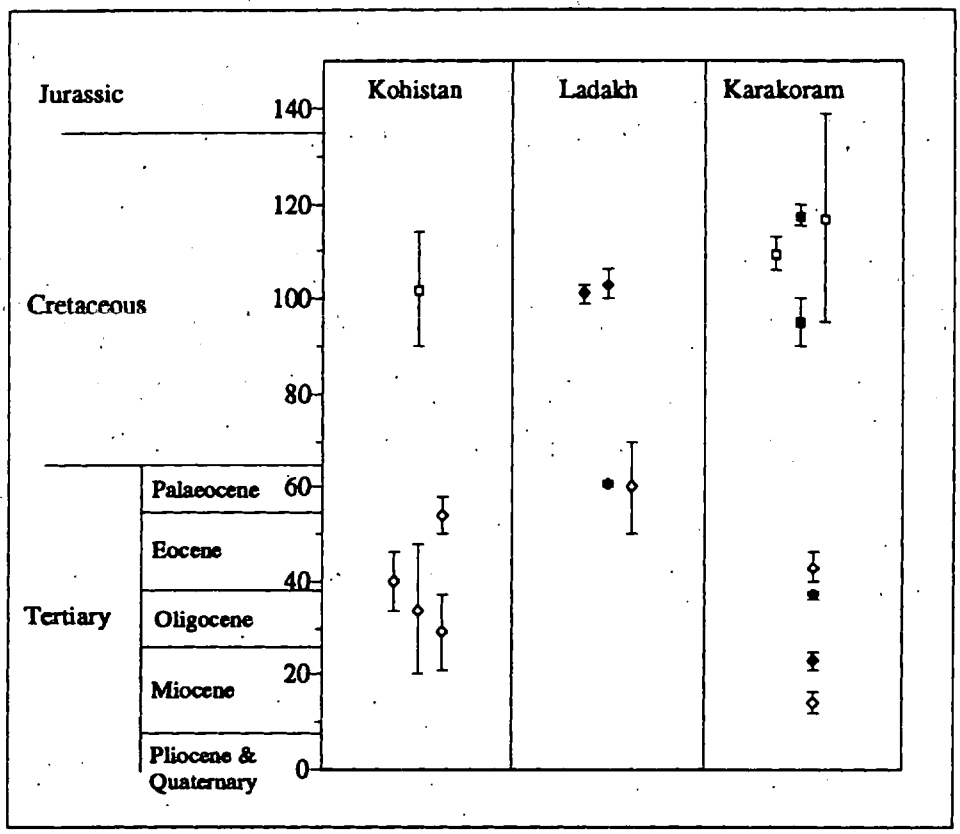

Fig. 1.8. Timing of granitoid magmatism in the Kohistan-Ladakh-Karakoram region. Diamonds = granitoids without penetrative deformation fabrics; squares = granitoids possessing penetrative deformation fabrics. Colourless symbols = Rb-Sr whole-rock ages; black symbols = U-Pb zircon ages. Kohistan data from Petterson and Windley (1985); Ladakh data from Honegger et al. (1982) and Scharer et al. (1984b); Karakoram data from Debon et al. (1987), Parrish and Tirrul (1989), Scharer et al. (1990), R. Parrish, *in* Searle and Tirrul (1991), Searle et al. (1992).

common, northward-directed subduction zone (Jan et al. 1981; Rex et al. 1988), or two separate subduction zones existing along both branches of the ITSZ (Fig. 1.9) (Debon et al. 1987; Crawford and Searle 1992). In either case, the higher initial Sr-isotope ratios observed for the Karakoram plutons than for their Kohistan-Ladakh equivalents indicates a greater contribution of relatively evolved crustal material in the genesis of the former (Debon et al. 1987).

The timing of closure of the suture zones has been controversial. The ITSZ melange is cut by intrusions of the Ladakh batholith, including a syenite which has a hornblende ^{40}Ar-^{39}Ar age of 82 ± 6 Ma (Brookfield and Reynolds 1981), whilst blueschists from the MMT in Kohistan have yielded phengite ^{40}Ar-^{39}Ar ages of 80 ± 5 Ma (Maluski and Matte 1984).

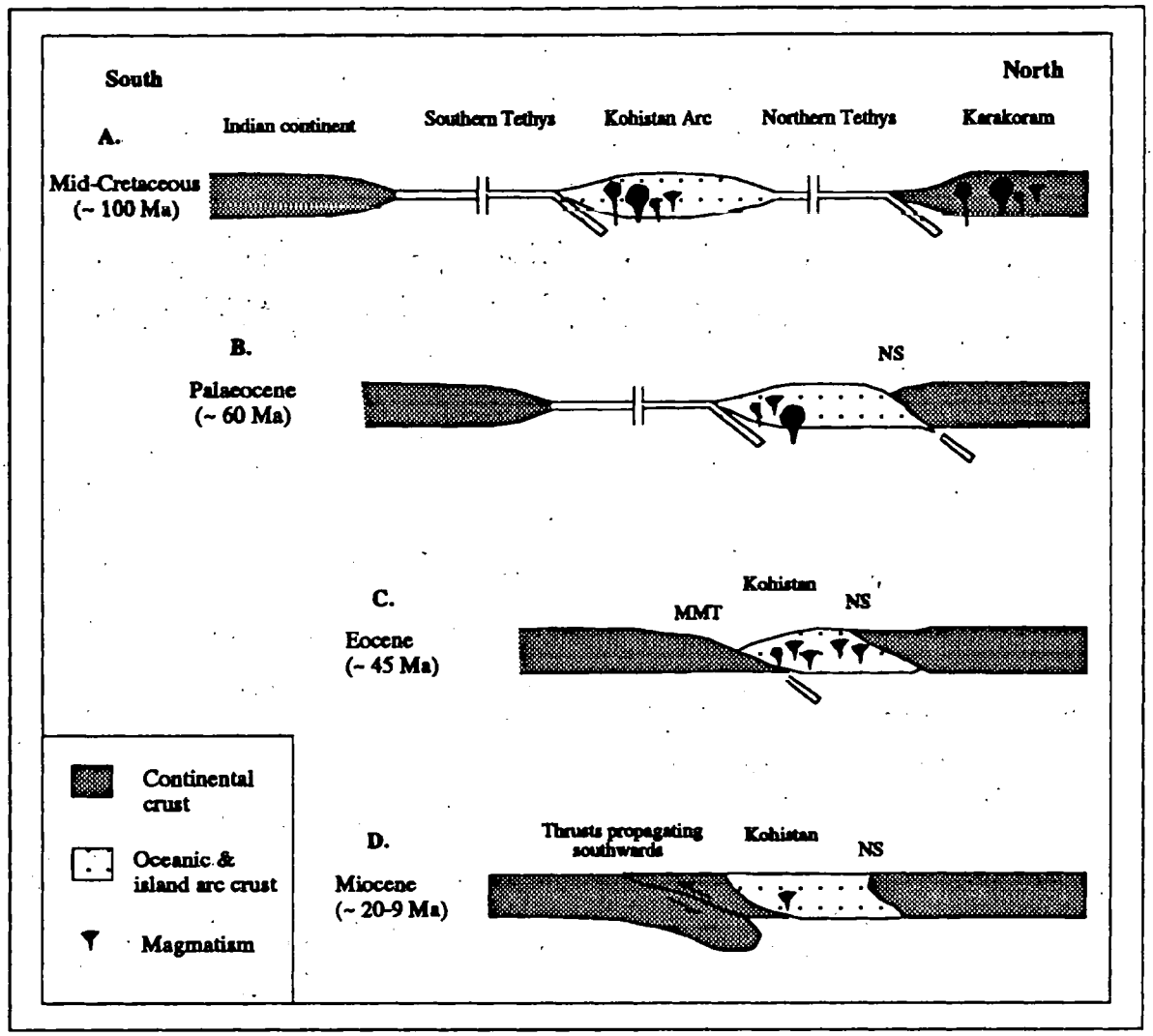

Fig. 1.9. Schematic tectonic evolution of the western Himalayan collision zone, after Debon et al. (1987). MMT = Main Mantle Thrust; NS = Northern suture.

Similarly, the Kamila shear zone suffered major, amphibolite-grade deformation before 80 Ma (Treloar et al. 1989a). These data have been interpreted by some workers as indicating a late Cretaceous time of collision between the arc and the Indian continent (Bard et al. 1980; Brookfield and Reynolds 1981; Bard 1983). However, an age of > 82 Ma for the collision between the Kohistan-Dras arc and India would be inconsistent with a model involving the generation of calc-alkaline plutons at 60 Ma or younger in the Kohistan-Ladakh arc. Brookfield and Reynolds (1981) suggested that the batholith formed on the northern margin of the Indian continental plate, after an earlier collision between India and the arc, and that the magmatism was related to southwards subduction which was terminated by closure of

the Shyok suture. However, Petterson and Windley (1985) and Pudsey et al. (1986) observed plutons of the Kohistan batholith extending to within 1 km of the Northern suture, and clearly post-dating the deformation associated with the suture. Palaeomagnetic studies on the Ladakh intrusives indicate that collision between the Indian continent and the Kohistan-Ladakh arc occurred at about 50 Ma (Klootwijk et al. 1979). Therefore, the consensus of opinion is that the obduction of melange along the ITSZ and deformation within the arc may have been related to earlier subduction processes, or to closure of the Northern suture (Maluski and Matte 1984; Coward et al. 1987; Le Fort 1989; Treloar et al. 1989a).

Many of the differences between the tectonic models proposed by earlier workers were due to uncertainties in the nature and age of the Northern suture in Ladakh (Shyok belt). Frank et al. (1977), Srimal (1986) and Srimal et al. (1987) suggested that this suture closed before the ITSZ, along a subduction zone which generated the I-type granites of the Karakoram. However, the presence of some Eocene and younger intrusives within the Karakoram, together with the discovery of apparently young volcanics (38 Ma) within the suture belt, led other workers to suggest that the Northern suture closed after the ITSZ (Tahirkheli et al. 1979; Rai 1982; Thakur and Misra 1984). A younger age for the Northern suture is at odds with the accepted evolutionary model for Tibet, whereby terranes are successively accreted from the south (Dewey et al. 1988). Furthermore, recent evidence suggests that the younger intrusives in the Karakoram batholith are related to crustal shortening and melting of metasediments, rather than being subduction-related (Searle et al. 1992). Finally, the discovery of oxygen isotopic exchange between the Shyok volcanics and a meteoric or hydrothermal system casts doubt on the K-Ar age (38 Ma) measured by Sharma et al. (1978) for these volcanics (Srimal et al. 1987).

In northern Kohistan, a tonalite deformed by fabrics thought to be associated with the closure of the Northern suture has yielded a whole-rock Rb-Sr age of 102 Ma (Petterson and Windley 1985). Furthermore, basic dykes in the same area that cut fabrics related to the closing of the Northern suture have yielded ^{40}Ar-^{39}Ar hornblende ages in the range 71-82

Ma (Treloar et al. 1989a). These data indicate that the Northern suture closed in the period 102-75 Ma, before the Eocene collision between the Kohistan-Ladakh arc and the Indian continent. The closure of the Northern suture probably caused the deformation of the majority of Cretaceous and Palaeocene intrusives in both the Karakoram and in Kohistan (Petterson and Windley 1985; Le Fort 1989). The 85-40 Ma calc-alkaline intrusives of the Kohistan-Ladakh batholith represent subduction-related magmatism occurring during continued oceanic subduction beneath a welded Karakoram-Island Arc terrane (Petterson and Windley 1985; Debon et al, 1987; Petterson and Windley 1991).

There is a marked absence of both lower crustal rocks and large-scale thrusts along the Northern suture. The consensus of opinion is therefore that the Northern suture represents the relatively passive closure, by either subduction or crustal shortening, of a marginal basin (Brookfield and Reynolds 1981; Thakur and Misra 1984; Coward et al. 1986; Pudsey et al. 1986; Srimal 1986; Hanson 1989). The belt has been widely affected by younger thrusting, possibly related to continued northwards convergence of India in post Eocene times (Srimal 1986; Searle et al. 1986; Hanson 1989).

Chapter 2
Field Relations and Petrography

2.1. Introduction

The aim of this chapter is to describe the field relations and petrographic characteristics of those areas within the Kohistan - NPHM region that have been the subject of detailed study, in order to provide a firm foundation for subsequent chapters. The petrography of many of the metamorphic rocks are described in more detail in Chapter 6, whilst the structures and fabrics associated with the shear zone that borders the western margin of the NPHM are described in detail in Chapter 3. The locations of the various field areas are shown in Fig. 2.1.

A relatively small part of the northern Kohistan Arc has been studied. This area extends from the Nanga Parbat-Haramosh massif westwards as far as the Bagrot valley and southwards as far as Jaglot (see Fig. 2.2; attached). Many of the exposures examined were well-developed road exposures. The region is dominated by a large body of metagabbro (Shuta gabbro of Madin et al. 1989) which has intruded a range of metasediments, volcaniclastics and gneisses. Both the metagabbro and its country rocks are themselves cut by swarms of granite sheets, which represent the youngest phase of magmatism in the Kohistan batholith.

Fieldwork in the NPHM was concentrated along the Indus valley eastwards from Sassi to just beyond Shengus, and in the Darchan, Phuparosh and Iskere valleys to the north of the Indus. Further detailed work was carried out in the Tato valley between Raikhot bridge and Fairy Meadows, and in the Liachar valley. Reconnaissance work was undertaken in the Astor valley, at Rupal and at Tarshing (Fig. 2.1).

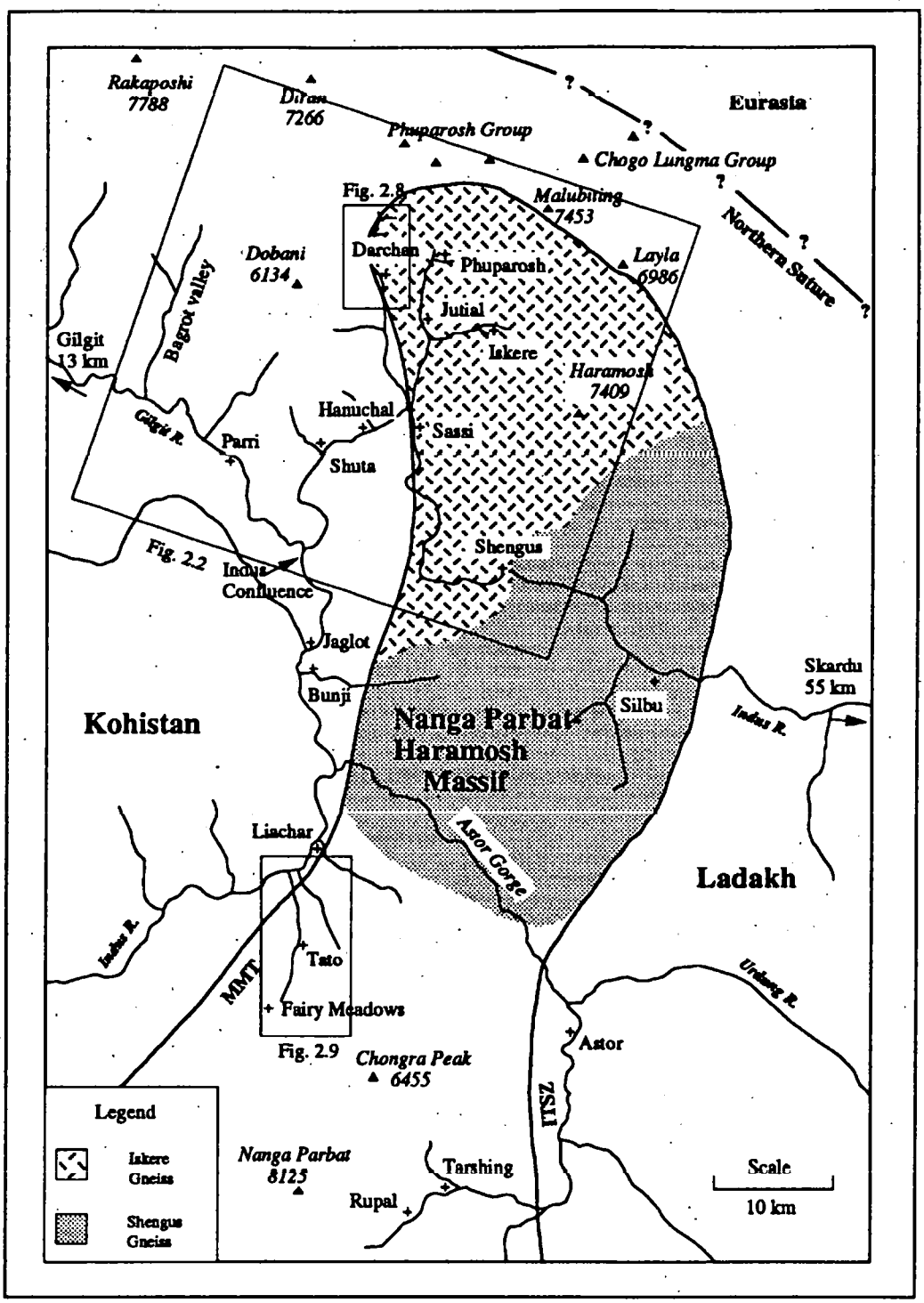

Fig. 2.1. Sketch Map of the Nanga Parbat-Haramosh Massif, showing the locations of further figures, and the distribution of the Iskere and Shengus gneisses (Madin et al. 1989) (other units undifferentiated). MMT = Main Mantle Thrust; ITSZ = Indus Tsangpo suture zone.

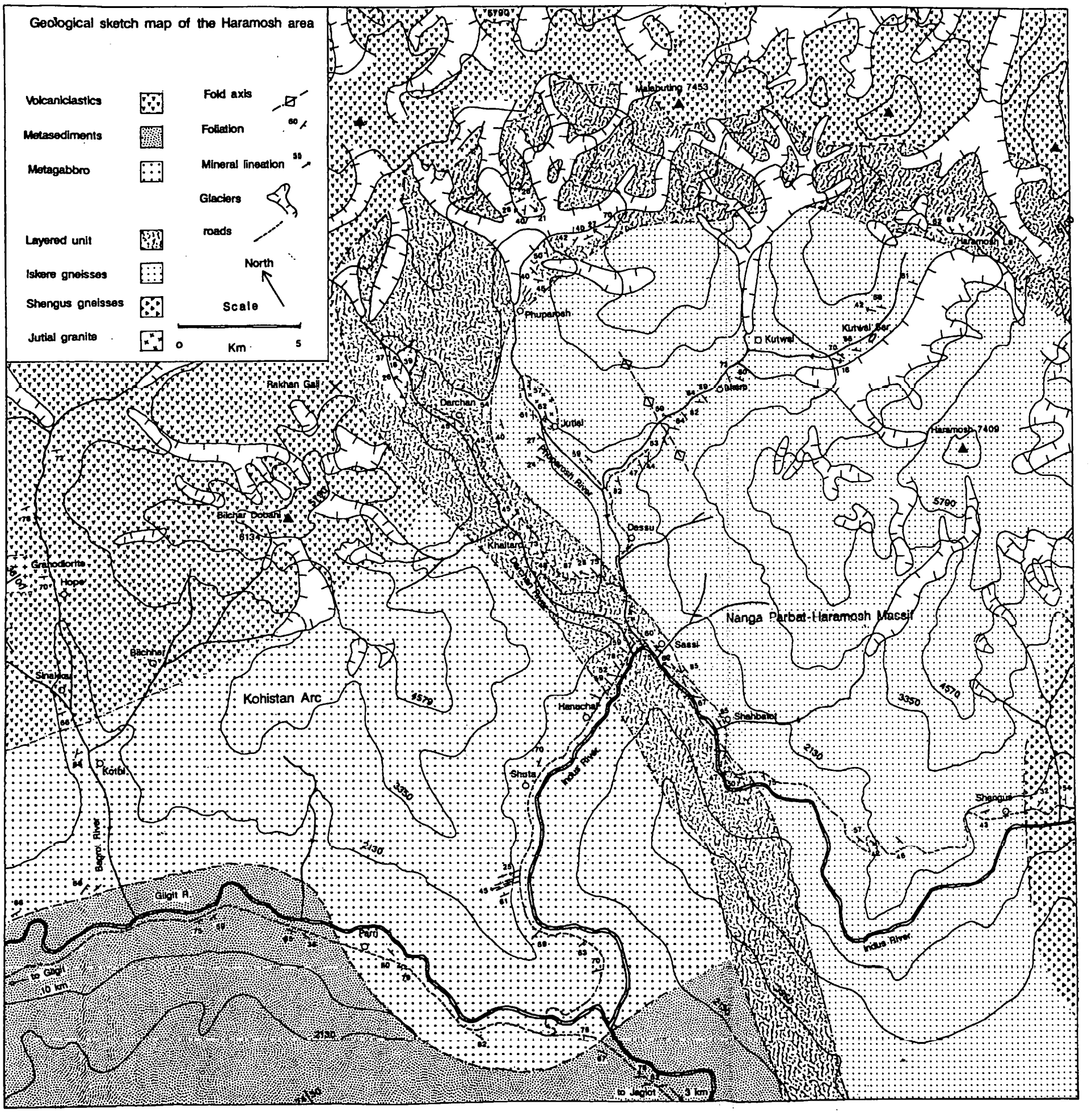

Fig. 2.2. Geological sketch map of the north-western part of the Nanga Parbat-Haramosh Massif, based on mapping by the author in August 1990, and some additional data supplied by R. W. H. Butler (*pers. com.*).

2.2. Field Relations and Petrography in Northern Kohistan

2.2.1. Previous work

Until relatively recently, the geology of northern Kohistan had only been the subject of brief reconnaissance studies. For example, Wadia (1932) suggested that the rocks in the vicinity of the NPHM were the metamorphosed equivalent of the Salkhala sedimentary series of Kashmir, and noted the abundance of epidiorites and basic intrusives in the region. Desio (1974) referred to the latter as the Middle Indus Noritic group. In the light of plate tectonic theory, the Kohistan sequence has been recognised as a relict island arc, separated from the Indian continent rocks by a major fault zone (Tahirkheli et al. 1979). The epidiorites and basic intrusives observed by Wadia (1932) are part of the Kohistan batholith which intrudes the northern part of the Kohistan arc (Petterson and Windley 1985). Petterson (1984) presented a detailed petrographic and geochemical account of the intrusive rocks of the Kohistan batholith in the Gilgit area (Fig. 2.3). Approximately a third of the plutons are part of a deformed, bi-modal suite consisting of gabbros and diorites, and tonalites. These intrusives pre-date the closure of the northern suture at 102-75 Ma (Petterson and Windley 1985). The remaining, second-stage plutons consist of gabbros, tonalites, granodiorites and granites which become progressively more acidic with time, and have not suffered a penetrative deformation. The country rocks to the Kohistan batholith include volcanics, volcaniclastics and metasediments (Petterson 1984), which Tahirkheli et al. (1979) described as a greenstone complex. The volcanic rocks (Chalt volcanics) occur in a strip to the south of the Northern Suture and consist mainly of lavas (some of which are pillowed), together with interbedded pyroclastics at epidote-chlorite grade (Petterson and Windley 1991). The metasedimentary rocks exposed in the region have not been mapped or studied in any detail by previous workers.

2.2.2. Metasediments and Volcaniclastics

In the Bagrot and Gilgit valleys, the metasediments and volcaniclastics dip steeply to

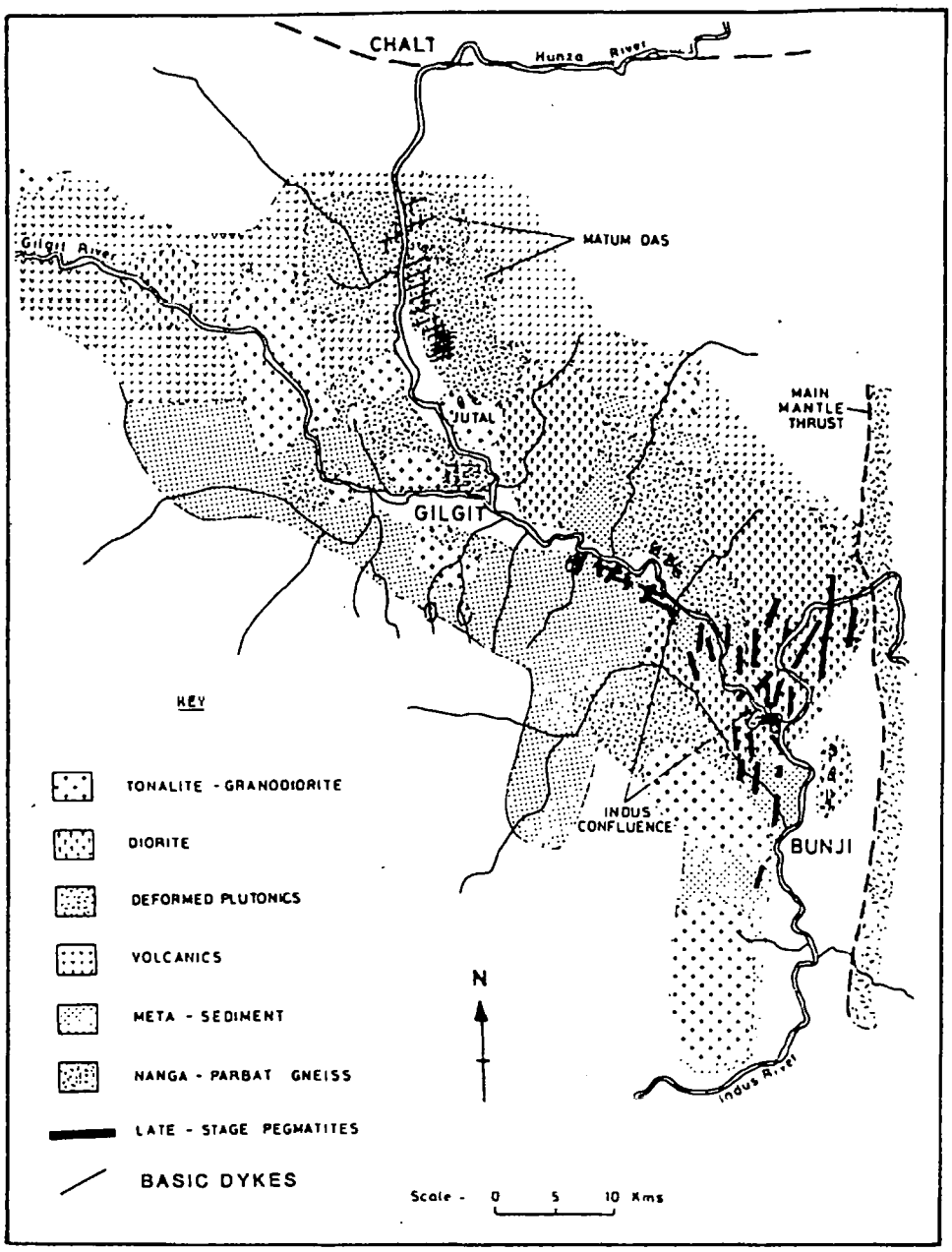

Fig. 2.3. The Kohistan batholith in the Gilgit area (Petterson 1984).

the south. Metasediments exposed 2 km north of Jaglot and between 4 and 11 km south of Jaglot dip steeply to the north (Fig. 2.2; Ahmed et al. 1977). This structural divergence has been termed the Jaglot syncline (Coward et al. 1982) (see Chapter 1).

The rocks exposed in the upper Bagrot valley consist of a uniform sequence of well-foliated, green-coloured and low-grade volcaniclastics. Great thicknesses of these upper-arc volcaniclastic rocks make up the head-wall of the Bagrot valley, continuing northwards towards Diran peak (Fig. 2.1). About 12 km to the east-northeast, similar metavolcanics lie

in the hanging-wall to the NPHM, at high and inaccessible levels in the head-walls of the Darchan and Phuparosh valleys (section 2.3.2). However, the along-strike continuity of the unit is uncertain.

In the upper Bagrot valley, the volcaniclastics are composed of fine grained chlorite (55 %), quartz (40 %) and opaque oxides (5 %). In the central Bagrot valley, the metavolcanics assume a darker colour and more massive character due to the presence of hornblende. In the village of Sinakkar (Fig. 2.2), the volcaniclastics are interbedded with muscovitic metasediments. Exposed in the western wall of the Bagrot valley is a large, undeformed granodiorite pluton which sharply cross-cuts metavolcanic wallrocks. This pluton contains streaky basic xenoliths and is characterised by the assemblage hornblende (15 %), plagioclase (15 %), altered k-feldspar (35 %), quartz (25 %), epidote (5 %) and secondary actinolite (3 %). The granodiorite was mapped by Petterson (1984), who considered the pluton to have been generated during the second intrusive stage of the Kohistan batholith.

The metasediments exposed in the Gilgit valley are dominantly medium-grained metagreywackes or semi-pelites at lower-amphibolite grade. In thin section, the metasediments contain the assemblage garnet (5-7 %), muscovite (6-20 %), biotite (25-40 %), plagioclase (An_{40-55}) (15-40 %), quartz (20-25 %), zoisite (1-3 %), opaque oxides (1-2 %) and accessory apatite (Plate 2.1). Petterson (1984) has observed rare staurolite in semi-pelites present in the Gilgit area. Garnet porphyroblasts are rounded, corroded and up to 2 mm in diameter. The garnets contain inclusions of sillimanite, quartz, zoisite, biotite and muscovite, and exhibit strong compositional zoning (see Chapter 4). The micas define a coarse foliation which is cut by rare blades of coarse, secondary muscovite. The samples are generally fresh and show few signs of post-metamorphic deformation, although some samples show slight cataclastic shearing around garnet porphyroblasts.

Pale, homogenous biotite gneisses outcrop sporadically in the Indus confluence area, and may represent granitoids of the Kohistan batholith that predate the closure of the

Northern Suture. Other metasedimentary lithologies in the region include amphibolites, marbles, slates, phyllites and calcsilicates, whilst migmatitic gneisses occur to the west of Gilgit (Petterson 1984; Ahmed et al. 1977). Petterson (1984) observed well-developed graded-bedding in some metasedimentary sequences.

2.2.3. Shuta Gabbro and included Metasediments

Occupying a large area to the north of the Indus Confluence (Fig. 2.2), the Shuta gabbro (Madin et al. 1989) is a medium to coarse grained, granular textured metagabbro or metadiorite. The intrusion lacks a penetrative deformation fabric but locally has been extensively sheared, for example in the lower Darchan valley. Late granite sheets that cross-cut the gabbro have been dated at 26-50 Ma (Chapter 7), giving a lower limit on the time of magma emplacement.

The Shuta gabbro has suffered a strongly retrogressive metamorphism, and there is little remaining evidence of the primary mineralogy. The typical assemblage consists of green-brown pleochroic hornblende (30-40 %), plagioclase (30-45 %), strongly zoned, often euhedral epidote (5-10 %), biotite (10-20 %), sphene (1-8 %) and interstitial quartz (2-5 %) with rare opaque oxides and apatite. The hornblende is poorly-shaped and sieved with inclusions of quartz and epidote. Similarly, large poikiloblastic epidote crystals up to 2 mm across enclose both biotite and hornblende, whilst plagioclase porphyroblasts sometimes enclose clusters of epidote inclusions. Petterson (1984) observed relict clinopyroxene cores in many hornblende crystals, and suggested that during crystallisation of the melt, hornblende replaced clinopyroxene as the major fractionating phase. The epidote was considered to be a retrogressive phase. However, the presence of epidote inclusions within hornblende, and the poor shape of the hornblende crystals, suggests that the hornblende-epidote-plagioclase assemblage is a reflection of sub-solidus growth and recrystallisation of the gabbro.

Large masses of coarse, dark-coloured hornblendite bodies, 700-800 metres across,

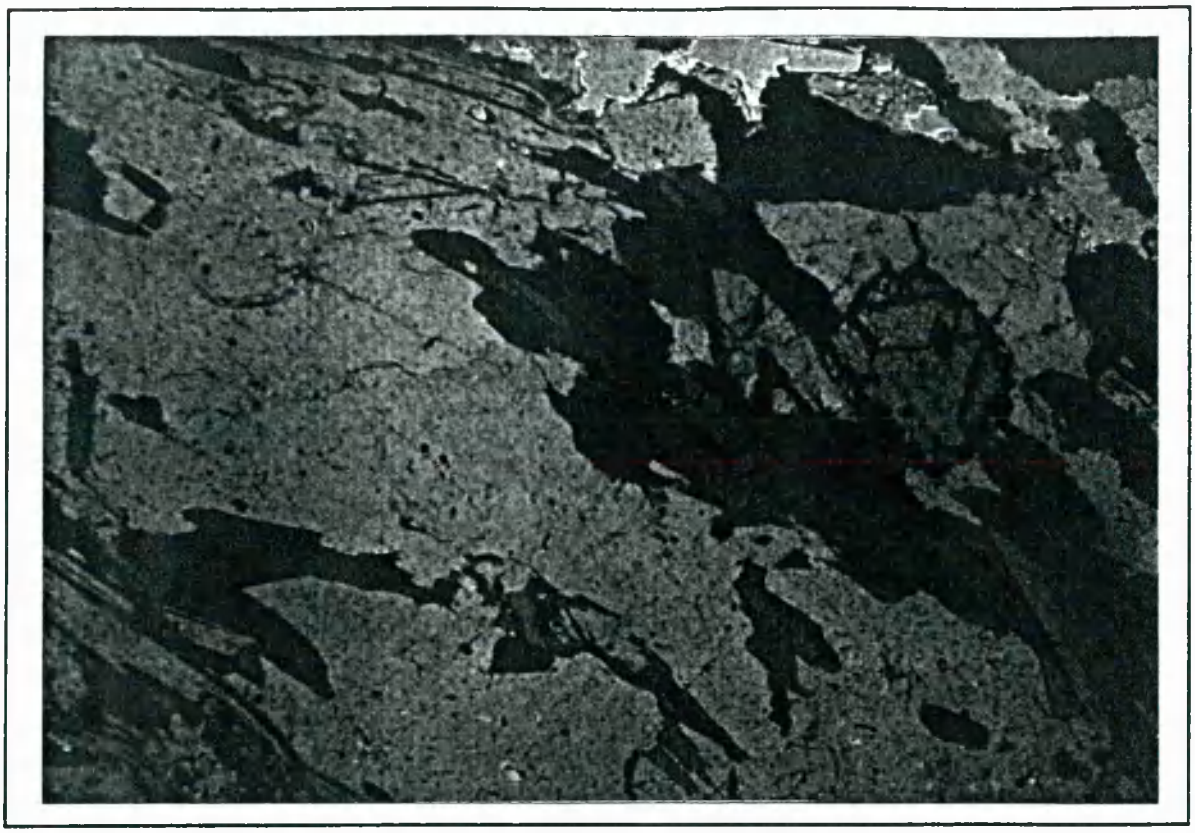

A

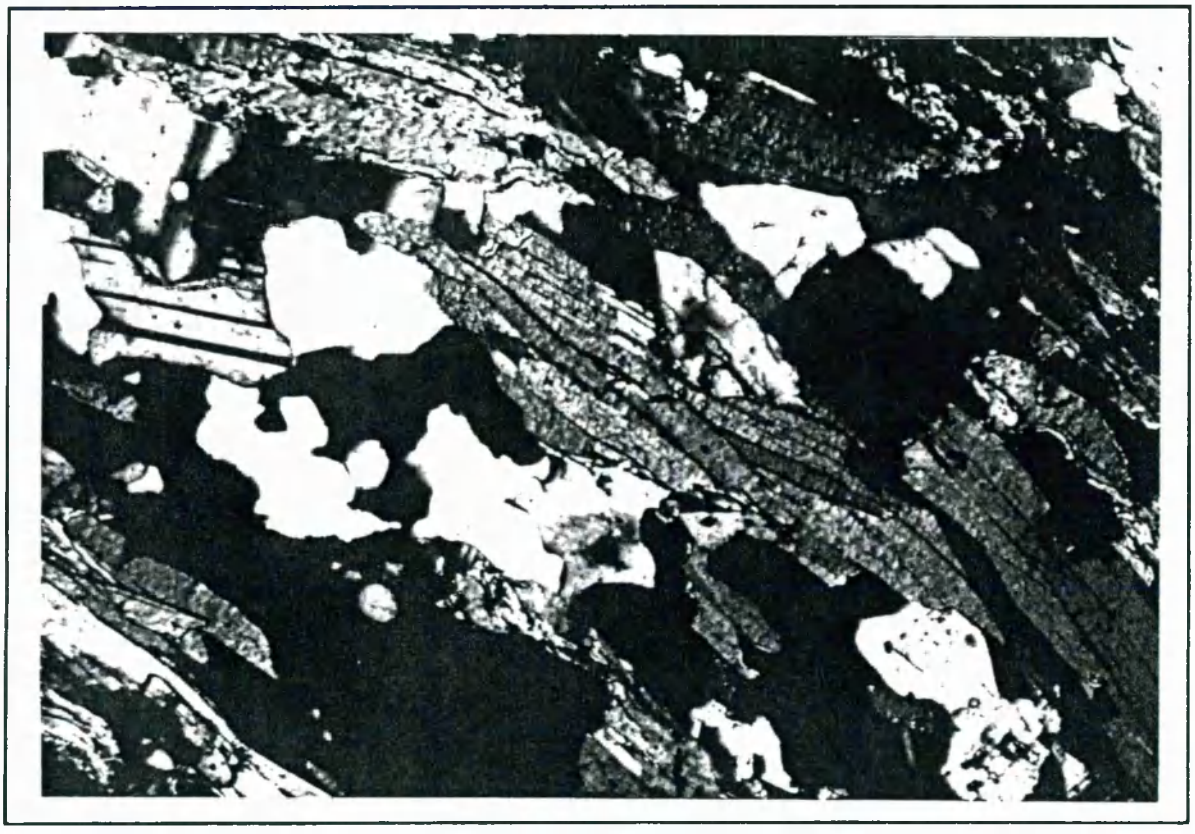

B

Plate 2.1. Photomicrographs of metasediment (sample G7) from Kohistan, collected from near the Indus confluence. **A** = PPL; **B** = XPL. Note the coarse foliation defined by muscovite and biotite. Plagioclase, quartz, garnet and zoisite are also visible. The zoisite occurs as high-relief, strongly-zoned grains that display anomalous blue interference colours.

A

B

Plate 2.2. Photomicrographs of metasediment (sample G20) from Kohistan, collected from a roof pendant enclosed by the Shuta gabbro. **A** = PPL; **B** = XPL. Biotite, plagioclase; quartz; garnet (gt) and epidote (ep) are all visible; hornblende also occurs in this sample. The garnet occurs as large corroded porphyroblasts containing inclusions of plagioclase (pl) and quartz.

occur within the Shuta gabbro (visible in Plates 2.3A & B). The hornblendite is dominantly composed of secondary hornblende replacing clinopyroxene (90-95 %), epidote (5-10 %), rare biotite (1-2 %) and interstitial quartz and plagioclase (3-4 %). Although no hornblendite-metagabbro contacts were accessible for examination, the hornblendite bodies are probably relict pods of cumulate pyroxenite, as suggested by Petterson (1984).

A 300-400 metre-thick wedge of well-foliated psammites, basic-schists and amphibolites occurs within the Shuta gabbro approximately 6 km north of the Indus confluence. Smaller rafts of metasediments have been observed in other parts of the metagabbro. The margins of the metasedimentary rafts, and their internal foliation planes, are orientated parallel to the weak fabric present in the metagabbro. The lithologies may be equivalent to the rocks bordering the western margin of the NPHM at Sassi (section 2.3.1). The presence of well-foliated metasediments coincides with a more marked foliation and presence of boudinage within the adjacent metagabbro. This observation may reflect the partitioning of deformation into those parts of the metagabbro that are characterised by a high proportion of relatively ductile metasedimentary inclusions. Although the age of this deformation is unknown, apparently at least some of the deformation suffered by the metasediments post-dates the intrusion of the gabbro. Both metagabbro and metasediments are cross-cut by the late granite sheets (section 2.2.4).

Structural data from the metasediments are plotted on a stereonet shown in Fig. 2.4. The foliation is steeply inclined and strikes east-northeast, in marked contrast to the orientation of the steep shear zone fabrics present at Sassi, which strike north-south. Tight microfolds are locally present, with fold axes plunging at 60-75° towards the north-east, whilst rare amphibole stretching lineations plunge moderately towards the south-west. However, the sparsity of consistent structural observations precludes firm conclusions on the kinematic origin of these fabrics from being drawn.

The basic-schists are composed of green, poikiloblastic and porphyroblastic hornblende (5-10 %), garnet (1-5 %), plagioclase (An_{40-60}) (35-50 %), biotite (20-45 %),

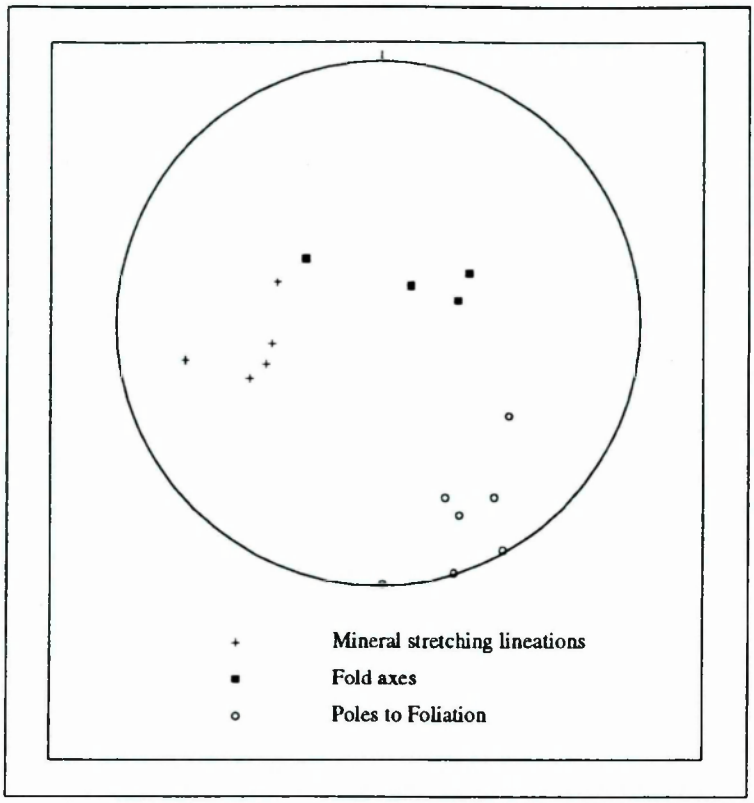

Fig. 2.4. Schmidt equal area projection of structural data from mafic-schists within the Shuta gabbro, Shuta.

quartz (10-15 %) and either epidote or zoisite (5-10 %), together with rare sphene and opaque oxides (Plate 2.2). The garnet occurs as colourless or pale-pink, corroded porphyroblasts up to 3 mm across, containing inclusions of quartz, hornblende, biotite and occasionally plagioclase. Epidote (or zoisite), hornblende and biotite grains are all intergrown, as was observed in the metagabbro. The foliation is defined by elongate hornblende crystals and platy biotite. Some samples contain large plagioclase (up to 5 mm) and epidote (up to 2 mm) porphyroblasts, around which there has been some cataclastic shearing. Slight deformation is also witnessed in kinked plagioclase twin lamellae.

2.2.4. Granite Sheets

Swarms of granite sheets intrude the eastern part of the Kohistan arc, locally giving the mountains in the region a spectacular striped appearance, as illustrated in Plate 2.3. Around the Indus confluence, the granites make up to 30 % of mountain exposure. The

approximate exposure limit of late granite sheets in the Gilgit valley area is shown in Fig. 2.5. Some of those sheets closer to Gilgit are probably genetically related to the large granitoid plutons mapped by Petterson and Windley (1985). However, all of the samples studied in this work were collected from exposures centred on the Indus confluence area, where no obvious parental granitoid is currently exposed. On the basis of mineralogy and geochemistry, Petterson and Windley (1985) divided the granites into the 'Indus Confluence Acid Sheets' and the 'Parri Acid Sheets', the former having biotite as the dominant mica, whereas for Parri granites muscovite predominates.

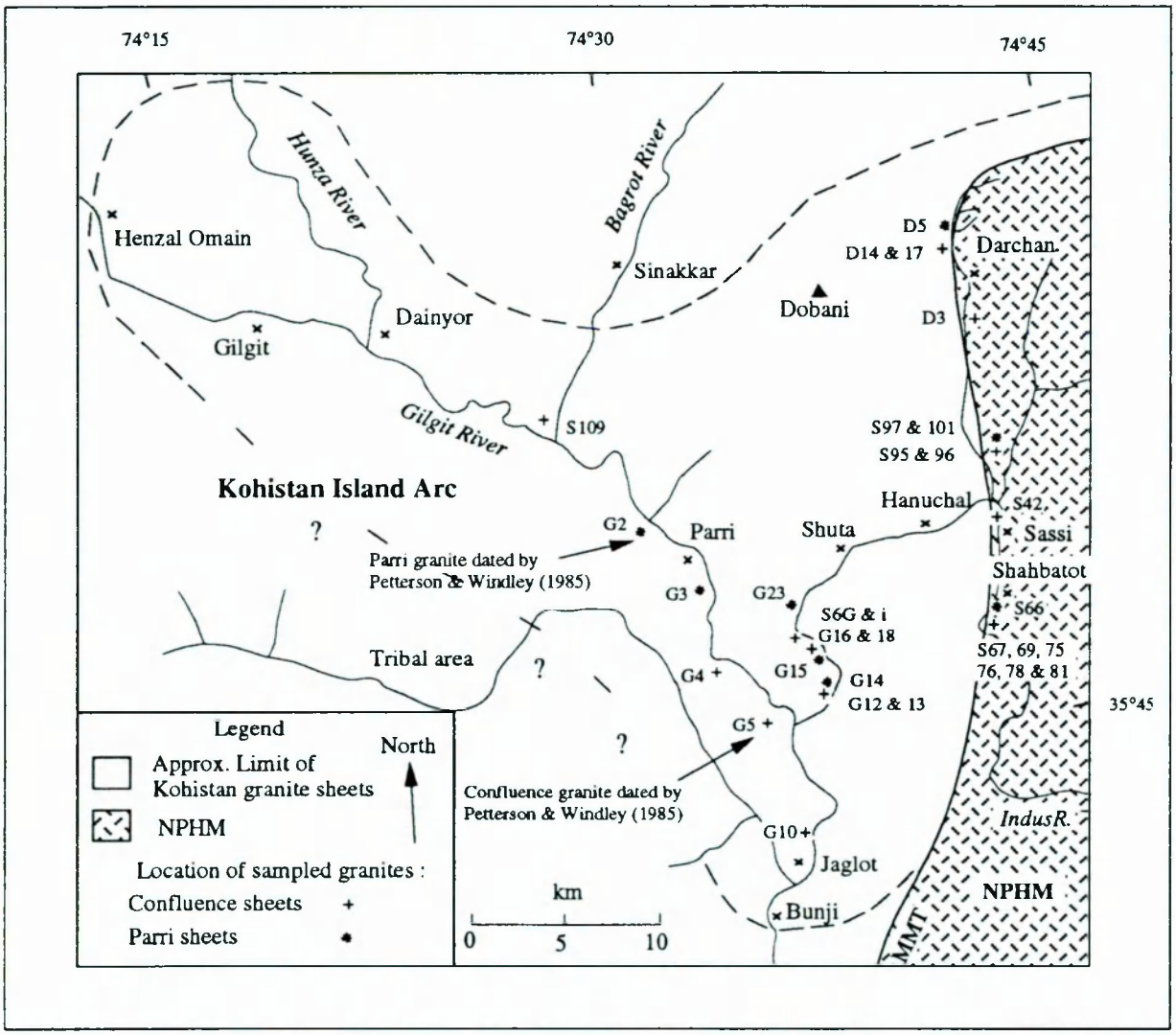

Fig. 2.5. Map showing the distribution of late granite sheets in northern Kohistan, together with the localities of those granites that have been sampled for XRF analysis (see Chapter 6). Five other Parri granite sheets were sampled near Sassi but are not shown. MMT = Main Mantle Thrust; NPHM = Nanga Parbat-Haramosh Massif. Granites collected from localities adjacent to the NPHM lie within the layered unit (not shown) and are deformed to varying degrees (see text for details).

2.2.4.1. The Confluence Granites

Undeformed Confluence granites intrude metasediments, biotite gneisses and metagabbro of the Kohistan arc, and were examined and sampled in the Indus valley between Jaglot and Shuta (Fig. 2.2). Further sheets were studied in the lower Bagrot valley. Confluence granites are generally medium-grained, biotite or muscovite-biotite granites that constitute about 60 % of the granite exposure in the study area. The Confluence granites usually occur as sheets between one and five metres thick (occasionally reaching 25 metres), that are traceable along strike for 10's-100's metres. However, in the Indus confluence area the Confluence granites locally occur as relatively homogenous, 200-metre wide plugs, as shown in Plate 2.4. Intrusive relations are complex, but in detail the plugs appear to have been generated by the coalescence of numerous thick sheets with varying orientations. The margins of the original sheets are often indistinct, reflecting homogenisation of separate magma batches during emplacement. Hutton (1992) has described multiple sheeting contributing to granite plutonism on a much larger scale (20-30 km), which is often associated with regional-scale shearing.

The Confluence granites have variable orientations, and individual sheets are often sinuous and branching. However, in general the Confluence sheets dip moderately to the north-west, as illustrated in Fig. 2.6A. In some areas, the Confluence sheets occur in dense swarms. For example, at the lower end of the Bagrot valley, a swarm of parallel Confluence sheets, each up to 7 metres thick, are separated by 1-5 metre thick strips of country rock. Two kilometres to the north of Jaglot, another swarm of steeply inclined Confluence granites occurs, intruding metasediments and biotite gneisses. Granite sheets that intrude the metagabbro often have a slightly different orientation to those sheets that intrude the metasediments and gneisses, suggesting that the thermal, structural and lithological characteristics of the country rocks exerted a strong control on the orientation of the granite sheets. For example, compared with the well-foliated metasedimentary lithologies, the Shuta metagabbro is probably to be relatively isotropic and structurally flawless. Those Confluence granites that intrude the Shuta gabbro may therefore be equivalent to Andersonian bodies

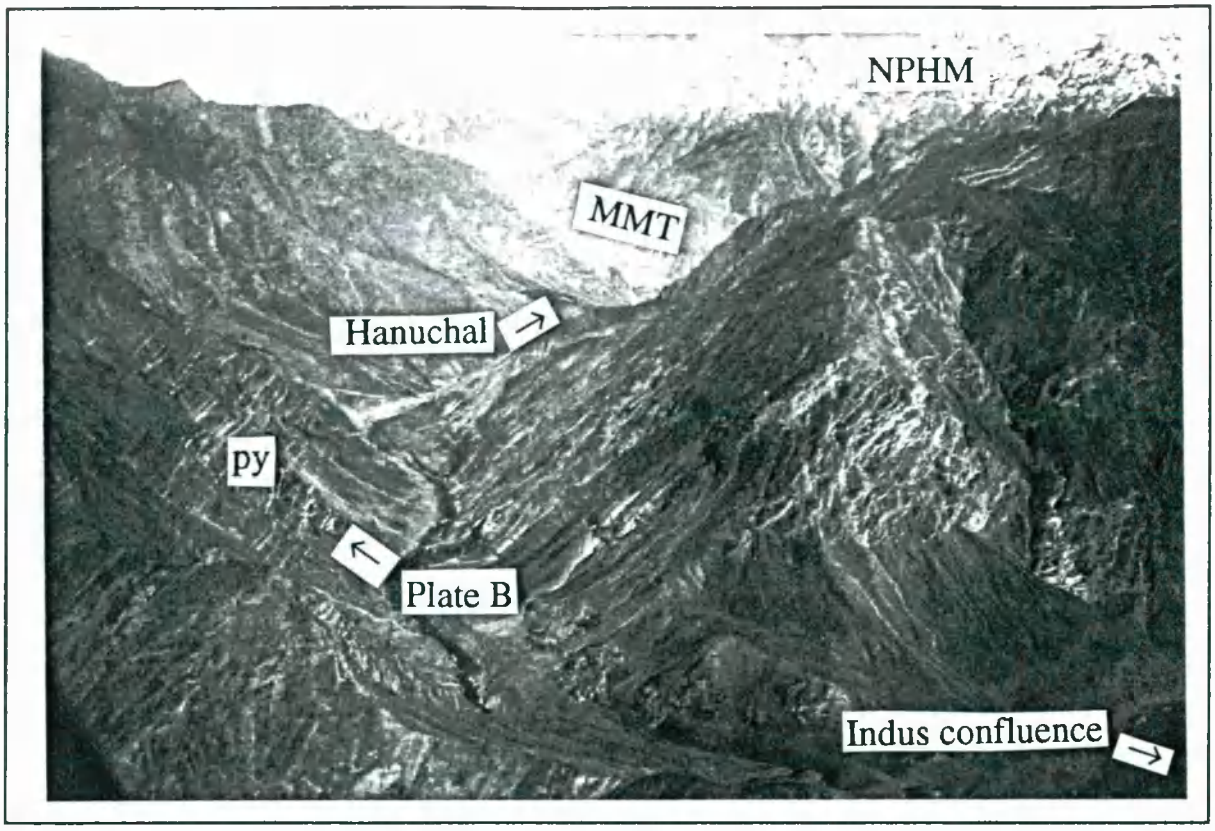

A

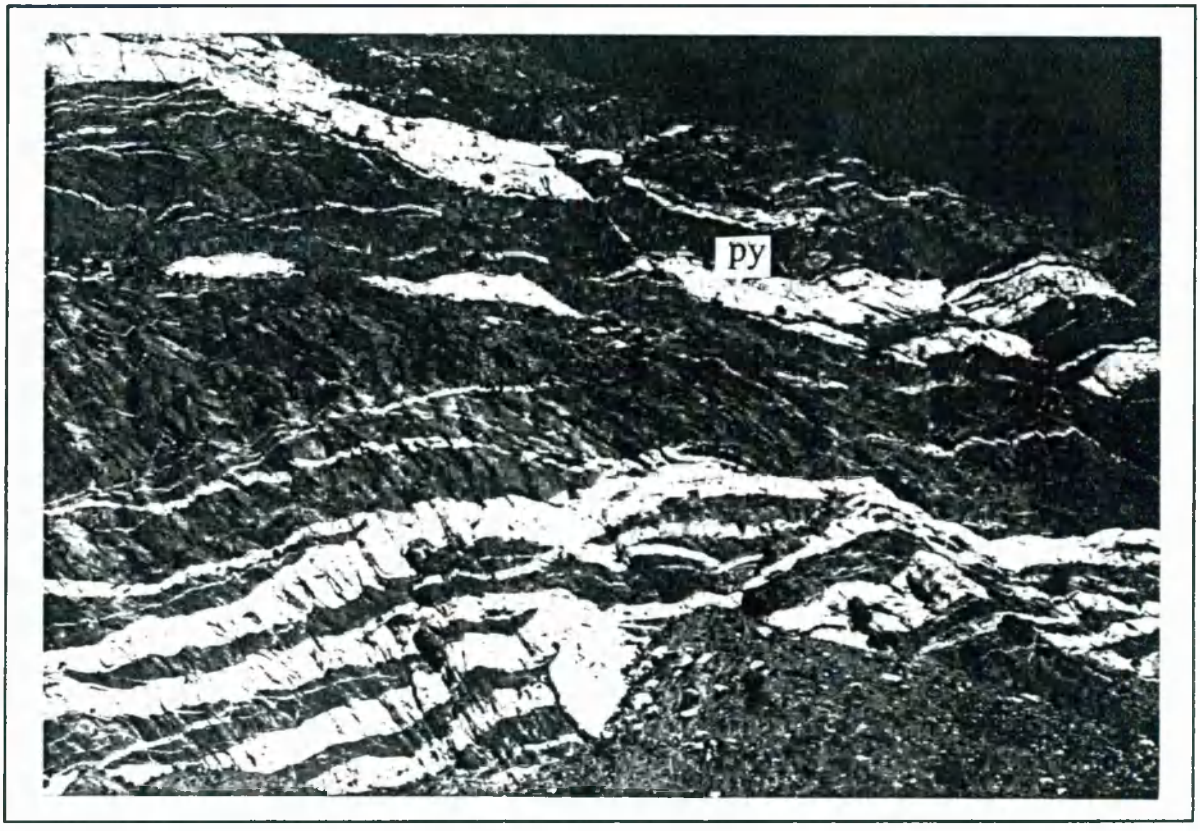

B

Plate 2.3. Confluence and Parri granites intruding the Shuta gabbro of the Kohistan batholith, Indus confluence area. **A** = Aerial view looking north-east along the Indus valley towards the Haramosh range (NPHM). MMT = Main Mantle Thrust; py = pyroxenite body. **B** = Closer view of 1-20 metre thick granite sheets intruding 1500 metre high cliff of metagabbro & pyroxenite.

Plate 2.4. 200-metre high plug of Confluence granite with radiating sheets, intruding and entraining metagabbro (Shuta gabbro of Madin et al. 1989); Indus confluence, Kohistan.

Plate 2.5. Abrupt magmatic layering in a 1.5-metre thick, composite Confluence granite sheet. The granite intrudes massive metagabbro, which is also present as angular xenoliths within the sheet. Shuta, Kohistan.

Plate 2.6. (right) Magmatic layering in a Confluence granite sheet, Indus Confluence. Sample G16 was collected from the relatively leucocratic portion; sample G18 was collected from the relatively biotite-rich portion : these two samples lie at opposite ends of the geochemical fractionation trends (see chapter 6).

Plate 2.7. (below) Photomicrograph of an undeformed Confluence granite (G13) (XPL). Plagioclase, k-feldspar, quartz, biotite and epidote are all visible; the epidote occurs as both a matrix phase and as inclusions in the biotite.

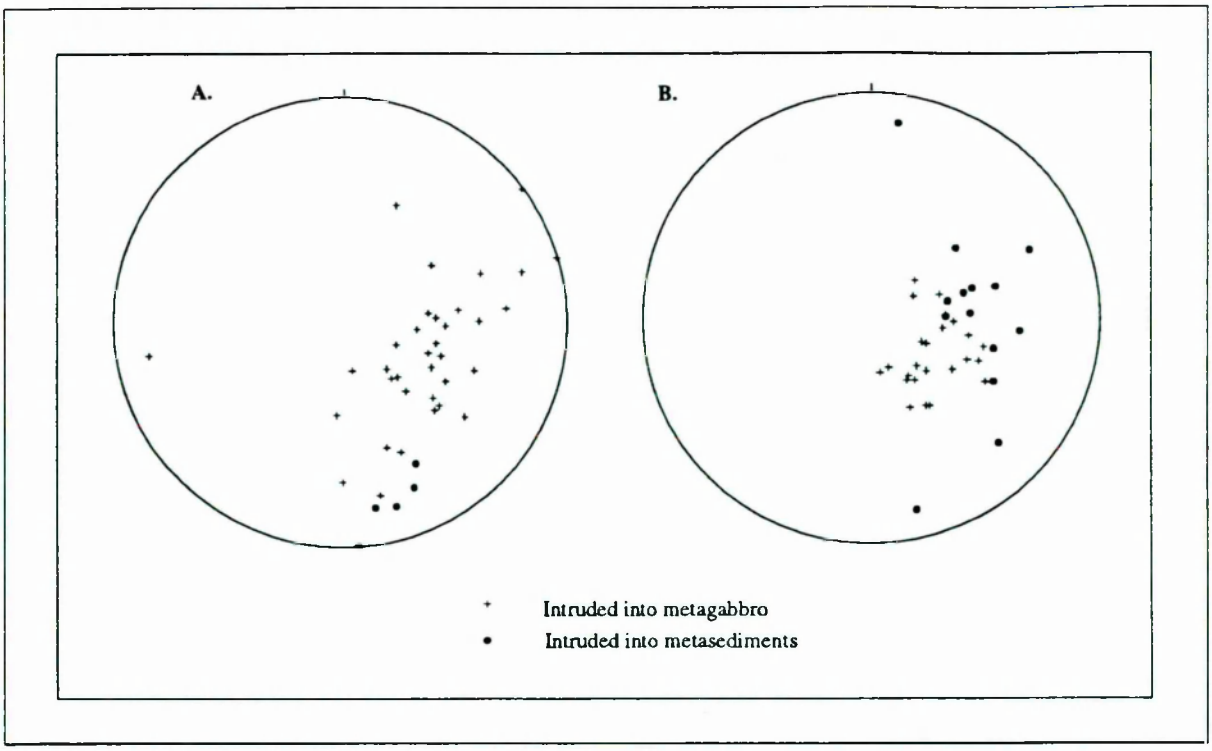

Fig. 2.6. Schmidt equal area projection for the orientations of Kohistan granite sheets (poles to sheet margins). **A**. Confluence granites; **B**. Parri granites.

(Anderson 1951), which are dyke intrusions that align themselves perpendicular to the minimum compressive stress. In contrast, the orientation of the granite sheets that were intruded into the metasedimentary lithologies were probably controlled mostly by local structural heterogeneities. The presence of geographically-distinct swarms of granite sheets with different orientations may reflect the emplacement of magma in a series of pulses, perhaps over an extended time period.

Blocks of country rock enclosed within the Confluence granites are common. In the larger sheets, the orientation of the foliation within the blocks demonstrates that they have been rotated, whereas in the smaller sheets, the magma usually appears to have been intruded more passively and xenoliths have not been rotated. Magmatic banding and layering is sometimes spectacularly developed and sharply defined, and reflects the intrusion of discrete pulses of magma of varying composition (Plates 2.5 and 2.6). Layers of coarse muscovite are sometimes preferentially developed near the margins of Confluence sheets, and chilled margins are absent. The intrusive contacts between Confluence granites and

country rocks are abrupt, and no contact metamorphic effects have been observed.

The undeformed Confluence granites are petrographically fresh and unaltered. The mineral assemblage consists of quartz (25-50 %), plagioclase (10-30 %), alkali feldspar (20-40 %), biotite (2-20 %), ± muscovite (< 5 %), ± epidote or zoisite (1-8 %). The epidote is present both as a groundmass phase, and as an inclusion phase within the biotite. Myrmekitic textures are common. Accessory minerals include apatite, magnetite and occasionally sphene, with rare garnet and zircon (Plate 2.7).

2.2.4.2. The Parri Granites

Parri granites which have not been affected by movements spatially related to the NPHM occur sporadically along the Gilgit and Indus valleys as shown in Fig. 2.5. Prior to this study, the Parri granites had only been studied at one locality, in the Gilgit valley, 2 km west of Parri village (Petterson 1984). Seventeen sheets have been sampled in the current study. The Parri intrusions generally occur as cross-cutting, 1-2 metre thick sheets, although occasionally they reach thicknesses of up to 20 metres. The Parri granites sometimes occur in swarms of parallel-sided sheets, and in general the sheets dip moderately towards the south-west, west or north-west, as shown in Fig. 2.6B. In detail, sheet orientations are variable and probably dependent on a wide range of factors, as discussed above for the Confluence granites.

The Parri granites are pale coloured due to their relatively low content of ferromagnesian minerals, however in this work they will not be termed 'leucogranites', in order to avoid confusion with those granites intruding the NPHM. The diagnostic mineralogy includes muscovite and usually garnet, with or without subsidiary biotite. The granites are often markedly heterogeneous, and grain sizes vary from medium to very coarse, even within individual sheets. Magmatic flow banding and layering often occurs, with alternating layers defined by slightly differing mineralogical compositions or grain sizes. Lozenge-shaped xenoliths of country-rock are frequently present, and are sometimes composed of Confluence-type biotite granite.

In thin section, the Parri granites have a fresh, granular texture, and signs of alteration or deformation are absent. The granites are characterised by quartz (20-50 %), plagioclase (10-30 %), alkali feldspar (20-50 %), muscovite (6-20 %), ± biotite (1-4 %) ± garnet (1-4 %), with subordinate contents of accessory phases such as apatite. The garnet occurs as small, euhedral and colourless crystals, although larger crystals up to 1 cm across have also been observed. As shown in Table 2.1, the garnet contains a relatively high spessartine component (Alm_{61-62} $Py_{2-2.5}$ $Gr_{5.7-6.5}$ Sp_{29-30}), which is indicative of an igneous paragenesis (Green 1977; Harris et al. 1992).

	Undeformed Parri		Deformed Parri			Deformed Parri			Leucogranite sheet	
Sample	G2	G2	G30	G30	G30	G43	G43	G43	I11	I11
Analysis	FGC	FGD	MGA	MGB	MGC	HGE	HGF	HGG	IGD	IGE
Location	Core	Rim	Core	Middle	Rim	Core	Middle	Rim	Core	Rim
SiO_2	37.41	37.64	38.78	38.67	38.65	38.99	38.54	38.67	37.06	37.26
TiO_2	0.12	0.07	0.02	0.02	0.02	0.02	0.02	0.02	0.05	0.05
Al_2O_3	21.05	21.11	21.69	21.58	21.72	21.8	21.68	21.6	20.88	20.87
FeO	26.53	27.47	33.59	34.23	34.66	34.7	34.83	34.26	26.64	29.92
MnO	13.22	12.47	0.78	0.84	0.98	1.05	1.41	1.15	16.36	12.42
MgO	0.59	0.56	5.65	5.28	4.94	4.92	3.07	3.76	0.37	0.58
CaO	2.09	2.26	0.95	1.01	1.3	1.17	2.96	2.72	0.37	0.38
Total	**101.0**	**101.6**	**101.5**	**101.6**	**102.3**	**102.7**	**102.5**	**102.2**	**101.7**	**101.5**
Si	3.018	3.021	3.019	3.017	3.006	3.018	3.013	3.019	3.001	3.015
Ti	0.007	0.004	0.001	0.001	0.001	0.001	0.001	0.001	0.003	0.003
Al	2.002	1.997	1.990	1.984	1.991	1.989	1.997	1.988	1.993	1.990
Fe	1.790	1.844	2.187	2.234	2.254	2.246	2.277	2.237	1.804	2.025
Mn	0.904	0.848	0.052	0.056	0.064	0.069	0.094	0.076	1.122	0.851
Mg	0.072	0.067	0.656	0.614	0.573	0.568	0.358	0.437	0.045	0.070
Ca	0.180	0.195	0.080	0.084	0.108	0.097	0.248	0.227	0.032	0.033
Total	7.97	7.98	7.98	7.99	8.00	7.99	7.99	7.99	8.00	7.99
X_{alm}	0.608	0.624	0.735	0.748	0.752	0.754	0.765	0.751	0.601	0.680
X_{sp}	0.307	0.287	0.017	0.019	0.021	0.023	0.031	0.025	0.374	0.286
X_{py}	0.024	0.023	0.221	0.206	0.191	0.190	0.120	0.147	0.015	0.024
X_{gr}	0.061	0.066	0.027	0.028	0.036	0.033	0.083	0.076	0.011	0.011

Table 2.1. Representative electron microprobe analyses of garnet samples obtained from four granite sheets in the Kohistan - NPHM region. All analyses recalculated to 12 formula oxygens. X = molar fraction of the almandine, spessartine, pyrope and grossular components. Sample locations : G2 - Parri (Kohistan); G30 and G43 - Sassi shear zone; I11 - Iskere village (NPHM). For analytical details, see Appendix 1.

Even at localities where both Confluence and Parri granites are present, the different sheets often have similar orientations, and therefore evidence for the relative chronology of granite intrusion is limited. Another problem lies in the unequivocal distinction between Confluence and Parri granites on the basis of mineralogy alone. For example, some granite sheets are characterised by muscovite with subordinate biotite, and could (in the absence of trace element data) be classified as either Confluence or Parri granites. However, a detailed study of several exposures suggests that the Parri granites are younger than the Confluence granites. In the lower Darchan valley, two medium-grained, 2-3 metre thick biotite granites that contain subsidiary muscovite, are cross-cut by relatively coarse and heterogeneous muscovite granites that reach thicknesses of seven metres (Fig. 2.7A). Trace element studies have confirmed that the biotite granites are typical Confluence granites, whilst the muscovite granites have the geochemical characteristics of Parri granites. In the vicinity of the Indus confluence, a plug of Confluence granite is locally cross-cut by younger, 1-2 metre thick sheets of muscovite-garnet granite. Theoretically it is possible that the Confluence and Parri granites were all intruded over a similar, extended time period, with the result that some overlap occurred between the intrusion of granites in the two suites. However, in addition to the field observations described above, the isotopic evidence (Chapter 7; Peterson and Windley 1985) also suggests that the Parri granites are younger than the Confluence granites.

Both Confluence and Parri granites may be cross-cut by coarse and often heterogeneous pegmatites that are generally less than 0.5 m thick. These pegmatites are characterised by biotite and muscovite in varying proportions, together with subsidiary garnet. The micas are locally extremely coarse (up to 30 cm long), and often orientated perpendicular to the sheet margins. In some cases, pegmatites have been preferentially intruded along the margins of larger granite sheets.

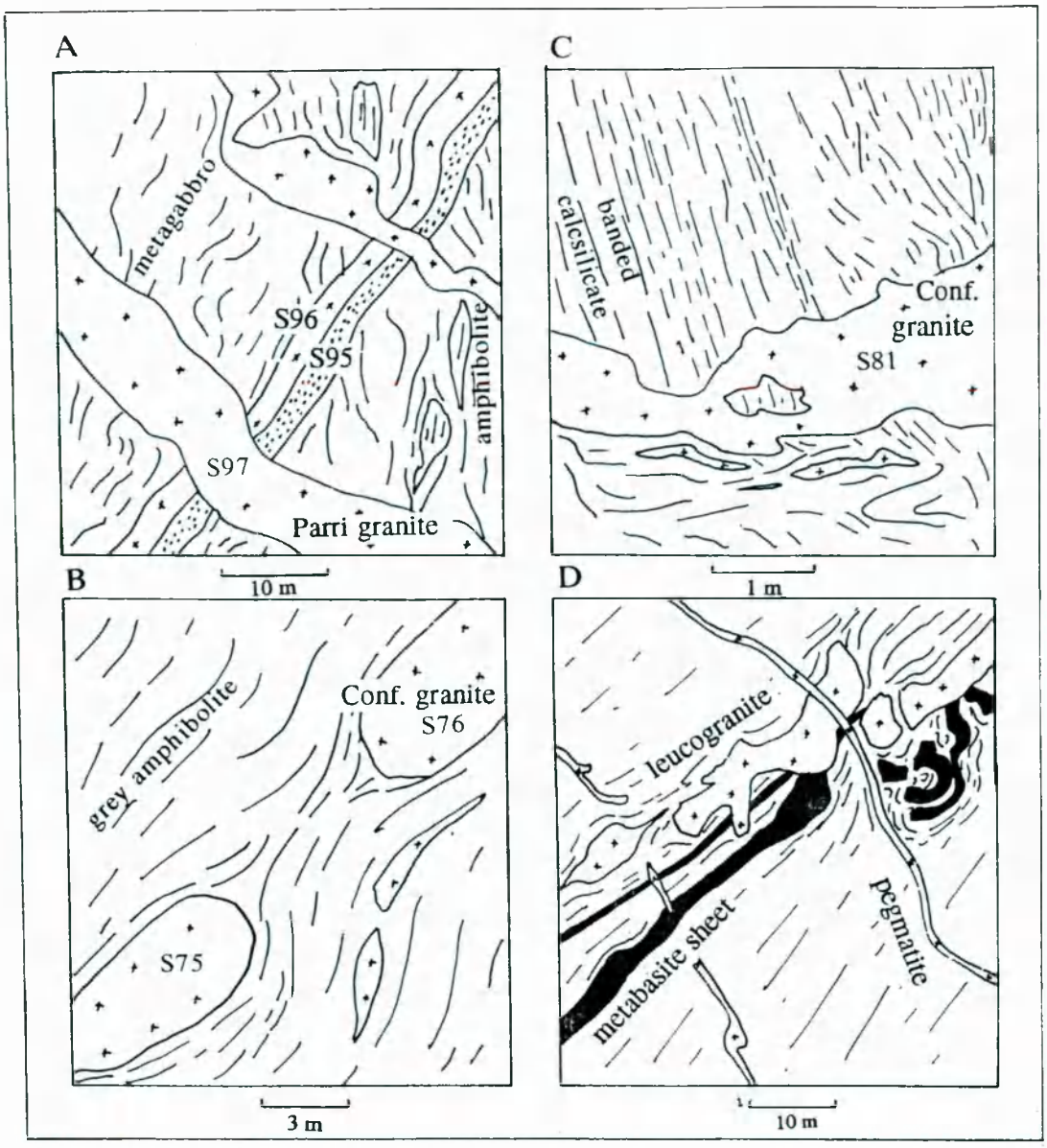

Fig. 2.7. Field sketches of igneous relations in the northern NPHM region. West is to the left in each case. **A**. Lower Darchan valley : coarse-grained muscovite granite sheets (Parri granites) (S97) cross-cutting medium-grained biotite granite sheets (Confluence granites) (S95 & S96), all intruding massive metagabbro and sheared amphibolite. **B**. Shahbatot : thick, boudinaged Confluence granite sheet (S75 & S76). **C**. Sassi : partially sheared Confluence granite sheet (S81) cross-cutting well-banded Indian continental calcsilicates. **D**. Indus gorge, NPHM interior. Concordant and folded metabasic dyke, cross-cut by a younger boudinaged leucogranite sheet, both cross-cut by younger pegmatites.

2.3. Marginal Regions of the Nanga Parbat-Haramosh Massif

2.3.1. The Western Margin between Shahbatot and Sassi

In the Indus gorge between Shahbatot and Sassi (Fig. 2.2), the contact between the Kohistan arc and the NPHM is marked by a 2-3 km-wide ductile shear zone containing a

wide range of intercalated metasedimentary and metabasic lithologies (Hanuchal amphibolites of Madin et al. 1989). This shear zone strikes north-south and generally dips steeply to the west, as shown in Plate 2.8. The contrasting lithologies are interleaved on a scale of metres, and the lithological banding is parallel to the strong mylonitic foliation. To the east, the metasedimentary and metabasic lithologies lie concordantly against the Iskere gneiss of the NPHM (see below), whilst to the west there is a 1-2 km gap in exposure before the Shuta gabbro is reached.

The sequence is dominated by grey, well-banded psammitic gneisses, green or grey-coloured amphibolites and buff-coloured marbles, whilst cream-coloured calcsilicates and well-cleaved pelitic schists form subsidiary intercalations. The majority of the amphibolites are thought to be derived from the Kohistan arc, whereas the pelites, calcsilicates and marbles probably originated in the Indian continental crust (Butler and Prior 1988a). This inference is supported by the following :

(i) The broad lithological characteristics of the NPHM and Kohistan terranes away from the shear zone. For example, compared with the Kohistan arc, the NPHM is dominated by metasedimentary and granitic lithologies, whilst amphibolites are relatively rare. In contrast, the Kohistan arc is dominated by amphibolitic lithologies, whilst calcsilicates and marbles have not been observed.

(ii) On traversing eastwards across the shear zone towards the NPHM, there is a marked decrease in the proportion of amphibolite and a corresponding increase in the proportion of pelite, calcsilicate and marble. There is also a rapid decline in the abundance of deformed Confluence and Parri granites (see below).

In the Babusar area, approximately 120 km to the south-west of Sassi, the MMT zone is also characterised by a sequence of highly sheared, intercalated amphibolites, calcsilicates and pelites, which have been interpreted as representing tectonically juxtaposed lithologies derived from the Indian continent and the Kohistan arc (Chamberlain et al. 1991).

The metasediments exposed at Sassi have been interpreted as a sedimentary cover of possible Phanerozoic age to the Indian continental basement (Butler and Prior 1988a).

However, it should be noted that metasedimentary rocks are not confined to the margins of the NPHM. For example, thick wedges of interbanded pelites, calcsilicates and amphibolites have a sporadic occurrence within the Iskere orthogneiss (section 2.4.2), and therefore in most cases original cover-basement relations have been obliterated by tectonism.

The basic schists or amphibolites are similar in mineralogical composition to those enclosed by the Shuta gabbro (section 2.2.3), although the amphibolites at Sassi generally do not contain primary epidote or zoisite. The Sassi basic schists are characterised by garnet (2-10 %), hornblende (25-50 %), biotite (5-30 %), plagioclase (An_{15-30}) (10-20 %), sphene (5-10 %) and quartz (5-20 %), sometimes k-feldspar (up to 20 %), and minor apatite, ilmenite and magnetite. Secondary minerals include rare chlorite and epidote. With a decrease in the modal abundance of biotite and an increase in the modal abundance of hornblende, the schists grade into amphibolites which contain up to 80 % hornblende, together with with plagioclase, quartz and sometimes garnet. Such hornblende-rich rocks are probably orthoamphibolites, and may have been derived from either Kohistan or the NPHM (see section 2.4.6)

The pelitic lithologies are characterised by the assemblage garnet (4-10 %), kyanite (up to 5 %), muscovite (5-45 %), biotite (10-40 %), plagioclase (An_{15-30}) (10-35 %) and quartz (10-45 %), together with rare opaque-oxides, secondary chlorite and occasional grains of fractured tourmaline. The calcsilicates and psammitic gneisses are similar to those found elsewhere within the NPHM, and are described below (section 2.4.2).

Both Confluence and Parri granites can be traced eastwards along the Indus gorge into the shear zone at Sassi (Butler and Prior 1988a), where they can be discriminated in the field on the basis of mineralogy. This distinction is confirmed by trace element analyses on collected samples (see Chapter 6). The majority of Kohistan granites in the shear zone are highly deformed and concordant with the mylonitic foliation (Fig. 2.7B; Plates 2.9 and 2.10). Many granites are strongly boudinaged or folded, and form useful kinematic indicators, as described in Chapter 4. The deformation fabrics within the granites vary from a poorly-defined foliation, characterised by the presence of recrystallised quartz around large alkali feldspar porphyroblasts (mortar texture) (Plate 2.11), to an intense penetrative foliation

(Plate 2.12).

The mylonitised granite sheets sometimes display gradational margins with their wallrocks, characterised by an increase in the mafic content towards the margins. Occasionally thin, discontinuous layers of more biotite-rich material are present within the interiors of deformed sheets, as shown in Plate 2.10. Deformed Parri granites locally contain highly fractured porphyroblasts of garnet which differ markedly to the euhdral grains that are present in the undeformed Parri sheets (Plate 2.13). These garnet grains are often surrounded by relatively coarse, recrystallised grains of biotite and quartz, contain abundant inclusions of quartz, mica and sillimanite, and often occur as trains of porphyroblasts that are orientated parallel to the foliation. Electron microprobe analysis shows that the garnet is relatively almandine-rich, and characterised by well-developed compositional zoning (Table 2.1). The chemical composition, and the zoning pattern, are similar to those observed in typical metamorphic garnets from the region (Chapter 4). All the evidence therefore suggests that the garnet porphyroblasts are xenocrystic metamorphic grains. The presence of xenocrystic garnet, together with the field observations described above, indicates that at some stage prior to crystallisation, melts intruding the shear zone were partially contaminated by either wall-rock or restite, an inference that is supported by isotopic and trace element studies (Chapters 6 and 7).

Butler and Prior (1988a) observed that the Kohistan granites become sheared by ductile, amphibolite-facies fabrics, the kinematics of which suggested a transport direction of top-to-the SSE. They concluded that the age of the arc granites was pre to syn-peak shearing along the 'Main Mantle Thrust', a conclusion supported by the apparent restriction of these sheets to Kohistan-derived units. However, locally, the Kohistan-derived granites truncate deformation fabrics, and intrude some of the intercalations of Indian continental material (Fig. 2.7C), suggesting that they post-date the initial suturing of the Kohistan arc with the NPHM. The fact that the majority of the granites have been sheared into parallelism with the mylonitic foliation, as illustrated in Plate 2.8, indicates that the granites were emplaced into an actively deforming shear zone, which resulted in the subsequent deformation of most of the granite sheets. The observations of Butler and Prior (1988a) may indicate that the

Plate 2.8. (right) The shear zone bordering the western margin of the NPHM near Sassi. The foliation is dipping steeply west (right). Numerous highly attenuated granite sheets (Confluence and Parri granites) lie concordant to the foliation; these sheets truncate fabrics in less-strained, higher-level horizons (top right corner). The cliff is about 700 metres high.

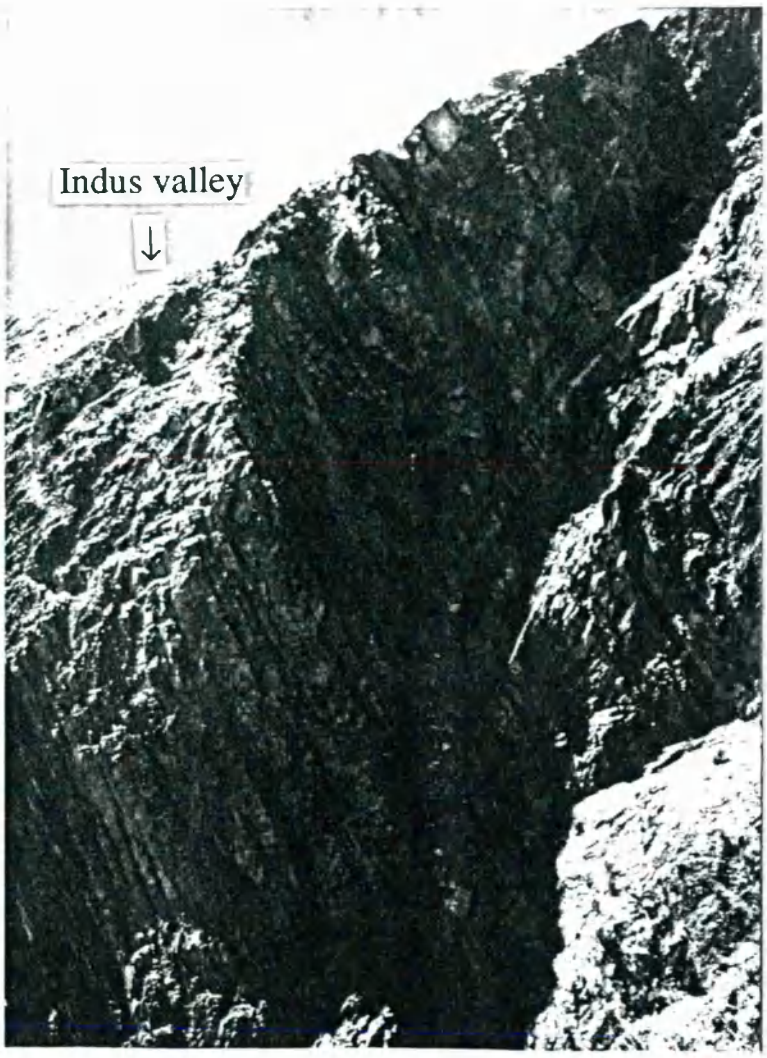

Plate 2.9. (below) Highly sheared granite sheets exposed on the west side of the upper Darchan valley. The wall rocks are well-layered paragneisses and amphibolites (Layered-unit of Butler et al. 1992). Confluence granite sample D17 was collected from this locality. SSF = strike-slip fault. Height of exposure is 5 metres.

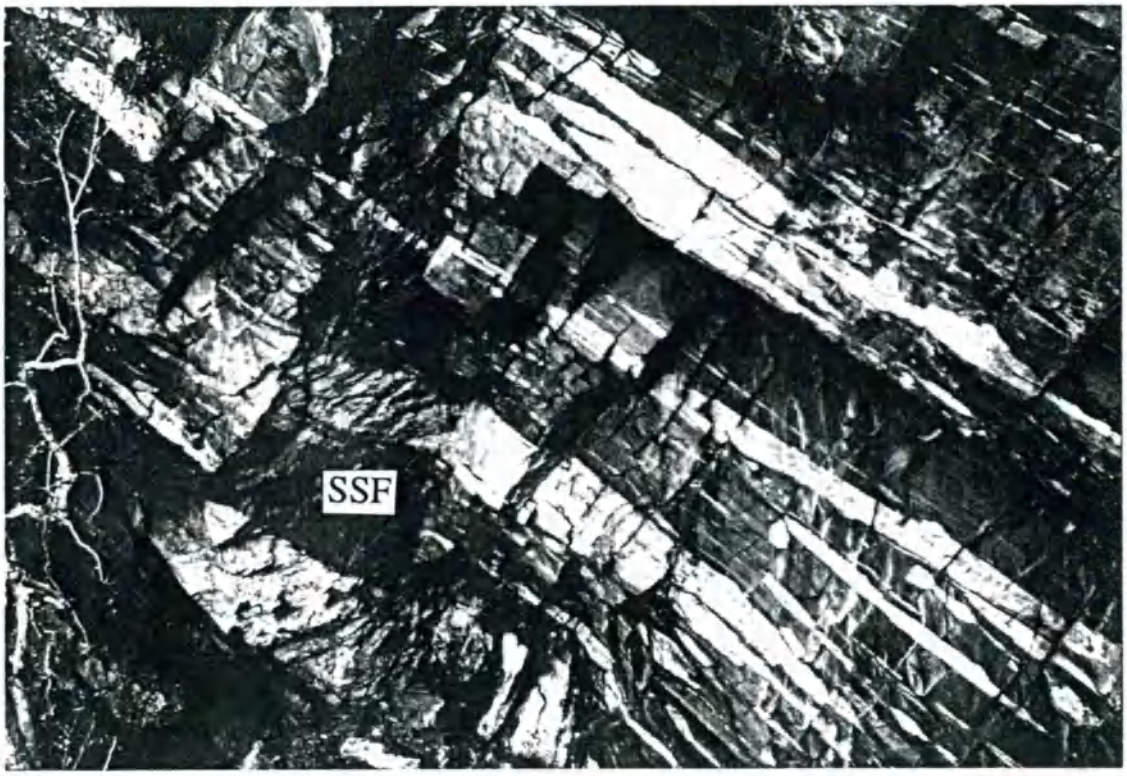

Plate 2.10. (right) Detail of highly-sheared body of biotite-muscovite-garnet (gt) granite (Parri granite), Sassi. Country rocks are well-foliated, locally migmatitic paragneisses, dipping steeply west (left). Granite samples S12, G34, G35, G36 were collected from this body. Hammer is 30 cm long.

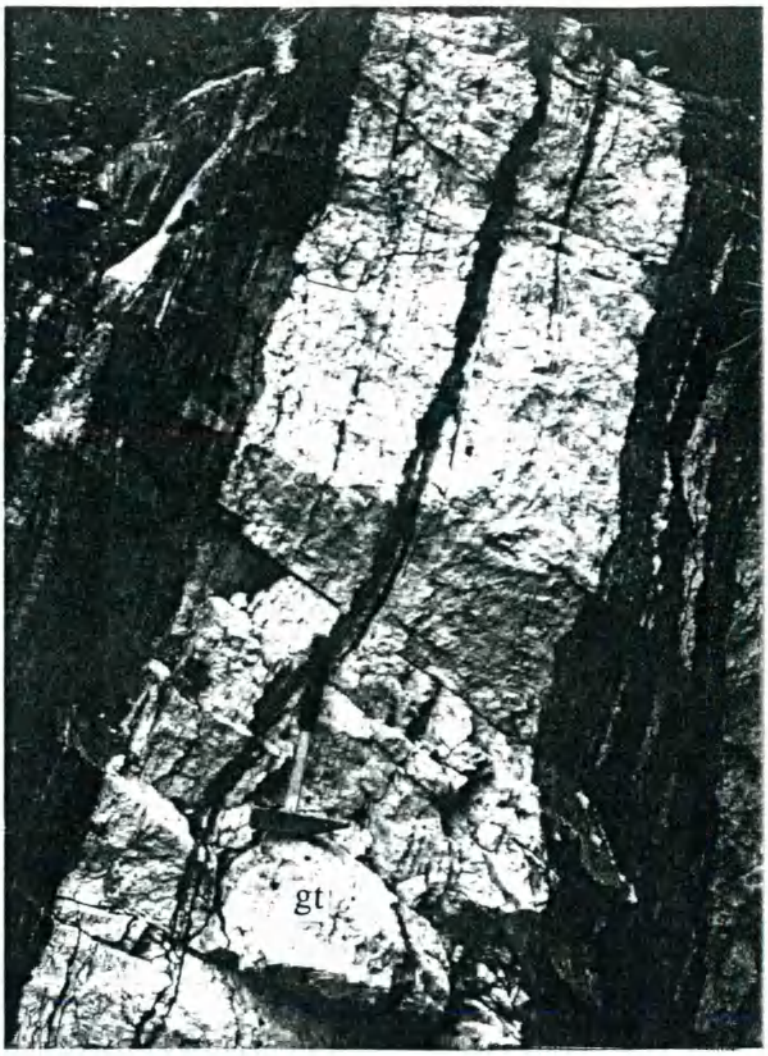

Plate 2.11. (below) Photomicrograph of a highly-deformed, mylonitic Confluence granite (sample S75) (XPL). Recrystallised ribbon quartz around large altered feldspar porphyroblasts, with fine-grained muscovite and biotite.

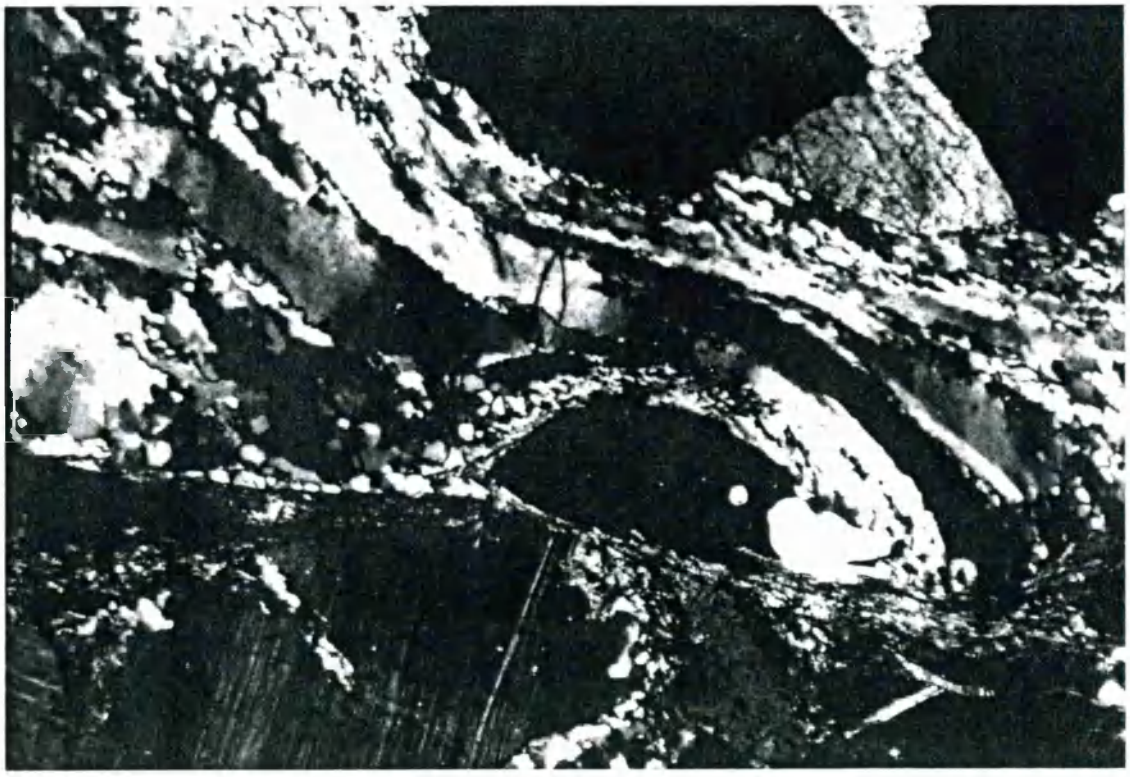

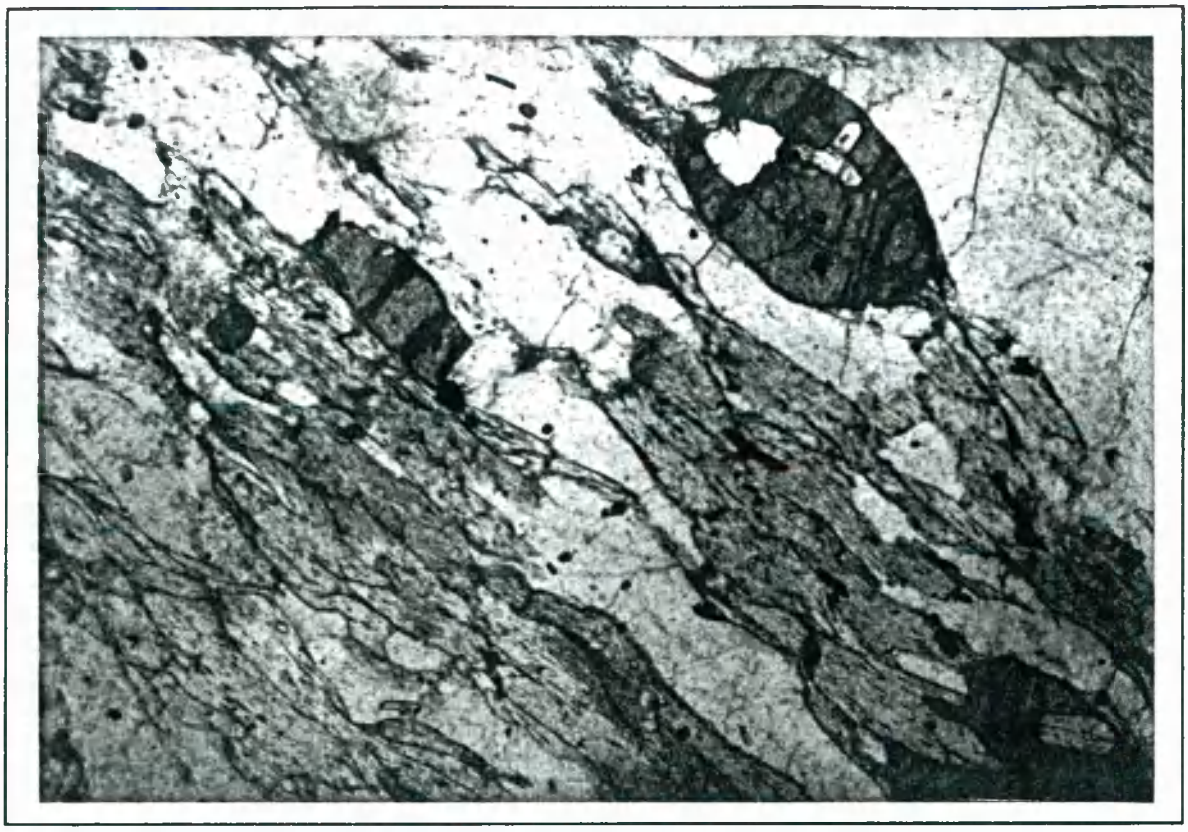

A

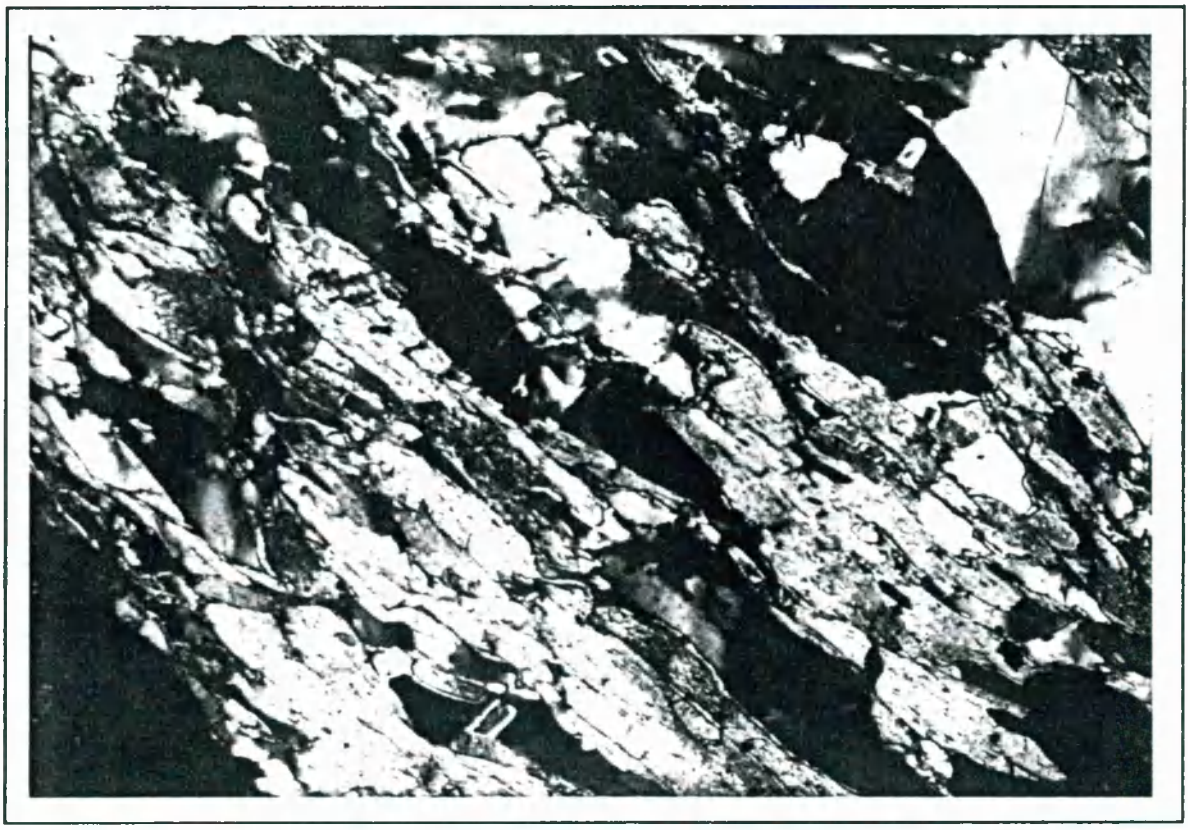

B

Plate 2.12. Photomicrographs of deformed Parri granite (sample G29) from the shear zone at Sassi. **A** = PPL; **B** = XPL. Fibrous muscovite and elongate quartz and feldspar define a well-developed foliation. High-relief, cracked porphyroblasts of garnet, containing inclusions of muscovite and quartz, are also present.

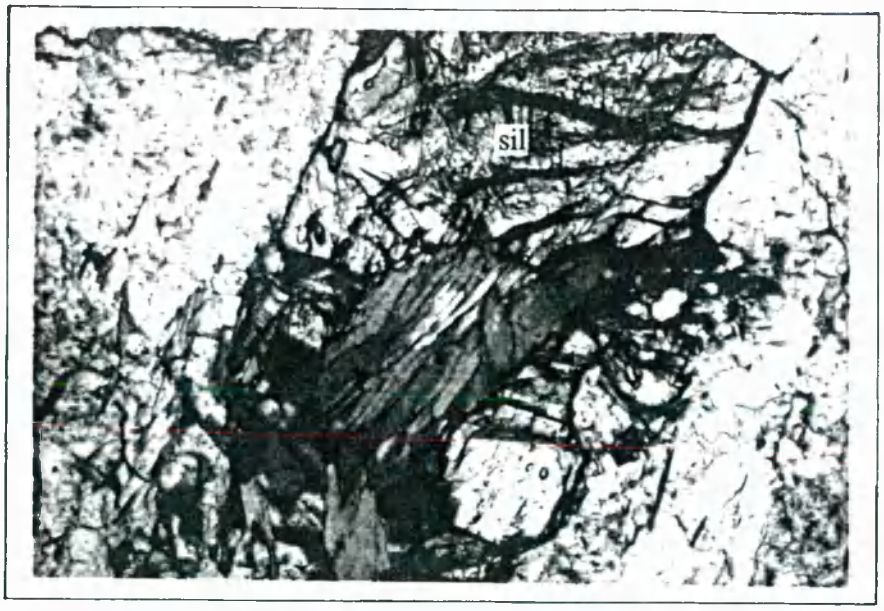

Plate 2.13. Photomicrograph of garnet crystal present in a deformed sheet of Parri granite, Sassi shear zone (sample G43) (PPL). The garnet is highly fractured and contains inclusions of fibrolitic sillimanite (sil) and biotite.

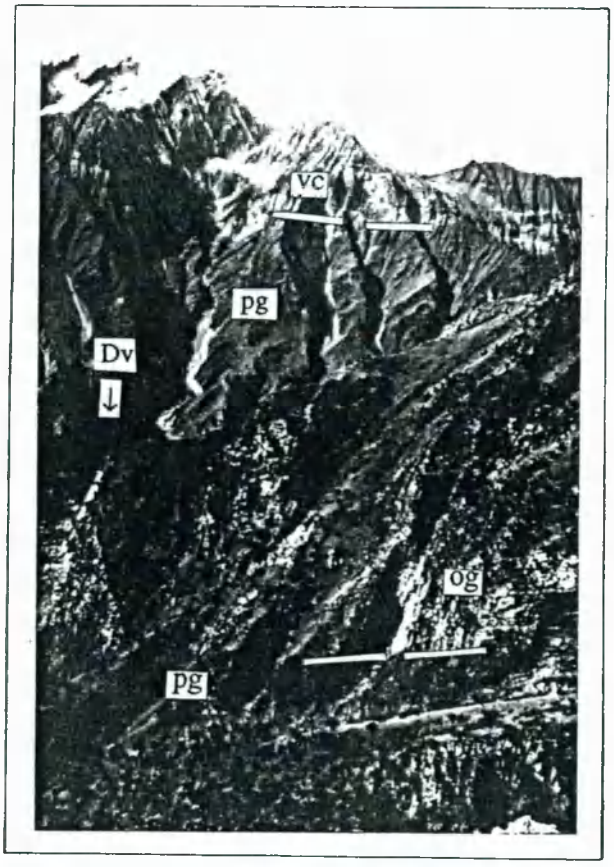

Plate 2.14. View across the upper Darchan valley (middle distance; Dv), looking westwards from the northern part of the NPHM. pg=paragneiss of the Layered-unit; og=orthogneiss of the NPHM; vc=upper arc volcaniclastics (Kohistan).

Plate 2.15. Well-layered paragneisses of the NPHM, exposed in the Indus gorge east of Shengus (Shengus unit of Madin et al. 1989). Note the normal fault with drag, and the hammer for scale. East is towards the right.

intrusion of granite sheets into the suture zone was followed by shearing along a transport direction of top-to-the SSE, but this will be discussed further in subsequent chapters.

Occasionally, heterogeneous biotite-tourmaline granite sheets and pegmatites are present within the shear zone. Although invariably deformed, these intrusive bodies exhibit varying orientations with respect to the shear zone fabrics. They occur both as sinuous veins that cross-cut the mylonitic foliation, and as boudinaged sheets that lie parallel to the foliation. These tourmaline-rich granites and pegmatites may be equivalent to the muscovite-tourmaline leucogranite bodies that occur elsewhere in the NPHM (section 2.4.7).

2.3.2. Northern Margin of the NPHM

Butler et al. (1992) mapped a 'Layered-unit' composed of well-layered ortho and paragneisses, together with subsidiary amphibolites, around the northern antiformal termination of the NPHM. The Layered-unit of Butler et al. (1992) is equivalent to the 2.5 km thick Haramosh schist of Madin et al. (1989). The unit can be readily examined in the upper parts (especially the headwalls) of the Iskere, Phuparosh and Darchan valleys (Fig. 2.2). In addition to the above lithologies, on the west side of the Darchan valley, the unit also contains numerous deformed sheets of biotite-granite, whilst on the east side of the Darchan valley, subordinate calcsilicate layers are present. In this work, the Layered-unit is considered to be equivalent to the sequence of intercalated metasedimentary and metaigneous rocks present in the Sassi-Shahbatot area (section 2.3.1).

A geological sketch map of the Darchan valley is presented in Fig. 2.8. On the western side of the valley is a sequence of well-foliated and interleaved amphibolites and paragneisses. This sequence reaches thicknesses of up to 50 metres, and is locally highly sheared. At higher elevations, the mountainside is dominated by more massive ortho and paragneisses, which can be traced along strike into the headwall of the Darchan valley to the north. The amphibolites are characterised by the assemblage epidote (up to 40 %), hornblende (30-40 %), plagioclase (10-25 %) and quartz (10-20 %). The paragneisses also contain a relatively high content of epidote, and are characterised by biotite (20-25 %), epidote (10-20 %), k-feldspar (5-20 %) plagioclase (20-40 %) and quartz (20-25 %), with

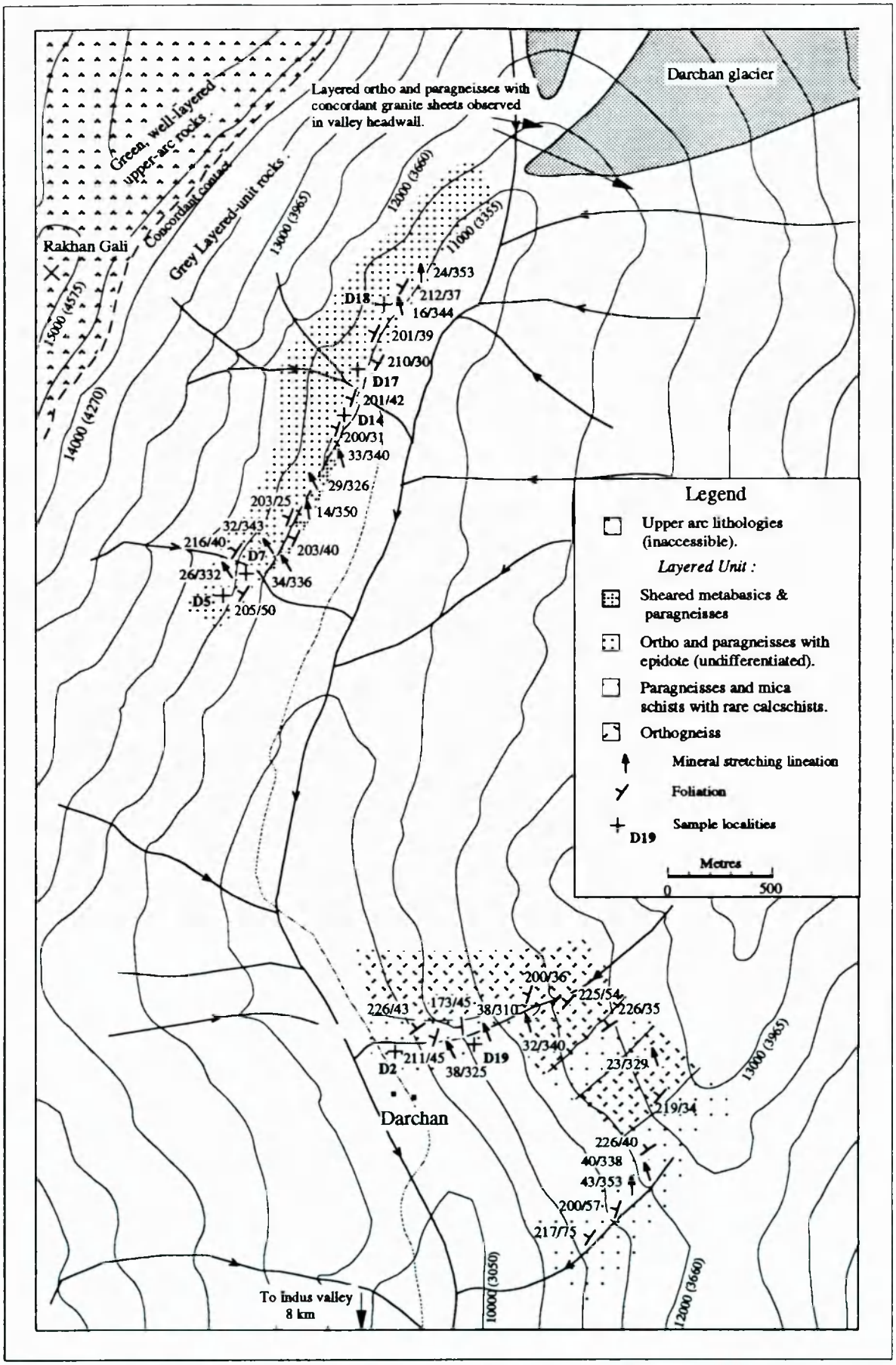

Fig. 2.8. Detailed Geological map of the upper Darchan valley. The localities of samples referred to in subsequent chapters are indicated. Contour intervals are 500 ft (1649 m), but contours are only approximate.

rare hornblende-rich horizons (2-3 mm thick). The orthogneisses are relatively massive, pale-grey rocks containing scattered garnet and approximately equal proportions of muscovite, biotite and epidote (3-4 % each).

Numerous, highly deformed and attenuated granite sheets are present in the sequence exposed on the west side of the Darchan valley (Plate 2.9). These granites lie parallel or sub-parallel to the dominant foliation, reach thicknesses of up to 5 metres, and are characterised by variable proportions of muscovite, biotite and garnet. The biotite-rich granites often contain subsidiary epidote and muscovite. The granites are similar to the deformed sheets present in the shear zone at Sassi, and appear to be the deformed equivalent of the Confluence and Parri sheets, an inference that has been confirmed by geochemical analysis.

The orthogneiss is characterised by a relatively primitive whole-rock strontium isotopic composition that is characteristic of the Kohistan arc (see Chapter 7). This observation, together with the abundance of Kohistan-derived granites, suggests that a high proportion of the Layered-unit that is exposed on the western side of the Darchan valley has been derived from Kohistan.

Compared with the sequence exposed on the west side of the Darchan valley, the sequence exposed on the east side of the valley is characterised by a greater proportion of pelitic gneiss, and the first horizons of calcsilicate are seen near the village of Darchan. There is a noticeable absence of concordant biotite-granite sheets, although coarse-grained, cross-cutting muscovite-tourmaline pegmatites and leucogranite dykes are occasionally present. The Layered-unit is conformably overlain by a relatively massive, grey-coloured biotite-orthogneiss that contains scattered garnet (Plate 2.14). This orthogneiss may be equivalent to the Iskere gneiss of Madin et al. (1989). In contrast to the orthogneiss unit exposed on the west side of the Darchan valley, the east Darchan orthogneiss is characterised by a relatively evolved whole-rock strontium isotopic composition, suggesting that the orthogneiss is part of the Indian continental basement (see Chapter 7).

A transitional, broadly concordant lithological contact occurs in the headwalls of the Phuparosh and Darchan valleys, at an elevation of about 5000 metres (Plate 2.14). From a

distance, this appears to separate green, well-layered upper-arc rocks of the Kohistan terrane from grey-coloured gneisses of the Layered-unit (Butler et al. 1992). The upper arc rocks are probably similar to the low-grade schists exposed in the upper Bagrot valley (section 2.2.2). In the south-east, the contact appears to lie to the east of the Haramosh La, since the pass itself lie within the Layered-unit, whilst the next peaks to the east are composed of green rocks believed to be representative of the Ladakh arc (Butler et al. 1992). Butler et al. (1992) correlated the lithological contact with the ductile MMT, defined at Sassi by Butler and Prior (1988a). The absence of low-grade upper-arc lithologies in the hanging-wall of the shear zone present at Sassi is presumably a reflection of a deeper level of erosion, or tectonic removal in the hanging-wall of the MMT.

2.4. Field Relations and Petrography in the Nanga Parbat-Haramosh Massif

2.4.1. Previous work

The rocks of the NPHM consist of a range of amphibolite-grade, often intensely deformed orthogneisses and paragneisses of the Indian continental crust, first described in detail by Wadia (1932). Other subordinate, but potentially important, lithologies include metabasic dykes and leucogranite sheets or sheet complexes, described further below. Wadia (1932) observed that the margins of the massif were dominated by biotite gneisses with subordinate metasediments, which Wadia grouped into the Precambrian Salkala series. Towards the core of the massif, there was both an increase in metamorphic grade, and an increase in proportion of orthogneiss, which was correlated with the Central Gneiss of the High Himalaya (now termed the High Himalayan crystalline). Wadia (1932) noted the frequent interbedding of orthogneisses and paragneisses, which was ascribed to lit-par-lit injection. However, in a classic study, Misch (1949) suggested that these migmatites were generated by sub-solidus, lit-par-lit granitisation of metasediments by alkali metasomatism. This process was believed to have occurred during Himalayan times, and may have involved the introduction of hot fluids during shearing. The evidence Misch used for such large-scale

metasomatic replacement included the close association between metamorphic grade and degree of granitisation, the gradational and conformable contacts between ortho- and para-gneisses, and the petrographically observed late-stage growth of alkali feldspar.

Madin et al. (1989) divided the rocks of the northern part of the NPHM, from structurally lowest to highest, into the Shengus gneiss, Iskere gneiss and Haramosh schist units. According to Madin et al. (1989), the Haramosh schists are a sequence of well-layered metasediments including schists, gneisses, calcsilicates and subordinate amphibolites, exposed on Layla and Haramosh peaks and occupying high, often inaccessible ground in the north-eastern part of the NPHM. The Haramosh schists are equivalent to the Layered-unit of Butler et al. (1992), which was mapped round the northern termination of the NPHM. In this work, the Layered-unit has been correlated with the intercalated sequence of metasediments present at Sassi, which are thought to have been derived from both the Kohistan arc and the Indian continent (Butler and Prior 1988a).

2.4.2. Iskere gneiss

This unit, exposed along the Indus gorge between Shahbatot and Shengus, and in the Haramosh valleys to the north, structurally overlies the Shengus gneiss unit (Madin et al. 1989). The contact between the Iskere and Shengus gneisses is marked by a band of sillimanite-bearing mylonites, modified by later brittle faulting (Treloar et al. 1991). In the Indus gorge, foliation in the Iskere unit generally strikes steeply north-south (Fig. 2.2).

The Iskere unit is dominated by a monotonous, relatively massive and coarse-grained biotite orthogneiss. The presence of streaky, deformed and concordant segregations of leucosome often gives the orthogneiss a migmatitic appearance. Elsewhere the orthogneiss is an augengneiss with coarse-grained feldspar porphyroblasts. The orthogneiss is typically characterised by the assemblage biotite (5-25 %), plagioclase (An_{20}) (10-30 %), k-feldspar (15-50 %) and quartz (20-40 %), together with minor sphene, allanite, zircon, apatite and opaque oxides, and secondary muscovite and chlorite after biotite. The feldspar is usually

sericitic and sometimes perthitic. Myrmekite is also often present. Garnets are very rare, but where present may reach 4 cm in diameter. Zircons from the Iskere orthogneiss have yielded U-Pb ages of ~1850 Ma (Zeitler et al. 1989).

In the Indus section, the Iskere gneisses enclose at least three separate, clearly-defined wedges of metasediments, each 30-40 metres-thick. These consist of conformable, well-foliated semi-pelitic and psammitic gneisses and amphibolites with occasional, 1-2 m thick horizons of calcsilicate. Further occurrences of paragneisses are found in the Haramosh area to the north, but true pelites are exceedingly rare in the region. The semi-pelites, psammites and orthogneisses often have transitional contacts or are interlayered on different scales, making rigorous mapping of the stratigraphy impossible.

The semi-pelites contain the assemblage garnet (4-5 %), muscovite (5-20 %), biotite (15-45 %), plagioclase (An_{25}) (10-30 %), quartz (20-50 %) and k-feldspar (< 20 %), together with minor secondary chlorite and opaque oxides. The garnets occur as corroded porphyroblasts up to 7 mm across, containing abundant inclusions of quartz and mica. The calcsilicates and amphibolites are generally coarser-grained rocks in which the foliation is less well-defined. The calcsilicates typically contain pale, olive-green diopside (30-55 %), plagioclase (30-35 %), quartz (15-30 %), epidote (2-6 %) and small, scattered garnet grains (4%), together with rare grains of sphene, calcite and opaque oxides. Secondary minerals include interstitial carbonate, chlorite and muscovite. The diopside crystals may be either small and blocky or large and poikiloblastic; alteration of diopside to actinolite is sometimes observed. The amphibolites contain rounded garnet porphyroblasts up to 7 mm across, sieved with quartz and opaque oxides (15 %), hornblende (10-40 %), biotite (10-25 %), plagioclase (An_{40}) (10-15 %) quartz (20-50 %) and sphene (2-6 %), with rare chlorite.

2.4.3. Shengus gneiss

The Shengus unit is exposed in the Astor gorge and to the east of Shengus village in the Indus gorge (Figs. 2.1 and 2.2). According to Madin et al. (1989) and Treloar et al.

(1991), the Shengus gneisses form the structurally lowest unit of the NPHM. Within the Shengus unit, kyanite-bearing gneisses overlie the sillimanite bearing gneisses, suggesting that significant post-metamorphic stacking has taken place (Treloar et al. 1991). The Shengus gneisses have yielded a U-Pb zircon age of about 500 Ma (Zeitler et al. 1989), and probably originally formed a cover to the Iskere gneiss unit.

In the Shengus area, the gneisses consist of a variable sequence of dark, biotite-rich pelitic gneisses, paler psammitic gneisses locally containing bands of coarse feldspar augen, garnet amphibolites and rare calcsilicate horizons. These rocks are well-layered and often finely-laminated, as shown in Plate 2.15. Migmatitic horizons rich in concordant segregations of leucosome, often containing garnet, are common. The foliation dips moderately towards the north near Shengus, whilst further to the east, the rocks assume an approximately north-south strike, dipping steeply either east or west. The sequence has suffered intense deformation, and both minor folds and faults are common (Plate 2.15).

Near Shengus, the garnet amphibolites are characterised by the assemblage garnet (4-10 %), coarse poikiloblastic hornblende (10-40 %), biotite (< 20 %), plagioclase (An_{35-60}) (10-30 %), quartz (15-25 %), sphene (1-5 %) and magnetite and ilmenite (2-5 %), with rare chlorite after biotite, and apatite. The garnet occurs as cracked, corroded, occasionally completely retrogressed porphyroblasts containing inclusions of hornblende, sphene, biotite and opaque oxides. The pelitic gneisses are characterised by sillimanite (5-8 %), muscovite (< 6 %), biotite (10-20 %), quartz (10-15 %), plagioclase (4-5 %) which is sometimes porphyroblastic, and minor secondary chlorite. The sillimanite occurs as fibrolitic porphyroblasts up to 2 mm across, aligned parallel to the foliation in the groundmass, and appears to be replacing fabric-forming muscovite. In some samples, the muscovite has been totally replaced, although rare blades of scecondary muscovite may be present. 1-2 mm thick veins and blebs of k-feldspar-plagioclase-quartz leucosome, orientated parallel to the foliation, are also common.

In the Astor gorge, highly strained, often migmatitic, pelitic and psammitic gneisses

dip steeply towards the west. These are composed of garnet (8-10 %), abundant small, blocky grains of kyanite (5-8 %), muscovite (10-25 %), biotite (20-25 %), k-feldspar (< 5 %), plagioclase (4-10 %) and quartz (15-40 %) with accessory tourmaline and rutile (Plate 2.16). Again, the plagioclase sometimes occurs as large twinned porphyroblasts. The garnet porphroblasts often contain inclusions of quartz, muscovite and rutile. In the larger garnet grains, fine grained biotite and rutile grains are sometimes preferentially developed near the margins (Plate 2.17).

2.4.4. Tarshing-Rupal Region

The southern part of the NPHM was not mapped by Madin et al. (1989). However, the dominant rock types appear to be similar to those of the Iskere unit to the north. In the Rupal valley (Fig. 2.1), the main lithology is a locally migmatitic orthogneiss, containing biotite and sometimes muscovite. Characteristic features of this gneiss include the presence of thick horizons containing feldspar augen and thin, concordant and sometimes boudinaged quartz veins and lenticles. Occasionally 0.5-1.0 m thick bands of granular calcite or calcsilicate are present. The foliation strikes northwest-southeast, being either vertical or steeply-dipping either north-east or south-west.

A thick sequence of well-foliated metasedimentary rocks is present about 3 km east of Tarshing (Fig. 2.1). These rocks include locally migmatitic pelitic and calcareous gneisses, characterised by varying proportions of garnet, muscovite, biotite, zoisite, plagioclase and quartz, together with rare ilmenite and rutile. The garnet porphyroblasts contain sinuous inclusion trails of opaque oxides and quartz, and are surrounded by asymmetric pressure shadows composed of recrystallised quartz. These features suggest that strong shearing deformation and rotation of the garnets occurred during their growth.

2.4.5. Tato Region

The dominant rock type in the Tato region is a coarse biotite orthogneiss. Concordant

Plate 2.16. Photomicrograph of garnet (gt)-kyanite (ky)-2-mica-gneiss from the Astor gorge (sample A3). PPL. Note the presence of quartz and biotite inclusions in the cracked garnet porphyroblast, and the presence of fabric-forming muscovite (mu) in the matrix.

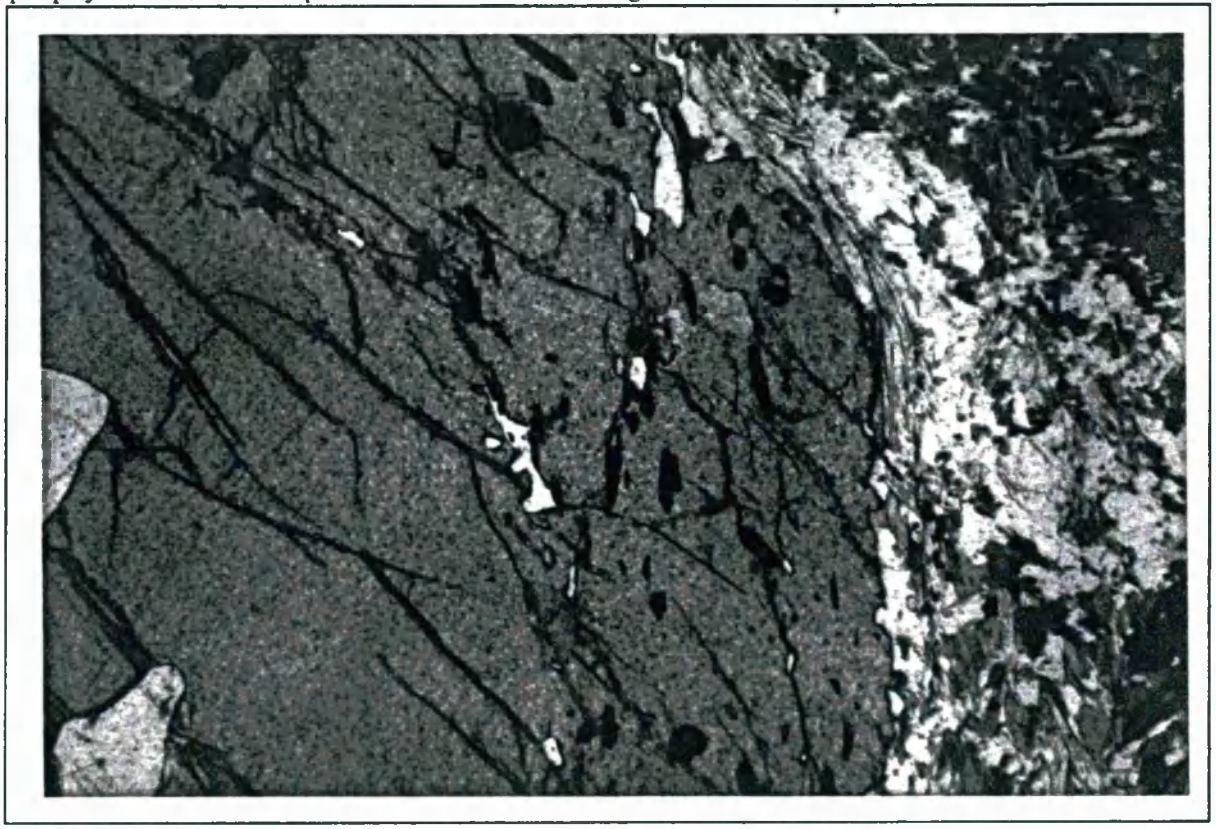

Plate 2.17. Detail of garnet porphyroblast present in kyanite-2-mica gneiss from the Astor gorge (sample A21) (PPL). The core of the garnet is characterised by large quartz inclusions (left margin); the rim of the garnet contains numerous rutile and biotite inclusions. Fine-grained muscovite, kyanite, biotite and rutile are visible in the matrix.

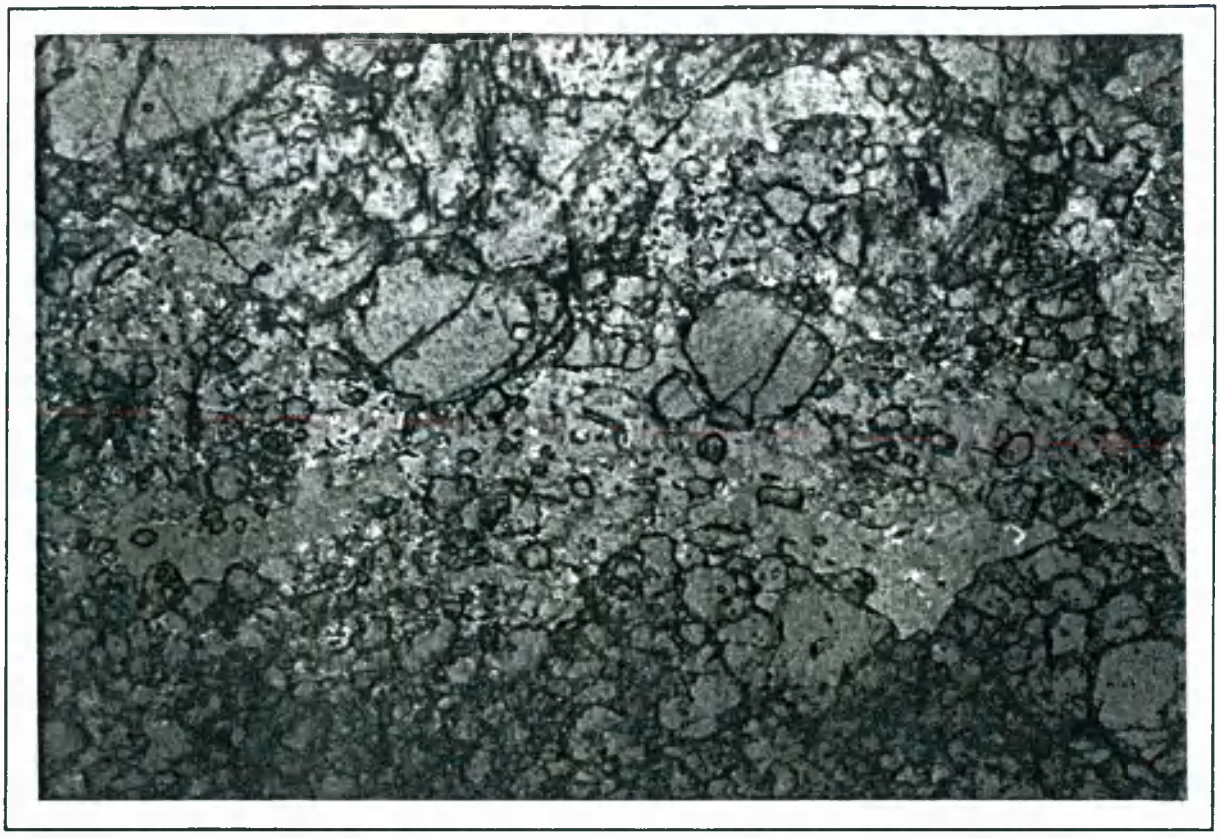

A

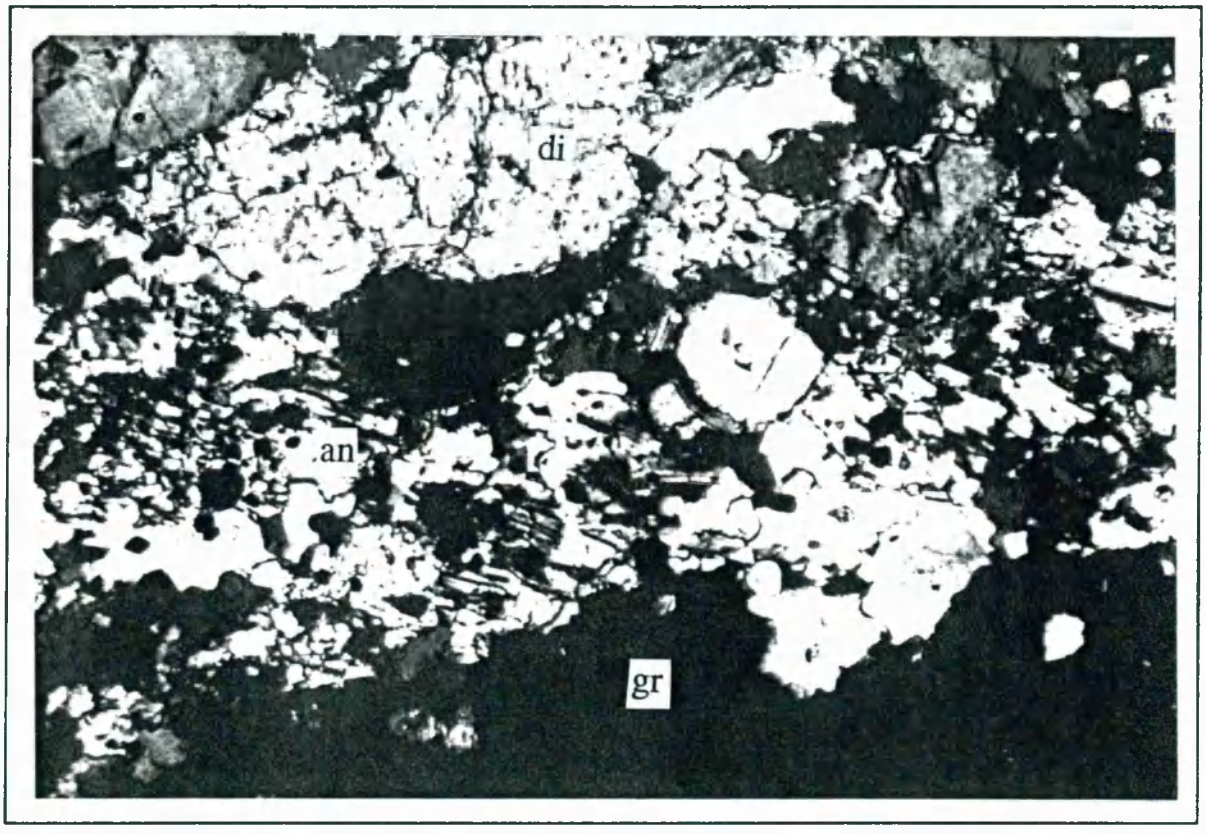

B

Plate 2.18. Photomicrographs of banded calcsilicate from the Liachar shear zone (sample T23). **A** = PPL; **B** = XPL. Coarse crystals of diopside showing second-order interference colours (di), anorthite showing repeated twinning (an), and granular grains of grossular garnet (gr) are all present, together with interstitial quartz.

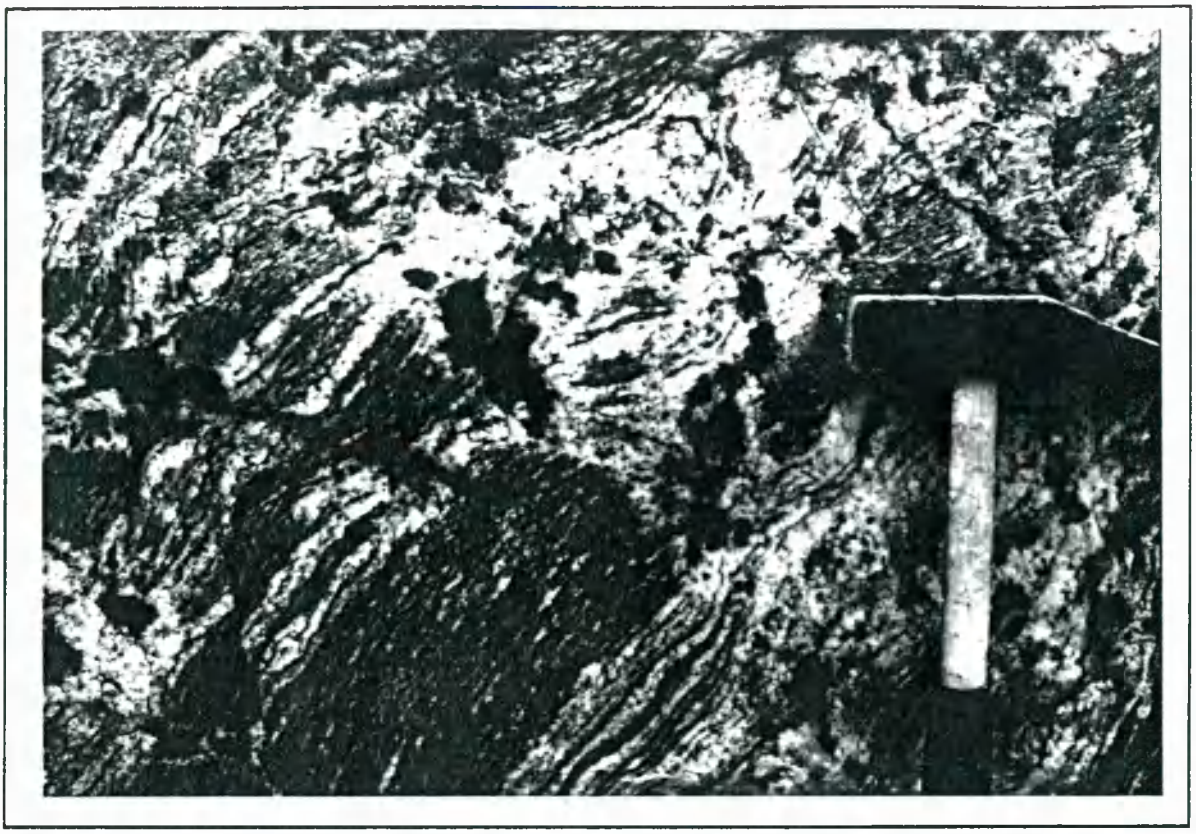

Plate 2.19. Detail of migmatitic pelitic gneiss present at Tato, NPHM. Fine stringers of leucosome locally truncate the metamorphic fabric. (The dark patches are lichen).

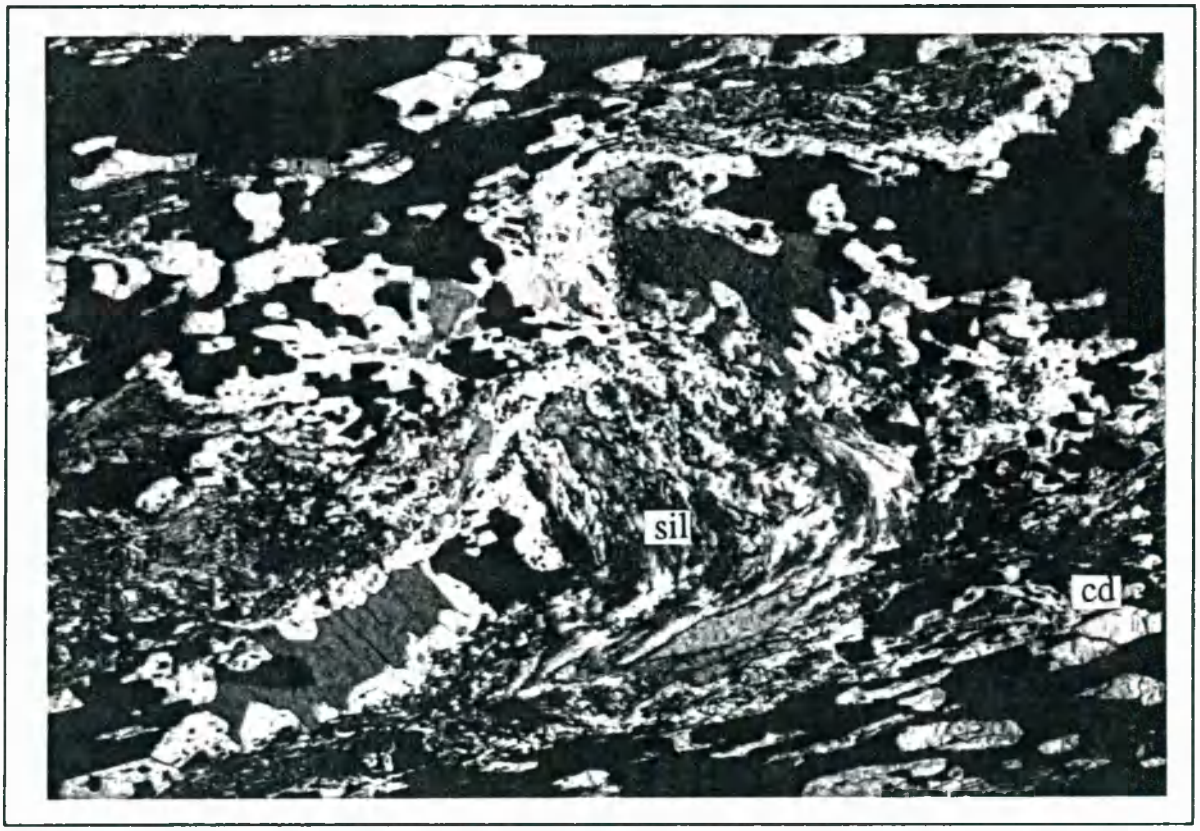

Plate 2.20. Photomicrograph of migmatite from Tato (sample M9) (XPL). Note the presence of fibrolitic sillimanite (sil) after biotite, and cordierite (cd).

packets of metasediments are also present. A newly constructed road between the Indus valley and Tato village presents excellent exposure across the strike of a typical sequence, southwards towards the interior of the NPHM. A structural map of the region is presented in Fig. 2.9, and a detailed lithologic log of a relatively metasedimentary-rich part of the road sequence is presented in Fig. 2.10.

The rocks in the Tato road traverse form a variable sequence of highly-deformed, amphibolite-grade lithologies dipping steeply southwards. For the first 2-3 km of the section, in the vicinity of the Liachar shear zone, the predominant lithology is a coarse-grained augengneiss with large feldspar porphyroblasts. In thin section, the orthogneiss is characterised by k-feldspar (30-50 %), plagioclase (10-30 %), biotite (15-35 %) and quartz (10-25 %), with accessory apatite and zircon. The enclosed metasediments include semi-pelites and psammites with subordinate amphibolites and calcsilicates, together with rare pelites (Fig. 2.9). Individual metasedimentary sequences reach thicknesses of 400 metres, but thin horizons of metasediment are often interbedded with the augengneisses on a scale of 1-2 metres.

The psammites and semi-pelites are medium-grained, well-foliated rocks characterised by the assemblage biotite (10-40 %), plagioclase (10-35 %), quartz (20-50 %) and sometimes muscovite (< 6 %) and tourmaline (< 5 %), together with opaque oxides and accessory phases such as apatite, sphene and zircon. Small, scattered grains of garnet (< 10 %) are occasionally present. Biotite locally shows slight retrogression to chlorite. The pelitic horizons contain muscovite and biotite in roughly equal proportions, together with scattered grains of tourmaline and garnet. According to Misch (1964) and Butler and Prior (1988b), kyanite is locally present, although none was found in this study. The tourmaline is found all along the Tato road, and occurs as highly-sheared, pulled-apart porphyroblasts lying within the main foliation. Inclusions of biotite and feldspar are sometimes present within the tourmaline.

The amphibolites and calcsilicates usually occur as well-defined, often intensely

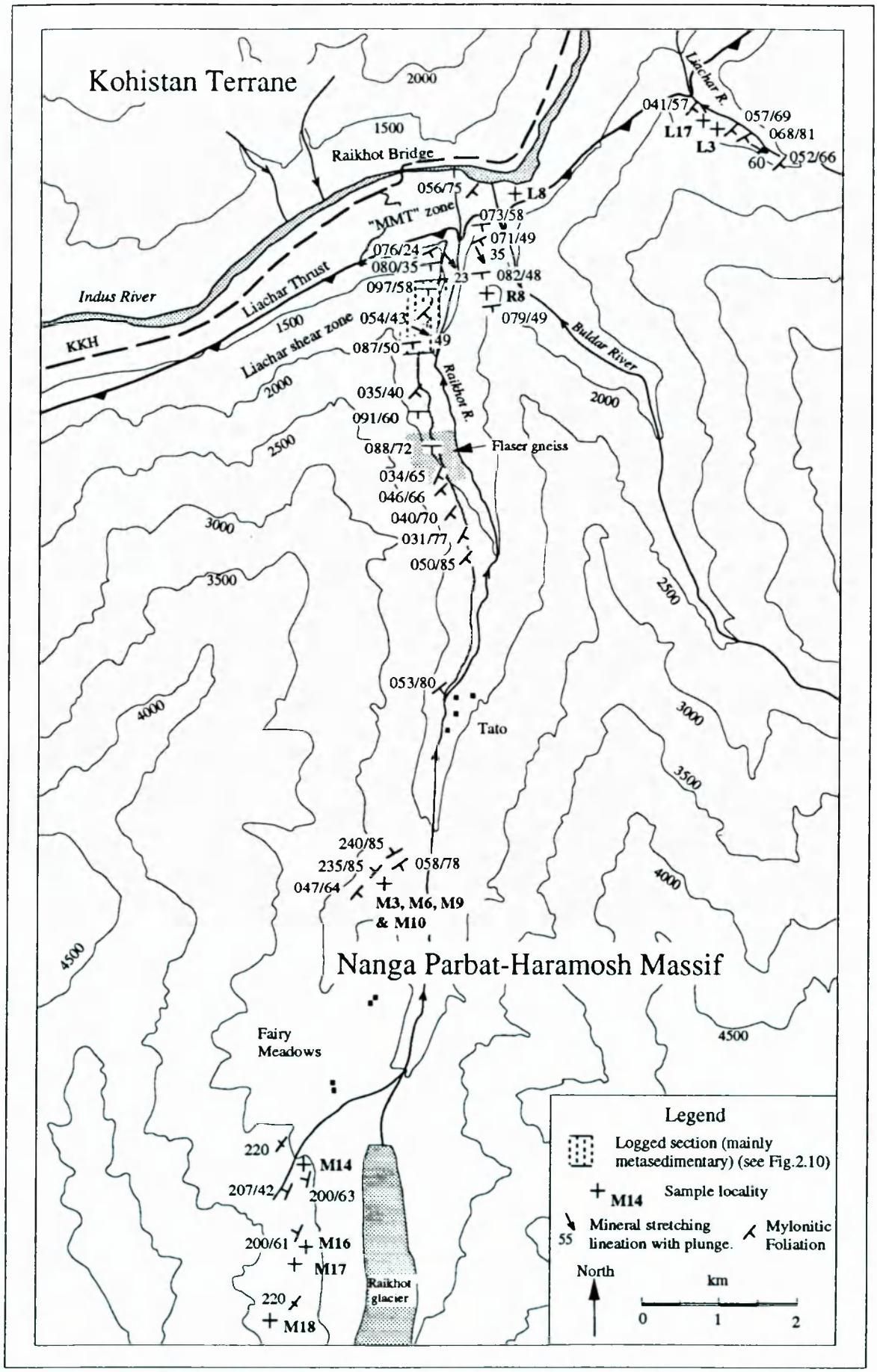

Fig. 2.9. Structural map of the Raikhot-Fairy Meadows Area, showing the localities of samples referred to in subsequent chapters. KKH = Karakoram highway. MMT = Main Mantle Thrust.Contours are in metres. For location, see Fig. 2.1.

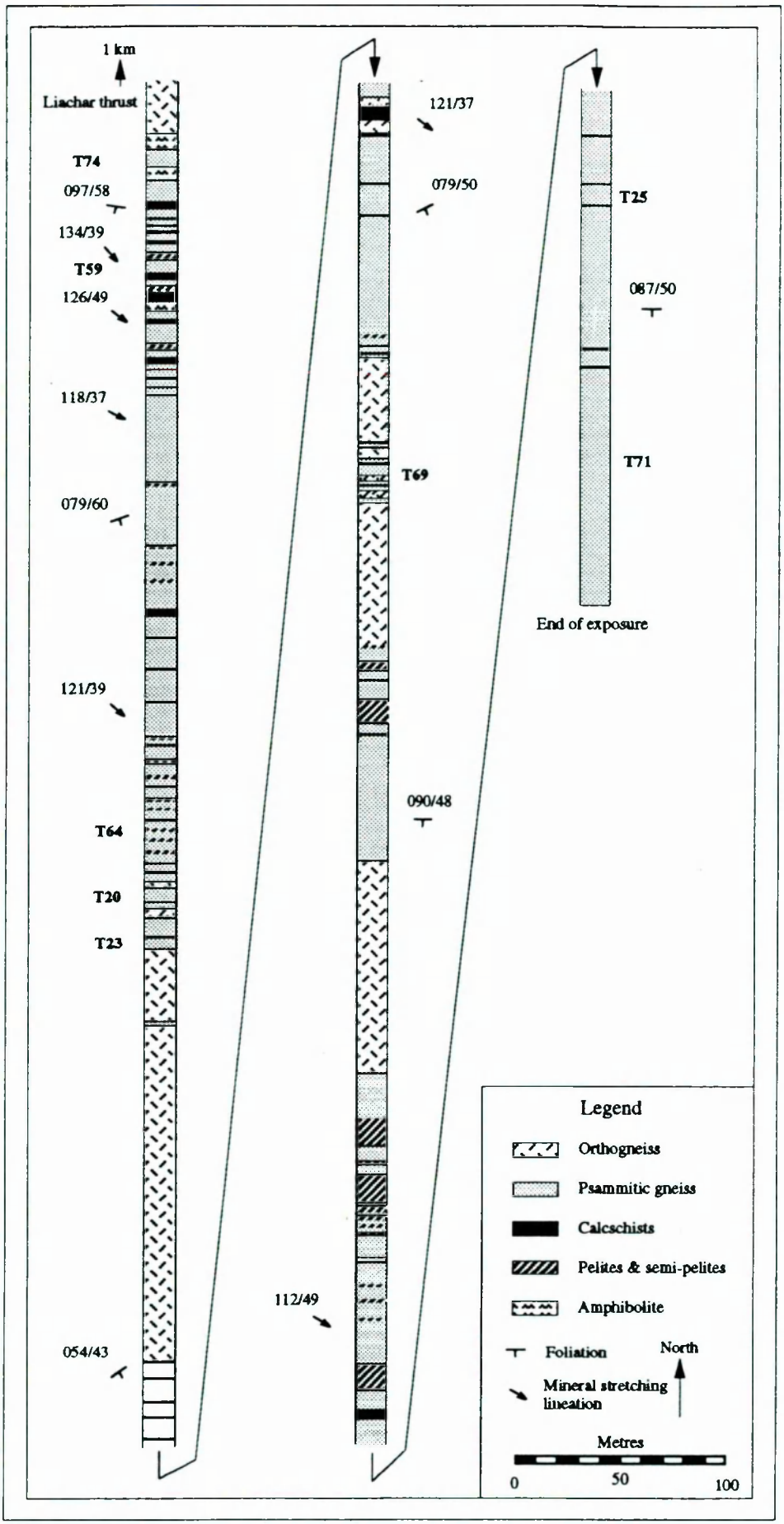

Fig. 2.10. Detailed lithological traverse through a typical metasedimentary sequence within the Liachar shear zone, Tato road section. Locations of samples referred to in later chapters are also indicated. For location of traverse, see Fig. 2.9.

sheared and boudinaged horizons between 0.5-2.0 metres thick. The amphibolites are dark, often highly-cleaved rocks which sometimes appear to have preferentially accommodated a high proportion of shear strain, since the adjacent gneisses are often more deformed than the gneisses further away. Thin sections indicate variable proportions of coarse, blocky hornblende and platy biotite, aligned in a quartz-feldspar groundmass. The typical assemblage is characterised by hornblende (20-50 %), biotite (10-60 %), plagioclase (5-30 %), quartz (10-30 %), sphene (1-8 %), ± k-feldspar (including rare microcline) (< 15 %), zoisite (< 5 %) and rare chlorite, apatite and opaque-oxides.

The calcsilicates are well-banded, pale-green, grey or cream rocks with variable mineralogical compositions. In thin section, the calcsilicates are characterised by relatively coarse, interlocking fabrics. The essential phases are quartz and plagioclase (An_{35-45}), with minor calcite, sphene, and either zoisite or epidote (Plate 2.18). Biotite and hornblende are also frequently observed. The plagioclase sometimes consists of large, often poikiloblastic grains of anorthite, showing marked repeated twinning and sericitic alteration. In addition, concentrated horizons occur which consist of coarse-grained, poikiloblastic diopside intergrown with granular, fine-grained and blocky grossular garnet.

Compositional layering on a millimetre-scale is common in all the metasediments, with metabasic hornblende-sphene horizons often alternating with more pelitic biotite-plagioclase horizons. The amphibolites grade into semi-pelites with a decrease in the proportion of modal hornblende, and they grade into calcsilicates with an increase in the proportion of zoisite and diopside. This fine layering, parallel to the foliation, may either reflect original sedimentary lamination, or later metamorphic differentiation.

In the middle of the section, an 800-metre thick, relatively massive body of biotite-flaser gneiss occurs (Fig. 2.10), which locally contains garnet. The margin between the flaser gneiss unit and the adjacent augengneisses is concordant and gradational. The presence of highly-deformed and streaked-out relicts of basic xenoliths, which reach lengths of up to one metre, indicates a magmatic origin for the flaser gneiss, although the age of

intrusion is unknown.

Near the village of Tato, approximately 8 km south-east of the Liachar fault, is a well-exposed sequence of inhomogenous and migmatitic metasediments. These include abundant interstratifications of calcsilicates, amphibolites and pelites, penetratively deformed and containing abundant, concordant, sheared segregations of leucosome. The interbanding of 'leucosome' and 'restite' occurs on all scales, from millimetres to several centimetres, but no large-scale masses of differentiated leucosome have been found. On a scale of centimetres, laterally discontinuous lenticles of leucosome, although themselves deformed, locally cross-cut the dominant metamorphic foliation, as shown in Plate 2.19.

The calcsilicates and amphibolites contain the same mineralogical assemblages as described above. However, the pelitic lithologies contain well-foliated biotite, plagioclase (An_{25}) and quartz, with sheared aggregates of fibrolitic sillimanite and cordierite (Plate 2.20). The leucosome consists of coarsely-grained quartz, k-feldspar and plagioclase, with varying proportions of biotite together with scattered garnet and sillimanite. The leucocratic segregations occur as sinuous veinlets or truncated blebs, locally making up to 40 % of the exposure. These are often indistinct, as the margins between the pale-coloured 'leucosome' and darker, more biotite-rich 'restite' are transitional. Aggregates of tourmaline are present in both portions of the migmatites.

The absence of muscovite, and the presence of restitic phases, suggests that the Tato migmatites were generated by in-situ melting. The absence of large segregations of melt, and the syn-kinematic nature of the migmatites, suggests that the melts may have been generated by the breakdown of muscovite (Patino Douce et al. 1991). The absence of restitic k-feldspar suggests that fluid-present conditions probably prevailed (Harris and Inger 1992)

2.4.6. Amphibolite Dykes

Amphibolite dykes and sheets occur sporadically throughout the NPHM. Whereas

the previously described amphibolites are associated with indisputably metasedimentary material (calcsilicates and pelites), the amphibolites that are discussed in this section show no such association, and are often found as isolated sheets within the larger orthogneiss units (such as the Iskere gneiss). Leake (1964) noted that the association between amphibolites and metasediments cannot be taken as complete proof of a sedimentary origin for the amphibolites, since such 'banded' amphibolites may also be generated by tectonic thinning of interbedded sequences of metabasic sills and metasediments, or by metamorphic segregation. On the other hand, the isolated amphibolite bodies present in the NPHM were probably originally basic dykes, although such an origin cannot be proved by the diagnostic geochemical trends of Leake (1964), owing to a shortage of geochemical data.

The amphibolitic dykes are generally one or two metres thick, although they occasionally reach nine or ten metres across. The amphibolites invariably possess penetrative deformation fabrics at amphibolite-grade. However, in many exposures, the dyke margins are demonstrably oblique to the regional metamorphic foliation. In the Iskere valley, metabasic dykes are folded within the Iskere antiform, but within the fold, dykes lie at a slightly oblique angle to the main foliation (see Fig. 3.1). These amphibolite dykes are also occasionally cut by undeformed pegmatites. Within the Liachar shear zone, the metabasic sheets are concordant, boudinaged and highly sheared by the simple shear fabrics. Throughout the NPHM, the metabasic dykes are commonly cross-cut by leucogranite sheets (Fig. 2.7D).

All of the amphibolites are characterised by retrogressive mineral assemblages and show only limited evidence for primary mineralogies. Some of the dykes are composed of hornblende and biotite in varying proportions, together with sphene, plagioclase and quartz. Other metabasites contain relict, rounded porphyroblasts of olivine (Fo_{54-64}) up to 2.5 cm across and/or corroded porphyroblasts of clinopyroxene up to 2-3 mm across (Plate 2.21). The olivine grains often have ragged, fractured margins rimmed with opaque-oxides, and contain abundant, randomly-orientated inclusions of secondary actinolite and chlorite. The olivine and pyroxene porphyroblasts lie within a fine-grained, highly-sheared groundmass

composed of chlorite, actinolite and opaque-oxides. The olivine porphyroblasts show little preferred orientation and give hand-specimens a characteristically spotted appearance. Presumably this reflects the hardness of olivine grains, which fracture before undergoing crystal-plastic deformation.

The presence of metabasic sheets in a predominantly granitic basement massif is an interesting phenomenon, and it is unfortunate that the dykes have not been dated. The fabric relationships indicate that the basement lithologies had suffered a penetrative deformation before intrusion of the basic dykes. Further deformation post-dated dyke intrusion, which, in the Iskere valley, involved large-scale folding on a north-south axis.

2.4.7. Leucogranites of the Nanga Parbat-Haramosh massif

Dykes and sheets of leucogranite have a widespread but scattered distribution across the NPHM. Whilst earlier workers (Coward et al. 1986) noted the presence of leucogranite bodies in the NPHM, this is the first detailed study of their field and geochemical characteristics. It should be emphasised that all of the leucogranites that have been studied in this work are clearly cross-cutting, and the amphibolite-grade wallrocks locally contain fabric-forming muscovite. Evidently the leucogranite magmas have been able to separate from their source regions. Clear evidence for in-situ melting has only been observed in the Tato region. Such allochthonous leucogranites should be differentiated from the syn-kinematic migmatites of unknown age that are widespread in the NPHM, and which led Misch (1949) to suggest that the massif had been widely affected by metasomatic granitisation.

Leucogranite dykes are generally 0.5-2.0 metres thick and traceable for 10-100 metres, although larger sheets at least 5 metres across were also observed in the region. The dykes are often coarse-grained and heterogeneous, with both grain-size and modal proportion of phases varying both along and across strike. In some areas of the NPHM, the leucogranite dykes occur in distinct swarms of parallel-sided bodies, often well-exposed on inaccessible mountainsides, whilst elsewhere they occur as more irregular bodies with

sinuous margins, or as isolated, planar bodies (Plate 2.22). The variable intrusive style presumably reflects a combination of factors such as the temperature, composition, water content, depth and size of intrusion, together with the temperature and structure of the country rocks. For example, the emplacement of the relatively planar bodies may have been controlled by brittle fracture of the country rocks. In contrast, the more sinuous bodies appear to have been emplaced relatively passively, perhaps due to higher contents of volatiles in the magma.

In the interior of the NPHM, the majority of leucogranite dykes are undeformed, although some dykes are affected by localised shearing. Leucogranite dykes are often orientated sub-parallel to the regional metamorphic fabric, suggesting that the foliation acted as a relative plane of weakness during intrusion. Elsewhere, leucogranite dykes strongly cross-cut the regional foliation. Where possible, the orientation of the relatively straight dykes was measured. The data shown in Fig. 2.11 confirm that many of the leucogranite dykes have intruded approximately parallel to the regional foliation, which in general trends steeply north-south, although leucogranites in different parts of the NPHM have contrasting orientations.

The Jutial granite is a relatively large, medium-grained pluton or sheet complex that can be traced for 2.5 km along the Phuparosh valley at an elevation of 2150 m (Fig. 2.2). In most exposures, the granite consists of a network of leucogranite sheets and irregular masses, locally showing magmatic flow-banding (Plate 2.23). The leucogranite bodies are separated by large roof-pendants of paragneiss, so that granite seldom makes-up more than 60 % of any given exposure. The roof-pendants maintain a constant orientation with respect to the regional foliation in the country-rocks, suggesting a fairly passive intrusion of magma. In general, the margins between the Jutial granite and its wallrocks are abrupt (Plate 2.24). However, the margins are locally characterised by foliation-parallel interleaving of 1-2 cm thick layers of leucosome and wallrock, as shown in Plate 2.25. This interleaving may have been generated by the following processes :

(i) Local segregation of partial melt in the high-grade wallrocks contributing to the magma.

Plate 2.21. Detail of highly-retrogressed basic dyke exposed in the Liachar shear zone, Liachar valley. Note the large rounded phenocrysts of olivine, the dark grains of clinopyroxene, and the chloritic groundmass.

Plate 2.22. View of scattered leucogranite sheets intruding well-layered Shengus gneisses, exposed in a 1000+ metre high mountainside above the Indus river.

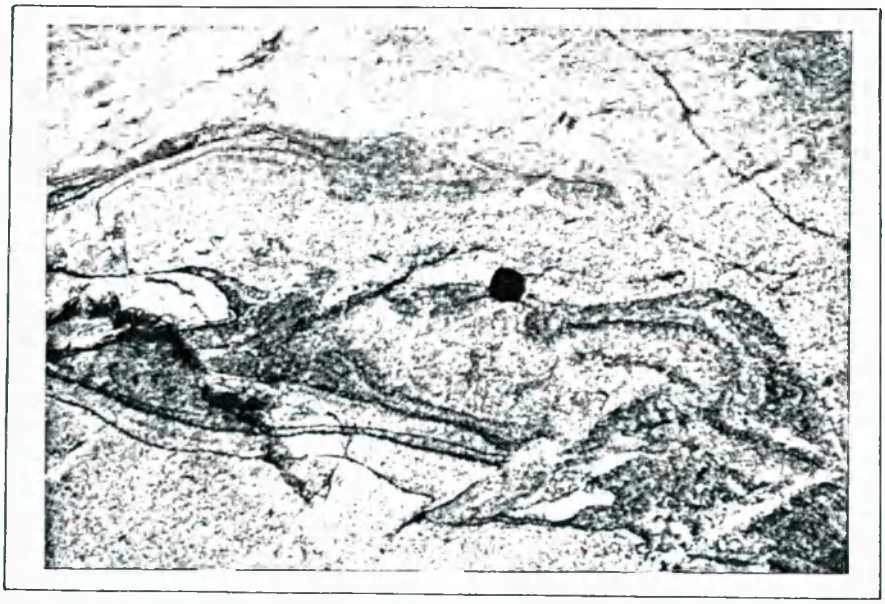

Plate 2.23. Magmatic flow banding in the Jutial granite, Jutial valley. Lens cap for scale.

Plate 2.24. Jutial granite sharply truncating the foliation of locally migmatitic wall-rock gneisses, Jutial valley. Hammer is 30 cm long. Samples J15, J16 & J17 were collected from this locality.

Plate 2.25. Detail of margin to the Jutial granite, showing local injection of leucosme along foliation planes of well-banded wall-rock gneisses (sample J18).

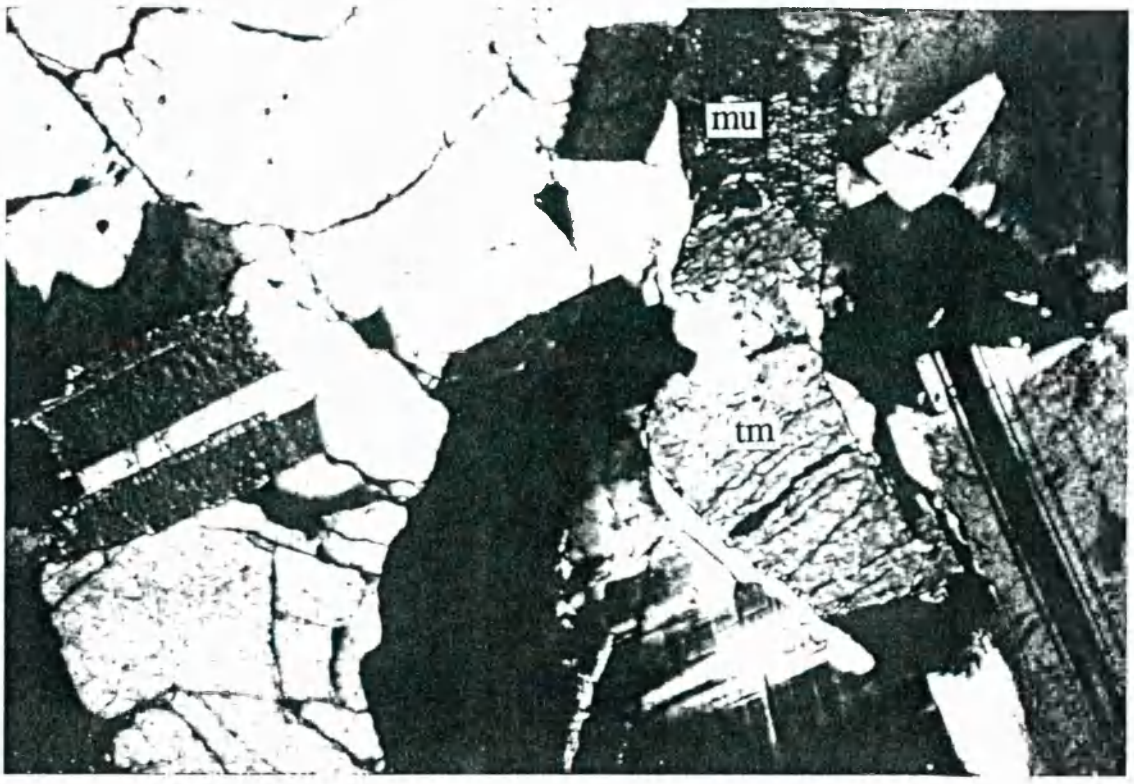

Plate 2.26. (above) Photomicrograph of undeformed leucogranite dyke collected from near Shengus in the Indus gorge (sample S92) (XPL). Note the presence of tourmaline (tm) and muscovite (mu).

Plate 2.27. (right) Detail of highly sheared, pegmatitic leucogranite dyke present in the Liachar shear zone. Note the segregation of quartz and tourmaline in the boudin neck, and the deformation-enhanced interlayering between the leucosome and the wall-rock.

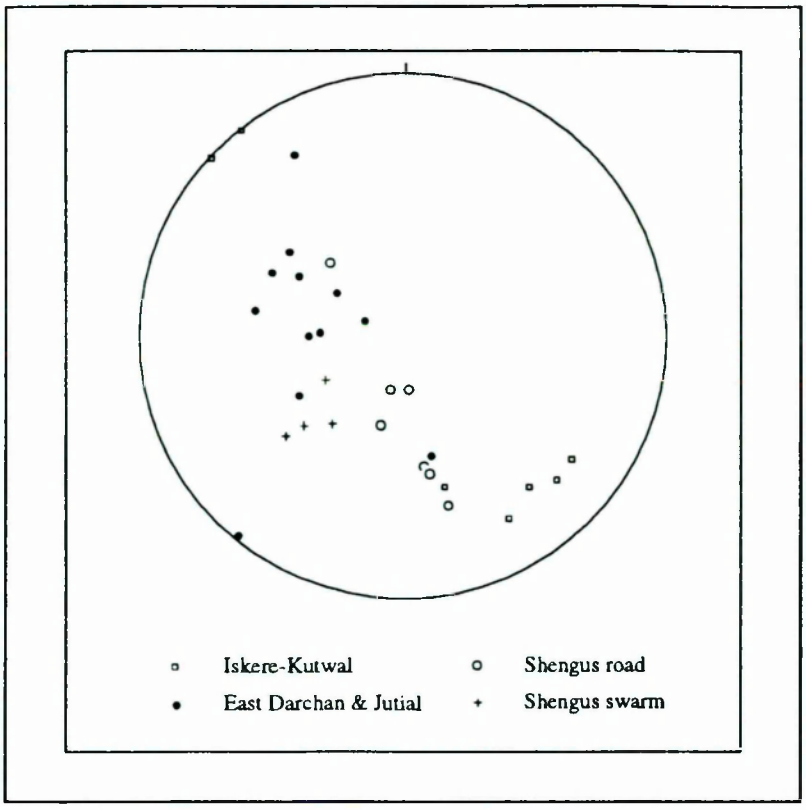

Fig. 2.11. Schmidt equal area projections of the Nanga Parbat-Haramosh massif leucogranites (poles to sheet margins).

(ii) Local injection of leucocratic melt from the Jutial granite into the wallrocks, parallel to the foliation, during granite emplacement.

The presence of fabric-forming muscovite in the wallrocks, and the absence of typical restitic phases, rules-out an origin by in-situ melting in the country rocks, and therefore the leucosome is thought to have an allochthonous origin.

On a large scale, the boundaries of the Jutial granite are difficult to define, partly due to lack of exposure, and partly because the margins of the complex are characterised by a gradual decrease (or increase) in the proportion of granite exposed, whilst the relative proportion of country-rock increases (or decreases).

The field evidence suggests that the NPHM leucogranites reflect a number of different intrusive pulses of magma. For example, at one locality, the Jutial granite cross-cuts an earlier biotite granite sheet. Similarly, in the Phuparosh area, numerous irregular

masses and heterogeneous sheets of two-mica leucogranite are locally cross-cut by younger leucogranite sheets which are characterised by a predominance of muscovite and tourmaline, together with subsidiary garnet. Thus the leucogranites of the NPHM were probably intruded over an extended time period. This accounts for much of the observed variation in intrusive style, orientation and composition of the leucogranites examined.

Larger bodies of leucogranite, up to 50 m thick, also occur in the Fairy Meadows area, and have also been described by Smith et al. (1992). These are relatively massive and well-jointed bodies, locally characterised by conspicuous clots of biotite, and intruded into a series of migmatitic metasediments (described in section 2.4.5). In the Haramosh region, near the village of Iskere, an undeformed, ten-metre thick body of coarse-grained quartz-diorite is present (see Chapter 6).

The Jutial granite is composed of equal proportions quartz, oligoclase and microperthite, together with biotite (5-10 %) and muscovite (2-10 %), with rare, skeletal tourmaline. Zircon and apatite are common accessory phases.

The leucogranite dykes are mineralogically variable, and are composed of equal proportions of quartz, plagioclase and k-feldspar, together with muscovite (5-15 %), ± biotite (< 4 %), ± tourmaline (< 10 %) (Plate 2.26). Garnets are occasionally present (< 1 %), and occur as small, corroded grains. These have relatively high spessartine contents ($Alm_{69}\ Py_2\ Gr_1\ Sp_{28}$) as shown in Table 2.1, which is indicative of an igneous paragenesis (Green 1977). Accessory minerals include apatite, zircon and occasionally sphene. The biotite is locally retrogressed to chlorite. The majority of leucogranites are muscovite-tourmaline bodies with variable proportions of biotite. However, dykes containing biotite and tourmaline, in the absence of muscovite, have also been frequently observed.

The tourmaline occurs as euhedral, well-zoned grains of schorl, and is believed to be magmatic in origin since it occasionally forms inclusions in garnet. The tourmaline is sometimes found preferentially developed adjacent to the margins of the leucogranite bodies, and the tourmaline grains are sometimes orientated perpendicular to these margins. The presence of tourmaline in most of these sheets distinguishes them in the field from the

Parri granites of the Kohistan arc (described above).

As mentioned above, in the interior of the NPHM, the majority of leucogranites are undeformed. In thin-section, these granites exhibit a granular, interlocking texture with no preferred orientation (Plate 2.26), although magmatic phases banding is occasionally present. However, some leucogranites exhibit a weak preferred orientation of quartz grains, sutured grain boundaries and associated secondary growth of chlorite and muscovite.

In contrast to the relatively undeformed leucogranites described above, a suite of highly deformed leucogranite dykes and pegmatites occurs within the recently-active Liachar shear zone. These are generally coarse-grained, extremely heterogeneous bodies characterised by varying proportions of biotite, muscovite and often highly fractured tourmaline. Feldspar tends to form relatively resistant porphyroblasts in a highly sheared matrix that is predominantly composed of aligned grains of quartz. The dykes are often highly attenuated, folded and boudinaged, and range in thickness from 10 cm to 2 metres. Some boudins show marked segregation of quartz within the 'pinches' relative to feldspar within the 'swells' (Plate 2.27). This feature was also observed in many of the highly boudinaged horizons of calcsilicate and amphibolite that are present in the shear zone, and is presumably due to differential diffusion during shearing. Individual bodies are mostly concordant with the dominant mylonitic foliation; however, locally they abruptly cross-cut the foliation over distances of 1-2 metres, where there is a noticeable increase in dyke thickness. Some leucogranites appear to have been deformed during intrusion, as suggested by the occurrence of thin veins of leucosome that have been partially sheared-out along the mylonitic foliation planes (Plate 2.27). These features suggest intrusion of leucogranite was synchronous with movements within the shear zone. Folded and sheared leucogranite sheets form useful kinematic indicators, as described in Chapter 3.

Chapter 3

The Structure and Origin of the Nanga Parbat-Haramosh Massif

3.1. Introduction

The anomalous structure of the Nanga Parbat-Haramosh massif was recognised by the earliest workers in the region, and has been the subject of increased research interest over the last decade or so. The aim of this chapter is to describe both the local and regional structural characteristics of the NPHM, and the origin of these structures within a tectonic framework. Emphasis will be placed on the interpretation of shear sense indicators in order to help define the local kinematics (Simpson and Schmidt 1983). Many of the areas that have been studied in detail in this work have also been described by previous workers (Butler and Prior 1988a, 1988b; Butler et al. 1989; Madin et al. 1989; Treloar et al. 1991). However, new kinematic data are presented from the western margin of the NPHM in the Sassi, Darchan and Liachar areas.

3.2. Previous Work

3.2.1. Structure of the Interior Region

The NPHM is unusual in that it exposes originally deeply-buried Indian continental crust more than 100 km north of its normal outcrop. This crust has been uplifted, from beneath the overthrust rocks of the Kohistan arc, within a north-trending antiformal structure with a half-wavelength of over 30 km (Coward 1985; Treloar et al. 1991). Recent studies have indicated that in detail, the interior of the NPHM is characterised by a series of separate, north-south trending folds, as shown in Fig. 3.1 (Butler et al. 1992, Treloar et al.

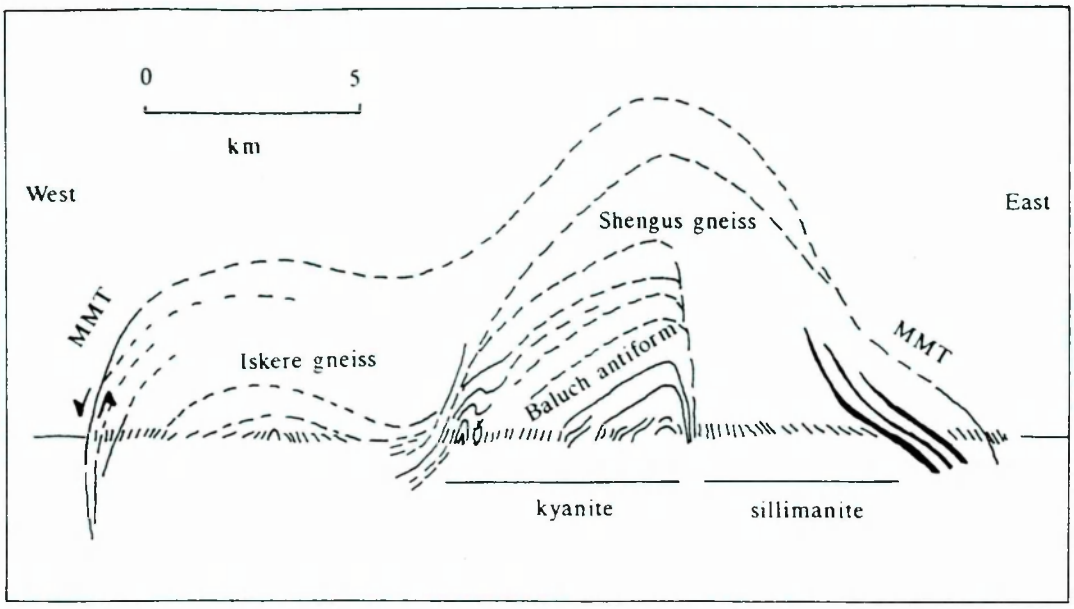

Fig. 3.1. The Indus section through the NPHM (after Treloar et al. 1991).

1992).

Coward (1985), Coward et al. (1986) and Treloar et al. (1991) have described the geology of the NPHM along the Indus section. The foliation is an intense ductile fabric, often mylonitic in character, within which a pervasive mineral stretching lineation plunges gently north or south. Near the western margin, however, the mineral stretching lineation takes on a steeper plunge towards the north-west, reflecting younger displacements along this margin (see below). The peak metamorphic assemblages are usually found to have been re-worked by intense shear-fabrics, but recrystallisation of microstructures generally prohibits any useful kinetic interpretation being made on these fabrics (Treloar et al. 1991). The shearing and the development of the main foliation and lineation probably record south-verging crustal thickening of the Indian crust in the foot-wall of the Main Mantle Thrust (MMT), presumably beneath the Kohistan arc (Treloar et al. 1992).

Coward (1985) and Coward et al. (1986) considered that the main foliation, and the original MMT, are F1 structures which have been folded by tight, asymmetric F2 structures facing east. According to Coward (1985), the F2 fold hinges trend NNW-SSE and are

approximately parallel to the mineral stretching lineations and to F1 and F2 sheath folds, which together suggest a SSE-directed overthrusting during F1 and F2. The F1 and F2 structures have been re-orientated about a large, crustal-scale F3 fold, which also caused the steepening of east-west trending fold axes in adjacent parts of Kohistan. However, using geochronological data, Treloar et al. (1991) showed that the F2 folds of Coward (1985) were related to the uplift of the NPHM at 3-4 Ma. The largest of these is the Baluche antiform which folds the Shengus gneisses, and has a half-wavelength of 15 km (Fig. 3.1). Other north-south trending folds occur within the Iskere gneisses, for example in the Iskere valley, where the gneisses are folded in the limbs of the large-scale Iskere antiform (Plate. 3.1). This antiform is the main structural manifestation of the NPHM fold in the Haramosh region. The fold axis strikes north-south across the valley just east of Barche and plunges gently towards the north. To the west of the fold axis, as far as the western margin of the NPHM, gneisses dip steeply westwards, whereas to the east of the axis, at least as far as Haramosh La, the gneisses dip steeply east (see Fig. 2.2).

3.2.2. Structure of the Marginal Regions

Relatively little work has been carried out on the eastern margin of the NPHM. According to Verplanck et al. (1985), in the Indus gorge the eastern margin of the NPHM is marked by an 8 km-wide, high-angle fault zone (the Stak fault) which in the south intersects the MMT. This fault zone has been recently active, as shown by offset stream channels and glacial till, together with hot-spring activity (Verplanck et al. 1985). However, according to Treloar et al. (1991) the eastern margin of the NPHM is a predominantly ductile, concordant contact equivalent to the MMT, which has been passively steepened during folding of the NPHM.

Recently active faulting has also been taking place along the western margin of the NPHM. In the Raikhot area (Fig. 3.2), brecciated fan-gravels and hot springs delineate a steeply-dipping fault zone which has a downthrow to the north or north-west (Lawrence and

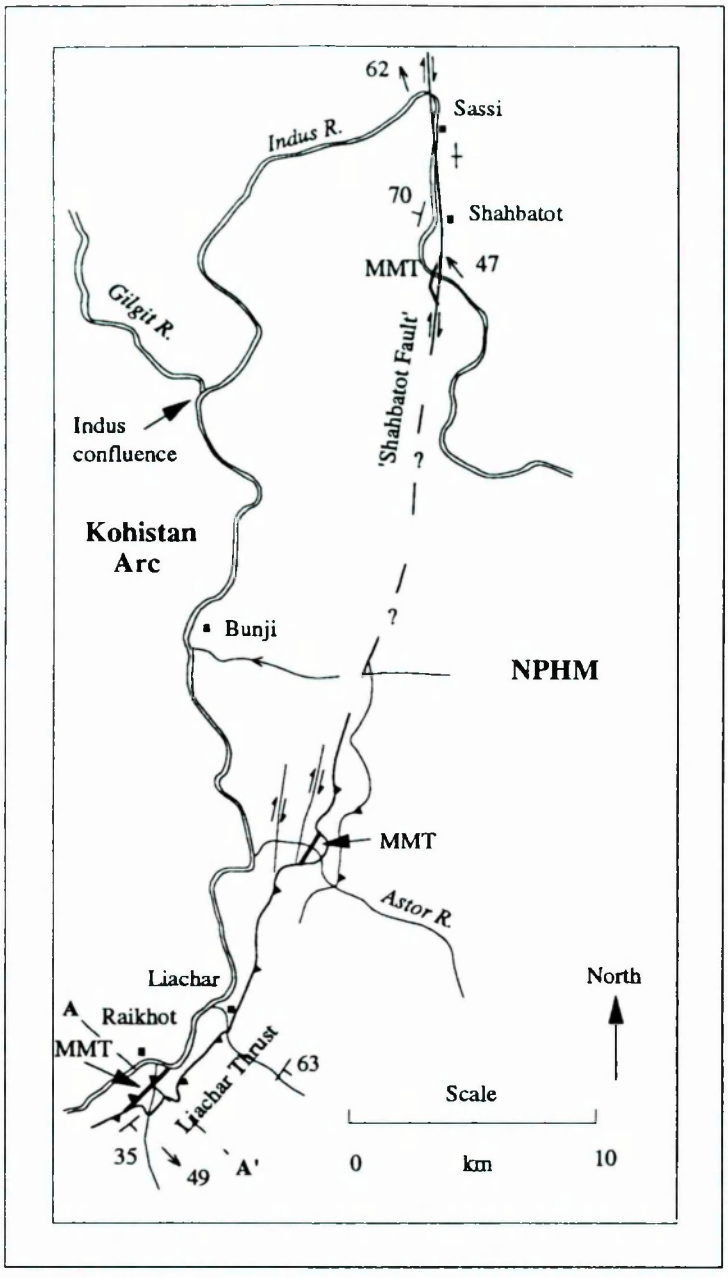

Fig. 3.2. Sketch map showing the broad structural characteristics of the western margin of the NPHM, after Butler et al. (1989). For location, see Fig. 2.1. MMT = Main Mantle Thrust. A - A' = location of Fig. 3.3. Refer to earlier figures for legend to structural symbols.

Ghauri 1983). Lawrence and Ghauri (1983) suggested that the fault zone had a reverse sense of movement, and may have accommodated some of the uplift of the NPHM. Butler and Prior (1988b) investigated the structure of this fault zone in more detail, which they called the Liachar thrust. In its type area in the lower Liachar valley, the thrust is a 20-metre thick zone of micro-brecciation and gouge, with kinematics indicating an overthrusting of Indian

crust northwards over the Kohistan arc (Fig. 3.3). Near Liachar village, the thrust zone over-rides Quaternary Indus valley sediments (Butler et al. 1989). Displacement on the Liachar thrust probably triggered the landslip which caused the great Indus flood of 1840-1841 (Butler et al. 1988).

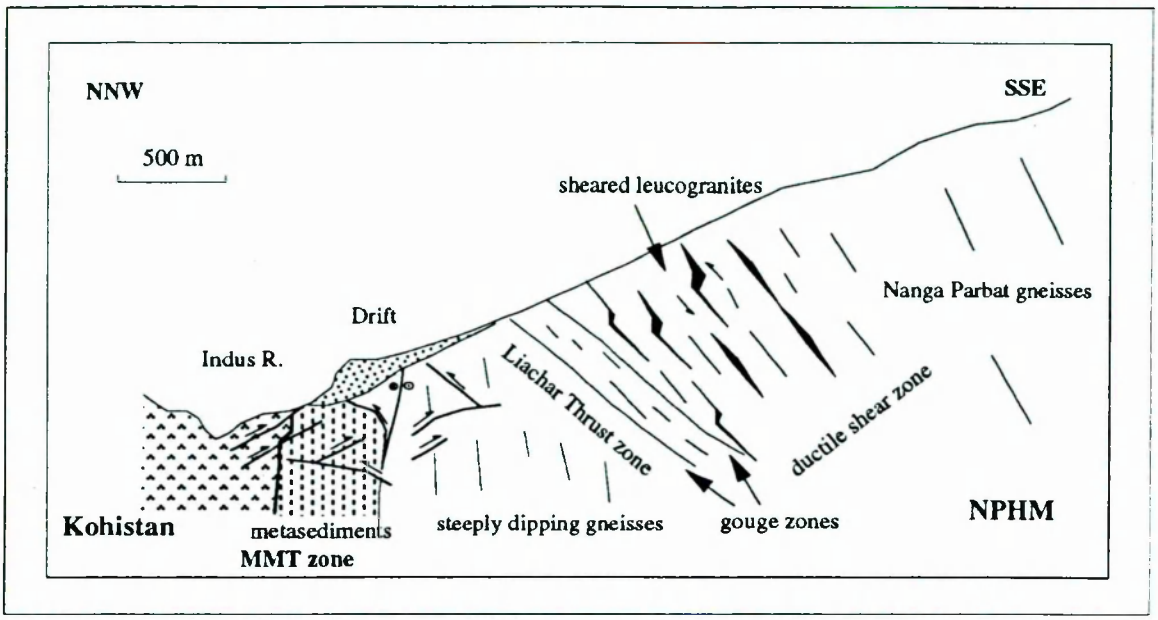

Fig. 3.3. Sketch section across the Liachar thrust zone (A-A', Fig. 3.2), after Butler et al. (1989). The north-west directed Liachar thrust is underlain by a steep belt of flattened Nanga Parbat gneisses and metasediments in the MMT zone.

The Liachar thrust carries in its hanging-wall the 3 km-wide, south-east dipping Liachar shear zone. This shear zone operated from amphibolite-facies to the present topographic surface, and shows the same kinematics as the underlying Liachar thrust (Butler and Prior 1988b).

In the immediate footwall of the Liachar thrust, a strip of steeply-inclined, high-grade and highly-sheared metasediments separate the NPHM from the Kohistan arc, and probably formed part of the original MMT sequence (Butler and Prior 1988b) (Fig. 3.3). According to Butler and Prior (1988b), these metasediments may represent a Phanerozoic cover to the Precambrian Indian basement. The metasediments contain stretching lineations which plunge towards the south-west, in contrast to the regional NNW plunge azimuth for the Indian continental crust. Strike-slip fault zones are also present, and locally have a dextral sense of

movement (Butler et al. 1989). The foliation was probably steepened, and the stretching lineations folded, during the uplift of the NPHM (Butler et al. 1989).

In the Sassi area, 50 km to the north of Liachar (Fig. 3.2), a range of metasedimentary and metabasic lithologies are deformed in a steeply-inclined, north-south trending shear zone. According to Butler and Prior (1988a) parts of this zone are characterised by an early penetrative deformation which, once latter structures have been untilted, indicates top to the SSE thrusting under amphibolite-facies conditions. Since this movement sense is consistent with the relative motions across the suture predicted by plate reconstructions, the ductile structure was correlated with the MMT. However, Butler and Prior (1988a) recognised that, as upper arc rocks are here juxtaposed against the Indian continent, this segment of the 'MMT' is not the primary suture, but instead may be a form of break-back thrust. The absence of ophiolitic rocks or blueschists in the shear zone also indicates that the original suture zone has been extensively modified.

The shear zone fabrics at Sassi are dominated by later dextral strike-slip, associated with the Shahbatot fault of Butler et al. (1989). Overprinting relationships suggest that this strike-slip zone has migrated southwards into the north-west directed Liachar thrust zone (Butler et al. 1989). According to Madin et al. (1989), the entire western margin of the NPHM consists of a dextral strike-slip zone (the Raikhot fault), which has a component of reverse-slip movement. Madin et al. (1989) argued that this fault zone was a late structure, accommodating much of the uplift of the NPHM, and completely removing the trace of the MMT. However, the work of Butler and co-workers (op. cit.) suggests that, firstly, the MMT zone is still present, albeit often modified by younger movements, and secondly that the structural character of the western margin of the NPHM varies in a north-south direction along strike.

Around the northern outcrop termination of the NPHM, the contact between the NPHM and the Kohistan arc is a broad, concordant and ductile fold structure which plunges

at about 20° towards the north, and which has been correlated with the MMT (Butler et al. 1992). According to Butler et al. (1992), the contact is associated with the interleaving of Indian plate and Kohistan lithologies, and overlies a sequence of well-banded Indian plate gneisses which Butler et al. (1992) termed the Layered-unit. However, as described in Chapter 2, this unit contains abundant sheets of deformed Kohistan-granite and metabasic material, and in this work is interpreted as being a continuation of the sequence of intercalated lithologies from Sassi (see Fig. 2.2).

Further structural data from the Sassi area, and also from the Darchan valley, are presented below.

3.3. Kinematics of the western Margin of the NPHM

3.3.1. Sassi-Darchan Region

The contact zone between the NPHM and the Kohistan arc is well exposed in the floor of the Indus valley between Hanuchal and Shahbatot, where the river flows parallel to the strike for about 6 km (Fig. 3.2; Plate 3.2). Here the western margin of the NPHM is marked by a wide zone of highly sheared, intercalated metasediments and metabasics (Chapter 2). The mylonitic foliation within this shear zone strikes north-south and generally dips steeply towards the west (Fig. 3.4), although to the south of the village of Shahbatot the dip of the foliation is locally more moderate. The shear zone can be traced northwards as far as the upper part of the Darchan valley, where the foliation has a moderate dip towards the NW (Fig. 3.5). The mylonitic foliation in the shear zone is often tightly folded on a scale that ranges from several centimetres to tens of metres. Relatively ductile calcsilicate horizons often exhibit intense folding, as shown in Plate 3.3. Granite sheets are also often caught-up by the folding (Plates 3.4 & 3.5). The axial planes of the folds are generally approximately parallel to the foliation, and the fold axes plunge towards the north-west, sub-parallel to the mineral stretching lineation (Fig. 3.4). Presumably, the folds have been rotated into the

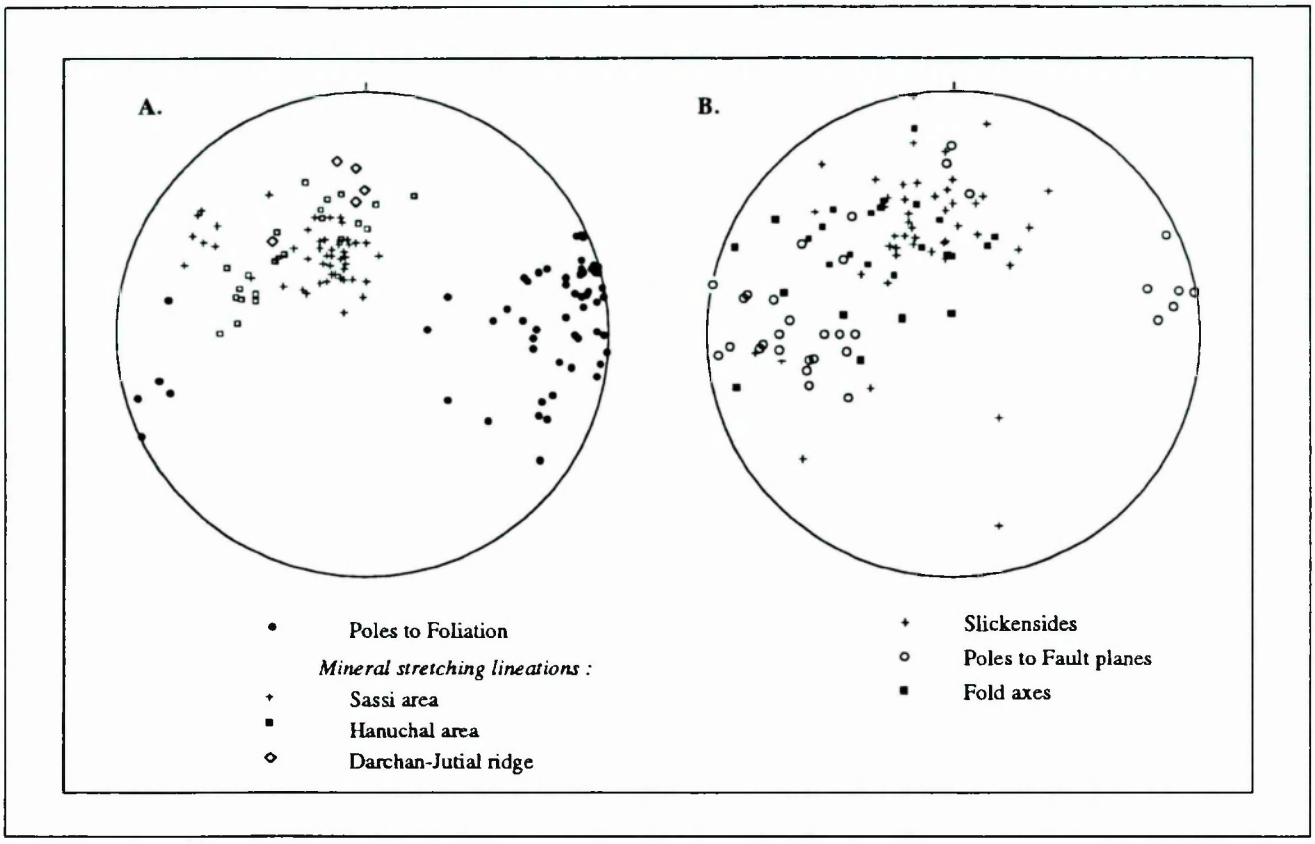

Fig. 3.4. Schmidt equal area projection of structural data from the Sassi-Hanuchal shear zone.

direction of maximum extension by the intense shearing.

The intercalated metasedimentary lithologies are generally intensely deformed, with a strong penetrative mylonitic foliation defined by elongate quartz and feldspar, and flakes of mica. Quartz-rich lithologies often display marked grain size reduction. The degree of ductile deformation varies markedly and abruptly across the strike of the shear zone, on a scale of millimetres to tens of metres. This varying ductility is probably due to variable lithology or fluid content, together with the accommodation of heterogeneous strain along discrete layers. In the central portion of the shear zone, calcsilicate layers are locally reduced to ultramylonite, characterised by highly sheared porphyroblasts of diopside and anorthite in a fine-grained, flow-banded groundmass (Plate 3.6).

Along the entire length of the Shahbatot-Darchan section (24 km), mineral stretching

Plate 3.1. (above) View of the Iskere antiform exposed in the north wall of the Iskere valley. Basic dykes are also folded, but locally lie oblique to the foliation (x).

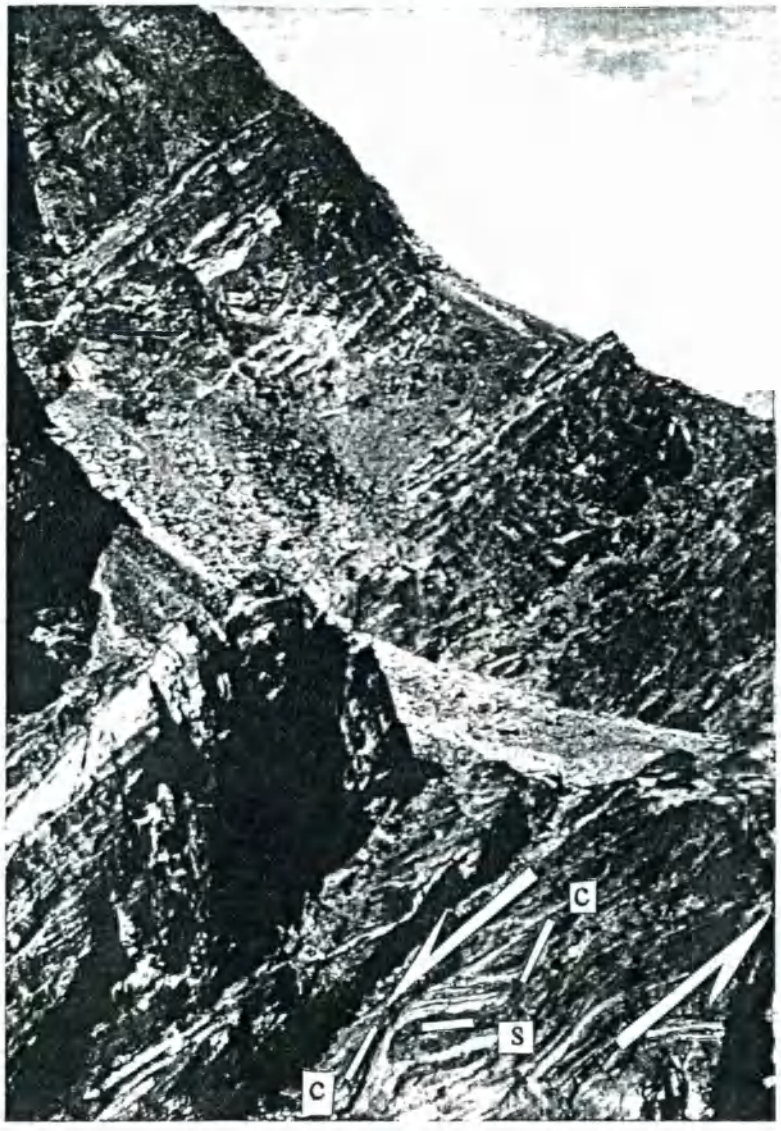

Plate 3.2. (right) View , looking north, of the shear zone bordering the western margin of the NPHM near Shahbatot. The foliation dips moderately towards the west (left). The upper levels of the shear zone are dominated by Kohistan lithologies which enclose highly deformed granite sheets (Confluence and Parri granites). The lower levels (bottom right) are characterised by pelites and calcsilicates with large-scale shear bands indicating extensional movement with hanging-wall down to the west.

Plate 3.3. Detail of isoclinally folded and contorted horizon of relatively ductile calcsilicate, enclosing a 10 cm thick horizon of amphibolite; Shahbatot. North is towards the left.

Plate 3.4. Highly deformed and folded sheet o muscovite-garnet granite (Parri granite) present in th shear zone at Sassi (sample G29). Note hammer fo scale.

Plate 3.5. Folded and boudinaged granite sheet present in the shear zone at Sassi, indicating a component of dextral shear. The foliation is approximately vertical. North is towards the right.

Plate 3.6A Photomicrograph of ultramylonite in a calcsilicate lithology, Sassi (sample S27) (PPL). The left half of the section is composed of coarse-grained quartz, diopside (di) and calcite (cc); the right half is composed of a ground-down, fine-grained ultramylonite with rare diopside and feldspar porphyroblasts.

Plate 3.6B. Detail of the ultramylonite sample (S27) (PPL). The diopside porphroblasts are locally characterised by folded tails of recrystallised material, a feature which is diagnostic of porphyroblast rotation during intense shear strain, and in this case indicative of sinistral shear. Field of view is 2.5 mm.

Plate 3.7 (right) Mineral stretching lineation in a marble at Sassi. The lineation is marked by elongate grains of opaque oxides, and plunges steeply towards the north-west.

Plate 3.8. (below) Large-scale shear band marked by attenuated and folded granite sheets, in the shear zone near Sassi (rucksack for scale). Granite sample G48 was collected from the 2-metre thick body visible in the top of the photograph. North is towards the right; the foliation is dipping into the rock-face. The shear band suggests a component of dextral shear.

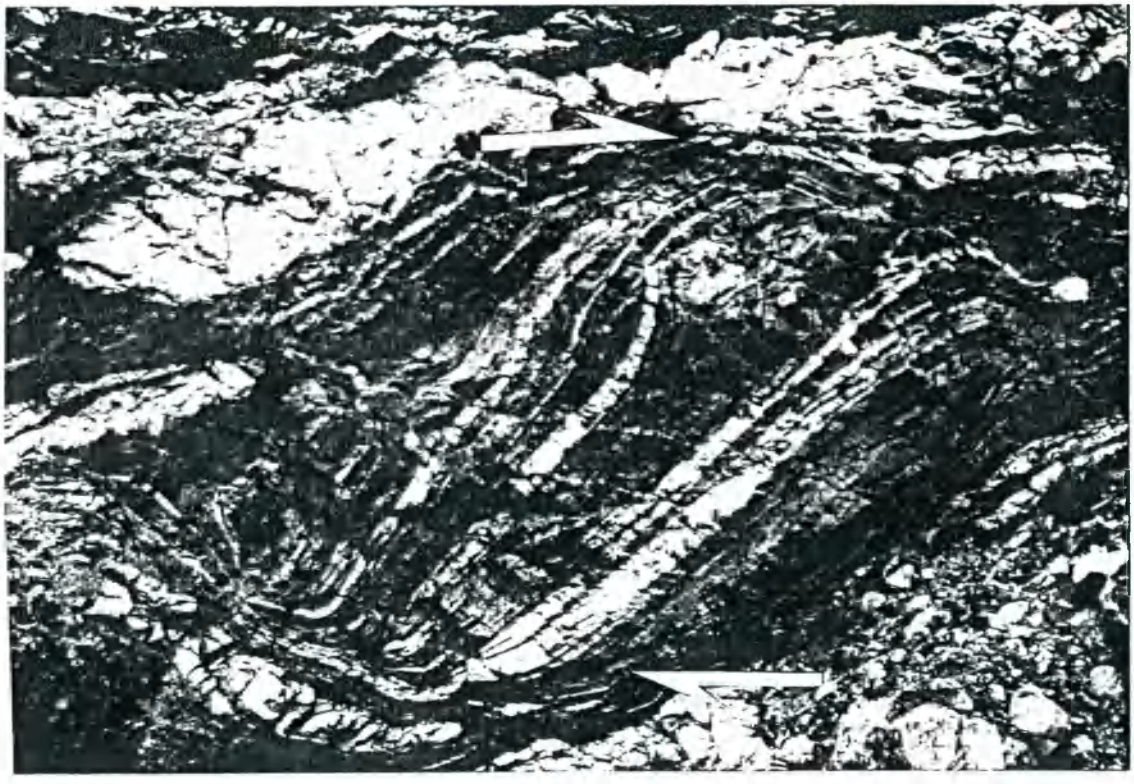

Plate 3.9. Small-scale shear band present in banded amphibolite and marble, Shahbatot. West is to the right : the shear sense is top-to-the-west.

Plate 3.10. Asymmetric boudin and lenticles of calcsilicate enclosed by amphibolitic gneisses. The foliation at this locality is vertical and east is towards the right. The shear sense is east-side-up.

Plate 3.11. Photomicrograph of muscovite mica fish present in semi-pelitic gneiss (sample S65) at Sassi (XPL). The s- and c-surfaces, which are indicated, make up a well-developed s-c fabric which indicates east-side-up, and an extensional west-side-down sense of movement.

Plate 3.12. Photomicrograph of amphibolite gneiss (sample S34), collected from the shear zone at Sassi (PPL). Note the retrogression of hornblende to biotite along a c-plane. Field of view is 1.5 mm.

lineations are well-developed, and are marked by the streaking of hornblende, quartz, or opaque oxides (Plate 3.7). In the Indus gorge, the lineations plunge on average 56 ° towards an azimuth of 326°, as shown in Fig. 3.4. In the upper Darchan valley, the lineations have a gentler plunge, on average 31° towards an azimuth of 343° (Fig. 3.5). Thus as the foliation changes in orientation as the northern part of the NPHM is approached, so too do the mineral stretching lineations.

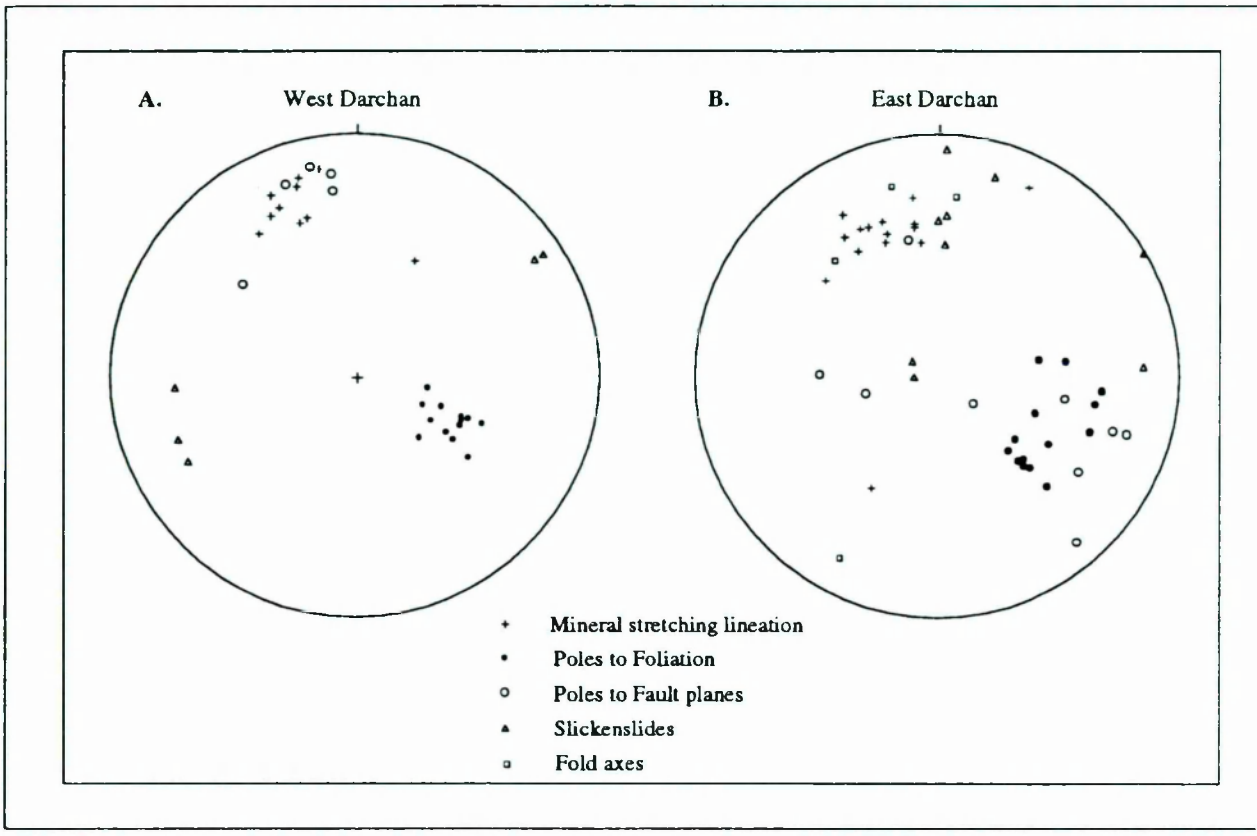

Fig. 3.5. Schmidt equal area projection of structural data from the upper Darchan valley. **A**. West side of the valley; **B**. East side of the valley.

Large-scale, ductile kinematic indicators within the shear zone include large shear bands which reach lengths of tens of metres (Plate 3.8). When these structures are exposed in a suitable orientation, they indicate a movement sense of east-side up. Discrete, small-scale ductile shears are also present, and these indicate the same movement sense, as shown in Plate 3.9.

Locally, horizons of psammitic gneiss contain bands containing concentrations of

large feldspar porphyroblasts. These occasionally have characteristic asymmetric shapes, with wedge-shaped recrystallisation tails defining shear bands (σ_b type of porphyroblast system of Passchier and Simpson 1986). Where present, these asymmetric augen indicate an east-side up movement sense. Another type of porphyroblast system is present in the rare ultramylonitised calcsilicate horizons (Plate 3.6B). These have narrow recrystallised tails with characteristic bends caused by the rotation of the porphyroblast, and lie in the δ–type porphyroblast category of Passchier and Simpson (1986). Asymmetric porphyroblasts such as these are only developed at high shear strain values, so that the rate of supply of new grains in the tails, by recrystallisation, is relatively low compared to the rate of deformation. The porphyroblasts examined in thin sections cut parallel to the mineral stretching lineation indicate a movement sense of east-side up, with a component of dextral-slip. Larger examples of δ–type asymmetric boudin in calcsilicates are also present, and indicate the same movement sense (Plate 3.10).

Throughout the length of the shear zone from Darchan to Shahbatot, but generally confined to the more micaceous lithologies scattered across the belt, the dominant mylonitic foliation is commonly affected by an extensional crenulation cleavage (Platt and Vissers 1980), and the rocks display the characteristics of s-c mylonites (Lister and Snoke 1984). The mylonitised granite sheets within the zone also locally display an extensional crenulation cleavage. In the field, the secondary cleavage is discontinuous, and does not mark a plane of fissility as a true cleavage does, making the measurement of the orientation of the cleavage problematic. However, in general, the secondary cleavage (c-surfaces) dips more steeply towards the west or west-north-west than does the mylonitic foliation (s-surfaces) (Fig. 3.6).

Twenty-five orientated thin sections have been cut parallel to the mineral stretching lineation and perpendicular to the dominant foliation, and clearly exhibit the distinctive s-c fabric. In detail, the micas which define the mylonitic foliation (s-surfaces) are deformed into a series of open microfolds (Plate 3.11). One set of limbs is highly attenuated and sheared,

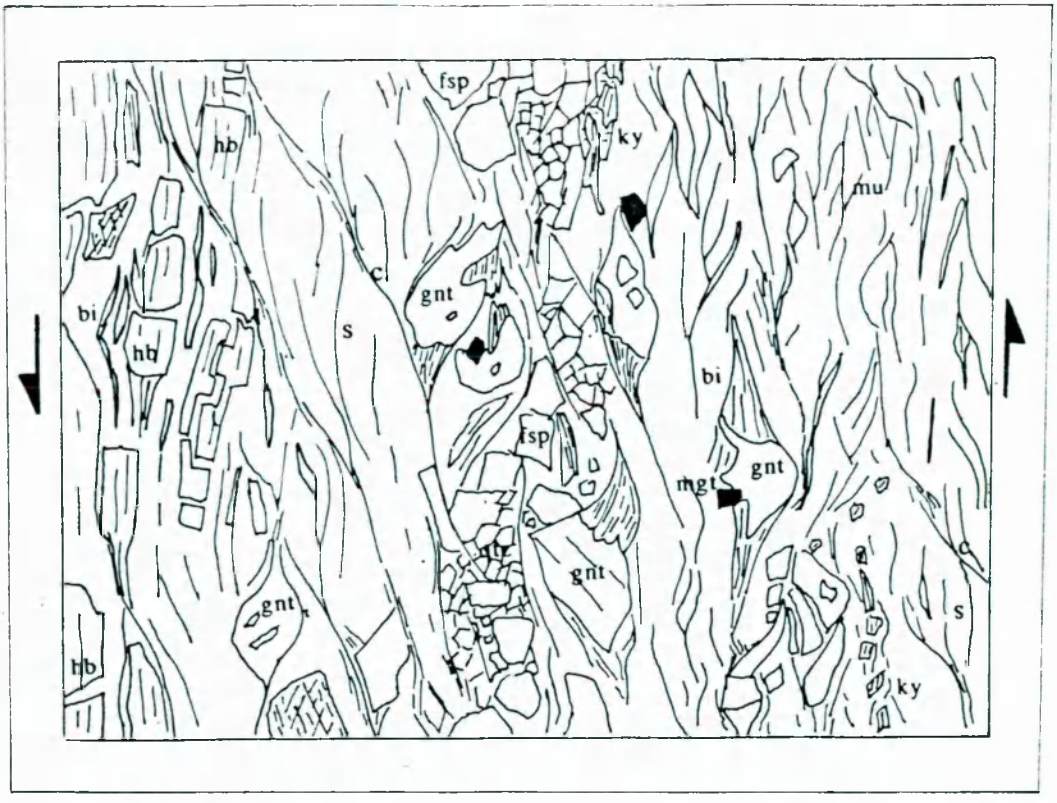

Fig. 3.6. Fabric relations in a pelitic schist (s-c mylonite) from the shear zone at Sassi. The field of view is 2 cm, and west is to the left. The c-surfaces dip steeply to the east, indicating east-side up movement sense. The sample is characterised by alternating hornblende and mica-rich laminae. Hb = hornblende; bi = biotite; mu = muscovite; gnt = garnet; fsp = feldspar; ky = kyanite; mgt = magnetite. Blocky kyanite crystals are cataclastically deformed and partially altered to muscovite. Hornblende is preferentially retrogressed to biotite along the c-planes. Garnet porphyroblasts are sheared and fractured, and locally have asymmetric shapes.

and defines a series of discontinuous shear planes or microscale shear bands (c-surfaces), which curve into the s-surfaces. The shear bands have a spacing of one or two millimetres. Within the c-planes, the micas show grain-size reduction, and this microstructural change probably initiated the softening which allowed the development of shear bands (Platt and Vissers 1980). The orientated thin sections indicate a consistent east-side up movement sense, with a large component of dextral strike-slip. Since the foliation dips steeply towards the west, the shear zone thus has a normal fault geometry, with dextral oblique-slip accommodating uplift of the NPHM (dextral transtension). In the upper Darchan valley, the mineral stretching lineation plunges more gently to the north-west than in the Indus gorge, and therefore there is a greater component of horizontal extension across the shear zone.

The mineralogical affects of the shear (c) planes on different phases can best be examined in those samples containing millimetre-scale alternations of micaceous and amphibolitic horizons. These show a slight retrogression of hornblende to biotite (Plate 3.12), indicating that the shearing operated at a temperature below the stability field of hornblende, in the greenschist-facies. In predominantly amphibolitic lithologies the hornblende appears to be stable, since these lithologies do not appear to have accommodated significant amounts of extensional shearing. Where primary metamorphic minerals such as garnet and kyanite are present, these are highly deformed and fractured by the shearing. Sometimes c-planes abut against the sides of garnet porphyroblasts, producing asymmetric shaped grains (Fig. 3.6).

Near Sassi, more brittle structures are evident as scattered, north-south trending faults, which either lie parallel to the foliation or dip steeply east (Fig. 3.4). These probably form part of the Shahbatot system of Butler et al. (1989). The east-dipping faults are occasionally marked by drag which indicates reverse-sense movement. These faults are locally characterised by thin trails of chlorite. The foliation-parallel faults possess abundant slickensides which plunge moderately towards a north-westerly azimuth (Fig. 3.4). Although the movement sense of these faults could not be reliably evaluated, according to Madin et al. (1989) and Treloar et al. (1991), they record a relatively late-stage dextral-oblique, east-side up movement sense. The similarity between the movement sense on these faults and that on the ductile, greenschist-facies structures described above, indicates that the shear zone evolved from greenschist to near-surface conditions along the same kinematic pathway. This may reflect the rapid cooling of the shear zone, possibly during the recent uplift of the NPHM (Chapter 5).

In summary, a variety of kinematic indicators from the shear zone between Shahbatot and upper Darchan have been used to help constrain the movement history within the zone. These consistently indicate that the lower amphibolite-greenschist grade shear fabrics were

developed during dextral-normal movement related to the uplift of the NPHM. The dextral component of this movement has already been recognised by previous workers (e.g. Butler et al. 1989; Madin et al. 1989; Treloar et al. 1991). Madin et al. (1989) interpreted the fabrics along the western margin of the NPHM as indicating dextral-transpression with an east-side up (reverse) movement direction, an interpretation which was based on the assumption that the foliation everywhere dips steeply east, whilst in this study, the dominant foliation was observed to generally dip steeply west. The orientation of the dominant foliation determines whether the movement sense is interpreted as being dextral-reverse or dextral-normal, and consequently the conclusion arrived at in this work is similar to that arrived at by Madin et al. (1989). Treloar et al. (1991) also interpreted the fabrics at Sassi as indicating an oblique dextral movement, east-side up on vertical surfaces. Indeed, Treloar et al. (1991) suggested that the younger, more brittle lineations have an increasingly shallow plunge, implying that the strike-slip movement has became more important with time.

There is uncertainty regarding the kinematic characteristics of the presumably original, amphibolite-grade fabrics developed in the shear zone during the earliest collision between the NPHM and the Kohistan arc. As already mentioned, Butler and Prior (1988a) interpreted moderately-dipping fabrics at Shahbatot as indicating sinistral overthrusting towards the SSE, which was related to the early 'MMT'. Unfortunately no evidence has been found in this study for the relation between the apparent MMT fabrics of Butler and Prior (1988a) and the later, lower-grade fabrics described above. It is possible that an early, thrust-sense shearing has been reactivated in the opposite sense by later ductile shearing related to the uplift of the NPHM. However, there is significant uncertainty attached to such an interpretation, since the age of the lineations and fabric described in this study is poorly-constrained. Any pre-existing fabric will have been rotated and affected by flattening during uplift of the NPHM. However, it should be noted that there is some geochronological evidence for tectonic and thermal activity in the shear zone at Sassi at about 6 Ma (Chapter 5). The available evidence suggests that the original suture zone between the Indian continent and the Kohistan arc has suffered an extended history of deformation, and that the

kinematics of this deformation have varied significantly through time.

3.3.2. Liachar shear zone

In the hanging-wall of the Liachar thrust, the Indian continental basement lithologies (described in Chapter 2) exhibit an intense, penetrative foliation which dips moderately towards the south and the SSE. Within the shear zone, there is locally marked grain-size reduction and mylonisation. Structural data from this shear zone are presented in Fig. 3.7. The foliation contains amphibolite to greenschist-grade mineral stretching lineations which plunge moderately towards the south or SSE. The dip of the foliation increases in a southerly direction towards the village of Tato (see Fig. 2.9). Near Tato village, a series of migmatised metasediments dips vertically or steeply towards the NNW, and the simple shear fabrics that are characteristic of the shear zone are no longer present.

In the Liachar shear zone, a variety of distinctive kinematic indicators demonstrate that movement involved ductile shearing characterised by SSE-side up, carrying the rocks of the NPHM out over the Kohistan arc. In the field, perhaps the most abundant shear sense indicators are asymmetric feldspar porphyroblasts, as shown in Plate 3.13. These occur as large grains with wedge-shaped recrystallisation trails, which curve away from the host grains to form a series of minor shear bands (σ_b type of Platt and Vissers 1980).

Larger shear bands also sporadically occur, although the relatively homogenous and massive orthogneisses, which form the greater proportion of the exposure in the shear zone, seem to be less susceptible to the formation shear bands than the metasedimentary sequence at Sassi. The shear bands constitute discontinuous planes or pairs of planes dipping less steeply towards the south or SSE than the mylonitic foliation. The bend-in fabrics which characterise these shear bands indicate the same sense of movement as described above. Occasionally the shears cut across well-defined, lithologically discrete layers such as leucogranite dykes, as illustrated in Plate 3.14. In such cases, the offsets are very noticeable

Plate 3.13. Detail of asymmetric feldspar-augen in an orthogneiss, Liachar shear zone. The foliation is dipping steeply to the south-east (left). The fabric indicates a thrust sense of top to the north-west.

Plate 3.14. Large-scale secondary shear planes truncating a leucogranite sheet present in the Liachar shear zone (Tato valley). The cliff is about 400 metres high; south-east is to the left. The shears indicate a thrust sense of top to the north-west.

Plate 3.15. Highly folded and boudinaged leucogranite sheets present in the Liachar shear zone, exposed in the 800-900 metre high side-wall of the Buldar valley. Shear sense is top to the north-west (left) .

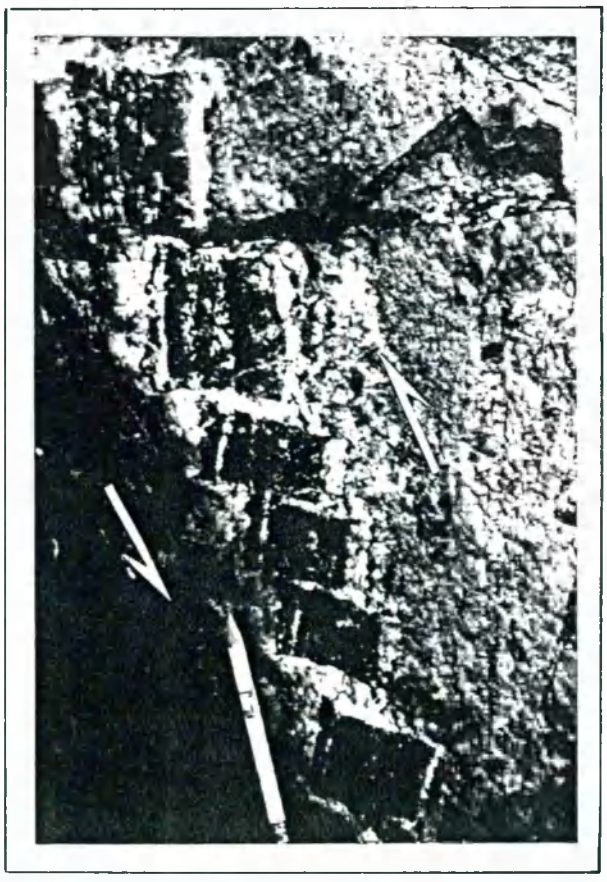

Plate 3.16. Domino shearing in calcsilicate, Liachar. Blocks composed of relatively competent diopside and hornblende have rotated in a carbonate matrix, indicating top to the north-west (left) shear sense.

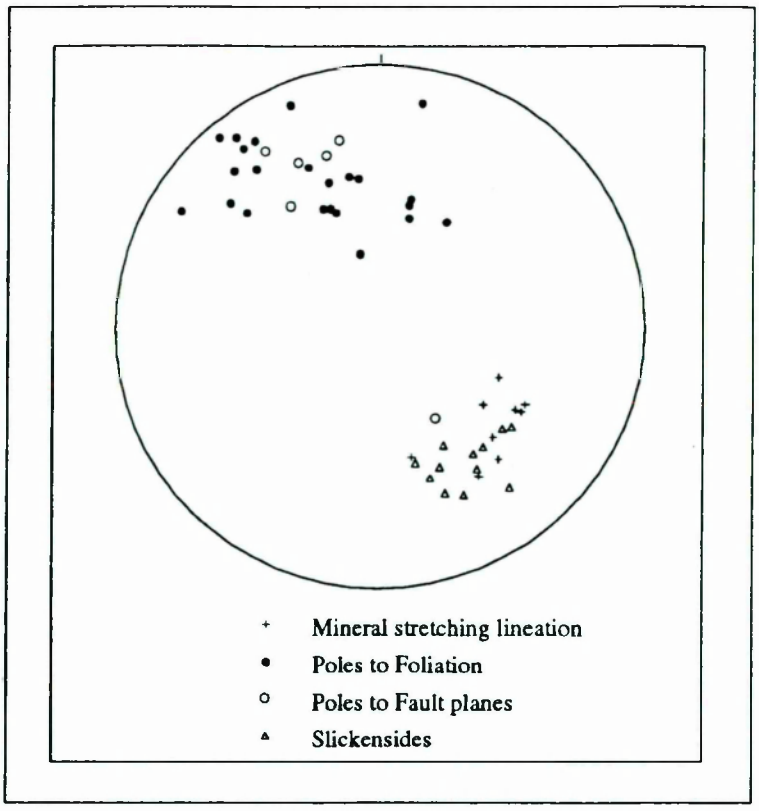

Fig. 3.7. Schmidt equal area projection of structural data from the Liachar shear zone.

and readily allow the reliable interpretation of shear sense.

Boudinaged, concordant horizons of leucogranite, calcsilicate or amphibolite are numerous throughout the shear zone. These are often characterised by highly sheared trains of 'swells', separated by attenuated 'pinches'. In some cases, examination of the relative orientation of the long axes of the swells, indicates that each one has been back-rotated in an antithetic sense to the shearing. These structures fall into the type 2a category of asymmetrical pull-aparts of Hanmer (1986). The shear sense is most discernible in those boudins where the 'pinches' have been affected by discrete shears, which have the same orientation as the shear bands described above (type 2b structures of Hanmer 1986).

Elsewhere, attenuated leucogranite sheets are sheared into spectacular isoclinal folds with limbs 10-20 m apart. These also indicate a strong vergence to the north-west, as shown in Plate 3.15. Locally, sheared horizons of banded calcsilicate exhibit domino-shearing

which also indicates a north-westerly movement sense (Simpson and Schmid 1983). This is characterised by the presence of relatively competent blocks of diopside and hornblende which have rotated within a relatively ductile calcite-quartz matrix, as shown in Plate 3.16.

Extensional crenulation cleavage, as described in the Sassi area, occurs occasionally within the Liachar shear zone. The secondary cleavage is well defined in the more mica-rich, schistose metasediments, such as the pelites and the biotite-rich amphibolite horizons. The s-c fabrics have been studied in a series of orientated thin sections, and confirm that the movement in the shear zone involved the north-westwards directed shearing of rocks of the NPHM. The amphibolite-grade, peak-metamorphic minerals are deformed by the simple-shear fabrics, with garnet being highly deformed and fractured, although not substantially retrogressed. As was seen in samples from Sassi, the shear planes are locally associated with the slight retrogression of hornblende to biotite, indicating an upper-greenschist grade of movement in parts of the shear zone.

Butler and Prior (1988b) noted the presence of numerous, foliation-parallel brittle faults within the shear zone. These are characterised by low-grade cataclastites, and contain slickensides which lie approximately parallel to the mineral stretching lineations. Thrusting thus appears to have continued from the formation of the amphibolite-grade fabrics to the present day (Butler and Prior 1988b). The apparent absence of lower greenschist-facies assemblages may indicate that in the later stages of uplift, the shear zone was rapidly cooled, perhaps by circulating groundwaters (Butler and Prior 1988b).

3.4. Origin of the NPHM

The fact that the NPHM experienced rapid and recent uplift is now well established (Chapter 5). As described in the above section, the structural accommodation of this uplift appears to have been complex, and probably involved a combination of crustal-scale folding (Coward et al. 1986), displacement on the Liachar thrust or Raikhot fault (Butler and Prior

1988b; Madin et al. 1989) and dextral-oblique transtension (this work). These different movements have operated in different parts of the NPHM, and probably at different times (Treloar et al. 1991).

Many workers have suggested possible causes for the recent growth of the NPHM. Early models were based on the indentor theory (Wadia 1961; Desio 1979). This theory proposes that the Indian crust in the vicinity of Nanga Parbat behaved as a rigid indentor into Asia, which was then preserved as a basement high. However, modern geochronological studies indicate that the NPHM structure was generated within the last 10 Ma (Treloar et al. 1991) whereas initial collision occurred at about 50 Ma (Chapter 1). By invoking the model of Richardson and England (1979), Zeitler (1985) suggested that uplift may have been delayed by the conversion of part of the Indian continental crust to eclogite during rapid underthrusting. In this model, after sufficient erosion and thermal re-equilibration has occurred, the conversion of eclogite back to granulite or amphibolite causes the buoyant uplift of the crust, characteristically along steeply-inclined shear zones. However, this theory does not explain the structural characteristics or detailed kinematics of the NPHM, such as the north-south orientated folds, north-west directed thrusts and dextral strike-slip faults.

The NPHM is one of a number of anomalous, north-south trending, regional-scale crustal antiforms in north Pakistan, which trend obliquely to the surrounding major fold and thrust belts, and also to relative plate motions (Coward et al. 1986). The other major structure is the Hazara fold, which deforms recent thrusts (including the Main Boundary thrust), and uplifts Palaeogene molasse of the external zone, and thus must have been active in the last 5 Ma (Treloar et al. 1991). The Besham fold, around which the MMT curves in a broad loop, was also recently active. All of these structures are characterised by anomalous topography, indicative of recent exhumation (Butler et al. 1989). All three antiforms lie in a wide zone of convergent thrusting, termed the Himalayan syntaxis by Wadia (1931), within which the strike of the mountain belt changes from being north-westerly in northern India, to north-easterly in northern Pakistan. In northern India, the dominant thrust direction is

towards the south-west, whilst in northern Pakistan, the direction is towards the SSE. The rapid change in direction of thrust propagation around the antiformal structures strongly suggests that the generation of these structures is related to the generation of the syntaxis itself.

The consensus of opinion is that the young, structurally-anomalous folds such as the NPHM reflect complex interference between thrust sheets with opposing movement senses, although the actual nature of this interference is not fully understood (e.g. Coward et al. 1987, 1988; Butler et al. 1989; Madin et al. 1989; Treloar et al. 1989c, 1991, 1992). The combination of observed structures in the NPHM supports an origin involving the inhibition or pinning of the lateral (south-westerly) propagation of one of the main Himalayan thrusts, currently cutting up through the southeast-verging north Pakistan thrust belt (Fig. 3.8) (Treloar et al. 1992). The pinning may have been caused by the relatively steep dip of the MMT or related thrust in the Pakistan thrust belt (Coward et al. 1986), or alternatively by the presence of the Kohistan arc (Coward et al. 1988; Treloar et al. 1992). The pinning of one of the main Himalayan thrusts is thought to have caused the local clockwise rotation of the thrust, and an increase in the amount of displacement towards the east, resulting in a combination of westerly-directed thrusting, dextral strike-slip and north-south trending folding. These movements effectively re-work the earlier structures developed in the Pakistani thrust system (Fig. 3.8) (Treloar et al. 1992). Such a model requires an earlier collision and subsequent crustal thickening in the western Himalaya than in the central Himalaya (Treloar et al. 1992).

In contrast, the Hazara structure may result from the reworking of a southwest-verging thrust stack by later south-verging thrusts of the Pakistani thrust system (Bossart et al. 1988). The Besham structure may have a similar origin to the NPHM, but is probably still in the early stages of development (Treloar et al. 1991).

Evidence for such a tectonic disturbance in the western Himalaya includes the zone

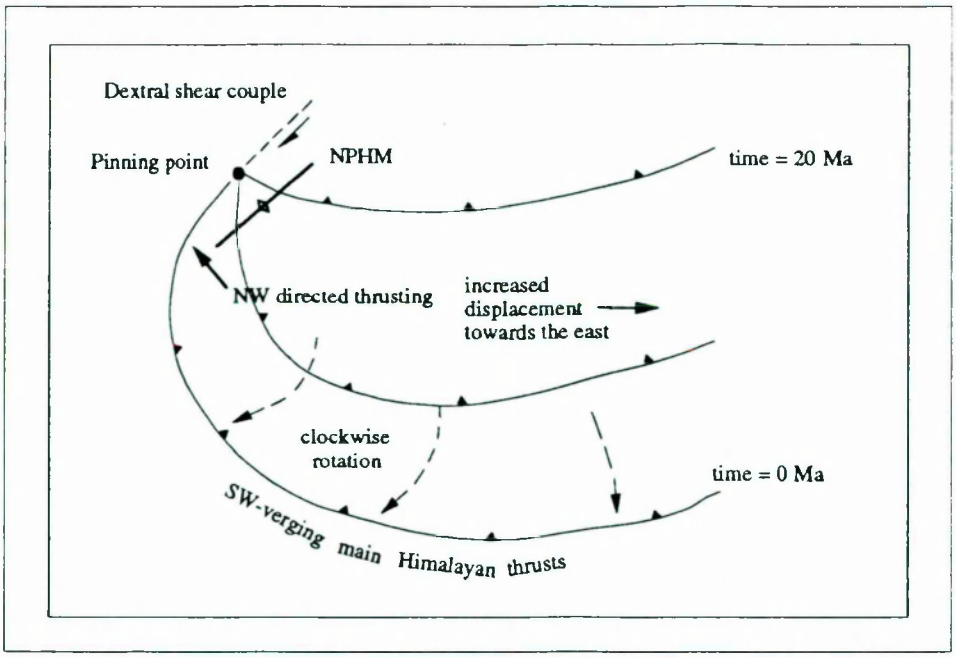

Fig. 3.8. Model for the formation of the NPHM at the lateral termination of one of the main Himalayan (Kashmiri) thrusts, after Treloar et al. (1991, 1992). Rotation of the movement vector towards the thrust tip resulted in NW-verging thrusting along the western margin. Tear faulting near the thrust tip resulted in southwards-migrating dextral strike slip, whilst the distribution of strain throughout the hanging wall of the thrust resulted in crustal-scale folding.

of important earthquakes recorded by Seeber et al. (1981), called the Indus-Kohistan seismic zone, which trends NNW from the Hazara fold. Further evidence comes from palaeomagnetic data, which suggests the substantial and systematic rotation of whole thrust sheets (Klootwijk et al. 1985).

3.5. Conclusions

The exhumation of the Indian continental crust of the NPHM has occurred by a combination of large-scale folding and thrusting. In general, this work has confirmed the conclusions reached by earlier workers, that the original suture bordering the western margin of the NPHM has been extensively modified by younger movements relating to the uplift of the NPHM. Furthermore, the kinematics of the fabrics exposed in the steep shear zone vary significantly in a north-south direction along strike.

In the Liachar-Raikhot area, Indian basement rocks have been thrust in a north-west direction back over Kohistan on the recently-active Liachar thrust. In contrast, in the Sassi-Darchan area, the greenschist-grade deformation is associated with a dextral-oblique sense of movement, involving extensional shearing directed steeply towards the north-west. This movement may reflect the relatively passive sliding of Kohistan rocks towards the north-west during active folding and growth of the NPHM.

The generation of the NPHM is probably related to the lateral pinning of a major, south-westerly propagating thrust at a deep crustal level within the western Himalayan syntaxis.

Chapter 4

Mineral Chemistry and Metamorphism of the Nanga Parbat-Haramosh Massif - Kohistan Region

4.1. Introduction

This chapter is a detailed study of the metamorphic conditions and evolution of rocks within the NPHM and the adjacent Kohistan arc. Structural and geochronological studies in the region (Chapters 3 & 5) constrain the post-metamorphic kinematic and cooling history across the western margin of the NPHM, which can be related to the uplift of the NPHM. However, the conditions and timing of peak metamorphism in the region, and the nature of the crustal thickening which presumably caused this metamorphism, are relatively unconstrained.

The consensus of opinion is that the early structural geometry of the region was characterised by the underthrusting of the Indian crust northwards beneath the Kohistan arc. The very presence of the NPHM, 100 km north of the bulk of the Indian crust outcrop, has been taken to indicate that Indian crust underlies much of the Kohistan-Ladakh arc (Coward et al. 1986). Such a conclusion is supported by the correlation between the 'MMT' in the Hazara area, where both structural and geophysical studies (Tahirkheli et al. 1979; Malinconico 1986) suggest that initial deformation was characterised by the northerly underthrusting of the Indian crust, with both the western (Tahirkheli et al. 1979; Butler and Prior 1988a) and eastern (Treloar et al. 1991) margins of the NPHM. Further support comes from the apparent MMT fabrics preserved along the western margin of the NPHM (Butler and Prior 1988a), and the ductile nature of the northern termination of the NPHM (Butler et al. 1992).

Numerical and theoretical models (Thompson and England 1984) have demonstrated

that the early thermal history of metamorphic terranes can be inferred from pressure-temperature-time (P-T-t) paths, and subsequently related to their tectonic evolution. In this section therefore, an analysis of the spatial and temporal variations of estimated P-T conditions recorded by samples from both the NPHM and the Kohistan arc is presented, in order to test the validity of the tectonic model summarised above.

This study involves detailed petrography combined with mineral chemistry and geothermobarometry. Major-element analyses have been obtained for garnet, biotite, muscovite, epidote, hornblende, plagioclase, k-feldspar and cordierite using wavelength dispersive spectrometry on a Cambridge Instruments Mark-9 electron microprobe (see Appendices 1 & 2). Five to ten grains of each mineral were analysed within each thin-section, whilst selected grains of garnet, plagioclase and zoisite were subjected to rigorous, multiple analysis in order to evaluate the degree of compositional zonation. P-T-t paths have been estimated from observations on inclusion phases in garnet and compositional zoning in garnet and feldspar, combined with Gibbs modelling of suitable samples (Spear and Selverstone 1983). Finally, a reconnaissance geochronological study, involving Nd-isotope dating of garnets, has been undertaken in order to help constrain the timing of metamorphism.

4.2. Previous Metamorphic Studies

There have been few studies of the metamorphism of either the NPHM or of the adjacent Kohistan arc. In early studies of the NPHM, Wadia (1932) and Misch (1949) observed that the grade of metamorphism increased from chlorite-grade to sillimanite-grade towards the core of the NPHM. However, at the time, the massif was not well-defined structurally, and part of the increase in grade inferred by these workers relates to the increase in grade between the island arc terrain and the NPHM. Wadia (1932) noted the frequent interbanding of orthogneiss and paragneiss within the NPHM, which was ascribed to lit-par-lit injection. However, in a classic study, Misch (1949) suggested that the NPHM migmatites were generated by sub-solidus, lit-par-lit granitisation of metasediments by alkali

metasomatism. This process was believed to have occurred during Himalayan times, and probably involved the introduction of hot fluids during shearing. The evidence that Misch (1949) used for such large-scale metasomatic replacement included the close association between metamorphic grade and degree of granitisation, the gradational and conformable contacts between ortho- and para-gneisses, and the petrographically observed late-stage growth of alkali feldspar.

Misch (1964) presented a detailed petrographic description of approximately fifty samples collected from the region around Nanga Parbat peak. On the basis of assemblages occurring in calcsilicate horizons, Misch divided the high-grade region into three somewhat indistinct zones, all of which lay in the amphibolite-facies. Table 4.1 shows the diagnostic mineral assemblages for the three zones. Zone 1, the highest grade (highest-T) zone, is characterised by the stable association of wollastonite and anorthite/bytownite, and roughly corresponds to the highest topographic elevation, immediately north of Nanga Parbat. In 1964, this was the first documented occurrence of wollastonite intergrown with anorthite. Locally, secondary grossular is present, and probably replaced the wollastonite/anorthite paragenesis in response to a temperature drop. In Zone 2, the wollastonite and grossularite pair is diagnostic. The assemblage grossular-anorthite/bytownite is stable throughout Zones 2 and 3. Zone 3 in characterised by the pair calcite-quartz, together with grossular and anorthite/bytownite, in the absence of wollastonite. The minerals diopside, hornblende, quartz and calcite are present in all three of the zones. Misch (1964) noted that, in the marginal areas of the NPHM, below Zone 3, calcsilicates are characterised by minerals such as scapolite, zoisite, andesine, garnet, calcite and quartz.

Within the NPHM, kyanite and sillimanite are sporadically present in pelitic lithologies of suitable composition. In the northern part of the NPHM, both kyanite and sillimanite are present in the Shengus gneiss unit exposed in the Indus valley (Treloar et al. 1991), and kyanite is also present in pelitic gneisses to the east of Haramosh peak (Zanetin 1964). In the southern part of the NPHM, Misch (1964) noted that euhedral sillimanite is only present in calcsilicate Zone 1, whereas fibrolitic sillimanite is present in both Zone 1

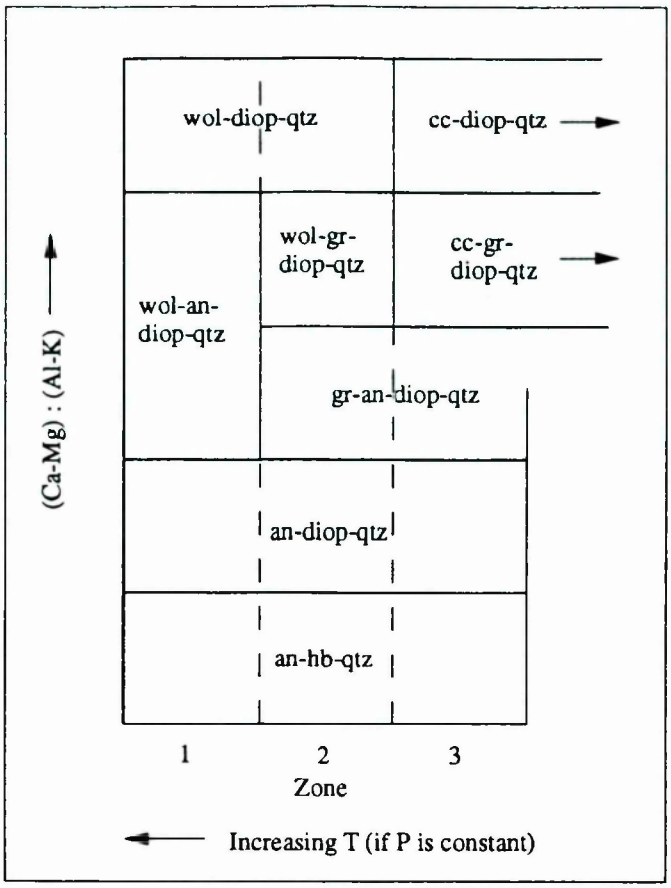

Table 4.1. Mineral assemblages in high grade calcschists from the NPHM, with excess quartz. From Misch (1964). In a given zone, the Ca-Al-Si phases present depend on the atomic ratio Ca/Al left over after the exhaustion of Mg and K in the formation of diopside (Ca) and k-feldspar (Al). See text for description of zones 1-3.

and in lower-grade zones, and was thought to have formed at the expense of biotite at a late stage of the metamorphism. In general, the assemblage sillimanite-k-feldspar in pelitic lithologies was only rarely observed by Misch (1964), whilst primary muscovite was found widely throughout the massif, indicating high P_{H_2O}. Kyanite is present in calcsilicate Zones 2 and 3 (Misch 1964).

From a study of mineral reaction textures, phase equilibria and Gibbs modelling of zoned garnets, Chamberlain et al. (1989) suggested that metamorphism in the NPHM was related to the underthrusting of the Indian crust beneath the Kohistan arc. These workers suggested that rocks of the Kohistan arc were metamorphosed on average at temperatures which were 100 °C higher than those in the NPHM, and subsequently followed a decreasing

pressure path. In contrast, rocks in the NPHM recorded an increasing P-T history. According to Chamberlain et al. (1989), the P-T-t paths of the two terranes converge, due to thermal equilibration following thrusting. Rocks initially buried deeper in the arc were thrust up over shallower-buried rocks of the Indian crust. This thrusting caused pressure increase in the lower plate (Indian crust) and pressure decrease in the upper plate (Kohistan), whilst the heat transfer between the hot overiding plate and the cooler lower plate caused an increase in temperature in the NPHM and decrease in temperature in the arc adjacent to the NPHM (Chamberlain et al. 1989). Peak metamorphic conditions in both the arc and the NPHM were estimated to have reached 613-650 °C and 7.5 kbar in the NPHM and 715 °C and 8.3 kbar in the adjacent arc (Chamberlain et al. 1989). These P-T results were based on the analysis of four samples from the NPHM (Astor gorge) and two samples from the Kohistan arc, one collected to the west of the NPHM and the other from near the eastern margin.

Zeitler and co-workers (Smith et al. 1992; Zeitler et al. 1993), have described a steep, southwards increase in grade in pelitic rocks in the Tato-Fairy Meadows area (part of the area studied by Misch 1964). They differentiated three metamorphic zones in pelitic lithologies, which were characterised by the diagnostic assemblages kyanite-muscovite, sillimanite-muscovite and sillimanite-cordierite-k-feldspar, respectively. The highest-grade rocks were highly migmatised and suffered peak metamorphism at 650 ± 50 °C and 6 ± 1 kbar, which was followed by isothermal decompression and melting at pressures of about 4 kbar (Zeitler et al. 1993).

4.3. Petrography and Mineral Chemistry

4.3.1. Kohistan Arc

Eight metamorphic samples have been examined from the north-eastern part of the Kohistan arc, five of which contained garnet and have subsequently been subjected to detailed compositional analysis (samples G1, G5, G7, G17 & G20). The petrography of

these samples has already been outlined in Chapter 2.

4.3.1.1. Metasediments

These typically contain the assemblage garnet + muscovite + biotite + zoisite + quartz + plagioclase (see plate 2.1).

Garnet forms colourless, somewhat corroded porphyroblasts which vary in size from 0.1-1.5 mm. The grains are generally free from alteration, although in sample G1, garnet is occasionally pseudomorphed by fine aggregates of zoisite, muscovite and plagioclase. Unorientated inclusions of quartz and biotite are abundant, whilst zoisite inclusions are sometimes present. In sample G7, fibrolitic sillimanite is present in the cores of the larger crystals. All of the garnets examined exhibit strong compositional zoning characterised by an increase in X_{gr} and Fe/(Fe+Mg) and decrease in X_{py}, X_{alm} and X_{sp} between core and rim. Garnet compositions, from core to rim, lie in the ranges X_{alm} = 0.78-0.51, X_{gr} = 0.05-0.26, X_{py} = 0.14-0.07 and X_{sp} = 0.11-0.07, respectively. In sample G7 (Fig. 4.1A), the most rapid change in garnet composition occurs near to the rim itself, whilst garnet in sample G9 (Fig. 4.1B) is characterised by a smoother zoning profile in the rim region. Garnet grains only show strong compositional zoning on well-preserved crystal faces. No textural discontinuities are associated with the changing garnet composition.

Plagioclase occurs as a fresh matrix phase showing repeated twinning. The grains usually lie in the compositional range An_{44-53}. However, in one sample from near Parri (G1), the feldspar grains have relatively anorthitic compositions which, although variable, reach An_{71}. Within this sample, individual feldspars also have variable anorthite contents, and sometimes show a decrease in anorthite content between core and rim.

Muscovite and Biotite occur as coarsely aligned platy crystals which define a crude metamorphic foliation. Rare grains of secondary muscovite cross-cut this foliation but have the same composition as the primary muscovite. Biotite is characterised by a high Ti content

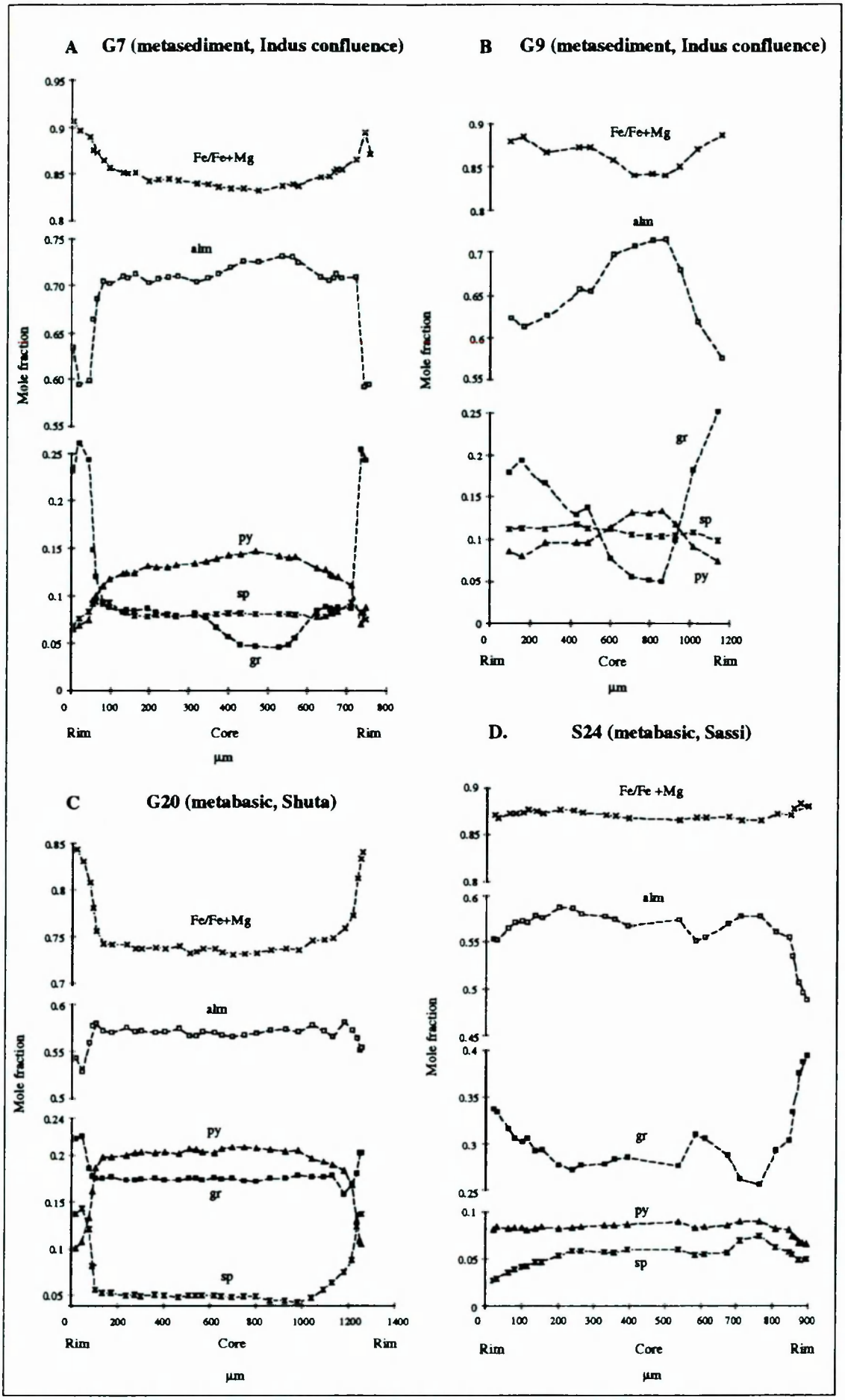

Fig. 4.1. Garnet compositional zoning traverses. alm=almandine; py=pyrope; gr=grossular and sp=spessartine.

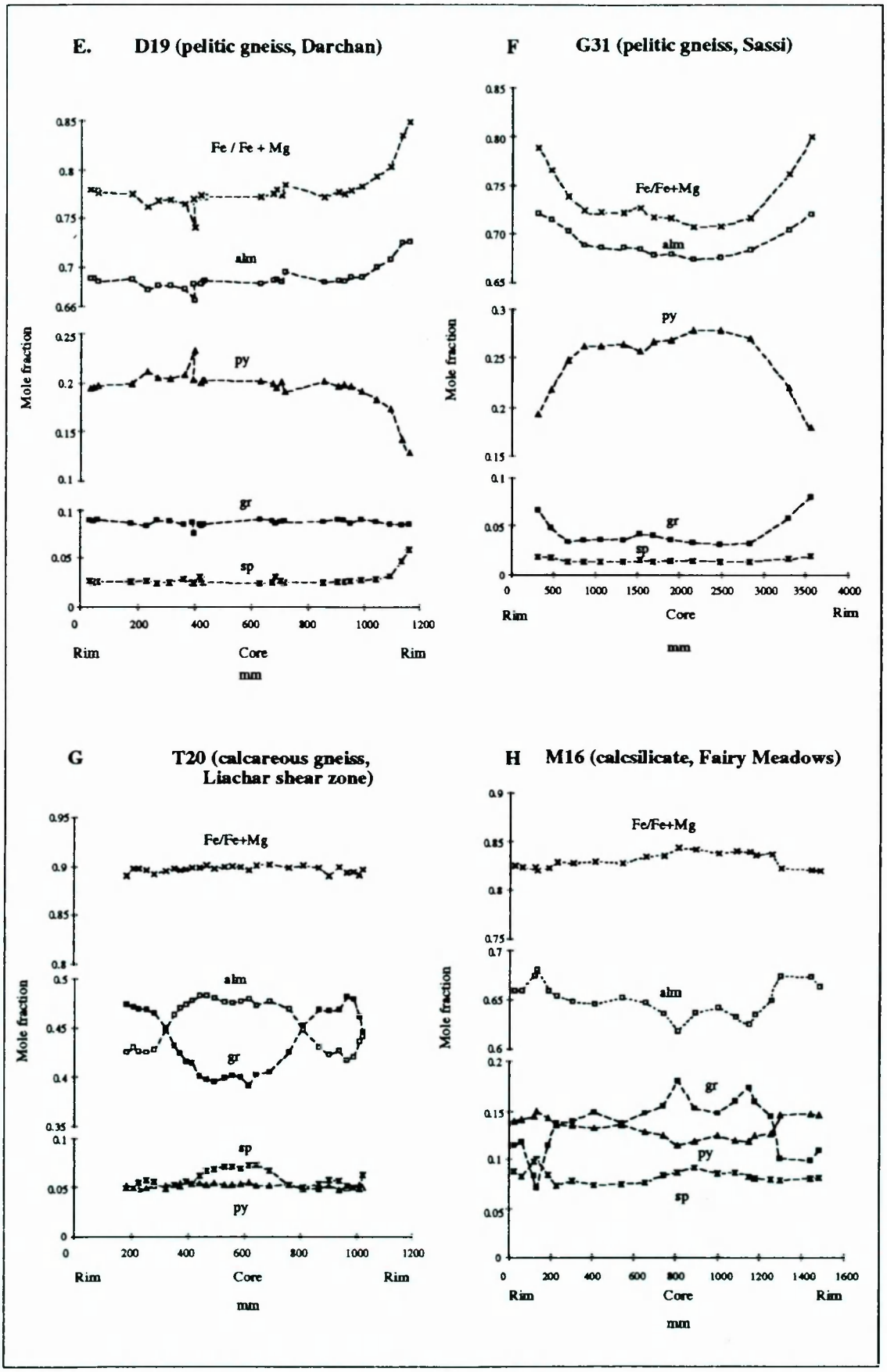
E. D19 (pelitic gneiss, Darchan)
Fe / Fe + Mg
alm
py
gr
sp
Mole fraction
Rim
Core
Rim
mm
F G31 (pelitic gneiss, Sassi)
Fe/Fe+Mg
alm
py
gr
sp
Mole fraction
Rim
Core
Rim
mm
G T20 (calcareous gneiss, Liachar shear zone)
Fe/Fe+Mg
alm
gr
sp
py
Mole fraction
Rim
Core
Rim
mm
H M16 (calcsilicate, Fairy Meadows)
Fe/Fe+Mg
alm
gr
py
sp
Mole fraction
Rim
Core
Rim
mm

Fig. 4.1. (cont.)

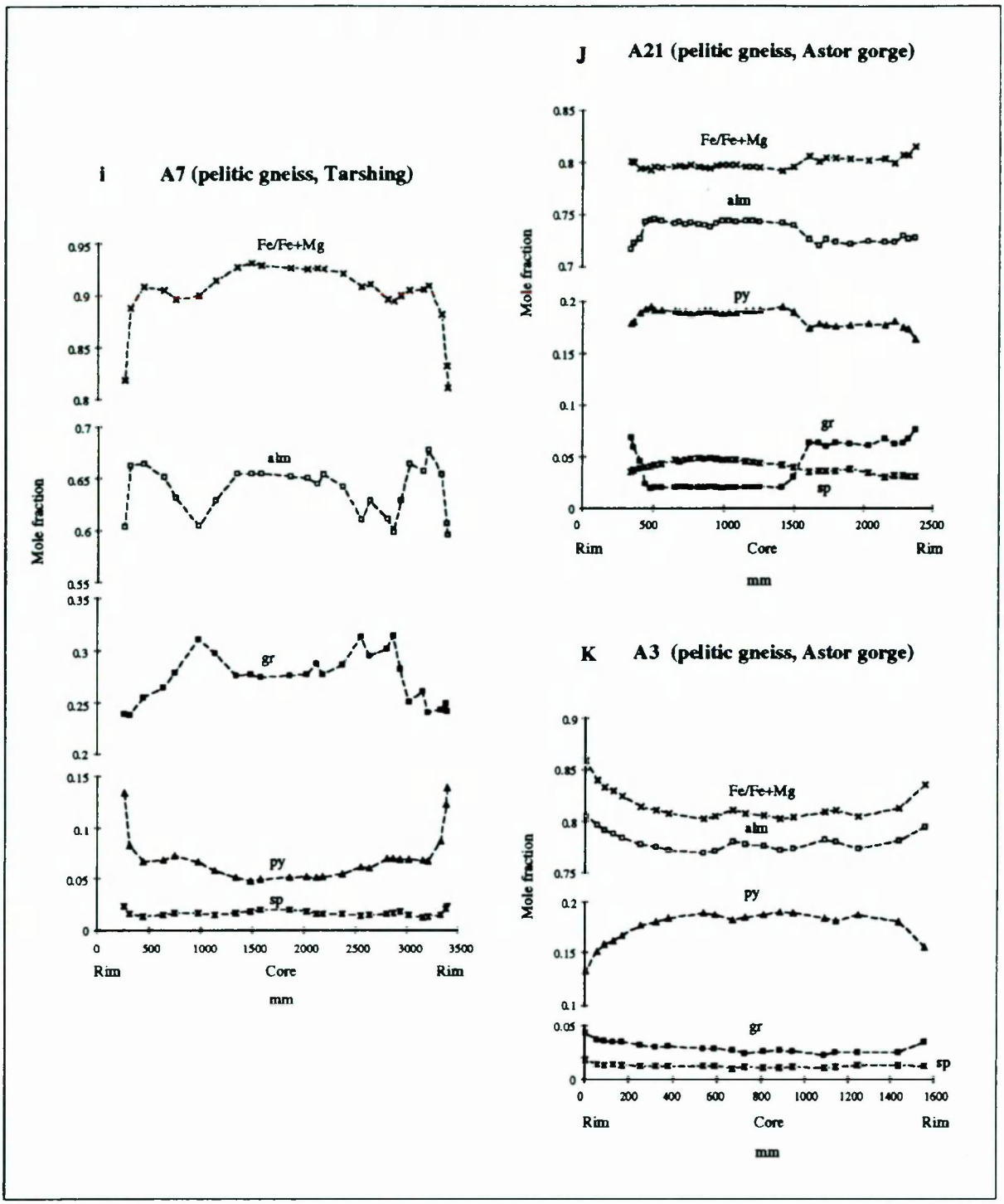
i
A7 (pelitic gneiss, Tarshing)
Fe/Fe+Mg
alm
gr
py
sp
Mole fraction
Rim
Core
Rim
mm
J
A21 (pelitic gneiss, Astor gorge)
Fe/Fe+Mg
alm
py
gr
sp
Mole fraction
Rim
Core
Rim
mm
K
A3 (pelitic gneiss, Astor gorge)
Fe/Fe+Mg
alm
py
gr
sp
Mole fraction
Rim
Core
Rim
mm

Fig. 4.1 (cont.)

(2-3 wt %) and X_{Mg} lies in the narrow range 0.45-0.49 (three samples). Within a given sample, the range of biotite composition is small, and individual matrix biotite grains are homogenous.

Zoisite occurs as high relief, colourless, often euhedral, tabular or pointed crystals. These crystals lie broadly within the metamorphic foliation. Many grains show characteristic anomalous blue interference colours. The compositional range of zoisite from the metasediments is fairly restricted, even between different samples. FeO contents lie in the range 4.3-6.2 wt %, whilst CaO lies in the range 23-24 wt %, for all samples. Compositional zoning is absent.

From an examination of the intergrowth textures and inclusion phases, all of the above minerals appear to be in equilibrium, at least with the garnet rims. The presence of calcic plagioclase together with zoisite suggests the epidote-amphibolite facies of metamorphism. This is supported by the presence of stable hornblende in adjacent metabasic rocks (see below). In sample G1, the compositional zoning present in garnet and plagioclase suggests that garnet growth occurred at the expense of plagioclase, which subsequently became more albitic. However, in other samples the plagioclase shows no consistent compositional variation, and consequently the relationship between garnet and plagioclase growth is less clear.

4.3.1.2. The Basic Schists

Rare horizons of basic and semi-pelitic schist occur within the Shuta gabbro, and two samples of basic schist containing garnet have been the subject of detailed compositional analysis (G17 & G20). These samples are characterised by the assemblage garnet + biotite + plagioclase + quartz + epidote (or zoisite) + sphene (see plate 2.2). None of the semi-pelitic schists contained garnet, although from the same area, Chamberlain et al. (1989) have described a pelitic gneiss characterised by the assemblage garnet + muscovite + biotite + kyanite + k-feldspar + quartz.

Garnet occurs as pink-coloured corroded grains up to 3 mm across. These contain inclusions of quartz, biotite, hornblende and occasionally plagioclase (Plate 2.2). A typical compositional traverse across garnet from sample G20 is shown in Fig. 4.1C. The pattern of compositional zoning is similar to that observed in the metasediments described above, although in this case there is also a marked increase in X_{sp} towards the rim region. Garnet compositions, from core to rim, lie in the ranges X_{alm} = 0.59-0.52, X_{gr} = 0.16-0.23, X_{py} = 0.20-0.10 and X_{sp} = 0.04-0.15, respectively.

Plagioclase in the matrix lies in the compositional range An_{40-60}. Individual feldspar grains also vary in composition, but in an inconsistent manner.

Epidote or Zoisite is present as large euhedral porphyroblasts which lie approximately parallel to the crude foliation. The epidote/zoisite contains inclusions of biotite and less frequently hornblende. In both samples, FeO contents lie in the range 7.5-9.1 wt % whilst CaO contents are 23-24 wt %. No compositional zoning was observed.

Biotite Coarse flakes of biotite define the crude foliation in the schists. X_{Mg} lies in the narrow range 0.5-0.6 for both samples, whilst TiO_2 contents are in the range 2.1-3.4 wt %.

Hornblende commonly forms poorly-shaped, poikiloblastic porphyroblasts containing inclusions of biotite and zoisite.

The stable association of hornblende, calcic plagioclase and zoisite indicates that the basic schists lie in the epidote-amphibolite facies.

4.3.2. The Nanga Parbat-Haramosh Massif

A large number of metamorphic samples have been examined from across a wide area of the NPHM (Fig. 4.2). In total, 28 samples have been the subject of detailed

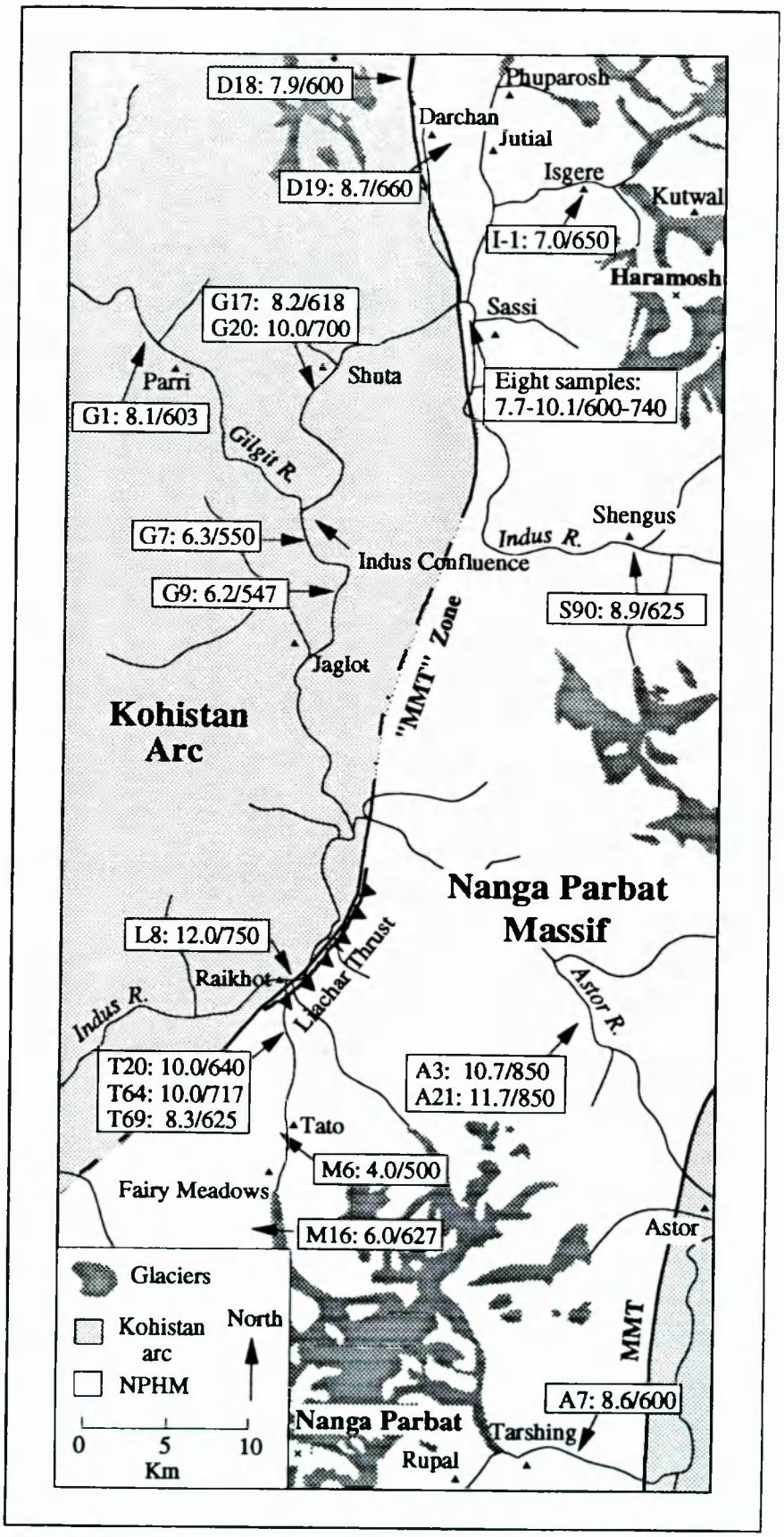

Fig. 4.2 Sketch map of the NPHM and adjacent Kohistan arc, showing sample localities and estimated P-T conditions. The sample number in each box is followed by estimated pressure (kbar) and finally temperature (°C). NPHM = Nanga Parbat-Haramosh massif. MMT = Main Mantle Thrust.

analytical study involving extensive use of the electron microprobe. A high proportion of these samples were collected from the western margin of the NPHM, from both the Liachar area in the south and from the Sassi-Darchan area to the north. The reasons for the sampling bias include the following:

(i) The structure and kinematics of the western margin of the NPHM is relatively well understood (see Chapter 3), and thus forms a suitable framework for a metamorphic study.

(ii) A high proportion of metasedimentary rocks containing garnet are exposed along the western margin of the NPHM.

(iii) The relative accessibility of the western margin of the NPHM.

4.3.2.1. Metasediments from the Sassi-Darchan shear zone.

The samples which are the subject of this section come from the shear zone extending northwards from Sassi towards Darchan. As described in chapter 2, the lithologies are pelitic and semi-pelitic gneisses, calcsilicates and basic schists. Thirteen samples have been subjected to detailed analysis. The pelitic gneisses contain the assemblage garnet + muscovite + biotite + plagioclase + quartz ± kyanite and the basic schists contain the assemblage garnet + hornblende + biotite + k-feldspar + plagioclase + quartz + sphene ± magnetite ± ilmenite. The calcsilicates are more variable, heterogeneous rocks composed of garnet ± hornblende ± biotite ± plagioclase ± zoisite ± diopside ± calcite ± quartz. Some samples (e.g. S28) are composed of 1-2 mm thick laminations of garnet + biotite + plagioclase (An_{50-60}) ± hornblende, alternating with more calcareous layers composed of garnet + diopside + plagioclase (An_{75-78}) + sphene ± zoisite. In such samples, there is no obvious variation in garnet composition with lithology. The stable association of calcite and quartz, together with the absence of wollastonite, places these samples in the high-grade Zone 3 of Misch (1964). This is consistent with the presence of kyanite in the adjacent pelitic gneisses.

Garnet The basic schists and pelitic gneisses contain abundant, rounded or corroded porphyroblasts of almandine garnet. In zones where the S-C fabric is well-developed, the garnets are often fractured and sometimes asymmetric. In many cases, the fractures seem to be extension fractures as they are orientated perpendicular to the dominant mylonitic foliation. The fractures are locally filled with secondary chlorite or muscovite. Inclusions of quartz, biotite and muscovite are common in garnets from the pelitic gneisses, whereas garnets from the metabasic lithologies contain inclusions of quartz, biotite and hornblende. The absence of any preferred orientation in the inclusions may indicate that garnet nucleation occurred before development of the foliation.

The composition range of garnet from four metabasic samples is relatively narrow. X_{alm} lies in the range 0.56-0.60; X_{gr} = 0.21-0.29; whilst both X_{py} and X_{sp} = 0.06-0.10. In the majority of metabasic samples from the shear zone, the garnet exhibits very little compositional zoning. Where present, the zoning is characterised by a slight decrease in X_{sp} towards the rim, whilst X_{py}, X_{gr} and Fe/(Fe+Mg) usually remain fairly constant. Garnet from metabasic sample S24 possesses unusually strong zoning, characterised by a strong decrease in X_{alm} and increase in X_{gr} towards the rim (see Fig. 4.1D).

Garnet from seven samples of pelitic gneiss has a wide compositional range due to whole-rock compositional variation. X_{alm} lies in the range 0.69-0.78; X_{gr} = 0.02-0.20; X_{py} = 0.11-0.20 and X_{sp} = 0.005-0.02. Compositional zoning tends to be better developed than in the adjacent metabasic lithologies, and is illustrated in Figs. 4.1E & F. The compositional zoning is characterised by a decrease in X_{py} and increase in Fe/(Fe+Mg) from core to rim. X_{gr} remains constant in some samples (e.g. D19; Fig. 4.1E), but in others increases towards the rim (e.g. G31; Fig. 4.1F). X_{sp} and X_{alm} usually increase towards the rim, but in some samples they decrease. In terms of compositional zoning, garnet from the metabasic schists differs from garnet from the pelitic gneisses in the absence of significant zonation in the Fe/(Fe+Mg) ratio in the former.

As expected, the calcsilicates contain garnet with a relatively high grossular content. X_{alm} lies in the range 0.40-0.50; X_{gr} = 0.37-0.47; X_{py} = 0.05-0.08 and X_{sp} = 0.01-0.10. The grossular-rich garnet often occurs as fine, rounded grains which may either be scattered, or concentrated in 1-2 mm thick layers. The type of compositional zoning observed varies greatly from sample to sample. In calcsilicate sample S28, X_{py}, X_{sp} and Fe/(Fe+Mg) decrease towards the rim whilst X_{gr} remains constant. In contrast, sample S34, which could be described as a calcareous amphibolite, contains compositionally zoned garnet which is characterised by an increase in X_{py} and X_{sp} and a decrease in X_{gr} and Fe/(Fe+Mg) between core and rim.

Feldspars The pelitic gneisses and metabasics contain fresh matrix plagioclase with a composition in the range An_{15-30}. The calcsilicates contain anorthite in the range An_{75-91}, although some samples additionally contain An_{50-60}, as already mentioned. The metabasics and psammitic gneisses also contain k-feldspar. In the pelitic gneisses, the plagioclase is usually unzoned. In contrast, plagioclase grains in the metabasics are strongly zoned and consistently have more anorthitic rims than cores (e.g. An_{25-30} from core to rim). Plagioclase present in calcsilicate samples is either unzoned, or displays an increase in anorthite between core and rim.

Kyanite From a collection of about 15 samples of pelitic gneiss collected from the shear zone, three contained kyanite. The mineral is present as tabular, high-relief matrix grains which lie parallel to the foliation. The crystals are generally highly deformed, as evidenced by fractures and bent cleavages, and sometimes show retrogression to muscovite.

Diopside This mineral is present as rounded porphyroblasts up to 1.5 mm across within the calcsilicates. The grains are high-relief, colourless or pale green, and often show substantial fracturing and retrogression to hornblende or tremolite.

Biotite is present in most lithologies and shows little compositional variation, with X_{Mg} lying in the range 0.41-0.49 and TiO_2 = 1.1-3.0 wt % for the majority of samples, although

one calcsilicate sample contains biotite with X_{Mg} = 0.55-0.58. Within individual samples there is little variation in biotite composition and no measurable compositional zoning. Biotite grains are often present as inclusions in garnet where they have the composition X_{Mg} = 0.39-0.41. Large biotite inclusions may be zoned, with decreasing X_{Mg} between core and rim. Core compositions of these larger biotite inclusions are similar to matrix biotite compositions, suggesting that the biotite inclusions have suffered Fe-Mg exchange with the adjacent garnet.

Muscovite is intergrown with the biotite in the pelitic gneisses. The two micas define the primary foliation and the lower-grade extensional shear fabric (see Chapter 3). There is no detectable difference in composition between the unsheared and sheared muscovite grains in samples exhibiting an S-C fabric.

Hornblende Stable hornblende is present both in calcsilicates and basic schists, and usually consists of elongate, green-coloured grains which lie parallel to the foliation. Where metabasic and pelitic lithologies are finely interlayered, extensional shear bands, defined by folded mica grains, can be traced into the metabasic layers, where the shears can be observed to cause the retrogression of hornblende to biotite (see Plate 3.12).

Epidote/Zoisite is absent from the basic schists within the shear zone at Sassi. However, the mineral is widespread in both psammitic and basic lithologies on the west side of the upper Darchan valley. Epidote in the former is relatively iron-rich, with FeO in the range 10.6-11.0 wt % and CaO = 21.1-23.1 wt %. Zoisite is also present in calcsilicates at Sassi, although in some cases the mineral may be secondary. In sample S28, zoisite lies in the range FeO = 7.2-8.5 wt %; CaO = 20.5-24.7 wt %, and shows compositional zoning towards more calcic and less iron-rich rims.

4.3.2.2. Liachar-Tato-Fairy Meadows Area

Six metamorphic samples from either side of the Liachar thrust, and a further three

samples from near Tato (Fig. 4.2) have been the subject of detailed analytical study, in order to compare the conditions of metamorphism and P-T-t paths of rocks in the footwall of the Liachar thrust with those in the immediate hanging-wall, and with those further away from the thrust, both along strike to the north (Sassi-Darchan area) and across strike to the east (Tato area). The metasediments in the Liachar area area contain the same metamorphic assemblages, and seem to be at the same metamorphic grade, as those exposed in the Sassi-Darchan area. Calcsilicates contain stable calcite and quartz together with diopside, anorthite ± hornblende ± biotite, whilst kyanite is present in the adjacent pelitic gneisses.

In the footwall of the Liachar thrust is a steeply-inclined imbricate zone trending north-south, containing lithologies derived from both Indian crust and Kohistan arc, and thus resembling the steep zone at Sassi. Sample L8 is a moderately calcareous, amphibolitic gneiss from this zone containing the stable assemblage garnet + biotite + hornblende + zoisite + plagioclase (An_{30-33}). Within this sample, the garnet varies in composition between different grains, in the range X_{alm} = 0.47-0.55; X_{gr} = 0.25-0.34; X_{py} = 0.16-0.17; X_{sp} = 0.02-0.03. Individual grains show similar zoning to garnets from the Sassi-Darchan area, with a slight increase in Fe/(Fe+Mg), X_{gr} and X_{sp} and a decrease in X_{py} between core and rim, whilst X_{alm} remains constant. Plagioclase is unzoned, but zoisite shows strong compositional zoning, with rims generally more calcic and less iron-rich than cores (e.g. 18-22 wt % CaO). The zoisite is sometimes present as inclusions in the garnet.

In the hanging-wall of the Liachar thrust, the metasediments enclosed by Indian plate orthogneisses are generally relatively calcareous, although not all are true calcsilicates, *sensu-stricto,* since characteristic minerals such as diopside and anorthite are not always present.

Garnet lies in the compositional range X_{alm} = 0.44-0.60; X_{gr} = 0.31-0.47; X_{py} = 0.02-0.05 and X_{sp} = 0.001-0.05. However, one calcsilicate sample (T23) contains grossularite with X_{gr} = 0.96 and X_{alm} = 0.04. This sample also contains An_{92-93} together with accessory apatite, whilst biotite is absent (see Plate 2.18). Out of the five analysed samples

from the hanging-wall of the Liachar thrust, three contain unzoned garnet. Garnets from the two remaining samples display slight decreases in X_{sp} and Fe/(Fe+Mg) between core and rim. In one of these samples (T20), X_{gr} increases strongly and smoothly from core to rim, as illustrated in Fig. 4.1G, whilst in the other sample (T69), X_{gr} remains constant.

Plagioclase in all five samples lies in the composition range An_{31-46}. Where zoned, the anorthite component of the feldspar increases towards the rim. In calcsilicate sample T20, the X_{an} in plagioclase increases from core to rim whilst contiguous garnet exhibits increasing X_{gr} from core to rim (Fig. 4.1G); the genesis of such calcic zoning in coexisting garnet and plagioclase is discussed at the end of section 4.3.

Biotite compositions are relatively uniform for individual samples but lie in the wider range X_{Mg} = 0.24-0.50 for all five samples.

Other phases have similar habits and compositions as already described for the Darchan-Sassi area.

Near Tato, packets of migmatitic metasediments within the Indian continental basement are common, as described in Chapter 2. The restitic portions of the pelitic gneisses are characterised by fibrolitic sillimanite intergrown with fine-grained cordierite, together with garnet, biotite (X_{Mg} = 0.33-0.43) and plagioclase (An_{24-29}), whilst muscovite is conspicuous by its absence (see Plate 2.20). The leucosome is composed of quartz, plagioclase and k-feldspar, together with minor sillimanite. Garnet porphyroblasts occur as large, corroded poikiloblastic grains with abundant inclusions of biotite. Garnet compositions are typically X_{alm} = 0.76, X_{gr} = 0.04; X_{py} = 0.11 and X_{sp} = 0.09. Slight compositional zoning is present, and is characterised by an increase in X_{sp} and Fe/(Fe+Mg) between core and rim, accompanied by a decrease in X_{py} and X_{gr}.

The calcsilicate assemblages present near Tato, and at Fairy Meadows, are similar to those already described from other areas, although no samples containing both stable calcite

and quartz were found. The assemblage is typically characterised by garnet + anorthite (An_{83-97}) + quartz ± plagioclase (An_{35-44}) ± diopside ± biotite ± sphene. Secondary minerals include calcite, muscovite, epidote, chlorite and zoisite. The garnets vary in composition according to the whole-rock composition, and the most grossular-rich garnet has the composition $X_{alm} = 0.26$, $X_{gr} = 0.73$, $X_{py} = 0.002$, and $X_{sp} = 0.006$. Garnet from a calcsilicate collected from a locality 3 km south of Fairy Meadows (M16) exhibits an unusual type of compositional zoning, characterised by a sharp decrease in X_{gr}, a slight decrease in Fe/(Fe+Mg), and a sharp increase in X_{alm}, between core and rim (Fig. 4.1H). Both anorthite and bytownite occur in separate, 1-2 mm thick laminae, reflecting fine variations in whole-rock composition, and exhibit compositional zoning characterised by an increase in anorthite between core and rim.

Although not found in this study, Misch (1964) identified wollastonite co-existing with anorthite in a sample from near Fairy Meadows. However, the sample also contained apparently stable grossular, leading Misch (1964) to conclude that the assemblage reflected conditions between Zones 1 and 2. Zone 2 calcsilicate assemblages have not been observed in the Tato area, either by Misch or in this study, but this probably reflects insufficient sampling. As mentioned above, pelitic samples in the Liachar area lie in the kyanite field, and the calcsilicates there contain stable quartz and calcite, diagnostic of Zone 3, which indicates that Zone 2 may locally be relatively thin (< 5 km wide).

4.3.2.3. Other Locations in the NPHM.

Detailed analytical work has been carried-out on seven other samples collected from scattered localities inside the NPHM. These samples are all amphibolitic or pelitic gneisses with variable mineralogical assemblages and compositions, and are discussed separately below.

Sample S86 is a pelitic schist from within the Iskere orthogneiss unit in the Indus gorge (see Fig. 4.2), and contains garnet, biotite ($X_{Mg} = 0.37$-0.39), muscovite, plagioclase

(An_{21-26}) and quartz. The garnet has the typical composition X_{alm} = 0.78, X_{gr} = 0.03; X_{py} = 0.12, X_{sp} = 0.7. The slight compositional zonation is characterised by an increase in X_{gr}, X_{sp} and Fe/(Fe+Mg) and decrease in X_{alm} and X_{py} between core and rim. Plagioclase grains often exhibit an increase in the anorthite component between core and rim.

Two samples of amphibolitic gneiss (S89 and S90) were collected from the Shengus paragneiss unit (Madin et al. 1989), near Shengus village. These samples are characterised by the assemblage garnet, biotite (X_{Mg} = 0.40-0.50), hornblende, quartz, plagioclase (An_{35-60}), sphene and sometimes k-feldspar, together with accessory ilmenite and magnetite. The garnet composition lies in the range X_{alm} = 0.49-0.63, X_{gr} = 0.27-0.36; X_{py} = 0.07-0.14 and X_{sp} = 0.03-0.07. Both garnet and plagioclase are unzoned, although adjacent plagioclase compositions sometimes vary considerably. Pelitic lithologies in the same area contain the assemblage quartz + k-feldspar + plagioclase + biotite + muscovite + fibrolitic sillimanite.

A sample of amphibolic gneiss from within the Iskere orthogneiss unit (I-1; Fig. 4.2) is characterised by the assemblage garnet, biotite, hornblende, quartz and plagioclase, and contains compositionally zoned garnet and plagioclase. The garnet, which has the composition X_{alm} = 0.63, X_{gr} = 0.16, X_{py} = 0.19 and X_{sp} = 0.03, exhibits a marked increase in X_{py} and a decrease in Fe/(Fe+Mg) between core and rim. X_{sp} shows a strong decrease from core to rim, whilst X_{gr} remains approximately constant. The plagioclase grains show strong zoning, with core compositions typically An_{35} compared to rim compositions of An_{64}.

A relatively calcareous, pelitic gneiss from close to the eastern margin of the NPHM, near Tarshing (A7), is composed of garnet, muscovite, biotite (X_{Mg} = 0.65-0.66), zoisite and plagioclase (An_{39-47}). Garnet has the typical composition X_{alm} = 0.55, X_{gr} = 0.23; X_{py} = 0.16 and X_{sp} = 0.06. As already mentioned in Chapter 2, the garnet is characterised by sinuous inclusion trails of quartz and opaque oxides, suggesting syn-kinematic garnet growth. The garnet also displays an unusual compositional zoning pattern (see Fig. 4.1I).

Between the core and a point half-way between core and rim, X_{gr} and X_{py} increase whilst X_{alm} and Fe/(Fe+Mg) decrease. In the outer half of the garnet, X_{gr} decreases and X_{py} increases smoothly towards the rim, whilst X_{alm} and Fe/(Fe+Mg) both increase strongly before a marked drop at the rim itself. Sample A7 is also unique in the present study in that plagioclase consistently exhibits zoning characterised by an increase in the albite component towards the rim.

Finally, two samples of pelitic gneiss from the Astor gorge have been studied in detail. These contain the assemblage garnet + kyanite + muscovite + biotite (X_{Mg} = 0.45-0.53) + plagioclase (An_{6-17}) + k-feldspar + quartz + rutile (see Plate 2.16). Plagioclase in unzoned, but the garnet is strongly zoned in both samples, as shown in Figs. 4.1J & K. Values for X_{gr} and Fe/(Fe+Mg) are higher, and values of X_{py} are lower, for rim compositions than core compositions. Although both samples are from the same locality, the overall shapes of the compositional profiles for garnet from each sample are different. In sample A21, the garnet profile is markedly stepped for all components except X_{sp}, whereas sample A3 contains garnet with a smoother profile typical of other garnets from the region. Some of the garnet grains in sample A21 exhibit a symmetrical zoning of inclusions, with large, irregularly shaped quartz inclusions in the core, and a zone rich in biotite and rutile inclusions near the rim (see Plate 2.17). However the marked step in composition does not coincide with this textural change. Another difference between samples A3 and A21 is that in detail, the changes in X_{sp} and X_{alm} from core to rim are in different directions; for example, garnet in sample A3 shows an increase in X_{alm} from core to rim, whereas garnet in A21 shows a decrease in X_{alm}. The step in composition profile is presumably due to a change in the continuous reaction involved in garnet growth; the absence of such a step in sample A3, but otherwise the similarity between the two profiles, makes it unlikely that the garnet in sample A21 is the result of two separate metamorphic episodes.

4.3.3. Summary

The type of compositional zoning observed in both plagioclase and garnet appears to

be more strongly related to lithology than to geographical location or structural level. Broadly speaking, samples from widely-spaced localities often have remarkably similar garnet zoning profiles. For example, pelitic gneisses from the Astor gorge, from the shear zone at Sassi, and from the Kohistan arc, all contain garnet which is characterised by increasing Fe/(Fe+Mg) and X_{gr} and decreasing X_{py} between core and rim (Figs. 4.1A, B, E, F, J, K). In comparison, metabasic samples from the region contain garnet which is characterised by constant Fe/(Fe+Mg) and X_{py}, decreasing X_{sp} and either constant or increasing X_{gr}, between core and rim (Fig. 4.1D).

Out of a total of 34 analysed samples from the Kohistan-NPHM region, only a handful contain garnet which is characterised by a decrease in Fe/(Fe+Mg) between core and rim. These include calcsilicate or calcareous amphibolite samples collected from scattered localites across the NPHM, including the shear zone at Sassi (S28 & S34), the Liachar shear zone (T20 & T69), Fairy Meadows (M16), Iskere (I-1), and from near to the eastern margin of the NPHM at Tarshing (A7). It is tentatively suggested that all of these samples preserve evidence of prograde garnet growth.

Some samples (e.g. S24, S86 & T20) contain garnet and plagioclase which are both characterised by an increase in X_{gr} and X_{an}, respectively, between core and rim. This is a surprising observation, since garnet which exhibits an increase in X_{gr} between core and rim is usually associated with plagioclase which exhibits a decrease in X_{an} between core and rim (Bergman 1992). Assuming that the garnet and plagioclase grew contemporaneously, this feature may be a reflection of the following :

(i) During garnet growth, the modal proportion of plagioclase decreased, and sodium cations were consumed by the growth of the paragonite component of white mica. Consequently the remaining plagioclase became increasingly calcic, in equilibrium with more grossular-rich garnet.

(ii) A third calcic phase was originally in equilibrium with the garnet core, and was

subsequently depleted during growth of both plagioclase and garnet.

Since there is no textural evidence for the presence of an additional calcic phase, the first option is preferred.

4.4. Geothermobarometry

The estimated conditions of peak metamorphism recorded by 26 metasedimentary samples have been calculated using the internally consistent thermodynamic dataset of Holland and Powell (1985, 1990) and the computer program *thermocalc* (Powell and Holland 1988). The dataset, which has been derived from all the experimental data simultaneously, includes tabulated data for the molar volume and enthalpy and entropy of formation of relevant phases. Uncertainties on the thermodynamic parameters are also given, thus allowing uncertainties to be calculated on the results of rock calculations using error propagation.

The program performs calculations on all independent reactions which can be written between end-members of co-existing minerals in a rock, thus minimising the problems associated with specific geothermobarameters. For each equilibrium assemblage, thermodynamic data are estimated from the same dataset, and are thus internally consistent. The results of these calculations can be combined to produce an optimum pressure or an optimum temperature within a user-specified window. The initial window is selected from the estimated grade of metamorphism and can be subsequently refined during operation of the program. A user-specified value for maximum acceptable uncertainty in pressure or temperature allows poorly constrained reactions to be removed from the calculations. Calculations are pressure-orientated since geobarometry is generally perceived to be less precise than geothermometry (Essene 1989). *Thermocalc* is particularly effective for low variance assemblages owing to the large number of reacting phases which help to constrain the equilibrium.

As for all methods of geothermometry and geobarometry, weight can only be attached to the results of *thermocalc* if the mineral phases involved in the calculations are in equilibrium. With the exception of sample G1, described above, none of the samples in this study contain phases with reaction rims or signs of significant retrogression, which are diagnostic features of non-equilibrium assemblages. In the case of sample G1, only fresh garnet grains together with contiguous matrix phases were selected for analysis. The presence of compositional zoning in garnet and plagioclase is evidence for disequilibrium in other samples. In order to select the appropriate phase compositions for use in *thermocalc*, it is important to have an appreciation of the origin of any observed growth zoning, including the effects of retrograde diffusion.

Diffusional homogenisation operates both during the growth of a crystal and during the subsequent cooling, and has the effect of erasing the P-T changes recorded by the garnet. Recent modelling of diffusion in garnet has indicated that the effect of diffusion will depend on variables such as the metamorphic assemblage, the size of the crystal and its initial zoning profile, the peak metamorphic temperature reached, the volumetric ratio of garnet to biotite and the cooling rate (Jiang and Lasaga 1990; Spear 1991). Diffusion rates are probably also enhanced by high strain rates. During prograde growth, the degree of homogenization of a zoning profile will depend on the rate of garnet growth relative to diffusion. According to de Bethune and Laduron (1975), evidence for post-growth retrograde resorption and diffusion may be the presence of sharp reversals in the trends of X_{sp} or X_{py} at the rim of a garnet. However, recent work (Spear 1989, 1991), has shown that it may be impossible to determine from an examination of a garnet zoning profile which garnet samples have been effected by diffusion, and consequently which compositions (if any) represent the equilibrium condition. The calculation of peak temperatures in prograde, amphibolite-facies pelitic schists may be impossible unless cooling rates are >100 °C / Ma or garnets are larger than about 1 cm. This is because peak metamorphic conditions in amphibolite-facies rocks are usually recorded by the composition of the outer rim of garnets, which are most easily destroyed by diffusion (Spear 1989; 1991). Peak metamorphic mineral compositions may also be effected by reactions (especially exchange reactions) operating during cooling, in

particular in granulite-facies rocks, and these reactions will also themselves affect rates of diffusion (Spear and Florence 1992).

For the majority of samples used in this study, rim compositions of closely co-existing phases have been used in the calculation of equilibrium metamorphic conditions. To some extent, the optimum set of end-member compositions can be selected by trial and error in running *thermocalc* with different end-member compositions, and examining the statistical fit of the resulting output data for each phase, as suggested by Powell and Holland (1988). For all the samples containing compositionally zoned phases, different combinations of core or rim compositions were used in *thermocalc* to to monitor the effect of changing composition on both estimated P-T and associated errors. The actual P-T results estimated for different combinations of core or rim compositions are similar, which is presumably a reflection of the rigorous nature of the *thermocalc* program. In contrast, the statistical fit of the ouput data, and subsequently the size of the final estimated errors, are variable. For example, garnet samples from the metasedimentary unit of the Kohistan arc exhibit strong increases in Fe/(Fe+Mg) and X_{gr} and a decrease in X_{py} between core and rim, as described above. Running the *thermocalc* program using the highly grossular-rich rim compositions together with the rim compositions of matrix phases generates good statistical fits and relatively low errors on P-T estimates. In contrast, when the garnet core compositions are used, there is a marked increase in the size of the resulting estimated errors, suggesting that matrix phases are out of equilibrium with the garnet core.

The cited error of a P-T estimate should incorporate both systematic and random uncertainties. Random uncertainties involve analytical errors, including errors in counting statistics together with mineral compositional variation, and represent a relatively small part of the total error. Random uncertainties probably lead to errors in the precision of a P-T estimate of 20-50 °C and 1.0-1.5 kbar (Hodges 1991). Systematic uncertainties include errors in the thermodynamic constants (calibration errors) and errors in mineral solution modelling due to imprecisely known activity-composition relationships. These errors are difficult to quantify, but are probably relatively large (Hodges and Crowley 1985). The

uncertainties in the thermodynamic parameters used in *thermocalc*, which have been derived from experimental studies, may have been underestimated, leading to unrealistically low estimated errors for the results of *thermocalc* (Hodges 1991). In this study, relative differences between different P-T estimates from the same area are important, and thus precision is more significant than accuracy. However, it should be noted that differences in P-T estimates between samples will only be solely due to analytical error (i.e. precision) for cases in which the same equilibria are used in the calculations. Since a range of different lithologies is used in *thermocalc* in this study, differences in P-T estimates between samples will also partly be a reflection of systematic uncertainty.

Previous workers have found inconsistency in P-T estimations between different geothermobarometers. For example, Boyle and Westhead (1992) found that *thermocalc* pressure estimates were systematically 1.5 kbar higher than estimates using the gnt-mu-plag-bi-qtz geobarometer of Ghent and Stout (1981), as modified by Hodges and Crowley (1985), and 1.1 kbar higher than pressure estimates using the gnt-hb-plag geobarometer of Kohn and Spear (1990). However, if a reasonable 1 kbar error is assigned to the results of both the gnt-mu-plag-bi-qtz and gnt-hb-plag geobarometers, the results lie within error of the estimates from *thermocalc*. Temperature estimates from *thermocalc* and conventional geothermometers were found to be in broad agreement, although *thermocalc* estimates indicated a wider range in temperature. Boyle and Westhead (1992) concluded that in general, *thermocalc* produced the most consistent P-T results.

Activities have been calculated using the Newton and Haselton (1981) solution models for garnet and feldspar. Default uncertainties are used for the activity-composition relationship, thus minimising the chance of underestimating this uncertainty. The most recent version of the application *activity* was used at the time of writing.

Many dehydration reactions are sensitive to water activity, and calculated temperatures may vary according to the value of water activity used. For example, Fig. 4.3 shows the variation in calculated temperature with changing water activity for pelitic gneiss

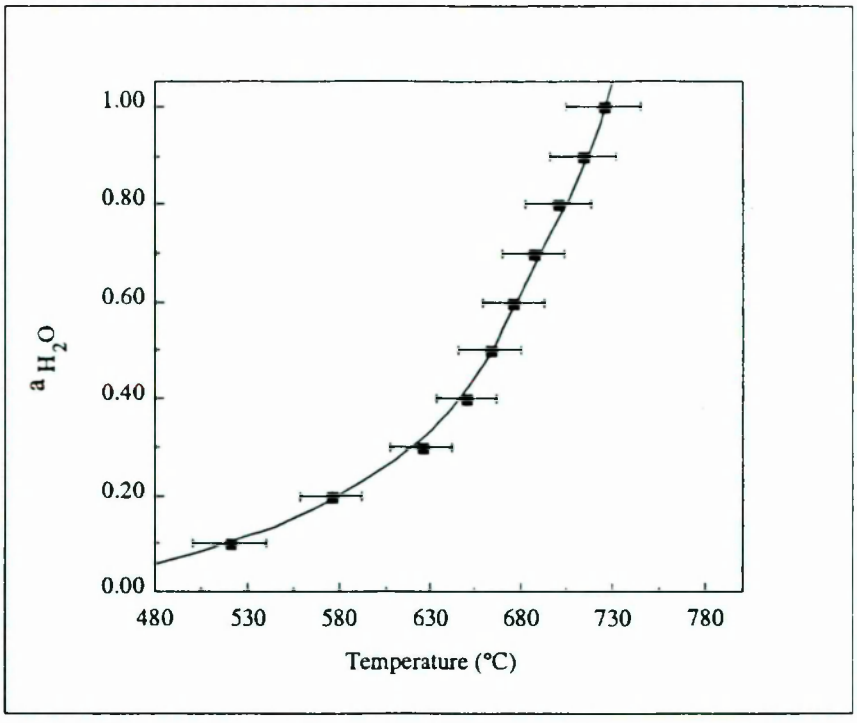

Fig. 4.3. Graph showing the variation in *thermocalc* temperature estimates with water activity, for pelitic gneiss sample G31.

sample G31. The calculated pressure remains relatively constant at 8.9-9.0 kbar. Although the total temperature range is > 200 °C, it should be noted that between a_{H_2O} 0.7-1.0, the calculated temperature varies by < 50 °C. Unfortunately independent estimates of water activity during metamorphism are not available. By comparing fluid-independent equilibria with fluid-dependant equilibria in pelitic schists from New Hampshire, Hodges and Spear (1982) found that $P_{H_2O} < P_{total}$. Muscovite is widely observed across the NPHM (Misch 1964), and all of the studied samples contain hydrous phases, and therefore it is reasonable to assume that the majority of samples contained a free fluid phase (water and/or CO_2) during metamorphism. However, the migmatitic, muscovite-free assemblages present at Fairy Meadows may be an exception, since the presence of a melt phase in these assemblages, in the absence of an external fluid source, would have had the effect of internally buffering the water activity. For example, Clemens and Vielzeuf (1987) predict a water activity of 0.8-0.9 for melting under fluid-absent conditions. In the light of these observations, in this work a water activity of 0.8 has been used for all calculations. Temperature results for samples constrained mainly by dehydration reactions may thus be minimum estimates if $a_{H_2O} > 0.8$.

Results of *thermocalc* calculations on twenty-six samples are given in Table 4.2, and data plotted in Fig. 4.4. Calculated temperatures lie in the range 500-850 °C and calculated pressures lie in the wide range 4-12 kbar. The magnitudes of the calculated errors are partly dependent on the mineral assemblage. Generally speaking, metabasic assemblages generate errors on P-T estimates of ~ 60 °C for temperature and > 0.9 kbar for pressure. Pelitic samples generally generate relatively small errors of ± 10-36 °C and < 1 kbar for temperature and pressure respectively, whilst errors on P-T estimates from calcsilicates are variable but also often relatively low. These differences demonstrate the importance of systematic error in the calculated uncertainties of P-T estimates. The most important systematic error probably originates from poorly-constrained activity-composition relationships for end-members such as hornblende (Holland and Powell 1990). Samples which contain the largest number of end-members also have the lowest errors in P-T estimates, as shown by samples which contain additional phases such as kyanite, zoisite or k-feldspar.

4.4.1. Kohistan Arc

Five samples collected from the Kohistan arc contained suitable assemblages for the calculation of P-T using *thermocalc*. Samples of pelitic gneiss from the Gilgit valley indicate consistent temperatures in the range 547-603 °C and pressures of 6.2-8.1 kbar (see Table 4.2). Metabasic samples collected from Shuta, closer to the NPHM, have somewhat higher temperatures and pressures in the range 618-700 °C and 8.2-10.0 kbar, indicating an increase in metamorphic grade towards the NPHM.

4.4.2. Northern NPHM

A total of eight samples collected from the shear zone at Sassi, contained suitable assemblages for use in *thermocalc* (Table 4.2). These samples are representative of the varied lithologies occurring within the shear zone, and were collected within close proximity to one another (< 1 km) and thus may help to give an indication of the precision of

Sample	Location	Lithology	Assemblage	P(Kb)	sd	T(°C)	sd
Kohistan							
G-1	Gilgit Valley	pel. gneiss	gt, bi, mu, pl, zo	8.1	0.3	603	10
G-7	Indus conf.	pel. gneiss	gt, bi, mu, pl, zo	6.3	0.1	550	6
G-9	Jaglot	pel. gneiss	gt, bi, mu, pl, zo	6.2	0.2	547	6
G-17	Shuta	amphib. gneiss	gt, bi, hb, pl, zo	8.2	0.3	618	14
G-20	Shuta	amphib. gneiss	gt, bi, hb, pl, zo	10.0	0.5	700	26
NPHM							
S-17	Sassi	amphib. gneiss	gt, bi, hb, pl	9.8	1.1	600	61
S-22	Sassi	amphib. gneiss	gt, bi, hb, pl, ksp	7.9	1.1	660	67
S-24	Sassi	amphib. gneiss	gt, bi, hb, pl	10.0	0.9	740	65
S-34	Sassi	calcsilicate	gt, bi, hb, pl	8.0	0.9	670	67
S-28	Sassi	calcsilicate	gt, bi, hb, pl, diop, zo	7.7	0.4	700	15
S-29	Sassi	pel. gneiss	gt, bi, mu, pl	8.0	0.9	660	36
S-62	Sassi	pel. gneiss	gt, bi, mu, pl, ky	10.1	1.0	700	27
G-31	Sassi	pel. gneiss	gt, bi, mu, pl, ky, ksp	9.1	0.8	700	18
D-18	W. Darchan	psam. gneiss	gt, bi, mu, pl, ep, ksp	7.9	0.5	600	18
D-19	E. Darchan	pel. gneiss	gt, bi, mu, pl	8.7	1.2	660	29
I-1	Isgere	amphib. gneiss	gt, bi, hb, pl	7.0	1.8	650	95
S-90	Shengus	amphib. gneiss	gt, bi, hb, pl	8.9	1.3	625	100
A-7	Tarshing	pel. gneiss	gt, bi, mu, pl, zo	8.6	0.2	600	7
A-3	Astor Gorge	pel. gneiss	gt, bi, mu, pl, ky, ksp	10.7	1.0	850	18
A-21	Astor Gorge	pel. gneiss	gt, bi, mu, pl, ky, ksp	11.7	1.7	850	55
T-20	Liachar SZ	calcsilicate	gt, bi, hb, pl	10.0	1.0	640	74
T-64	Liachar SZ	calcsilicate	gt, bi, hb, pl, diop	10.0	1.2	717	58
T-69	Liachar SZ	amphib. gneiss	gt, bi, hb, pl, ksp	8.3	0.7	625	48
L-8	Liachar SZ	amphib. gneiss	gt, bi, hb, pl, zo	12.0	0.5	750	18
M-6	Tato village	calcsilicate	gt, bi, hb, pl, diop	4.0	0.9	500	31
M-16	Fairy Meadow	calcsilicate	gt, bi, hb, pl	6.0	1.7	627	88

Table 4.2. P-T estimates from the Nanga Parbat-Haramosh massif and adjacent Kohistan terrane, using the program *thermocalc* (Powell & Holland 1988). Quoted overall uncertainties (sd) are to two sigma. Liachar SZ = Liachar shear zone. gt = garnet; bi = biotite; mu = muscovite; hb = hornblende; pl = plagioclase; ksp = k-feldspar; diop = diopside; zo = zoisite; ep = epidote; ky = kyanite.

thermocalc. The metabasic lithologies are assumed to have an origin in the Kohistan arc, and the calcsilicates and pelites are more likely to have originally formed a part of the ancient Indian continental crust ("cover" of Butler and Prior 1988a).

Estimates of temperature for these eight samples are relatively consistent, and in most

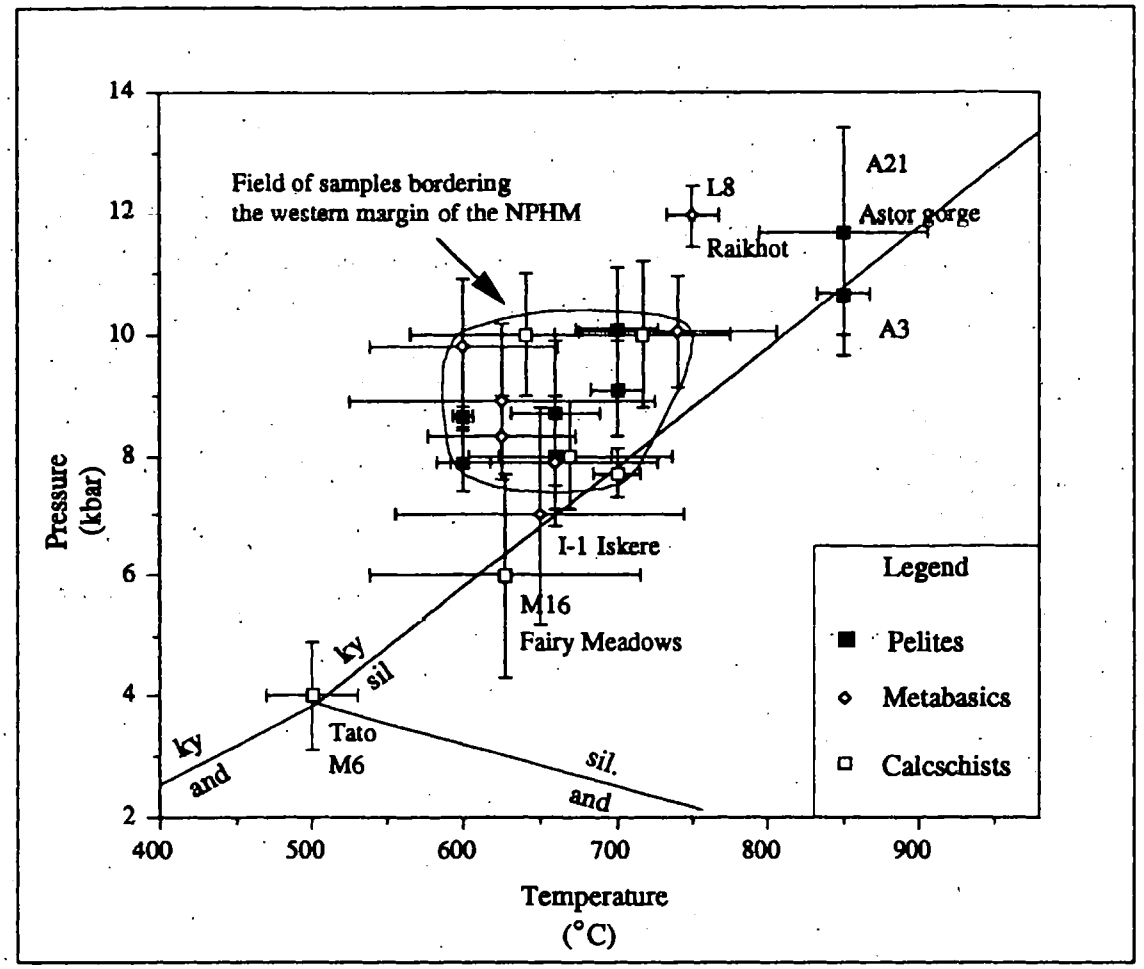

Fig. 4.4. P-T diagram for the NPHM. Al_2SiO_5 triple point after Holdaway (1971). The majority of samples plot in the field defined by samples bordering the western margin of the NPHM; other samples are labelled.

cases overlap within error, as shown in Table 4.2. The range of calculated temperature is 600-740 °C (540-805 °C within the total error bracket). Calculated pressures are more variable, and lie in the range 7.7-10.1 kbar (6.8-11.1 kbar within error). In contrast to the size of the error (as discussed above), the size ot the estimated P and T recorded by a sample appears to be unrelated to the metamorphic assemblage, as illustrated in Fig. 4.4. Nor is there any consistent change in P-T across the strike of the shear zone. The cause of the slight variation in calculated pressure between samples may reflect a real variation in pressure of metamorphism recorded by samples in different parts of the shear zone. Given the fact that the shear zone has been the site of substantial, post metamorphic ductile oblique-slip, the samples may have originated from different structural levels in the crustal stack. Alternatively, the pressure variation may simply reflect experimental error combined with the

underestimation of propagated uncertainties in *thermocalc*.

Four other samples from the northern part of the NPHM generate P and T estimates within the ranges defined by the Sassi suite. The two samples from the upper Darchan valley (D18 and D19) straddle the northern extension of the shear zone, and have yielded P-T estimates in the range 600-660 °C and 7.9-8.7 kbar. These show that there is no marked P-T change (within error) along the strike of the shear zone for approximately 50 km from north to south. These samples also show that there is no consistent P-T change across the strike of the shear zone in the upper Darchan valley. The other two samples (I-1 and S-90) were collected from localities outside the shear zone, within the NPHM. Sample S-90 is from the Shengus gneiss unit of Madin et al. (1989), in which the pelitic lithologies contain fibrolitic sillimanite, whereas sample I-1 is representative of the Iskere orthogneiss unit. These samples yield estimates of P-T in the range 625-650 °C and 7.0-8.9 kbar. It can be concluded that there is no consistent variation in P-T across this part of the NPHM, nor is there any measurable difference in P-T conditions between the Iskere and Shengus gneisses.

4.4.3. Southern NPHM

Four samples were collected from the western margin of the NPHM in the southern area. Three of these (T20, T64 and T69; Table 4.2), come from the Liachar shear zone in the hanging-wall of the Liachar thrust (Butler and Prior 1988b), at a spacing between sample localities of < 0.5 km. Calculated average temperatures and pressures for these samples are 625-717 °C and 8.3-10.0 kbar, and lie within error of those from the Sassi suite. The fourth sample (L8) comes from Raikhot, in the footwall of the Liachar thrust, and yields estimated P-T of 750 ± 18 °C and 12.0 ± 0.5 kbar. The estimated peak pressure is significantly higher than for other samples from the western margin of the NPHM, which presumably indicates that some samples presently exposed in the shear zone experienced relatively deep burial.

The pressure and temperature calculated for a calcareous gneiss assemblage collected from near to the eastern margin of the NPHM (sample A7, Table 4.2) are 600 °C and 8.6

kbar, respectively. These estimates lie within error of the P-T conditions recorded by most samples from the western margin. However, migmatitic samples of pelitic gneiss from the Astor gorge, in the core of the NPHM (Shengus unit of Madin et al. 1989), record markedly higher temperatures (850 ± 55 °C) than other samples from the NPHM, supporting Misch's (1964) contention that the peak metamorphic grade increases towards the core of the NPHM. These gneisses contain scattered, concordant, 1-2 mm thick layers of quartz-k-feldspar leucosome, but the age of the migmatisation is unconstrained. Primary muscovite appears to be stable in these rocks (see Plate 2.16), and sillimanite is absent. According to Vielzeuf and Holloway (1988), extensive breakdown of biotite occurs in pelitic rocks at around 850 °C at 10 kbar, above the temperature required for the dehydration of muscovite. This may indicate that *thermocalc* has slightly over-estimated the approximate peak metamorphic temperatures for the Astor gorge samples. Alternatively, during prograde metamorphism, the fluid-absent solidus may have been overstepped due to the delayed nucleation of new phases in the incongruent melting reaction (Rubie and Brearley 1990).

Samples M16 and M9 from the Tato-Fairy meadows area have yielded equivocal results for pressures and temperatures of metamorphism, and demonstrate some of the potential pitfalls involved in such calculations.

Sample M16 is a calcareous, amphibolitic gneiss characterised by fine, compositionally distinct laminations of garnet, biotite, plagioclase (An_{35-44}) and hornblende, alternating with garnet, biotite and plagioclase (An_{83-87}). On the basis of errors propagated in *thermocalc*, the anorthitic plagioclase appears to be out of equilibrium with the garnet and biotite contained in the sample, although there is no textural evidence for this. When the anorthite phase is used in *thermocalc*, the optimum pressure conditions within the temperature window lie outside the overlap of optimum temperature conditions in the pressure window. However, this problem is not encountered using An_{35-44}, when good fits are generated in the data output. The final estimated errors are further improved in this sample by excluding the tremolite and ferro tremolite end-members, although the exclusion of these end-members produces a slight shift in the results to higher temperatures. Calculated

temperature and pressure for sample M16 are approximately 500 ± 105 °C and 5.8 ± 2.1 kbar respectively, using all end-members, whilst the results are 627 ± 88 °C and 6.0 ± 1.7 kbar if reactions involving tremolite and ferro-tremolite are excluded. The removal of these end-members can be justified since they have very low activities and correspondingly high default uncertainties, and since the shift in the results is within error.

Sample M9 is a migmatitic, pelitic gneiss containing the assemblage garnet, sillimanite, cordierite, biotite, k-feldspar and quartz. The calculated temperature from five independent reactions is approximately 550 °C, but this result lies outside the temperature window of the calculated pressures. The situation is not improved by selectively removing end-members or changing positions of windows, indicating that the assemblage is substantially out of equilibrium, with the result that no acceptable P-T calculation is possible for this sample. However, a calcsilicate from near Tato village (M6; Table 4.2) generates relatively low estimates of temperaturesand pressure (T = ~ 500 °C; P ~ 4 kbar), which is consistent with the presence of cordierite in the associated pelitic gneisses.

In summary, conditions of metamorphism in the Tato-Fairy Meadows area are rather poorly constrained, but lie in the range 500-630 °C and 4-6 kbar. In comparison, Zeitler et al. (1993) determined peak metamorphic conditions on four pelitic samples to be approximately 650 ± 50 and 6 ± 1 kbar.

4.5. Evolution of Metamorphic Conditions ('P-T-t paths')

The range of P-T conditions under which garnet crystallised has been estimated using Gibbs modelling of compositionally-zoned garnets (Spear and Selverstone 1983, Spear 1988), a technique which relies on the capacity of garnet to preserve a record of changing P-T conditions during either prograde or retrograde growth. In the past, the early portions of metamorphic P-T-t paths were constrained by the interpretation of diagnostic reaction textures, such as cordierite overgrowths on garnet (Hollister 1982). As discussed by Spear et al. (1991) and Frost and Tracy (1991), evidence from such reaction textures,

together with observations of metamorphic phase relations, compositional variation in thin-section and structural evidence, should be used in combination with Gibbs modelling to constrain the thermal evolution of a metamorphic rock.

The Gibbs method involves analytically formulating the phase equilibria of a given mineral assemblage so that compositional changes of co-existing minerals can be related to changes in pressure and temperature. A series of simultaneous linear differential equations are solved which include a Gibbs-Dunhem equation for each phase present, and equations for the conditions of heterogeneous equilibrium and the variation in phase composition. The solutions are carried out by finite difference techniques which resolve the changing temperature and pressure from garnet rim to garnet core, given an initial (rim) reference temperature and pressure. The phases quartz, muscovite and H_2O are assumed to be pure. The equilibrium crystallisation model can be used which assumes that all parts of all phases are homogenous and always in equilibrium; P-T path calculations using the Gibbs method are not affected by fractional crystallisation because only intensive variables in the system are used (Spear 1988).

The Gibbs method makes three important assumptions :

(i) Garnet zoning is due to continuous reactions occurring during growth, and post-growth modification of growth zoning by diffusion is negligible.

(i) The metamorphic assemblage present at all stages of garnet growth is known.

(iii) Local equilibrium existed between all phases at all times during garnet growth.

If these assumptions are unjustified, P-T paths calculated from the Gibbs method are subject to considerable uncertainty. The extent to which the garnet zoning profiles of the studied samples have been effected by diffusion is difficult to evaluate, as already discussed. Post-growth diffusion has the effect of shortening P-T paths, and, due to different cation

diffusion rates, slightly modifying their slope. The deviation of calculated growth history from the true growth history is the greatest for the early part of the garnet history (Spear and Selverstone 1983; Spear 1991). According to Tracy et al. (1976), diffusion rates in garnet at amphibolite grade are probably slow. Furthermore, the presence of strong, often finely-detailed garnet zoning profiles in samples from the NPHM, together with the consistent relation between lithology and pattern of garnet zoning, argues against significant diffusional homogenization, despite relatively high metamorphic temperatures (> 700 °C). The rapid cooling rates for metamorphic rocks from the region (see Chapter 5) may have helped to preserve the garnet zoning profiles. Thus the garnet zoning patterns illustrated in Fig. 4.1 are interpreted as reflecting the prograde or retrograde continuous reactions in which the garnet is involved.

If the metamorphic assemblage has changed during garnet growth, the slope of the P-T path may be significantly in error (Frost and Tracy 1991). The presence of most matrix phases as inclusions in the garnet samples in this study supports the assumption that the same assemblage was present throughout garnet growth. Further support comes from the observation that the garnet zoning profiles for most samples are relatively smooth, since any new garnet-producing reaction which began during garnet growth would probably be reflected in a discontinuity in the profile (Bergman 1992).

Unfortunately, the majority of garnet samples do not contain plagioclase inclusions, and subsequently the methods of Thompson et al. (1977) and St Onge (1987) cannot be used as additional constraints. Zoned matrix plagioclase may help in deducing reaction histories, but as noted by other workers (Frost and Tracy 1991), such zoning is often patchy rather than concentric, and rarely unambiguous. According to Spear and Florence (1992), variable zoning observed in matrix plagioclase may be a reflection of the fact that only a proportion of plagioclase has reacted with the garnet. Where the variance of the assemblage is > 3, and plagioclase inclusions are not present, it must be assumed that the matrix plagioclase core was in equilibrium with the garnet core. Clearly this may not be the case, and results must be treated with caution.

Other uncertainties in the calculation of P-T paths involve errors in the analytical and thermodynamic parameters, which may be assessed by error propagation through the calculations (Spear and Rumble 1986; Kohn 1993). For example, Kohn (1993) estimated typical errors on P-T paths to lie in the range ± 0.3-0.4 kbar and ± 8-50 °C for different assemblages, taking into account uncertainties in endmember thermodynamic data, monitor parameters and initial P-T estimates. The largest source of error was found to be derived from the uncertainty associated with the monitor parameters. Since these propagated errors are relatively small compared with the total path lengths, the largest uncertainties in the use of the Gibbs method are attributed to assumptions concerning the mineral assemblage during garnet growth, and to correlations between garnet zoning and plagioclase zoning (Spear et al. 1990), uncertainties which to a large extent cannot be quantified.

P-T paths have been calculated for seven different samples from widely separated locations within the NPHM and adjoining Kohistan arc. Results are shown in Table 4.3 and plotted in Figs. 4.5A & B. All calculations have been carried out assuming ideal mixing in garnet, biotite and plagioclase, since the choice of mixing model makes little difference to the final result (Spear and Selverstone 1983). Initial P-T conditions are derived from *thermocalc* calculations (see above). Although *thermocalc* may generate slightly different absolute P-T from the package of Spear (1988), it should be emphasised that the object of this part of the study is to evaluate the relative change of P-T with time. All of the samples contain garnet with a significant X_{gr} component and subsidiary X_{sp} component, together with plagioclase, and consequently all the modelling was carried out in the system KNCFMMASH (i.e. with Ca +Na +Mn).

4.5.1. Trivariant Assemblages

Three samples of pelitic gneiss contain the assemblage garnet, kyanite, muscovite, biotite plagioclase, k-feldspar and quartz. Garnets porphyroblasts contain inclusions of kyanite, muscovite, biotite and quartz, and it is assumed that the garnet always grew in the

Sample	Δalm	Δsp	Δgr	Δan	Δzo	ΔP (kbar)	ΔT (°C)
Trivariant							
A3	0.027	0.007	0.019	0.074(1)	-	-3.2	-57
A21	-0.016	-0.016	0.056	0.133(1)	-	-1.9	-33
G31	0.047	0.005	0.034	0.216(1)	-	-3.7	-65
Quadrivariant							
A7	-0.104	0.013	0.022	-0.072	-0.021 (1)	2.8	69
G1-1	0.020	-0.010	0.037	-0.276	-0.075 (1)	2.7	53
G1-2	0.020	-0.010	0.037	-0.052	-0.109 (1)	1.5	72
S24	-0.021	-0.033	0.061	0.068	-	-0.7	47
T20	-0.055	-0.024	0.082	0.054	-	-0.1	22

Table 4.3. Results of Gibbs modelling of garnet. The total measured compositional change for each phase between core and rim is shown (individual, modelled compositional steps are not shown). alm = almandine; sp = spessartine; gr = grossular; an = anorthite and zo = zoisite. (1) = the calculated compositional change for plagioclase or zoisite.

same assemblage. In the KNCFMMASH system, the samples are trivariant, thus requiring the input of three compositional parameters. Since the matrix plagioclase in all three of these samples is unzoned, and plagioclase inclusions in garnet are absent, the parameters selected must be ΔX_{gr}, ΔX_{alm} and ΔX_{sp}.

Modelling of sample G31, collected from Sassi, indicates garnet growth during ΔT = - 65 °C and ΔP = - 3.7 kbar, using a rim reference point of 700 °C at 9.1 kbar. The X_{an} component of the plagioclase is simultaneously increased during the calculations from An_5 to An_{27} (core to rim), as shown in Table 4.3.

Sample A3, collected from the Astor gorge, grew during ΔT = - 57 °C and ΔP = - 3.2 kbar, using rim reference conditions of 850 °C at 10.6 kbar. The program again calculated an increase in the anorthite component of the plagioclase from An_4 (core) to An_{11} (rim).

Sample A21, from the same locality as sample A3, contains garnet which grew during ΔT = - 34 °C and ΔP = - 1.9 kbar, using a rim reference point of 850 °C at 11.7 kbar. In this case, the plagioclase composition was modelled to increase from An_2 (core) to An_{16} (rim).

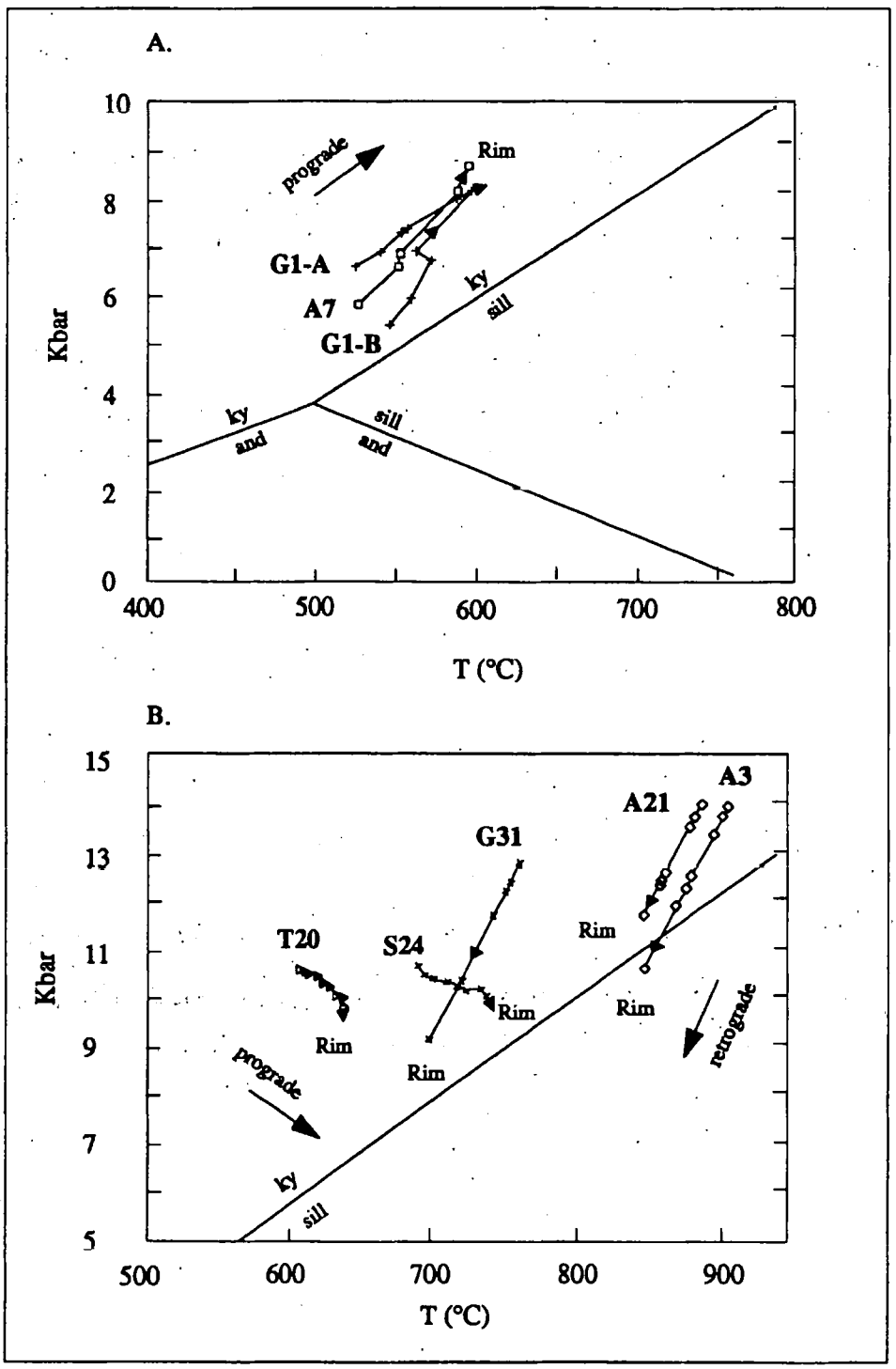

Fig. 4.5. P-T Paths from Gibbs modelling of garnet zoning. A: Apparent prograde paths for sample G1 from the Kohistan arc(see text for discussion), and also a prograde path for sample A7 from near Tarshing (NPHM). B : Retrograde paths for samples from the Astor gorge (NPHM; A21 & A3) and shear zone at Sassi (G31), together with prograde paths for samples from Sassi (S24) and the Liachar shear zone (T20; NPHM). Aluminosilicate triple point after Holdaway (1971).

The garnets in all of these samples exhibit broadly similar compositional zoning profiles, characterised by increasing X_{gr} and Fe/(Fe+Mg), and decreasing X_{py}, from core to rim, although the profiles have markedly different shapes (see Fig. 4.1). For example, garnets from samples G31 and A3 exhibit smooth profiles from core to rim, indicative of gradual growth during a single metamorphic event. In contrast, the compositional profile across garnet from sample A21 has a marked step, which could be interpreted as indicating two periods of growth. However, the P-T path of sample A21 lies in a straight line in P-T space, and is comparable to the path recorded by adjacent sample A3, which contains garnet which exhibits relatively smooth growth zoning. Points recorded by analyses from either side of the compositional step in sample A21 are relatively spaced-out, suggesting that the 'step' records a period of more rapid growth, along the same path. The decreasing temperatures recorded by Gibbs modelling of these samples is consistent with the observed increase in Fe/(Fe+Mg) between garnet core and rim.

The calculation of an increase X_{an} in the anorthite component of plagioclase between core and rim is supported by the widespread presence of reversely-zoned plagioclase in the NPHM, recorded both in this work and by Misch (1964). The fact that all three trivariant samples contain unzoned plagioclase suggests that the matrix plagioclase in high-grade samples from the NPHM has locally suffered retrograde diffusion, eradicating the original zoning profiles. The assumption of constant plagioclase composition during garnet growth is therefore hazardous, undermining its role as a compositional parameter in Gibbs modelling (Chamberlain et al. 1989).

4.5.2. Quadrivariant Assemblages

Four samples with quadrivariant assemblages have been modelled using the Gibbs method. Samples S24 and T20 contain the assemblage garnet, hornblende, biotite, plagioclase, k-feldspar and quartz. Garnets contain inclusions of biotite and hornblende, and it is assumed that the garnets grew in the above assemblage. Samples A7 and G1 contain the assemblage garnet, zoisite, muscovite, biotite, plagioclase and quartz. Although plagioclase

inclusions in garnet are absent, all four samples contain matrix plagioclase which consistently exhibits compositional zoning. Since four compositional parameters must be used, it is assumed that the matrix plagioclase cores are in equilibrium with the garnet cores. Furthermore, it is assumed that the changes in plagioclase composition are dispersed smoothly over the zoning profile, so that the change in plagioclase composition from core to rim can be correlated with the growth of garnet from core to rim. Thus for each step, the value of X_{an} is decreased or increased by a pre-determined amount (Spear and Selverstone 1983). This is a reasonable assumption since in a closed system in which garnet and plagioclase are the only calcic phases, growth of garnet requires the consumption of plagioclase. Previous workers have successfully modelled quadrivariant assemblages, despite the higher degree of uncertainty in the calculated P-T paths (Bergman 1992; Spear et al. 1990). According to Spear et al. (1990), the amount of plagioclase zonation is probably underestimated, since recrystallisation of plagioclase during garnet growth tends to obliterate the pre-existing zonation preserved in the plagioclase, and hence the modelled ΔP may be a minimum estimate.

Samples S24 and T20 are characterised by the same mineral assemblages, and contain similarly zoned garnets. Both samples possess matrix plagioclase which exhibits a measured increase in the anorthite component from core to rim. This plagioclase co-exists with garnet which shows an increase in the grossular component from core to rim. Sample S24 from the shear zone at Sassi grew during $\Delta T = +47$ °C and $\Delta P = -0.7$ kbar. Although the bulk of the compositional change occurs near to the garnet rim, the observed temperature increase prohibits this from being solely the effect of retrograde diffusion. Sample T20 from the Liachar shear zone possesses relatively strong garnet compositional zoning (see Fig. 4.1G), but this zoning records a relatively minor P-T change of $\Delta T = +22$ °C and $\Delta P = -0.1$ kbar. This demonstrates that the degree of compositional zoning in a garnet is not necessarily directly related to the degree of P-T change that has occurred.

Sample A7 (Table 4.3) contains matrix plagioclase which consistently shows a decrease in X_{an} from core to rim, whilst the garnet displays a decrease in X_{gr} from core to

rim. Modelling of this sample indicates $\Delta T = +70$ °C and $\Delta P = +2.8$ kbar during garnet growth, which is consistent with the strong decrease in Fe/(Fe+Mg) observed in the rim region. The P-T path (Fig. 4.5A) is remarkably straight, given the complexity of the garnet zoning profile.

A complete garnet compositional profile for sample G1 from the Gilgit valley (Kohistan) is not available, but similar profiles for garnets from adjacent samples are given in Figs. 4.1A & B. Sample G1 contains matrix plagioclase which shows substantial variation in composition between different grains. Individual grains usually show a decrease in X_{an} between core and rim. Consequently the garnet has been modelled, firstly, by using the change in composition of a single plagioclase grain adjacent to the garnet, and secondly by using the maximum preserved change in plagioclase composition throughout the sample. In the first case, the modelling indicates $\Delta T = +72$ °C and $\Delta P = +1.5$ kbar. Using a larger modelled change in X_{an} for each finite differential step produces $\Delta T = +53$ °C and $\Delta P = +2.7$ kbar. As expected, the two modelled P-T paths become more divergent towards the garnet core, as shown in Fig. 4.5A.

The two P-T paths for sample G1 are similar to the P-T path modelled for sample A7, described above, despite diferences in the garnet zoning profiles for the two samples. Given the fact that, in sample G1, the Fe/(Fe+Mg) ratio increases strongly between the garnet core and rim, the calculated increase in temperature is surprising. In other metasedimentary samples collected from Kohistan, sillimanite is locally present in garnet cores but absent from the surrounding matrix, suggesting that the metamorphic assemblage has changed during garnet growth and that progressive reactions have eliminated sillimanite from the equilibrium assemblage. Both the measured increase in Fe/(Fe+Mg) ratio between the garnet core and rim, together with the presence of sillimanite in some garnet cores, suggest that reactions may actually have been retrogressive, and therefore no weight can be attached to the results of Gibbs modelling for sample G1.

In summary, P-T paths determined from the NPHM appear to be highly variable.

Three relatively well-constrained trivariant samples record major retrogressive P-T paths. Cygan and Lasaga (1982) also found that garnet characterised by a decrease in X_{py} and an increase in X_{alm} from core to rim appeared to have grown during a retrograde event. The three trivariant samples contain the same pelitic assemblage, and in two cases were collected from the same structural level. The similarity between path lengths and path orientations between different samples lends support to the results. Peak metamorphic conditions are constrained to be 750-900 °C and 13-14 kbar. Contrasting, poorly-constrained prograde P-T paths are provided by quadrivariant samples. Two of these samples (S24 & T20) were collected from the western margin of the NPHM, although from localities approximately 50 km apart. These samples are characterised by similar metamorphic assemblages and garnet zoning profiles, and record a slight temperature increase and pressure decrease during garnet growth. A single sample collected from the eastern side of the NPHM (A7) has the most unusual garnet zoning profile observed in the region, consistent with a modelled growth path along increasing temperature and pressure. No reliable, quantitative P-T paths are available from the Kohistan arc, although samples from this region have probably followed retrogressive pathways.

4.6. Geochronological Evidence for the Timing of Metamorphism

4.6.1. Previous Constaints

To the south-west of the NPHM, the deformation intensity and associated metamorphic grade increases northwards towards the Main Mantle Thrust, which there bounds the southern margin of the Kohistan arc (Treloar et al. 1989b & c). The relation between structure and metamorphism, as in other sections of the Himalaya, suggests a Himalayan-age for the dominant metamorphic fabric present in the Indian continental crust. Geochronological studies indicate that this metamorphism occurred before ~ 40 Ma (Treloar et al. 1989a; Treloar and Rex 1990a &b). However, in detail, some areas of the Indian crust exposed in northern Pakistan retain both textural and geochronological evidence for earlier

metamorphic events (Williams et al. 1988).

In the NPHM, the age of metamorphic fabrics is also subject to some uncertainty (Smith et al. 1992). Scattered, amphibolite-grade metabasic dykes within the NPHM locally lie oblique to the dominant foliation, but are themselves folded and highly deformed. Although the age of the dykes is unknown, a complex long-term deformational and metamorphic history for the NPHM can be inferred (Butler et al. 1989; Treloar et al. 1991).

Muscovite, biotite and hornblende Rb/Sr, Ar-Ar and K-Ar mineral ages for the NPHM have variable but 'Himalayan' (< 40 Ma) ages (see Chapter 5). However, these are cooling ages, and either reflect simple cooling through the relevent blocking tempertaure, or the resetting of the appropriate isotopic system for the relevant phase during a young heating event (which does not necessarily correspond to the 'peak' metamorphism). Given the fact that the blocking temperature for strontium in muscovite and for argon in hornblende is about 500 °C (Cliff 1985), and that the peak metamorphic temperatures for the NPHM are generally 600-750 °C, mineral ages only place a minimum constraint on the time of metamorphism.

U-Pb conventional and ion microprobe zircon dating of the metamorphic rocks of the NPHM indicate protolith ages of 1.9 Ga for the Iskere gneisses and 400-500 Ma for the Shengus gneisses (Zeitler et al. 1989). However, metamorphic zircons are often characterised by high-U overgrowths which have yielded ages in the range 2-11 Ma (Zeitler et al. 1989). These are similar to the ages of zircons from leucogranite dykes intruding the NPHM (1-7 Ma) (Zeitler and Chamberlain 1991; Zeitler et al. 1993). Furthermore, metamorphic monazites collected from widely separated localities within the NPHM, including the Indus gorge, the Astor gorge and Fairy Meadows, have yielded U-Pb ages in the range 3-11 Ma (Smith et al. 1992; Zeitler et al. 1993). Given the relatively high blocking temperatures thought to apply to zircon and monazite, these studies have been used to infer a young, late-Himalayan age for the metamorphism recorded by the rocks of the NPHM (Smith et al. 1992).

4.6.2. Sm-Nd Dating of Garnet

A reconnaissance isotopic study of metamorphic garnets from the NPHM has been carried out in an attempt to further constrain the timing of metamorphism in the region. Three samples were selected which contained suitably fresh, relatively inclusion-free grains. Garnet samples were handpicked in order to separate and discard any grains containing inclusion phases. Details of subsequent experimental techniques are described in Appendix 1. Following earlier studies (Burton and O' Nions 1991), an attempt was made to run the garnets for both strontium and neodymium isotopic compositions. However, during the course of the study, it was found that the garnet samples contained insufficient concentrations of strontium (< 1.5 ppm) for accurate determination of their strontium isotopic ratios.

Results of the garnet neodymium-isotope work are presented in Table 4.4. Neodymium concentrations in the garnets are relatively high (up to 46 ppm) and consequently Sm/Nd ratios are correspondingly low. Samples D19 and A3 are pelitic gneisses from the Darchan and Astor valleys, respectively. In both cases, the garnet is characterised by a similar neodymium isotopic composition to the corresponding whole-rock. Unfortunately, the long half-life of the neodymium decay scheme, coupled with the relatively small differences in Sm/Nd ratios between garnet and whole-rock, makes the precise resolution of an age for these garnets impossible. However, the equation for the radiogenic decay of ^{147}Sm can be used to place an upper constraint on the time of isotopic equilibration between the garnet and the whole-rock. In the case of sample D19, equilibration must be younger than ~20 Ma since, for an interval of > 20 Ma, the difference in neodymium isotopic ratio between the garnet and whole rock would be greater than the two-sigma error attached to these ratios. In the case of garnet sample A3, which is characterised by a smaller Sm/Nd ratio, the time since last equilibration must be < ~25 Ma. If it is assumed that one-sigma differences between neodymium isotope ratios are detectable, then equilibration of the neodymium isotopic system of the garnets must have occurred since

Sample	Rb	Sr	Sm	Nd	Sm/Nd	$^{147}Sm/^{144}Nd$	$^{143}Nd/^{144}Nd$	2σ	Age (Ma)
D19 WR	175	181	4.50	20.62	0.2182	0.1314	0.51129	1	
D19 gnt	5.1	1.5	1.50	5.91	0.2533	0.1525	0.51131	2	no age
A3 WR	375	77.4	6.78 (1)	36.10 (1)	0.1878	0.1131	0.51174	1	
A3 gnt	n/d	n/d	9.30	45.94	0.2023	0.1218	0.51174	2	no age
G31 WR	129	115	5.74	27.44	0.2091	0.1259	0.51168	1	
G31 gnt	n/d	n/d	5.02	18.30	0.2744	0.1652	0.51177	1	363.7 ± 63

Table 4.4. Rb-Sr and Sm-Nd isotope data for garnet samples from the Nanga Parbat-Haramosh massif (A3) and Sassi-Darchan shear zone (D19 & G31). WR = whole-rock; (1) = Sm and Nd concentrations by INAA; all other Sm and Nd concentrations are by isotope dilution. Rb and Sr concentrations are by isotope dilution (garnet) or XRF (whole-rock). See text for discussion.

10-13 Ma.

It should be noted that the time of last equilibration of the Sm-Nd system may not correspond to the time of peak metamorphism. The closure temperature for neodymium diffusion in garnet is the subject of some debate and estimates range from around 700 °C to 600 ± 30 °C (Mezger et al. 1992; Burton and O' Nions 1991). The relatively high peak metamorphic temperatures experienced by samples D19 and A3 may imply that the neodymium isotope compositions of the garnets reflect the radiogenic decay that has occurred since the rocks passed through the neodymium blocking temperature (i.e, the 'ages' may be cooling ages). However, the data require that either garnet growth or isotopic resetting occurred at least within the last 25 Ma, and probably more recently. The data are thus consistent with U-Pb zircon and monazite studies of Zeitler and co-workers (Smith et al. 1993), which suggest that the rocks presently exposed in the NPHM experienced a late-Himalayan (< 10 Ma) metamorphic event.

Samples G31 is a pelitic gneiss collected from the shear zone at Sassi, and yields an Sm-Nd garnet-whole rock age of 364 ± 63 Ma. No meaningful geological interpretation can be applied to such an age, and the isotopic systematics may be a reflection of the following :

(i) The date is a mixing age, caused by the partial resetting of an old (possibly Precambrian) neodymium isotopic system by a Himalayan-age heating event.

(ii) The age reflects the presence of inclusions of monazite within the garnet (Vance and O'Nions 1990; Chaudhary et al. 1992). The inclusions must contain a significantly higher neodymium content than the garnet, and must have remained closed to re-equilibration during Himalayan metamorphism, whilst the garnet was isotopically homogenised.

(iii) The age reflects open-system behaviour in the shear zone, possibly due to the influx of fluids characterised by a low $^{143}Nd/^{144}Nd$ ratio from relatively evolved Indian continental crust. Unless at tempertures > ~ 600 °C, such fluids would not be expected to affect the neodymium composition of the garnet, but may well have caused a reduction in the $^{143}Nd/^{144}Nd$ of matrix phases, thus leading to an elevated garnet - whole-rock age.

The first two possibilities both require that at least part of the garnet population contained in sample G31 grew in pre-Himalayan times. The compositional zoning profiles displayed by the garnet are relatively smooth, suggesting a single growth event, an inference which is supported by the garnet P-T path (see Fig. 4.1). Furthermore, the sample contains only one texturally and compositionally recognisable garnet generation. These observations indicate that, if the isotope data is simply a reflection of Himalayan-age isotopic resetting, the garnet must have grown entirely in pre-Himalayan times. However, the metamorphic P-T conditions calculated for the the sample are within error of those estimated for other samples from the shear zone, and it therefore seems unlikely that the sample represents an isolated slice of a pre-Himalayan fabric. Garnets containing monazite inclusions tend to be characterised by relatively high neodymium contents and low $^{147}Sm/^{144}Nd$ ratios (Vance and O'Nions 1990). However, compared with samples D19 and A3, garnet G31 fails to display either of these characteristics, which is further evidence against the involvment of inherited inclusions.

Having excluded the first two alternatives, it is tentatively concluded that the data is a

reflection of local neodymium open-system behaviour in the shear zone. Further evidence for such open system behaviour comes from the study of the isotope systematics of deformed granites within the shear zone (see Chapter 7). Furthermore, there are crustal sources available in the NPHM that could potentially yield fluids characterised by relatively low $^{143}Nd/^{144}Nd$ ratios (see Table 7.4).

4.7. Discussion

4.7.1. Peak P-T conditions

The use of *thermocalc* has proven useful in comparing the metamorphic grade of a variety of metamorphic assemblages from across the region, particularly given the relative scarcity of aluminosilicates. It should be borne in mind that the estimated P-T conditions recorded by porphyroblast rims do not necessarily represent the maximum P-T conditions experienced by a particular sample. Firstly, peak temperatures may be underestimated due to the effects of retrograde diffusion (Spear 1989). Secondly, thermal modelling has indicated that along some clockwise P-T paths, the peak metamorphic temperature may only be reached following a period of decompression, and thus the pressure actually recorded at the peak metamorphic temperature does not correspond to the peak metamorphic pressure experienced (England and Thompson 1984). This is a reflection of the fact that chemical equilibration is most likely to be attained at peak temperature but not necessarily at peak pressure. Finally, in high-grade rocks, temperature-sensitive and pressure-sensitive reactions may close at different times (Frost and Chacko 1989).

The metamorphism of the NPHM and adjacent Kohistan arc cannot be completely described since most of the area has yet to be sampled and mapped. However, broadly speaking, the measured P-T variations are consistent with the stability fields of the observed mineral assemblages present in the region. For example, the relatively high-temperatures estimated for samples from the Astor gorge are consistent with the migmatitic nature of these samples. Similarly, the presence of cordierite in samples collected from near Tato village is

consistent with the lower pressures estimated for these samples. However, given the variable whole-rock composition of the metasediments from the area, it should be noted that the presence or absence of typical 'zonal' index minerals is an unreliable monitor of changing metamorphic conditions.

An examination of the data shown in Table 4.2 and plotted in Fig. 4.4 shows that along both the western and eastern margins of the NPHM, and in the Haramosh area, the metamorphic grade deduced from about seventeen samples is relatively consistent, and in the range 600-750 °C and 7-10 kbar. Samples collected from the Astor gorge, from the footwall of the Liachar thrust and from the Tato-Fairy Meadows area introduce some variation into the range of P-T estimates from the NPHM.

An important result of the *thermocalc* study is that there appears to be a systematic spatial variation in estimated equilibrium P-T conditions, characterised by a general increase in temperature and pressure preserved on traversing eastwards between the Gilgit valley and the NPHM, as shown in Fig. 4.6. The systematic variation is observable despite a rather large variation in P-T existing between widely-spaced samples within both the NPHM and Kohistan. The observed gradual increase in metamorphic grade towards the NPHM is in strong contrast with the findings of Chamberlain et al. (1989), who concluded that the rocks in the Kohistan arc had been metamorphosed at higher P-T than rocks in the adjacent NPHM. There is no marked change in P-T across the western margin of the NPHM. Furthermore, metabasic lithologies within the shear zone, thought to have been derived from the Kohistan arc, and pelitic and calcareous lithologies, thought to have been predominantly derived from the Indian continental crust, are at the same metamorphic grade. These observations would be consistent with there having been a single, Himalayan-age regional metamorphism in the region, which post-dated suturing between the Indian continent and the Kohistan arc. Furthermore, the increase in metamorphic grade on traversing eastwards into the NPHM is consistent with metamorphism following overthrusting, with higher P-T preserved in the deeper thrust sheets in the footwall of the Main Mantle Thrust (now within the NPHM), than in the adjacent hanging-wall (Kohistan). However, the available

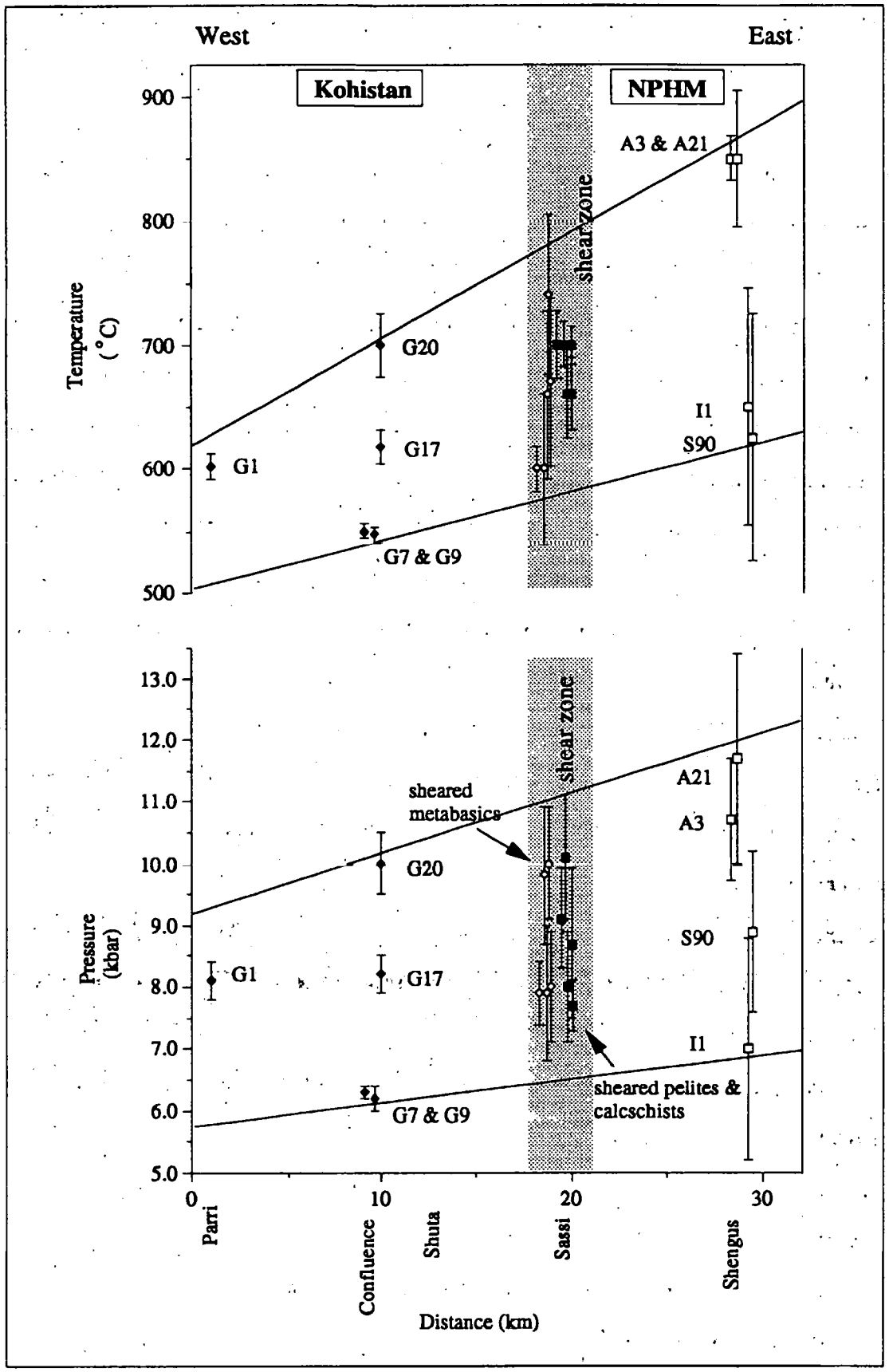

Fig. 4.6. P-T traverse between the Kohistan arc and the Nanga Parbat-Haramosh Massif (NPHM). Black diamonds = Kohistan; open diamonds = shear zone basic schists; black squares = shear zone pelites and calcsilicates; open squares = NPHM. Samples from outside the shear zone have sample numbers beside them (see Table 4.2).

geochronological data contradict such a simple relation between metamorphism and tectonics in the NPHM region, as discussed in section 4.7.3.

Despite the sparse sample coverage, there seem to be few abrupt changes in metamorphic grade in the Kohistan-NPHM region, and it has not been possible to draw metamorphic isograds in this study. The observation by Misch (1964) that the metamorphic grade increases isobarically towards the core of the NPHM is probably correct for some parts of the NPHM, for example in the Astor gorge region. However, in the Fairy Meadows region, assemblages are characterised by garnet, cordierite and sillimanite and reflect peak metamorphism under relatively low pressure. Unfortunately diagnostic melt-reaction textures have not been observed, and furthermore the assemblage appears to be locally out of equilibrium. However, cordierite-producing reactions tend to have a strong pressure-dependence, due to the large molar volume of cordierite (Schreyer and Seifert 1969), and consequently the presence of cordierite suggests a pressure decrease along this part of the P-T path, a feature that would fit with the rapid cooling history of the Fairy Meadows area (see Chapter 5). The assemblages present at Fairy Meadows may represent a relatively young (~ 3 Ma) metamorphism associated with rapid exhumation and anatexis, as discussed by Zeitler et al. (1993).

4.7.2. P-T-t Variations during Metamorphism

According to Tracy et al. (1976), garnet zoning is a complex function of the following :

1. Whole-rock bulk composition
2. Specific continuous reactions in which the garnet is involved
3. P-T history of the rock
4. Diffusion within garnet
5. Availability of metamorphic fluids

For example, a proportion of the compositional zoning in a garnet may be due to Rayleigh fractionation (Hollister 1966), in which cations such as manganese are preferentially taken-up during continuous reactions between a growing garnet and surrounding matrix. The result is a garnet with 'normal' compositional zoning, characterised by X_{sp} and X_{gr} richer cores, X_{alm} and X_{py} richer rims, and typical bell-shaped compositional profiles. However, this type of zoning can only be successfully modelled if the garnet is involved in a single continuous reaction (Tracy et al. 1976). According to Frost and Tracy (1991), some apparent P-T paths may be due to, or affected by, isothermal and isobaric growth of garnet undergoing Rayleigh fractionation of, for example, calcium. None of the analysed samples contain 'normal' garnet zoning for amphibolite-grade pelitic rocks, suggesting that other factors such as temperature change are involved.

It is thought that the rates of diffusion in garnet, and the availability of fluids, would be similar for adjacent samples within the shear zone. Hence the observed differences between zoning profiles for garnets from different lithologies within the shear zone at Sassi are most likely due to the differences in whole-rock composition between basic and pelitic schists, and consequently differences between the continuous reactions in which garnet is involved. This is supported by the fact that the equilibrium P-T estimates for the different lithologies lie within error.

The reactions involved in garnet growth are difficult to deduce in the region, owing to the absence of lithologies of sub-garnet-grade. Many garnet samples show strong zoning of X_{gr}, suggesting control of garnet growth by continuous reactions involving the calcium cation. Calcium is involved in reactions between plagioclase + garnet ± epidote, and also in reactions involving Ca, Na and K between muscovite + plagioclase ± k-feldspar ± epidote. The origin of the strikingly grossular-rich rims in garnets from the metasediments of the Kohistan arc is somewhat problematical. In a study concerning the formation of garnet in a pelitic schist, McAteer (1976) proposed that an increase in the grossular content of the garnet was due to the reaction :

epidote + calcite + quartz = grossular + anorthite + H_2O + CO_2

The petrographic evidence for this involved the simultaneous disappearance of epidote inclusions and increase in the grossular content in the garnet, together with the increase in anorthite content of matrix plagioclase. However, in the case of samples from the Kohistan arc, matrix zoisite appears to be stable with the grossular-rich garnet rim whilst zoisite inclusions are occasionally found in garnet cores, and therefore a different equilibrium must be involved to that suggested by NcAteer (1976).

The calculation of the P-T paths shown in Fig. 4.5 is entirely based on Gibbs modelling of compositionally zoned garnet, and therefore the results should be treated with some caution. It is unfortunate that garnet from the NPHM seldom contains inclusions of plagioclase or diagnostic aluminosilicates. Another problem is that relatively simple, radial zoning traverses may be insufficient to deduce the compositional history of a garnet (Thompson et al. 1977).

Despite the marked compositional zoning measured in the majority of garnets from the region, P-T paths estimated by the Gibbs method suggest relatively small changes in pressure and temperature occurred during garnet growth. In most cases the derived P-T paths are consistent with the zoning of Fe/(Fe+Mg), confirming that Fe/(Fe+Mg) ratios can be used subjectively as an effective monitor of changing metamorphic temperature (Spear et al. 1991). In this study, where the P-T path is not consistent with the measured Fe/(Fe+Mg) ratio, there is evidence that the metamorphic assemblage has changed during growth of the garnet (e.g. sample G1). The relation between P-T path and Fe/(Fe+Mg) ratio can thus be used to deduce the metamorphic evolution of high-variance assemblages which cannot be modelled using the Gibbs method. For example, samples D19 and G20 contain garnet characterised by an increase in the Fe/(Fe+Mg) ratio between core and rim, suggesting that garnet growth occurred during decreasing temperatures.

In contrast to the Fe/(Fe+Mg) ratio, the results of Gibbs modelling show that no

subjective assumptions can be made concerning changing metamorphic pressure solely on the basis of X_{gr} zonation in garnet. For example, although previous workers have inferred that an increase in X_{gr} between garnet core and rim is indicative of growth during increasing pressure (Crawford 1977), pelitic rocks in the NPHM region contain garnet characterised by strongly increasing X_{gr}, which grew during decreasing pressure conditions. As Spear et al. (1991) concluded, there is no reliable single-phase ΔP monitor, and inferences about ΔP can only be made considering plagioclase and garnet together.

The results of Gibbs modelling indicate variable P-T paths were followed for samples collected from different localities in the NPHM, as follows :

(i) Decrease in both temperature and pressure (G31, A21 & A3).

(ii) Increase in temperature and a decrease in pressure (T20, S24).

(iii) Increase in both temperature and pressure (A7).

The retrogressive P-T paths (1 above) indicate that late stages of metamorphism in the NPHM were taking place during early unroofing of the metamorphic pile, and that the P-T recorded by equilibrium rim assemblages for these samples do not represent peak P-T conditions. In some garnet samples which exhibit an increase in the Fe/(Fe+Mg) ratio between core and rim (e.g. G20, Fig. 4.1C), the inner portion of the garnet profile is relatively flat, whereas steep concentration gradients are present in the rim region. This feature may be partly the result of homogenization of the earlier-formed garnet at higher grades by volume diffusion, with preservation of latter-formed growth zoning at lower grades (Cygan and Lasaga 1982). In all samples which yield retrograde growth paths, high temperatures appear to have destroyed the evidence for earlier prograde growth. This type of retrograde garnet zoning (i.e. increasing X_{alm} and X_{gr} and decreasing X_{py}), is commonly observed in granulite-facies rocks which have apparently undergone isobaric cooling (Frost and Chacko 1989).

The paths which record an increase in temperature and a decrease in pressure (2 above) may reflect a relatively early exhumation history for some rocks now present in the NPHM, whilst they were still undergoing prograde metamorphism. This exhumation may be a manifestation of early tectonic uplift along the western margin of the NPHM.

Samples from the shear zone at Sassi display both prograde and retrograde P-T paths. Evidence for this comes both from a comparison of the garnet zoning present in different lithologies (e.g. samples S28 and S34 compared with samples D19 and G31), and the Gibbs modelling of samples S24 and G31. This observation may be due to the following :

(i) Different lithologies come from different structural levels, and suffered different P-T histories during metamorphism, before being juxtaposed during later shearing. However, this is considered unlikely, given that the samples suffered similar peak metamorphic conditions.

(ii) The samples suffered the same P-T history, but different portions of this P-T path were preserved by different samples, according to their lithological characteristics. This inference is supported by the strong lithological contrast between samples G31 (pelite) and S24 (amphibolite). The onset and period of garnet growth for a particular sample is probably dependant on bulk composition and possibly also kinetic factors, so that garnet growth is not necessarily simultaneous in different lithologies.

Lithological contrasts may partly account for the wide range of P-T paths seen across the region. Thus rocks currently exposed in the shear zone along the western margin of the NPHM were probably all still enjoying prograde metamorphism during early exhumation, which was then followed by a long history of retrograde metamorphism. Different lithologies record different portions of the same clockwise P-T path. The similar P-T paths for sample G31 (Sassi) and samples from the Astor gorge may indicate that the Astor gorge

samples also followed the same P-T path. Alternatively, Astor gorge samples, originally occupying relatively deep structural levels below the MMT, may have experienced slightly different prograde P-T paths, since these rocks would be expected to have experienced peak metamorphism slightly later than higher-level rocks (Oxburgh and England 1980). As in other metamorphic terrains, there is a shortage of information concerning the prograde history of rocks of the NPHM. This is unfortunate, as it is the prograde portion of P-T paths which can best be used to distinguish between different tectonic settings.

The single sample (A7) from the NPHM which followed a prograde history accompanied by a pressure increase comes from an unconstrained structural setting. However, presumably this P-T path reflects metamorphism during crustal thickening in the footwall of the Main Mantle Thrust, with no evidence in this case for early exhumation. Support for this interpretation comes from the presence of distinctive synkinematic inclusion trails preserved in the garnet, a texture which is not present in any other samples collected from the region.

Unfortunately, P-T paths from samples collected from the Kohistan arc are probably unreliable. However, the garnet zoning measured in samples from Kohistan is characterised by strongly increasing Fe/(Fe+Mg), diagnostic of growth during decreasing temperature. This is supported by the presence of sillimanite locally in garnet cores, whereas sillimanite is absent from the matrix assemblage of these samples.

No support has been found for the preliminary conclusions of Chamberlain et al. (1989), made on the basis of six samples. In this study, the majority of samples from both the Kohistan arc and the NPHM appear to have suffered metamorphism during decreasing P-T conditions. Metamorphic rocks in the NPHM show little evidence for loading by an overiding Kohistan arc, as garnet growth during increasing temperature and pressure has only been identified in a single sample from the eastern margin. It seems likely that the metamorphism in the NPHM was a complex, dynamic process which cannot be realistically modelled in terms of the P-T effects of simple underplating of one crustal slab by another.

4.7.3. Timing of Metamorphism

Hornblende $^{40}Ar/^{39}Ar$ cooling ages for samples in the vicinity of the Indus confluence place a minimum age of ~ 30 Ma on the metamorphism that occurred in this part of the Kohistan arc (Treloar et al. 1989a; Chapter 5). Furthermore, this part of Kohistan has also been intruded by post-metamorphic, cross cutting granite sheets dated at > 26 Ma (Chapter 7). The available evidence from field observations combined with metamorphic studies suggest that this (> 30 Ma) metamorphism has also affected the adjacent part of the NPHM, as follows :

(i) Similar lithologies in both the NPHM and Kohistan contain garnets that are characterised by similar compositional zoning profiles, suggesting synchronous garnet growth occurred in similar lithologies across the whole region

(ii) Peak metamorphic conditions recorded in this study increase gradually between the NPHM and the Kohistan arc, and furthermore there is no abrupt metamorphic discontinuity discernible across the shear zone between the two terranes (Fig. 4.6).

(iii) Within the shear zone, imbricated lithologies thought to have been derived from both the Indian continental crust and the Kohistan arc have suffered identical peak metamorphic conditions.

(iv) The numerous granite sheets exposed in the shear zone that borders the NPHM are mineralogically and geochemically the deformed equivalent of the Confluence and Parri granites (Chapter 6), and have locally been observed to cross-cut metamorphic fabrics preserved in Indian continent -derived lithologies.

These observations suggest that Indian continental crust and the Kohistan arc were already sutured together before being affected by a regional metamorphism that occurred at >

30 Ma. However, as described above, the available Sm-Nd garnet and U-Pb monazite (Smith et al. 1992) data indicate that the rocks presently exposed in the NPHM have suffered a high-grade (> 600 °C) metamorphic event within the last 10 Ma. Thus the geochronological data apparently contradict the hypothesis that the entire region has been affected by the same metamorphism. This dilemma can be resolved when account is taken of the dynamic nature of metamorphic processes. The high-grade metamorphic rocks within the NPHM may have suffered metamorphism at ~ 30 Ma during crustal shortening associated with early Himalayan collision, but probably remained at high metamorphic-grade at depth within the thrust stack until rapidly exhumed within the last 10 Ma, during the growth of the NPHM. The current distribution of metamorphic rocks in the NPHM-Kohistan region is primarily related to the degree of local exhumation that has occurred, and therefore cannot be simply related in time to the distribution of metamorphic rocks in the Kohistan arc, since different structural levels are exposed.

4.8. Conclusions

(i) A total of 36 metamorphic samples from the NPHM - Kohistan region have been subjected to detailed microprobe analysis. A high proportion of samples contain garnet that displays marked compositional zoning. The style of garnet compositional zoning is more strongly related to lithology than to structural setting, an observation that is thought to be a reflection of varying times of garnet nucleation and growth in differing lithologies.

(ii) Peak metamorphic conditions recorded by a total of 26 samples have been estimated using *thermocalc*. The majority of P-T estimates for the NPHM lie in the range 600-750 °C and 7-10 kbar, although samples from Fairy Meadows, Raikhot and from the Astor gorge throw considerable variation into this range. Samples from near the Indus confluence in Kohistan yield P-T estimates of 550-600 °C and 6-8 kbar.

(iii) Igneous relations and mineral cooling ages (Chapter 5) from the Indus confluence area place a 30 Ma lower limit on the timing of metamorphism in the northern Kohistan arc.

Furthermore, igneous relations at Sassi indicate that metamorphic fabrics within Indian continental rocks locally predate 30 Ma.

(iv) Garnet Sm-Nd data indicate that the metamorphic rocks exposed in the NPHM were last isotopically-equilibrated (> ~ 600 °C) in the period 25-0 Ma. These data are consistent with the U-Pb monazite ages of Smith et al. (1992) and Zeitler et al. (1993), which suggest that the rocks presently exposed in the NPHM have been at temperatures > ~ 650 °C within the last 10 Ma. In general, these observations reflect the recent, rapid exhumation of high-grade metamorphic rocks from relatively deep structural-levels.

(v) Within the Kohistan arc, peak metamorphic conditions increase steadily towards the NPHM. There are no obvious metamorphic breaks associated with the shear zone that borders the north-western margin of the NPHM. However, the geochronological data described above indicate that no simple comparison is possible between the metamorphism experienced by rocks presently exposed in the Kohistan arc with the metamorphism experienced by rocks presently exposed within the NPHM. It is thought that contrasting structural and metamorphic levels have been exposed during differential exhumation of the region, although this exhumation has not resulted in the generation of any obvious metamorphic breaks.

(vi) Variable P-T paths estimated using the Gibbs method are consistent with zoning of Fe/(Fe+Mg). In the majority of samples from the region, garnet growth occurred during decreasing pressure and temperature, although locally P-T paths indicate prograde garnet growth during decreasing pressure. In general, the contrasting P-T paths recorded in this study are thought to reflect lithological differences, rather than differences in the thermal histories experienced by contrasting samples. As mentioned above (i), this may result from the fact that available mineral reactions determine which section of the P-T-t loop is recorded, and hence the preserved P-T-t path is, at least partly, a function of lithology. Hence the garnet present in amphibolite samples grew relatively early and recorded the earliest portion of the exhumation history, whilst the garnet present in pelitic samples

nucleated at a later time and consequently recorded a later portion of the exhumation history. It can be hypothesised that samples originally buried the deepest in the thrust stack are likely to contain garnet that records the most extended P-T path during exhumation, although the analysis of the P-T paths of more samples would be required to verify this suggestion.

(vii) Whilst in the majority of samples from the NPHM, garnet growth occurred during exhumation, a single sample collected from near to the eastern margin of the NPHM contains garnet that records prograde growth during increasing pressure. This may be a reflection of a relatively slow rate of exhumation along the estern margin of the NPHM compared with the western margin, resulting in the preservation of metamorphic assemblages along the eastern margin that were equilibrated at a relatively early stage of crustal thickening. The structural studies of Butler and Prior (1988b) and Treloar et al. (1991) also indicate that the degree of exhumation has strongly varied within the NPHM, with a high proportion of active tectonic uplift occurring along the western margin. This hypothesis may be tested when more geochronological data become available for samples exposed along the eastern margin of the NPHM.

Chapter 5

The Cooling History of the Nanga Parbat-Haramosh Massif - Kohistan Region

5.1. Introduction

Modern geological studies of collisional mountain belts aim to unravel the interplay between regional tectonics and the metamorphic and structural evolution of rocks currently at the Earth's surface. Important evidence for the thermal development of rocks originally at mid-crustal levels comes from establishing the cooling histories of different structural levels. Such cooling histories may be deduced from the radiometric dating of different mineral phases using different isotope systems. This approach is based on the concept of closure temperature (T_C), which is the temperature at which the diffusion of a particular element within a particular mineral effectively ceases (Dodson 1973), so that, below this temperature the daughter products of radiogenic decay are retained in a mineral structure. Closure temperatures may be either calculated experimentally, using the volume diffusion equation of Dodson (1973), or estimated empirically (Jäger et al. 1967). If the closure temperatures of different minerals to diffusion of different elements are known, it is possible to construct a temperature - time profile for the rock sample studied and by analysing a number of different samples, temporal and spatial variations in the thermal evolution of a region may be illustrated. If assumptions are made concerning the size and stability of the geothermal gradient, cooling ages may be interpreted in terms of exhumation rate, which refers to the rate at which a particular geological horizon approaches the surface (England and Molnar 1990).

The Nanga Parbat-Haramosh Massif (NPHM) region in northern Pakistan is especially suited to a detailed study of thermal and tectonic exhumation, given the relative abundance of previously determined cooling ages, the well-constrained structural history of

the massif, and the rapid and recent differential uplift experienced by the NPHM (Zeitler 1985; Zeitler et al. 1993). This chapter presents over fifty Rb-Sr and $^{40}Ar/^{39}Ar$ mica ages from the NPHM and adjacent rocks of the Kohistan arc. Following an evaluation of the uncertainty involved in the assignment of closure temperature, these ages are discussed in terms of regional variations, temperature-time paths and exhumation rates.

5.2. Previous Geochronological Studies

Recently, Zeitler and co-workers (Smith et al. 1992; Zeitler et al. 1993) have documented remarkably young U-Pb ages from parts of the NPHM. Zircons from two samples of the Iskere orthogneiss (Madin et al. 1989) collected from the Indus gorge were found to have thin, relatively high-U rims which yielded scanning high-resolution ion microprobe (SHRIMP) ages of 2-11 Ma (Zeitler et al. 1989). A sample of Shengus gneiss (Madin et al. 1989), also collected from the Indus gorge, was characterised by zircons with relatively high-U rims, although these rims were not dated. In the Fairy Meadows area (Fig. 5.1), near Nanga Parbat itself, zircon separated from a migmatite was also characterised by young overgrowths (< 5 Ma), whilst monazite from the same sample yielded a conventional monazite U-Pb age of 3.3 Ma (Zeitler et al. 1993). Samples of schist and gneiss from widely-spaced localities in the NPHM yield conventional monazite U-Pb ages in the range 4-11 Ma (Smith et al. 1992). These U-Pb ages have been used as evidence for a Neogene metamorphism in the NPHM, an interpretation which relies on the assumption that monazite U-Pb ages date the crystallisation of this accessory phase during upper-amphibolite grade metamorphism, rather than reflecting closure of the U-Pb system following a period of cooling (Smith and Barreiro 1990). The young metamorphism in the region appears to have been culminated in many areas by the intrusion of leucogranite dykes, which have yielded SHRIMP U-Pb igneous zircon ages in the range 1-7 Ma (Zeitler and Chamberlain 1991; Zeitler et al. 1993).

Other geochronological studies have documented the remarkably rapid, recent cooling of the NPHM. In a regional study, Zeitler (1985) showed that fission-track and

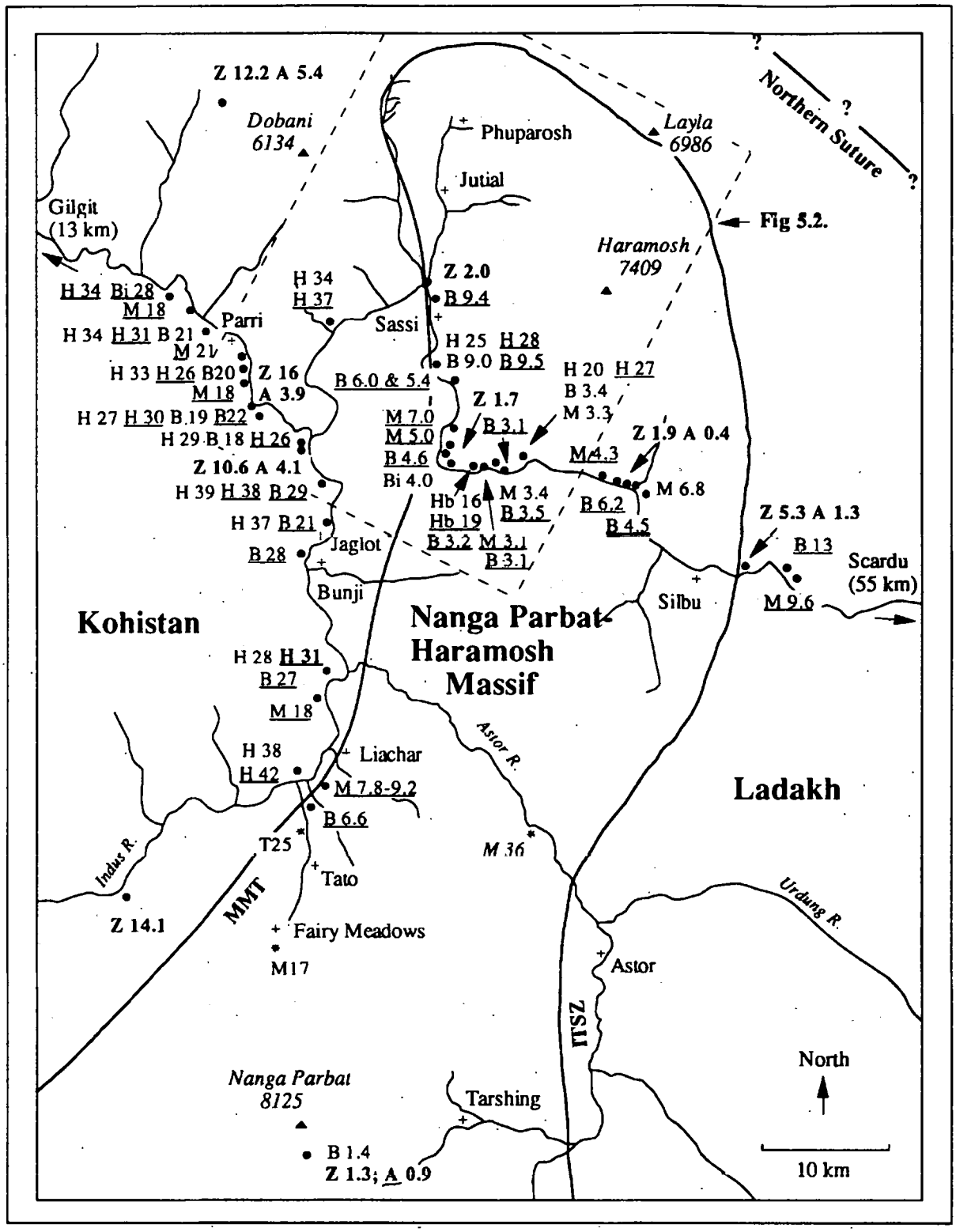

Fig. 5.1. Sketch map of the Nanga Parbat-Haramosh Massif, showing location of previously published regional cooling ages (Coward et al. 1986, Zeitler 1985, Zeitler et al. 1989, Treloar et al. 1989a and 1991). * = location of the two samples dated in this work from the Tato-Fairy Meadows area. MMT= Main Mantle Thrust; ITSZ = Indus Tsangpo suture zone. H = hornblende; B = biotite; M = muscovite; Z = zircon; A = apatite. Numbers in plane text are $^{40}Ar/^{39}Ar$ ages, those underlined are K-Ar ages, those in bold are fission-track ages whilst those in italics are Rb-Sr ages. Large dashed square indicates location of Fig. 5.2.

$^{40}Ar/^{39}Ar$ cooling ages decreased rapidly from the Kohistan arc towards the NPHM. For example, apatite fission-track ages, which are thought to reflect cooling through ~ 120 °C, were observed to decrease from 4.1 Ma at the Indus confluence to 0.4 Ma within the NPHM in the Indus gorge. Further $^{40}Ar/^{39}Ar$ and K-Ar cooling ages from the Gilgit and Indus valleys, for samples collected from both the NPHM and from adjacent parts of the Kohistan arc, have been presented by Coward et al. (1986), Treloar et al. (1989a), Zeitler et al. (1989) and Treloar et al. (1991). These ages, together with those of Zeitler (1985), are shown in Fig. 5.1.

Hornblende $^{40}Ar/^{39}Ar$ cooling ages for three samples from the Indus gorge section through the NPHM lie in the range 16-25 Ma, whilst hornblende K-Ar ages for the same samples lie in the range 19-28 Ma (Zeitler et al. 1989; Fig. 5.1). However, on the basis of younger monazite U-Pb ages (see above), Smith et al. (1992) suggested that these hornblende ages were overestimates due to the undetected presence of excess argon. $^{40}Ar/^{39}Ar$ mica ages for samples from the core of the NPHM, where the Indus gorge trends approximately east-west, are 3.3 Ma, 3.4 Ma and 6.8 Ma for muscovite, and 4.0 Ma and 3.4 Ma for biotite. K-Ar ages from the same area are similar to the $^{40}Ar/^{39}Ar$ ages, and lie in the ranges 3.1-7.0 Ma for muscovite and 3.1-6.2 Ma for biotite. Biotite $^{40}Ar/^{39}Ar$ and K-Ar ages increase towards the western margin, where they lie in the range 5.4-9.4 Ma (Zeitler 1985; Zeitler et al. 1989; Treloar et al. 1991). In general, the relatively young cooling ages for the NPHM have been interpreted as documenting rapid, recent differential uplift of the NPHM relative to the surrounding regions (Zeitler 1985).

$^{40}Ar/^{39}Ar$ and K-Ar cooling ages for adjacent parts of the Kohistan arc, within 20 km of the NPHM, lie in the ranges 27-39 Ma ($^{40}Ar/^{39}Ar$) and 26-42 Ma (K-Ar) for hornblende; 18-21 Ma (K-Ar) for muscovite; and 18-21 Ma ($^{40}Ar/^{39}Ar$) and 21-29 Ma (K-Ar) for biotite (Fig. 5.1; Treloar et al. 1989a; Zeitler et al. 1989). Over a distance of about 40 km, cooling ages in the Kohistan arc decrease towards the NPHM, and regional cooling rates increase towards the NPHM, observations which are interpreted as evidence for both younger and more rapid uplift towards the NPHM (Treloar et al. 1989a).

5.3. Aims

Both conventional Rb-Sr and laser probe $^{40}Ar/^{39}Ar$ techniques have been employed on closely-spaced samples in order to establish the small-scale spatial variation in cooling ages and the derived cooling paths within the region. Although previous work has shown that the NPHM is characterised by markedly young cooling ages compared with the adjacent Kohistan arc terrane (Zeitler 1985), few ages have been published either for samples from the shear zone bordering the NPHM, or for samples collected from areas to the north of the Indus gorge. In this study, the variation in cooling ages across the region is investigated in an east-west traverse approximately perpendicular to the western margin of the NPHM, and also in a north-south direction, parallel to the western margin of the NPHM.

5.4. Samples

Samples selected for this geochronologial study come from the north-eastern part of the Kohistan arc, the north-western part of the NPHM and from the wide shear zone separating the two areas (Fig. 5.2). Two samples come from more southerly locations in the NPHM, and were collected during reconnaissance fieldwork (see Fig. 5.1). Only fresh, unaltered, medium to coarse-grained samples were selected for dating purposes. Samples containing polyphase mica growth were avoided, and all micas analysed were fabric forming. All the samples were sieved, and clean, inclusion-free mineral separates were hand-picked to ensure optimum purity.

5.4.1. Nanga Parbat-Haramosh Massif

Sampled units from the northern part of the NPHM include cross-cutting, tourmaline-muscovite-biotite leucogranites (J11 and S92), psammitic gneisses (J21, I6) and semi-pelitic gneisses (J13, J14, I9 and I10). Samples J13 and J14 come from roof pendants enclosed by the Jutial granite (J11). The psammitic gneisses are characterised by the

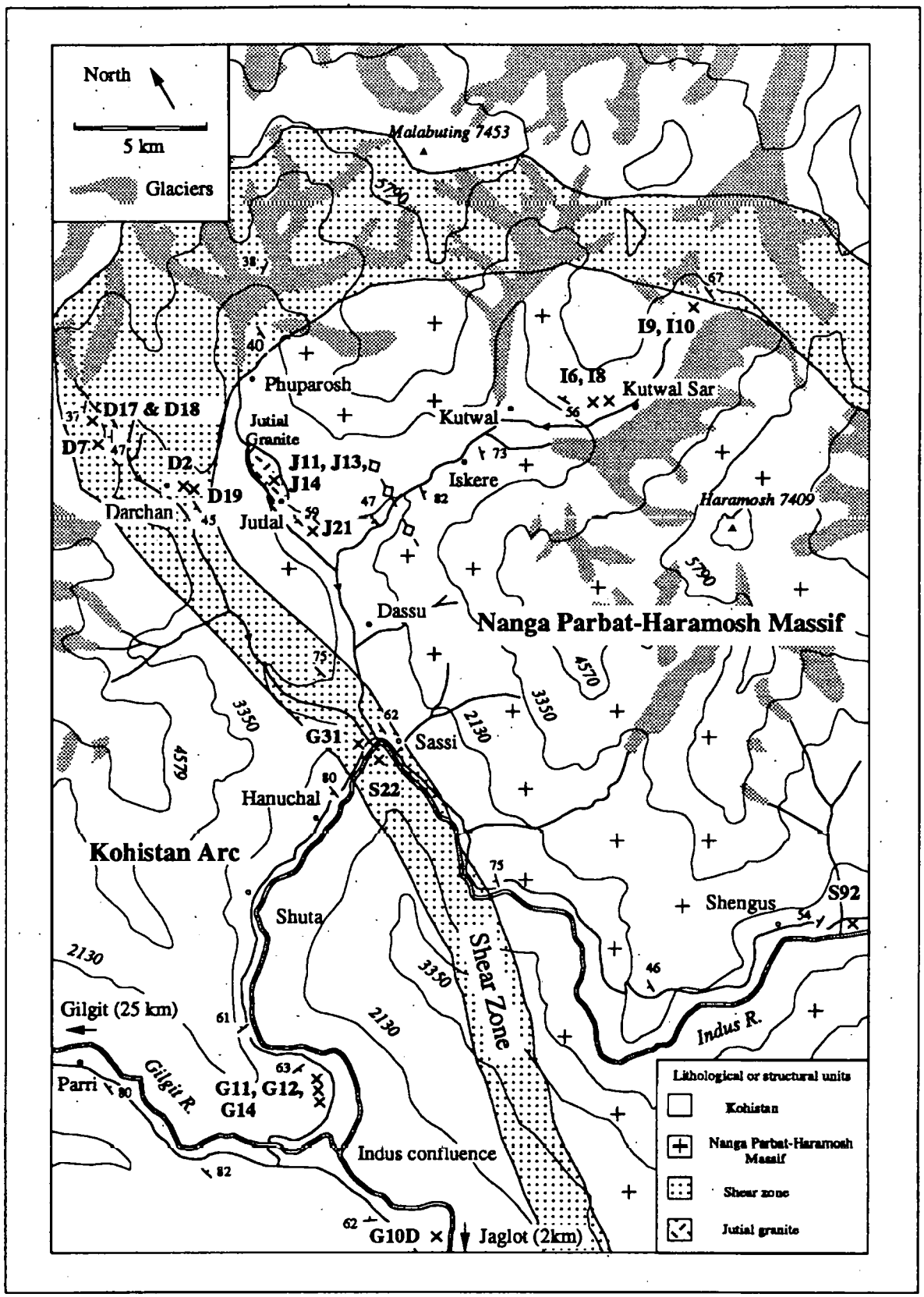

Fig. 5.2. Sketch map of the north-western margin of the Nanga Parbat-Haramosh massif and adjoining Kohistan arc, showing the location of dated samples. Lithological units are not differentiated, although the exposure of the Jutial granite is shown. The shear zone is an imbicate zone containing lithologies from both terranes, and corresponds partly to the Layered-unit of Butler et al. (1992). The orientation of the regional foliation is indicated together with dip amount; contours are in metres.

assemblage k-feldspar + plagioclase + biotite + quartz , whereas the semi-pelitic gneisses also contain muscovite.

The two samples from the south of the region include a calcsilicate (M17) from an elevation of 3500 near Fairy Meadows, characterised by the assemblage diopside + plagioclase + biotite + hornblende + quartz + sphene, and a semi-pelitic gneiss from the Liachar shear zone (T25) (Fig. 5.1), characterised by the assemblage k-feldspar + plagioclase + quartz + biotite + muscovite.

The basement lithologies of the NPHM locally contain concordant, deformed segregations of leucosome of unknown age, although in most cases the segregations are demonstrably older than the cross-cutting leucogranites. One such deformed migmatite was sampled from the Astor gorge (sample A3), and is characterised by the assemblage garnet + k-feldspar + plagioclase + biotite + quartz + muscovite + kyanite.

5.4.2. Sassi - Darchan shear zone

A total of seven samples have been studied from the shear zone bordering the western margin of the NPHM, between the villages of Sassi and Darchan. The range of dated lithologies reflects the variability of rock-types present in the shear zone, which have been derived from both the Kohistan arc and the NPHM. Samples D17, D18 and D7 were collected from the western side of the Darchan valley (Fig. 5.2). The latter two samples, collected from exposures about 1.5 km apart, are representative of a relatively massive orthogneiss unit exposed along the western wall of the Darchan valley, and characterised by the assemblage k-feldspar + plagioclase + quartz + biotite ± muscovite ± garnet ± epidote. The relatively unradiogenic strontium isotopic ratio of whole-rock sample D7 (see Table 5.2) suggests a derivation for this orthogneiss unit in the Kohistan arc, rather than the isotopically-evolved Indian continental crust.

Samples D2 and D19 were collected from near to Darchan village, on the eastern side of the Darchan valley, from exposures approximately 400 m apart across the strike of the shear zone (Fig. 5.2). Both samples are highly sheared pelitic or semi-pelitic gneisses characterised by the assemblage plagioclase + quartz + biotite + muscovite ± garnet. The relatively evolved strontium isotopic ratios of these whole-rock samples is diagnostic of an origin in the Indian continental crust, although as discussed in Chapter 7, such an interpretation should be treated with caution given that there may have been significant strontium isotope mobility within the shear zone.

The other two samples both come from the shear zone at Sassi, approximately 10 km southwards along strike from Darchan village. Sample G31 is a highly sheared pelitic gneiss characterised by the assemblage plagioclase + quartz + biotite + muscovite + kyanite + garnet + k-feldspar, whilst sample S22 is an amphibolite characterised by the assemblage plagioclase + k-feldspar + quartz + biotite + hornblende + garnet + sphene.

5.4.3. Kohistan

The studied samples from the Kohistan arc come from two separate localities near the Indus confluence, 8-9 km west of the NPHM. They include representatives of the final stage of granite magmatism in the Kohistan batholith, termed the Confluence (two-mica) granite sheets (samples G10 and G12) and Parri (muscovite ± garnet) granite sheets (sample G14) (see Chapters 2 & 6; Petterson and Windley 1985), together with the epidote-amphibolite facies metabasic country rocks to these granite intrusions (sample G11), composed of plagioclase + biotite + hornblende + quartz + sphene + epidote. Samples G11, G12 and G14 come from a single exposure 2 km to the north of the Indus confluence, whilst sample G10 comes from a single granite sheet exposed to the south of the Indus confluence (Fig. 5.2).

5.5. $^{40}Ar/^{39}Ar$ Results

Results of $^{40}Ar/^{39}Ar$ determinations are given in Table 5.1. Analyses quoted in Table 5.1 represent the amount of argon x ($2x10^{-10}$) cc STP. Ages in Table 5.1 were calculated using the decay constant of Steiger and Jäger (1977) and uncertainties are quoted at the 1σ level.

In the calculation of $^{40}Ar/^{39}Ar$ mineral ages, correction must be made for the presence of non-radiogenic ^{40}Ar. This correction is carried out by measurement of ^{36}Ar, based on the assumption that the ^{36}Ar is derived from the modern atmosphere which possesses an $^{40}Ar/^{36}Ar$ ratio of 295.5 (Faure 1988). However, a mineral may trap argon which has a different $^{40}Ar/^{36}Ar$ ratio to atmospheric argon, during either initial crystallisation or subsequent deformation. If the ratio of the trapped argon > 295.5, there will be an excess of radiogenic argon, leading to the over-estimation of mineral ages.

Duplicate analyses, derived by ablating different grains of the same sample, were undertaken on all dated samples. Where sufficient duplicates are available, the initial $^{36}Ar/^{40}Ar$ composition of the inherited argon component in each sample can be established by plotting the data in the form of an $^{36}Ar/^{40}Ar$ vs $^{39}Ar/^{40}Ar$ correlation diagram, as shown in Fig. 5.3. The majority of samples show no evidence for the presence of excess argon, since the duplicates fall on a mixing-line that intercepts the $^{36}Ar/^{40}Ar$ axis near to the atmospheric composition. However, the two amphibole samples collected from the NPHM (M17 and J13) are characterised by variable and heterogeneous excess argon components and consequently fail to yield geologically meaningful ages (e.g. Fig. 5.3H; Table 5.1). In contrast, the biotite coexisting with the hornblende in both of these samples is apparently unaffected by excess argon (e.g. Fig. 5.3G). One of the duplicate analyses of biotite sample G12 (Fig. 5.3A) is characterised by a relatively high $^{36}Ar/^{40}Ar$ ratio, which may be a reflection of slight alteration to chlorite. Consequently the relatively young age (11.9 Ma) calculated for this sample has been ignored in the calculation of the weighted mean age. Reproducibilities on the $^{40}Ar/^{39}Ar$ duplicates that show no evidence for the presence of

Sample	a	T_c	^{40}Ar	±	^{39}Ar	±	^{36}Ar	±	$^{*40}Ar/^{39}Ar$	±	Age (Ma)	±	Mean (Ma)	±
Kohistan Arc														
Confluence granite														
GIO-B-1	0.5	334	2.53148	0.00686	1.06152	0.00214	0.00520	0.00021	0.93663	0.05940	17.6	1.1	17.4	0.8
GIO-B-2			4.51195	0.00593	1.34589	0.00194	0.01111	0.00029	0.91270	0.06405	17.2	1.2		
GIO-M-1	0.5	409	1.18006	0.00223	0.75024	0.00282	0.00079	0.00017	1.26115	0.06844	23.9	1.3	22.2	0.6
GIO-M-2			1.48238	0.00339	1.28687	0.00211	0.00001	0.00014	1.15193	0.03289	21.8	0.7		
metagabbro														
GI1-B-1	1.0	356	8.08661	0.01617	1.59976	0.00317	0.01911	0.00040	1.52495	0.07414	28.7	1.4	29.6	0.8
GI1-B-2			5.16716	0.01677	1.29616	0.00379	0.01046	0.00021	1.60076	0.04983	30.1	1.0		
GI1-Hb-1	1.0	587	1.04410	0.00223	0.54787	0.00096	0.00076	0.00014	1.49571	0.07503	28.3	1.4	27.9	0.8
GI1-Hb-2			1.58495	0.00212	0.89266	0.00136	0.00092	0.00014	1.46947	0.04599	27.8	0.9		
Confluence granite														
GI2-B-1	0.8	349	4.59653	0.00556	2.36221	0.00355	0.01056	0.00032	0.62428	0.04042	11.9	0.8		
GI2-B-2			3.03271	0.00628	2.70296	0.00337	0.00144	0.00019	0.96430	0.02042	18.3	0.4	17.8	0.3
GI2-B-3			2.56256	0.00692	2.49820	0.00141	0.00093	0.00014	0.91518	0.01733	17.4	0.4		
Parri granite														
GI4-B-2	1.0	356	0.70661	0.00219	0.36860	0.00157	0.00137	0.00019	0.82078	0.15500	15.5	2.9	16.5	2.0
GI4-B-3			0.30308	0.00162	0.26738	0.00095	0.00019	0.00013	0.92025	0.14777	17.3	2.8		
GI4-M-1	1.0	433	2.01941	0.00351	1.74840	11.00134	0.00062	0.00015	1.05048	0.02464	19.9	0.5	18.5	0.2
GI4-M-2			6.35584	0.03543	6.53904	0.02485	0.00026	0.00013	0.96016	0.00888	18.2	0.2		
Shear zone														
Confluence granite														
DI7-B-1	1.3	375	3.09079	0.00587	1.95836	0.00620	0.00576	0.00019	0.70964	0.02864	13.5	0.6	13.3	0.3
DI7-B-2			4.76533	0.00306	4.52309	0.00815	0.00546	0.00020	0.69662	0.01338	13.2	0.3		
DI7-M-1	1.3	455	3.92927	0.00667	3.87178	0.00502	0.00293	0.00018	0.79096	0.01409	14.9	0.3	14.6	0.2
DI7-M-2			4.53560	0.00914	4.09664	0.01429	0.00492	0.00022	0.75207	0.01653	14.2	0.3		
orthogneiss														
DI8-M-1	0.8	437	1.34338	0.00353	1.79614	0.00226	0.00021	0.00015	0.71358	0.02454	13.5	0.5	13.3	0.4
DI8-M-2			0.73820	0.00299	1.08027	0.00222	0.00006	0.00017	0.66681	0.04559	12.6	0.9		
NPHM														
paragneiss														
I9-B-1	1.0	375	3.01466	0.00897	2.98090	0.00558	0.00733	0.00017	0.28475	0.01737	5.4	0.3		
I9-B-2			4.00653	0.00964	4.83145	0.00934	0.00938	0.00031	0.25552	0.01882	4.9	0.4	5.3	0.2
I9-B-3			2.68955	0.00284	3.31758	0.00328	0.00590	0.00020	0.28535	0.01757	5.4	0.3		
I9-M-1	1.0	455	1.85012	0.00719	2.71711	0.00889	0.00360	0.00019	0.28917	0.02109	5.5	0.4	5.1	0.4
I9-M-2			0.54561	0.00159	1.98705	0.00659	0.00015	0.00013	0.25162	0.01939	4.8	0.4		
leucogranite														
JI1-B-1	1.0	375	2.10524	0.00594	0.79831	0.00137	0.00621	0.00017	0.33769	0.06293	6.4	1.2	5.3	0.4
JI1-B-2			4.48837	0.01026	3.11798	0.00686	0.01229	0.00023	0.27433	0.02210	5.2	0.4		
JI1-M-1	1.4	468	7.76976	0.00592	2.83216	0.00470	0.02126	0.00041	0.52490	0.04286	9.9	0.8	-	
JI1-M-3			3.34463	0.00705	8.22711	0.00993	0.00305	0.00018	0.29704	0.00653	5.6	0.1	5.6	0.1
paragneiss														
JI3-B-1	1.0	375	1.80060	0.00388	1.52384	0.00207	0.00422	0.00015	0.36336	0.02911	6.9	0.6		
JI3-B-2			3.96759	0.01408	4.15219	0.00461	0.00827	0.00026	0.36703	0.01912	7.0	0.4	6.9	0.3
JI3-B-3			1.83878	0.00317	2.21519	0.00268	0.00352	0.00018	0.36015	0.02441	6.8	0.5		
JI3-Hb-1			5.16432	0.02040	0.11833	0.00059	0.00130	0.00016	40.38592	0.48768	637.8	8.4	-	
JI3-Hb-2			1.77791	0.00422	0.54365	0.00133	0.00101	0.00014	2.72338	0.07600	50.9	1.5	-	
paragneiss														
JI4-B-2	1.0	375	1.20207	0.00211	0.76328	0.00188	0.00326	0.00013	0.31399	0.05098	5.9	1.0		
JI4-B-3			9.14775	0.01355	8.18567	0.04752	0.02232	0.00039	0.31187	0.01431	5.9	0.3	6.0	0.2
JI4-B-4			0.65014	0.00199	1.58050	0.00502	0.00038	0.00014	0.33939	0.02678	6.4	0.5		
JI4-M-1	1.0	455	1.84068	0.00339	1.56088	0.00387	0.00434	0.00021	0.35791	0.04014	6.8	0.8		
JI4-M-2			1.24165	0.00399	2.09691	0.00626	0.00213	0.00014	0.29154	0.01934	5.5	0.4	5.8	0.3
JI4-M-3			0.62701	0.00223	0.88367	0.00148	0.00119	0.00016	0.31276	0.05457	5.9	1.0		
leucogranite														
S92-B-1	0.8	368	5.27971	0.00742	0.64269	0.00130	0.01715	0.00016	0.32747	0.07232	6.2	1.4		
S92-B-2			2.56989	0.00373	0.90387	0.00434	0.00754	0.00024	0.37946	0.07758	7.2	1.5	3.7	0.5
S92-B-3			4.86681	0.00719	1.69678	0.00457	0.01520	0.00017	0.22093	0.03031	4.2	0.6		
S92-M-1	0.8	447	3.25688	0.00654	6.29016	0.00947	0.00686	0.00029	0.19550	0.01343	3.7	0.3	3.6	0.1
S92-M-2			3.11333	0.00592	8.83317	0.00818	0.00493	0.00027	0.18747	0.00915	3.5	0.2		
calcschist														
M17-B-1	0.5	393	1.88887	0.00493	1.10249	0.00238	0.00603	0.00025	0.09801	0.06748	1.9	1.3		
M17-B-2			2.98630	0.00426	2.57060	0.00618	0.00924	0.00020	0.09991	0.02277	1.9	0.4	1.6	0.2
M17-B-4			4.92202	0.00991	7.40670	0.01368	0.01470	0.00023	0.07823	0.00925	1.5	0.2		
M17-Hb-2			3.10570	0.00452	0.22607	0.00041	0.00851	0.00026	2.61557	0.33523	48.9	6.2	-	
M17-Hb-3			0.50392	0.00289	0.42509	0.00125	0.00113	0.00016	0.39962	0.11316	7.6	2.1	-	
M17-Hb-4			0.50436	0.00154	0.37162	0.00087	0.00162	0.00013	0.07051	0.10283	1.3	1.9	-	
M17-Hb-5			1.67443	0.00239	5.66253	0.00697	0.00687	0.00017	-0.06293	-0.00897	-1.2	0.2	-	

Table 5.1. Laser ^{40}Ar-^{39}Ar data for samples from the Nanga Parbat-Kohistan region. Measured values in voltage = value x (2E-10) cc STP. Errors shown were calculated to 1σ. * = radiogenic argon; a = mean grain radius along (001); Tc estimated maximum closure temperature, assuming effective diffusion distance is equivalent to the measured grain radius and using diffusion data of Harrison et al. (1985) for biotite, Harrison (1981) for hornblende and Hamilton et al. (1989) for muscovite. WR = whole-rock; B = biotite; M = muscovite; Hb = hornblende.

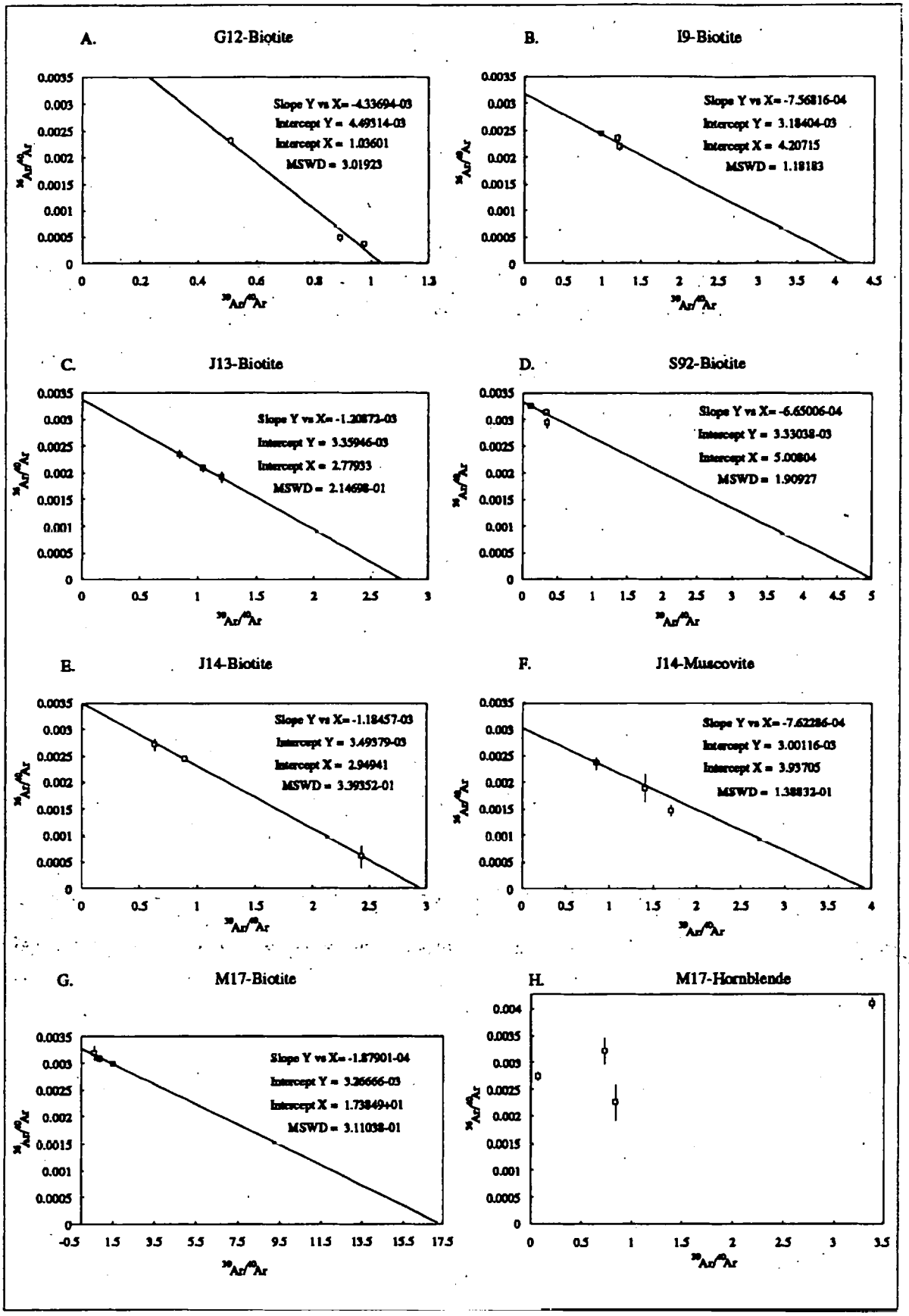

Fig. 5.3. Argon isotope correlation diagrams for dated minerals. Samples uncontaminated by excess argon should plot on an isochron with a Y-intercept = 0.00338 (^{40} Ar/^{36} Ar ratio of the present atmosphere). In such cases, the gradient of the line reflects the true cooling age.

excess argon are variable, and lie in the range 2-21 % for muscovite (mean = 10.7%) and 2-40 % for biotite (mean = 11.3 %). The $^{40}Ar/^{39}Ar$ ages discussed in this study are the weighted means of the duplicate analyses for each sample.

$^{40}Ar/^{39}Ar$ ages from the northern part of the NPHM lie in the range 3.6-5.8 Ma for muscovite and 3.7-6.9 Ma for biotite. At Fairy Meadows, biotite from a calcsilicate horizon has yielded an $^{40}Ar/^{39}Ar$ age of 1.6 Ma, whereas the coexisting hornblende contained excess argon such that no age could be determined, as already mentioned.

Previous attempts at $^{40}Ar/^{39}Ar$ dating of micas from the shear zone at Sassi have proved futile due to the incorporation of excess radiogenic argon, which was probably derived from the Indian continental crust (Zeitler et al. 1989). Consequently, in this study the $^{40}Ar/^{39}Ar$ dating of strongly-deformed samples from the shear zone has not been attempted. However, two relatively undeformed samples, collected from the western side of the Darchan valley, have yielded three mica $^{40}Ar/^{39}Ar$ ages in the range 13.3-14.6 Ma.

$^{40}Ar/^{39}Ar$ ages from Kohistan lie in the range 18.5-22.2 Ma for muscovite and 16.6-17.4 Ma for biotite, with one unusually old biotite age of 29.6 Ma.

5.6. Rb-Sr Results

The results from the Rb-Sr determinations are given in Table 5.2. Uncertainties are quoted at the 1σ level. All Rb-Sr ages quoted were calculated by whole-rock - mica regression, except where indicated.

The high Rb-Sr ratios for the granite gneisses and leucogranites of the NPHM make these rocks ideally suited for Rb-Sr dating. For samples where sufficient phases or duplicates have been analysed, the strontium isotope systematics have been plotted on isochron diagrams, as shown in Fig. 5.4A-J. For all samples, both muscovite and biotite have much higher Rb/Sr ratios than their corresponding whole rocks, allowing reliable

Sample	Rb(ppm)	Sr(ppm)	Rb/Sr	$^{87}Rb/^{86}Sr$	$^{87}Sr/^{86}Sr$	±	Age ± 1σ
Kohistan Arc							
Confluence granite							
G10D-WR	92.0	482.0	0.19	0.55	0.70521	1	
G10-D-B	520.5	19.8	26.30	76.01	0.72323	2	16.8 ± 0.1
G10-D-M	250.8	106.7	2.35	6.79	0.70725	1	23.0 ± 1.0
Parri granite							
G14-WR	31.0	93.0	0.33	0.96	0.70581	1	
G14-M	612.1	20.4	29.96	86.59	0.73733	4	25.8 ± 0.2
Shear Zone							
orthogneiss							
D7-WR	80.0	353.0	0.23	0.65	0.70440	1	
D7-B	447.2	45.5	9.83	28.41	0.70939	13	12.7 ± 0.1
D7-B duplicate					0.70863	3	10.7 ± 0.1
D7-M	260.9	42.3	6.17	17.83	0.70854	2	16.9 ± 0.2
Confluence granite							
D17-WR	38.0	427.0	0.09	0.26	0.70812	1	
D17-M	369.4	47.7	7.75	22.39	0.71394	4	18.5 ± 0.2
paragneiss							
D2-WR	227.0	81.5	2.79	8.05	0.96392	1	
D2-M	409.9	4.6	89.97	260.01	1.00792	5	11.9 ± 0.1
paragneiss							
D19-WR	175.0	181.0	0.97	2.79	0.77990	1	
D19-B	595.8	16.1	36.94	106.76	0.78850	1	5.8 ± 0.1
D19-B-duplicate	552.8	13.7	40.23	116.27	0.78958	14	5.9 ± 0.1
D19-M	344.8	86.7	3.98	11.49	0.78334	1	27.6 ± 0.3
D19-M-duplicate	356.1	85.3	4.17	12.05	0.78313	6	24.4 ± 0.5
D19-Pl	3.6	388.0	0.01	0.03	0.77965	1	5.9 ± 0.1 (1)
amphibolite							
S22-WR	115.0	212.0	0.54	1.57	0.73540	1	
S22-B	625.1	48.0	13.01	37.61	0.74760	1	23.7 ± 0.2
S22-Hb	95.4	147.3	0.65	1.87	0.73473	2	25.2 ± 0.2 (2)
paragneiss							
G31-WR	129.0	115.0	1.12	3.24	0.75943	1	
G31-M	259.4	166.1	1.56	4.51	0.76469	3	288.1 ± 8.8
NPHM							
Jutial granite							
J11-WR	309.0	110.0	2.81	8.12	0.88438	1	
J11-B	1514.0	3.5	431.09	1245.85	0.93832	3	3.0 ± 0.1
J11-M	603.5	9.4	63.98	184.90	0.90100	3	6.5 ± 0.1
paragneiss							
J13-WR	264.0	124.0	2.13	6.15	0.87565	1	
J13-B	883.3	5.3	167.36	483.67	0.85792	4	no age.
J13-B-duplicate	860.3	7.3	118.09	341.28	0.85367	1	
paragneiss							
J14-WR	455.0	88.1	5.16	14.92	0.87851	4	
J14-B	2352.0	8.5	278.04	803.55	0.91470	2	3.2 ± 0.1
paragneiss							
J21-WR	206.0	159.0	1.29	3.74	0.80384	9	
J21-B	821.3	26.9	30.50	88.17	0.80796	2	3.4 ± 0.1
paragneiss							
I6-WR	248.0	152.0	1.63	4.71	0.83941	1	
I6-B	893.4	8.7	102.25	295.50	0.84872	1	2.2 ± 0.1
leucogranite							
I8-WR	296.0	17.0	17.40	50.32	0.80485	5	
I8-B	2829.0	2.4	1203.30	3477.60	0.92642	27	2.4 ± 0.1
I8-M	809.5	1.9	417.30	1206.00	0.86622	24	3.7 ± 0.1
paragneiss							
I9-WR	108.9	151.1	0.72	2.08	0.76613	2	
I9-B	1244.0	8.6	143.90	416.10	0.77664	3	1.8 ± 0.1
I9-M	249.2	17.0	14.60	42.26	0.76868	3	4.4 ± 0.8
I9-M-duplicate	311.9	21.9	14.22	41.10	0.77043	3	7.7 ± 0.1
paragneiss							
I10-WR	150.4	285.8	0.53	1.52	0.76878	4	
I10-B	516.5	9.2	56.36	162.90	0.77999	8	1.7 ± 0.1
I10-M	284.3	18.7	15.24	44.03	0.77244	2	6.0 ± 0.1
I10-ksp	167.1	109.3	1.53	4.42	0.76869	1	no age
leucogranite							
S92-WR	389.0	25.0	15.56	44.97	0.83016	1	
S92-B	1939.0	1.0	1960.57	5666.05	0.94490	26	1.4 ± 0.1
S92-M	865.7	3.1	275.61	796.51	0.86564	3	3.3 ± 0.1
S92-M-duplicate	928.0	3.4	275.15	795.18	0.86019	3	2.8 ± 0.1
paragneiss							
A3-WR	375.0	77.4	4.84	14.00	0.83808	1	
A3-M	966.9	23.3	41.43	119.72	0.89377	6	36.4 ± 0.3
paragneiss							
T25-WR	291.0	163.0	1.79	5.16	0.83800	1	
T25-M	872.6	31.1	28.08	81.15	0.84180	2	3.5 ± 0.1

Table 5.2. Strontium isotope data for dated samples, with derived ages (see text for analytical details). Errors shown were calculated to one sigma. (1) = biotite age calculated using regression to plagioclase; (2) = biotite age calculated using regression to hornblende; all other ages calculated by regression to whole-rock. WR = whole-rock; B = biotite; M = muscovite; Hb = hornblende; Pl = plagioclase; ksp = k-feldspar.

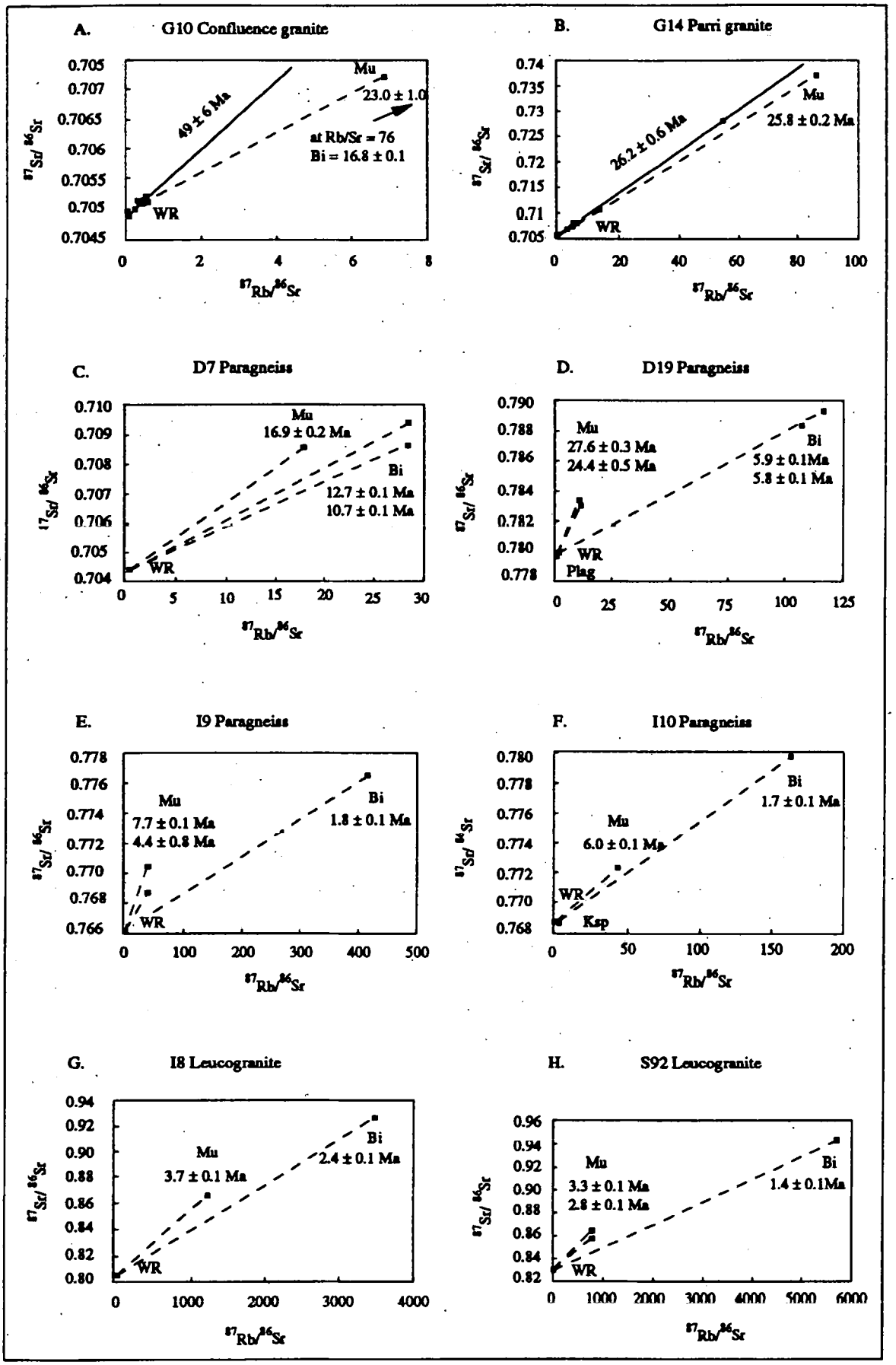

Fig. 5.4. Strontium isotope systematics for samples from the Kohistan arc (G10 & G14), the shear zone (D7, D19) and the NPHM (I9, I10, I8, S92, J11 & J13). WR = whole-rock; Mu = muscovite; Bi = biotite. Data for strontium whole-rock isochrons (Figs A & B) are given in Chapter 7. All errors are quoted to one sigma.

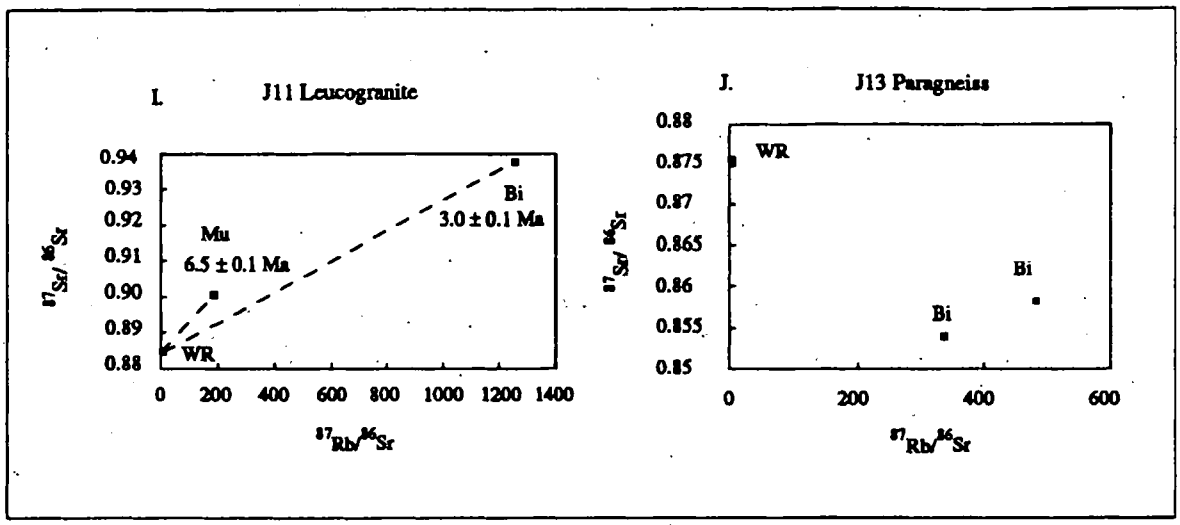

Fig. 5.4 (cont.).

Rb-Sr age determinations to be made on relatively young mica samples. In contrast, the Rb/Sr ratios of the analysed feldspar and hornblende separates lie too close to the corresponding whole rock ratios to give precise dates.

The interpretation of Rb-Sr whole-rock - mineral isochrons is based on the assumption that at the time of closure to strontium, muscovite or biotite were in isotopic equilibrium with the whole-rock. This assumption is probably correct for muscovite, since in the studied samples muscovite was probably the first phase to close to strontium diffusion, and therefore the whole-rock represents the true composition with which the muscovite equilibrated. However, strontium diffusion between biotite and a co-existing phase is likely to continue down to a relatively low temperature, after the closure of other phases in the rock to strontium. Consequently, the closure temperature of biotite will partly be dependant on the diffusivity of the last phase to exchange strontium with the biotite, since the closure of this phase also forces the closure of the biotite (Giletti 1991). For example, the relatively low strontium retentivity of apatite suggests that coexisting apatite and biotite may sometimes be the residual open phases (Forver and Giletti 1989). As a result, the initial isotopic ratio of the biotite (i.e. the ratio existing at the time that isotopic exchange between biotite and the coexisting phase ceased) can only be evaluated when the identity of the last phase to be in isotopic equilibrium is known. Use of the whole-rock initial ratio to calculate Rb-Sr biotite ages in this study is therefore based on an unrealistic simplifying assumption

(i.e. whole-rock - biotite equilibrium at the time of biotite closure). However, this assumption probably generates only a small error for the following reasons :

(i) Feldspar forms the most important strontium reservoir in the studied samples, and the Rb/Sr ratios of both feldspars and whole-rocks are generally relatively low. Consequently the isotopic compositions of the whole-rock and feldspar for a given sample are likely to be very close, an inference which is supported by the data for sample D19 (Fig. 5.4D; Table 5.2).

(ii) The mica samples from the NPHM show extreme enrichment in $^{87}Sr/^{86}Sr$, and consequently a slight error in the estimation of the initial strontium isotopic composition produces only a slight error in the calculated age.

The true accuracies on the ages are difficult to assess; errors incorporate the uncertainties in both isotopic ratios and Rb/Sr elemental ratios, and also to a large extent the degree of dispersion existing in the Rb-Sr ratio of the two points. Repeat analyses were performed on five samples, hand-picked at different times from the same mesh sizes (i.e. not 'duplicates' *sensu stricto*). Biotite samples show a reproducibility of 8 % and 3 %, whilst three muscovite samples have reproducibilities of 12 %, 16 % and 54 % (sample I10). The poor reproducibility for some samples is probably a reflection of sample inhomogeneity (e.g. undetected feldspar inclusions).

Rb-Sr ages from the northern part of the NPHM lie in the range 2.8-7.7 Ma for muscovite and 1.4-3.4 Ma for biotite. As shown in Fig. 5.4J, duplicate biotite Rb-Sr analyses of sample J13 define negative isochrons with respect to the whole rock, indicating that the sample is substantially out of isotopic equilibrium on a whole-rock scale.

In the central zone of the NPHM, the migmatite sample collected from the Astor gorge has yielded a muscovite Rb-Sr age of 36.4 Ma. In contrast, muscovite collected from the Liachar shear zone has an Rb-Sr age of 3.5 Ma.

In the Sassi-Darchan shear zone, muscovite Rb-Sr ages from the western side of the Darchan valley are 16.9 Ma and 18.5 Ma, whilst biotite from sample D7 has yielded duplicate ages of 12.7 Ma and 10.7 Ma. Rb-Sr ages from other parts of the shear zone are highly variable. Muscovite duplicates from sample D19 have yielded Rb-Sr ages of 24.4 and 27.6 Ma. In contrast, the plagioclase, whole-rock and biotite from sample D19 lie on a three-point isochron (Fig. 5.4D) which yields an age of 5.9 Ma, indicating that strontium exchange between plagioclase and biotite ceased at this time. Sample D2, collected only 400 metres away from sample D19, has yielded an Rb-Sr muscovite age of 11.9 Ma. Both biotite and hornblende separates have been analysed from metabasic lithology S22, and have yielded biotite-hornblende and biotite-whole rock Rb-Sr ages of 24-25 Ma. Sample G31 has yielded a muscovite Rb-Sr age of 288 Ma.

Samples from the Kohistan arc have yielded mica Rb-Sr ages in the range 16.8-25.8 Ma.

5.7. Closure Temperatures

In order to interpret the above cooling ages in terms of temperature variation with time, the closure temperatures of the relevant phases must be estimated for each isotopic system. Such closure temperatures (T_C) may be either estimated empirically, or calculated using experimentally derived diffusion data using the iterative (but rapidly converging) equation of Dodson (1973), which assumes volume diffusion during linear cooling :

$$T_C = \frac{E/R}{\ln\{(ART^2D_o/a^2)/EdT/dt\}}$$

where E is the activation energy, A is a geometrical constant, R is the gas constant, D_o is the diffusion coefficient and a is the diffusion distance.

Unfortunately, reliable experimental data are often unavailable, and even where such data are available, information on cooling rate and effective diffusion radius are also required in order to calculate closure temperatures. Furthermore, diffusion rates may be dependent on factors such as major element composition and structural or crystallographic state (Cliff 1985; Hodges 1991). Empirical estimates of closure temperature are highly variable but do at least reflect real geological situations.

5.7.1. $^{40}Ar/^{39}Ar$

Harrison (1981) and Harrison et al. (1985) have calculated argon diffusion parameters for hornblende and biotite, respectively. However, there are no reliable experimental diffusion data available for argon in muscovite, and empirical estimations of the temperature of muscovite closure to argon diffusion are variable. For example, Purdy and Jäger (1976) estimated that muscovite closure to argon occurred at about 350 °C, whilst from a study of partial argon loss from muscovite in an orebody, Snee et al. (1988) estimated that closure occurred at ~ 325 °C during rapid cooling and ~ 270 °C during slow cooling. By comparing biotite and hornblende $^{40}Ar/^{39}Ar$ ages on a well-constrained cooling path, Blanckenburg et al. (1989) estimated argon closure in muscovite to occur at ~ 410 °C (cooling rate ~ 40 °C/Ma^{-1}). The kinetic parameters for argon diffusion in muscovite have been inferred by Hamilton et al. (1989). Using these parameters, together with those for diffusion in hornblende and biotite (Harrison 1981 and Harrison et al. 1985), the closure temperatures for argon diffusion in all three phases have been calculated using equation 1, as shown in Table 5.1.

The calculation of closure temperatures also requires constraints on both the cooling rate of the sample and on the effective diffusion radius of the grain analysed. In general, changing the cooling rate only has a minor effect on the estimation of the closure temperature; e.g. for a 1 mm biotite T_C is 367 °C at 40 °C/Ma, 378 °C at 80 °C/Ma and 385 °C at 120 °C/Ma. Approximate cooling rates can be estimated by simply using empirical estimates of the closure temperature of different minerals for which ages have been obtained.

Although this argument is circular to some extent, the small dependence of closure temperatures on cooling rate means that this does not significantly affect the results. Cooling rates used to calculate the closure temperatures in Table 5.1 are 20 °C/Ma for samples from the Kohistan arc, 40 °C/Ma for samples from the shear zone on the western margin of the NPHM and 67 °C/Ma for samples from the NPHM.

Changing the effective diffusion distance also has an effect on the calculated closure temperature. For example, at a cooling rate of 20 °C/Ma, biotite with a half-width of 0.5 mm has a closure temperature of 356°C, whilst biotite with a half-width of 0.25 mm has a closure temperature of 334°C. Because of this grain size effect, it is important to point out that the closure temperatures given in Table 5.1 are maximum estimates because the diffusion radius measured is a maximum. It is more likely that the effective diffusion radius is smaller than that measured because of imperfections within the mineral lattice, as observed by previous workers (Harrison and Fitz-Gerald 1986; Baldwin et al. 1990). Various empirical studies have found a strong correlation between grain size and blocking temperature up to a critical grain size (Foland 1974; Kelley 1988; Goodwin and Renne 1991; Cosca et al. 1992). The results of hydrothermal heating experiments give an indication of the variation in effective diffusion radius between different samples. For example, values for three different hornblende samples were estimated to be > 60 μm, 36-65 μm and < 25 μm (Harrison 1981; Baldwin et al. 1990). In contrast, using a laser probe, Kelley and Turner (1991) observed diffusion domains in hornblende of up to 500 μm. Harrison et al (1985) found that the maximum diffusion distance in a biotite sample was approximately 150 μm. In the light of these experimental results, the measured grain size of the samples used in this study (generally ~ 1 mm) is unlikely to represent the effective diffusion distance. Consequently, the calculated closure temperatures given in Table 5.1 are probably overestimates and may therefore be geologically unreasonable.

Given the uncertainty on the effective diffusion distance for each sample, cooling paths will be constructing using approximate closure temperatures of 500 ± 50 °C for hornblende and 300 ± 50 °C for biotite (Cliff 1985). This allows comparison between the

$^{40}Ar/^{39}Ar$ ages presented in Table 5.1 and those of previous studies, and also comparison between the $^{40}Ar/^{39}Ar$ and the Rb-Sr ages from the same samples (Tables 5.1 & 5.2).

5.7.2. Rb-Sr

There are no reliable experimental data for strontium diffusion in muscovite or biotite, and consequently closure temperatures for strontium diffusion in these phases are even less well-constrained than for argon diffusion, and no control exists on the variation of T_C with either cooling rate or grain size. Empirical observations provide only very broad approximations of closure temperatures for strontium. For example, in a contact aureole study, Hart (1964) found that argon diffusion in biotite occurred more readily than strontium diffusion in biotite. Using the diffusion data for argon in biotite of Harrison et al. (1985), Harrison and McDougall (1980) estimated that the difference in activation energy calculated by Hart (1964) was compatible with a 30-40 °C higher closure temperature for strontium in biotite than argon in biotite. However, as pointed out by Cliff (1985), at Alpine cooling rates, the difference between the resulting ages is not likely to be resolvable. Consequently, in most previous studies, biotite Rb-Sr and $^{40}Ar/^{39}Ar$ ages for the same samples have generally been found to be concordant (Armstrong et al. 1966; Hurford 1986; Blanckenburg et al. 1989).

Empirical studies suggest that the muscovite closure temperature for strontium is close to the hornblende closure temperature for argon (~ 500 °C; Cliff 1985). For example, in the central Alps, muscovite closed to strontium shortly after the closure of hornblende to argon, whereas in the Tauern window, muscovite closure to strontium occurred first, observations which also serve to confirm the strong relation between closure temperature and local factors such as cooling rate and lithology (Blanckenburg et al. 1989). By extrapolating a cooling path to higher temperatures, Blanckenburg et al. (1989) estimated that strontium closure in phengite occurs at 550 °C.

By comparing pre-Alpine and Alpine mica cooling ages to metamorphic isograds, Jäger and co-workers (Jäger et al. 1967; Purdy and Jäger 1976; Wagner et al. 1977) estimated the closure temperature for strontium in biotite to be 300 ± 50 °C and strontium in muscovite to be 500 ± 50 °C. Although this approach was based on the assumption that the peak age of Alpine metamorphism was uniform over the whole area, as discussed by Blanckenburg et al. (1989), the estimates of closure temperature have appeared to be relatively reliable when tested at other metamorphic grades and in different areas. Consequently, in common with previous studies (Cliff et al. 1985) the closure temperatures of Jäger and co-workers are used in the following discussion.

In summary, the assignment of precise values to closure temperatures is problematic, and it should be born in mind that there remain significant uncertainties attached to all of the values of T_C used in this study. However these uncertainties do not reflect the general conclusions regarding relative differences in the cooling histories of the NPHM and Kohistan arc.

5.8. Discussion

5.8.1. Regional Distribution

Cooling ages from the NPHM-Kohistan region have a distinct regional distribution, confirming that age differences have a geological significance. Fig. 5.5 is an east-west projected profile from eastern Kohistan into the northern part of the NPHM. The leucogranite sample (S92) from the Indus gorge has not been included for reasons outlined below. Muscovite and biotite $^{40}Ar/^{39}Ar$ and Rb-Sr ages all decrease dramatically from Kohistan into the NPHM. In general, the age separation between different phases from the same area or sample also decreases in an eastwards direction, showing that cooling rates have been more rapid in the NPHM. The shear zone bordering the western margin of the NPHM thus separates two terrains with strongly contrasting post-metamorphic cooling histories.

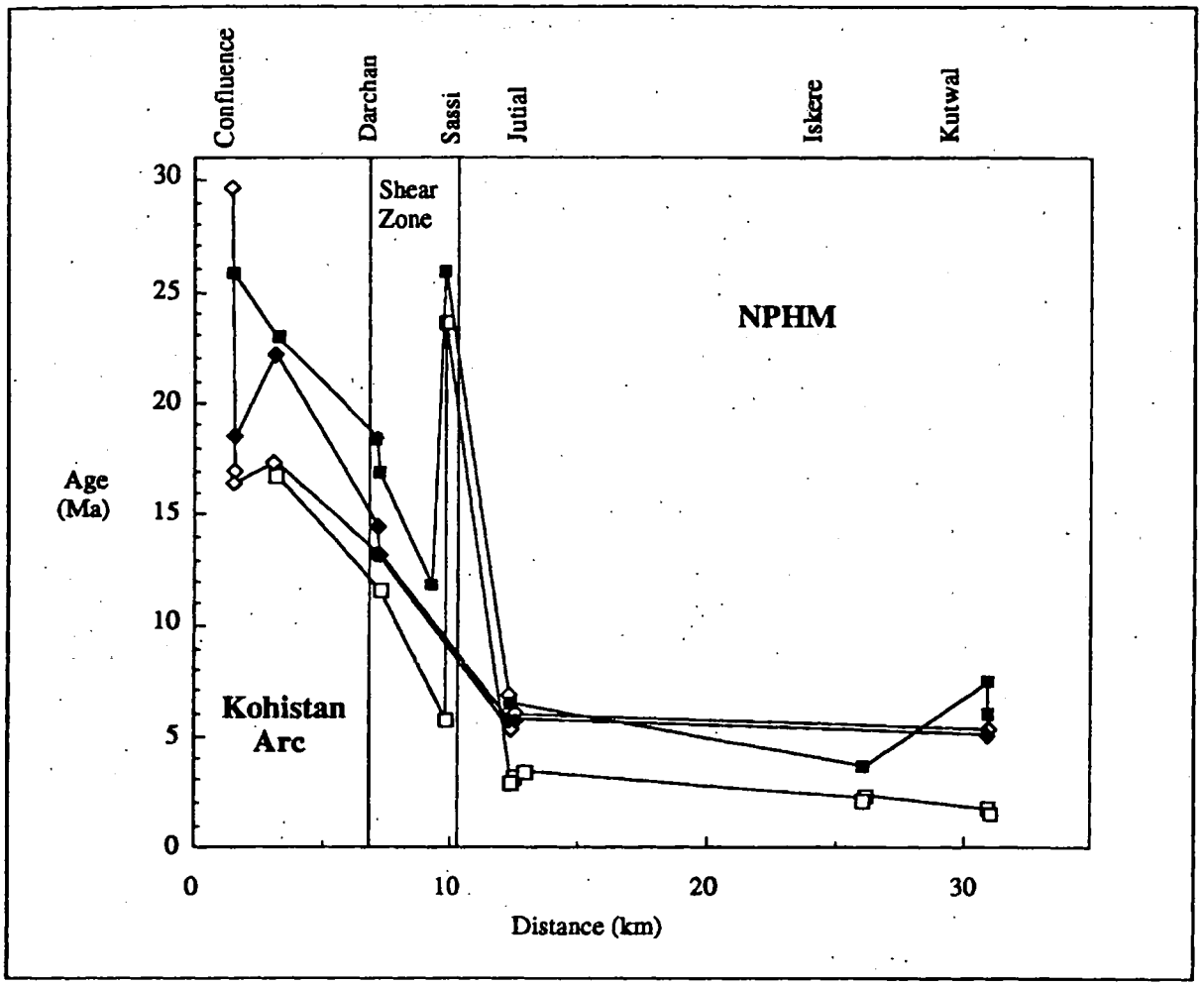

Fig. 5.5. East-west, projected cooling-age traverse across the western margin of the NPHM. Squares : Rb-Sr (open - biotite, closed - muscovite); diamonds : $^{40}Ar/^{39}Ar$ (open - biotite, closed - muscovite).

Within the shear zone, mineral ages are highly variable, which is probably a reflection of an extended history of deformation and exhumation within the zone (see below). However, it should be noted that the youngest ages from the shear zone are older than the majority of mineral ages from adjacent parts of the NPHM. Thus in the northern part of the NPHM, there is no geochronological evidence for young exhumation preferentially occurring along the western margin, as has occurred in the Liachar area (Fig. 5.1) (Butler and Prior 1988b). The structural nature of the northern margin of the NPHM in the Sassi-Darchan area is also markedly different to the margin in the Liachar area. Structural studies show that the Sassi-Darchan shear zone is characterised by dextral oblique-slip with a relative movement sense of NW side (Kohistan) down (Chapter 3), whereas in the Liachar area, there has been large-scale, greenschist to amphibolite-grade overthrusting of NPHM rocks north-westwards over the Kohistan arc. Thus the exhumation of the northern part of

the NPHM has probably occurred by a combination of folding within the NPHM, and transtensional shearing along the contact zone that borders the western margin.

5.8.2. Local Mineral Age Variation

In the following section, the mineral ages from closely-spaced samples for each geographical area will be discussed separately. Where there is sufficient data available, cooling paths have been constructed in order to enable comparison to be made between the thermal histories of different structural levels within the NPHM (Fig. 5.6). Each cooling path has been constrained by as many different phases and closure temperatures as possible, and average cooling rates have been estimated for different intervals along each cooling path. Such cooling rates for individual samples from different areas are given in Table 5.3. Cooling rates between 350 °C and 300 °C are constrained by $^{40}Ar/^{39}Ar$ muscovite and biotite ages; Rb-Sr biotite ages are considered to be rather less reliable than $^{40}Ar/^{39}Ar$ biotite ages. Errors in the cooling rates take into account uncertainties in both the closure temperatures and ages. Estimated cooling rates between the smallest intervals have the largest uncertainty, since the age difference between the relevant phases is relatively small (and in some cases, smaller than the errors on the ages).

5.8.2.1. Nanga Parbat-Haramosh Massif

Within the northern NPHM, mica $^{40}Ar/^{39}Ar$ and Rb-Sr ages for post-metamorphic, cross-cutting leucogranite dykes and plutons lie within error of ages from the metamorphic rocks of the NPHM, and consequently, with one possible exception (sample S92, discussed below), all of the leucogranite mineral ages presented in this study are interpreted as being tectonically-related cooling ages. For example, the Jutial granite contains large roof pendants of paragneiss which have similar biotite and muscovite $^{40}Ar/^{39}Ar$ and biotite Rb-Sr ages as the granite itself. These ages are similar to the ages obtained from more distal metamorphic

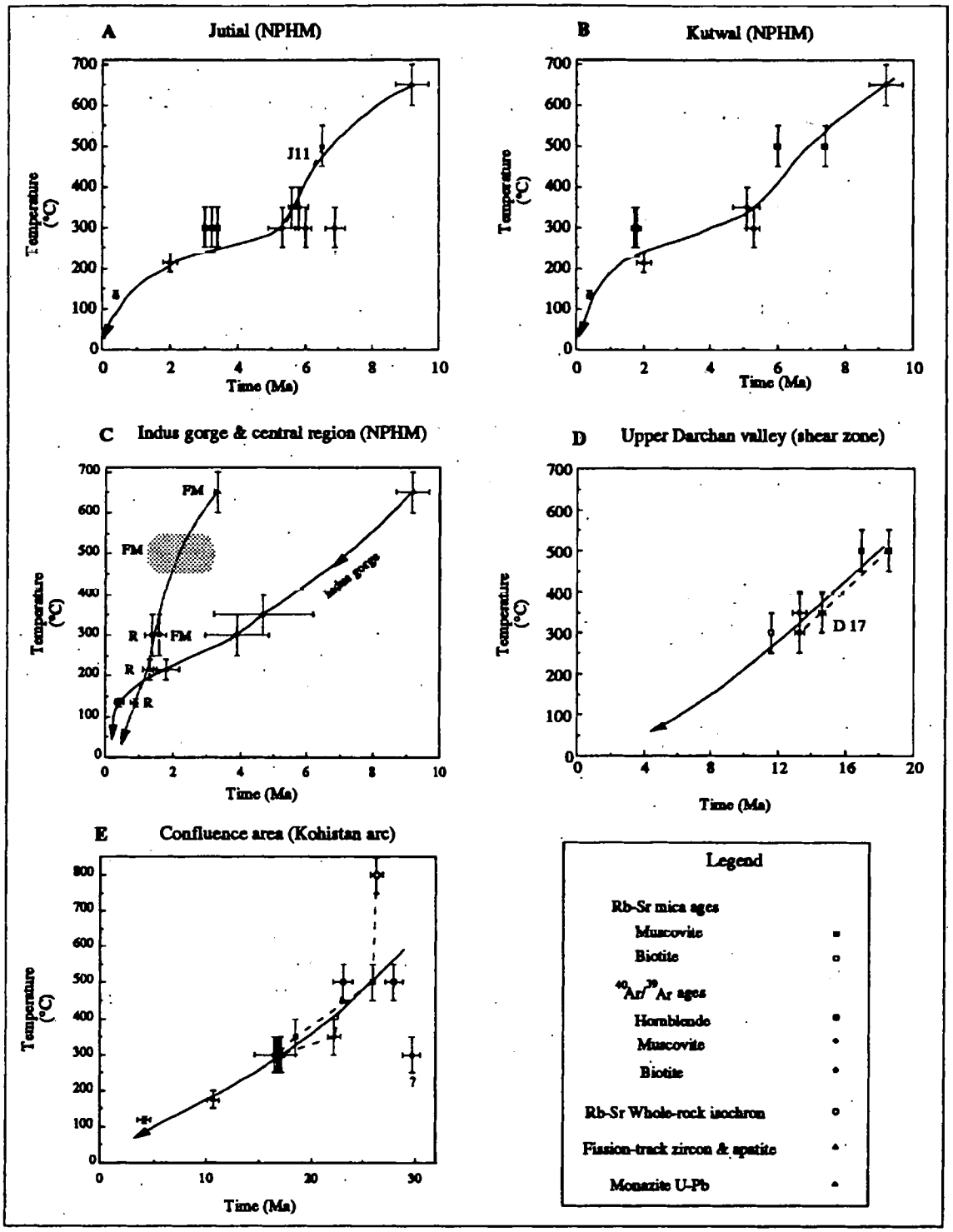

Fig. 5.6 . Cooling Paths from the Kohistan-NPHM region. **A** : Jutial (NPHM), derived from samples J11, 13, 14, & 21 (J11 samples joined by dashed lines); **B** : Kutwal (NPHM), derived from samples I9 & I10; **C** : Indus gorge (solid line), and Fairy Meadows (FM) - Rupal (R) area (dashed line); **D** : Darchan valley shear zone, derived from samples D7, D17 & D18 (D17 samples joined); **E** : Kohistan arc, derived from samples G11, 12, 14 & 20 (samples G10 & G14 joined). Rb-Sr whole-rock ages from Chapter 7; fission-track zircon and apatite data from Zeitler (1985). Monazite U-Pb ages from Smith et al. (1992) (Indus gorge) and Zeitler et al. (1993) (Fairy Meadows). Each point represents a separately-determined age, with the exception of biotite D7 and muscovite I9, which are the weighted mean of duplicates, and monazite U-Pb and zircon fission-track data from the Indus gorge, which are shown as a the mean ages of two samples. Indus gorge mica ages represent means of all previously determined $^{40}Ar/^{39}Ar$ and K-Ar ages from the Indus gorge transect through the NPHM (Treloar et al. 1989a, 1991; Zeitler et al. 1989). The shaded field on the Fairy Meadows curve represents the range of saddle shaped hornblende $^{40}Ar/^{39}Ar$ spectra determined by Zeitler et al. (1993) for float samples. All errors are calculated to one sigma.

Location & Sample	Method	Time period (Ma)	Cooling Rate (°C / Ma)	Uplift rate mm/yr
Kohistan				
Confluence (G14)	Sr WR - Sr Mu	26.2-25.8	625 ± 1.7	-
	Sr Mu - Ar Mu	25.8-18.5	20.5 ± 0.5	0.7 ± 0.02
	Ar Mu - Ar Bi	18.5-16.5	25.0 ± 2.5	0.8 ± 0.08
	Ar Bi - FT Z	16.5-10.6	21.0 ± 0.6	0.7 ± 0.02
	FT Z - FT Ap	10.6-4.1	8.4 ± 0.5	0.3 ± 0.02
	FT Ap - Sur	4.1-0	~ 26.8	~ 0.9
Confluence (G10)	Sr Mu - Ar Mu	23.0-22.2	187.5 ± 1.6	-
	Ar Mu - Ar Bi	22.2-17.4	10.4 ± 1.6	0.3 ± 0.02
NPHM				
Darchan (D17)	Sr Mu - Ar Mu	18.5-14.6	38.5 ± 0.5	1.3 ± 0.02
	Ar Mu - Ar Bi	14.6-13.3	38.5 ± 1.4	1.3 ± 0.05
	Ar Bi - Sur	13.3-0	~ 21.8	~ 0.7
Jutial (J11)	Sr Mu - Ar Mu	6.5-5.6	167.0 ± 0.5	5.6 ± 0.02
	Ar Mu - Ar Bi	5.6-5.3	167.0 ± 1.6	5.6 ± 0.05
	Ar Bi - Sur	5.3-0	~ 54.7	~ 1.8
Kutwal (I9 & 10)	Sr Mu - Ar Mu	6.7-5.1	93.7 ± 0.6	3.0 ± 0.02
	Ar Mu - Sur	5.1-0	~ 66.7	~ 2.2
Indus gorge	Pb M [1]- Ar Mu [2]	9.2-4.7	67.0 ± 0.4	2.2 ± 0.01
	Ar Mu - Ar Bi [2]	4.7-3.9	62.5 ± 2.6	2.1 ± 0.09
	Ar Bi - FT Z [3]	3.9-1.8	40.0 ± 0.8	1.3 ± 0.03
	FT Z - FT Ap [3]	1.8-0.4	57.0 ± 0.4	1.4 ± 0.01
	FT Ap - Sur	0.4-0	~ 312.5	~ 7.8
Fairy Meadows	Pb M [4]- Ar Bi	3.3-1.6	206 ± 0.3	6.8 (4.1) ± 0.01
	Ar Bi - FT Z [3]	1.6-1.3	283 ± 1.2	9.4 (5.7) ± 0.04
	FT Z - FT Ap [3]	1.3-0.9	186 ± 0.6	6.2 (3.7) ± 0.02
	FT Ap - Sur	0.9-0	143 ± 0.2	4.8 (2.9) ± 0.01

Table 5.3. Estimated cooling rates and derived exhumation rates for different intervals along measured cooling paths. Exhumation rates calculated assuming a 30 °C/km geotherm, except in the case of fission track ages from the Indus gorge (40 °C/km). Furthermore, the exhumation rates for Fairy Meadows that are given in parentheses were calculated assuming a 50 °C/km geotherm. Sr = Rb/Sr age; Ar = ^{40}Ar-^{39}Ar age; FT = fission track age; Pb = U-Pb age. WR = whole-rock isochron age; Mu = muscovite; Bi = biotite; Z = zircon; Ap = apatite; M = monazite; sur = surface. [1] Smith et al. (1992); [2] mean ages after Treloar et al. (1989a, 1991); [3] Zeitler (1985); [4] Zeitler et al. (1993).

rocks (e.g. J21), thus ruling-out an interpretation that involves the resetting of mineral ages in wallrock samples during granite intrusion. The Jutial granite also has a similar muscovite Rb-Sr age to metamorphic samples collected from Kutwal, 20 km to the east. These observations indicate that the granite undoubtedly intruded whilst its country rocks were still at temperatures of > 350 °C, and probably whilst its country rocks were at temperatures > 500 °C, and therefore intrusion took place at a considerable depth in the crust.

(i) Jutial and Kutwal areas

Fig. 5.6A shows a cooling path for the rocks in the vicinity of the Jutial granite, and Fig. 5.6B shows a cooling path for the rocks of the Kutwal area. In these figures, the high temperature portions of the cooling paths are roughly constrained by the monazite U-Pb age from the Indus gorge (Smith et al. 1992). The closure temperature of the monazite has been arbitrarily fixed at 650 ± 50 °C. The lower temperature portions of the cooling paths are constrained by the fission track dating of Zeitler (1985), using zircon and apatite ages of 1.8 Ma and 0.4 Ma respectively, again for samples from the Indus gorge.

It should be noted that the Indus gorge is here at an altitude of 1900 m, approximately 700 m lower than the Haramosh valleys the to north, and therefore fission-track ages for the Haramosh area would be expected to be slightly younger than in the Indus valley. Any correction made to the Indus gorge fission-track ages requires the assumption of a particular exhumation rate, which is dependant on estimates of both closure temperature and the geothermal gradient. For example, in the case of apatite fission-track ages, if an exhumation rate of 8 mm/yr is assumed (see below, Table 5.3), then a crustal thickness of 700 m would be exhumed in only 0.09 Ma, whereas if an exhumation rate of 3 mm /yr is assumed, the same crustal section would take 0.23 Ma to exhume. Apatite dated from the Indus gorge has yielded an age of 0.4 ± 0.1 Ma, and therefore corrected apatite ages could lie anywhere in the range 0.1-0.4 Ma, depending on the exhumation rate. Given the analytical errors on determined ages, the uncertainties on closure temperatures and the uncertainties on the geothermal gradient (discussed further below), fission track ages plotted in Figs. 5.6A & B have not been corrected for the altitude differences between sampling localities, and therefore they provide only a poor control on the low temperature portion of the cooling paths.

All the mica samples plotted in Fig. 5.6A were collected from the vicinity of the Jutial granite, and, with the exception of the biotite sample J21, come from within 500 m of each other. The biotite $^{40}Ar/^{39}Ar$ ages overlap the muscovite $^{40}Ar/^{39}Ar$ ages, and in one case

the biotite and muscovite ages for the same sample lie within error. The biotite which has yielded the oldest age (6.9 Ma; sample J13), co-exists with hornblende that contains excess argon. However, correlation diagrams show that there are no detectable signs of excess argon present in either this or other biotite samples. In general, the overlap between $^{40}Ar/^{39}Ar$ biotite and muscovite ages implies very rapid cooling through the argon blocking temperatures for these micas. Mineral ages from the Jutial granite (J11) indicate that the cooling rate between 6.5-5.3 Ma was approximately constant at a rate of about 170 $°C/Ma^{-1}$. The granite then cooled at a time-averaged rate of about 55 $°C/Ma^{-1}$ to the present day.

In Fig. 5.6B, cooling ages from Kutwal samples plot with an even greater scatter than the Jutial samples, although in this case, the mica samples were collected from within 30 cm of each other. Again, the biotite and muscovite $^{40}Ar/^{39}Ar$ ages from the same sample lie within error of each other, indicating rapid cooling through the mica blocking temperatures, whilst three muscovite samples have yielded variable Rb-Sr ages in the range 4.4-7.7 Ma. The Kutwal samples cooled from ~ 500 °C to ~ 350 °C at a rate of about 94 $°C/Ma^{-1}$.

Rb-Sr analyses of biotite from sample J13, a roof pendant within the Jutial granite, define negative isochrons with respect to the whole-rock, indicating that the sample is substantially out of isotopic equilibrium on a whole-rock scale, due to open system behaviour. The roof pendant is characterised by the presence of concordant layers of quartz-k-feldspar leucosome, which in the field appears to extend into the adjacent portions of the Jutial granite (see Plate 2.24). The Jutial granite has an evolved strontium isotopic composition of 0.875-0.892 (see Chapter 7), and sample J13 has a similar whole-rock composition of 0.875 (Table 5.2). Consequently, it is suggested that during intrusion, the injection of isotopically evolved melt (dominantly quartz and k-feldspar) from the Jutial granite into its wall-rock, a distance of 1-2 metres, has caused the elevation of the $^{87}Sr/^{86}Sr$ ratio of the whole rock roof-pendant samples, whereas the isotopic composition of the biotite is primarily controlled by the isotopic composition of the pre-existing country rock to the Jutial granite. In other words, the cooling age of the biotite cannot be calculated since the

initial ratio of the biotite cannot be constrained. It should be noted that such an interpretation would not be valid if the wall-rocks to the granite were isotopically homogenised on the cm-scale during granite emplacement.

(ii) Indus gorge

The mica cooling ages from the Indus gorge, where the Indus River trends east-west through the NPHM (Fig. 5.2), are broadly similar to mica ages from the Haramosh region. Using average mineral ages (Zeitler 1985; Zeitler et al. 1989; Treloar et al. 1989a, 1991; and Smith et al. 1992), a cooling path for the Indus gorge has been drawn for comparison with the cooling paths already described above (Fig. 5.6C). There is some doubt as to the high-temperature cooling history of this path, as discussed by Smith et al. (1992). Although Zeitler et al. (1989) reported hornblende $^{40}Ar/^{39}Ar$ and K-Ar ages for samples collected from the Indus gorge in the range 16-28 Ma (blocking temperature ~ 500 °C), two samples of metamorphic monazite have yielded U-Pb ages of 8.7 Ma and 9.7 Ma (Smith et al. 1992). Since Smith et al. (1992) suggested that the hornblende ages may be overestimates due to the undetected presence of excess argon, in Fig. 5.6A the high temperature portion of the cooling curve is constrained solely by the monazite ages. The cooling rate decreased slightly between 9.2-2.0 Ma. The single apatite fission-track age from the Indus gorge indicates a rapid, recent increase in cooling rate to about 300 °C/Ma^{-1}, as also noted by Zeitler (1985). The variable slope in the cooling curves indicate a complex, varying exhumation history for the northern NPHM.

The one-metre thick leucogranite dyke sampled in the Indus gorge (S92) has a duplicated muscovite Rb-Sr age of 2.8-3.3 Ma and biotite and muscovite $^{40}Ar/^{39}Ar$ ages within error of each other at 3.6-3.7 Ma (Tables 5.1 & 5.2). The similarity between muscovite Rb-Sr and both biotite and muscovite $^{40}Ar/^{39}Ar$ ages indicates very rapid cooling of this granite, at a rate which is not resolvable using currently available geochronological techniques. This observation, together with the presence of older hornblende and monazite ages from the Indus gorge, is consistent with the intrusion of the granite dyke at relatively

high structural levels, into rocks which were already at temperatures < 500 °C, causing very rapid post-emplacement crystallisation and cooling of the granite. Thus in some areas of the NPHM, muscovite Rb-Sr (and possibly mica $^{40}Ar/^{39}Ar$ ages) from leucogranite bodies may be close to their intrusion ages.

(iii) Fairy Meadows

The biotite $^{40}Ar/^{39}Ar$ age of 1.6 ± 0.2 Ma from a calcsilicate near Fairy Meadows is comparable with biotite and hornblende $^{40}Ar/^{39}Ar$ step-heating ages from the same area, which lie in the range 1.0-2.4 Ma and 1.5-2.8 Ma, respectively (Zeitler 1985 and Zeitler et al. 1993). Also at Fairy Meadows, a migmatite has yielded a monazite U-Pb age of 3.3 ± 0.1 Ma. Samples collected from an altitude of 4440 m beneath the Rupal face have yielded fission track ages of 1.3 Ma (Zircon) and 0.9 Ma (Apatite) (Fig. 5.2) (Zeitler 1985). These data enable a cooling curve to be plotted for the central Nanga Parbat region (Fig. 5.6C), which shows an extremely rapid, gently decreasing cooling rate in the range 143-280 °C/Ma^{-1} for the last 3.3 Ma .

Cooling ages from Fairy Meadows, lying at a relatively high topographic elevation, are significantly younger than cooling ages for samples from the Liachar shear zone (see below), which borders part of the western margin of the NPHM. This shear zone is thought to have accommodated substantial amounts of uplift by overthrusting rocks of the NPHM back over the Kohistan arc (Butler and Prior 1988b). The simplest interpretation of the young ages from Fairy Meadows is that they reflect extremely rapid, recent uplift on some (as yet unmapped) structure other than the Liachar thrust.

Metamorphic studies in the NPHM indicate that the metamorphic grade increases from kyanite-amphibolite facies to (locally) granulite facies, as Nanga Parbat is approached (Misch 1964; Zeitler et al. 1993; Chapter 4), and consequently the area with the highest topographic elevation and the youngest cooling ages also coincides with the area having the highest metamorphic grade. This is a similar situation as that existing in the Alps, where the

youngest cooling ages are seen in the higher-grade rocks which originally occupied the deepest structural levels. However, the temporal and spatial correlation between the high-grade metamorphic fabrics in the core and the amphibolite-grade fabrics along the margin of the NPHM is uncertain. The metamorphism and migmatisation observed at Fairy Meadows has been dated at < 3 Ma (Zeitler et al. 1993), but the age of other fabrics in the NPHM is poorly constrained. It is possible that the muscovite-free migmatitic assemblages observed sporadically throughout the NPHM may reflect a young metamorphism which has locally overprinted the earlier (? Himalayan) amphibolite-facies assemblages. Evidence for this comes from P-T studies, which indicate that the metamorphism at Fairy Meadows took place under significantly lower (5-6 kb) pressure conditions than the widespread, amphibolite-grade metamorphism in the NPHM (7-10 kb) (Chapter 4; Zeitler et al. 1993). Thus, whereas previous studies have documented rapid, near isothermal uplift of hot migmatites towards the surface (Jones and Brown 1990), in the core of the NPHM, metamorphism and migmatisation appears to have taken place at a relatively high level, and was followed by rapid, post-metamorphic cooling.

(iv) Astor gorge

The single muscovite Rb-Sr age of 36 Ma from the Astor gorge contrasts strongly with younger cooling ages from other parts of the NPHM, which may be a reflection of strong regional differences in the thermal history of the NPHM. However, it should be noted that three paragneiss samples from the Astor gorge have yielded conventional monazite U-Pb ages of 5-10 Ma, which have been used as evidence for a young metamorphism in the region (Smith et al. 1992). Consequently, the dating of further samples from the Astor gorge is required before the thermal history of the region can be understood.

5.8.2.2. *The Western Margin of the NPHM*

(i) Liachar shear zone

Cooling ages from the Liachar shear zone, a structure which is thought to have accommodated a large amount of recent uplift of the NPHM (Butler and Prior 1988b; Chapter 3), are significantly older and more variable than ages from Fairy Meadows. This study has yielded a muscovite Rb-Sr age of 3.5 Ma, whereas numerous mica K-Ar ages lie in the range 6.6-9.2 Ma (Coward et al. 1986; Treloar et al. 1991). In the same vicinity, a metamorphic monazite has been dated at 11 Ma (Smith et al. 1992), whilst zircon from a pegmatite has been dated at 2.2 Ma (Zeitler et al. 1993). There is insufficient reliable data available for the construction of a cooling curve for the shear zone.

(ii) Sassi-Darchan shear zone

Samples from the west side of the Darchan valley (D7, D17 and D18; Fig. 5.3) are the least-strongly deformed samples collected from the shear zone, and yield relatively consistent mica $^{40}Ar/^{39}Ar$ and Rb-Sr ages. These ages reflect closure through ~ 500 °C at 16.9-18.5 Ma, closure through ~ 350 °C at about 14 Ma, and through ~ 300 °C at about 12 Ma (see Fig. 5.6D). The similarity between muscovite Rb-Sr ages for a deformed Confluence granite and its wall rocks indicates that by ~ 500 °C, the granites and their country rocks were following the same cooling path. The cooling rate remained at about 38 $°C/Ma^{-1}$ during the interval 18-13 Ma. The rocks then experienced a time-averaged cooling rate of about 22 $°C/Ma^{-1}$ to the present day.

In contrast, the samples from the east side of the Darchan valley (D2 and D19) and from Sassi (G31 and S22) have yielded exceedingly variable mica Rb-Sr ages. These samples are intensely deformed, and the pelitic lithologies possess a strong s-c fabric, related to transtensional movements in the shear zone (see Chapter 3)). Along the c-planes, mica has been reorientated, and hornblende shows signs of retrogression to biotite, indicating that this

fabric was generated under greenschist-facies conditions. The discordance in these Rb-Sr ages greatly exceeds the analytical uncertainty involved. The geological interpretation and significance of such variable cooling ages in equivocal, and may reflect one or a combination of the following processes:

(1) Variable closure temperatures for different samples, due to variable diffusion parameters or cooling rates (Blanckenburg et al. 1989). Diffusion parameters may be dependant on factors such as the effective diffusion radius, the presence of fluid, the crystallographic structure or chemical composition, factors which may themselves be strongly affected by degree of shearing. However, samples from closely-spaced localities (e.g. D2 and D19) yield remarkably different cooling ages, and there appears to be no obvious correlation between lithology or structural state and mineral age. For cooling rate to be an important factor would also require the maintenance of relatively fine-scale thermal gradients in the shear zone during deformation.

(2) Variable resetting of mineral ages during two separate thermal events in Himalayan times, with an early metamorphism (M1) at ~30 Ma, and a later, weaker event (M2) at < 10 Ma. The petrological and P-T data presented in Chapter 4, together with the granite geochronology presented in Chapter 7, support the existence of M1, whilst the U-Pb studies of Zeitler et al. (1989, 1993) and Smith et al. (1992) provide evidence for a younger metamorphism in the region. The different thermal events are not easily separable in shear zone rocks due to incomplete requilibration during M2. The younger event caused the complete resetting of the biotite-plagioclase pair in sample D19, whereas muscovite in the same sample was thermally unaffected. Other samples, such as muscovite D2, were partially rejuvenated during M2. The metamorphic event at < 10 Ma seems to have been at least temporally associated with the widespread intrusion of leucogranites in the NPHM at this time. Factors such as the duration of heating, and the fluid content or grain size of a particular sample are likely to have an important affect on the degree to which resetting occurred.

(3) Juxtaposition by shearing of different structural levels which have experienced different thermal histories. For example, sample S22 appears to be representative of one of the many imbricates of Kohistan-derived metabasic material lying within the shear zone, and has a similar biotite age to some of the samples collected from the Kohistan arc. Such imbricates must have been brought into their present structural positions after shear zone temperatures had fallen below the temperature for strontium diffusion in the biotite-plagioclase pair, in order to prevent resetting.

The old muscovite age recorded by sample G31 may be a mixing age containing a large component of ^{87}Sr preserved from pre-Himalayan times. However, metamorphic studies show that sample G31 was metamorphosed under identical P-T conditions to other shear zone samples, and therefore it seems unlikely that the sample represents an isolated, preserved slice of pre-Himalayan fabric in such a zone of young and intense deformation. Alternatively, therefore, the age may reflect a degree of localised open-system behaviour in some parts of the shear zone, possibly related to a degree of strontium mobility in circulating fluids. Independent evidence for such open-system behaviour comes from a study of the granites present in the shear zone (see Chapter 6).

All of the above theories are problematic. For example, lithological or structural effects are unlikely to account for such a wide variation in mineral ages, since cooling ages are primarily affected by temperature (Cliff 1985). Polymetamorphism fails to explain why only samples collected from the shear zone display such a wide variation in mineral ages, whereas such strong variation is relatively rare elsewhere in the region. Furthermore, in the Indus gorge M2 appears to have been a sufficiently high grade to have caused either the crystallisation or the isotopic resetting of monazite, whereas in the shear zone muscovite Rb-Sr ages have not been reset locally. Finally, structural juxtaposition of different rock units within the shear zone fails to explain the contrasting muscovite and biotite Rb-Sr ages for sample D19.

The thermal evolution of rocks in the Sassi-Darchan shear zone is complex, and may involve a combination of the processes or factors described above. However, it should be noted that, firstly, the most scattered mineral ages obtained in this study come from shear-zone samples, and secondly, that the majority of these mineral ages lie within the range of possible tectonothermal activity for the region in Himalayan times. During deformation, a combination of grain-size reduction, dynamic recrystallisation and lattice dislocation may substantially reduce mineral ages preserved either during slow cooling or later thermal resetting (Kelley 1988; Kligfield et al. 1986). For example, Kligfield et al. (1986) obtained muscovite K-Ar ages in the range 13-26 Ma for different size fractions from a single, highly crenulated sample. A full understanding of the complex thermal evolution of the zone will therefore require denser sampling, and the analysis of more phases in order to constrain the degree of strontium isotopic disequilibrium.

5.8.2.3. Kohistan Arc

(i) North of the Indus confluence

Parri granite whole-rock sample G14 lies on an eleven-point isochron which yields an age of 26.2 ± 0.6 Ma (MSWD = 5.9) (Chapter 7). The Parri granites are cross-cutting S-type granites that were probably generated by fluid absent melting (see Chapter 6) and emplaced at temperatures of 750 ± 50 °C (Clemens and Wall 1981), as shown on Fig. 5.6E. A muscovite Rb-Sr age of 25.8 Ma for sample G14 is within error of the crystallisation age and indicates rapid, post-emplacement cooling of the granite to approximately 500 °C at a rate of about 625 °C/Ma^{-1} (Table 5.3). The similarity between the whole-rock and muscovite Rb-Sr ages for this sample may also reflect a higher closure temperature for strontium in muscovite at the inferred cooling rate, since initial, rapid cooling from high temperatures causes rapid closure (Harrison and McDougall 1980). The Parri granite has also yielded muscovite and biotite $^{40}Ar/^{39}Ar$ ages of 18.5 Ma and 16.5 Ma respectively. The metabasic country rock (G11) to the Parri granite sheet has yielded a hornblende $^{40}Ar/^{39}Ar$ age of 27.9 Ma (Table 5.1). This age is similar to other hornblende $^{40}Ar/^{39}Ar$ ages for metamorphic

rocks in the vicinity of the Indus confluence (Treloar et al. 1989a; see below), demonstrating that, firstly, the hornblende ages close to the granite sheets have not been isotopically reset during granite intrusion, and secondly that the Parri granite was intruded into country rocks that had only recently passed through ~ 500 °C. A biotite sample (G12) from a Confluence granite sheet at the same exposure has yielded an $^{40}Ar/^{39}Ar$ age which is within error of a biotite age from the adjacent Parri granite, indicating that the Confluence and Parri granites cooled simultaneously through the biotite blocking temperature to argon. A biotite sample from metabasic sample (G11) has inexplicably yielded an unusually old age of 29.6 Ma, although there is no detectable excess argon present.

(ii) South of Indus confluence

The Confluence granite dated (sample G10) lies on a ten-point errorchron which yields a poorly-constrained age of 49.1 ± 6 Ma (MSWD = 11). The same sample has yielded a muscovite Rb-Sr age of 23 Ma and muscovite and biotite $^{40}Ar/^{39}Ar$ ages of 22.2 Ma and 17.4 Ma, respectively. These mica cooling ages are similar to those for samples from the exposure to the north of the Indus confluence, and thus mineral ages from both locations are plotted on Fig. 5.6E. The low-temperature portion of this cooling path is constrained by the fission track dating of zircon and apatite samples collected from the same area (Zeitler 1985). Since approximately 23-25 Ma, cooling rates in Kohistan have gently decreased, at rates of < 30 °C/Ma^{-1}, with a rather greater variation in cooling rate over the last 10 Ma (Table 5.3).

Previous hornblende step-heating $^{40}Ar/^{39}Ar$ ages from near to the Indus confluence lie in the range 27-39 Ma (Treloar et al. 1989a; Zeitler et al. 1989), although some of these ages may be slight overestimates due to the presence of excess argon. Peak metamorphic temperatures for samples from near the Indus Confluence are 550-650 °C (Chapter 4), and subsequently these hornblende ages place an additional constraint on the timing of regional metamorphism, as already suggested by Zeitler et al. (1989). The variation existing between the hornblende ages is probably a reflection of both the presence of excess argon in some

samples, together with a variation in post-metamorphic cooling and exhumation histories for different samples.

Previously-determined muscovite $^{40}Ar/^{39}Ar$ ages for granites and their country rocks from near to the Indus confluence lie in the range 18-21 Ma, whereas biotite K-Ar and $^{40}Ar/^{39}Ar$ ages from the same area mostly lie in the range 18-25 Ma (Treloar et al. 1989a; Zeitler et al. 1989). These ages confirm that the Kohistan granites and their country rocks passed together through the argon closure temperature in biotite and muscovite.

5.8.3. Discordance between biotite $^{40}Ar/^{39}Ar$ and Rb-Sr ages

As shown in Fig. 5.5, the biotite Rb-Sr ages obtained from both leucogranites and metamorphic rocks in the NPHM are consistently younger than the biotite $^{40}Ar/^{39}Ar$ ages for the same samples. This result is surprising, given the apparently similar diffusivities of argon and strontium in biotite, and the fact that previous workers have generally recorded concordant biotite Rb-Sr and $^{40}Ar/^{39}Ar$ ages for the same samples (Armstrong et al. 1966; Hurford 1986; Blanckenburg et al. 1989). The consistency of the observed difference between biotite Rb-Sr and $^{40}Ar/^{39}Ar$ ages makes it unlikely that the differences are due to the effects of excess argon. Relevant factors which may be important in accounting for the variable behaviour of the two isotopic systems are the exceptionally high uplift rates in the NPHM, and the relatively coarse grain size of the samples. Two possible explanations are suggested :

(i) Imprecise correction for initial strontium in the calculation of Rb-Sr mica ages, as discussed by Cliff et al. (1985). However, it is unlikely that this would have produced such a marked discordance between biotite Rb-Sr and $^{40}Ar/^{39}Ar$ ages. Furthermore, use of a whole-rock isotopic composition would be expected to overestimate a mica age if significant volume diffusion had occurred after mica closure, since such diffusion would have the effect of increasing the strontium isotopic composition of the biotite relative to the whole-rock.

(ii) Kwan et al. (1992) found that a rapidly-cooled granite intrusion in west Malaysia had younger biotite Rb-Sr ages than biotite $^{40}Ar/^{39}Ar$ ages, which was thought to reflect preferential leaching of ^{87}Sr from the biotite during a brief period of fluid circulation. This was supported by the experimental work of Krahenbuhl (1984), which showed that during isotopic requilibration with a fluid, Rb-Sr ages of biotite samples were more reduced for coarse fractions than the corresponding K-Ar ages, whereas for fine fractions, K-Ar ages were more reduced than the Rb-Sr ages. This was ascribed to the rapid loss of ^{87}Sr from the crystallographic lattice during initial grain size reduction, compared to the more gradual loss of ^{40}Ar. Thus the results from the NPHM may reflect the involvement of fluid interaction, combined with the relatively coarse grain size of the dated samples. Interestingly, Zeitler and Williams (1988) originally interpreted 2-10 Ma zircon overgrowths observed in metamorphic samples from the Indus gorge as indicating a period of post-metamorphic fluid flow within the NPHM, at temperatures of ~ 500-200 °C.

In summary, the cause of the discordant biotite ages in not fully understood, but the role of fluid movement in the NPHM during uplift may be an important contributing factor.

5.8.4. Heat Flow and Exhumation Rates

Continental surface heat flow is thought to be generated by a combination of radiogenic heat production in the upper crust and a background heat flux ('reduced heat flow') from the lower lithosphere and mantle (Sclater et al. 1980). Young orogens tend to have a relatively high internal heat production due to the enrichment of radiogenic elements in the upper layers, but the distribution of heat sources with depth is difficult to constrain, and is dependant on factors such as metamorphic grade and erosion. According to Vitorello and Pollack (1980), continental heat flow is augmented by residual heat associated with the last deep-seated orogenesis, a component which will be particularly important in Cenozoic orogens. The effects of such a thermal perturbation are difficult to model, but they may be prolonged by extending the disturbed zone to greater depths or reducing the heat lost downwards towards the lower crust. England and Richardson (1980) stressed the

importance of rapid erosion in removing heat-producing elements, whilst at the same time introducing a strong transient heat flow by bringing relatively warm rocks towards the surface. Geothermal gradients and PTt paths followed by rocks in continental collision zones are also dependant on factors such as the style and timing of both the crustal thickening and of the subsequent thinning (England and Thompson 1986).

From the above discussion, it is apparent that there is a large number of variables that can influence the thermal structure of a young orogen, and this probably acounts for the variability of the measured heat flow data from such regions (Sclater et al. 1980). The majority of models concerning the thermal evolution of orogenic belts assume instantaneous doubling of crustal thickness by thrusting, or homogenous thickening of the whole lithosphere, accompanied by metamorphism, and followed by a long (~ 100 Ma) history of erosion or extension (England and Thompson 1986; Day 1987; DeYoreo et al. 1989). Such models assume constant thermal conductivity and do not take into account horizontal temperature gradients. Clearly, these simplifying assumptions are not applicable to the Nanga Parbat-Haramosh structure, which is effectively a crustal-scale fold that has been generated exceedingly rapidly by homogenous shortening, and at a relatively late stage in the evolution of the Himalayan collision zone. The thermal state of the Indian continental crust before fold generation took place is somewhat unconstrained but is likely to have been complex. For example, the crust was probably already thicker than average, and probably contained a relatively high content of radiogenic elements, since the radiogenic heat production calculated for pelitic and psammitic gneisses from the NPHM lies in the range 1.8-8.2 $\mu W/m^{-3}$ (average of sixteen samples = 3.73 $\mu W/m^{-3}$). In contrast, a deformed amphibolite present in the Sassi shear-zone (probably originally part of the Kohistan terrane) has a heat production of 0.6 $\mu W/m^{-3}$.

Cooling recorded by rocks presently exposed in the NPHM region may reflect thermal relaxation either following metamorphism or magmatism, or cooling related to exhumation. The cooling ages from the leucogranite dyke sampled in the Indus gorge (S92), together with the muscovite Rb-Sr date for the Parri granite (G14), are probably

magmatically-related cooling ages. All of the other ages presented in this study are interpreted as being related to cooling due to the upwards movement of rock relative to the surface (exhumation). Support for this assumption comes from the presence of high-grade metamorphic rocks currently exposed at the surface that are thought to have been metamorphosed at an average pressure of 7-10 kbar during the Himalayan orogeny (see Chapter 4). Cooling rates deduced from such cooling ages can be used to calculate exhumation rates although assumptions must be made concerning the size and stability of the geothermal gradient that existed during unroofing. It should be noted, however, that such exhumation rates are not necessarily equivalent to rates of either rock uplift or surface uplift (England and Molnar 1990). Hubbard et al. (1991) have emphasised the difficulty in constraining uplift histories on the basis of cooling rates, even when supplementary thermobarometric data are available.

Palaeogeotherms are difficult to estimate for the NPHM region, since there are no heatflow or thermal conductivity data currently available. The presence of hot springs along the western margin of the NPHM (Butler and Prior 1988b) suggests that the present thermal structure of the NPHM is complex and probably out of equilibrium. Numerical experiments on the thermal structure of metamorphic terrains confirm that geothermal gradients during orogenesis are complex, and probably never reach equilibrium for any appreciable length of time (Hodges 1991; Royden 1993). For example, rapid uplift may cause a transient steepening of near-surface geothermal gradients through updoming of isotherms, since the uplift rate will exceed the rate of cooling by thermal equilibration (Vitorello and Pollack 1980; England and Richardson 1980). The result is a delay in the rate of initial cooling, which then increases with time (Zeitler 1983). According to Royden (1993), high heat production coupled with rapid erosion may also lead to anomalously steep geothermal gradients; clearly this is likely to be the case in the NPHM.

In this study, a constant geotherm of 30 °C/km has generally been used to calculate the approximate exhumation rates given in Table 5.3. However, following Zeitler (1985), a geotherm of 40 °C/km has been used for the fission-track data from the Indus gorge, whilst a

geotherm of 50 °C/km has been used for the Fairy Meadows area, in order to take into account the increased near-surface geotherm due to rapid uplift. The quoted uncertainties in calculated exhumation rates were calculated by propagating uncertainties in closure temperatures and mineral ages, but not uncertainties in the geothermal gradient, and subsequently the actual uncertainties in calculated exhumation rates are larger.

As would be expected for a tectonically active region, calculated exhumation rates for the NPHM are extremely variable, and lie in the range 1-10 mm/yr (km/Ma). In contrast, exhumation rates for Kohistan are < 1 mm/yr. On the basis of young fission-track apatite ages from the Indus gorge, Zeitler (1985) concluded that cooling and exhumation rates within the NPHM have accelerated dramatically over the last 2 Ma (see Fig. 5.6C). The mica ages presented in this study document an earlier portion of the cooling path than that defined by the fission-track ages. Relatively low time-integrated cooling rates (55-67 °C/Ma) have been calculated from mica ages for both Jutial and Kutwal (Table 5.3), compared with those obtained from fission track ages, since the Jutial and Kutwal cooling rates are not constrained by fission-track ages. In general, the results from the Indus, Jutial and Kutwal areas suggest a slightly decreasing cooling and exhumation rate in the interval 10-8 Ma, and a rapid acceleration of this rate in the last 2 Ma, as shown in Figs. 5.6A, B & C.

Theoretically, pressure estimates of metamorphism may help to constrain the exhumation rates in the NPHM region. Metamorphic assemblages exposed in the northern part of the NPHM record 'peak' metamorphic pressures of 9 ± 1 kbar, corresponding to a crustal thickness of 29-40 km, but unfortunately the timing of metamorphism in this part of the NPHM is poorly constrained. If the metamorphism recorded by these assemblages took place at 30 Ma (see Chapter 4), then a time-integrated exhumation rate of 1.0-1.3 mm/yr can be inferred, whilst if metamorphism occurred at 10 Ma (see Smith et al. 1992), the calculated rate is 2.9-4.0 mm/yr. Such estimates are only of limited use, since they are an indication of time-integrated exhumation rate over tens of millions of years, whereas T-t paths give an indication of the variations in exhumation rate over a much smaller timescale.

The Fairy Meadows area appears to be a thermally anomalous part of the NPHM that has experienced a relatively rapid but decreasing rate of cooling over the last 3 Ma, as shown in Fig. 5.6C. Interpretation of the Fairy Meadows-Rupal data in terms of exhumation is subject to additional uncertainty, since, firstly, the dated samples come from widely separated localities, and secondly, the remarkably rapid exhumation of the region over the last 3 Ma will have probably resulted in a high (but unconstrained) geothermal gradient (England and Richardson 1980; Royden 1993). The metamorphic assemblages at Fairy Meadows record pressures of about 5 ± 2 kbar (see Chapter 4), which suggests that 11-25 km of crust have been exhumed over the last 3.3 Ma (Zeitler et al. 1993), which corresponds to a time-integrated exhumation rate of 3.3-7.6 mm/yr. This exhumation rate agrees broadly with the results inferred from the cooling ages presented in this Chapter (Table 5.3).

The extreme topography of the NPHM indicates that uplift in the region is (or has recently been) taking place at a greater rate than denudation, since at some time the rate of surface uplift of the NPHM has been greater than the rate of surface uplift in Kohistan. This inference is supported by the fact that major landslides have taken place in the Indus gorge in historical times (Butler et al. 1988). Furthermore, the observation that an abrupt change in topography approximately coincides with the geological margin of the NPHM suggests that tectonic uplift is more important than isostatic uplift. The high exhumation rates calculated for the region (Table 5.3) make it unlikely that a 30°C/km geotherm is geologically reasonable. In reality, the transient geothermal gradient within the NPHM would have been increasing with time during the period of rapid uplift and may well have averaged 50 °C/km or more, as suggested by Zeitler (1985), in which case the apparent exhumation rates are overestimates. In any case, the exhumation rates given in Table 5.3 are apparently a reflection of rapid tectonic uplift, although they only provide a maximum constraint on the rate of exhumation.

It will only be possible to calculate exhumation rates within the NPHM with more certainty when heat flow data are available from the region.

5.9. Conclusions

(1) The mineral ages presented in this study confirm the relatively rapid and recent exhumation of the NPHM compared with the adjacent Kohistan arc, as observed by previous workers (Zeitler 1985).

(2) The majority of leucogranites in the NPHM, together with the majority of Confluence and Parri granites in Kohistan, were intruded at depth into relatively warm (> 350 °C) country rocks, probably shortly following regional metamorphism. Mica ages from such granites are thus cooling ages that are thought to reflect exhumation-related cooling. However, cooling ages derived from granites in both terranes may locally reflect rapid, magmatic-related cooling following granite emplacement.

(3) The geochronological data from the Jutial and Kutwal areas document similar cooling histories for these areas to those experienced by rocks present in the Indus gorge. In general, the variable slope of the cooling curves suggests a complex, varying exhumation history for the northern NPHM. Within both the Jutial and Kutwal areas, cooling paths are rather poorly defined, even for closely-spaced samples. This poor definition is related to the following factors :

(i) The poorly constrained closure temperatures for strontium and argon in both muscovite and biotite.

(ii) The relatively poor precision of muscovite Rb-Sr ages.

(iii) The poorly-understood discordancy between biotite Rb-Sr and $^{40}Ar/^{39}Ar$ ages.

(iv) The similarity between biotite and muscovite $^{40}Ar/^{39}Ar$ ages due to rapid rates of cooling.

(v) The absence of geochronological data from other phases other than muscovite and biotite.

(4) Strongly deformed shear-zone samples (D2, D19, G31 and S22) yield highly variable Rb-Sr mica ages that probably reflect closure temperature variation, polymetamorphism, or relatively late structural juxtaposition (without isotopic homogenistion). Although locally there appears to have been isotopically open-system behaviour (G31), the fact that the majority of mineral separates yield 'Himalayan' ages indicates that open-system behaviour is unlikely to have been a widespread phenomenon.

(5) The discordance between different mineral ages from relatively small areas, such as the Indus gorge ($^{40}Ar/^{39}Ar$ hornblende versus U-Pb monazite), the Astor gorge (Rb-Sr muscovite versus U-Pb monazite) and the Sassi-Darchan shear zone (Rb-Sr mica), observed in both this work and in previous studies (Smith et al. 1992), suggests that the dating of more samples from the NPHM region is urgently required, together with information on heat flow and thermal conductivities from the region.

(6) The rapid exhumation rates calculated for the NPHM, coupled with the unusually high radiogenic heat production calculated for the basement lithologies, suggest that geothermal gradients during the last 10 Ma have been anomalously steep. Rapid exhumation of sufficiently fertile lithologies would thus allow crustal melting and generation of the NPHM leucogranites (see Chapter 6).

Chapter 6

Geochemistry of Post-Metamorphic Granite Intrusions in the Kohistan - Nanga Parbat-Haramosh Massif region

6.1. Introduction

Granitoid bodies of varying size, structural state and mineralogy have a widespread distribution across the Kohistan - Nanga Parbat-Haramosh Massif region. For example, the presence of large orthogneiss bodies within the NPHM has long been recognised (Wadia 1932; Misch 1949), whilst approximately 40 % of the Kohistan batholith exposed in the Gilgit area is composed of large, either undeformed or deformed plutons of granite, granodiorite or tonalite composition (Petterson 1984). However, the majority of the granites that are the subject of this chapter are relatively minor, sheet or dyke-like intrusions, typically only a few metres thick. These granite bodies cross-cut the regional metamorphic fabrics, although, as described in Chapter 2, they may locally be considerably deformed by late-stage shearing. Such post-metamorphic granites have been studied since they should yield important information on the magmatic and thermal state of the crust following crustal thickening, during on-going continental collision. Consequently the granites may be used as a further constraint on the tectonic evolution of the region.

This chapter describes the major and trace element geochemistry of the granites and discusses their petrogenesis. Inevitably, isotopic systematics contribute to the models discussed, but the isotopic constraints are discussed more fully in Chapter 7.

The granites are divided spatially and mineralogically into the Confluence and Parri granites that intrude the Kohistan arc, and the leucogranite bodies that intrude the Indian continental basement of the NPHM. The Confluence and Parri granites in the Indus

confluence area have also been studied by Petterson (1984), who termed the granites the Indus Confluence acid sheets and the Parri acid sheets, respectively. A further granite sheet in the same area was termed the Sainallah body, which in this work has been grouped as a Confluence granite. Petterson's (1984) study was based on the geochemical analysis of 22 samples of Confluence granite collected from six separate localities, and on the geochemical analysis of eight samples from a single intrusion of Parri granite exposed near Parri (the type locality).

There have been no previous petrological or analytical studies of the leucogranite dykes and bodies of the NPHM.

The principle field relations and petrography of all of the granites, together with their sampling localities, have already been described in Chapter 2, but the pertinent features are summarised below.

6.1.1. Summary of Field Relations and Petrography

6.1.1.1. Confluence and Parri granites

These granites are well-exposed in the Indus confluence area, where they are present as swarms of sheets that make up to 30 % of mountainside exposure (see Plate 2.3). Confluence granites occur both as 1-2 metre-thick sheets (occasionally thicker), and plugs up to 200 metres across. The Parri granites occur solely as sheets, and are less abundant than the Confluence granites, although both the Confluence and Parri granites outcrop over a similar geographical area. Locally, Parri granite sheets are observed to cross-cut and/or contain inclusions of Confluence granite. In the Indus confluence area, the Confluence and Parri granites display fresh, undeformed igneous fabrics. The granites are demonstrably post-metamorphic and cross-cutting, and furthermore the country rocks to the granites are not at a sufficient metamorphic grade to be the source rocks (see Chapter 4). Evidently the granite magmas were sufficiently mobile to have been able to leave their source regions.

The Confluence bodies are characterised by biotite with a typical modal proportion of 6-15 %, together with subsidiary epidote and muscovite. The Parri granites are relatively leucocratic, and are characterised by muscovite, often accompanied by biotite and/or garnet. Both granite types may exhibit marked magmatic layering, and coarse pegmatitic layers are commonly observed.

The Confluence and Parri granites may be traced eastwards along the Indus gorge into the 2-3 km wide shear zone at Sassi, as was also noted by Butler and Prior (1988a). Within the shear zone, the granites are highly sheared and attenuated, and lie parallel to the dominant mylonitic foliation. Locally, however, granite sheets are observed to cross-cut the shear zone fabrics present in imbricates of Indian-continent derived calcschists and pelites. Across the shear zone, the proportion of granite to wall-rock rapidly decreases as the NPHM is approached, and no Confluence or Parri granites have been found within the NPHM.

It should be noted that Confluence and Parri granites may not always be readily separated on the basis of mineralogy. For example, within the shear zone, some of the deformed granite sheets are characterised by biotite with minor garnet, or muscovite and biotite in equal proportions, and such granites may, on the basis of mineralogical evidence alone, fall into either category.

6.1.1.2. NPHM Leucogranites

1-2 metre-thick leucogranite dykes have a widespread distribution across the NPHM. The dykes are often coarse-grained, rather heterogeneous bodies, and have a variable intrusive style. The leucogranites are mineralogically variable, although they are typically characterised by the presence of muscovite and tourmaline, with subsidiary biotite. Dykes and veins of tourmaline leucogranite and pegmatite are also present in the shear zone at Sassi, where they are commonly observed to cross-cut shear zone fabrics, although locally they have been affected by late-stage shearing.

The Jutial granite is a sheet complex at least 2.5 km wide, composed of cross-cutting two-mica granite. Tourmaline within the Jutial granite is rare, but the granite is locally cross-cut by younger tourmaline-muscovite leucogranite dykes. An undeformed, ten-metre thick body of quartz diorite has also been found within the NPHM at Iskere. This is a coarse-grained intrusion characterised by the presence of plagioclase and biotite, with subordinate amounts of quartz and k-feldspar.

6.1.2. Aims

The aim of this chapter is to describe the geochemical characteristics of the youngest stages of granite magmatism in both the Kohistan arc and the NPHM, and to resolve the factors that influence the compositional variation observed in in each granite suite. The three specific aims are as follows :

(i) To categorise the contrasting granite suites found in the region. These suites have already been broadly identified on the basis on petrography (Chapter 2).

(ii) To evaluate the causes of the geochemical variation exhibited by the granites in the region, and in particular those granites that have been deformed in the shear zone bordering the western margin of the NPHM.

(iii) To deduce the potential source regions and petrogenesis of each granite type. In the case of the NPHM, where potential source rocks of the leucogranites are exposed at the surface, the metamorphic rocks will be geochemically characterised in order to constrain possible melt processes during magmagenesis.

This chapter presents major and trace element data for the Confluence and Parri granites, the leucogranites of the NPHM, and a range of metamorphic lithologies from the NPHM. All of the samples have been analysed by wavelength dispersive X-ray fluorescence

(XRF), whilst a subset of representative samples has been analysed for Rare Earth Elements (REE) and Th, Ta, Hf, U, Co and Sc by instrumental neutron activation analysis (INAA). Analytical techniques are described in Appendix 1, whilst major and trace element data are listed in Appendix 3.

6.1.3. Sample Description

6.1.3.1. Confluence granites

A total of 29 samples of Confluence granite have been analysed, which come from 18 different intrusions. Eighteen of these samples are from undeformed granites exposed in the Gilgit valley and Indus confluence area (see Fig. 2.5). These undeformed granites are equivalent to the Indus Confluence acid sheets and Sainallah body studied by Petterson (1984). The other eleven samples were collected from the shear zone bordering the western margin of the NPHM, between the villages of Shahbatot and Darchan, and come from intensely-deformed granite sheets that have varying orientations with respect to the shear zone fabrics.

Three Confluence granites were examined in order to deduce the amount of intra-sheet geochemical variation (Table 6.1). Samples G16 and G18 come from lithologically-distinct layers of a three-metre thick, undeformed Confluence granite exposed near the Indus confluence. The layers are relatively homogenous, are characterised by varying proportions of biotite, and show sharp magmatic contacts (see Plate 2.6). Samples S6G and S6I were collected from a ten-metre thick, relatively homogenous, undeformed granite sheet, also exposed in the Indus Confluence area. Samples S75 and S76 come from separate, two-metre thick, highly sheared boudins of a granite sheet at Sassi. The two boudins are part of a train, and occur at a spacing of about 20 metres (see Fig. 2.7B).

	Undeformed Conf.		Undeformed Conf.		Deformed Conf.		Deformed Parri	
	G16 B-Ep-(M)	G18 B-Ep-(M)	S6G B-M-(Ep)	S6I B-M-(Ep)	S75 B-M-Ep	S76 B-M-Ep	G35 M-G-(B)	G36 M-G-(B)
SiO_2	75.41	69.07	72.21	72.45	73.13	71.34	71.94	74.77
TiO_2	0.071	0.377	0.274	0.276	0.044	0.139	0.048	0.019
Al_2O_3	14.13	16.94	14.88	14.85	15.58	16.56	16.55	15.34
Fe_2O_3(1)	0.42	2.57	1.83	1.81	0.31	1.18	0.32	0.31
MnO	0.007	0.046	0.029	0.028	0.009	0.023	0.013	0.120
MgO	0.10	0.76	0.58	0.55	0.10	0.46	0.14	0.04
CaO	1.46	3.80	2.14	2.09	3.32	3.60	1.70	1.99
Na_2O	3.63	5.20	4.17	4.12	5.51	5.61	4.15	4.73
K_2O	4.96	1.22	3.65	3.62	0.44	0.76	4.79	3.20
P_2O_5	0.014	0.116	0.095	0.094	0.006	0.052	0.014	0.011
LOI	0.31	0.33	0.32	0.26	0.34	0.47	0.96	0.28
Total	**100.5**	**100.4**	**100.2**	**100.2**	**98.8**	**100.2**	**100.6**	**100.8**
Rb	87	47	85	83	8	19	198	122
Sr	320	551	385	392	676	670	194	165
Y	1	5	4	3	1	4	9	14
Zr	41	108	155	152	3	50	20	48
Nb	2	7	4	5	1	2	24	3
Ba	485	188	908	946	131	260	588	250
Pb	33	15	20	18	14	14	82	55
Th	3	5	9	9	0	2	1	1
U	1	1	1	1	1	1	4	1
Sc	2	4	4	1	3	2	5	2
V	8	39	25	27	5	15	14	0
Cr	6	12	11	16	6	6	8	14
Co	0	3	1	1	0	0	0	0
Ni	4	3	4	4	4	6	4	2
Cu	14	21	38	25	17	13	2	2
Zn	11	57	49	46	10	16	5	6
Ga	13	20	17	16	13	14	25	16

Table 6.1. Intra-sheet variation for the Kohistan granite sheets. (1) = all Fe calculated as Fe_2O_3. B = biotite; Ep = epidote; M = muscovite; G = garnet. Parentheses indicate a subsidiary phase. The two undeformed Confluence granites are from the Indus confluence area; the two deformed granite sheets are from the shear zone at Sassi. Samples were collected 1-2 metres apart, except in the case of samples S75 and S76, which were collected from separate boudin of the same deformed sheet.

6.1.3.2. Parri granites

A total of thirteen samples of Parri granite have been analysed, which come from twelve different sheets. Five of these samples are from entirely undeformed granite sheets exposed in the Gilgit valley and Indus confluence area (see Fig. 2.5), and are therefore equivalent to the Parri granite studied by Petterson (1984). The other eight samples are deformed granites collected from the shear zone at Sassi. Samples G35 and G36 (Table 6.1) were collected from the central portion of the same deformed granite sheet, at a one-metre spacing (Plate 2.6).

Confluence and the Parri granites that have pegmatitic layers and veins have been avoided in this geochemical study, since they do not represent magmatic compositions.

6.1.3.3. NPHM Leucogranites and Metamorphic Basement

A total of 25 samples have been analysed from 21 different leucogranite dykes intruding the NPHM. The sampled dykes are from widely-separated localities, from the Indus, Jutial and Iskere valleys in the northern part of the NPHM, and from the Fairy Meadows, Tato, Liachar and Rupal areas in the southern part of the NPHM. Two leucogranite bodies were examined in order to evaluate the amount of intra-sheet geochemical variation (Table 6.2). Three samples were collected from a ten-metre thick, cross-cutting leucogranite sheet at Rupal (A9, 10 and 14), whilst a further three samples were collected from a highly sheared, two-metre thick leucogranite sheet in the Liachar shear zone (L17E, F and G).

A further twelve samples come from the Jutial granite, and were collected from within 2 km of each other. A single sample has been analysed from the quartz diorite intrusion at Iskere.

A total of 22 samples of varying metamorphic lithology have been collected and analysed from the NPHM basement. These include both metasedimentary and metaigneous rock types, and come from similar areas as the leucogranites mentioned above.

6.2. Major Element Geochemistry

6.2.1. Confluence granites

The Confluence granites are characterised by SiO_2 contents in the range 66-75 oxide wt. %. The Confluence granites are either metaluminous or weakly peraluminous, with values of (A/CNK) in the range 0.96-1.14, as shown in Fig. 6.1. (A/CNK) is a measure of aluminium saturation defined by the molar ratio of Al_2O_3 to the sum of ($CaO+Na_2O+K_2O$) (Shand 1949). On a Streckeisen diagram (Streckeisen 1976), both the undeformed and

	Undeformed leucogranite Rupal			Deformed leucogranite Liachar shear zone		
Mineralogy	A9 M-T	A10 M-T	A14 M-T	L17E T-(B)	L17F T-(B)	L17G T-(B)
SiO_2	75.25	74.22	74.28	74.74	74.60	73.80
TiO_2	0.052	0.057	0.053	0.023	0.021	0.024
Al_2O_3	14.83	14.85	14.78	14.76	15.23	15.34
Fe_2O_3 (1)	0.89	1.58	1.00	0.22	0.20	0.23
MnO	0.019	0.026	0.022	0.028	0.047	0.021
MgO	0.05	0.13	0.12	0.03	0.02	0.04
CaO	0.94	0.95	1.00	0.89	0.95	0.79
Na_2O	4.42	4.17	4.14	5.26	5.90	4.98
K_2O	2.25	2.39	3.56	3.89	3.22	4.93
P_2O_5	0.068	0.129	0.126	0.012	0.013	0.011
LOI	0.73	0.91	0.50	0.37	0.39	0.21
Total	99.5	99.4	99.6	100.2	100.6	100.4
Rb	252	224	290	388	318	419
Sr	11	12	25	15	15	21
Y	42	55.8	22	78	60	48
Zr	42	65	28	40	31	26
Nb	22	12	6	18	16	34
Ba	0	9	0	7	4	6
Pb	28	34	43	68	56	66
Th	16	18	5	11	9	11
U	25	40	18	12	9	10
Sc	4	3	2	1	1	2
V	5	2	3	3	3	4
Cr	10	13	9	8	5	7
Co	0	1	0	0	0	0
Ni	5	6	4	9	5	5
Cu	0	0	0	2	2	0
Zn	28	52	30	11	9	8
Ga	32	28	21	25	26	26

Table 6.2. Intra-sheet geochemical variation for two leucogranite bodies intruding the NPHM. (1) = all Fe calculated as Fe_2O_3. M = muscovite; T = tourmaline; (B) = subsidiary biotite. Samples A9, A10 & A14 were collected from a 10-metre thick sheet from the Rupal valley, whilst samples L17E, F & G were collected from a 2-metre thick sheet, deformed within the Liachar shear zone.

deformed Confluence granites define a range of compositions from granites (*sensu stricto*) and granodiorites to tonalites (Fig. 6.2A). It should be noted that, in this study, the normative proportions of the quartzo-feldspathic phases (volume %) have been used for the Streckeisen classification (rather than modal proportions), since point-counting is considered to be inaccurate given the coarse grain size of many of the granites.

Conventional CIPW norms are inappropriate for granites, since all K_2O is recalculated as k-feldspar, with excess Al_2O_3 recalculated as corundum. Since no account is taken of the K_2O present in mica, the normative proportion of k-feldspar present in granitic rocks may be overestimated. This overestimation is especially marked for relatively mica-

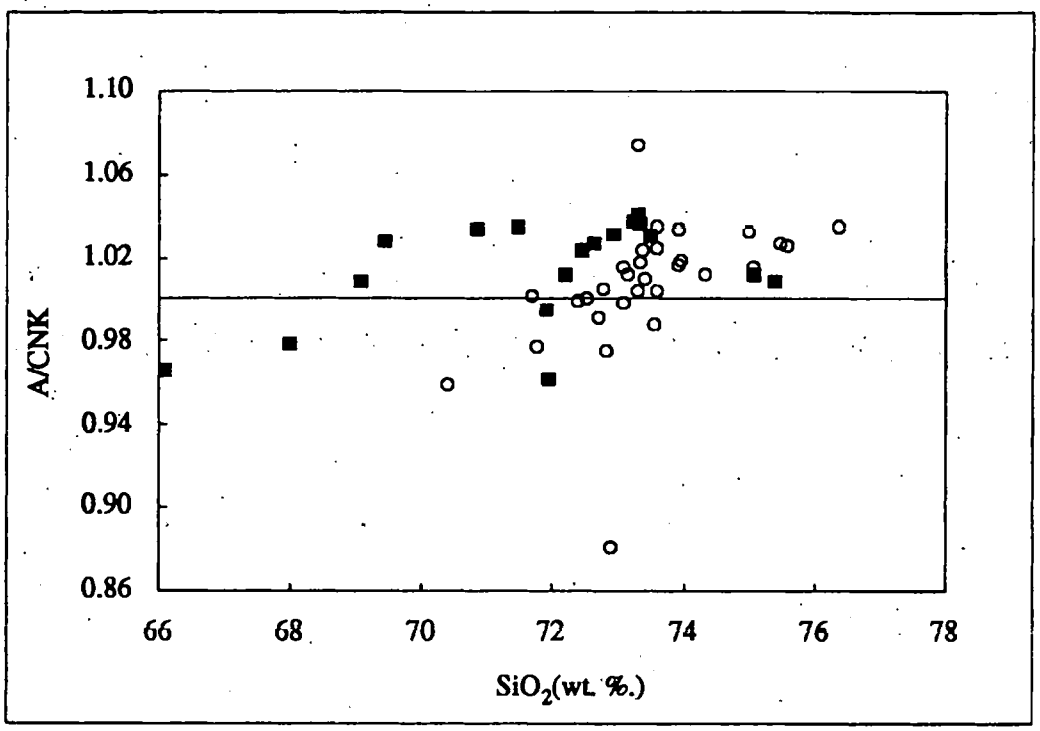

Fig. 6.1. Variation in aluminosity (A/CNK; molecular proportions) against silica for the undeformed Confluence granites. ■ = this chapter; ○ = data from Petterson (1984).

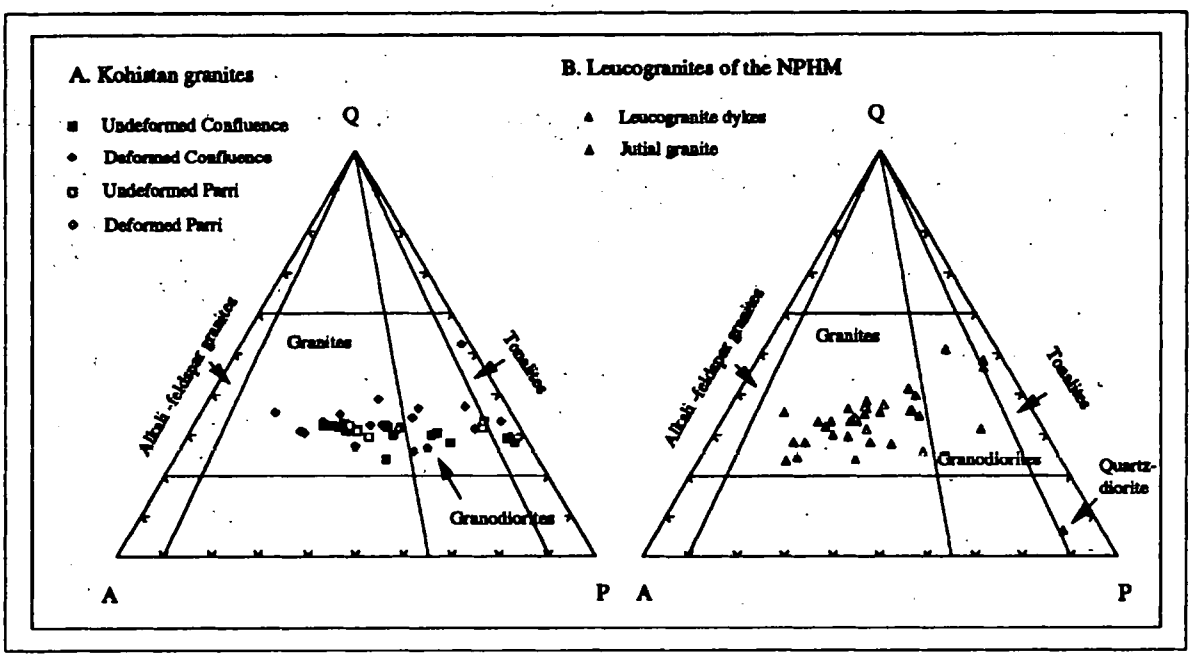

Fig. 6.2. Streckeisen classification of the studied granites, based on the *Grannorm* normative mineral content (in vol. %). Q = quartz; A = alkali feldspar; P = plagioclase. Q + A + P = 100.

rich granites, such as the Confluence sheets described in this chapter. Consequently, normative compositions used in this work were calculated using the program *'Grannorm'* (Harris and Marriner 1980), which is based on the assignment of potassium to both mica and k-feldspar depending on Al availability. However, it is uncertain how representative any normative calculations are of original liquid compositions, since such calculations do not take into account the presence of inherited restitic crystals, entrained peritectic phases from the melt reaction, or xenocrysts incorporated from wall rocks.

A comparison between the normative compositions of the granites studied in this work and the approximate, experimentally-determined compositions of minimum melts at varying pressure, anorthite content and water activity, may potentially yield information on the physical and chemical conditions of melting. The four-component system SiO_2-$NaAlSi_3O_8$-$KAlSi_3O_8$-H_2O (Fig. 6.3) is the haplogranite system originally studied by Tuttle and Bowen (1958). In this system, the quartz and k-feldspar liquidus fields are divided by a cotectic line which is characterised by a temperature minimum of 670 °C at a pressure of 2 kbar (note that the experimentally-determined compositions of the minimum melts shown in Fig. 6.3 are generally the compositions that exist at 15-20 °C higher than the true beginning of melting; Winkler 1967). The position of the cotectic line and the temperature minimum shift towards the albite apex with an increase in pressure, as shown in Fig. 6.3. At pressures greater than about 3.6 kbar, two different alkali feldspars may exist with the quartz, and therefore the temperature minimum is replaced by a eutectic. Consequently, the composition of the first melt (minimum melt) is dependant on the position of the eutectic rather than on the whole-rock composition. At the eutectic composition, albite, orthoclase, quartz, melt and water are all in equilibrium.

Von Platen (1965) showed that the An/Ab ratio of the source strongly controls the composition of the minimum melt. The phase $CaAl_2Si_2O_8$ may be considered as forming the apex of a tetrahedron, whose base is formed by the equilibrium quartz-albite-k-feldspar. This effect can be demonstrated by projecting the thermal minimum onto the isobaric quartz-albite-k-feldspar diagram at different An/Ab ratios, as shown on Fig. 6.3 at a pressure of 2

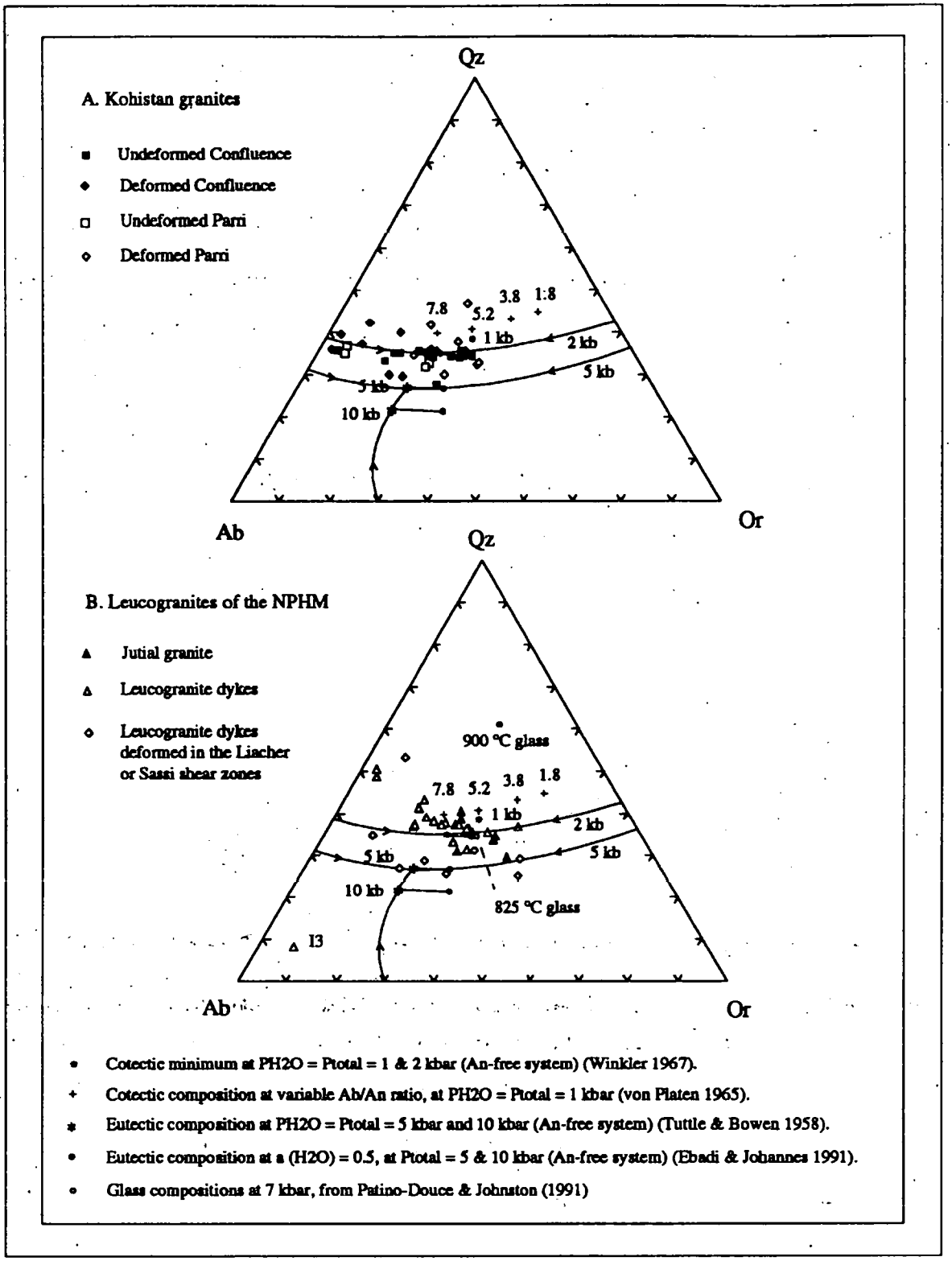

Fig. 6.3. Comparison between the normative granite compositions calculated for samples in this study, and experimentally determined phase relations in the quaternary system Quartz - Albite - Orthoclase - water. The glass composition at 825 °C corresponds to muscovite breakdown; the glass composition at 900 °C approximately corresponds to biotite breakdown (Patino-Douce & Johnston 1991).

kbar. An increase in the anorthite component causes a shift in the thermal minimum towards the quartz-k-feldspar tie-line, and consequently the melt becomes less albite-rich, although this effect must be extrapolated for higher pressures. The minimum melt temperatures are also decreased slightly by an increase in the Ab/An ratio, with the result that during anatexis, the pelitic horizons characterised by the most albitic plagioclase are most likely to be the first to melt (Winkler 1967).

By varying the H_2O-CO_2 ratio of the fluid, Ebadi and Johannes (1991) demonstrated that, at a given pressure, the k-feldspar/albite ratios of eutectic or minimum melt compositions increase with decreasing water activity (Fig. 6.3). If water-undersaturated melt crystallises at constant pressure, the water activity of the residual melt will increase (Burnham and Ohomoto 1980). However, according to the data from water-saturated melts, if the melt crystallises whilst the magma is ascending, the reduction in pressure will also effect the minimum melt composition, moving the composition from albite-rich to more quartz and k-feldspar-rich compositions (Tuttle and Bowen 1958). As noted by Johannes and Holtz (1990), the net effect of a pressure decrease combined with an increase in water activity is to decrease the k-feldspar content of the melt and increase the quartz content, whilst the albite content remains approximately constant. This is almost perpendicular to the evolutionary trend predicted for the effect of pressure decrease on water-saturated melts.

The presence of the halogens fluorine and chlorine may also affect minimum melt compositions by causing a shift away from the quartz apex, and also by lowering the solidus temperature (von Platen 1965; Manning 1981). Increasing the alumina content of the haplogranite system, under different water activities, causes minimum melt compositions to shift slightly towards the quartz apex, whilst the solidus temperature is also lowered (Holz et al. 1992).

Clearly, the large number of variables that may influence minimum melt compositions make any comparisons with real data hazardous. Furthermore, it should be noted that the majority of experimental studies have been based on the fluid-present

haplogranite system, in which the initial charges are simple mixtures of quartz and feldspar (with or without normative corundum) in varying proportions, whereas real granites are likely to result from the melting of a wide range of crustal lithologies, usually under fluid-absent conditions.

Several experimental studies involving the fluid-absent melting of pelites have yielded glasses that are characterised by variable compositions (Le Breton and Thompson 1988; Vielzeuf and Holloway 1988; Patino-Douce and Johnston 1991). Le Breton and Thompson (1988) conducted melting experiments on three different pelitic charges, and at 850 °C and 10 kbar, the glass microprobe compositions were found to lie in the ranges 2.2-4.7 wt % K_2O, 0.9-4.3 wt. % Na_2O, and 56-77 wt. % SiO_2, although some of this scatter was due to biotite contamination in the probe mounts. Patino-Douce and Johnston (1991) produced a glass at 7 kbar and 825 °C which was thought to represent fluid-absent muscovite breakdown of a pelite, whilst a glass produced at 900 °C was thought to approximately correspond to biotite breakdown. The normative compositions of the glasses are plotted on Fig. 6.3B. Clearly, the lower temperature glass plots close to the experimental granite minimum, which is an encouraging result, given the number of variables (described above) that can effect minimum melt compositions.

In the light of the uncertainties described above, the normative granite compositions of the natural crustal melts that have been calculated in this study can only be tentatively related to conditions of melting by reference to the experimental haplogranite system.

Normative granite compositions in this study have been plotted on the haplogranite system in Fig. 6.3. On Fig. 6.3A, the Confluence granite compositions are observed to lie in a belt that extends along the quartz-albite cotectic towards the orthoclase apex. The high silica compositions lie at the orthoclase-rich end of this trend and are equivalent to minimum melts at about 2 kbar and $aH_2O = 1.0$-0.5 (anorthite-free). The presence of magmatic epidote in these granites, however, suggests rather higher pressures than 2 kbar (Zen and Hammarstrom 1984). The minimum melt may therefore have been generated at a relatively

high pressure (e.g. 5 kbar), but in a source characterised by a relatively low Ab/An ratio (e.g. 2-4). Such an interpretation would be consistent with melting of amphibolitic source rocks in the Kohistan arc, since such rocks would be characterised by relatively high calcium contents. If an origin controlled entirely by melting processes is invoked, the low orthoclase, low-silica samples may be the result of a higher melt fraction from a quartz-plagioclase rich source, from which the orthoclase was exhausted (see section 6.7.2 for further discussion).

On Harker variation diagrams (Fig. 6.4), the Confluence granites display systematic major element variations that reflect control by magmatic processes. The oxides TiO_2, Al_2O_3, Fe_2O_3, MgO, MnO, CaO and Na_2O exhibit linear decreases in concentration with increasing silica content. K_2O displays an inverse relationship with increasing silica to that displayed by the above elements, suggesting that the trends are caused by a common process (see section 6.7). A single Confluence granite (S109) with the lowest silica content analysed for the suite (66 wt. %), displays relatively low concentrations of Al_2O_3, CaO, Na_2O and MnO, and a relatively high content of K_2O. However, this sample was collected from a locality about 20 km west of the Indus confluence, outside the main granite sheet swarm, and thus may not be comagmatic. This sample has therefore not been included in the undeformed Confluence granite field in Fig. 6.4.

As shown in Table 6.1, the two samples of undeformed Confluence granite (S6G and I) analysed from the same, relatively homogenous sheet, display virtually identical major element compositions. In contrast, the samples collected from adjacent magmatic layers of another undeformed sheet (G16 and G18), display strongly contrasting major element compositions with silica values from 69.0 to 75.4 wt. %, which are consistent with the magmatic trends described above.

The deformed granites present in the shear zone tend to exhibit greater major element variation than the undeformed granites, increasing the geochemical dispersion either side of the trends defined by the undeformed samples, an effect that is particularly marked for the alkalis. In general, deformed Confluence granites display relatively high Na_2O and low K_2O

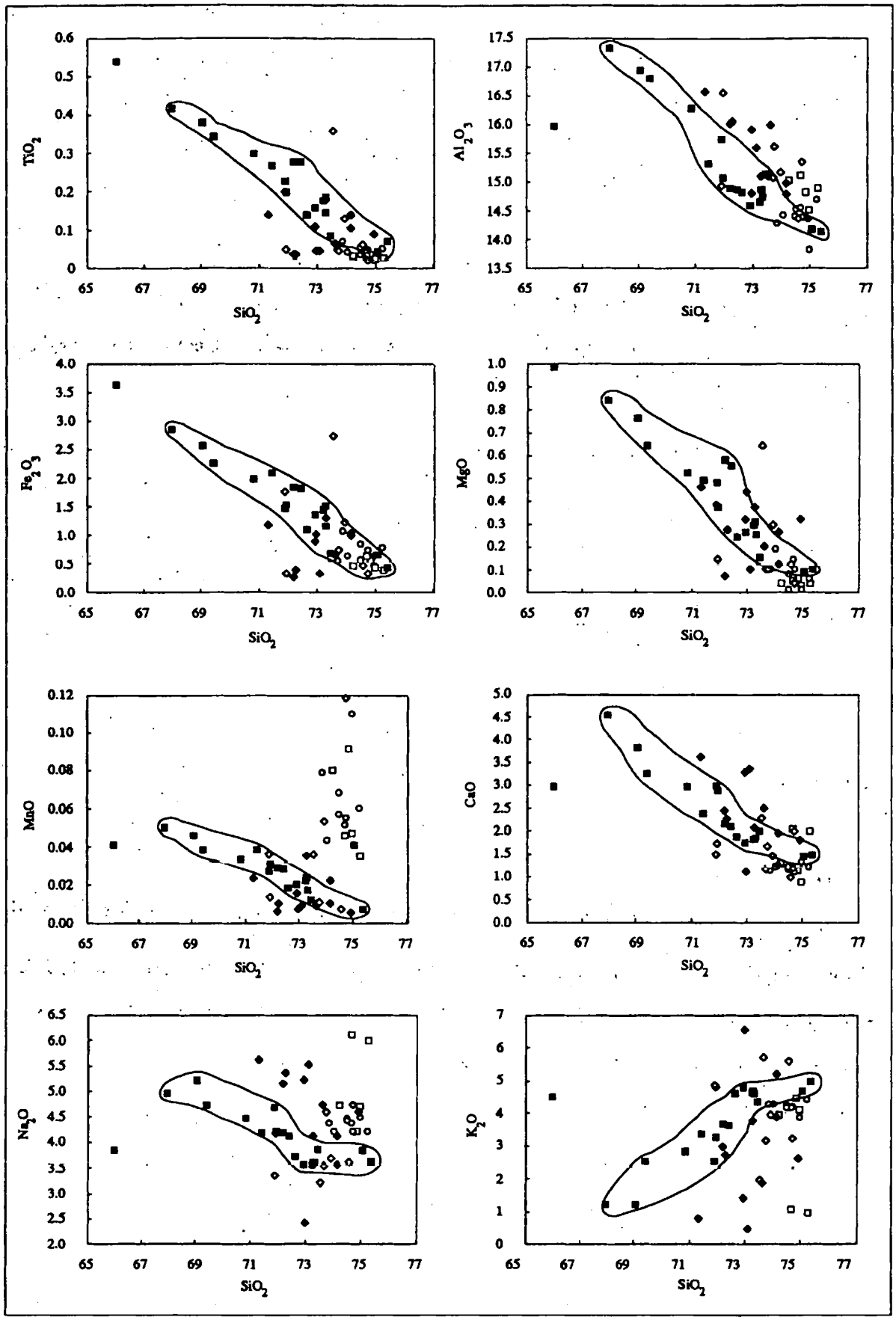

Fig. 6.4. Harker variation diagrams for the granite sheets of the Kohistan arc, northern Pakistan. All values are in wt %. ▪ = undeformed Confluence granites from the Gilgit valley-Indus confluence area; ◆ = deformed Confluence granites from the shear zone bordering the western margin of the NPHM between Shahbatot and Darchan; ▫ = undeformed Parri granites; ◇ = deformed Parri granites; ○ = data from Petterson (1984) for an undeformed Parri granite exposed at the type locality near Parri village. With the exception of sample S109 (SiO_2 = 66%), the fields for the undeformed Confluence granites are outlined.

compared with undeformed granites. Some deformed Confluence granites are also characterised by relatively low contents of Fe_2O_3 and TiO_2, and relatively high contents of CaO and Al_2O_3 compared with undeformed samples, at similar silica values.

The two samples from the boudinaged granite sheet in the shear zone (S75 and S76) are also characterised by contrasting major element compositions (Table 6.1). The variations observed for the majority of elements are consistent with the magmatic trends described above. However, both samples display a relatively high Na_2O content and a relatively low K_2O content at their respective silica contents. Furthermore, the differences in alkali contents between samples S75 and S76 do not appear to reflect magmatic processes, since the sample with the highest silica content is characterised by the lowest potassium content.

6.2.2. Parri granites

Compared with the Confluence granites, the Parri granites are relatively siliceous, and display only a minor variation in their silica content of 72-76 wt. %. An additional Parri granite (S66), displaying otherwise 'Parri-type' geochemical characteristics, possesses a relatively high silica content (78 wt. %). This sample may have been affected by silica mobility in sub-solidus fluids, and therefore may be unrepresentative of a true magmatic composition; consequently sample S66 will not be discussed further in this chapter. The Parri granites are weakly peraluminous, with values of (A/CNK) in the range 1.02-1.17, although one of the deformed sheets (G30) is characterised by (A/CNK) = 1.31.

On a Streckeisen diagram (Fig. 6.2A), the Parri granites mostly lie in the granite field. However, two undeformed samples with relatively low K_2O contents (G14 and G15) plot on the boundary between the granodiorite and tonalite fields, whilst one of the deformed samples (G30) plots within the tonalite field.

Plotted onto the haplogranite system (Fig. 6.2A), the majority of Parri granites lie around the 2 kbar cotectic minimum ($P_{H_2O} = P_{total}$). The relatively low potassium content

displayed by two of the undeformed Parri granites is once again illustrated (these samples are discussed further in section 6.7). The origin of the scatter for the Parri granites may be partly due to variable conditions of melting (e.g. water activity), variable source composition, or selective entrainment of restitic phases.

No magmatic trends can be detected on Harker major element plots (Fig 6.3), partly due to the small silica range. In general, TiO_2, Fe_2O_3 and MgO contents are lower than for the Confluence granites, reflecting a lower modal proportion of biotite in the Parri granites. The Parri granites are characterised by relatively high and variable MnO contents relative to the Confluence granites. The MnO content seems to be related to the variable modal proportion of spessartine garnet present, since the granites that possess relatively low MnO contents (< 0.02 wt. %) are those intrusions that do not contain modal garnet. Electron microprobe analysis has confirmed that the garnet present in the Parri granite is spessartine-rich and therefore of igneous origin (see Chapter 2). The Parri granites are also depleted in K_2O and enriched in Na_2O relative to the Confluence granites.

The deformed Parri granites exhibit a much greater variation in major element composition than the undeformed sheets. For the majority of elements, this variation does not appear to be systematic, although deformed granites frequently possess lower Na_2O contents than the undeformed samples. The two samples (G35 and G36) analysed from the same deformed Parri granite display variable major element compositions (Table 6.1), presumably due to alteration by sub-solidus processes.

6.2.3. NPHM Leucogranites

The NPHM leucogranites are peraluminous granites characterised by (A/CNK) in the range 1.04-1.13 (Jutial granite) and 1.00-1.33 (leucogranite dykes), whilst silica contents lie in the range 70-76 wt. %. The majority of leucogranite samples from the NPHM plot in the granite field in the Streckeisen diagram, although several samples plot in the granodiorite

field (Fig. 6.2B). The coarse-grained, biotite-rich intrusion at Iskere is classified as a quartz diorite.

In the experimental granite system (Fig. 6.3B), the leucogranites show considerable scatter, but are centred on the 1.5 kbar cotectic minimum for haplogranite (anorthite-free system). As expected, the Iskere quartz diorite (I3) is characterised by a relatively albite-rich composition. The majority of leucogranites display a systematic trend towards either increasing or decreasing orthoclase content at a relatively constant quartz/albite ratio. Much of the non-systematic scatter present in Fig. 6.3B is probably caused by sub-solidus alteration, since granite sheets that are sheared within the Liachar shear zone show extremely variable normative compositions. Some of the scatter is probably also due to compositional variation in the source region, or to non-representative sampling of coarse grained leucogranites.

In general, the major element compositions of the Jutial granite and the leucogranite dykes are similar. However, the Jutial granite samples are characterised by higher TiO_2 and Fe_2O_3 contents than the latter, a feature that reflects the relatively high biotite content of the Jutial granite. On the basis of major elements alone, the leucogranites of the NPHM are indistinguishable from the Parri granites described in section 6.2.2.

On Harker diagrams (Fig. 6.5), the leucogranite dykes display few distinct magmatic trends, due partly to the relatively narrow silica range, and the presence of several non-magmatic compositions with $SiO_2 > 75$ %. However, Al_2O_3 content is observed to decrease slightly with increasing silica. The Jutial granite displays a more consistent, although still somewhat scattered, major element variation. The elements TiO_2, Fe_2O_3, Al_2O_3, MgO and K_2O are observed to decrease with increasing silica, whilst Na_2O increases with increasing silica, except where $SiO_2 > 75$ %.

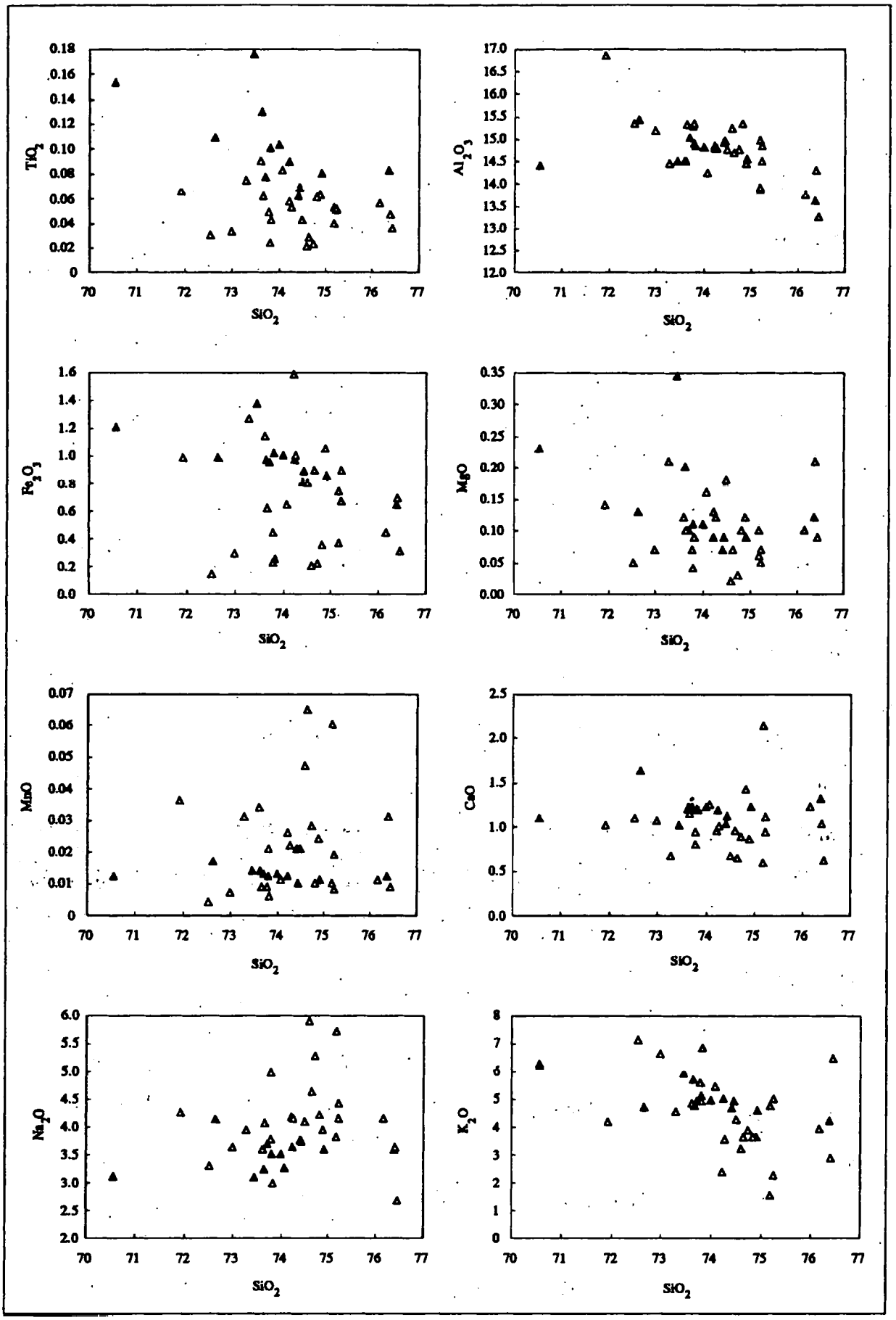

Fig. 6.5. Harker major element variation diagrams for the leucogranites of the Nanga Parbat-Haramosh Massif. All values are in oxide wt. %. ▲ = Jutial granite; △ = leucogranite dykes and sheets.

6.3. Trace Element Geochemistry

6.3.1. The Confluence granites

The Confluence granites display variable trace element compositions, and are characterised by Rb/Sr ratios in the range 0.01-0.4. The large ion lithophile elements (LILE) Rb, Sr and Ba lie in the ranges 8-130 ppm, 280-740 ppm and 100-2000 ppm respectively. Th contents are generally 1-10 ppm, whilst Nb and Y contents are < 12 ppm.

The undeformed granites yield relatively coherent and linear trends on Harker variation diagrams (Fig. 6.6). The LILE Rb and Ba behave incompatibly with increasing silica, the elements Sr, Y, Nb and Zr behave compatibly, whilst the elements Th and U do not exhibit any consistent trends. The sample characterised by the lowest silica content (S109), is characterised by relatively high Rb and Ba, and low Sr but, as already mentioned, may not be comagmatic.

The relatively homogenous, undeformed Confluence granite that has been analysed in order to evaluate the degree of intra-sheet geochemical variation, displays relatively homogenous trace element compositions (Table 6.1; samples S6G and S6I). In contrast, the samples collected from the adjacent magmatic layers of the other undeformed Confluence granite (G16 and G18) display contrasting trace element compositions. As was observed for the major elements, the two lithological types lie at opposite ends of the different magmatic trends.

The deformed Confluence granites exhibit significant dispersion in trace element contents compared with the undeformed sheets, and absolute abundances of many trace elements tend to be relatively low for deformed granite samples. For example, an examination of Fig. 6.6 shows that deformed Confluence granites display marked reductions in Rb, Th, and Zr, and to a lesser extent, in Nb, Y and Ba, for a given silica content. The average trace element contents of the undeformed and deformed Confluence granites may be

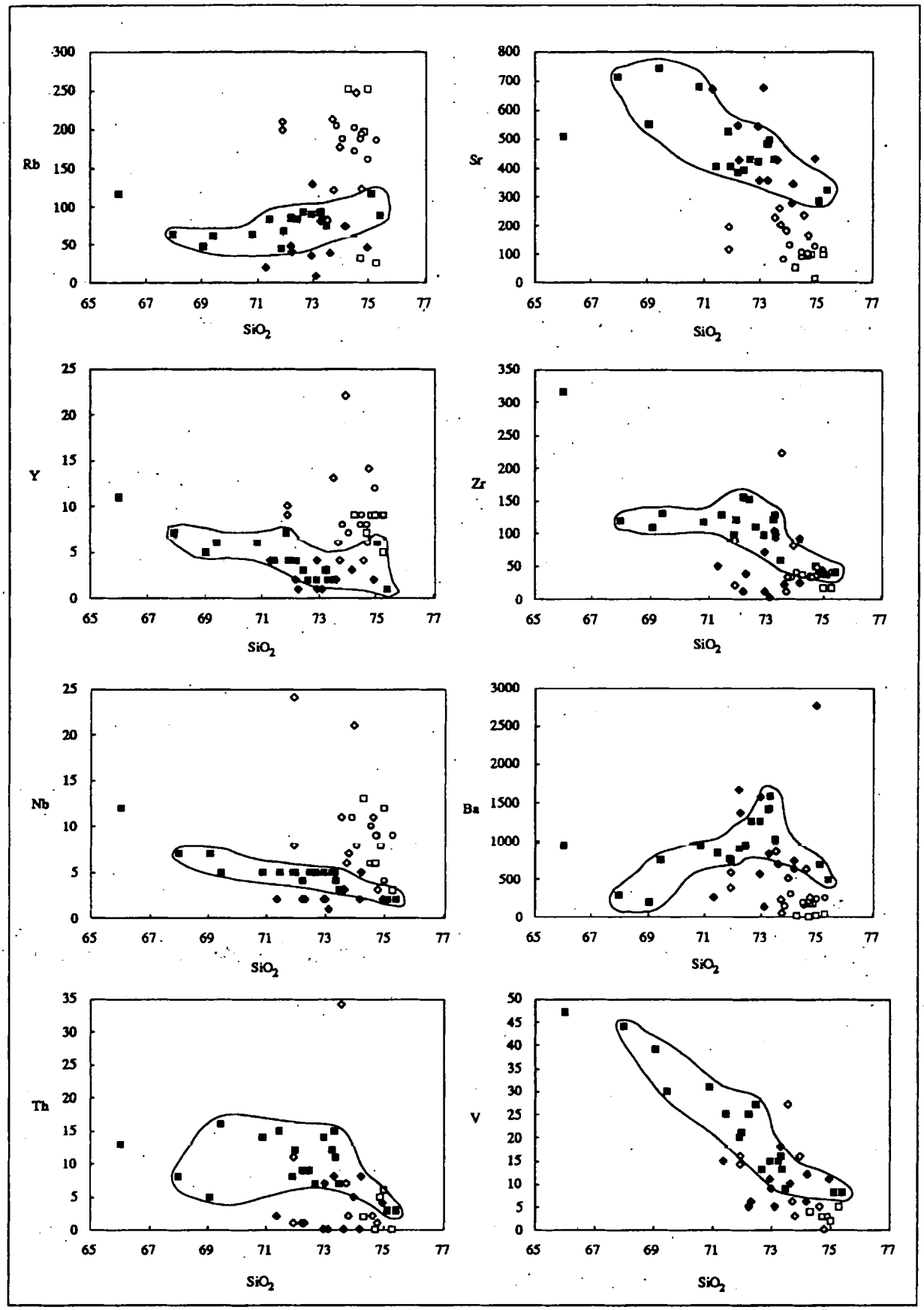

Fig. 6.6. Harker trace element variation diagrams for the Confluence and the Parri granites. Values of SiO_2 are in oxide wt. %; all other values are in ppm. ▪ = undeformed Confluence granites; ♦ = deformed Confluence granites; ▫ = undeformed Parri granites. ◇ = deformed sheets; ○ = data for the undeformed Parri granite of Petterson (1984). With the exception of sample S109 (SiO_2 = 66 %), the fields for undeformed Confluence are outlined.

compared on a spidergram, where trace element abundances have been normalised to a hypothetical ocean ridge granite (ORG; Pearce et al. 1984) (Fig. 6.7A). This comparison illustrates the relatively low contents of Rb, Th, Nb, Zr and Y for the deformed Confluence granites compared with the undeformed Confluence granites.

The two samples collected from separate boudins of the same deformed granite sheet (S75 and S76; Table 6.1) are characterised by contrasting trace element compositions. The variation observed for the majority of elements between these samples can be ascribed to fractionation trends. However, the variations observed for Ba and Sr with silica are inconsistent with the magmatic trends mentioned above, since the sample with the highest silica content is characterised by a higher Sr content and a lower Ba content than the sample with the lower silica content. This is presumably a reflection of sub-solidus alteration involving fluid transport.

Chondrite normalised REE plots for undeformed Confluence granites are displayed in Fig. 6.8A. These include three samples from a single sheet (this study), together with the average of two further sheets (Petterson 1984). The REE profiles are relatively fractionated, with La/Yb ratios in the range 74-119. Europium anomalies are either flat or slightly positive.

6.3.2. Parri granites

The Parri granites display a wide range of trace element compositions, and are characterised by Rb/Sr ratios that are usually in the range 0.6-2.0, although one undeformed sheet is characterised by Rb/Sr = 19.3. The elements Rb, Sr and Ba lie in the ranges 30-250 ppm, 10-260 ppm and 0-869 ppm, respectively. Th contents are generally 1-10 ppm, Zr contents lie in the range 10-90 ppm, whilst Y and Nb contents lie in the range 3-38 ppm.

Harker trace element variation diagrams for the Parri granites (Fig. 6.6) display no consistent trends with increasing silica content. Undeformed Parri granites display relatively

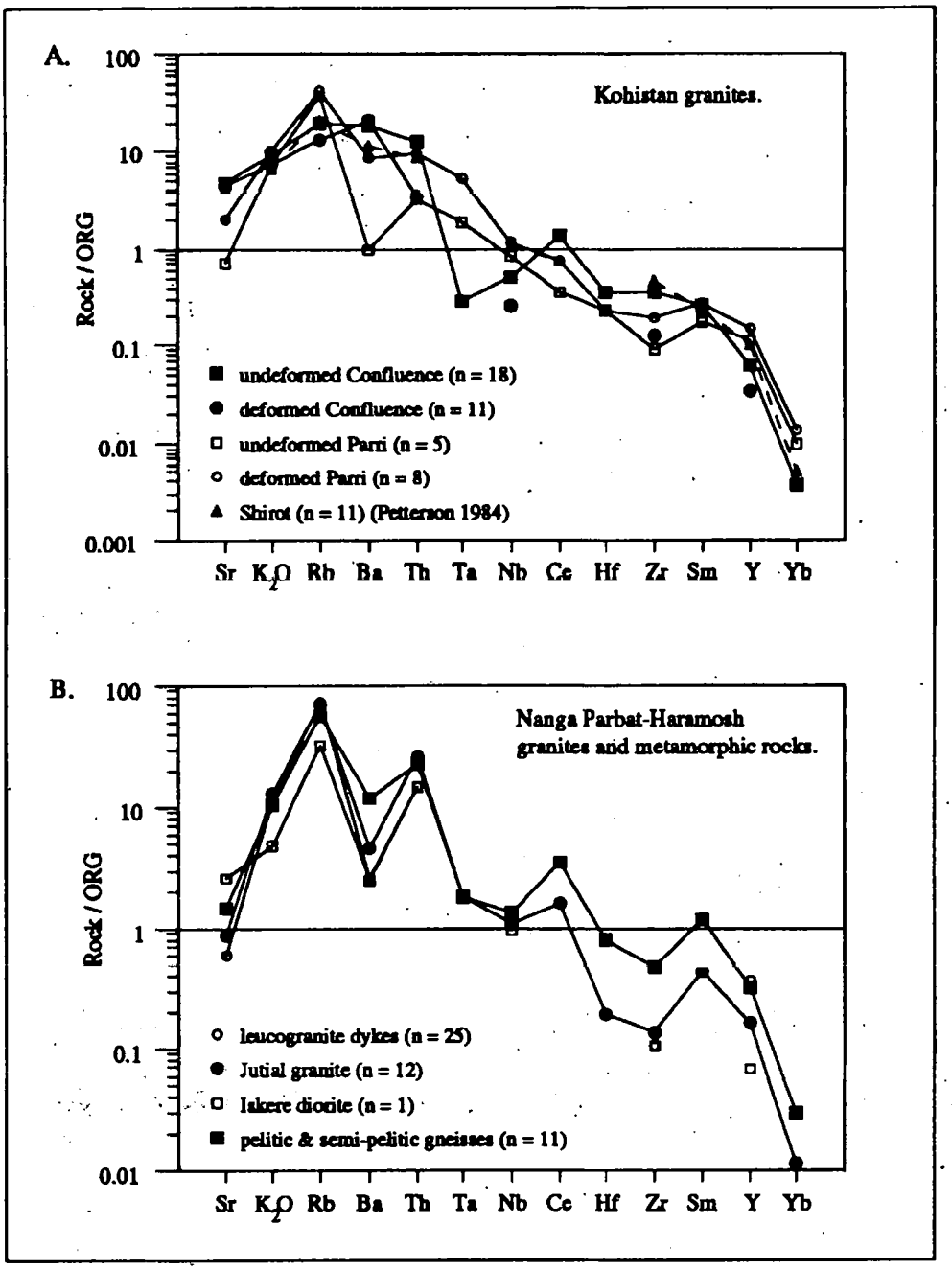

Fig. 6.7. Average trace element abundances, normalised against Ocean Ridge Granite (Pearce et al. 1984), for (A) Kohistan granites, and (B) leucogranites and gneisses of the NPHM. n = number of samples for all elements except REE (Ce, Sm, Yb), Ta & Hf. For the REE, Ta & Hf, n = 3 for undeformed Confluence granites (from the same granite sheet); n = 1 for undeformed Parri granites; n = 2 for deformed Parri granites; n = 6 for the Jutial granite and n = 4 for NPHM gneisses.

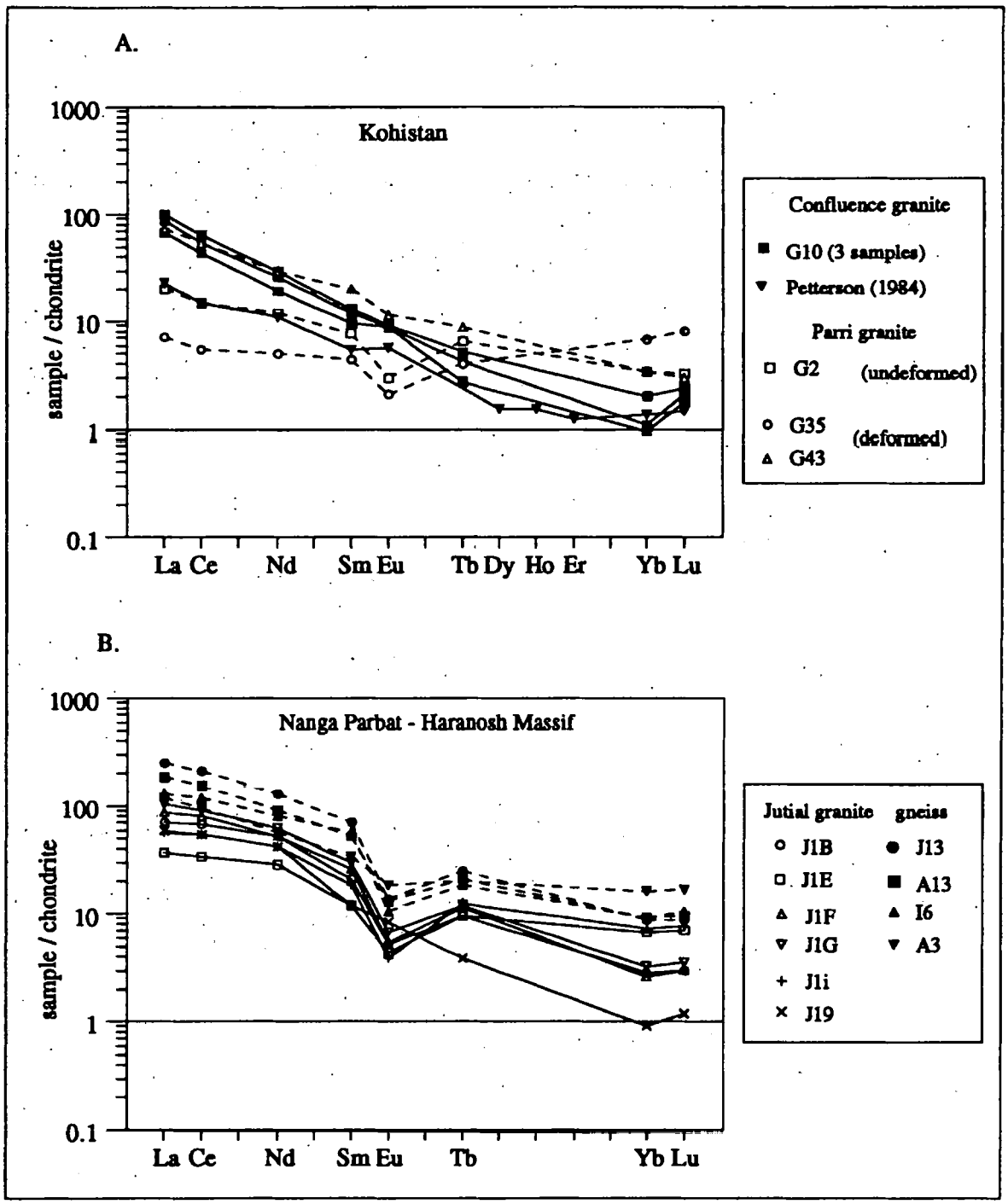

Fig. 6.8. Chondrite normalised REE plots for granites from the NPHM-Kohistan region. **A.** Kohistan arc : Confluence granites (solid lines) and Parri granites (dashed lines). Three samples were analysed from the undeformed Confluence granite 'G10'. The data from Petterson (1984) are the mean of two analyses of an "Indus Confluence Acid Sheet" (equivalent to an undeformed Confluence granite). **B.** NPHM : Jutial granite (solid lines) and pelitic gneisses (dashed line). Chondrite values from Nakamura (1974).

uniform trace element abundances, although the concentration of Y varies widely, correlating with the proportion of modal garnet, whilst the two samples that are characterised by relatively depleted K_2O contents (G14 and G15), also exhibit relatively low concentrations of Rb.

The deformed Parri granites display extremely variable trace element contents compared with the undeformed granite sheets. On the Harker variation diagrams (Fig. 6.6), the relatively high contents of Sr and Ba for the deformed sheets can be readily observed. A comparison between the mean trace element contents of the undeformed and deformed Parri granites (see Table 6.3; Fig. 6.7A) demonstrates that the deformed granites are also relatively enriched in the HFSE, Ta and Zr compared with the undeformed Parri sheets.

In general, the Parri granites are characterised by flat REE profiles compared with the Confluence granites, due to lower contents of LREE and higher contents of HREE (Fig. 6.8A). The Parri granite exposed at the type locality in the Gilgit valley (G2) is characterised by a La/Yb ratio of 8.8, whilst sample G35 collected from the shear zone at Sassi is characterised by an even flatter profile (La/Yb = 1.5). The other deformed Parri granite from the shear zone (G43) is unusual in displaying a relatively steep profile due to relatively high absolute LREE abundances (La/Yb = 33). Presumably the relatively high (but variable) content of HREE in the Parri granites is a reflection of the presence of modal garnet. All the Parri granites exhibit negative Eu anomalies.

6.3.3. NPHM Leucogranites and Metamorphics

6.3.3.1. Leucogranites

The NPHM leucogranites are characterised by Rb and Sr concentrations in the ranges 80-360 ppm and 10-144 ppm, respectively, leading to Rb/Sr ratios in the range 1-27 ppm for the leucogranite dykes, and 2-8 ppm for the Jutial granite. However, it should be noted that only five separate leucogranite dykes (9 samples), out of a total of 21 dykes studied,

	Kohistan				Nanga Parbat-Haramosh Massif			
	Confluence		Parri		Leucogranite		Iskere	Pelitic
	Undef. n = 18	Def. n = 11	Undef. n = 5	Def. n = 8	Dyke n = 25	Jutial n = 12	Qtz-Di. n = 1	Gneiss n = 11
SiO_2	71.82	73.20	74.83	73.54	74.41	73.86	61.60	69.39
TiO_2	0.23	0.09	0.03	0.11	0.05	0.10	0.20	0.53
Al_2O_3	15.34	15.46	14.86	15.26	14.79	14.69	22.27	15.12
Fe_2O_3 (1)	1.68	0.78	0.50	1.01	0.65	0.97	1.48	4.76
MnO	0.03	0.01	0.06	0.04	0.02	0.01	0.02	0.08
MgO	0.44	0.27	0.04	0.23	0.10	0.14	0.51	1.45
CaO	2.43	2.31	1.46	1.58	1.02	1.21	4.00	1.27
Na_2O	4.10	4.57	5.13	3.85	4.11	3.55	6.90	2.35
K_2O	3.66	2.91	2.90	4.14	4.39	5.08	1.92	4.16
P_2O_5	0.08	0.04	0.02	0.04	0.07	0.04	0.07	0.13
LOI	0.45	0.38	0.40	0.67	0.54	0.61	0.67	1.07
Total	100.3	100.0	100.2	100.5	100.1	100.3	99.6	100.3
Rb	80	54	151	171	294	288	128	229
Sr	480	458	70	196	59	87	256	147
Y	4	2	8	10	26	11	5	23
Zr	118	43	31	67	36	46	36	164
Nb	5	3	8	11	12	11	10	14
Ba	912	1016	50	435	128	230	125	594
Pb	27	28	38	76	60	75	49	31
Th	10	3	3	8	12	21	12	18
U	1	1	4	3	12	19	3	5
Sc	3	2	2	4	2	3	5	9
V	23	10	3	11	3	5	11	67
Cr	10	15	5	10	10	8	6	76
Co	1	0	0	1	0	0	1	14
Ni	3	5	3	4	5	4	9	27
Cu	19	10	1	5	2	1	0	13
Zn	40	16	24	21	20	26	34	72
Ga	16	13	19	19	21	20	29	19

Table 6.3. Average granite and gneiss compositions. n = number of samples. (1) = all Fe calculated as Fe_2O_3. Undef. = undeformed; Def. = deformed; Qz-Di. = quartz diorite from Iskere.

record Rb/Sr ratios > 10. Ba contents generally lie in the range 50-340 ppm, although four leucogranite samples are characterised by concentrations > 500 ppm. Th contents generally lie in the range 10-38 ppm.

Harker variation diagrams (Fig. 6.9) demonstrate the widely ranging trace element compositions of the NPHM leucogranites. Compared with the leucogranite dykes, the Jutial granite is characterised by a more uniform trace element composition. Indistinct fractionation trends for the Jutial granite include slight decreases in Rb, Zr, Th and U with increasing silica, although there is a large amount of scatter. The leucogranite samples that are characterised by relatively high MnO contents also display unusually high Y contents,

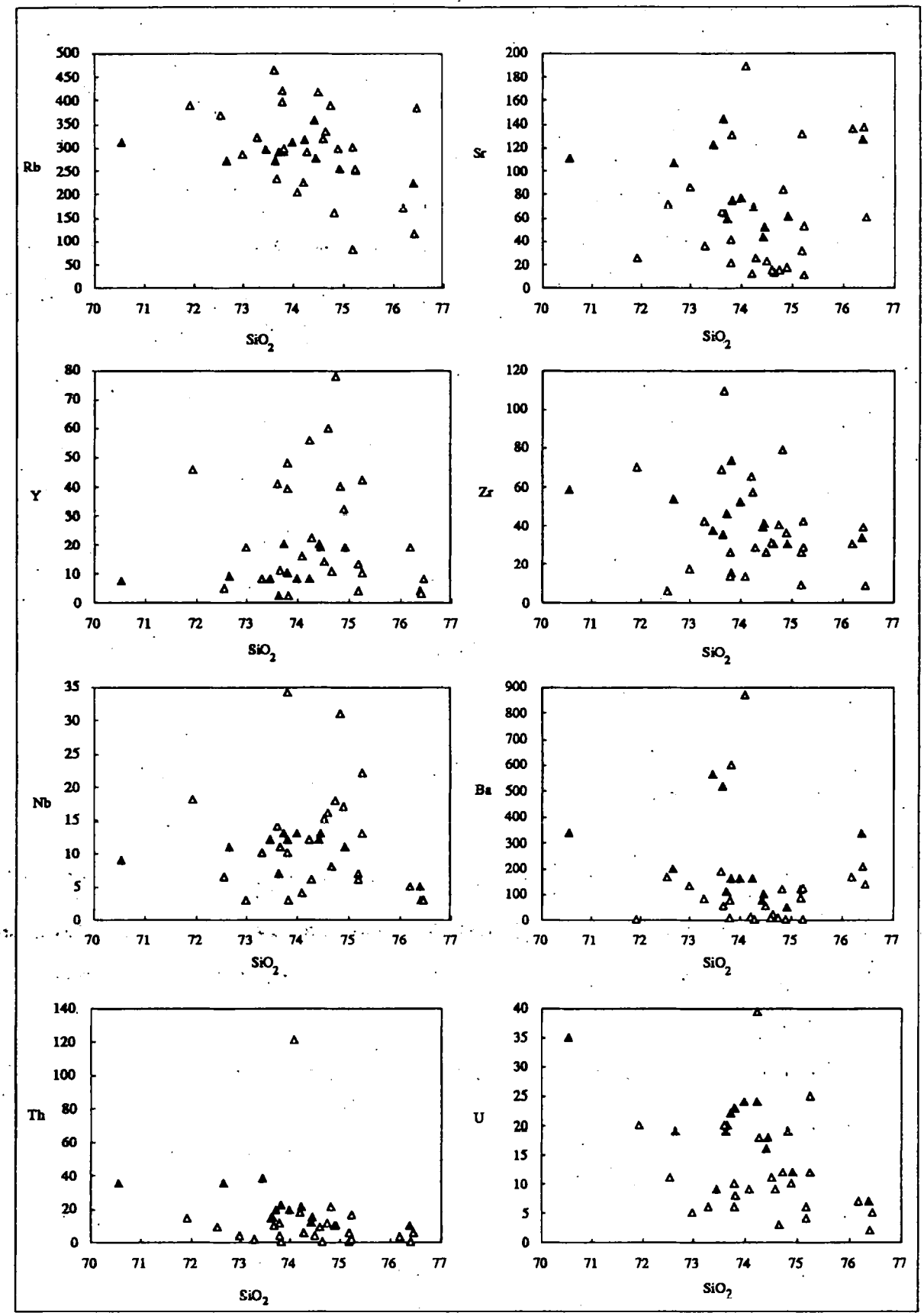

Fig. 6.9. Harker trace element variation diagrams for the leucogranites of the Nanga Parbat-Haramosh Massif. Values of SiO_2 are in oxide wt. %; all other values are in ppm. ▲ = Jutial granite; △ = leucogranite dykes.

reflecting variable proportions of modal garnet. The average trace element content of the Jutial granite and the leucogranite dykes may be compared in Table 6.3 and on the spidergram in Fig. 6.7B. The dykes are generally characterised by higher Y, and lower Sr, Ba and Th contents compared with the Jutial granite, indicating the relatively evolved nature of the leucogranite dykes compared with the Jutial granite.

As shown in Table 6.2, individual leucogranite dykes show remarkably little trace element variation, even where intensely deformed, as in the case of the leucogranite body exposed in the Liachar shear zone (sample L17; Table 6.2). The elements Y and Nd are the most variable within individual sheets.

Different samples collected from the Jutial granite display variable abundances of REE (Fig. 6.8B). However in general the REE profiles are steep, with La/Yb mostly in the range 10-50. Sample J19 displays relatively low HREE contents (La/Yb = 96), which may be a reflection of equilibrium between the melt and either garnet or zircon. The relatively low content of Y present in this sample suggests the involvement of garnet. All of the REE profiles are marked by negative europium anomalies.

The quartz diorite intrusion at Iskere exhibits an unusual major and trace element geochemistry (Table 6.3), and, as expected, the sample does not fall into any of the granite suites already described. The quartz diorite is weakly peraluminous (A/CNK = 1.07), and is characterised by a relatively low silica content (62 wt. %), and an Rb/Sr ratio of 1.6. Compared with the leucogranites of the NPHM, the quartz diorite is characterised by a relatively high Sr content and a relatively low Rb content.

6.3.3.2. Metamorphic Samples

Although the cross-cutting nature of all of the sampled leucogranites indicates that melting did not occur at the present exposure level, the upper-amphibolite grade (Chapter 4) and isotopic characteristics (Chapter 7) of the basement rocks of the NPHM makes them

potential leucogranite source rocks. Experimental work has indicated that the optimum mode for crustal melting is approximately 38 % biotite, 32 % quartz, 22 % plagioclase and 8 % aluminosilicate (Patino-Douce and Johnston 1991). Consequently, in this study, the geochemical compositions of the eleven most micaceous of the gneisses from the NPHM are evaluated for comparison with the geochemical compositions of the leucogranites. These samples contain both modal muscovite and biotite, with total mica in the range 10-40 %. The aluminium saturation (A/ACK) lies in the range 1.1-2.8 (average = 1.5).

The average major and trace element composition of the eleven semi-pelitic gneisses is given in Table 6.3. The average abundances of most trace elements are considerably greater than those for the NPHM leucogranites, as shown in Fig. 6.7B. In particular, the metamorphic samples display relative enrichments in the LILE Sr and Ba and depletion in Rb. With the exceptions of Ta and Nb, the HFSE are also extremely enriched in the metamorphic samples relative to the Jutial granite.

Four metasedimentary samples from the NPHM have been analysed for REE, including the semi-pelitic wallrock to the Jutial granite (J13), two samples of psammitic gneiss from Rupal (A13) and Iskere (I6), and a migmatitic gneiss from the Astor gorge, characterised by the assemblage kyanite, garnet, biotite, muscovite, plagioclase and k-feldspar (A3). These four samples are characterised by relatively high REE abundances compared with the Jutial granite, but the shape of the chondrite-normalised REE profiles for the pelitic gneisses and Jutial granite are similar. La/Yb ratios for the pelitic gneisses lie in the range 11-43 (Fig. 6.8B). As expected, the single metamorphic sample that contains modal garnet (A3) exhibits a relatively high HREE content.

6.4. Summary of Major and Trace Element Geochemistry

The granites studied in this work have been divided on the basis of mineralogy and geochemistry into three distinct suites. Given the geochemical variability of the granites, the concentration of no single trace element is independently diagnostic of granite type. The

division of granites into suites has required an evaluation of all the available mineralogical and trace element data. In general, the Confluence granites, Parri granites and NPHM leucogranites may best be distinguished on a Rb versus Sr plot (Fig. 6.10), on which the more evolved granites are characterised by lower Sr and higher Rb contents than less evolved granites.

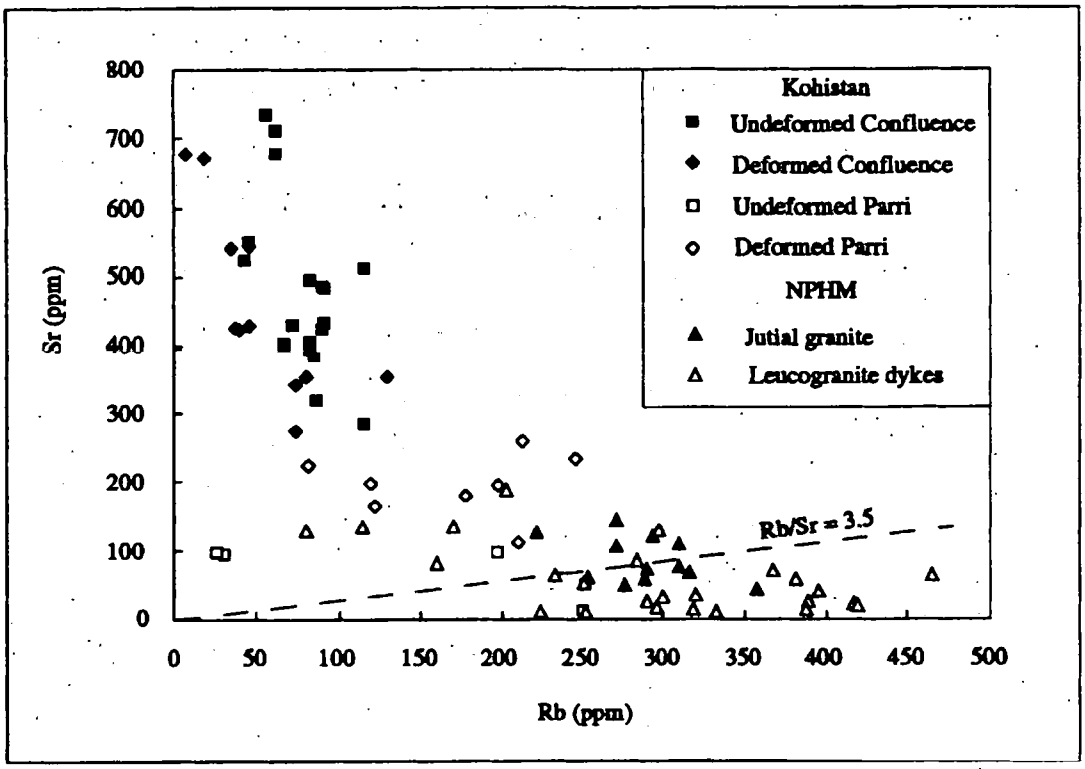

Fig. 6.10. Covariation diagram for Rb and Sr, allowing the discrimination of the different granite suites present in the Nanga Parbat - Kohistan region. Rb/Sr ratios > 3.5 can only be obtained under fluid-absent conditions, regardless of source composition, unless feldspar fractionation has occurred (Harris et al. 1993).

The Confluence granites are mineralogically and geochemically the most homogenous suite, and display characteristic magmatic trends over a wide range of silica. In terms of the LILE, the Confluence granites are relatively enriched in Sr and Ba and depleted in Rb. Contents of the HFSE Ta, Nb and Y are also relatively low. Chondrite-normalised REE profiles are relatively steep and are characterised by flat or slightly positive europium anomalies. The deformed Confluence granites display greater geochemical variation than their undeformed equivalents outside the shear zone, and are characterised by relatively high Na_2O and low K_2O, Rb, Th and Zr contents.

The Parri granites exhibit variable geochemical compositions that overlap with those of the Confluence granites. The trace element abundances of the two suites may be conveniently compared on a spidergram (Fig. 6.7A). Compared with the Confluence granites, the Parri granites are characterised by relatively high Rb/Sr ratios and (usually) relatively low Ba contents. The Parri granites also exhibit relatively high concentrations of Nb, Y, Ta, Yb and the HREE, and relatively low concentrations of the LREE, compared with the Confluence granites. However, it should be noted that, in the case of Ta and Yb, data are only available for a single undeformed Parri granite and a single undeformed Confluence granite, and therefore any comparison between the Ta and Yb contents of the different granite suites can only be speculative. The Parri granites are also characterised by negative europium anomalies. The deformed Parri granites exhibit extreme geochemical dispersion, and are characterised by relatively high contents of Sr, Ba, Zr and Ta compared with their undeformed equivalents outside the shear zone.

In view of their relatively leucocratic nature and high modal proportion of muscovite, the Parri granites are broadly similar to the NPHM leucogranites. However, the NPHM leucogranites are usually characterised by the presence of tourmaline, display even higher Rb/Sr ratios, and usually possess greater concentrations of Th and U. As will become apparent in Chapter 7, the distinction between NPHM leucogranites and the deformed Parri granites is important, since both types occur in the shear zone bordering the western margin of the NPHM. The average trace element contents of deformed Parri granite and NPHM leucogranite are compared in Table 6.3 and Fig. 6.11A. In addition to the above-mentioned differences, the spidergram indicates that the deformed Parri granites are also characterised by higher contents of Ba and the HFSE Ta and Zr, and lower contents of LREE, compared with the NPHM leucogranites. Furthermore, the NPHM leucogranites display steeper REE profiles than the Parri granites, whilst the europium anomalies are more marked (see Fig. 6.8).

The NPHM leucogranites share a similar trace element geochemistry to the Miocene High Himalayan leucogranites exposed in other parts of the Himalaya. For example, as

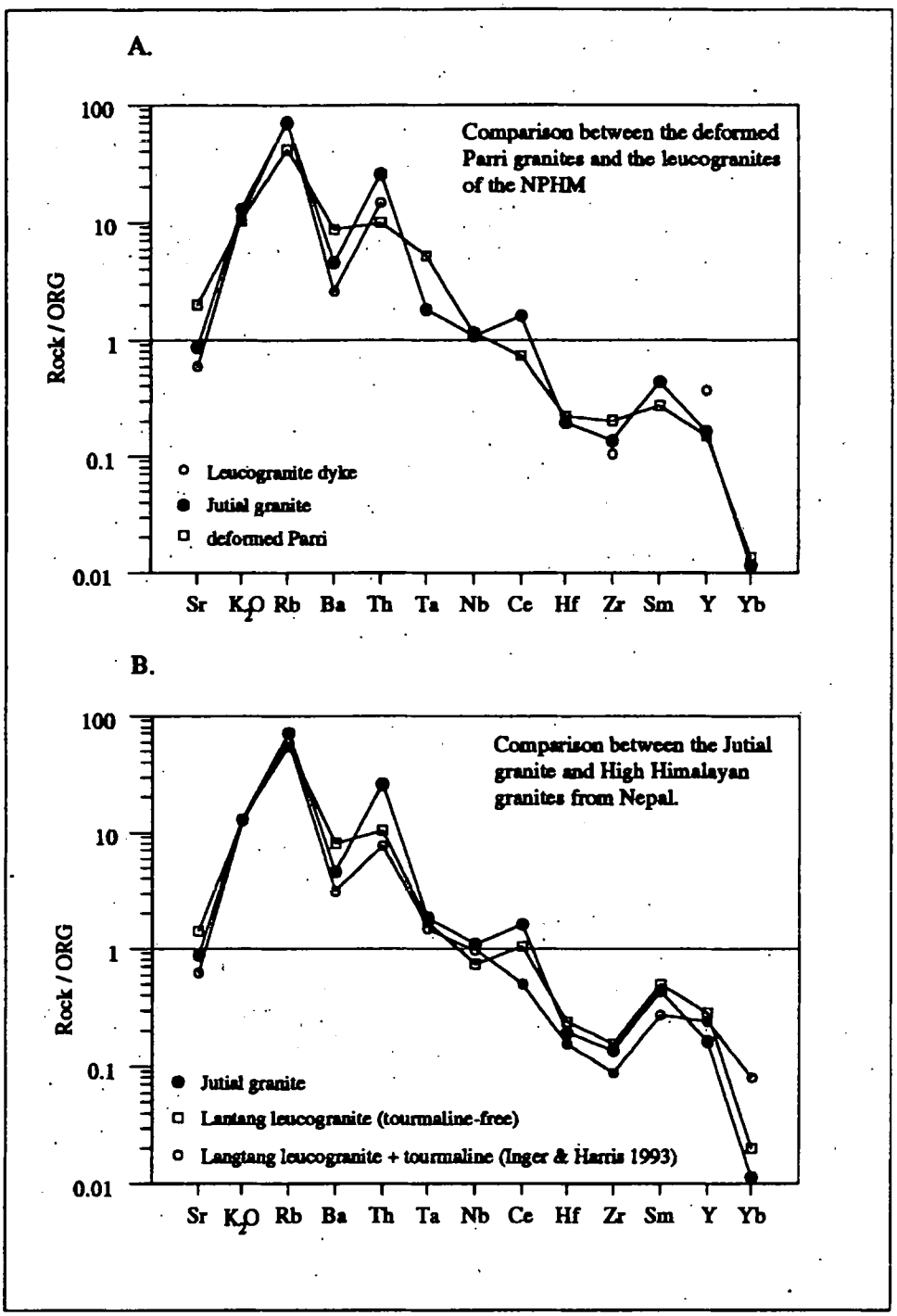

Fig. 6.11. Comparison between average trace element abundances for the leucogranites of the NPHM and, (A) deformed Parri granites, and (B) other High Himalayan leucogranites (Inger & Harris 1993). ORG = Ocean ridge Granite (Pearce et al. 1984).

shown in Fig. 6.11B, the geochemistry of the Jutial granite is broadly comparable to that of the tourmaline-free facies of the Langtang leucogranite in Nepal (Inger and Harris 1993), although the Jutial granite is somewhat enriched in Th, Nb and LREE.

The potential source rocks of the leucogranites are relatively enriched in Sr and Ba and depleted in Rb compared with the NPHM leucogranites. The metamorphic rocks are also characterised by relatively high contents of the REE, and of the HFSE Hf, Zr and Y.

6.5. Tectonic Discrimination Diagrams

Numerous workers have stressed the close relationship between granite type and tectonic setting, which, in the widest sense, occurs because different tectonic settings are characterised by distinct source lithologies, and also because distinct petrogenetic processes may occur in different tectonic settings (Pitcher 1982). It may thus be possible to distinguish between the three granite suites in this study by using the tectonic discrimination diagrams of Pearce et al. (1984) and Harris et al. (1986) (Figs. 6.12A and B).

As expected, the Confluence granites plot within the volcanic arc field of Pearce et al. (1984) and Harris et al. (1986). The Parri granites exhibit significant scatter on the discrimination diagrams, straddling the boundaries between syn-collision and volcanic arc granites. Some of the leucogranites of the NPHM also straddle the boundaries between syn-collision and volcanic arc fields, although the majority of samples lie in the syn-collision granite fields.

The usefulness of the tectonic discrimination diagrams in this study is somewhat equivocal. Whilst such a tectonic discrimination may be valid on a global scale, where 'generalised' tectonic settings may be relatively easily differentiated, on a smaller scale, and/or in a tectonically active region, the precise distinction in time and space between different tectonic settings may not be possible. Thus in this study, a wide range of granite types has been observed, although all of the granites were actually intruded into broadly the

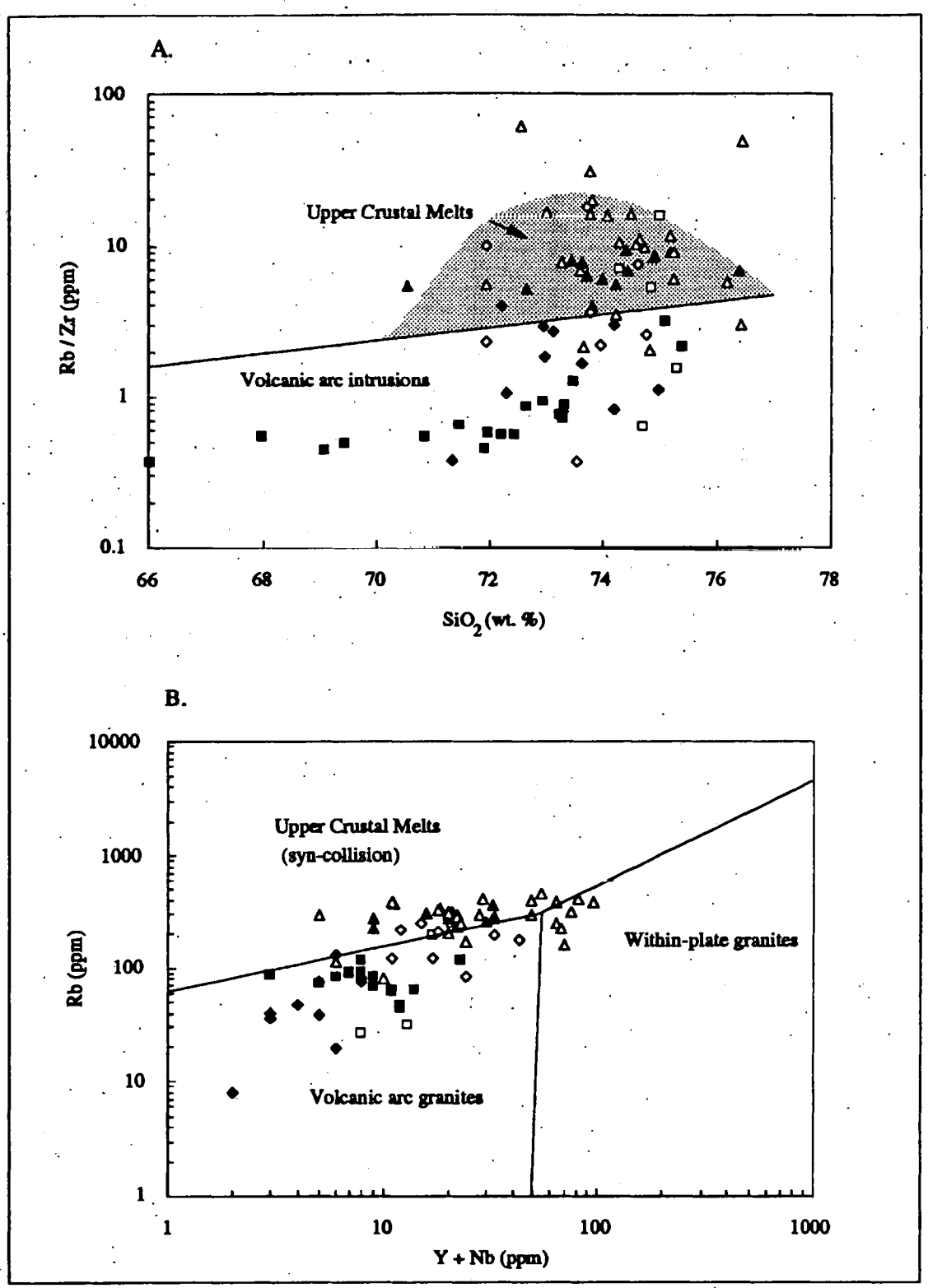

Fig. 6.12. Tectonic discrimination diagrams for granites of the Nanga Parbat - Kohistan region. A = Rb/Zr versus silica (Harris et al. 1986); B = Rb versus Y + Nb (Pearce et al. 1984). ■ = undeformed Confluence granites; ◆ = deformed Confluence granites; □ = undeformed Parri granites; ◇ = deformed Parri granites; ▲ = Jutial gramite (NPHM); △ = leucogranite dykes (NPHM).

same tectonic setting. All of the granites were emplaced at some time after the initial continental collision (during continued convergence), but are characterised by strongly contrasting compositions that are primarily dependant on the local variation in source composition.

Previous workers have also noted the problems involved in the use of tectonic discrimination diagrams. For example, on the Rb versus (Y+Nb) diagram, the distinction between subduction-related magmatism and some examples of post-collision magmatism may not be clear cut (Pearce et al. 1984), although, in some cases, the distinction between such granites may be improved by an evaluation of associated rock types (Rogers and Greenburg 1990). The high Rb, low HFSE 'syn-collision' field of Pearce et al. (1984) may also encompass post-collisional crustal melts, as noted by Harris et al. (1988). Clearly, this field is not necessarily diagnostic of collision magmatism, but only of crustal melting. Following Harris et al. (1988), the syn-collision field in this work has been relabelled the 'Upper Crustal Melt' field.

In the case of the Rb/Zr versus silica diagram (Harris et al. 1986), samples plotting below the crustal melt field may have been generated in an island arc setting, or a crustal source of intermediate composition (Harris et al. 1988). Alternatively, such samples may be crustal melts that have incorporated accessory zircon during melting, resulting in unusually low Rb/Zr ratios.

On the basis of trace element contents alone, the Confluence granites may be considered to be either associated with active subduction and formation of the Kohistan batholith (Petterson and Windley 1985), or the result of post-collision magmatism in the Kohistan arc. Field relations and isotopic systematics (Chapter 7) indicate a post-collisional origin. The Confluence granites thus appear to fall in the post-orogenic category of Rogers and Greenburg (1990).

The tectonic discrimination diagrams confirm that both the Parri granites and the NPHM leucogranites are crustal melts, although such a geochemistry is not uniquely a consequence of syn-collision magmatism.

6.6. Compositional Variation of granites from the Sassi Shear Zone

One of the interesting aspects that has emerged from this study is the chemical variation displayed by the granite sheets present in the shear zone bordering the western margin of the NPHM. The smooth geochemical variation patterns displayed by the undeformed Confluence granites, and the relatively uniform compositions of the undeformed Parri granites, contrast strongly with the variable geochemical compositions of the deformed Confluence and Parri granites present in the shear zone.

The deformed Confluence granites are characterised by consistently lower contents of K_2O, Rb, Ba, Th and Zr and the HFS elements Nb and Y, and higher contents of Na_2O, compared with the undeformed Confluence granites outside the shear zone, for a given silica content (silica contents do not appear to have been systematically affected). The geochemical affects of shear zone processes on the Parri granites are difficult to resolve, since firstly, analyses of only five undeformed Parri granites are available for comparison, and secondly the Parri granites do not display any consistent magmatic trends. In general, deformed Parri granites are characterised by relatively low contents of Na_2O, and relatively high contents of Sr, Ba, Ta and Zr compared with the undeformed Parri sheets.

It is thought that the undeformed and deformed granites in each suite are co-magmatic, and were generated in similar source regions, for the following reasons :

(i) The swarm of undeformed granite sheets present in the Indus confluence area can be traced along the Indus gorge into the shear zone at Sassi, which marks the eastern exposure

limit of Kohistan granite sheets. There is no discontinuity in granite exposure between the shear zone and the Indus confluence.

(ii) In terms of mineralogy and major element composition, the undeformed and deformed granites in each suite are similar.

The observation that the most geochemically variable Confluence and Parri granites are exposed in the shear zone, strongly suggests that this variation is caused by shear zone processes such as fluid transport. However, there is some evidence that the composition of the deformed Parri granites is at least partly a function of crustal contamination, as discussed below.

6.6.1. Crustal Contamination

As described in Chapter 2, field and petrographic observations indicate that some of the deformed Parri granites have been partially contaminated by either wall-rock or restite. The strontium and neodymium isotope systematics of the deformed Parri granites suggest that the contamination occurred by the interaction between the melt and relatively evolved, Indian continental lithologies present in the wall rocks (see Chapter 7). Given the average composition of pelitic gneiss from the NPHM compared with the average composition of undeformed Parri granite (Table 6.3), incorporation of such pelitic material would account for the observed enrichment in Sr, Ba, Ta and Zr, and depletion in Na_2O, between deformed and undeformed Parri granites.

The possibility that the Parri granites that were intruded closest to the NPHM underwent magma-mixing, with contamination by anatectic melts derived from the NPHM, leading to the distinctive geochemical signatures of the deformed Parri granites, cannot be entirely ruled out. However, there is no evidence for the occurrence of magmatism in the NPHM at about 30 Ma (see Chapter 7), whilst such a hypothesis would fail to account for the strong association between deformation and geochemical alteration.

In contrast, the deformed Confluence granites show little petrographic evidence for contamination by wall-rock or restite. A single deformed Confluence granite has been found to contain rare grains of garnet, but is not known whether these are magmatic crystals or xenocrysts. An examination of Table 6.3 shows that the observed geochemical differences between deformed and undeformed Confluence granites could not not be due to contamination by material of 'average pelite' composition.

6.6.2. Metasomatism

In order to account for the geochemical differences between deformed and undeformed Confluence granites, some process other than crustal assimilation is required. The importance of shear zones in providing conduits for fluid movement through the crust is well known (Etheridge et al. 1983). Fluids are often confined to shear zones due to the relatively low confining pressures in these zones. They may create their own permeability by hydraulic fracturing, or alternatively they may migrate by grain-boundary diffusion. Compositional changes in mylonite zones are usually the result of fluid flow (Tobisch et al. 1991) and therefore it is possible that the deformed Confluence granites have been affected by elements transported by fluids being channelled along the shear zone.

In general, the chemical changes that take place during mylonitisation of granitoids is poorly understood. Geochemical data from different shear zones show that affects are variable, but the elements that are most commonly modified are SiO_2, K_2O, Al_2O_3, CaO, Sr and Rb (Beach 1976; Sinha et al. 1988; Dipple et al. 1990; Tobisch et al. 1991). The relative chronology of deformation, fluid flow and chemical change in a ductile shear zone may be complex, especially where cyclical fluid influx occurs through a heterogeneous network of anastomosing mylonite zones. Fluid flow and deformation are often accompanied by the growth of retrogressive minerals, which are the petrographic expression of the geochemical changes (Sinha et al. 1988; Tobisch et al. 1991). Although retrogressive minerals are not present in significant proportions, the deformed Confluence granites are characterised by

slightly lower modal contents of biotite (generally < 5 %) compared with the undeformed Confluence sheets (generally 6-15 %). This observation is consistent with the lower abundancies of K_2O, Rb, Ba and Th present in the deformed sheets, whilst the lower content of Zr may indicate that this element is largely present in zircon inclusions present within the biotite.

Despite the fact that the HFSE and Th are generally considered to be relatively resistant to fluid mobility, the variability of these elements in the deformed Confluence granites relative to the undeformed granites suggest that they have been modified by sub-solidus processes in the shear zone. This may be a reflection of a high activity of acidic ligands such as F^- and Cl^- in the circulating fluids (Harris 1981; Eugster 1985).

In order to evaluate the geochemical changes experienced by a granitoid present in a shear zone, the original composition of the granitoid must be well characterised. Even where this is possible, the geochemical variation displayed by a deformed granitoid may be the result of a wide range of interelated processes. For example, according to Tobisch et al. (1991), the most influential factors that control the geochemical modification of granitoid intrusions present in a shear zone are the primary composition, mineralogy and texture (e.g. grain size) of the granitoid, together with the pressure, temperature, strain rate, fluid-rock ratio, fluid source and porosity. Given the large number of variables, geochemical changes are best studied in cases where a shear zone cuts a single, homogenous intrusion, so that the greatest compositional changes occur in the most strained parts of the shear zone (Beach 1976). Unfortunately, in the case of the Confluence granites, the original compositions of the deformed bodies are poorly constrained, since the undeformed granites exposed outside the shear zone exhibit a range of major and trace element compositions. Consequently it is not possible to evaluate precisely the sub-solidus geochemical changes experienced by the Confluence granites, or to model these changes in terms of mass balance calculations (Dipple et al. 1990).

6.6.3. Summary

The composition of the deformed Confluence granites is thought to be dominantly controlled by fluid transport in the shear zone. The composition of the deformed Parri granites appears to have been partly controlled by wall-rock contamination, although sub-solidus processes may also have played a role. Alternatively, fluid flux through the shear zone may have already terminated before intrusion of the Parri granites at 26 Ma (see Chapter 7). These two alternatives cannot be separated on the basis of the available data from the Parri granites, since the geochemical effects of metasomatism appear to be relatively minor compared with the effects of crustal assimilation. However, the deformed Confluence granites show little evidence for assimilation of Indian continental crust. It is unknown why the Parri granites appear to have been affected by crustal assimilation, whilst the Confluence granites have not. A higher temperature for the Confluence granites is indicated by the lower SiO_2 contents of the least evolved endmembers, and therefore the Confluence granites would be expected to have been more susceptible to crustal contamination than the Parri granites. It is possible that, at the time of intrusion of the Confluence granites, Kohistan and Indian continental lithologies had not yet been thoroughly interleaved, and therefore the Confluence granites were able to rise with relative ease through the crust. By the time that the Parri granites were intruded, extensive imbrication between Kohistan and Indian continental lithologies along the Main Mantle Thrust had occurred, and therefore the Parri granites were more likely to assimilate LILE and HFSE-enriched Indian continental material during their emplacement.

6.7. Petrogenesis of Undeformed Granites

6.7.1. Introduction

Geochemical variation in granitoid rocks may be ascribed to a range of processes that include partial melting of a heterogeneous source region (Deniel et al. 1987), incomplete separation between melt and restite (Chapell et al. 1987), or processes that result in the

modification of magma during ascent and emplacement, such as magma mixing, fractional crystallisation or wallrock assimilation-fractional crystallisation (AFC) (De Paolo 1981; Hildreth and Moorbath 1988). Geochemical signatures are also influenced by the style and rate of melt separation, and by a variety of sub-solidus processes. Unfortunately, it is rare to obtain unequivocal evidence that identifies one of these processes as the unique cause of variation within a given granite or granite suite. In this section, the geochemical contraints on the petrogenesis of the granites from Kohistan and the Nanga Parbat-Haramosh Massif are discussed, whilst the isotopic constraints are discussed in Chapter 7.

Successful modelling of melting and fractionation processes in basic or intermediate rocks has been based on an evaluation of the relative trace element abundances in these rocks, and rests on the equilibrium distribution of elements between melt and magma (McCulloch and Gamble 1991). However, the behaviour of many trace elements during granite petrogenesis is poorly understood. A large proportion of the trace element budget of a granite is incorporated in accessory phases such as allanite, zircon, monazite, sphene and apatite (Hanson 1978; Fourcade and Allègre 1981). This has two important implications. Firstly, the concentrations of many trace elements in the melt will not be determined by the major phases in the source, but by the solubilities of accessory phases in the magma. For example, the concentrations of LREE, Ta, Hf, Zr, Th and U will be controlled by the solubilities of such phases as zircon, monazite and sphene in the melt. The solubilities of some of these phases have are been determined experimentally, and are primarily controlled by melt composition (Watson 1979; Watson and Harrison 1983). Secondly, tiny accessory phases are likely to be entrained in the melt, so that true magmatic trace element contents cannot be determined. The result is that the behaviour of many of the trace elements present in granites does not reflect true equilibrium between melt and restite. In granites, only the trace elements that are hosted by the major phases mica and feldspar can yield well-constrained petrogenetic information, since during melting, the concentrations of these elements in melt and restite are likely to remain in equilibrium (Fourcade and Allègre 1981). The result is that formal petrogenetic modelling of granites may only be based on the LILE, Rb, Sr and Ba (Harris and Inger 1992).

Petrogenetic modelling of granites that show evidence for fractionation may also be hazardous, due to the fact that such granites are often intruded as crystal-liquid mushes. Textural evidence for the presence of pre-existing crystals during magma emplacement includes the identification of zoned phenocrysts and magmatic flow fabrics. The crystals present in any given sample from a granite that was intruded as a crystal-liquid mush have probably precipitated in different places and equilibrated with different melt compositions. In other words, the compositions and relative proportions of minerals in a granite may not reflect true melt-crystal equilibria (Zen 1986).

In the last ten to fifteen years, the importance of water availibility in controlling partial melting in the crust has become clear. The presence of large volumes of fluids during high-grade regional metamorphism is unlikely, especially given the low porosity of high-grade metamorphic rocks (Clemens and Wall 1981). Furthermore, most granite magmas are water-undersaturated, and therefore the presence of a free aqueous phase would require the presence of components such as CO_2 or CH_4 (Clemens and Wall 1981). Although such carbon-bearing components could be derived from metasedimentary source regions, the consensus of opinion is that most crustal melting takes place under that fluid-absent conditions (Burnham and Ohomoto 1980; Clemens and Wall 1981; Miller 1985; Clemens and Vielzeuf 1987). Even where initial melting takes place under fluid-present conditions, the high solubility of water in melts (especially at high pressure) results in the rapid attainment of fluid-absent conditions (Clemens and Vielzeuf 1987). Thus large volumes of magma are almost certainly generated under fluid-absent conditions, unless there happens to be a large and continuous supply of free fluid.

The fluid required for crustal melting is derived from the dehydration breakdown of the hydrous phases hornblende, biotite and muscovite, with the amount of melt generated in each case strongly dependent on the modal proportion of the relevent phase in the source (Clemens and Vielzeuf 1987). As a result, the water activity is buffered by the magma; addition of external fluid results in the generation of more melt to consume the water, whilst

if the water activity is reduced (e.g. by the addition of CO_2), part of the melt will crystallise (Johannes and Holtz 1990). Fluid-absent melting reactions leave anhydrous restites including minerals such as quartz, aluminosilicate, k-feldspar, plagioclase, garnet or cordierite.

Fluid-absent muscovite breakdown in pelitic rocks takes place at about 675 °C at 5 kbar (Clemens and Vielzeuf 1987), via reactions such as :

Muscovite + Quartz + Plagioclase = Sillimanite + K-feldspar + melt

Such reactions lead to the generation of strongly peraluminous, near-minimum melts with > 8 wt. % water, which crystallise at > 3 kbar (Burham and Ohomoto 1980).

The fluid absent breakdown of biotite takes place in the lower granulite-facies, in the temperature range 800-850 °C at 10 kbar (Burnham and Ohomoto 1980; Rutter and Wyllie 1988; Vielzeuf and Holloway 1988), via reactions such as :

Biotite + Quartz + Plagioclase = Garnet + K-feldspar + melt

or Biotite + Sillimanite + Quartz + Plagioclase = Garnet + k-feldspar + melt.

Such high temperatures may be produced by the emplacement of mafic magma into the crust (Clemens and Wall 1981). The resulting melts are strongly water-undersaturated, with water contents of ~ 4 wt. %, and consequently the melts are able to rise to high crustal levels without crystallising. Such liquids may also depart significantly from the minimum melt composition (Clemens and Wall 1981). Fluid-absent biotite breakdown is probably the dominant melt reaction in rocks of intermediate composition, and relatively large volumes of magma may be produced.

Relatively high temperatures of 950-1000 °C are required for hornblende dehydation in rocks of intermediate composition at 10 kbar, and the resulting liquids contain > 2.7 wt. % water (Burnham and Ohomoto 1980; Rutter and Wyllie 1988).

The water content of a water-undersaturated magma will vary during ascent through the crust. The dissolved water will be expelled during crystallisation, leaving melts saturated in water. Further crystallisation causes the separation of more water (retrograde boiling), resulting in pressure increase (or volume changes) and the subsequent forceful ejection of water into the country rocks (Burnham and Ohomoto 1980).

6.7.2. Undeformed Confluence Granites

As described above, the undeformed Confluence granites display clear geochemical trends relative to silica (Figs. 6.4 & 6.6). The trends are remarkably smooth for some of the major elements, a feature which may be partly related to the 'dilution effect' of increasing silica. The more variable trends displayed by trace elements such as Sr and Rb may give a better indication of the degree of complexity involved in the magmatic processes.

The presence of numerous pegmatitic layers and lenses in some of the Confluence granites suggests that there must have been local concentrations of residual volatile phases during late crystallisation, as also noted by Petterson (1984). However, the preservation of the magmatic trends indicates that geochemical modification of the sampled granites by sub-solidus fluid activity has been minimal. The geochemical trends are in some cases slightly curved (e.g. silica versus alkalis; Fig. 6.4), and no obvious cumulate textures have been observed, and consequently the trends are not thought to be the result of variable restite unmixing (Chapell et al. 1987), although such a mechanism cannot be entirely disproved. Confirmation of purely magmatic geochemistry for the undeformed Confluence granites requires isotopic constraints, as presented in Chapter 7. To summarise these findings here, a slight isotopic heterogeneity is observed in the undeformed Confluence granites, even within single sheets, which may be due to a limited amount of wall-rock - melt interaction, or minor

sub-solidus fluid activity. However, the geochemical trends are primarily interpreted as being a reflection of magmatic processes.

The magmatic trends displayed by the Confluence granites may be a reflection of varying melt fractions derived from a single source, or due to fractionation processes occurring during magma ascent and emplacement. Since it is unlikely that in-situ fractionation can have been a significant process in such minor intrusive bodies, the individual granite sheets that show the same magmatic trends must have been generated by the multiple injection of melt derived from a source undergoing crystal fractionation, or by varying degrees of partial melting. This inference is supported by the fact that mineralogically and geochemically distinct layers within the same sheet are often separated by sharp magmatic boundaries (see Plate 2.6). Since the available evidence suggests that the Confluence granites were generated in a relatively deep-seated source (see below), the observation that some of the granites are composite intrusions generated by the multiple emplacement of relatively thin sheets, with compositions that can be related by fractional crystallisation, suggests that the magma underwent crystal fractionation at a relatively high structural level, perhaps within a large pluton, as suggested by Petterson (1984).

Interestingly, the Confluence granites display a positive correlation between the degree of aluminium saturation and silica content, as shown in Fig. 6.1, which is a commonly observed characteristic of calcalkaline magmas. Since the most primitive Confluence granite compositions are characterised by (A/CNK) < 1, the correlation suggests that the magma has been affected by fractionation of a phase with (A/CNK) < 1 (diopside-normative), such as hornblende, pyroxene, sphene or epidote (Miller 1985). The reverse trend would have been produced by the fractionation of feldspar or mica, since these phases would have reduced the aluminium saturation of the most primitive Confluence granites. Although modal hornblende has not been observed in the Confluence granites, hornblende is locally present in some of the larger, but geochemically similar, granitoid plutons of the Kohistan batholith (Petterson 1984). For example, the more basic parts of the Shirot granitoid, described further below, contain up to 20 % modal hornblende (Petterson 1984).

The observation that the elements TiO_2, Fe_2O_3, MgO, CaO, Na_2O, Al_2O_3, Sr, Y, Nb and Zr all behave compatibly with increasing silica content is interpreted as reflecting the fractionation of plagioclase which incorporates CaO, Na_2O and Sr, ilmenite which incorporates TiO_2, Fe_2O_3 and Nb and either biotite or hornblende which incorporate TiO_2, Fe_2O_3 and MgO, together with zircon which incorporates Zr and Y and apatite which incorporates LREE, CaO and Sr. Biotite and/or hornblende fractionation can be inferred from the behaviour of MgO. Assuming that biotite fractionation has occurred, the incompatible behaviour of K_2O, Rb and (to some extent) Ba, may be a reflection of the synchronous fractionation of hornblende (see below). K-feldspar fractionation does not appear to have been a significant process, contrary to the suggestion of Petterson (1984).

The parental magmas of the Confluence granites must be characterised by silica contents of < 66 wt. %. The presence of magmatic epidote suggests relatively high pressures of emplacement (Zen and Hammarstrom 1984) (see also Chapter 7), whilst the voluminous nature of the Confluence granites, and the high content of Ba, suggest that the granites were generated by the relatively high-temperature fluid-absent breakdown of biotite. In general, the geochemical characteristics of the Confluence granites suggests a source relatively enriched in LILE and LREE. The strontium isotope systematics of the undeformed Confluence granites (Chapter 7) indicate that the source was isotopically primitive, and free from the influence of evolved continental material.

The undeformed Confluence granites are either weakly peraluminous, or metaluminous, with (A/CNK) in the range 0.96-1.04. In terms of constraining the nature of the source area, such values are equivocal. For example, the majority of voluminous peraluminous magmas are generated by anatexis of weakly metaluminous or weakly peraluminous quartzofeldspathic sources, which may be either sedimentary (e.g. greywacke) or igneous (e.g. granitoid) (Miller 1985). Experimental studies show that relatively small volumes of peraluminous magmas may be generated by anatexis of a metaluminous mafic source (such as an amphibolite) at relatively low temperatures (< 1000 °C), or by the

fractionation of phases such as hornblende, sphene or epidote from a mafic magma (Cawthorn and Brown 1976; Heltz 1976; Miller 1985; Ellis and Thompson 1986; Zen 1986). However, according to Ellis and Thompson (1986), peraluminous melts may only be generated by the partial melting of a mafic source under fluid-present conditions, whilst the fractionation of diopside-normative phases such as hornblende from a mafic magma must take place under high P_{H_2O}. Dehydration (fluid-absent) melting of a mafic source generates marginally metaluminous melts (Ellis and Thompson 1986).

As noted by Petterson (1984), the Confluence granites display either a positive or flat europium anomaly despite the fact that the available evidence indicates that plagioclase fractionation has occurred. However, the positive europium anomaly is unlikely to be a reflection of the incorporation of cumulate or restitic feldspar, as suggested by Petterson (1984), given the relatively low silica content of some of the Confluence granites. According to Rutter and Wyllie (1988), during the partial melting of a mafic source, any k-feldspar initially present goes into the first, relatively evolved melt fractions. Similarly, during the fractionation of a mafic or intermediate magma, the k-feldspar will be a relative late phase to fractionate, and there is unlikely to be excess k-feldspar in the system. The observed positive europium anomaly may be at least partly a reflection of the presence of restitic hornblende in the source region (Hanson 1978). Such a source mineralogy would be also be consistent with the typical amphibolitic nature of the Kohistan arc crust, and the weakly peraluminous to metaluminous nature of the Confluence granites.

Evidence for the involvement of hornblende in the generation of the Confluence granites may come from an evaluation of REE contents. Hornblende has significantly larger distribution coefficients for the middle and heavy REE than the light REE . Consequently, the presence of restitic hornblende, or the fractionation of hornblende, leads to an increase in the LREE concentration and La/Yb ratio of the magma, but only a slight enrichment (or even a depletion) in the middle and heavy REE. In some cases, hornblende fractionation may produce characteristic, concave-up REE profiles (Romick et al. 1992). Hornblende distribution coefficients for the REE are also strongly dependent on melt composition,

temperature and pressure. For example, at constant pressure, distribution coefficients increase with decreasing temperature and increasing silica content, and thus intermediate magmas are more affected by hornblende fractionation than basic magmas. As a result, with increasing silica content, magmas that have been affected by hornblende fractionation show increasing La/Yb ratios (Romick et al. 1992).

The Confluence granites display remarkably steep REE profiles (La/Yb = 74-119) (Fig. 6.8A). HREE depletion may be caused by the presence of restitic garnet or zircon (Hanson 1978), but the lack of correlation between Zr and Y suggests that zircon fractionation cannot have played a significant role in controlling the REE behaviour of the Confluence granites. Where data for Dy, Ho and Er are available (Petterson 1984), the REE profiles for Confluence granites exhibit the concave-up shape that is characteristic of equilibrium between the melt and hornblende, rather than between melt and garnet (Fig. 6.8A). Although REE data are only available for seven samples of Confluence granite, La/Yb ratios have been plotted against silica in Fig. 6.13. The figure exhibits a large dispersion in La/Yb ratio, and between different Confluence sheets there is no correlation between La/Yb and silica. This may be a reflection of the important role played by accessory phases in controlling REE behaviour in granitic melts. Despite the lack of correlation on Fig. 6.13, the available REE data suggest that hornblende fractionation may have occurred in the formation of the Confluence granites, although modal hornblende is absent. Plagioclase is characterised by similar bulk distribution coefficients for the majority of the REE (with the exception of Eu), and therefore plagioclase fractionation will not significantly affect the La/Yb ratio (Romick et al. 1992). Thus, in the case of the Confluence granites, plagioclase fractionation occurring at a later stage than hornblende fractionation will have resulted in the differentiation of a more evolved magma containing higher abundances of all the REE (with the exception of Eu), a reduced positive or flat Eu anomaly, and an unaffected (high) La/Yb ratio.

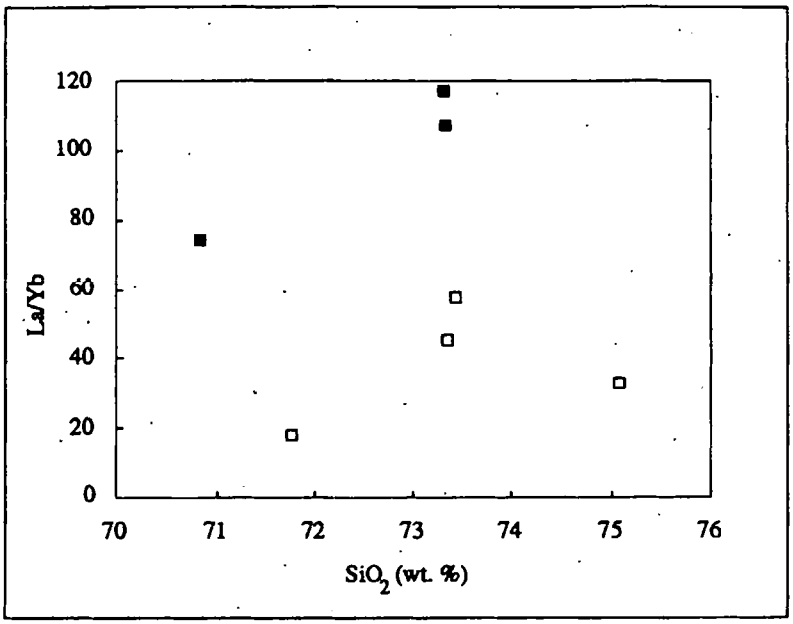

Fig. 6.13. Plot of La/Yb versus silica for the undeformed Confluence granites. ■ = data from this work (same sheet; G10); □ = data from Petterson (1984). A positive correlation suggests the involvment of hornblende in magma petrogenesis (Romick et al. 1992).

Hornblende fractionation may also account for some of the trends on the Harker variation diagrams described above. For example, hornblende fractionation would remove CaO, MgO and Fe_2O_3 from the melt, leaving the magma relatively enriched in K_2O and TiO_2. Significant hornblende fractionation may have also depleted the melt in Sr, together with the transition elements Ni, Cr, Co and Sc.

The Confluence granites have a broadly similar geochemical composition and age (see Chapter 7) to the relatively large, undeformed granitoids that were emplaced into the Kohistan batholith at 40-54 Ma, such as the 'main Shirot granitoid' exposed near Gilgit (Petterson and Windley 1985). The Shirot granitoid was intruded at 40 Ma, and is characterised by a silica content in the range 67-76 wt. %. This intrusion is characterised by slightly higher contents of MgO, Fe_2O_3 and TiO_2 than the Confluence granites, reflecting a greater modal proportion of biotite (~ 20 %). The average trace element compositions of the Confluence granites and the Shirot granitoid are compared in Fig. 6.7A. The Shirot granite displays slightly higher contents of Nb and Y, and a slightly lower content of Ba, than the Confluence granites, but the concentrations of most trace elements are similar. The Shirot

and Confluence granites also display similar fractionation trends, and similar, relatively steep REE profiles that are characterised by either flat or slightly positive europium anomalies. The initial strontium isotopic composition of the Shirot granitoid is 0.7044, whilst the initial ratio for the Confluence granites lies in the range 0.7045-0.7048, indicating that the different granites were generated in similar, isotopically primitive source regions.

The geochemical and isotopic similarity between the Confluence granites and larger granitoid plutons in the Kohistan batholith suggests that the Confluence granites are part of an important, volumetrically-significant phase of granite magmatism in the batholith.

6.7.3. Undeformed Parri Granites

As already described, the geochemical compositions of the Parri granites show some overlap with the Confluence granites, and this raises the question as to whether the two granite types may be genetically related. The evidence against any such relationship is as follows :

(i) Although the Parri and Confluence granites were intruded in close proximity, they form discrete intrusions that do not grade into each other.

(ii) Both field evidence and isotopic evidence suggests that the Parri granites are younger than the Confluence granites, and were generated in a source that was characterised by a slightly higher $^{87}Sr/^{86}Sr$ ratio (see Chapter 7).

Compared with the Confluence granites, the undeformed Parri granites have slightly higher (and more variable) Rb/Sr ratios (Fig. 6.10), and are slightly more peraluminous, with values of (A/CNK) in the range 1.0-1.1 (Appendix 3). Small volumes of granite with such a peraluminosity may be generated either by partial melting in a peraluminous source (Miller 1985), or by the fractionation of a diopside-normative phase from a metaluminous source (Zen 1986). The restricted silica range and the relatively high Rb/Sr ratios suggest

either extreme fractionation or small-degree partial melting of a mica-rich source (Harris and Inger 1992). The wide geochemical variation of the Parri granites suggests an origin by partial melting of a rather variable crustal source. The presence of spessartine-rich garnet on the liquidus of such peraluminous granites indicates moderate to shallow emplacement depths in the crust (Green 1977). The strontium isotope systematics of the undeformed Parri granites (Chapter 7) indicate that the source was isotopically primitive, and free from the influence of evolved continental material.

If generated by partial melting, the Rb/Sr ratios of ~ 1-2 would be consistent with either the fluid-absent melting of a feldspar-rich metasediment (such as a greywacke), or the melting of a pelite under conditions of low water activity (Harris and Inger 1992). Both processes would be consistent with the negative europium anomaly displayed by the Parri granites, since feldspar remains in the restite during fluid-absent or fluid-deficient melting.

The lower Ba abundances compared with the Confluence granites suggests that temperatures were insufficiently high to deplete biotite in the source. A lower temperature in the source is also supported by the more restricted range of silica displayed by the Parri granites. If the Confluence and Parri granites have equilibrated with zircon in their respective sources, the Zr abundances allow approximate temperatures of melts to be determined (Watson and Harrison 1983), which are calculated at 750 °C and 660 °C, respectively. However, since incongruent melting of biotite is implicated by the Ba abundances, at least for the Confluence granites, the actual melt temperatures are likely to have been higher (> 850 °C; Vielzeuf and Holloway 1988). Hence the melts were undersaturated in Zr, indicating rapid extraction from the source region. In general, this study confirms that the Parri granites were generated at shallower, cooler crustal levels than the Confluence granites, as suggested by Petterson and Windley (1991).

The two undeformed sheets of Parri granite from the Indus Confluence that have tonalitic compositions (G14 and G15) (Fig. 6.2) are characterised by relatively low contents of K_2O and Rb and relatively high contents of CaO and Na_2O (see Figs. 6.3, 6.4 and 6.6).

The unusual compositions of these samples cannot be related to the other Parri granites by simple magmatic processes, since there is no accompanying systematic variation in silica. However, the samples fall on the 26 Ma Rb-Sr isochron for the Parri granites (see Chapter 7), ruling out sub-solidus alteration as the cause of the variation. There is thus no clear explanation for the geochemical compositions of samples G14 and G15, although it can be tentatively suggested that the different Parri granites were generated at the same time by the partial melting of geochemically contrasting source compositions that were nevertheless characterised by similar strontium isotopic compositions.

6.7.4. Leucogranites of the Nanga Parbat-Haramosh Massif

Compared with the Parri granites, the NPHM leucogranites are characterised by extreme Rb/Sr ratios, whilst the presence of tourmaline in the majority of leucogranite dykes indicates a relatively high boron activity during crystallisation. Broadly speaking, the leucogranite dykes and sheets that contain significant modal proportions of tourmaline (2-10 %) are characterised by high Rb/Sr ratios (mostly in the range 7-27) and relatively low Ba (< 100 ppm), whilst the dykes that do not contain modal tourmaline, or contain insignificant tourmaline, are characterised by Rb/Sr ratios in the range 1-5, together with higher contents of Ba (> 100 ppm). Thus the tourmaline-rich leucogranites appear to be either extreme fractionates, or small-degree melt fractions derived under conditions of low water activity (Harris and Inger 1992).

The majority of Himalayan leucogranites are characterised by relatively homogenous and unfractionated major-element compositions, that fall close to the granite eutectic, implying near-perfect separation of minimum melt from a relatively homogenous source (Dietrich and Gansser 1981; Le Fort 1981; Deniel et al. 1987; Scaillet et al. 1990). However, as already descibed, the leucogranites of the NPHM display a range of geochemical compositions. In the haplogranite system, the majority of leucogranites define a broad trend towards increasing or decreasing k-feldspar at constant quartz/albite ratio. According to Johannes and Holtz (1990), this trend may be a reflection of crystallisation

during the ascent of water-underaturated magma. Alternatively, the trend may be caused by the incorporation of peritectic k-feldspar from the melt forming reaction (see section 6.7).

The Jutial granite displays some evidence for magmatic fractionation. The elements Fe_2O_3, TiO_2, Al_2O_3, K_2O, Rb, Zr, Th and U decrease slightly with increasing silica, whilst there are no distinct trends for CaO, Sr or Ba, suggesting control by biotite and accessory phases. The leucogranite dykes display a wider geochemical variation than the Jutial granite, and show no evidence for magmatic fractionation . There is no evidence that the geochemical variation is due to restite unmixing, since the leucogranites do not contain characteristic refractory phases such as sillimanite or almandine garnet, or strongly zoned plagioclase crystals. Furthermore, according to Clemens and Wall (1981), the entrainment of a high proportion of restite crystals is unlikely at small melt fractions. Restite unmixing may be an important process for relatively large melt fractions (e.g. 30-35 vol. %), when parts of the pelitic source region loose their structural rigidity and become gravitational unstable, with the result that both melt and restite ascend *en masse*.

Local sub-solidus deformation and fluid activity may have caused some of the observed geochemical dispersion. This is supported by the observation that those leucogranites that have been affected by shearing often plot away from the haplogranite minimum (Fig. 6.3). The leucogranites that are characterised by $SiO_2 > 75$ % have almost certainly been affected by varying degrees of sub-solidus fluid activity.

Of the three samples collected from the thick leucogranite sheet exposed at Rupal, two are characterised by relatively low contents of K_2O (see Table 6.2). These two samples are classified as tonalites in Fig. 6.2, and plot adjacent to quartz-albite tie-line in Fig. 6.3B. Accounting for such low potassium contents in these samples by magmatic processes is problematic, since potassium is the only element that has been significantly affected, and there is no evidence for fractionation trends (e.g. varying silica content) between the three samples. The Rupal granite may have been affected by sub-solidus alteration, causing variable leeching of potassium. The presence of cataclastic deformation features within the

granite lends some support to such a process. Interestingly, the whole-rock samples of the Rupal granite appear to be in strontium isotopic equilibrium (see Chapter 7), suggesting that the trace elements Rb and Sr have not been significantly affected by such a process.

In general, individual leucogranite dykes, or closely-spaced leucogranite dykes (e.g. M14 and M18 from Fairy Meadows), are characterised by distinct geochemical and isotopic compositions, whereas the total range in both geochemical and isotopic compositions for all the sampled leucogranites is large. This observation suggests that leucogranite geochemistry is mainly controlled by source composition, and therefore the geochemical variation displayed by the leucogranite dykes is mostly a reflection of the fact that the dykes were collected from widely-spaced localities across the NPHM. There is no observable relationship between leucogranite geochemistry and geographical or structural setting within the NPHM; for example, leucogranites exposed in the northern part of the NPHM show no consistent geochemical differences to those exposed in the southern part of the NPHM.

The peraluminous nature of the NPHM leucogranites (A/CNK = 1.0-1.3) suggests a mature metasedimentary source (Miller 1985). The petrogenesis of the NPHM leucogranites may be resolved by an evaluation of the covariation between the LILE, Rb, Sr and Ba. Fig. 6.14 displays a broad correlation between Rb/Sr and Ba content, for NPHM leucogranites characterised by Rb/Sr < 10 ppm. The trend in Fig. 6.14 could be the result of either the vapour-absent melting of a metasedimentary source by the incongruent melting of muscovite (Harris and Inger 1992), or about 30 % fractional crystallisation of k-feldspar.

Significant fractionation of k-feldspar in relatively minor, viscous magma bodies is considered unlikely, due both to the lack of density contrast between crystals and melt, and due to the fact that such bodies are likely to cool and crystallise relatively rapidly. The relatively high Rb/Sr ratios of the leucogranites (mostly > 3.5; Fig. 6.10) rules out an origin involving fluid-present melting (Harris et al. 1993). The available evidence therefore suggests that the NPHM leucogranites have been generated by the vapour-absent melting of a rather variable pelitic source. Such an interpretation is supported both by the negative

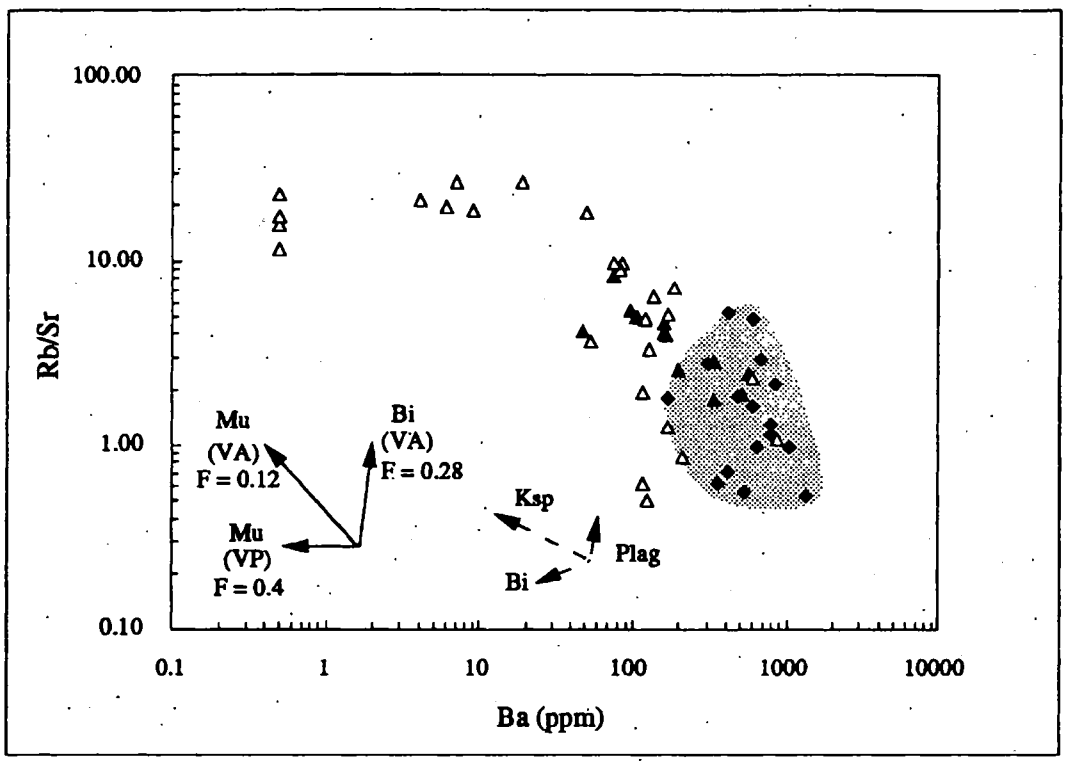

Fig. 6.14. Rb/Sr variation against Ba abundance for leucogranites and metamorphic rocks from the NPHM. ▲ = Jutial granite; △ = leucogranite dykes; ◆ = pelitic gneisses, outlined by the stippled field. Four samples containing no detectable Ba have been plotted on the log scale at Ba = 0.5 ppm. Solid vectors : modelled partial melting trends for the vapour-absent (VA) or vapour present (VP) melting of muscovite (Mu) or biotite (Bi). F = maximum melt fraction from an average pelite, using values of k_D for silicic melts from Henderson (1982). The length of the vectors is fixed by the protolith mineralogy. Dashed vectors : modelled change in magma composition with 10 % fractional crystallisation of k-feldspar (Ksp), plagioclase (Plag) and biotite (Bi).

europium anomalies displayed by the NPHM leucogranites, and their small volume. Fluid-absent melting generates melts that are able to leave their source region without crystallising, due to the positive slope of the vapour-absent solidus (Cann 1970), and therefore the cross-cutting, intrusive nature of the studied leucogranites is also consistent with their generation by fluid-absent melting. In contrast, the vapour-present generation of eutectic granites from a pelitic source is likely to generate relatively large melt fractions, causing a depletion of the source in feldspar, and leading to melts with relatively high Sr/Ba ratios and low Rb/Sr ratios (< 3.5) (Harris et al. 1993). Furthermore, for the NPHM leucogranites to have been produced by fluid-present melting would have required a copious fluid source during melting (Le Fort 1981), whilst the resulting melts would have had to have been sufficiently superheated to achieve the mobility required to leave the source region, conditions which are considered unlikely to have been present.

In general, the relatively evolved, tourmaline-rich leucogranites that are characterised by the highest Rb/Sr ratios, are most likely to be representative of the earliest melt fractions generated during fluid-absent muscovite breakdown. However, leucogranite dykes that are characterised by Rb/Sr > 10 cannot be modelled in terms of fluid-absent melting (Harris et al. 1993). Such leucogranites may not represent magmatic compositions, possibly due to interaction with sub-solidus fluids. This suggestion is supported by the poor correlation between K_2O and Rb observed for the NPHM leucogranites (Fig. 6.15).

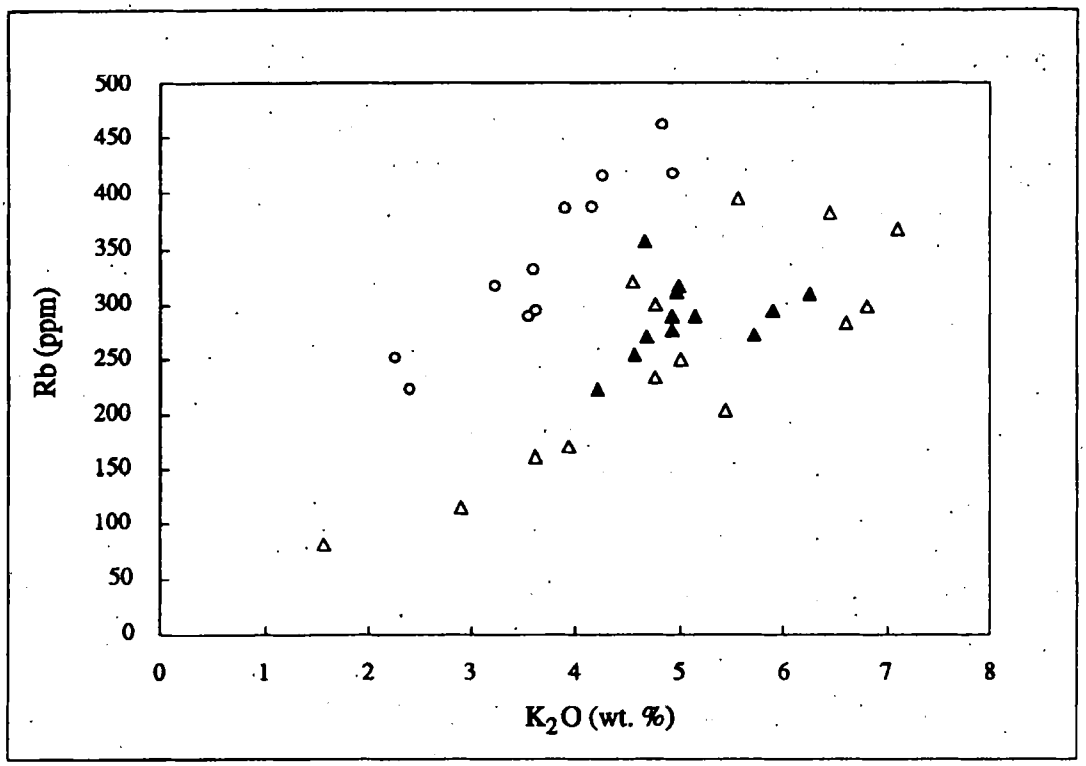

Fig. 6.15. Covariation between K_2O and Rb for the leucogranites of the NPHM. ▲ = Jutial granite; △ = leucogranite dykes with Rb/Sr < 10. ○ = leucogranite dykes characterised by Rb/Sr > 10.

The most fertile of the pelitic gneisses present in the NPHM, thought to be equivalent to the source rocks of the leucogranites, are characterised by relatively high contents of Ba and Sr, and a low content of Rb, compared with the leucogranites (see Fig. 6.7B). The relative concentrations of LILE in the pelitic gneisses compared with the leucogranites would be consistent with the generation of the leucogranites by fluid-absent melting, as described

above. The limited Rb enrichment in the leucogranites compared with the gneisses also suggests that muscovite, as opposed to biotite, was probably the dominant mica involved in the melting reactions (Harris and Inger 1992).

The leucogranites are also strongly depleted in the HFSE Zr, Hf, Y and the REE compared with their potential source rocks, an observation that has also been made for leucogranites in other parts of the Himalaya (Vidal et al. 1984; Le Fort et al. 1987). Ion microprobe studies indicate that the NPHM leucogranites contain significant amounts of inherited zircon (Zeitler et al. 1989), suggesting that, as expected, the behaviour of the HFSE and REE is controlled by accessory phase behaviour. It is unlikely that a garnet-bearing source has resulted in the strong Y and HREE depletion observed in the leucogranites, because at the inferred low temperatures of leucogranite formation (< 750 °C; Vielzeuf and Holloway 1988), diffusion of REE is too sluggish for equilibrium to be reached between melt and restite garnet (Harris and Inger 1992). Hence the depletion in HFSE and REE in the leucogranites reflects near-complete separation of melt from refractory phases in the source. Rapid extraction of melt from its source would also result in low concentrations of these elements due to disequilibrium between melt and accessory phases (Wickham 1987). Zr abundances in the leucogranites suggest that melt temperatures exceeded 700 °C if undersaturation of Zr occurred (Watson and Harrison 1983).

Chapter 7
Isotope Geology

The Tectonic Implications of Contrasting Granite Magmatism between the Kohistan Island Arc and the Nanga Parbat-Haramosh Massif, Pakistan Himalaya

Mark T. George, Nigel B. W. Harris and Robert W. H. Butler [1]

Department of Earth Sciences, Open University, Milton Keynes, MK7 6AA, UK
[1] Department of Earth Sciences, University of Leeds, Leeds, LS2 9JT, UK

In : Treloar P. J. and Searle M. K. (eds), Himalayan Tectonics Geological Society London Special Publication, No 74, pp.

Authors note : Since publication, new isotope data have become available which have been incorporated into this chapter. These include seven new strontium isotope analyses and twelve new neodymium analyses. However, the original conclusions that were made still hold, and the bulk of the text has not been altered.

7.1. Abstract

In northern Pakistan, an integrated structural and geochemical study across the contact between the Cretaceous-Tertiary Kohistan island arc and Indian crust of the Nanga Parbat-Haramosh massif (NPHM) has identified strongly contrasting source regions contributing to post-50 Ma magmatism, which constrains the tectonic evolution of the region. Nd-model ages of Tertiary intrusives increase dramatically across the contact from ~700 Ma in the Kohistan terrane to ~2500 Ma in the NPHM.

Following collision between the Indian continent and the Kohistan island arc terrane at ~50 Ma, biotite granite sheets (Confluence granites) were emplaced into the Kohistan batholith at 50-30 Ma, followed by muscovite granite sheets (Parri granites) at ~26 Ma. These are geochemically distinct, with the Confluence granites comprising a range of granitic compositions with high Sr and Ba abundances and the Parri granites forming granite sheets enriched in Rb. Undeformed granites in both suites have $(^{87}Sr/^{86}Sr)_i$ in the range 0.7045-0.7054 and $\varepsilon_{Nd}(T)$ of +0.1 to +2.7, suggesting that both groups may be derived from juvenile arc sources. Detailed structural studies verify that the Kohistan granite sheets postdate the initial collision of the northern Kohistan terrane with the Indian continent, but are pre- or syntectonic with respect to underthrusting of the Indian continent below the Kohistan arc. These results, together with the isotopic evidence from the undeformed granite sheets, suggest that significant underthrusting of northern Kohistan by the Indian continental crust could not have occurred until after 26 Ma.

Along the western margin of the NPHM, deformed granite sheets show a marked increase in $(^{87}Sr/^{86}Sr)_i$ (0.7075-0.7784), with decreased $\varepsilon_{Nd}(T)$ (-13 to -26). These trends are thought to be due to a combination of sub-solidus fluid infiltration and assimilation of crustal material, with fluids or material derived from the adjacent, isotopically evolved NPHM crust.

The NPHM (Indian continent) has been intruded by a series of tourmaline leucogranite

dykes and plutons at 2-12 Ma. These intrusives have trace-element signatures consistent with a generation by vapour-absent melting of a pelitic source. Sr-Nd isotope systematics indicate derivation from metasediments such as are currently exposed in the basement rocks of the massif, although melting at the present exposure level is generally precluded by subsolidus metamorphic grades in the country rock. Extreme heterogeneities in radiogenic Sr ($(^{87}Sr/^{86}Sr)_i > 0.9$) are observed in leucogranite dykes from the Liachar thrust zone, probably indicating subsolidus fluid infiltration. In general the NPHM leucogranites result from rapid exhumation of metasediments characterised by unusually high heat productivity.

7.2. Introduction

Collision orogenesis commonly involves the stacking of lithospheric levels through large-scale thrusting. Charting the juxtaposition of these different materials during orogenesis is of fundamental importance in understanding how collision belts evolve. Where available, geophysical methods, particularly deep seismic reflection profiling, provide insights on the modern geometry of mountain belts. An alternative line of evidence comes from the chemistry and chronology of syn-orogenic magmatism. The variation in Sr or Nd isotopic ratios in granitoids across terrane boundaries can provide critical information on the nature of the crustal stack at depth (Geist et al. 1988).

In this contribution we examine the Tertiary magmatism on the western flank of the Nanga Parbat massif, along the contact between the Kohistan island arc and the Indian subcontinent (Fig. 7.1). Granites which post-date the Eocene collision between India and Eurasia occur on either side of this zone, and provide contrasting geochemical and isotopic signatures that can be related to the varying source regions available in the two terranes during post-collisional tectonics. Consequently, an evaluation of the timing and geochemistry of magmatism combined with detailed structural studies of the relationship between intrusion and deformation, can be used as evidence in reconstructing the tectono-metamorphic evolution of the suture zone.

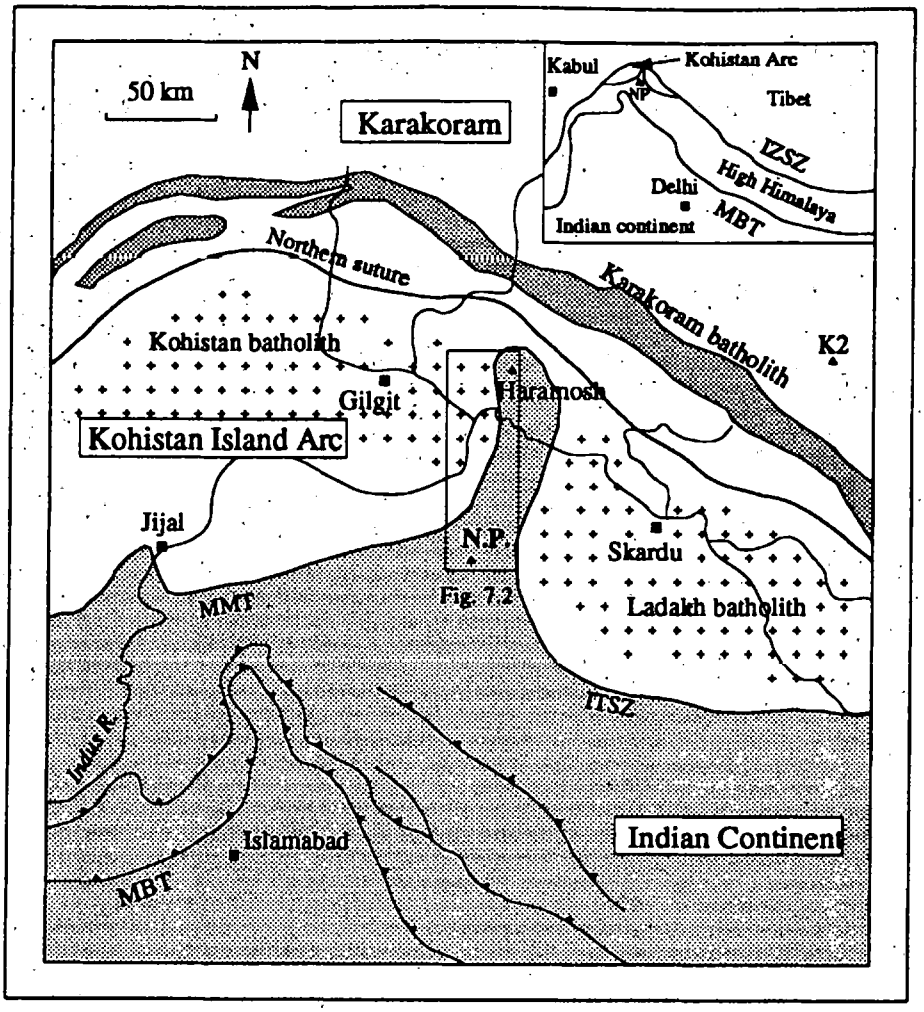

Fig. 7.1. Sketch map of the NW Himalaya, showing positions of the major tectonic terrancs. MMT = Main Mantle Thrust; MBT = Main Boundary Thrust; N.P. = Nanga Parbat. Inset shows the location of the Kohistan arc in the Himalayan chain (ITSZ = Indus Tsangpo suture zone).

7.3. Regional structure of the Tertiary suture zone

In the Himalayas the principal Tertiary (Indus-Tsangpo) suture between the Indian subcontinent in the south and Eurasia in the north appears readily traceable as a major tectonic break (Fig. 7.1), decorated by small remnants of ophiolitic material (Le Fort 1989). Plate-tectonic reconstructions of the opening of the Indian Ocean and palaeomagnetic data led Patriat and Achache (1984) to conclude that collision occurred between *ca.* 55 and 52 Ma. Besse et al. (1984) conclude from palaeomagnetic data in the eastern Himalayas that suturing occurred at 53-47 Ma, whereas in the western Himalayas collision has been dated by a change in sedimentation from marine to continental environments in early-mid Eocene times between 44 and 55 Ma (Le Fort 1989).

The tectonic evolution of the western Himalayas is complicated by the presence of the Cretaceous-Tertiary Kohistan-Ladakh island arc terrane (Tahirkheli et al. 1979; Honegger et al. 1982), thought to have sutured to Eurasia (Karakoram block) in the late Cretaceous (Klootwijk et al. 1979; Pudsey 1986). The northern part of the arc is dominated by a range of calcalkaline intrusives dated at ~100-40 Ma, related to the northwards subduction of Tethyan oceanic lithosphere and representing the westward continuation of the Trans-Himalayan batholith (Petterson and Windley 1985; Honegger et al. 1982). Along the southern margin of the Kohistan arc, the Indus-Tsangpo suture zone has been traced as the Main Mantle Thrust (MMT). This structure, which carries peridotites and high pressure granulites of the Kohistan island arc terrane in its hanging-wall, was defined by Tahirkheli et al. (1979) along the Indus valley in the Hazara area, near the town of Jijal (Fig. 7.1). The adjacent footwall rocks derived from the Indian continent have been stacked up into a post-collisional thrust belt (Coward et al. 1988). These metamorphic rocks had cooled through the blocking temperature for Ar in hornblende (*ca.* 500°C) by 39 Ma (Treloar et al. 1989b). These and other isotopic data are consistent with suturing between the Kohistan terrane and the Indian continent at Hazara, with displacements occurring on the MMT, at ~ 50 Ma.

Since the pioneering work of Tahirkheli and colleagues (Tahirkheli 1979 a & b) the MMT has been traced to the NE, from its type area at Hazara, to define the western flank of the NPHM. This represents the northernmost outcrops of Indian continental rocks. The eastern boundary of the massif can be traced in Ladakh to link with the main trace of the Indus-Tsangpo suture (Fig. 7.1; Tahirkheli et al. 1979). The northern contact between the Nanga Parbat-Haramosh Massif (NPHM) and the Kohistan terrane has now been identified (Butler et al. 1992) thus linking the map traces of the MMT with the Indus-Tsangpo suture. On both sides of the massif the primary contact is a high strain zone of ductile deformation preserving structures that developed under amphibolite-facies conditions (Treloar et al. 1991). It is tempting to link these ductile structures in time to those at the MMT at Hazara. There are however, strong indications that this temporal correlation is not appropriate.

Butler and Prior (1988a) studied the kinematics of the contact between the Kohistan arc and the NPHM in the Sassi area (Fig. 7.2). They found evidence for an early, penetrative deformation marked by top to the SSE thrusting under amphibolite facies conditions. As this is consistent with the relative motions across the suture predicted by plate reconstructions, they inferred this ductile structure to be the MMT. However, Butler and Prior (1988a) recognise that, as upper arc rocks are juxtaposed against the Indian continent, this segment of the 'MMT' cannot be the primary suture, but instead may be a form of break-back thrust. Regardless of the nature of the early ductile contact, it has certainly been modified by later structures developed under decreasing metamorphic conditions. Detailed structural mapping on the western margin of the massif at Sassi has indicated that younger movements in this area are dominated by dextral-transtension under greenschist-facies conditions, reflecting uplift of the NPHM relative to the Kohistan arc (see also Butler et al. 1989). The present structure of the contact between the Kohistan arc and the NPHM is thus very different to the type-section of the MMT seen in the Hazara area.

Further south in the Nanga Parbat area, the Liachar shear zone (Fig. 7.2) carries rocks of the NPHM north-westwards, back over the Kohistan arc. This recently active shear zone operated from amphibolite-facies conditions to the present surface, and probably accommodated substantial amounts of uplift of the NPHM (Butler and Prior 1988b).

7.4. Granite Sheets of the Kohistan Arc

7.4.1. Field Relations and Petrography

Late stage magmatism within the Kohistan batholith has been studied near to the eastern edge of the Kohistan arc (see Fig. 7.2), where swarms of granite sheets, 0.5-10 m thick, locally make up to 30 % of exposure. Away from the contact between the Kohistan arc and the NPHM, the sheets are undeformed and sharply cross-cut the country rocks, which consist of semi-pelites and metagabbros at epidote-amphibolite grade. On the basis of mineralogy and geochemistry, Petterson and Windley (1985) divided the granites

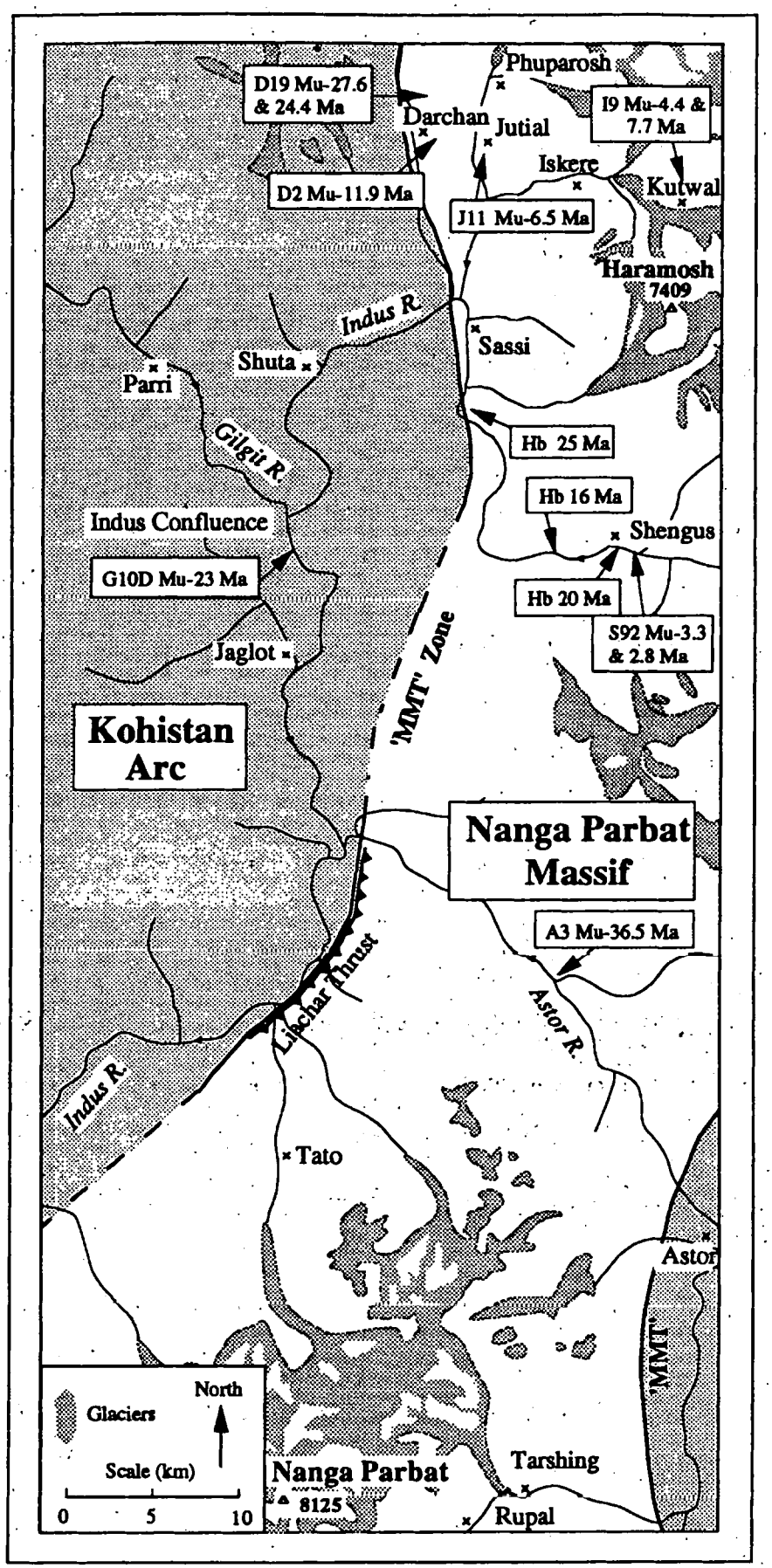

Fig. 7.2. Sketch map of the NPHM region, showing the sample localities for Rb-Sr muscovite (Mu) (Table 7.3) and ^{40}Ar-^{39}Ar hornblende (Hb) (Zeitler et al. 1989) dating.

into the 'Indus Confluence Acid Sheets' and the 'Parri Acid Sheets', the former having biotite as the dominant mica, whereas for Parri granites muscovite predominates. This study has enlarged the geochemical and isotopic database of the granites by sampling a greater number of different sheets, particularly necessary for the Parri granites which had, until now, only been studied at one locality.

The Confluence granites constitute about 70 % of the granite exposure in the studied area. They form medium grained, two-mica granites occurring both as dykes and more massive plugs up to 50 m thick. The mineral assemblage consists of quartz (25-50 %), plagioclase (10-30 %), alkali feldspar (20-40 %), biotite (2-20 %), ± muscovite (< 5 %), ± epidote or clinozoisite (1-8 %), sometimes enclosed by biotite. Myrmekitic textures are common. Accessory minerals include apatite, magnetite and occasionally sphene, with rare garnet and zircon.

The Parri granite sheets are mineralogically more variable, and have been observed to cross-cut the Confluence granites. The diagnostic mineral assemblage of Parri granites is quartz (20-50 %), plagioclase (10-30 %), alkali feldspar (20-50 %), muscovite (6-20 %), ± biotite (1-4 %) ± garnet (1-4 %), with subordinate and similar accessory mineral contents to the Confluence granites. The Parri granites are leucogranites, but to avoid confusion with those granites intruding the NPHM, are referred to by their type locality.

7.4.2. Major and Trace Element Geochemistry

The main geochemical features of the Confluence and Parri sheets have been detailed by Petterson (1984) and are summarized below. The Confluence granites are peraluminous with SiO_2 varying between 64-75 %: antipathetic trends between Mg, Fe, Ti, Mn and Ca and silica can be linked to fractionation of micas and feldspars during crystallisation. The Parri granites are also peraluminous but are uniformly siliceous ($SiO_2 > 71$ %), although Petterson (1984) noted some fractionation trends within a single intrusion.

Average trace-element abundances (Table 7.1) are plotted for both suites and are found to be distinct (Fig. 7.3A). The Confluence granites have low Rb and high Ba compared to the Parri granites. High-field-strength-element (HFSE) abundances are similar, although Confluence granites display a strong depletion in Ta and Nb and are more depleted in Y and HREE. The two suites of granite sheets can be most easily distinguished on a Rb versus Sr plot (Fig. 7.4), where Confluence granites are characterised by low Rb/Sr (0.01-0.4) compared to Parri granites that show higher, and more variable Rb/Sr ratios (generally 1-2).

	Confluence granites *n=29*	Parri granites *n=13*	Leucogranite dykes *n=25*	Jutial granite *n=12*
SiO_2	72.35	74.04	74.41	73.86
TiO_2	0.18	0.08	0.05	0.10
Al_2O_3	15.39	15.10	14.79	14.69
Fe_2O_3 (1)	1.34	0.81	0.65	0.97
MnO	0.02	0.05	0.02	0.01
MgO	0.37	0.16	0.10	0.14
CaO	2.38	1.53	1.02	1.21
Na_2O	4.28	4.34	4.11	3.55
K_2O	3.37	3.66	4.39	5.08
P_2O_5	0.06	0.03	0.07	0.04
LOI	0.42	0.57	0.54	0.61
Total	**100.17**	**100.37**	**100.14**	**100.26**
Rb	70	163	294	288
Sr	472	148	59	87
Y	4	9	26	11
Zr	89	53	36	46
Nb	4	10	12	11
Ba	951	287	128	230
Pb	27	61	60	75
Th	7	6	12	21
U	1	4	12	19
Ta	0.17	2.4	-	1.3
Hf	3.1	2.9	-	1.7
Ce	46.9	40.9	-	55.4
Sm	2.3	3	-	4
Yb	0.3	1	-	0.9

Table 7.1. Average whole-rock major and trace element abundances of granites from the NPHM and Kohistan. (1) = all Fe calculated as Fe_2O_3. Ta, Hf, Ce and Yb were analysed by instrumental neutron activation; all other elements by XRF. n = number of analyses.

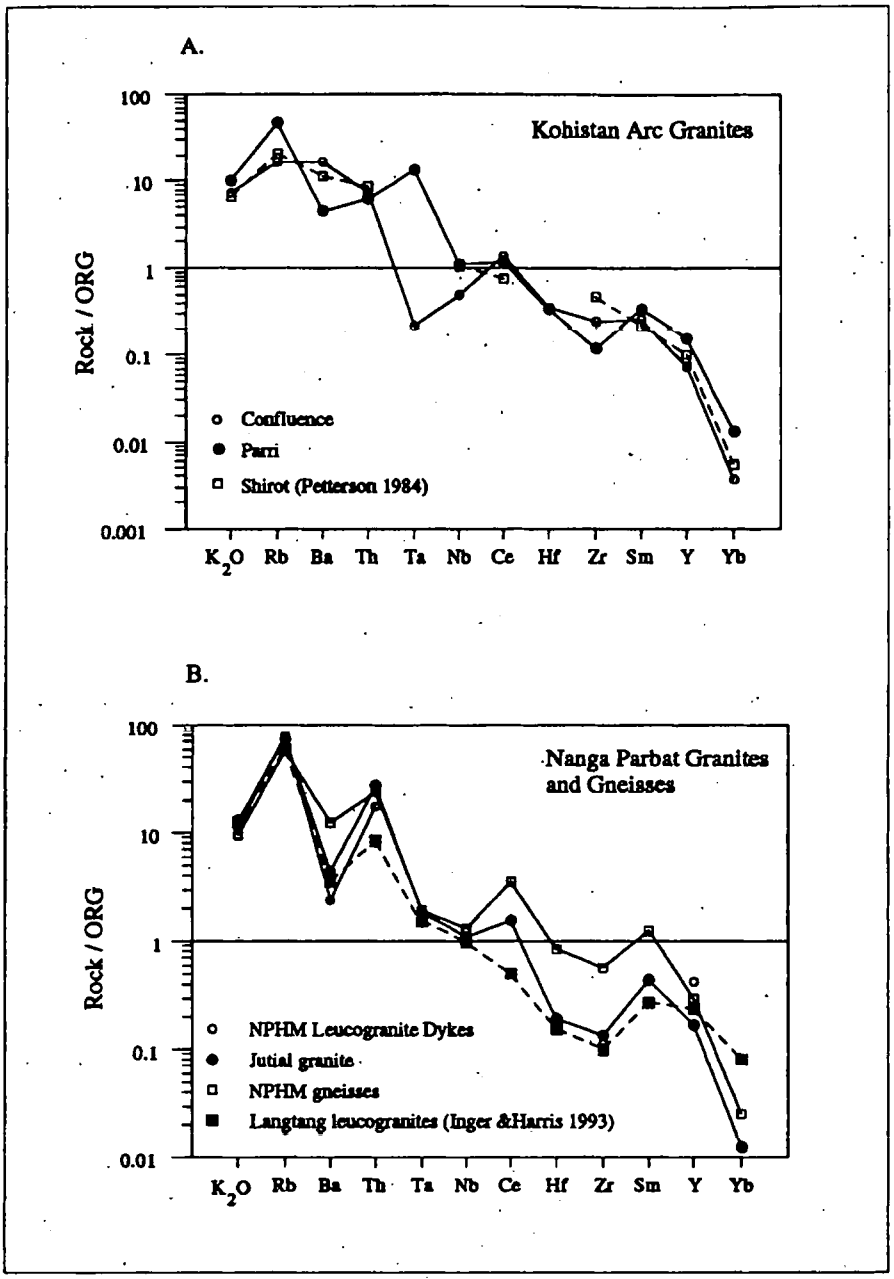

Fig. 7.3. Variations in trace-element abundances, normalised against Ocean Ridge Granite (Pearce et al. 1984) for (A) Kohistan granites, (B) Leucogranites and gneisses of the NPHM. The Langtang leucogranite is the tourmaline-present sub-type (Inger and Harris 1993).

The Confluence granites have broadly similar geochemical compositions to relatively large, evolved plutons, such as the main Shirot granitoid, which intruded the Kohistan batholith between 40 and 54 Ma (Petterson and Windley 1985). The Shirot granitoid shows a wide range in geochemical composition, and was probably generated by the fractionation of a magma derived from a variably-metasomatised mantle source (Petterson and Windley 1991). Detailed petrogenetic modelling is beyond the scope of this study, but fractionation trends suggest that the Confluence granites may share a similar petrogenesis to plutons such

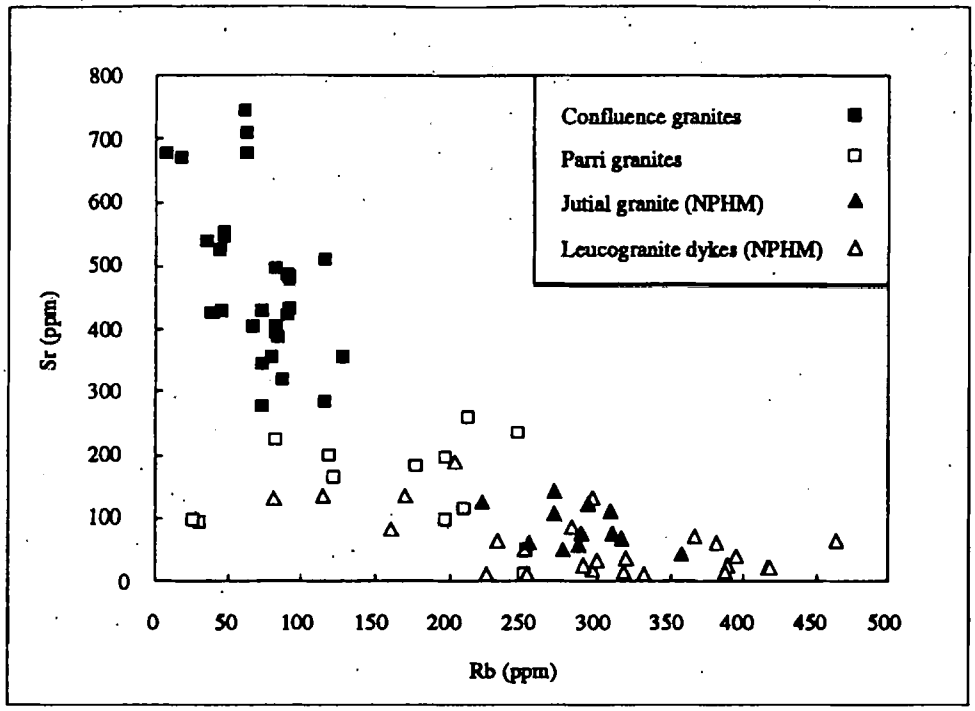

Fig. 7.4. Covariation between Rb and Sr abundances observed in granites from the Kohistan arc and the NPHM.

as the Shirot granitoid. Alternatively, as suggested by Petterson and Windley (1991), the fractionation trends displayed by the Confluence granites may result from varying degrees of partial melting of juvenile, possibly crystalline, arc crust. In either case, the high Ba (up to 2000 ppm) of the Confluence granites would imply that temperatures in the source region were sufficiently high to exhaust biotite, whilst, following the reasoning of Zen and Hammarstrom (1984), the presence of magmatic epidote would suggest that pressures in the source region were also moderately high.

The high Rb/Sr ratios of the Parri granites (Fig. 7.4) suggest either extreme fractionation or small-degree partial melting of a mica-rich source (Harris and Inger 1992). It is probable that the Parri granites were derived at shallower, cooler crustal levels, such that mica was retained in the protolith, thus limiting the Ba abundance in the melt. Although the metasediments exposed in the Gilgit valley would be a potential source for the Parri granites, their epidote-amphibolite grade precludes partial melting of these rocks at the present exposure level.

7.4.3. Age of intrusion

Field evidence shows that the Parri granites are younger than the Confluence granites. Petterson and Windley (1985) obtained poorly constrained, whole-rock errorchrons for a Confluence and a Parri granite yielding ages of 34 ± 14 Ma (2σ) (MSWD = 0.74, $(^{87}Sr/^{86}Sr)_i$ = 0.7045) and 29 ± 8 Ma (MSWD = 0.2, $(^{87}Sr/^{86}Sr)_i$ = 0.7052) respectively. Whole-rock data from undeformed and deformed granites together (this study, Table 7.2, Fig. 7.5) do not define an isochron for either Confluence or Parri suites. However, the data from the four undeformed Parri granites, collected from widely separated localities, do define an errorchron yielding an age of 26.8 ± 2.6 Ma (MSWD = 15, $(^{87}Sr/^{86}Sr)_i$ = 0.7054). These data can be combined with the seven isotopic ratios from the Parri granite analysed by Petterson (1984), which yields an improved errorchron indicating an age of 26.2 ± 1.2 Ma (MSWD = 5.9, $(^{87}Sr/^{86}Sr)_i$ = 0.7054).

Petterson (1984) was unable to date a granite exposed 3 km south of the Indus Confluence (the Sainallah leucogranite) due to the restricted range in Rb/Sr ratios for this granite. Sr-isotope data from an adjacent sheet at Jaglot (this study) can be combined with the Sainallah data to define a ten point errorchron with an age of 49.1 ± 11 Ma (MSWD = 11; $(^{87}Sr/^{86}Sr)_i$ = 0.70485 ± 4). Whilst the age has significant uncertainties, it does suggest that proximal Confluence granites may be co-eval. On the basis of present whole-rock data we can conclude that the Confluence sheets were emplaced at 50-30 Ma, whereas the Parri sheets were intruded at ~26 Ma.

The time of granite emplacement is further constrained by a range of cooling ages from granites and metamorphic rocks in the arc (Treloar et al. 1989b; Zeitler et al. 1989). K-Ar and ^{40}Ar-^{39}Ar studies indicate closure for Ar at 26-38 Ma for hornblende, 18-36 Ma for biotite and 18-21 Ma for muscovite. A muscovite Rb-Sr age from the Jaglot granite of 23 ± 1 Ma (Table 7.3) places a lower limit on the time of granite emplacement, and the coincidence of ages in the granites and their country rocks indicates that the granites were intruded into relatively warm country rocks which had not yet cooled below the blocking

Sample	Location	Rb/Sr	$^{87}Rb/^{86}Sr$	$^{87}Sr/^{86}Sr$	2σ	$(^{87}Sr/^{86}Sr)_{30}$
Confluence Granites						
G10-A [1]	Jaglot	0.21	0.62	0.70535	2	0.70509
G10-D [1]	Jaglot	0.19	0.55	0.70521	2	0.70498
G10-E [1]	Jaglot	0.08	0.24	0.70501	2	0.70491
G10-F [1]	Jaglot	0.21	0.61	0.70512	6	0.70486
G10-G [1]	Jaglot	0.17	0.48	0.70511	5	0.70491
G10-H [1]	Jaglot	0.09	0.27	0.70501	2	0.70503
S95	L. Darchan	0.23	0.65	0.70488	3	0.70460
S6G	Indus conf.	0.22	0.64	0.70480	2	0.70453
G18	Indus conf.	0.08	0.25	0.70476	2	0.70466
S81 *	Shahbatot	0.27	0.77	0.70786	2	0.70753
D17 *	W. Darchan	0.09	0.26	0.70812	2	0.70801
S67 *	Shahbatot	0.06	0.19	0.70846	2	0.70838
S75 * [2]	Shahbatot	0.01	0.03	0.70969	2	0.70967
S76 * [2]	Shahbatot	0.03	0.08	0.70820	2	0.70816
Parri Granites						
G2	Gilgit valley	2.03	5.87	0.70752	2	0.70502
G3	Gilgit valley	19.31	55.80	0.72832	2	0.70455
G14	Indus conf.	0.33	0.96	0.70581	2	0.70540
G15	Indus conf.	0.27	0.77	0.70627	2	0.70594
G23	Shuta	5.04	14.57	0.71076	2	0.70456
S97 *	L. Darchan	0.82	2.38	0.73546	2	0.73445
G43 *	Sassi	1.86	5.37	0.76032	2	0.75803
G35 * [3]	Sassi	1.02	2.95	0.72505	2	0.72379
G36 * [3]	Sassi	0.74	2.14	0.70838	9	0.70747
G48 *	Sassi	0.98	2.82	0.75640	5	0.75520
S66 *	Shahbatot	1.89	5.45	0.75842	5	0.75610
D5 *	W. Darchan	0.60	1.74	0.72350	2	0.72276
G30 *	Sassi	0.37	1.06	0.74051	2	0.74006

Table 7.2. Whole rock Sr-Isotopic Data for the Kohistan Granites. Rb and Sr data from XRF. $^{87}Sr/^{86}Sr$ ratio determinations were made on a Finnigan MAT 261 multi-collector. $(^{87}Sr/^{86}Sr)_i$ calculated for an age of 30 Ma. * = deformed granites; [1], [2], [3] = samples from the same granite sheets. L. Darchan = lower Darchan; Indus conf. = Indus confluence; L. Darchan = lower Darchan.

temperature (500-550 °C) for Sr in muscovite (Purdy and Jager 1976; Cliff 1985).

7.4.4. Sr and Nd Isotope systematics

Sr-isotope data from fourteen Confluence granite samples, representing eight separate sheets, and thirteen Parri granite samples, from twelve separate sheets, are shown in Table 7.2. The majority of the undeformed samples were collected from the Gilgit valley-Indus confluence area, whilst all the deformed samples come from within the ductile shear zone bordering the NPHM (MMT of Butler and Prior 1988a). The isotopic composition of each suite is variable, with $(^{87}Sr/^{86}Sr)_{30}$ in the range 0.704-0.710 for the Confluence

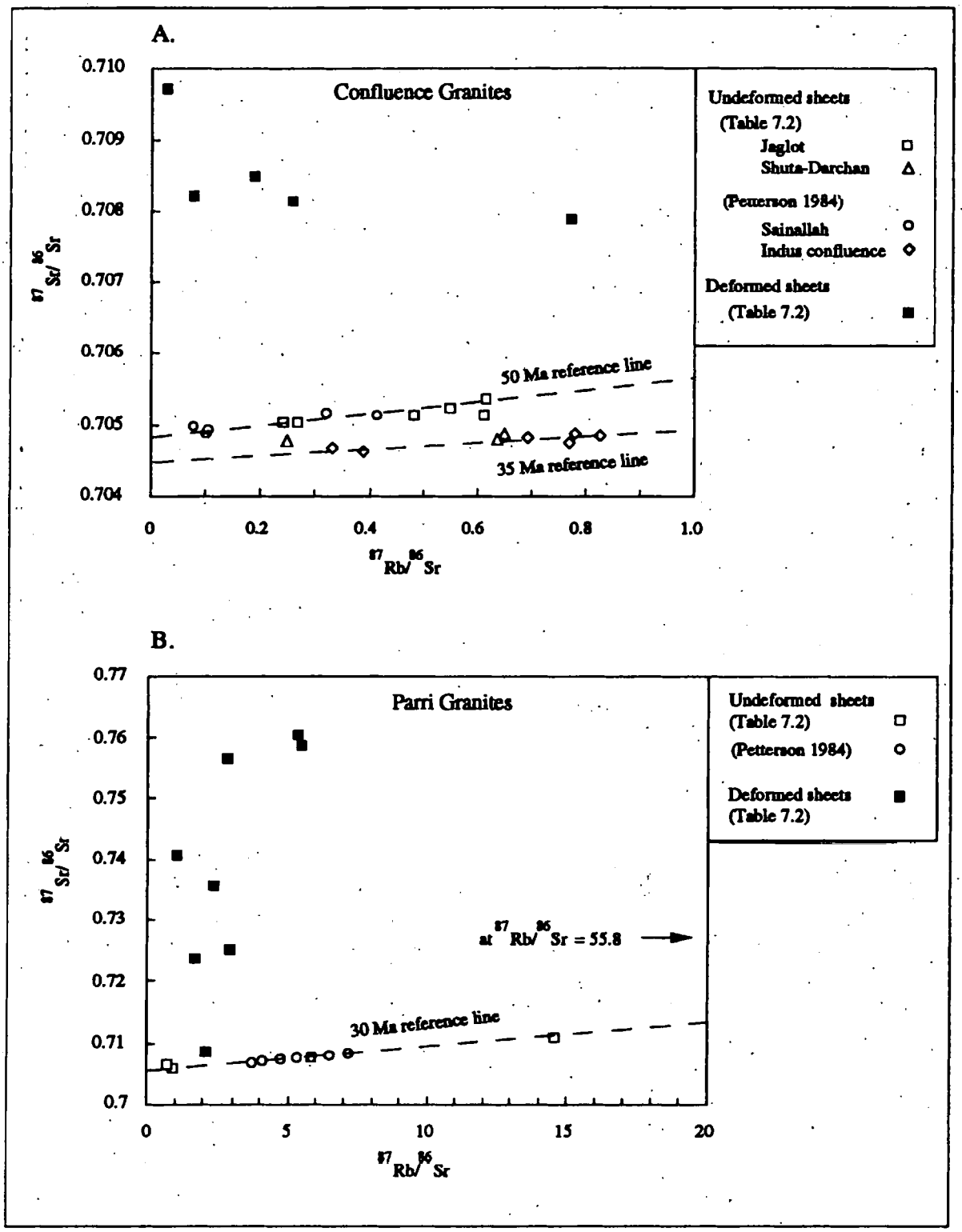

Fig. 7.5. Rb-Sr isochron diagrams for granite sheets from the Kohistan arc. (A) Confluence granites; (B) Parri granites. The Jaglot and Sainallah (Petterson 1884) sheets (from 3 km south of the Indus confluence) have yielded a poorly-constrained age of 49 ± 11 Ma. The undeformed Parri sheets have yielded an age of 26 ± 1 Ma.

Sample and Lithology	Rb(ppm)	Sr(ppm)	Rb/Sr	$^{87}Rb/^{86}Sr$	$^{87}Sr/^{86}Sr$	2σ	Age (Ma)
Kohistan Arc							
Jaglot Granite							
G10-D WR	92	482	0.19	0.55	0.70521	2	
G10-D-M	250	106	2.35	6.79	0.70725	2	23.0 ± 1.0
NPHM							
Jutial Granite							
J11 WR	309	110	2.81	8.12	0.88438	3	
J11-M	603	9.43	64.0	184.9	0.90010	6	6.5 ± 0.04
Leucogranite Dyke							
S92 WR	389	25	15.6	44.97	0.83015	2	
S92-M	865	3.14	275	796.5	0.86564	6	3.3 ± 0.02
S92-M-dup	928	3.37	275	795.2	0.86019	5	2.8 ± 0.02
Orthogneiss							
D2 WR	227	81.5	2.79	8.05	0.96392	3	
D2-M	409	4.56	90.0	260.0	1.00792	9	11.9 ± 0.08
Paragneiss							
I9 WR	109	151	0.72	2.08	0.76613	4	
I9-M	249	17.0	14.6	42.26	0.76868	7	4.4 ± 0.78
I9-M-dup	311	21.9	14.2	41.10	0.77043	3	7.7 ± 0.08
Paragneiss							
A3 WR	375	77.4	4.84	14.00	0.83808	2	
A3-M	967	23.3	41.4	119.7	0.89377	12	36.3 ± 0.3
Paragneiss							
D19 WR	175	181	0.97	2.79	0.77988	2	
D19-M	344	86.7	3.98	11.49	0.78333	3	27.6 ± 0.3
D19-M dup	356	85.3	4.17	12.05	0.78313	11	24.4 ± 0.5

Table 7.3. Sr-isotope data for muscovite samples. The derived ages were calculated by regression to the whole-rocks. The Rb and Sr concentrations in the muscovites are by isotope dilution and the Rb and Sr concentrations in the whole-rocks are by XRF. All errors on the ages were calculated using $^{87}Rb/^{87}Sr \pm 2$ %, and are to one sigma. WR = Whole-rock; M = muscovite; dup = duplicate dissolution and analysis.

granites and 0.705-0.758 for the Parri granites.

The lack of isotopic homogenisation within whole-rock samples of peraluminous granites is well-documented and is generally attributed either to isotopically distinct source regions, coupled with lack of homogenisation in viscous intrusions (Deniel et al. 1987) or to subsolidus fluid infiltration (Cliff et al. 1991). It is clear from Fig. 7.5 that the deformed Confluence and Parri granites show an enrichment in radiogenic Sr compared with their undeformed counterparts outside the shear zone. For the Parri granites for example, undeformed samples are characterised by $(^{87}Sr/^{86}Sr)_{30} < 0.705$, but this ratio rises up to 0.758 in deformed sheets near Sassi. Individual Parri and Confluence granite sheets in the shear zone also show marked isotopic disequilibrium on the whole-rock scale. This is demonstrated by samples S75 and S76, which were collected about 20 metres apart from separate, two-metre thick boudins of the same Confluence sheet, and samples G35 and G36,

which were collected at a one-metre spacing from the same Parri sheet.

Undeformed Parri granites from widely separated localities define an isochron with $(^{87}Sr/^{86}Sr)_i = 0.7054$, as described above, showing that these granite sheets are co-eval. Whole-rock samples of undeformed Confluence granites show slight isotopic heterogeneities, both between granite sheets and within the same intrusion (e.g. G10). Such fine scale heterogeneities may reflect processes occurring just prior to crystallisation, such as wall-rock contamination or sub-solidus fluid interaction. The Confluence granites yield $(^{87}Sr/^{86}Sr)_i$ of 0.7045 and 0.7048. The initial-Sr isotopic ratios of the undeformed Confluence and Parri granites are low compared with Miocene leucogranites from the Central Himalayas, derived from metapelites (Deniel et al. 1987; Inger and Harris 1993), indicating less radiogenic source regions for the former.

Further constraints on the nature of the source of the Kohistan granites are provided by Nd isotopic data obtained from four samples of Confluence granite and six samples of Parri granite (Table 7.4). The Confluence granites are characterised by $\varepsilon_{Nd}(T)$ in the range + 0.7 to + 1.3, and two undeformed Parri granites have $\varepsilon_{Nd}(T) \sim +0.2$ and + 2.7. In contrast, four deformed Parri granites from the western margin of the NPHM have $\varepsilon_{Nd}(T) \sim -13$ to -26. This depletion in $^{143}Nd/^{144}Nd$ for granites within the shear zone is clearly coupled with an enrichment in $^{87}Sr/^{86}Sr$, as can be seen from an $\varepsilon_{Nd}(T)$-$\varepsilon_{Sr}(T)$ plot (Fig. 7.6), in which these data are expressed relative to the isotope ratios of bulk earth at the approximate time of granite formation. The undeformed Confluence and Parri granites plot within the field defined by arc-derived magmas from Kohistan and Ladakh (Allègre and Ben Othman 1980; Petterson et al. 1993). Both Nd and Sr data are consistent with a juvenile source for the undeformed Kohistan granites, similar to the source of the Kohistan-Ladakh batholith.

The age of igneous protoliths can be constrained by Nd model ages (Table 7.4) that represent the time passed since a sample, or its crustal protolith, was extracted from a mantle reservoir. The underlying assumption for such ages is that Sm/Nd has not fractionated during the crustal residency of the source regions. The interpretation of such ages has been

	Location	Sm/Nd	$^{147}Sm/^{143}Nd$	$^{143}Nd/^{144}Nd$	2σ	$^{143}Nd/^{144}Nd_i$	ε_{Sr} (T)	ε_{Nd} (T)	T^{Nd}_{DM} (Ga)
Kohistan									
Confluence granites									
G10-D	Jaglot	0.15	0.087	0.51267	1	0.51265	4.5	1.0	0.7
G10-H	Jaglot	0.15	0.089	0.51266	1	0.51265	3.3	0.9	0.7
S6-G	Indus conf.	n/d	-	0.51269	1	0.51267	-1.9	1.3	0.6
G18	Indus conf.	n/d	-	0.51266	1	0.51264	-0.1	0.7	0.7
Parri granites									
G2	Gilgit valley	0.21	0.124	0.51276	3	0.51274	5.1	2.7	0.5
G3	Gilgit valley	n/d	-	0.51263	4	0.51261	-1.8	0.2	0.7
G30 *	Sassi	0.17	0.103	0.51190	2	0.51188	502	-14.1	1.7
G43 *	Sassi	0.21	0.127	0.51196	2	0.51193	757	-13.0	1.7
S97 *	L. Darchan	n/d	-	0.51166	2	0.51164	423	-18.8	2.1
S66 *	Shahbatot	n/d	-	0.51129	1	0.51129	730	-26.0	2.6
NPHM									
Jutial granite									
J19	Jutial	0.09	0.057	0.51132	2	0.51131	2496	-25.7	2.5
J1G	Jutial	0.15	0.092	0.51130	1	0.51129	2607	-26.1	2.6
J1i	Jutial	0.14	0.083	0.51127	2	0.51126	2568	-26.6	2.6
J1B	Jutial	0.13	0.077	0.51129	1	0.51128	2609	-26.3	2.6
Leg dykes									
G39	Sassi	n/d	-	0.51127	4	0.51125	1045	-26.4	2.6
J7	Phuparoch	n/d	-	0.51138	2	0.51138	1730	-24.3	2.4
S92	Shengus	n/d	-	0.51136	1	0.51135	1690	-24.6	2.5
M18	Fairy M'dws	n/d	-	0.51139	1	0.51138	2464	-24.3	2.4
Quartz diorite									
I3	Iskere	n/d	-	0.51141	1	0.51140	1930	-23.9	2.4
Gneisses									
I6	Iskere	0.22	0.135	0.51162	1	0.51161	1902	-19.8	2.1
I9	Kutwal	n/d	-	0.51100	3	0.51100	868	-31.8	3.0
J14	Jutial	n/d	-	0.51125	2	0.51125	544	-26.8	2.6
D19	E. Darchan	0.22(1)	0.131	0.51129	1	0.51129	1062	-26.2	2.6
G31	Sassi	0.21(1)	0.126	0.51168	1	0.51167	770	-18.7	2.0
S102	L. Darchan	0.21(1)	0.124	0.51125	1	0.51124	758	-27.1	2.6
A3	Astor gorge	0.19	0.113	0.51174	2	0.51173	1865	-17.5	2.0
L3	Liachar SZ	n/d	-	0.51117	2	0.51117	1153	-28.4	2.7
A13	Rupal	0.18	0.111	0.51130	1	0.51129	2498	-26.1	2.6

Table 7.4. Whole rock Nd-isotope data for the NPHM and the Kohistan Arc. n/d = no data (average crustal value for $^{147}Sm/^{144}Nd$ value assumed). (1) = data from isotope dilution; all other Sm-Nd data from INAA. ε_{Sr}, ε_{Nd} and T^{Nd}_{DM} calculated using the following ages : 10 Ma for the Jutial granite and NPHM gneisses, 30 Ma for the Kohistan arc granites. T_{DM} relative to depleted mantle of De Paolo (1981). * = deformed Parri granites. Indus conf. = confluence between Indus and Gilgit rivers; L. Darchan = lower Darchan valley; Liachar SZ = Liachar shear zone.

widely discussed in the literature (Arndt and Goldstein 1987; Harris et al. 1988; Cliff et al. 1991) but for this study the low Sm/Nd ratios of many granites suggest that accessory phase behaviour has resulted in depletion of Sm/Nd during crustal anatexis. In order to circumvent problems of intracrustal Sm/Nd fractionation, Nd model ages have been calculated by assuming an average crustal value for Sm/Nd (0.19) between the time of extraction from a depleted mantle and crustal anatexis. For undeformed granites of both suites, Nd model ages lie in the range 500-700 Ma (Table 7.4; Petterson et al. 1993). They are similar to the Nd model ages obtained from the large plutons of the Kohistan-Ladakh batholith, which lie in

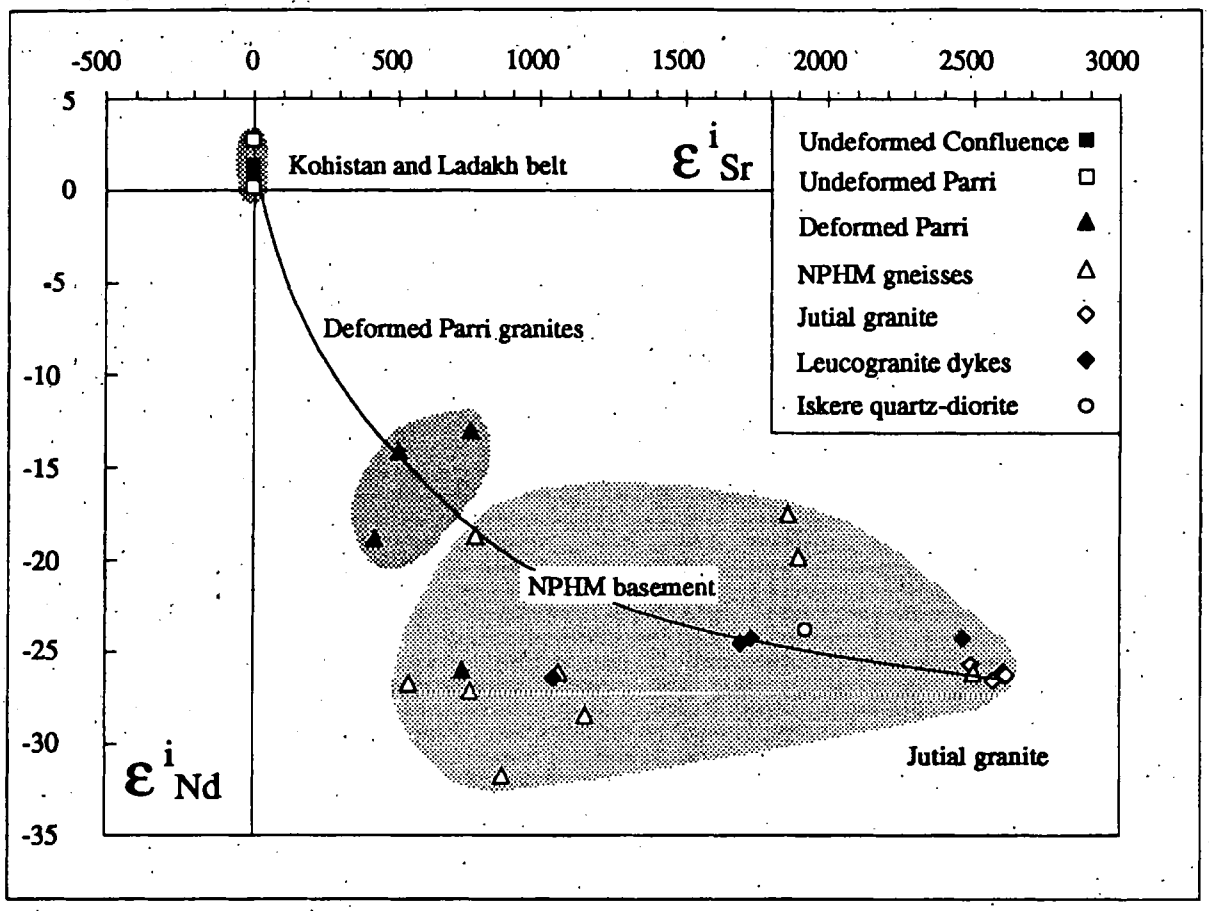

Fig. 7.6. $\varepsilon_{Nd}(T)$-$\varepsilon_{Sr}(T)$ plot for samples of granite and gneiss collected from Kohistan and the NPHM. T = 30 Ma for Kohistan granites and T = 10 Ma for NPHM gneisses and granites. Field of Ladakh and Kohistan from Allègre and Ben Othman (1980) and Petterson et al. (1992). The curved line is a mixing line between undeformed Parri granite and leucogranite derived from the NPHM basement at 30 Ma.

the range 300-800 Ma (Allègre and Ben Othman 1980; Petterson et al. 1993). All of these intrusives have model ages which are considerably older than their age of emplacement, indicating that limited continental material has contributed to their protolith. This may reflect the subduction of continental-derived sediments during the evolution of the island arc.

The cause of the enrichment in $^{87}Sr/^{86}Sr$ observed in those Confluence and Parri granites which have been deformed along the western margin of the NPHM is equivocal. One explanation for such a marked disturbance to the Sr isotopic system is the infiltration of fluids through the shear zone. This interpretation is supported, firstly by isotopic heterogeneities within individual deformed sheets (Table 7.2), and secondly by analyses of amphibolitic and pelitic gneisses present within the shear zone, which are characterised by

similar initial-Sr isotope ratios ($(^{87}Sr/^{86}Sr)_{30}$ = 0.74-0.78; Table 7.5), suggesting that the wallrocks to the granites may have also been affected by fluids. The enrichment trend is less marked in the Confluence sheets, perhaps because higher elemental abundances of Sr in these sheets makes them less sensitive to isotopic shifts induced by fluid infiltration. The elevation of $(^{87}Sr/^{86}Sr)_{30}$ in the deformed granites indicates that if fluids were involved, they must have been relatively radiogenic, suggesting a derivation from the Indian crust. However, significant mobility of REE by fluid infiltration is unusual, and consequently the depleted, crustal Nd signatures seen in the deformed Parri granites are unlikely to have been caused by sub-solidus fluids. Furthermore, REE data available for two of the deformed samples contain no geochemical anomalies which might be expected if the REE had been mobilised by fluids.

A second explanation for the evolved isotopic signatures of the deformed granite sheets, is that sources in both the arc and the NPHM have contributed to the melts. In this case, data from such magmas should plot on a mixing line between endmember compositions from each source. It can be seen from Fig. 7.6 that only one of the deformed sheets (G30) lies close to such a line, if we assume that the NPHM source was similar to that of the Jutial granite. The wide variation in the Sr and Nd isotopic ratios from the three deformed sheets may only be the result of magma mixing if the contributing melts from the NPHM were characterised by highly variable isotopic characteristics. However, there is presently no evidence to suggest that melting in the arc and in the NPHM was synchronous. This, coupled with the close association between deformation and the modification of isotope ratios, makes a mechanism involving magma mixing unlikely.

A third explanation is that fragments of material from the Indian plate have been assimilated by melts derived from the arc, within the shear zone. Given the radiogenic Sr and Nd isotopic composition of the NPHM crust (Tables 7.4 & 7.5), assimilation of such material might have caused the isotopic characteristics of the deformed granites. A study of the garnets from two deformed Parri granites (G43 and G30) provides some evidence for wallrock contamination during emplacement of the magma. Garnets in these granites have

Sample	Assemblage	Location	Rb/Sr	$^{87}Rb/^{86}Sr$	$^{87}Sr/^{86}Sr$	2σ	$(^{87}Sr/^{86}Sr)_{10}$
Northern NPHM							
I6	Bi, Pl, Ksp	Iskere	1.63	4.71	0.83941	2	0.83874
J13	Bi, Pl, (Mu), (Hb)	Jutial	2.13	6.15	0.87565	3	0.87478
J14	Bi, Mu, Pl	Jutial	5.16	14.93	0.87851	7	0.87639
J21	Bi, Pl, Ksp	L. Jutial	1.30	3.74	0.80397	6	0.80344
D2	Gnt, Mu, Bi, Pl	E. Darchan	2.79	8.05	0.96392	3	0.96278
I9	Bi, Mu, Pl, Ksp	U. Kutwal	0.72	2.07	0.76613	4	0.76584
I10	Bi, Mu, Pl, Ksp	U. Kutwal	0.52	1.52	0.76878	9	0.76857
J6	Bi, Pl, Ksp	Phuparosh	0.60	1.75	0.73173	3	0.73148
Southern NPHM							
S91	Bi, Si, Pl	Shengus	1.85	5.35	0.76962	2	0.76887
A3	Gnt, Mu, Bi, Ky, Pl, Ksp	Astor gorge	4.84	14.00	0.83808	2	0.83609
A7	Gnt, Mu, Bi, Pl	Tarshing	0.55	1.60	0.71708	2	0.71685
A13	Bi, Pl, Ksp (Mu)	Rupal	2.91	8.40	0.88193	2	0.88074
L3	Bi, Pl, Ksp	Liachar SZ	0.98	2.83	0.78633	2	0.78593
T25	Bi, Mu, Pl, Ksp	Liachar SZ	1.79	5.16	0.83801	3	0.83728
M10	Bi, Sil, Pl	Tato	6.64	19.19	0.97311	2	0.97038
M3-L	Bi, Pl, Ksp, (Si)	Tato	0.78	2.26	0.8438	2	0.84347
M3-R	Bi, Si, Cd, Pl	Tato	1.42	4.10	0.85084	3	0.85026
Shear zone							
D19	Gnt, Mu, Bi, Pl	E. Darchan	0.97	2.79	0.77989	2	0.77950
G31	Gnt, Mu, Bi, Ky, Pl	Sassi	1.12	3.24	0.75943	2	0.75897
S102	Gnt, Hb, Bi, Pl	L. Darchan	0.62	1.79	0.75839	6	0.75813
S22	Gnt, Hb, Bi, Pl, Ksp	Sassi	0.54	1.57	0.73535	3	0.73513
Kohistan							
D7	Bi, Mu, Ep, Pl, Ksp	W. Darchan	0.23	0.65	0.70440	2	0.70431

Table 7.5. Whole rock Sr-Isotope Data for metamorphic rocks of the NPHM, the Sassi-Darchan shear-zone, and Kohistan. Details as for Table 7.2. $^{87}Sr/^{86}Sr_i$ calculated for an age of 10 Ma. M3-L = migmatite leucosome; M3-R = migmatite restite. All the assemblages include quartz. Gnt = garnet; Hb = hornblende; Bi = biotite, Mu = muscovite, Pl = plagioclase; Ksp = k-felspar; Ep = epidote; Ky = kyanite; Cd = cordierite; Si = sillimanite. L. Jutial = lower Jutial valley; U. Kutwal = upper Kutwal valley; Liachar SZ = Liachar shear zone.

similar morphology and geochemical composition to garnets in adjacent amphibolite-grade metasedimentary rocks, suggesting that they are xenocrysts. The grains are highly fractured and corroded, and contain quartz, mica and sillimanite inclusions. Electron microprobe studies show that these garnets have the average composition $Alm_{74}\,Py_{18}\,Gr_6\,Sp_2$. In contrast, garnets within undeformed Parri granites are generally small, undeformed, euhedral and inclusion-free grains. These garnets have relatively high spessartine contents ($Alm_{62}\,Py_2\,Gr_6\,Sp_{30}$), indicative of an igneous paragenesis (Green 1977; Harris et al. 1992). Given the high REE content of garnet, it is probable that inclusion of garnet

xenocrysts into some granites has strongly altered the whole-rock Nd isotopic compositions of these samples, although confirmation of this theory would require an analysis of the Nd isotopic compositions of the garnets themselves. Assimilation of Indian crust by arc-derived granites also suggests that at the time of intrusion, considerable imbrication between arc and continental lithologies had already occurred along the western margin of the NPHM. However, the observed shift in Nd isotopes cannot result entirely from the assimilation of garnet, since another deformed Parri granite (S66) shows an even greater depletion in radiogenic Nd ($\varepsilon_{Nd}(T) \sim -26$) but contains no modal garnet. It is probable that other phases and possibly other processes, such as fluid transport, were involved.

In summary, the correlation between the enrichment in radiogenic Sr and the depletion in radiogenic Nd for deformed Parri granites from the shear zone indicates the involvement of ancient crust with an evolved isotopic signature. This may have been incorporated into the melt geochemistry through fluid infiltration, magma hybridisation or crustal assimilation, or indeed a combination of these processes.

7.5. Field Relationships at Sassi

In the Indus gorge at Sassi (Fig. 7.2), the contact between the Kohistan arc and the NPHM is marked by a 2.5 km-wide, steeply inclined ductile shear zone containing intercalated lithologies typical of the upper part of the Kohistan island arc (metabasic volcanics and intrusives) together with marbles, para and granitic orthogneisses thought to be derived from the Indian continent (Butler and Prior 1988a). Butler et al. (1992) mapped this zone of intercalation (their 'layered unit') northwards around the antiform defining the northern termination of the Nanga Parbat massif.

Both Confluence and Parri granites can be traced eastwards along the Indus gorge into the shear zone at Sassi where they can be discriminated in the field on the basis of mineralogy. This distinction is confirmed by trace element analyses on collected samples. Butler and Prior (1988a) recognised that in this zone, Kohistan arc granites become sheared

and that the kinematics of the shearing fabrics that deform the sheets are top-to-the SSE. The ductile fabrics are at amphibolite facies and are found both within and outside the granites. They concluded that the age of the arc granites is pre to syn-peak shearing along the 'MMT', a conclusion supported by the apparent restriction of these sheets to Kohistan-derived units.

The majority of Kohistan granites in the shear zone are highly deformed and concordant with the banding in the rocks. The deformation fabrics within the granites vary from an intense penetrative foliation to a more poorly defined foliation with recrystallised quartz around large alkali feldspar porphyroblasts. Detailed work associated with this study has found rare localities where Confluence-type granites (e.g. sample S81) cross-cut deformation fabrics, and intrude some of the intercalations of Indian continental material. Since the geochemical and isotopic evidence suggests that the Confluence granites are a relatively coherent group with presumably a restricted intrusion age, these relationships clearly indicate that the arc-derived granites post-date initial collision of the arc with the Indian continent. Furthermore, the granites were emplaced into an actively deforming shear zone, which resulted in the subsequent deformation of many granite sheets. These observations have important tectonic implications, discussed further below. The apparent lack of any significant penetration of the arc granites into the Indian plate may be due to the thermal contrast between the two terranes at the time of granite intrusion, or to continued displacements in the shear zone.

7.6. Nanga Parbat-Haramosh Massif Leucogranites

7.6.1. Field Relations and Petrography

Dykes and small plutons of leucogranite have a widespread but scattered distribution across the NPHM. The dykes are heterogeneous and coarse-grained, and generally 1-3 m thick. They generally have sharp margins, and individual dykes can commonly be traced for 10-100 metres. Whilst the majority of leucogranites cross-cut the regional metamorphic fabrics of the NPHM, locally they are deformed by both cataclastic and ductile shears.

Deformation of leucogranites is particularly marked in the recently active Liachar shear zone (Butler and Prior 1988b).

Leucogranite dykes were sampled in the Nanga Parbat area at Rupal, Tato and Liachar and in the Haramosh area from the Indus gorge northwards into the Iskere and Phuparosh valleys (Fig. 7.2). The leucogranites are composed of quartz (15-50 %), plagioclase (10-40 %), alkali-feldspar (25-45 %), muscovite (5-15 %), ± biotite (< 4 %), ± tourmaline (< 10 %). Garnets are rarely observed (< 1 %), and have relatively high spessartine contents ($Alm_{69}\,Py_2\,Gr_1\,Sp_{28}$), indicative of an igneous paragenesis. The tourmaline is believed to be magmatic in origin since it occasionally forms inclusions in garnet. Zircon and apatite are common accessory phases. The usual presence of tourmaline in these sheets distinguishes them in the field from the Parri granites of the Kohistan arc. The Jutial granite is a larger, medium-grained pluton composed of biotite (5-10 %) and muscovite (2-10 %) with rare tourmaline, and can be traced for 2.5 km along the Phuparosh valley (Fig. 7.2). Numerous leucogranite dykes and pegmatites cross-cut the margins of the Jutial granite. Large roof pendants of paragneiss within the granite maintain a constant orientation with respect to the country rocks, suggesting a fairly passive intrusion of magma.

The country rocks of the leucogranites are a range of partially migmatised orthogneisses intercalated with metasediments, and paragneisses (termed Iskere and Shengus gneisses respectively by Madin et al. 1989). The pelitic lithologies contain kyanite and occasionally sillimanite, and are at upper amphibolite grade. All of the sampled leucogranites cross-cut these rocks with abrupt contacts, indicating that the melts have been able to effectively leave their sources.

7.6.2. Major and Trace Element Geochemistry

The NPHM leucogranites are peraluminous with a high, restricted silica range (71-75 %), high Rb/Sr ratios (3-23 in the dykes, 2-8 in the Jutial pluton), and depleted HFSE abundances. They have similar trace element chemistries to the Miocene leucogranites from

the central Himalaya (Fig. 7.3B), except for relatively high Th and LREE concentrations of the NPHM leucogranites (Table 7.1). Compared with the Parri sheets of Kohistan, NPHM leucogranites are characterised by even higher Rb/Sr ratios (Fig. 7.4).

A range of metamorphic lithologies sampled from the NPHM basement include pelites (biotite+muscovite+garnet± kyanite/sillimanite), semi-pelites (biotite± muscovite) and orthogneisses. Compared with the leucogranites, the gneisses are enriched in both Ba and Sr (Fig. 7.3B), with Rb/Sr ratios in the range 0.5-5. The relative concentrations of LILE, together with the high Rb/Sr ratios in the leucogranites, are consistent with vapour-absent melting of a metapelite source by incongruent melting of muscovite (Harris and Inger 1992). For example, an Rb/Sr ratio of 8 can result from a 0.15 melt fraction from a pelitic source under vapour-absent conditions (Harris et al. this volume). The limited Rb enrichment in the leucogranites compared with the gneisses may indicate that muscovite, as opposed to biotite, was the dominant mica involved in the melting reactions. Depletion in HFSE in the granites, such as Zr, Hf, Y and REE, is consistent with their retention in accessory phases that were largely residual during melting.

7.6.3. Age of intrusion

The Sr isotope ratios for ten widely-spaced samples from the Jutial granite do not define an isochron (Table 7.6; Fig. 7.7). However, work by Zeitler and Chamberlain (1991) on young zircon overgrowths from three leucogranite dykes has yielded concordant spreads in ages of 2.2-4.3 Ma; 5-8 Ma; and 7-12 Ma. In each case, the youngest age is interpreted by these authors as the leucogranite intrusion age. Interestingly, three whole-rock samples of a ten-metre thick leucogranite from Rupal define an approximate age of 2.8 ± 0.1 Ma ($(^{87}Sr/^{86}Sr)_i$ = 1.0056), although the small number of samples on such a young age makes the calculated uncertainty highly unrealistic.

A further constraint on the age of the leucogranite magmatism comes from Rb-Sr muscovite ages, interpreted as the time of cooling through a 500-550 °C blocking

Sample	Location	Rb/Sr	$^{87}Rb/^{86}Sr$	$^{87}Sr/^{86}Sr$	2σ	$(^{87}Sr/^{86}Sr)_{10}$
Jutial Granite						
J1A	Jutial	5.41	15.64	0.88723	2	0.88501
J1B	Jutial	4.58	13.24	0.89041	3	0.88853
J1C	Jutial	4.08	11.79	0.89199	3	0.89031
J1E	Jutial	4.15	11.99	0.88839	3	0.88668
J1F	Jutial	3.91	11.29	0.89171	3	0.89011
J1G	Jutial	2.55	7.36	0.88947	2	0.88842
J1i	Jutial	4.97	14.35	0.88769	2	0.88565
J1D	Jutial	2.40	6.94	0.87465	2	0.87366
J19	Jutial	1.88	5.44	0.88132	2	0.88055
J11	Jutial	2.80	8.09	0.88438	3	0.88323
Leucogranite Dykes						
G39	Sassi	1.92	5.55	0.78072	4	0.77836
S47	Sassi	0.62	1.79	0.83405	2	0.83379
J7	Phuparosh	3.64	10.52	0.82808	2	0.82659
I11	Kutwal	9.67	27.95	0.80804	2	0.80407
I8	Iskere	17.41	50.32	0.80485	10	0.79770
S87	Shengus	3.32	9.59	0.87362	3	0.87225
S92	Shengus	15.50	44.80	0.83015	2	0.82379
S93	Shengus	1.26	3.64	0.75584	4	0.75532
M-18	Fairy M'dws	7.22	20.86	0.88122	2	0.87826
L17-F (1)	Liachar SZ	21.20	61.27	1.06583	3	1.05712
L17-E (1)	Liachar SZ	26.77	77.35	1.07385	5	1.06286
L17-G (1)	Liachar SZ	19.95	57.66	0.94990	3	0.94172
A14 (2)	Rupal	11.60	33.52	1.00696	3	1.00220
A10 (2)	Rupal	18.67	53.96	1.00780	2	1.00014
A9 (2)	Rupal	22.91	66.21	1.00831	6	0.99891
Quartz-Diorite						
I3	Iskere	0.50	1.44	0.84091	2	0.84070

Table 7.6. Whole-rock Sr-Isotope Data for the NPHM Leucogranites. Details as for Table 7.2. $^{87}Sr/^{86}Sr_i$ calculated for an age of 10 Ma. (1), (2) = samples from the same granite dykes. Liachar SZ = Liachar shear zone.

temperature (Purdy and Jäger 1976; Cliff 1985). The Jutial granite has a muscovite age of 6.5 Ma, compared with muscovite ages of 2.8 and 3.3 Ma for a leucogranite dyke in the Haramosh area (Table 7.3).

Muscovite Rb-Sr ages from metamorphic rocks in the NPHM are extremely variable and lie in the range 4-36 Ma (Fig. 7.2; Table 7.3), indicating contrasting thermal histories for different parts of the NPHM. The blocking temperature for Ar in hornblende is similar to the blocking temperature for Sr in muscovite ($\approx$ 500 °C, Harrison 1981), although both are affected by cooling rate. Thus the older muscovite Rb-Sr ages noted above correspond

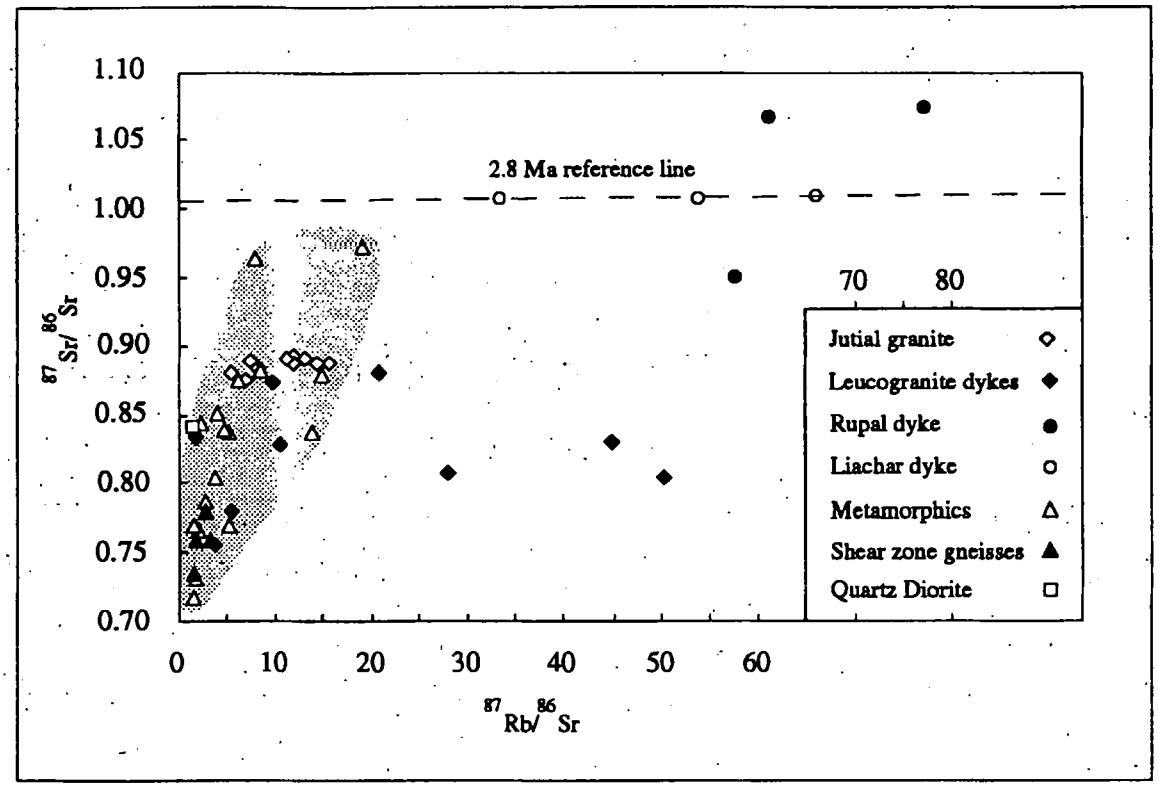

Fig. 7.7. Rb-Sr isochron diagram for leucogranites and gneisses from the MPHM. Dashed line is a 2.8 Ma reference line for the Rupal granite. The shaded region delineates the field of NPHM crust. Shear zone samples include both pelitic and amphibolitic gneisses.

broadly to hornblende ^{40}Ar-^{39}Ar ages of 16-25 Ma from the NPHM (Zeitler et al. 1989), also shown in Fig. 7.2 . Interestingly, the Rb-Sr muscovite ages for the NPHM are locally very young (4.4-7.7 Ma). These are similar to the young monazite ages (4-11 Ma) recorded by Smith et al. (1992), suggesting that at least some parts of the NPHM experienced a much younger metamorphic event, or more recent cooling. However, in general, the younger muscovite ages from the leucogranites suggest that the leucogranites intruded after their country rocks had cooled below about 500 °C. For example, from Shengus (Fig. 7.2), Zeitler et al. (1989) obtained a metamorphic hornblende ^{40}Ar-^{39}Ar age of 20 Ma, which contrasts with Rb-Sr muscovite ages of 3.3-2.8 Ma for a leucogranite from this locality. Magmatic cooling rates will be affected by volume and depth of intrusion, but in general post-magmatic closure to Sr in muscovite occurs shortly after crystallisation. Following from this, the variable leucogranite muscovite cooling ages above may indicate a slightly older age for the Jutial granite than leucogranite sheets at Haramosh and Rupal, although detailed U-Pb zircon dating would be required to confirm this.

In summary, the timing of leucogranite magmatism is rather poorly constrained, but probably took the form of separate magma batches intruded between 2 and 12 Ma.

7.6.4. Sr and Nd Isotope systematics

Initial Sr-isotope ratios from all leucogranites in the NPHM are > 0.75, and generally in excess of values observed in the Kohistan granites (Table 7.6). Whereas widely spaced samples of the Jutial granite have $(^{87}Sr/^{86}Sr)_{10}$ ratios in the range 0.87-0.89, leucogranite dykes with a wide geographical spread across the NPHM have more variable ratios of 0.75-0.87, probably reflecting isotopically distinct source regions. Extreme Sr-isotope ratios (0.98-1.06) have been identified in leucogranite dykes from the Liachar thrust zone and at Rupal. Twenty-one samples of Indian crust material from across the NPHM have varied $(^{87}Sr/^{86}Sr)_{10}$ in the range 0.72-0.97. There is no obvious correlation between metamorphic lithology or grade and the Sr-isotope composition. However, metamorphic samples collected from border regions of the NPHM often display relatively low $(^{87}Sr/^{86}Sr)_{10}$ compared with samples collected from more central regions (Iskere and Shengus gneisses of Madin et al. 1989). For example, samples from the shear zone at Sassi, from near Kutwal and Phuparosh, and from near Tarshing, are characterised by $(^{87}Sr/^{86}Sr)_{10}$ in the range 0.72-0.78. The majority of these samples come from the Layered unit of Butler et al. (1992), suggesting a distinct isotopic history for this unit compared with the bulk of the NPHM. The Sr-isotope compositions of the analysed gneisses encompass the range of all the leucogranites except the extremely radiogenic bodies mentioned above (Fig. 7.7). Even in these cases, it is possible that further analyses of basement gneisses could yield potential source materials. Alternatively, the very high Sr-isotope compositions locally observed in the NPHM leucogranites may be the result of disequilibrium melting of a mica-rich protolith, where the radiogenic Sr of the reactant mica is incorporated in the melt, and the melt extracted before isotopic equilibration is reached between melt and restite phases.

The significance of heterogeneous Sr isotopic compositions, observed not only

between different granites but also within individual intrusions such as the Jutial granite, is equivocal, though it must reflect the characteristics of the source region, possibly modified by wall-rock assimilation or subsolidus fluid infiltration. In the light of the variable isotopic compositions of the NPHM gneisses, together with the geochronological evidence which indicates emplacement of magmas as separate pulses over several million years, the isotopic variation existing between and within different granites can be accounted for by batch melting of heterogeneous lithologies within the ancient Indian crust, similar to those now exposed in the NPHM basement.

A leucogranite dyke from Liachar, deformed in the hanging wall of the Liachar thrust, provides an example of extreme isotopic heterogeneity within a single body (L17, Table 7.6). In an isotopic study of another leucogranite at Liachar, Cliff et al. (1991) noted isotopic disequilibrium between adjacent phases, even at a millimetre scale, which was ascribed to the action of sub-solidus fluids. Further evidence for the action of fluids in the Liachar thrust comes from oxygen-isotope disequilibrium between minerals in pegmatites (Barnett et al. 1991). Thus it seems that fluid infiltration has resulted in Sr mobility within those NPHM leucogranites which have been deformed in the Liachar shear zone.

Samples of the Jutial granite have uniform Nd-isotope compositions with $\varepsilon_{Nd}(T)$ of ~-26 (Fig. 7.6). Four leucogranite dykes from the NPHM have $\varepsilon_{Nd}(T)$ in the range -24 to -26, comparable to a deformed dyke at Liachar which has $\varepsilon_{Nd}(T) = -24.3$ (Cliff et al. 1991). Nine samples of NPHM gneiss with a wide geographical spread have $\varepsilon_{Nd}(T)$ in the range -17 to -32. On the basis of Sr and Nd isotope systematics, the leucogranites could have been derived from the NPHM at 2-12 Ma ago.

The mineralogy, peraluminous composition, high Rb/Sr ratio and radiogenic Sr and Nd isotopic compositions of NPHM leucogranites indicate a derivation by partial melting of an ancient, highly evolved crustal source. Model Nd ages for the leucogranites lie between 2.4 and 2.6 Ga, within the range provided by the sampled gneisses (2.0-3.0 Ga). These compare with somewhat younger model ages (1.6-2.0 Ga) for High Himalayan

leucogranites (Deniel et al. 1987; Inger and Harris 1993) indicative of the relative ages of the metasedimentary protoliths from these two regions of the Himalayan orogen.

A crustal source for the NPHM leucogranites is also suggested by the common inheritance of radiogenic Pb seen in zircons from these intrusives (Zeitler and Chamberlain 1991). Conventional and ion microprobe zircon U-Pb ages of ~1.9 Ga (Iskere gneisses) and 400-500 Ma (Shengus gneisses) have been obtained (Zeitler et al. 1989) from country rocks to the leucogranites, providing suitably ancient potential sources for the granites. Furthermore, xenocrystic zircons from leucogranites intruding both the Iskere and Shengus gneisses have the same age as the Iskere gneisses. This suggests that the Iskere gneisses are more likely to have been the source of the leucogranites (Zeitler and Chamberlain 1990; Zeitler et al. 1989), although this work has shown that, in general, the melting zone is not presently exposed. Unfortunately, Sr-isotope studies cannot resolve any significant difference in isotopic composition between the Iskere gneisses and the Shengus gneisses.

In most cases, the Sr-isotope ratios of leucogranites do not correspond to the ratios observed in their immediate country rocks. For example, the Rupal dyke has $(^{87}Sr/^{86}Sr)_i$ = 1.005 compared with an adjacent gneiss (sample A13) which is characterised by $(^{87}Sr/^{86}Sr)$ = 0.882. These observations, together with the cross-cutting nature of the leucogranites, indicate that the magma was sufficiently mobile to leave its source. This is consistent with the younger muscovite cooling ages observed in the leucogranites, and the widespread presence of stable muscovite in the country rocks. Thus there is little evidence for widespread, Himalayan age, *in-situ* melting in the massif at present exposure levels, although locally sillimanite-grade assemblages and migmatites are observed.

7.7. Discussion

Field, petrographic, geochemical and isotopic data enable us to distinguish between three suites of granites adjacent to the the western margin of the NPHM. As expected, the most significant isotopic and geochemical contrasts exist between granites intruding the arc

and the relatively young leucogranites intruding the NPHM, due to primary differences between the source characteristics of the two terranes. This contrast is exemplified by Nd model ages for intrusives which increase dramatically across the contact from ~700 Ma in the Kohistan terrane to ~2500 Ma in the Indian Plate.

Two suites of Kohistan granite sheets can be traced into the shear zone. The majority of the Confluence and Parri granites which have been deformed in the shear zone show elevated whole-rock ($^{87}Sr/^{86}Sr$) ratios relative to their undeformed counterparts in the arc. Compared with the undeformed granites in the Kohistan arc, granites within the shear zone also show increased scatter in ($^{87}Sr/^{86}Sr$) ratios between different granites, and extreme heterogeneity has even been preserved within single granite sheets. These variations are consistent with infiltration of sub-solidus fluids through the shear zone. However, an evaluation of the Nd isotopic data suggest that incorporation of ancient crustal material into the melts during ascent has also played a role in the isotopic evolution of the granites within the shear zone.

Deformed leucogranites in the Liachar thrust zone also provide evidence of fluid infiltration effecting Sr-isotope ratios (Cliff et al. 1991; this contribution). Interestingly, the similarity in $\varepsilon_{Nd}(T)$ between these leucogranites and undeformed dykes within the NPHM could be taken as confirmation that Sr, but not Nd, can be mobilised by fault-related fluids. The absence of melting associated with fluid infiltration suggests that advection through the shear zone occurred after amphibolite-grade ductile deformation. The fluids may be associated with crystallisation of leucogranite bodies within the NPHM basement < 12 Ma ago.

Ion probe U-Pb depth-profiling of basement zircons reveals young overgrowths with ages of 2-10 Ma, possibly reflecting post-metamorphic fluid flow at temperatures of 200-500 °C (Zeitler and Williams 1988). These ages are comparable to the ages of NPHM leucogranite magmatic zircons (Zeitler and Chamberlain 1991), and coincide with the time of young, rapid uplift of the NPHM (Zeitler 1985), suggesting that leucogranite magmatism

within the NPHM, pervasive fluid flow and rapid uplift are contemporaneous and possibly related.

Petterson and Windley (1991) suggested that frictional heating and dehydration of the Indian continental crust during underthrusting below the arc caused anatexis of lower arc crust and generation of the undeformed Confluence and Parri granites, whilst Petterson et al. (1993) proposed that fluids derived from the Indian crust had enriched the Sr isotopic composition of the source of the Parri granites. The data presented in this study are consistent with an arc source for post-50 Ma magmatism in Kohistan. However, if fluids from the underthrusting Indian continental crust had caused melting or metasomatism in the arc, the isotope systematics of the 26-50 Ma, undeformed arc granites should record a continental input, which is not observed. The absence of Archean signatures in such young granites in the arc is perhaps surprising, because the present crustal levels of the Indian continent exposed in the NPHM include thick wedges of metasediments with evolved, radiogenic isotopic compositions (Table 7.5). During underthrusting, such hydrous assemblages would be expected to undergo partial melting (Patino-Douce et al. 1990), generating melts with the isotopic and geochemical characteristics of the leucogranites currently exposed in the NPHM. The presence of isotopically juvenile melts in northern Kohistan, rather than NPHM-type leucogranites, therefore suggests that significant underthrusting of northern Kohistan by Indian continental crust did not occur before 26 Ma. We should emphasise, however, that this study does not constrain the time at which either collision or crustal thickening was initiated, but places a maximum constraint of 26 Ma on the time of large-scale underthrusting of the Indian crust in northern Kohistan.

The monazites of the Miocene Baltoro plutonic unit (BPU) in the Karakoram (Searle et al. 1989) share similar geochemical characteristics to the Confluence granites. The BPU is characterised by low $(^{87}Sr/^{86}Sr)_i$ ratios thought to reflect large scale melting of the lower Karakoram crust during homogenous crustal thickening, and enrichment of LILE possibly caused by melts derived from the mantle wedge (Searle et al. 1992). Significantly, there is no evidence for the involvement of ancient Indian crust (Rex et al. 1988; Searle and Tirrul,

1991). Crawford and Windley (1990) identified the BPU as a "type b" collision-related leucogranite, with melting at the base of the crust being triggered by an input of heat or material from the mantle wedge. If northern Kohistan was still underlain by a Tethyan mantle wedge at 50-30 Ma, as would be the case if underthrusting had not occurred until then, then the Confluence granites may share a similar origin to the BPU. However, if melting in the arc had been triggered by a mantle heat source after underthrusting, fertile Indian continental material would be expected to melt before juvenile arc crust, although this would also be dependant on the initial crustal temperatures. Again, the absence of mature crustal melts intruding the Kohistan arc therefore suggests, if the mantle was indeed the heat source, that underthrusting of continental material beneath the northern arc may not have occurred until after ~30 Ma. Interestingly, the BPU has been dated at 21-25 Ma (U-Pb zircon, Parrish and Tirrul, 1989; Scharer et al. 1990), slightly younger than the Confluence and Parri granites of Kohistan to the south. This may therefore reflect crustal thickening and melting progressively migrating northwards from the collision zone, as predicted by England and Searle (1986).

Cross-cutting igneous relations at Sassi show that the Kohistan granites post-date the closure of the collisional suture, observations which are supported by geochronology. Kinematic work shows that the same granites have been deformed by a top to the SSE shearing, associated with underthrusting of the Indian continental crust below Kohistan (Butler and Prior 1988a). If underthrusting had commenced during the initial collision, then either this deformation phase must have lasted for at least 20 Ma, or there have been two separate deformation phases characterised by top to the SSE shearing. Alternatively, either the initial collision in north-eastern Kohistan occurred later than in the Hazara area (for which there is no evidence), or significant underthrusting of Kohistan by the Indian craton did not occur until after 26 Ma. Both structural and isotopic evidence therefore suggest that before 26 Ma, continental underthrusting below northern Kohistan was limited.

The trace element contents of the NPHM leucogranites are consistent with vapour-absent melting of a metapelite source (Harris and Inger 1992). The high Rb/Sr of the

leucogranites and Sr and Nd isotope systematics suggest that the sources of the leucogranites were similar to the NPHM gneisses currently exposed, although there is little evidence at the surface for Himalayan-age *in-situ* melting. Low volume, batch melting of these ancient, evolved and isotopically heterogeneous gneisses occurred over a period of about 2-12 Ma. The association of rapid, young uplift in the NPHM (Zeitler 1985) with young leucogranite magmatism suggests an origin by decompression melting (Zeitler and Chamberlain, 1991). For a crustal exhumation from 20 to 10 km depth, a melt fraction of F = 0.1 can be produced from sub-solidus temperatures if exhumation is sufficiently rapid for adiabatic ascent (Harris et al. this volume). Melting during decompression would be enhanced by the high concentrations of U and Th in pelites within the NPHM, which result in extremely high heat production (2-8 μWm^{-3}). Thus the unusually young leucogranites intruding the NPHM were derived from crustal rocks with high heat productivities, buried beneath an insulating layer of Kohistan rocks before extremely rapid uplift and exhumation.

Acknowledgements

This work was supported by a NERC studentship (MTG) and fieldwork expenses (RWHB & NBWH) were funded by a Royal Society study visit to Pakistan and a NERC research grant (GR3/6113). We are indepted to Munir Ghazanfar and Nawaz Chaudary of the Punjab University, Lahore, for hospitality and logistical support in the field. We acknowledge the advice given by Pete Treloar and two anonymous reviewers of an earlier draft, and MTG thanks Peter van Calsteren and Mabs Johnston for support in the laboratory.

Chapter 8
Summary and Conclusions

The Nanga Parbat-Haramosh massif is a large-scale, antiformal complex of Indian continental crust which lies obliquely to the regional trend of the Himalayan orogen. The NPHM is one of a number of such structural re-entrants within the western Himalaya. Previous structural and geochronological studies have shown that the NPHM has been rapidly exhumed from beneath the Kohistan-Ladakh island arc, probably within the last 10 Ma (Treloar et al. 1991). The main objective of this study was to investigate the metamorphic and magmatic history of the NPHM and the adjacent Kohistan arc, and to discuss the significance of the results in terms of the structural history of the NPHM and thus the tectonic evolution of the western Himalaya as a whole. Since the NPHM is composed of Precambrian crust with presumably a complex, extended thermal history, it was of particular interest to determine the thermal affects of Himalayan orogenesis, and to ascertain the timing of thermal events in the region during the Himalayan orogeny. Fortunately, modern geochronological techniques have the potential to discriminate very young thermal events in crust affected by Tertiary orogenesis, due to the relatively small uncertainties attached to young mineral ages.

The exhumation of the NPHM has been at least partly accommodated by active folding and thrusting. Detailed structural observations along the western margin of the NPHM indicate that the MMT zone has been significantly affected by younger movements, the kinematics of which vary along strike. In the Liachar area, Indian continental rocks have been thrust back in a north-westerly direction over Kohistan, as described by earlier workers (Butler and Prior 1988b and Butler et al. 1989). In contrast, in the Sassi-Darchan area, the steep contact zone between Kohistan and the NPHM has been affected by dextral-transtension, involving the oblique movement of the present hanging-wall rocks down towards the north-west, relative to the footwall rocks.

A detailed study of the mineral chemistry and metamorphism in the region indicates that metamorphic rocks presently exposed within the NPHM have equilibrated under relatively high-grade temperature and pressure conditions compared with those present in northern Kohistan. Calculated P-T for the NPHM region mostly lie in the range 600-750 °C and 7-10 kbar, whilst samples in the adjacent Kohistan arc yield P-T estimates in the range 550-700°C and 6-8 kbar. Furthermore, there is a systematic increase in preserved metamorphic pressure and temperature on traversing eastwards across Kohistan towards the NPHM. There is no marked P-T change across the Sassi-Darchan shear zone. These observations could be taken as evidence that rocks in both Kohistan and the NPHM have been affected by a synchronous regional metamorphism, with higher P-T preserved at deeper structural levels below the MMT. However, a consideration of the available geochronological data suggests that such a simple model, requiring a close association between metamorphism and tectonics, may not be appropriate.

Garnet Sm-Nd data indicate that the metamorphic rocks exposed in the NPHM were last isotopically equilibrated within the last 20-25 Ma. These data are consistent with the proposal of Zeitler and co-workers (Smith et al. 1992) that the rocks exposed within the NPHM structure have been metamorphosed within the last 10 Ma. However, in contrast, the metamorphic fabrics present in the adjacent part of Kohistan are truncated by late granite sheets which were intruded before ~ 30 Ma. Furthermore, hornblende $^{40}Ar/^{39}Ar$ cooling ages for metamorphic rock samples collected from Kohistan offer a weak constraint on the lower limit of metamorphism. In the Indus confluence area (Kohistan), this study has yielded a hornblende $^{40}Ar/^{39}Ar$ cooling age of 28 ± 1 Ma. The metamorphic rocks exposed in the Kohistan and NPHM regions were thus last equilibrated at markedly different times.

Taken together, these findings are interpreted in terms of the rapid exhumation of high-grade Indian continental rocks within the NPHM, from relatively deep structural levels. In contrast, the rocks presently exposed in northern Kohistan have not been exposed to such high rates of recent exhumation, and therefore these rocks last equilibrated at relatively high structural levels at > 30 Ma. An important conclusion that can be drawn is that contrasting

structural and metamorphic levels may be exposed within an orogen during rapid differential exhumation, without the generation of obvious metamorphic breaks. It is interesting to speculate whether apparent evidence for separate metamorphic events in some orogens is, at least partly, a function of varying degrees of exhumation of metamorphic rocks from different structural levels.

P-T paths derived from garnet compositional zoning in the northern NPHM include major retrogressive (decreasing P and T) paths provided by pelitic samples, and less-well constrained prograde (increasing T, decreasing P) P-T paths provided by amphibolitic and calcareous lithologies. It is thought that samples present in the northern part of the NPHM (at least) experienced the same P-T history, but preserve different portions of the P-T path due to non-simultaneous garnet nucleation and growth in contrasting lithologies. The overall P-T history is thought to consist of a poorly-constrained period of prograde metamorphism, which probably developed during thrusting along the leading edge of the Indian continental plate, followed by a long history of retrograde metamorphism during exhumation, involving decompression by at least ~ 2-4 kbar. Some samples presently exposed along the western margin of the NPHM may have still been enjoying prograde metamorphism during early exhumation. From a consideration of the available geochronological data, this exhumation, recorded by garnet growth, is interpreted as being related to the evolution of the NPHM structure.

Some of the observed variation in recorded metamorphic conditions and P-T paths for different samples collected from the NPHM region probably relates to varying degrees of exhumation of metamorphic rocks from different structural levels. Thus samples from the Astor gorge were buried to depths corresponding to at least 14 kbar, before an extended exhumation history involving decompression by 2-3 kbar, when final metamorphic equilibration occurred, and then by a further 10-11 kbar during exhumation to the present topographic surface. Samples exposed near to the eastern margin of the NPHM locally record a history of prograde metamorphism under increasing pressure, which may reflect early equilibration during crustal thickening. Such samples may have been preserved due to

the lower rates of exhumation that are thought to have occurred along the eastern margin of the NPHM compared with the western margin.

The NPHM and Kohistan terranes are characterised by Himalayan-age magmatism of strongly contrasting geochemistry, which primarily reflects the available source composition. The granites are best distinguished on the basis of the LILE (Rb, Ba and Sr), reflecting the fact that these trace elements reside in the major phases, and therefore during melting, equilibrium is maintained for these elements between melt and restite.

In Kohistan, the Confluence intrusives are biotite ± muscovite granite bodies that display consistent fractionation trends, enriched LILE contents and fractionated REE profiles. The Parri granites are relatively siliceous, peraluminous muscovite-garnet ± biotite leucogranite sheets characterised by lower Rb/Sr ratios and flatter REE profiles than the Confluence granites.

The Confluence granites are part of a volumetrically significant phase of granitoid magmatism in the Kohistan batholith. They were probably generated by fluid-absent biotite breakdown in an isotopically-juvenile, LILE and LREE-enriched source at a relatively deep level in the Kohistan crust. The melts were affected by fractionation of plagioclase, biotite, ilmenite, zircon, apatite and probably hornblende, either within the source or at a higher crustal level. Individual Confluence sheets are locally characterised by slightly heterogeneous strontium isotopic compositions, and magmatic layering is common. These features probably reflect multiple injection of magma from a slightly isotopically-heterogeneous, fractionating source. Alternatively, the isotopic heterogeneities may have been caused by limited wall-rock interaction or sub-solidus processes.

The Parri granites are probably low-degree partial melts of a peraluminous, isotopically-juvenile, metasedimentary source present in the upper crust of the Kohistan arc.

The primitive initial Sr and Nd isotopic compositions of both the Confluence and

Parri granites intruded in the vicinity of the Indus confluence indicate that significant underthrusting of this part of Kohistan by Indian continental crust, required by the tectonic models of Butler and Coward (1989), could not have occurred until after 26 Ma. However, elevated Nd model ages indicate that limited continental material has contributed to the protolith, as has also been observed in the Ladakh batholith (Allègre and Ben Othman 1980). This may reflect the subduction of continental-derived sediments during the evolution of the island arc. Furthermore, it should be noted that, at the time of intrusion of the late Kohistan granite sheets, the initial suturing between the Kohistan arc and the Indian continent had already occurred. Thus the source regions of the Kohistan granites distal to the MMT were geochemically and isotopically unaffected by the early continental collision between the Indian continent and Kohistan.

The NPHM leucogranites are peraluminous, geochemically variable tourmaline-muscovite-biotite leucogranites, characterised by high or extreme Rb/Sr ratios. Geochemical and isotopic data suggest that the leucogranites have been generated by fluid-absent incongruent melting of muscovite in geochemically variable pelitic source regions within the high-grade Indian continental crust, and subsequently intruded as a succession of independent magma batches. The scattered distribution of the leucogranites is probably a reflection of the distribution of suitably fertile (pelitic) protoliths at depth within the NPHM. The leucogranites were probably intruded as small melt fractions along fractures and shears in the crust; these fractures may have been generated by the local increase in volume associated with partial melting (Rubie and Brearley 1990).

It should be noted that the intrusive leucogranites that have been studied in this work represent magma batches that have been effectively separated from their source regions. The metamorphic grade of the country rocks to the NPHM leucogranites (600-750 °C) is generally close to that required for the breakdown of muscovite (~ 675 °C; Clemens and Vielzeuf 1987), and therefore scattered occurrences of migmatites within the NPHM may reflect local in-situ melting during Himalayan times. However, many of the syn-kinematic, concordant migmatites present in the NPHM are part of the Precambrian basement complex,

as shown by U-Pb zircon dating (Zeitler et al. 1989). In general, it should be emphasised that the structural and metamorphic relations of the migmatites present in the NPHM have not yet been fully explored. The migmatitic metasediments present at Tato have suffered a relatively low-pressure metamorphism. The apparently anomalous thermal history of the Tato area is supported by a 3 Ma monazite U-Pb age (Zeitler et al. 1993) and a 1.6 Ma biotite ^{40}Ar-^{39}Ar cooling age. Clearly, although in general the NPHM has experienced rapid denudation over a wide area during the last 10 Ma, there has also been intense, localised exhumation of high-grade Indian continental rocks within the core of the NPHM. Future research should be directed at resolving the structural mechanism for such rapid and localised exhumation.

The NPHM leucogranites have yielded U-Pb zircon ages of < 10 Ma (Zeitler and Chamberlain 1991; Zeitler et al. 1993), and thus the leucogranites are significantly younger than the major period of metamorphism and crustal thickening that occurred in the western Himalaya (~ 40-50 Ma). Since theoretical modelling indicates that mobile, post-kinematic granites are generally intruded within 10 Ma of crustal thickening (Patino-Douce et al. 1990), the leucogranites were probably generated by decompression melting that occurred during the rapid uplift of previously-thickened Indian continental crust (Zeitler and Chamberlain 1991). Geochemical data show that the metamorphic basement is characterised by a relatively high radiogenic heat productivity. Furthermore, the thickened crust may have been insulated beneath a low-conductivity cover of upper arc rocks before rapid exhumation in the last 10 Ma (Jaupart and Provost 1985). Thus the generation of the NPHM leucogranites is readily explicable in terms of an anomalously steep, transient geothermal gradient associated with rapid tectonic uplift and erosion of relatively hot Indian continental crust.

The mineral ages described in this study confirm that the NPHM has been subjected to relatively rapid and recent differential exhumation compared with the adjacent Kohistan arc. When consideration is taken of the kinematics of the recently-active Liachar thrust, the anomalously high topography of the NPHM compared with the surrounding regions, and

the occurrences of major landslips in historic times along the Indus gorge, it can be inferred that a substantial proportion of the recent exhumation has been caused by active tectonic uplift and associated erosion. The mineral ages also indicate that exhumation rates within the NPHM have varied both temporally and spatially, suggesting that, as expected, the thermal evolution of the region has been complex. Ironically, uplift rates are difficult to quantify due to the fact that the crustal exhumation has been so rapid and focussed on such a small area, and therefore the palaeogeothermal gradients are unconstrained. Another problem lies in the uncertainty attached to closure temperature estimates for strontium and argon in both muscovite and biotite (especially in a region that has experienced such rapid cooling), and the lack of geochronological data for other phases in many parts of the NPHM.

A subsidiary part of this work has been concerned with the geochemical and isotopic processes associated with the regional shear zone that borders the north-western margin of the NPHM. The structural, petrological and isotopic observations that have been made in the shear zone have been summarised in Fig. 8.1. Both the Confluence and Parri granites can be traced into the shear zone, with the result that simple geochemical and isotopic comparisons can be made between undeformed and deformed granites. Unfortunately, there is some doubt as to whether all of the Parri granite sheets are cogenetic. However, in general, the deformed granite sheets exhibit variable trace element contents (including the HFSE), and variably enriched strontium and depleted neodymium isotopic compositions. These observations are thought to reflect a combination of assimilation of Indian crustal material present in the wallrocks, and element mobility in sub-solidus fluids being channelled through the shear zone. Evidence for further open-system behaviour in the shear zone is provided by an isotopic study of metamorphic garnet. One garnet sample has yielded an elevated Sm-Nd age, which is probably a reflection of the activity of fluids that have been derived from the isotopically-evolved Indian continental crust. Since the REE and HFSE are generally thought to be relatively immobile in aqueous fluids, the fluids may have contained significant proportions of CO_2, F^- or Cl^- (Harris 1981; Eugster 1985; Tait and Harley 1988).

The most deformed samples collected from the Sassi-Darchan shear zone have

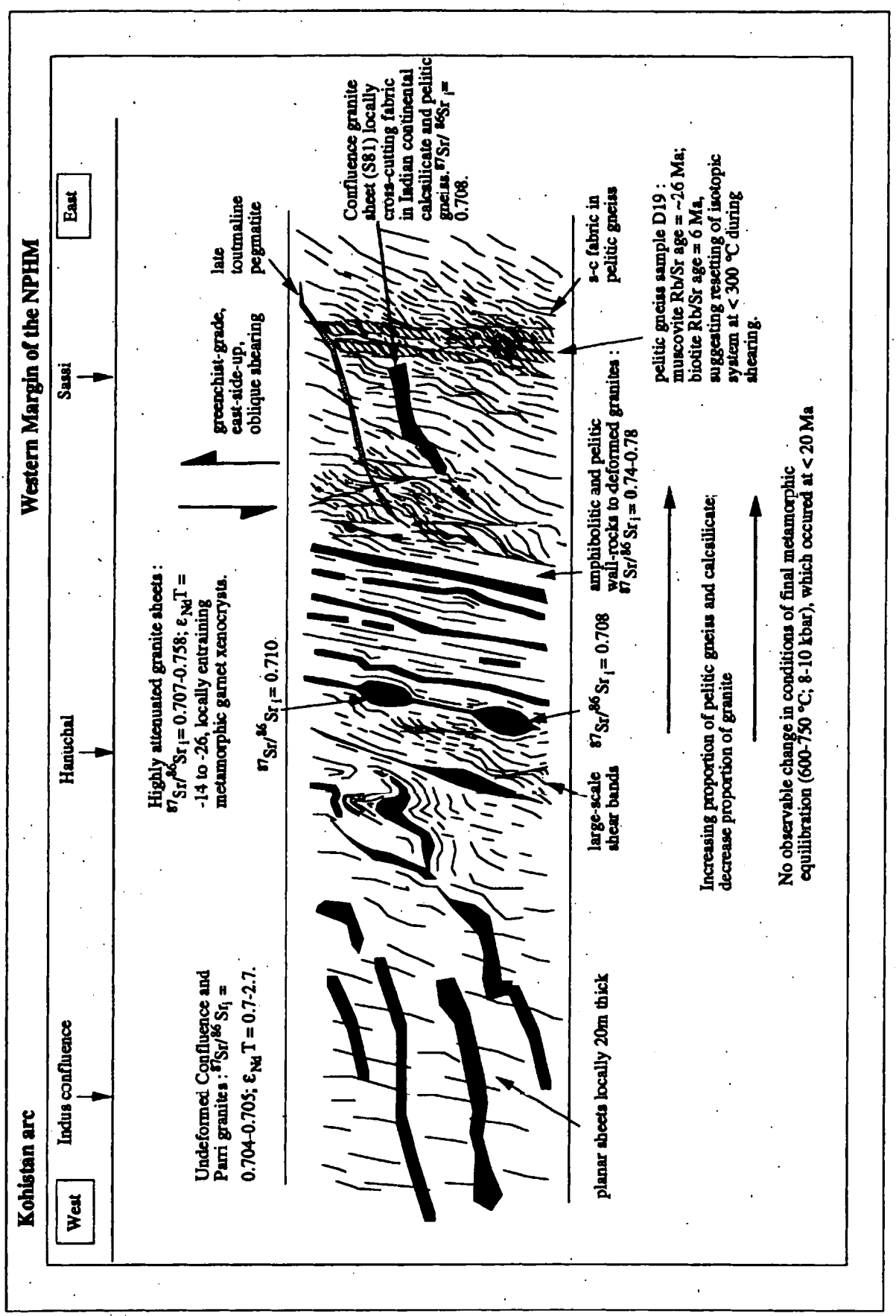

Fig. 8.1. Geological sketch section across the shear zone bordering the western margin of the NPHM in the Sassi area (not to scale). This figure combines structural observations with petrological, isotopic and metamorphic data from the shear zone.

yielded exceedingly variable Rb-Sr mineral cooling ages, and even individual samples have yielded strongly contrasting biotite and muscovite ages. Although a single muscovite sample probably reflects strontium isotopic open-system behaviour, the majority of ages are 'Himalayan', and therefore probably reflect the complex, evolving thermal structure of the shear zone over an extended period of time. Although a full understanding of this thermal evolution awaits further geochronological data and thermal modelling, the variable mineral ages probably reflect a combination of variable closure temperatures between samples with widely varying fluid content, strain state and lithology, juxtaposition of samples that have suffered contrasting thermal histories by late, relatively low-temperature shearing, and discrete (but indistinct) metamorphic or retrogressive events in the region. Unfortunately, cooling ages offer rather poor constraints on the timing of fabric formation, as concluded by Sinha et al. (1988). The entire spectrum of fabrics in the shear zone may have been formed during a single continuous deformation event occurring during decreasing metamorphic conditions.

Any fluid mobility within the shear zone is likely to have been complex. Fluid processes may not have been pervasive along and across the shear zone, and different lithologies are likely to have been effected to varying extents due to varying element mobility. Fluids may also cause thermal changes in a shear zone, due to the thermal expansion of hot fluids ascending from depth in the crust, since these fluids are able to maintain a higher temperature than the surrounding geothermal gradient (Beach 1976). The suture zone bordering the western margin of the NPHM has undoubtedly been the focus of a complex thermal, deformation and fluid history, but more research is required to evaluate this history.

In general, this study has emphasised the thermal and magmatic complexity of the western Himalayan syntaxis. This complexity is a reflection of an extended tectonic history involving an initial collision, followed by a period of marked differential uplift and unroofing which occurred contemporaneously with continued convergence across the collision orogen. It is likely that steady-state thermal conditions in such tectonically active

regions are rarely achieved, since crustal deformation proceeds much faster than heat diffusion in rocks. Intermittent or localised deformation and uplift, together with crustal anatexis and local advection of heat during magma ascent, are likely to result in purely transient geothermal structures in evolving collision zones. However, initial constraints on the geological histories of such areas come from integrated studies such as this one, which combine detailed field study with modern geochemical, metamorphic and geochronological techniques. Such studies of tectonically-active regions are crucial in understanding the tectonic and thermal histories of ancient collision belts.

References

Ahmed, Z., Hussain, S. and Awan, A. 1977. Petrology of Thelichi area, Gilgit Agency. *Geol. Bull. Punjab University*, **4**, 27-38.

Allègre, C. J. and Ben Othman, D. 1980. Nd-Sr isotopic relationships in granitoid rocks and continental crust : a chemical approach to orogenesis. *Nature*, **296**, 335-342.

Allègre, C. J. and 34 other workers 1984. Structure and Evolution of the Himalaya-Tibet orogenic belt. *Nature*, **307**, 17-22.

Anderson, E. M. 1951. *The Dynamics of Faulting and Dyke Emplacement.* Oliver & Boyd, Edinburgh, 206 pp.

Armstrong, R. L., Jäger, E. and Eberhardt, P. 1966. A comparison of K-Ar and Rb-Sr ages on Alpine biotites. *Earth Planet. Sci. Lett.*, **1**, 13-19.

Arndt, N. T. and Goldstein, S. L. 1987. Use and abuse of crust-forming ages. *Geology*, **15**, 893-895.

Baldwin, S. L., Harrison, T. M. and Fitz Gerald, J. D. 1990. Diffusion of ^{40}Ar in metamorphic hornblende. *Contrib. Mineral. Petrol.*, **105**, 691-703.

Bard, J. P. 1983. Metamorphism of an obducted island arc : Example of the Kohistan Sequence (Pakistan) in the Himalayan collided range. *Earth Planet. Sci. Lett.*, **65**, 133-144.

Bard, J. P., Maluski, H., Matte, Ph. and Proust, F. 1980. The Kohistan sequence : crust and mantle of an obducted island arc. *Spec. Iss. Geol. Bull. Univ. Peshawar*, **13**, 87-94.

Barnett, D. E. 1991. Oxygen Isotope Constraints on the Genesis of Young (< 5 Ma) Leucogranites from the Nanga Parbat Haramosh Massif (abstract). *Eos Trans*, AGU, **72**.

Barnicoat, A. C. and Treloar, P. J. 1988. Collision tectonics in the western Himalaya : suture zone P-T paths (abstract). *Geol. Soc. Am*, 20.7, A322.

Beach, A. 1976. The interrelations of fluid transport, deformation, geochemistry and heat flow in early Proterozoic shear zones in the Lewisian complex. *Phil. Trans. R. Soc. Lon.*, **280**, 569-604.

Bergman, S. 1992. P-T paths in the Handol area, central Scandinavia : record of Caledonian accretion of outboard rocks to the Baltoscandian margin. *J. Metamorphic Geol.*, **10**, 265-281.

Besse, J., Courtillot, V., Pozzi, J. P., Westphal, M. and Zhou, Y. X. 1984. Paleomagnetic estimates of crustal shortening in the Himalayan thrusts and Zangbo suture. *Nature*, **311**, 621-626.

Béthune, P. de. and Laduron, D. 1975. Diffusion Processes in Resorbed Garnets. *Contrib. Mineral. Petrol.*, **50**, 197-204.

Bird, P. 1978. Initiation of intracontinental subduction in the Himalayas. *J. Geophys. Res.*, **83**, 4975-4987.

Blanckenburg, F., Villa, I. M., Baur, H., Morteani, G. and Steiger, R. H. 1989. Time calibration of a P-T path from the Western Tauern Window, Eastern Alps : the problem of closure temperatures. *Contrib. Mineral. Petrol.*, **101**, 1-11.

Blattner, P., Dietrich, V. and Gansser, A. 1983. Contrasting ^{18}O enrichment and origins of High Himalayan and Transhimalayan intrusives. *Earth Planet. Sci. Lett.*, **65**, 276-286.

Bossart, P., Dietrich, D., Greco, A., Ottiger, R. and Ramsay, J. G. 1988. The tectonic structure of the Hazara-Kashmir-Syntaxis, southern Himalayas, Pakistan. *Tectonics*, **7**, 273-297.

Boyle, A. P. and Westhead, R. K. 1992. Metamorphic peak geothermobarometry in the Furulund Group, Sulitjelma, Scandinavian Caledonides : implications for uplift. *J. Metamorphic Geol.*, **10**, 615-626.

Brookfield, M. E. 1981. Metamorphic distributions and events in the Ladakh range, Indus suture zone and Karakorum mountains. In : Saklani, P. S. (ed.), *Metamorphic Tectonites of the Himalaya*, pp. 1-14.

Brookfield, M. E. and Reynolds, P. H. 1981. Late Cretaceous emplacement of the Indus suture zone ophiolitic melanges and an Eocene-Oligocene magmatic arc on the northern edge of the Indian plate. *Earth Planet. Sci. Lett.*, **55**, 157-162.

Burchfield, B. C. and Royden, L. H. 1985. North-south extension within the convergent Himalayan region. *Geology*, **13**, 679-682.

Burg, J. P., Brunel, M., Gapais, D., Chen, G. M. and Liu, G. H. 1984. Deformation of leucogranites of the crystalline Main Central Thrust Sheet in southern Tibet (China). *J. Structural Geol.*, **6**, 535-542.

Burnham, C. W. and Ohomoto, H. 1980. Late-stage Processes of Felsic Magmatism. *Mining Geol. Spec. Iss*, **8**, 1-11.

Burton, K. W. and O'Nions, R. K. 1991. High-resolution garnet chronometry and the rates of metamorphic processes. *Earth Planet. Sci. Lett.*, **104**, 649-671.

Butler, R. W. H. and Coward, M. P. 1989. Crustal scale thrusting and continental subduction during Himalayan collision tectonics on the NW Indian plate. In : Sengor, A. M. C. (ed.), *Tectonic Evolution of Tethyan regions*. Spec. Pub. NATO Ad. Sud. Inst., pp. 387-413.

Butler, R. W. H. and Prior, D. J. 1988a. Anatomy of a continental subduction zone: the main mantle thrust in northern Pakistan. *Geologische Rundschau*, **77**, 1, 239-255.

Butler, R. W. H. and Prior, D.J. 1988b. Tectonic controls on the uplift of the Nanga Parbat Massif, Pakistan Himalayas. *Nature*, **333**, 247-250.

Butler, R. W. H., George, M. T., Harris, N. B. W., Jones, C., Prior, D. J., Treloar, P. J. and Wheeler, J. 1992. Geology of the Northern part of the Nanga Parbat massif, Northern Pakistan, and its implications for Himalayan tectonics. *J. Geol. Soc. Lon.*, **149**, 557-567.

Butler, R. W. H., Owen, L. and Prior, D. J. 1988. Flashfloods, earthquakes and uplift in the Pakistan Himalayas. *Geology Today*, **4**, 197-201.

Butler, R. W. H., Prior, D. J. and Knipe, R. J. 1989. Neotectonics of the Nanga Parbat Syntaxis, Pakistan, and crustal stacking in the N.W.Himalayas. *Earth Planet. Sci. Lett.*, **94**, 329-343.

Cann, J. R. 1970. Upward movement of granite magma. *Geol. Mag.*, **107**, 335-340.

Cawthorn, R. G. and Brown, P. A. 1976. A model for the formation and crystallisation of corundum-normative calc-alkaline magmas through amphibole fractionation. *J. Geol.*, **84**, 467-476.

Chang, C. F. and Cheng, H. 1973. Some tectonic features of the Mount Jolmo Lungma area, southern Tibet, China. *Scientia Sinica*, **16**, 257-265.

Chappell, B. W., White, A. J. R. and Wyborn, D. 1987. The importance of residual source material (Restite) in granite petrogenesis. *J. Petrol.*, **28**, 1111-1138.

Chamberlain, C. P., Jan, Q. and Zeitler, P. K. 1989. A Petrologic record of the collision between the Kohistan island arc and the Indian plate, northwest Himalaya. In : Malinconico, L. L. and Lillie, R. J. (eds.), Tectonics of the western Himalayas. *Geol. Soc. Am. Spec. Pub.*, **232**, 23-32.

Chamberlain, C. P., Zeitler, P. K. and Erickson, E. 1991. Constraints on the Tectonic evolution of the northwestern Himalaya from Geochronolgic and Petrologic studies of Babusar Pass, Pakistan. *J. Geol.*, **99**, 829-849.

Chaudhary, A. K., Harris, N. B. W., Calsteren, P. Van and Hawkesworth, C. J. 1992. Pan-African charnockite formation in Kerala, South India. *Geol. Mag.*, **129**, 257-264.

Clemens, J. D. and Vielzeuf, D. 1987. Constraints on Melting and Magma Production in the Crust. *Earth Planet. Sci. Lett.*, **86**, 287-306.

Clemens, J. D. and Wall, V. J. 1981. Origin and Crystallisation of some Peraluminous (S-type) granitic magmas. *Can. Min.*, **19**, 111-131.

Cliff, R.A. 1985. Isotopic Dating in Metamorphic Belts. *J. Geol. Soc. Lon.*, **142**, 97-110.

Cliff, R. A., Barnicoat, A. C. and Treloar, P. J. 1991. Generation and Migration of Isotopically Extreme Partial Melts in Active Fault Zones (abstract). *Eos Trans*, AGU, **6**, 489.

Cliff, R. A., Droop, G. T. R. and Rex, D. C. 1985. Alpine metamorphism in the south-east Tauern Window, Austria : 2. Rates of heating, cooling and uplift. *J. Metamorphic Geol.*, **3**, 403-415.

Cosca, M. A., Johannes, J. C., Hunziker, S. H. and Masson, H. 1992. Radiometric age constraints on mineral growth, metamorphism and tectonism of the Gummfluch Klippe, Brianconnais domain of the Préalpes, Switzerland. *Contrib. Mineral. Petrol.*, **112**, 439-449.

Coward, M. P. 1985. A section through the Nanga Parbat Syntaxis, Indus valley, Kohistan. *Geol. Bull. Univ. Peshawar*, **18**, 147-152.

Coward, M. P. and Butler, R. W. H. 1985. Thrust tectonics and the deep structure of the Pakistan Himalaya. *Geology* , **13**, 417-420.

Coward, M. P., Butler, R. W. H., Asif Khan, M. and Knipe, R. J. 1987. The tectonic history of Kohistan and its implications for Himalayan Structure. *J. Geol. Soc. Lon.*, **144**, 377-391.

Coward, M. P., Butler, R. W. H., Chambers, A. F., Graham, R. H., Izatt, C. N., Asif Khan, M., Knipe, R. J., Prior, D. J., Treloar, P. J. and Williams, M. P. 1988. Folding and imbrication of the Indian crust during Himalayan collision. *Phil. Trans. R. Soc. Lon.*, **326**, 89-116.

Coward, M. P., Jan, M. Q, Rex, D., Tarney, J., Thirwall, M. and Windley, B. F. 1982. Geo-tectonic framework of the Himalaya of N. Pakistan. *J. Geol. Soc. Lon.*, **139**, 299-308.

Coward, M. P.,Windley, B. F., Broughton, R. D., Luff, I. W., Petterson, M. G., Pudsey, C. J., Rex, D. C.and Asif Khan, M. 1986. Collision Tectonics in the NW Himalayas. In : Coward, M. P., and Ries, A., (eds.), Collision Tectonics, *Geol. Soc. Lon. Spec. Publ.*, **19**, 203-219.

Crawford, M. L. 1977. Calcium zoning in almandine garnet, Wissahickon Formation, Philadelphia, Pennsylvania. *Can. Min.*, **15**, 243-249.

Crawford, M. B. and Searle, M. P. 1992. Field relationships and geochemistry of pre-collisional (India-Asia) granitoid magmatism in the central Karakoram, northern Pakistan. *Tectonophysics*, **206**, 171-192.

Crawford, M. B. and Windley, B. F. 1990. Leucogranites of the Himalaya/Karakoram: implications for magmatic evolution within collisional belts and the study of collisional-related leucogranite petrogenesis. *J. Volcanol. Geothermal Res.*, **44**, 1-19.

Cygan, R. T. and Lasaga, A. C. 1982. Crystal growth and the formation of chemical zoning in garnets. *Contrib. Mineral. Petrol.*, **79**, 187-200.

Day, H. W. 1987. Controls on the apparent thermal and baric structure of mountain belts. *J. Geol.*, **95**, 807-824.

Debon, F., Le Fort, P., Dautel, D., Sonet, J. and Zimmermann, J. L. 1987. Granites of W. Karakorum and northern Kohistan (Pakistan) : A composite mid-Cretaceous to upper Cenozoic magmatism. *Lithos*, **20**, 19-40.

Deniel, C., Vidal, P., Fernandez, A., Le Fort, P. and Peucat, J. J. 1987. Isotopic study of the Manaslu granite (Himalaya, Nepal): inferences of the age and source of Himalayan leucogranites. *Contrib. Mineral. Petrol.*, **96**, 78-92.

DePaolo, D. J. 1981. Nd isotope systematics in the Colorado Front Range and crustal mantle evolution in the Proterozoic. *Nature*, **291**, 193-196.

DePaolo, D. J. and Wasserburg, G. L. 1976. Nd isotope variations and petrogenetic models. *Geophys. Res. Lett.*, **3**, 249-252.

Desio, A. 1974. Geological reconnaissance in the Middle Indus valley between Chilas and Besham Quila, Pakistan. *Boll. Soc. Geol. Ital.*, **9**, 345-368.

Desio. A. 1979. Geologic evolution of the Karakorum. In : Farah, A., and DeJong, K. A. (eds), *Geodynamics of Pakistan*, Quetta, pp. 111-124.

Desio, A., Tongiorgi, E. and Ferrara, G. 1964. On the geological age of some granites of the Karakoram, Hindu Kush and Badakhshan (central Asia). *Proc. 22nd Int. Geol. Congress*, **11**, 479-496.

Dewey, J. F. and Burke, K. 1973. Tibetan, Variscan and Precambrian basement reactivation: products of continental collision. *J. Geol.*, **81**, 683-692.

Dewey, J. F., Cande, S. and Pitman, W. C. 1989. Tectonic evolution of the India/Eurasia collision zone. *Eclogae geol. Helv.*, **82**, 717-734.

Dewey, J. F, FRS, Shackleton, R. M, FRS, Chengfa, C., Yiyin, S. 1988. The Tectonic evolution of the Tibetan Plateau. *Phil. Trans. R. Soc. Lon.*, **327**, 379-413.

De Yoreo, J. J., Lux, D. R. and Guidotti, C. V. 1989. The role of crustal anatexis and magma migration in the thermal evolution of regions of thickened continental crust. In : Daly, J. S., Cliff, R. A. and Yardley, B. W. D. (eds.), Evolution of Metamorphic Belts, *Geol. Soc. Lon. Spec. Pub.*, **43**, 187-202.

Dietrich, V. and Gansser A. 1981. The leucogranites of the Bhutan Himalaya (Crustal anatexis versus mantle melting). *Schweiz. Mineral. Petrogr. Mitt.*, **61**, 177-202.

Dietrich, V. J., Wolfgang. F. and Honegger, K. 1983. A Jurassic-Cretaceous island arc in the Ladakh-Himalayas. *J. Volcanol. Geothermal Res.*, **18**, 405-433.

DiPietro, J. A. 1991. Metamorphic pressure-temperature conditions of Indian plate rocks south of the Main Mantle Thrust, lower Swat, Pakistan. *Tectonics*, **10**, 742-757.

Dipple, G. M., Wintsch, R. P. and Andrews, M. S. 1990. Identification of the scales of differential element mobility in a ductile fault zone. *J. Metamorphic Geol.*, **8**, 645-661.

Dodson, M. H. 1973. Closure Temperature in Cooling Geochronological and Petrological Systems. *Contrib. Mineral. Petrol.*, **40**, 259-274.

Ebadi, A. and Johannes, W. 1991. Beginning of melting and composition of first melts in the system Qz-Ab-Or-H_2O-CO_2. *Contrib. Mineral. Petrol.*, **106**, 286-295.

Ellis, D. J. and Thompson, A. B. 1986. Subsolidus and Partial melting reactions in the quartz-excess CaO+MgO+Al_2O_3+SiO_2+H_2O system under water excess and water deficient conditions to 10 kb : Some implications for the origin of peraluminous melts from mafic rocks. *J. Petrol.*, **27**, 91-121.

England, P. and Houseman, G. A. 1986. Finite strain calculations of continental deformation 2 : comparison with the India-Asia collision zone. *J. Geophys. Res.*, **91**, 3664-3676.

England, P. and Molnar, P. 1990b. Surface uplift, uplift of rocks, and exhumation of rocks. *Geology*, **18**, 1173-1177.

England, P. C. and Richardson, S. W. 1980. Erosion and age dependence of continental heat flow. *Geophys. J. R. Ast. Soc.*, **61**, 421-437.

England, P. and Searle, M. P. 1986. The Cretaceous-Tertiary deformation of the Lhasa block and its implications for crustal thickening in Tibet. *Tectonics*, **5**, 1-14.

England, P. C. and Thompson, A. B. 1984. Pressure-temperature-time paths of regional metamorphism. Heat transfer during the evolution of regions of thickened continental crust. *J. Petrol.*, **25**, 894-928.

England, P. C. and Thompson, A. B. 1986. Some Thermal and Tectonic models for crustal melting in Continental Collision zones. In : Coward, M. P. and Ries, A. (eds.), Collision Tectonics, *Geol. Soc. Lon. Spec. Pub.*, **19**, 83-94.

Essene, E. J. 1989. The current status of thermobarometry in metamorphic rocks. In : Daly, J. S., Cliff, R. A. and Yardley, B. W. D. (eds.), Evolution of Metamorphic Belts, *Geol. Soc. Lon. Spec. Pub.*, **43**, 1-44.

Etheridge, M. A., Wall, V. J. and Vernon, R. H. 1983. The role of the fluid phase during regional metamorphism and deformation. *J. Metamorphic Geol.*, **1**, 205-226.

Eugster, H. P. 1985. Granites and hydrothermal ore deposits : a geochemical framework. *Min. Mag.*, **49**, 7-23.

Farver, J. R. and Giletti, B. J. 1989. Oxygen and strontium diffusion kinetics in apatite and potential applications to thermal history determinations. *Geochem. Cosmochim. Act.*, **53**, 1621-1631.

Faure, G. 1986. *Principles of Isotope Geology*. John Wiley & Sons, 589 pp.

Foland, K. A. 1974. Ar^{40} diffusion in homogenous orthoclase and an interpretation of Ar diffusion in k-feldspars. *Geochem. Cosmochim. Act.*, **38**, 151-166.

Fourcade, S. and Allègre, C. J. 1981. Trace Element Behaviour in Granite Genesis : a case study. The Calc-alkaline plutonic association from the Querigut complex (Pyrenees, France). *Contrib. Mineral. Petrol.*, **76**, 177-195.

France-Lanord, C. and Le. Fort, P. 1988. Crustal melting and granite genesis during the Himalayan collision orogenesis. *Trans. R. Soc. Edin.*, **79**, 183-195.

Frank, W., Gansser, A. and Trommsdorff, V. 1977. Geological observations in the Ladakh area (Himalayas). A preliminary report. *Schweiz. mineral. petrogr. Mitt.*, **57**, 89-113.

Frost, B. R. and Chacko, T. 1989. The Granulite uncertainty principle : Limitations on Thermobarometry in granulites. *J. Geol.*, **97**, 435-450.

Frost, B. R. and Tracy, R. J. 1991. P-T paths from zoned garnets : some minimum criteria. *Am. J. Sci.*, **291**, 917-939.

Gansser, A. 1964. *Geology of the Himalayas*. Interscience publishers, London, 289 pp.

Gansser, A. 1980. The division between Himalaya and Karakorum. *Spec. Iss. Geol. Bull. Univ. Peshawar*, **13**, 9-22.

Gariepy, C., Allègre, C. J. and Xu, R. H. 1985. The Pb-isotope geochemistry of granitoids from the Himalaya-Tibet collision zone : implications for crustal evolution. *Earth Planet. Sci. Lett.*, **74**, 220-234.

Geist, D., J., Frost, C. D., Kolker, A. and Frost, B. R. 1988. A geochemical study of magmatism across a major terrane boundary: Sr and Nd isotopes in Proterozoic granitoids of the southern Laramie Range, Wyoming. *J. Geology*, **97**, 331-342.

Ghent, E. D. and Stout, M. Z. 1981. Geobarometry and geothermometry of plagioclase-biotite-garnet-muscovite assemblages. *Contrib. Mineral. Petrol.*, **76**, 92-97.

Giletti, B. J. 1991. Rb and Sr diffusion in alkali feldspars with implications for cooling histories of rocks. *Geochim. Cosmochim. Act.*, **55**, 1331-1343.

Goodwin, L. B. and Renne, P. R. 1991. Effects of progressive mylonisation on Ar retention in biotites from the Santa Rosa mylonite zone, California, and thermochronologic implications. *Contrib. Mineral. Petrol.*, **108**, 283-297.

Green, T. H. 1977. Garnet in silicic liquids and its possible use as a P-T indicator. *Contrib. Mineral. Petrol.*, **65**, 59-67.

Hamilton, P. J., Kelley, S. and Fallick, A. E. 1989. K-Ar dating of Illite in hydrocarbon reservoirs. *Clay Minerals*, **24**, 215-231.

Hanmer, S. 1986. Asymmetrical pull-aparts and foliation fish as kinematic indicators. *J. Structural Geol.*, **8**, 111-122.

Hanson, N. G. 1978. The application of Trace Elements to the Petrogenesis of Igneous Rocks of granitic composition. *Earth Planet. Sci. Lett.*, **38**, 26-43.

Hanson, C. R. 1989. The Northern Suture in the Shigar valley, Baltistan, northern Pakistan. In : Malinconico, L. L. and Lillie, , R. J. (eds.), Tectonics of the Western Himalayas. *Geol. Soc. Am. Spec. Paper*, **232**, 203-215.

Harris, N. B. W. 1981. The Role of Fluorine and Chlorine in the Petrogenesis of a Peralkaline complex from Saudi Arabia. *Chem. Geol.*, **31**, 303-310.

Harris, N. B. W. and Inger, S. 1992. Trace Element modelling of Pelite-derived Granites. *Contrib. Mineral. Petrol.*, **110**, 46-56.

Harris, N. B. W. and Marriner, G. F. 1980. Geochemistry and Petrogensis of a Peralkaline granite complex from the Midian Mountains, Saudi Arabia. *Lithos*, **13**, 325-337.

Harris, N., Inger, S. and Massey, J. 1993. The role of fluids in the formation of High Himalayan Leucogranites. In : Treloar, P. J. and Searle, M. P (eds.). Himalayan Tectonics, *Geol. Soc. Lon. Spec. Pub.*, **74**, 391-400.

Harris, N. B. W., Pearce, J. A. and Tindle, A. G. 1986. Geochemical characteristics of collision-zone magmatism. In : Coward, M. P. and Ries, A. (eds.), Collision Tectonics, *Geol. Soc. Lon. Spec. Pub.*, **19**, 67-81.

Harris, N. B. W., Xu, R., Lewis, C. L. and Chengwei, J. 1988a. Plutonic rocks of the 1985 Tibet Geotraverse, Lhasa to Golmud. *Phil. Trans. R. Soc. Lon.*, **327**, 145-168.

Harris, N. B. W., Xu, R., Lewis, C.L., Hawkesworth, C.J. and Zhang Yuquan 1988b. Isotope geochemistry of the 1985 Tibet Geotraverse, Lhasa to Golmud. *Phil. Trans. R. Soc. Lon.*, **327**, 263-285.

Harris, N. B. W., Gravestock, P. and Inger, S. 1992. Ion-microprobe determinations of trace-element concentrations in garnets from anatectic assemblages. *Chemical Geology*, **100**, 41-49.

Harrison, T. M. 1981. Diffusion of argon in hornblende. *Contrib. Mineral. Petrol.*, **78**, 324-331.

Harrison, T. M. and Fitz Gerald, J. G. 1986. Exsolution in hornblende and its consequences for $^{40}Ar/^{39}Ar$ age spectra and closure temperatures. *Geochim. Cosmochim. Act.*, **50**, 247-253.

Harrison, T. M. and McDougall, I. 1980. Investigations of an Intrusive contact, northwest Nelson, New Zealand -1. Thermal, chronological and isotopic constraints. *Geochim. Cosmochim. Act.*, **44**, 1985-2003.

Harrison, T. M., Copeland, P., Kidd, W. S. F. and Yin, A. 1992. Raising Tibet, *Science*, **255**, 1663-1670.

Harrison, T. M., Duncan, I. and McDougall, I. 1985. Diffusion of ^{40}Ar in Biotite : Temperature, pressure and compositional effects. *Geochim. Cosmochim. Act.*, **49**, 2461-2468.

Hart, S. R. 1964. The petrology and isotopic-mineral age relations at a contact zone in the Front Ranges, Colorado. *J. Geol.*, **72**, 493-525.

Helz, R. T. 1976. Phase relations of basalts in their melting ranges at P_{H_2O} = 5 kbar. Part 2 : melt compositions. *J. Petrol.*, **17**, 139-193.

Henderson, P. 1982. *Inorganic Geochemistry*. Pergamon Press, Oxford, 353 pp.

Herren, E. 1987. Zanskar shear zone : northeast-southwest extension within the Higher Himalayas (Ladakh, India). *Geology*, **15**, 409-413.

Hildreth, W. and Moorbath, S. 1988. Crustal contributions to arc magmatism in the Andes of Central Chile. *Contrib. Mineral. Petrol.*, **98**, 455-489.

Hodges, K. V. 1991. Pressure-Temperature-Time paths. *An. Rev. Earth Planet. Sci.*, **19**, 207-236.

Hodges, K. V. and Crowley, P. D. 1985. Error estimation and empirical geothermobarometry for pelitic systems. *Am. Min.*, **70**, 702-709.

Hodges, K. V. and Silverburg, D. S. 1988. Thermal evolution of the greater Himalaya, Garhwal, India. *Tectonics*, **7**, 583-600.

Hodges, K. V. and Spear, F. S. 1982. Geothermometry, geobarometry and the Al_2SiO_5 triple point at Mt. Moosilauke, New Hampshire. *Am. Min.*, **67**, 1118-1134.

Holdaway, M. J. 1971. Stability of andalusite and the aluminosilicate phase diagram. *Am. J. Sci.*, **271**, 97-131.

Holland, T. J. B. and Powell, R. 1985. An internally consistent thermodynamic dataset with uncertainties and corrections : 2. Data and Results. *J. Metamorphic Geol.*, **3**, 343-370.

Holland, T. J. B. and Powell, R. 1990. An enlarged and updated internally consistent thermodynamic dataset with uncertainties and correlations : the system K_2O-Na_2O-CaO-MgO-MnO-FeO-Fe_2O_3-Al_2O_3-TiO_2-SiO_2-C-H_2-O_2. *J. Metamorphic Geol.*, **8**, 89-124.

Hollister, L. S. 1966. Garnet zoning : an interpretation based on the Rayleigh fractionation model. *Science*, **154**, 1647-1651.

Hollister, L. S. 1982. Metamorphic evidence for rapid (2 mm/yr) uplift of a portion of the Central Gneiss Complex, Coast Mountains, British Columbia. *Can. Min.*, **20**, 319-332.

Holz, F., Johannes, W. and Pichavant, M. 1992. Peraluminous granites : the effect of alumina on melt composition and coexisting minerals. *Trans. R. Soc. Edin.*, **83**, 409-416.

Honegger, K., Dietrich, V., Frank, W., Gansser, A., Thoni, M. and Trommsdorff, V. 1982. Magmatism and metamorphism in the Ladakh Himalaya (the Indus-Tsangpo suture zone). *Earth Planet. Sci. Lett.*, **60**, 253-292.

Honegger, K., Le Fort, P., Mascle, G. and Van Haver, T. 1985. Presence de Schistes Bleus a Glaucophane dans la zone de suture de l'Indus au Ladakh (abstract). *Terra Cognita*, **5**, 257.

Hubbard, M., Royden, L. and Hodges, K. 1991. Constraints on Unroofing Rates in the High Himalaya, Eastern Nepal. *Tectonics*, **10**, 287-298.

Hurford, A. J. 1986. Cooling and uplift patterns in the Lepontine Alps, South Central Switzerland, and an age of vertical movement on the Insubric fault line. *Contrib. Mineral. Petrol.*, **92**, 413-427.

Hutton, D. H. W. 1992. Granite sheeted complexes : evidence for the dyking ascent mechanism. *Trans. R. Soc. Edin.*, **83**, 377-382.

Inger, S. and Harris, N. B. W. 1992. Tectonothermal evolution of the high Himalayan Crystalline sequence, Langtang valley, northern Nepal. *J. Metamorphic Geol.*, **10**, 439-452.

Inger, S. and Harris, N. 1993. Geochemical constraints on leucogranite magmatism in the Langtang Valley, Nepal Himalaya. *J. Petrol., in press.*

Jäger, E., Niggli, E. and Wenk, E. 1967. Rb-Sr Altersbestimmungen an Glimmern der Zentralalpen. *Beitr. Geol. Karte Schweiz, NF Liefg.* **134.**, Kümmerly and Frey, Bern.

Jan, M. Q. and Howie, R. A. 1980. Ortho- and clinopyroxenes from the pyroxene granulites of Swat Kohistan, northern Pakistan. *Min. Mag.*, **43**, 715-726.

Jan, M. Q. and Howie, R. A. 1981. The mineralogy and geochemistry of the metamorphosed basic and ultrabasic rocks of the Jijal complex, Kohistan, NW Pakistan. *J. Petrol.*, **22**, 85-126.

Jan, M. Q., Asif, M., Tahirkheli, T. and Kamal, M. 1981. Tectonic subdivision of granite rocks of north Pakistan. *Geol. Bull. Univ. Peshawar*, **14**, 159-182.

Jaupart, C. and Provost, A. 1985. Heat focussing, granite genesis and inverted metamorphic gradients in continental collision zones. *Earth Planet. Sci. Lett.*, **73**, 385-397.

Jiang, J. and Lasaga, A. C. 1990. The effect of post-growth thermal events on growth-zoned garnet : implication for metamorphic P-T history calculations. *Contrib. Mineral. Petrol.*, **105**, 454-459.

Johannes, W. and Holtz, F. 1990. Formation and composition of H_2O-undersaturated granitic melts. In : Ashworth, J. R. and Brown, M. (eds.), *High-temperature metamorphism and crustal Anatexis*. Unwin Hyman, London, pp. 87-101.

Johnson, B. D., Powell, McA., Veevers, J. J. 1976. Spreading history of the eastern Indian ocean, and greater India's northward flight from Antartica and Australia. *Geol. Soc. Am. Bull.*, **87**, 1560-1566.

Jones, K. A. and Brown, M. 1990. High-temperature 'clockwise' P-T paths and melting in the development of regional migmatites : an example from southern Brittany, France. *J. Metamorphic Geol.*, **8**, 551-578.

Kazmi, A. H., Lawrence, R. D., Dawood, H., Snee, L. W. and Hussain, S. S. 1984. Geology of the Indus suture zone in the Mingora-Shangla area of Swat, N. Pakistan. *Geol. Bull. Univ. Peshawar*, **17**, 127-144.

Kelley, S. 1988. The relationship between K-Ar mineral ages, mica grain sizes and movement on the Moine Thrust Zone, NW Highlands, Scotland. *J. Geol. Soc. Lon.*, **145**, 1-10.

Kelley, S. P. and Turner, G. 1991. Laser probe ^{40}Ar-^{39}Ar measurements of loss profiles within individual hornblende grains from the Giants Range Granite, northern Minnesota, USA. *Earth Planet. Sci. Lett.*, **107**, 634-648.

Khan, M. A., Jan, M. Q., Windley, B. F., Tarney, J. and Thirlwall, M. F. 1989. The Chilas mafic-ultramafic igneous complex; the root of the Kohistan island arc in the Himalaya of northern Pakistan. In : Malinconico, L. L. and Lillie, R. J. (eds.), Tectonics of the western Himalayas. *Geol. Soc. Am. Spec. Paper*, **232**, 75-93.

Kligfield, R., Hunziker, J., Dallmeyer, R. D. and Schamel, S. 1986. Dating of deformation phases using K-Ar and $^{40}Ar/^{39}Ar$ techniques : results from the Northern Apennines. *J. Structural Geol.*, **8**, 781-798.

Klootwijk, C. T., Conaghan, P. J. and Powell, C. McA. 1985. The Himalyan Arc : Large-scale continental subduction, oroclinal bending and back-arc spreading. *Earth Planet. Sci. Lett.*, **75**, 167-183.

Klootwijk, C., Sharma, M. L., Gergan, J., Tirkey, B., Shah, S. K. and Agarwal, V. 1979. The extent of greater India, 2. Palaeomagnetic data from the Ladakh intrusives at Kargil, NW Himalayas. *Earth Planet. Sci. Lett.*, **44**, 47-64.

Kohn, M. J. 1993. Uncertainties in differential thermodynamic (Gibbs' method) P-T paths. *Contrib. Mineral. Petrol.*, **113**, 24-39.

Kohn, M. J. and Spear, F. S. 1990. Two new geobarometers for garnet amphibolites, with applications to southeastern Vermont. *Am. Min.*, **75**, 89-96.

Krähenbühl, R. 1984. Petrographisch-geologische Untersuchungen in der Silvrettamasse vom Flüela Wisshorn zum Gorihorn und Rosställispitz (Graubünden). *PhD. Thesis*, University Berne, Switzerland (unpublished).

Kwan, T. S., Krähenbühl, R. and Jäger, E. 1992. Rb-Sr, K-Ar and fission-track ages for granites from Penang Island, West Malaysia : an interpretation model for Rb-Sr whole-rock and for actual and experimental mica data. *Contrib. Mineral. Petrol.*, **111**, 527-542.

Laurence, R. D. and Ghauri, A. A. K. 1983a. Evidence of active faulting in Chilas district, N. Pakistan. *Geol. Bull. Univ. Peshawar*, **16**, 185-186.

Lawrence, R. D. and Ghauri, A. A. K. 1983b. Observations on the structure of the Main Mantle Thrust at Jijal, Kohistan, Pakistan. *Geol. Bull. Univ. Peshawar*, **16**, 1-10.

Lawrence, R. D., Snee, L. W. and Rosenberg, P. S. 1985. Nappe structure in a crustal scale duplex in Swat, Pakistan (abstract). *Geol. Soc. Am., Abstr. Progr.*, **17**, 640.

Le Breton, N. and Thompson, A. B. 1988. Fluid-absent (dehydration) melting of biotite in metapelites in the early stages of crustal anatexis. *Contrib. Mineral. Petrol.*, **99**, 226-237.

Le Fort, P. 1975. Himalaya : the collided range. Present knowledge of the continental arc. *Am. J. Sci.*, **275**, 1-44.

Le Fort, P. 1981. Manaslu Leucogranite : A collision signature of the Himalaya. A model for its genesis and emplacement. *J. Geophys. Res.*, **86**, 10545-10568.

Le Fort, P. 1989. The Himalayan Orogenic Segment. In : Sengor, A. M. C. (ed.) *Tectonic Evolution of the Tethyan Region*. NATO ASI Series C, **259**, 289-386.

Le Fort, P., Cuney, M., Deniel, C., France-Lanord, C., Sheppard, S. M. F., Upreti, B. N. and Vidal, P. 1987. Crustal generation of the Himalayan Leucogranites. *Tectonophysics*, **134**, 39-57.

Le Fort, P., Debon, F. and Sonet, J. 1980. The lesser Himalayan cordierite granite belt. Typology and age of the pluton of Manserah (Pakistan).. *Spec. Iss. Geol. Bull. Univ. Peshawar*, **13**, 51-61.

Le Fort, P., Michard, A., Sonet, J. and Zimmermann, J. L. 1983. Petrography, geochemistry and geochronology of some samples from the Karakoram axial batholith (northern Pakistan). In : Shams, F. A. (ed.), *Granites of Himalayas Karakoram and Hindu Kush*. Inst. Geol., Punjab Univ., Lahore, Pakistan, pp. 377-387.

Leake, B. E. 1964. The Chemical distinction between Ortho- and Para-amphibolites. *J. Petrol.*, **5**, 238-254.

Lister, G. S. and Snoke, A. W. 1984. S-C Mylonites. J. *Structural Geol.*, **6**, 617-638.

Madin, I. P., Lawrence, R. D. and Ur-Rahman, S. 1989. The northwestern Nanga-Parbat Haramosh Massif, evidence for crustal uplift at the N.W. corner of the Indian Craton. In : Malinconico, L. L. and Lillie, R. J. (eds.), Tectonics of the Western Himalayas. *Geol. Soc. Am. Spec. Paper*, **232**, 169-182.

Malinconico, L. L. 1986. The structure of the Kohistan-Arc terrane in northern Pakistan as inferred from gravity data. *Tectonophysics*, **124**, 297-307.

Maluski, H. and Matte, P. 1984. Ages of Alpine Tectonometamorphic events in the NW Himalaya by $^{40}Ar/^{39}Ar$ method. *Tectonics*, **3**, 1-18.

Maluski, H., Proust, F. and Xiao, X. C. 1982. $^{40}Ar/^{39}Ar$ dating of the Transhimalayan calcalkaline magmatism of southern Tibet. *Nature*, **298**, 152-154.

Manning, D. A. C. 1981. The effect of fluorine on liquidus phase relationships in the system Qz-Ab-Or with excess water at 1 kbar. *Contrib. Mineral. Pet.*, **76**, 206-215.

Mattauer, M. 1986. Intracontinental subduction, crust-mantle decollement and crustal stacking wedge in the Himalayas and other collision belts. In : Collision Tectonics, Coward, M. P., and Ries, A., (eds.), Collision Tectonics, *Geol. Soc. Lon. Spec. Pub.*, **19**, 37-50.

McAteer, C. 1976. Formation of garnets in a rock from Mallaig 1976. *Contrib. Mineral. Petrol.*, **55**, 293-301.

McCulloch, M. T. and Gamble, J. A. 1991. Geochemical and geodynamical constraints on subduction zone magmatism. *Earth Planet. Sci. Lett.*, **102**, 358-374.

Mercier, J. L., Armijo, R., Tapponnier, P., Carey-Gailhardis, E. and Lin, H. T. 1987. Change from late Tertiary compression to quaternary extension in southern Tibet during India-Asia collision. *Tectonics*, **6**, 275-304.

Mezger, K., Essene, E. J. and Halliday, A. N. 1992. Closure temperature of the Sm-Nd system in metamorphic garnets. *Earth Planet. Sci. Lett.*, **113**, 397-409.

Miller, C. F. 1985. Are Strongly Peraluminous Magmas derived from Pelitic Sedimentary Sources ? *J. Geol.*, **93**, 673-689.

Misch, P. 1949. Metasomatic granitisation of batholithic dimensions. *Am. J. Sci.*, **247**, 209-245.

Misch, P. 1964. Stable association wollastonite-anorthite and other calcsilicate assemblages in amphibolite-facies crystalline schists of Nanga Parbat, Northwest Himalayas. *Contrib. Mineral. Petrol.*, **10**, 315-356.

Molnar, P. and England, P. 1990. Late Cenozoic uplift of mountain ranges and global climate change : chicken or egg ? *Nature*, **346**, 29-34.

Molnar, P. and Tapponnier, P. 1975. Cenozoic Tectonics of Asia : Effects of a continental collision. *Science*, **189**, 419-426.

Nakamura, N. 1974. Determination of REE, Ba, Fe, Mg, Na and K in carbonaceous and ordinary meteorites. *Geochem. Cosmochim. Acta.*, **38**, 757-775.

Newton, R. C. and Haselton, H. T. 1981. Thermodynamics of the garnet-plagiclase-Al_2SiO_5-quartz geobarometer. In : Newton, R. C., Navrotsky, A. and Wood, B. J. (eds.), *Thermodynamics of Minerals and Melts*, Springer-Verlag, New York, pp. 131-147.

Ni, J. and Barazangi, M. 1984. Seismotectonics of the Himalayan Collision zone : geometry of the underthrusting Indian plate beneath the Himalaya. *J. Geophys Res.*, **89**, 1147-1163.

Oxburgh, E. R. and England, P. C. 1980. Heat flow and the metamorphic evolution of the Eastern Alps. *Eclogae. Geol. Helv.*, **73**, 379-398.

Parrish, R. and Tirrul, R. 1989. U-Pb age of the Baltoro granite, northwest Himalaya, and implications for monazite U-Pb systematics. *Geology*, **17**, 1076-1079.

Passchier, C. W. and Simpson, C. 1986. Porphyroblast systems as kinematic indicators. *J. Structural Geol.*, **8**, 831-843.

Patino-Douce, A. E., Humphreys, E. D. and Johnston, A. D. 1990. Anatexis and metamorphism in tectonically thickened crust exemplified by the Sevier hinterland, western North America. *Earth Planet. Sci. Lett.*, **97**, 290-315.

Patino-Douce, A. E. and Johnston, A. D. 1991. Phase equilibria and melt productivity in the pelitic system: implications for the origin of peraluminous granitoids and aluminous granites. *Contrib. Mineral. Petrol.*, **107**, 202-218.

Patriat, P. and Achache, J. 1984. India-Eurasia collision chronology has implications for Crustal Shortening and Driving mechanism of Plates. *Nature*, **311**, 615-621.

Pearce, J. A., Harris, N. B. W. and Tindle, A. G. 1984. Trace Element Discrimination Diagrams for the tectonic Interpretation of Granitic rocks. *J. Petrol.*, **25**, 956-983.

Petterson, M. G. 1984. The structure, petrology and geochemistry of the Kohistan batholith, Gilgit, Kashmir, N.Pakistan. *PhD. Thesis*, Leicester (unpublished).

Petterson, M. G. and Windley, B. F. 1985. Rb-Sr dating of the Kohistan arc-batholith in the Trans-Himalaya of north Pakistan, and tectonic implications. *Earth Planet. Sci. Lett.*, **74**, 45-57.

Petterson, M. G. and Windley, B. F. 1991. Changing source regions of magmas and crustal growth in the trans-Himalayas: evidence from the Chalt batholith, Kohistan, northern Pakistan. *Earth Planet. Sci. Lett.*, **102**, 326-341.

Petterson, M. G., Crawford, M. B. and Windley, B. F. 1993. Petrogenetic implications of neodymium isotope data from the Kohistan batholith, North Pakistan. *J. Geol. Soc. Lon.*, **150**, 125-129.

Pinet, C. and Jaupart, C. 1987. A thermal model for the distribution in space and time of the Himalayan granites. *Earth Planet. Sci. Lett.*, **84**, 87-99.

Pitcher, W. S. 1982. Ganite type and tectonic environment. In : Hsü, K. J. (ed.), *Mountain Building Processes*. Academic Press, London, pp. 19-40.

Platt, J. P. and Vissers, R. L. M. 1980. Extensional structures in anisotropic rocks. *J. Structural Geol.*, **2**, 397-410.

Potts, P. J., Williams Thorpe, O., Isaacs M. C. and Wright, D. W. 1985. High precision instrumental neutron activation analysis of geological samples employing simulataneous counting with both planar and coaxial detectors. *Chem. Geol*, **48**, 145-155.

Powell, C. McA. 1986. Continental underplating model for the rise of the Tibetan plateau. *Earth Planet. Sci. Lett.*, **81**, 79-94.

Powell, C . McA. and Conaghan, P. J. 1973. Plate Tectonics and the Himalaya. *Earth Planet. Sci. Lett.*, **20**, 1-12.

Powell, R. and Holland, T. J. B. 1988. An internally consistent dataset with uncertainties and correlations : 3. Applications to geobarometry, worked examples and a computer program. *J. Metamorphic Geol.*, **6**, 173-204.

Pudsey, C. J. 1986. The northern suture, Pakistan: margin of a Cretaceous island arc. *Geol. Mag.*, **123**, 405-423.

Pudsey, C. J., Schroeder, R. and Skelton, P. W. 1985. Cretaceous (Aptian/Albian) age for island arc volcanics, Kohistan, N. Pakistan. In : Gupta, V. J. (ed.), Geology of the western Himalayas, *Contributions to Himalayan Geology*, **3**, 150-168.

Pudsey, C. J., Coward, M. P., Luff, I. W., Shackleton, R. M., Windley, B. F. and Jan, M. Q. 1986. Collision zone between the Kohistan arc and the Asian plate in N.W.Pakistan. *Trans. R. Soc. Edin.*, **76**, 463-479.

Purdy, J. W. and Jäger, E. 1976. K-Ar Ages on Rock-Forming Minerals from the Central Alps. *Memorie degli Instituti di Geologia e Mineralogia dell'Universita di Padova*, **30**, 1-31.

Rai, H. 1982. Geological evidence against the Shyok Palaeo-suture, Ladakh Himalaya. *Nature*, **297**, 142-144.

Raz, U. and Honegger, K. 1989. Magmatic and tectonic evolution of the Ladakh block from field studies. *Tectonophysics*, **161**, 107-118.

Rex, A. J., Searle, M. P., Tirrul, R., Crawford, M. B., Prior, D. J., Rex, D. C. and Barnicoat, A. 1988. The geochemical and tectonic evolution of the central Karakoram, northern Pakistan. *Phil. Trans. R. Soc. Lon.*, **326**, 229-255.

Reynolds, P. H., Brookfield, M. E. and Mc Nutt, R. H. 1983. The age and nature of Mesozoic-Tertiary magmatism across the Indus suture zone in Kashmir and Ladakh (NW India and Pakistan). *Geol. Rund.*, **72**, 981-1004.

Richardson, S. W. and England, P. C. 1979. Metamorphic consequences of crustal eclogite production in overthrust orogenic zones. *Earth Planet. Sci. Lett.*, **42**, 183-190.

Rogers, J. J. W. and Greenberg, J. K. 1990. Late-orogenic, post-orogenic and orogenic granites : distinction by major-element and trace element-chemistry and possible origins. *J. Geol.*, **98**, 291-309.

Romick, J. D., Kay, S. M. and Kay, R. W. 1992. The influence of amphibole fractionation on the evolution of calc-alkaline andesite and dacite tephra from the central Aleutians, Alaska. *Contrib. Mineral. Petrol.*, **112**, 101-118.

Royden, L. H. 1993. The Steady State Thermal Structure of Eroding Orogenic Belts and Accretionary Prisms. *J. Geophys. Res.*, **98**, 4487-4507.

Rubie, D. C. and Brearley, A. J. 1990. A model for rates of disequilibrium melting during metamorphism. In : Ashworth, J. R. and Brown, M. (eds.), *High-temperature metamorphism and crustal Anatexis*. Unwin Hyman, London, pp. 57-84.

Rutter, M. J. and Wyllie, P. J. 1988. Melting of vapour-absent tonalite at 10 kbar to simulate dehydration-melting in the deep crust. *Nature*, **331**, 159-160.

Saxena, M. N. and Miller, J. A. 1972. Metamorphism, Magmatism and Orogeny in the light of radiometric dates in north-western Himalayas. *Bull. Ind. Geol. Ass.*, **5**, 63-69.

Scaillet, B., France-Lanord, C. and Le Fort, P. 1990. Badrinath-Gangotri plutons (Garwal, India) : Petrological and geochemical evidence for fractionation processes in a High Himalayan leucogranite. *J. Volcanol. Geothermal Res.*, **44**, 163-188.

Scharer, U., Copeland, P. Y, Harrison, T. M. and Searle, M. 1990. Age, cooling history and origin of post-collisional leucogranites in the Karakoram batholith; a multi-system isotope study. *J. Geol.*, **98**, 233-251.

Scharer, U., Xu., R. H. and Allègre, C. J. 1984a. U-Pb geochronology of Gangdese (Transhimalyan) plutonism in the Lhasa-Xigase region, Tibet. *Earth Planet. Sci. Lett.*, **69**, 311-320.

Scharer, U., Hamet, J. and Allègre, C. J. 1984b. The Transhimalayan (Gangdese) plutonism in the Ladakh region : a U-Pb and Rb-Sr study. *Earth Planet. Sci. Lett.*, **67**, 327-339.

Scharer, U., Xu., R. H. and Allègre, C. J. 1986. U-(Th)-Pb systematics and ages of Himalayan leucogranites, south Tibet. *Earth Planet, Sci. Lett.*, **77**, 35-48.

Schreyer, W. and Seifert, F. 1969. High-pressure phases in the system MgO-Al_2O_3-SiO_2-H_2O. *Am. J. Sci.*, **267**, 407-443.

Sclater, J. G., Jaupart, C. and Galson, D. 1980. The Heat Flow through Oceanic and Continental Crust and the Heat Loss of the Earth. Rev. Geophys. *Space Phys.*, **18**, 269-311.

Searle, M. P. 1983. Stratigraphy, structure and evolution of the Tibetan-Tethys zone in Zansgar and the Indus suture zone in the Ladakh Himalaya. *Trans. R. Soc. Edin.*, **73**, 205-219.

Searle, M. P. 1986. Structural evolution and sequence of thrusting in the High Himalayan, Tibetan-Tethys and Indus suture zones of Zanskar and Ladakh, western Himalaya. *J. Structural Geol.*, **8**, 923-936.

Searle, M. P. and Rex, A. J. 1989. Thermal model for the Zanskar Himalaya, *J. Metamorphic Geol.*, **7**, 127-134.

Searle, M. P. and Tirrul, R. 1991. Structural and Thermal evolution of the Karakoram crust. *J. Geol. Soc. Lon.*, **148**, 65-82.

Searle, M. P., Crawford, M. B. and Rex, A. J. 1992. Field relations, geochemistry, origin and emplacement of the Baltoro granite, Central Karakoram. *Trans. R. Soc. Edin. Earth Sciences*, **83**, 519-538.

Searle, M. P., Parrish, R. R., Tirrul, R. and Rex, D. C. 1990. Age of crystallisation and cooling of the K2 gneiss in the Baltoro Karakoram. *J. Geol. Soc. Lon.*, **147**, 603-606.

Searle, M. P., Rex, A. J., Tirrul, R., Windley, B. F., St. Onge, M. and Hoffman, P. 1986. A geological profile across the Baltoro Karakoram range, N. Pakistan. *Geol. Bull. Univ. Peshawar*, **19**, 1-12.

Searle, M. P., Rex, A. J., Tirrul, R., Rex, D. C., Barnicoat, A. and Windley, B. F. 1989. Metamorphic, magmatic and tectonic evolution of the central Karakorum in the Biafo-

Baltoro-Hushe regions of northern Pakistan. In : Malinconico, L. L. and Lillie, R. J. (eds.), Tectonics of the Western Himalayas. *Geol. Soc. Am. Spec. Paper*, **232**, 47-73.

Seeber, L., Armbruster, J. G. and Quittmeyer, R. C. 1981. Seismicity and continental subduction in the Himalayan arc. *Am. Geophys. Union, Geodyn. Ser.*, **5**, 215-242.

Shah, S. K., Sharma, J. T., Gergan, J. T. and Tara, C. S. 1976. Stratigraphy and structure of the western part of the Indus suture belt, Ladakh, northwest India. *Him. Geol.*, **6**, 543-556.

Shams, F. A. 1972. Glaucophane-bearing rocks from near Topsin, Swat - first record from Pakistan. *Pakistan J. Sci. Res.*, **24**, 343-345.

Shand, S. J. 1949. *Eruptive Rocks*. John Wiley and sons, New York, 488 pp.

Sharma, K. K., Sinha, A. K., Bagdasarian, G. P. and Gukasain, R. C. 1978. Potassium argon dating of Dras Volcanics, Shyok volcanics and Ladakh granite, Ladakh, northwest Himalaya. *Himalayan Geol.*, **8**, 288-295.

Simpson, C. and Schmid, S. M. 1983. An Evaluation of Criteria to deduce the sense of movement in sheared rocks. *Bull. Geol. Soc. Am.*, **94**, 1281-1288.

Sinha, A. K., Hewitt, D. A. and Rimstidt, J. D. 1988. Metamorphic petrology and strontium isotope geochemistry associated with the development of mylonites : an example from the Brevard fault zone, North Carolina. *Am. J. Sci.*, **288**, 115-147.

Smith, H. A. and Barreiro, B. 1990. Monazite U-Pb dating of staurolite grade metamorphism in pelitic schists. *Contrib. Mineral. Petrol.*, **105**, 602-615.

Smith, H. A., Chamberlain, C. P. and Zeitler, P. K. 1992. Documentation of Neogene regional metamorphism in the Himalayas of Pakistan using U-Pb in monazite. *Earth Planet. Sci. Lett.*, **113**, 93-105.

Snee, L. W., Sutter, J. F. and Kelly, W. C. 1988. Thermochronology of Economic mineral Deposits : Dating the stages of Mineralisation at Panasqueira, Portugal, by high-precision $^{40}Ar/^{39}Ar$ Age Spectrum Techniques on Muscovite. *Econ. Geol.*, **83**, 335-354.

Spear, F. S. 1988. Metamorphic fractional crystallisation and internal metasomatism by diffusional homogenisation of zoned garnets. *Contrib. Mineral. Petrol.*, **99**, 507-517.

Spear, F. S. 1989. Relative thermobarometry and metamorphic P-T paths. In : Daly, J. S., Cliff, R. A. and Yardley, B. W. D. (eds.), Evolution of Metamorphic Belts. *Spec. Pub. Geol. Soc. Lon.*, **43**, 63-81.

Spear, F. S. 1991. On the Interpretation of peak metamorphic temperatures in the light of garnet diffusion during cooling. *J. Metamorphic Geol.*, **9**, 379-388.

Spear, F. S. and Florence, F. P. 1992. Thermobarometry in granulites : Pitfalls and new approaches. *Precamb. Res.*, **55**, 209-241.

Spear, F. S. and Rumble, D. 1986. Pressure, Temperature and Structural Evolution of the Orfordville belt, west-central New Hampshire. *J. Petrol.*, **27**, 1071-1093.

Spear, F. S. and Selverstone, J. 1983. Quantitative P-T paths from zoned minerals : Theory and Tectonic Applications. *Contrib. Mineral. Petrol.*, **83**, 348-357.

Spear, F. S., Hickmott, D. D. and Selverstone, J. 1990. Metamorphic consequences of thrust emplacement, Fall Mountain, New Hampshire. *Bull. Geol. Soc. Am.*, **102**, 1344-1360.

Spear, F. S., Kohn, M. J., Florence, F. P. and Menard, T. 1991. A model for garnet and plagioclase in pelitic schists : implications for thermobarometry and P-T path determinations. *J. Metamorphic Geol.*, **8**, 683-696.

Srimal, N. 1986. India-Asia collision : implications from the geology of the eastern Karakoram. *Geology*, **14**, 523-527.

Srimal, N., Basu, A. R. and Kyser, T. K. 1987. Tectonic inferences from oxygen isotopes in volcano-plutonic complexes of the India-Eurasia collision zone, NW. India. *Tectonics*, **6**, 261-273.

Steiger, R. H. and Jäger, E. 1977. Subcommision on geochronology : convention on the use of decay constants in geo- and cosmo-chronology. *Earth Planet. Sci. Lett.*, **36**, 359-362.

St. Onge, M. R. 1987. Zoned Poikiloblastic Garnets : P-T paths and syn-metamorphic uplift through 30 km of structural depth, Wopmay orogen, *Canada. J. Petrol.*, **28**, 1-21.

Streckeisen, A. 1976. To each plutonic rock its proper name. *Earth Planet. Sci. Lett.*, **12**, 1-33.

Tahirkheli, R. A. K., Mattauer, M., Proust, F. and Tapponnier, P. 1979. The India Eurasia suture zone in northern Pakistan: synthesis and interpretation of recent data at plate scale. In : Farah, A. and De Jong, K. A., (eds.), *Geodynamics of Pakistan*. Geol. Surv. Pakistan, Quetta, pp. 125-130.

Tahirkheli, R. A. K. 1979a. Geotectonic Evolution of Kohistan. *Spec. Iss. Geol. Bull. Univ. Peshawar*, **11**, 113-130

Tahirkheli, R. A. K. 1979b. Geology of Kohistan, Karakorum Himalaya, northern Pakistan. *Spec. Iss. Geol. Bull. Univ. Peshawar*, **11**, 1-30.

Tait, R. E. and Harley, S. L. 1988. Local processes involved in the generation of migmatites within mafic granulites. *Trans. R. Soc. Edin.*, **79**, 209-222.

Tapponnier, P. and Molnar, P. 1976. Slip-line field theory and large-scale continental tectonics. *Nature*, **264**, 319-324.

Tapponnier, P., Peltzer, G., Le Dain, A. and Armijo, R. 1982. Propagating extrusion tectonics in Asia : New insights from simple experiments with plasticene. *Geology*, **10**, 611-616.

Thakur, V. C. and Misra, D. K. 1984. Tectonic framework of the Indus and Shyok suture zone in eastern Ladakh, northwestern Himalaya. *Tectonophysics*, **101**, 207-220.

Thompson, A. B. and England, P. C. 1984. Pressure-temperature-time paths of regional metamorphism 2. Their inference and interpretation using mineral assemblages in metamorphic rocks. *J. Petrol.*, **25**, 929-955.

Thompson, A. B., Tracy, R. J., Lyttle, P. T. and Thompson, J. B., Jr. 1977. Prograde reaction histories deduced from compositional zonation and mineral inclusions in garnet from the Gassetts Schist, Vermont. *Am. J. Sci.*, **277**, 1152-1167.

Tobisch, O. T., Barton, M. D., Vernon, R. H. and Paterson, S. R. 1991. Fluid-enhanced deformation : transformation of granitoids to banded mylonites, western Sierra Nevada, California, and southeastern Australia. *J. Structural Geol.*, **13**, 1137-1156.

Tracy, R. J., Robinson, P. and Thompson, A. B. 1976. Garnet composition and zoning in the determination of temperature and pressure of metamorphism, central Massachusetts. *Am. Min.*, **61**, 762-775.

Treloar, P. J. and Rex, D. C. 1990a. Cooling and uplift histories of the crystalline thrust stack of the Indian plate internal zones west of Nanga Parbat, Pakistan Himalaya. *Tectonophysics*, **180**, 323-349.

Treloar, P. J. and Rex, D. C. 1990b. Post-metamorphic cooling history of the Indian plate crystalline thrust stack, Pakistan Himalaya. *J. Geol. Soc. Lon.*, **147**, 735-738.

Treloar, P, J., Brodie, K. H., Coward, M. P., Jan, M. Q., Khan, M. A., Knipe, R. J., Rex, D. C. and Williams, M. P. 1990. The evolution of the Kamila shear zone, Kohistan, Pakistan. In : Salisbury, M. H. and Fountain, D. M. (eds.), *Exposed Cross-Sections of the Continental Crust*. pp. 175-214.

Treloar, P, J., Broughton, R. D., Williams, M. P., Coward, M. P. and Windley, B. F. 1989b. Deformation, metamorphism and imbrication of the Indian plate, south of the Main Mantle Thrust, north Pakistan. *J. Metamorphic Geol.*, **7**, 111-125.

Treloar, P, J., Coward, M. P., Chambers, A. F., Isatt, C. N and Jackson, K. C. 1992. Thrust geometries, inferences and rotations in the Northwest Himalaya. In : McClay, K. R. (ed.), *Thrust Tectonics*, pp. 325-342.

Treloar, P, J., Potts, D. J., Wheeler, J. and Rex, D. C. 1991. Structural evolution and asymmetric uplift of the Nanga Parbat Syntaxis, Pakistan Himalaya. *Geologische Rundschau*, **80**, 411-428.

Treloar, P, J., Rex, D. C., Guise, P. G., Coward, M. P., Searle, M. P., Windley, B. F., Petterson, M. G., Jan, M. Q. and Luff, I. W. 1989a. K-Ar and Ar-Ar geochronology of the Himalayan collision in N.W.Pakistan: Constaints on the timing of suturing, deformation, metamorphism and uplift. *Tectonics*, **8**, 881-909.

Treloar, P, J., Williams, M. P.and Coward, M. P. 1989c. Metamorphism and crustal stacking in the North Indian Plate, North Pakistan. *Tectonophysics*, **165**, 167-184.

Tuttle, P. F. and Bowen, N. L. 1958. Origin of granite in the light of experimental studies in the system $NaAlSi_3O_8$-$KAlSi_3O_8$-H_2O. *Mem. Geol. Soc. Am.*, **74**, pp. 45.

Vance, D. and O'Nions, R. K. 1990. Isotopic chronometry of zoned garnets : growth kinematics and metamorphic histories. *Earth Planet. Sci. Lett.*, **97**, 227-240.

Verplanck, P. L., Snee, L.W. and Lund, K. 1985. The boundary between the Nanga Parbat massif and the Ladakh island arc terrane, northern Pakistan: a cross fault on the main mantle thrust (abstract). *E.O.S. Trans*, **66**, 1074.

Vidal, Ph., Bernard-Griffiths, J., Cocherie, A., Le Fort, P., Peucat, J. J. and Sheppard, S. M. F. 1984. Geochemical comparison between Himalayan and Hercynian leucogranites. *Phys. Earth Planet. Interiors*, **35**, 179-190.

Vielzeuf, D. and Holloway, J. R. 1988. Experimental determination of the fluid-absent melting relations in the pelitic system. *Contrib. Mineral. Petrol.*, **98**, 257-276.

Vitorello, I. and Pollack, H. N. 1980. On the variation of continental heat flow with age and the thermal evolution of continents. *J. Geophys. Res.*, **85**, 983-995.

Von Platen, H. 1965. Experimental anatexis and genesis of Migmatites. In : Pitcher, W. G. and Flinn, G. W. (eds.), *Controls of Metamorphism*. Oliver & Boyd, Edinburgh, pp. 202-218.

Wadia, D. N. 1931. The Syntaxis of the North-West Himalaya : Its rocks, tectonics and orogeny. *Rec. Geol. Sur. Ind.*, **65**, 190-220.

Wadia, D. N. 1932. Note on the Geology of Nanga Parbat (Mt. Diamir) and adjoining portions of Chilas, Gilgit district, Kashmir. *Rec. Geol. Sur. Ind.*, **66**, 212-235.

Wadia, D. N. 1961. *Geology of India*, 3rd ed., New York, Mac Millan, 536 pp.

Wagner, G. A., Reimer, G. M. and Jäger, E. 1977. Cooling ages derived by apatite fission-track, mica Rb-Sr and K-Ar dating : the uplift and cooling history of the central Alps. *Memorie degli Instituti di Geologia e Mineralogia dell'Universita di Padova*, **30**, 1-27.

Watson, E. B. 1979. Zircon saturation in felsic liquids : experimental data and applications to trace element geochemistry. *Contrib. Mineral. Petrol.*, **70**, 407-419.

Watson, E. B. and Harrison, T. M. 1983. Zircon saturation revisited : temperature and composition effects in a variety of crustal magma types. *Earth Planet. Sci. Lett.*, **64**, 295-304.

Wickham, S. M. 1987. Crustal anatexis and granite petrogenesis during low-pressure regional metamorphism : the Trois Seigneurs Massif, Pyrenees, France. *J. Petrol.* **28**, 127-169.

Williams, M. D., Treloar, P. J. and Coward, M. P. 1988. More evidence of pre-Himalayan orogenesis in northern Pakistan. *Geol. Mag.*, **125**, 651-652.

Windley, B. F., Coward, M. P. and Jan, M. Q. 1986. *The geology and tectonic evolution of the Karakoram-Kohistan range of the Himalaya of N. Pakistan.* Proc. 66 th An. Symp. Mesozoic and Cenozoic Geol., Beijing, China, pp. 455-467.

Winkler, H. G. F. 1967. *Petrogenesis of Metamorphic Rocks.* Springer-Verlag, New York, 237 pp.

Xu, R. H., Scharer, U. and Allègre, C. J. 1985. Magmatism and Metamorphism in the Lhasa block (Tibet) : A geochronological study. *J. Geol.*, **93**, 41-57.

Yamamoto, H. 1993. Contrasting metamorphic P-T time paths of the Kohistan granulites and tectonics of the western Himalayas. J. *Geol. Soc. Lon.*, **150**, *in press.*

Zanettin, B. 1964. Geology of the Haramosh-Mango Gusor Area : Desio's Italian expeditions to the Karakoram and Hindu Kush. *Scient. Rep.*, **3**, Brill. Leiden.

Zeitler, P. K. 1983. Uplift and Cooling history of the NW Himalaya, northern Pakistan - Evidence from Fission-track and $^{40}Ar/^{39}Ar$ cooling ages. *Ph.D. Thesis*, Dartmouth college, Hanover, New Hampshire (unpublished).

Zeitler, P. K. 1985. Cooling history of the N.W.Himalaya, Pakistan. *Tectonics*, **4**, 127-151.

Zeitler, P. K. and Chamberlain C. P. 1991. Petrogenetic and Tectonic Significance of Young Leucogranites from the Northwestern Himalaya, Pakistan. *Tectonics*, **10**, 729-741.

Zeitler, P. K. and Williams, I. S. 1988. U-Pb dating of Metamorphic Zircon Overgrowths by means of depth profiling with an ion microprobe (abstract). *EOS Trans*, **69**, 464.

Zeitler, P. K., Tahirkheli, R. A. K., Naeser, C. W. and Johnson, N. M. 1982. Unroofing history of a suture zone in the Himalaya of Pakistan by means of fission-track annealing ages. *Earth Planet. Sci. Lett.*, **57**, 227-240.

Zeitler, P. K., Sutter, J. F., Williams, I. S., Zartman, R. and Tahirkheli, R. A. K. 1989. Geochronology and temperature history of the Nanga-Parbat-Haramosh massif, Pakistan. In : Malinconico, L. L. and Lillie, R. J. (eds.), Tectonics of the western Himalayas. *Geol. Soc. Am. Spec. Paper,* **232**, 1-22.

Zeitler, P. K., Chamberlain, C. P. and Smith, H. A. 1993. Synchronous anatexis, metamorphism, and rapid denudation at Nanga Parbat (Pakistan Himalaya). *Geology*, **21**, 347-350.

Zen, E-An. and Hammarstrom J. M. 1984. Magmatic epidote and its petrological significance. *Geology*, **12**, 515-518.

Zen, E-An. 1986. Aluminium Enrichment in Silicate Melts by Fractional Crystallisation : Some Mineralogic and Petrographic constraints. *J. Petrol.*, **27**, 1095-1117.

Zhao, W. L. and Morgan, W. J. 1985. Uplift of Tibetan Plateau. *Tectonics*, **4**, 359-369.

Appendix 1 - Analytical Techniques

1.1. Sample Powder and Mineral Separate Preparation

Whole-rock samples were split into ~5 cm sized fragments using a hydraulic splitter, and any weathered material removed. Approximately 1 kg of the sample was then crushed in a hardened steel jaw crusher, and a representative 100 g portion of the crushate taken by cone and quartering. This fraction was powdered in an agate tema mill for ~12 minutes to produce a powder of less than 200 mesh grain size.

Mineral separates were obtained by sieving a portion of the crushate from the jaw crusher, followed by handpicking under a binocular microscope. The separates were then rinsed twice with distilled water in an ultrasonic bath. Garnet separates were cleaned in a similar manner before being crushed to a fine powder in an agate pestle and mortar.

1.2. XRF Sample Preparation and Analysis

Rock powders were dried overnight to eliminate moisture. Glass discs for major element analysis were made by mixing lithium metaborate/tetraborate flux (Spectraflux 100B) to rock powders in the ratio 5 : 1. The resulting mixtures were placed in a furnace and fused in Pt - 5 % Au crucibles for 20 minutes. The fused mixtures were poured into heated, 3.6 cm diameter moulds to produce 1.5 mm thick discs. Loss on ignition (LOI) for each sample was calculated by igniting the sample at 1000 °C for 20 minutes and measuring the percentage mass loss.

Powder pellets for trace element analysis were prepared by mixing ~10 g rock powder and 8-10 drops of polyvinylpyrollidone (PVP)-methyl cellulose binder. The mixtures were pressed into 3.8 cm diameter pellets in a hydraulic press at a pressure of 105 Pa. The pellets were then dried for 12 hours at 80 °C before analysis.

All major and trace element analyses were carried out by wavelength dispersive XRF spectrometry at the Open University. X-rays were generated using a 3 kW Rh anode end-window X-ray tube, and the diffracting crystals used were AX06, PET, Ge111, LiF200 and LiF220. Elemental intensities were corrected for background and known peak overlap interferences. Instrumental intensity drift was taken into account using a drift monitor. Count times for most trace elements were selected to achieve 2σ precision better than 2 ppm or 2 % relative at concentrations > 100 ppm. Major element matrix corrections employed the empirical Traill-Lachance procedure; trace element matrix corrections usually involved ratioing with the Compton scattered tube lines.

1.3. Instrumental neutron activation analysis (INAA)

INAA was used to determine the concentrations of the rare earth elements La, Ce, Nd, Sm, Eu, Tb, Yb and Lu together with Th, U, Co, Ta and Hf. 0.3 g pre-dried rock powder was weighed into a polythene capsule and sealed. Nine samples and two standards were stacked into a cylinder, with weighed lacquered iron foil between each capsule to monitor the neutron flux variation along the length of the cylinder. The two standards used in each cylinder were an irradiation standard AC-2 (Ailsa Craig microgranite) and a sample from the Whin Sill which was used as an internal standard.

Samples were irradiated in the core tube at the Imperial College Reactor Centre, Ascot, in a thermal neutron flux of 5×10^{12} ncm^2 sec^{-1} for 24-30 hours. The samples were left for a week before analysis to allow short lived radioactive isotopes to decay; details of counting conditions, peak fitting, calibration and corrections are described in Potts et al. (1985).

1.4. Wavelength Dispersive Microprobe Analysis

Electron microprobe analyses were carried out on a wavelength dispersive Cambridge Instruments Microscan Mk-9. This instrument has two spectrometers and uses standard PET, TAP and LiF crystals. The probe operates at an accelerating potential of 20kV, a beam current of 30 nA and a column vacuum better than 10^{-5} torr. Typical spot sizes are 10-15 μm. Analyses were carried out on 40-50 μm-thick polished thin sections which had been carbon-coated using an Edwards vacuum coater. Counting times varied from 30-50 seconds. The instrument was calibrated daily using mineral standards, and drift was monitored by analysing an internal standard 'ABG' (a basaltic glass).

1.5. Radiogenic Isotope Analysis

1.5.1. Sample dissolution and separation techniques

All isotopic analyses and preparations were carried out in a clean-air laboratory in which a positive air pressure was maintained. All solutions used in the dissolutions were made up with either quartz distilled or Milli-Q reverse osmosis purified water (ROW). Prior to use, beakers and bombs were rinsed in ROW, soaked in ~15M HNO3 (aq) at ~80 °C for at least 24 hr, then rinsed and soaked in ROW overnight.

Between 100 and 150 mg of rock powder was subjected to a HNO3 + HF digestion, and repeatedly treated with hot 15M HNO3 and 6M HCl. For mineral separates, between 150-200 mg were required. The majority of samples were left in covered teflon beakers overnight. However, teflon oven bombs were required for samples of garnetiferous granite, and all metamorphic samples, to ensure complete dissolution of accessory phases and garnet. The bombs were fitted with sleeves, placed in monel jackets, and left in an oven at 180 °C for several days. Garnet separates required up to two weeks at the HNO3 + HF stage before clear solutions were obtained.

The mica and garnet solutions were each split into two aliquots for either spiking and subsequent isotope dilution, or determination of isotope ratios. Mica samples were spiked with one drop of ^{85}Rb-^{86}Sr HI solution, whilst garnet samples were spiked with one drop of ^{150}Sm-^{149}Nd solution. All solutions were evaporated to dryness and the residues redissolved in 1ml 2.5M HCl. Rb and Sr were separated using carefully calibrated ion-exchange columns of 10 ml preconditioned Bio-rad AG50W X8 200-400 mesh resin. 20 cm-long cation exchange columns were used for all mica samples to ensure optimum separation of Rb from Sr. For the separation of Sm and Nd, the MREE fraction was collected in 3M HNO3 and evaporated to dryness. This residue was dissolved in 1 ml 0.25M HCl, and Sm and Nd separated using preconditioned reverse ion-exchange columns composed of 1g teflon powder (Voltalef 300LD PL micro) and 100 g DEP (di(2-ethylhexyl)phosphate).

1.5.2. Mass spectrometry

Spiked samples for Rb, Sr, Sm, Nd isotope dilution analysis were analysed on a Vacuum Generators Isomass 54E solid source, single-collector mass spectrometer. All other analyses were carried out on a Finnegan M80 261 solid source, multi-collector mass spectrometer, interfaced with a HP 9836 computer using software designed by D.W. Wright and P.W.C van Calsteren. Filaments for both mass spectrometers were outgassed before loading for 5 minutes at 4.5A in a vacuum better than 10^{-6} torr. Sr was loaded in phosphoric acid on single Ta filaments, and the measured $^{87}Sr/^{86}Sr$ ratios were exponentially fractionation corrected within each run to $^{86}Sr/^{88}Sr = 0.1194$. During the period of laboratory work, 21 measurements of the machine standard NBS 987 gave an average $^{87}Sr/^{86}Sr$ ratio of 0.710237 ± 17 (1σ) . Total procedural strontium blanks were in the range 1.2-5.5 ng/g.

Nd was loaded on Ta filaments (a Re ionisation filament was used) and run as metal ions. $^{143}Nd/^{144}Nd$ ratios were exponentially fractionation corrected to $^{146}Nd/^{144}Nd = 0.72190$. Eight analyses of an internal J&M Nd standard over the period of analysis had a mean value of 0.511820 ± 12 (1σ standard deviation).

1.5.3. Age corrections and constants

The natural abundances of ^{87}Rb, ^{86}Sr, ^{147}Sm and ^{144}Nd were used to calculate $^{87}Rb/^{86}Sr$ and $^{147}Sm/^{144}Nd$ for each sample from the elemental ratios measured by XRF or isotope dilution :

$$^{87}Rb/^{86}Sr = 2.891 Rb/Sr$$

$$^{147}Sm/^{144}Nd = 0.602 Sm/Nd$$

All initial isotope ratios and evolution diagrams have been calculated using the age equations :

$$(^{87}Sr/^{86}Sr)_{measured} = (^{87}Sr/^{86}Sr)_{initial} + ^{87}Rb/^{86}Sr(e^{l1t} - 1)$$

$$(^{143}Nd/^{144}Nd)_{measured} = (^{143}Nd/^{144}Nd)_{initial} + ^{147}Sm/^{144}Nd(e^{l2t} - 1)$$

where $l1 = 1.42 \times 10^{-11}\ y^{-1}$ and $l2 = 6.54 \times 10^{-12}\ y^{-1}$.

Epsilon notation follows the definitions of DePaolo and Wasserberg (1976), and model Sr and Nd ages are reported relative to depleted mantle. The following constants have been used :

$^{87}Rb/^{86}Sr_{Bulk\ earth}=0.0847$ $\quad$ $^{147}Sm/^{144}Nd_{CHUR}=0.1967$

$^{87}Sr/^{86}Sr_{Bulk\ earth}=0.7047$ $\quad$ $^{143}Nd/^{144}Nd_{CHUR}=0.51264$

$^{87}Sr/^{86}Sr_{DM}=0.70306$ $\quad$ $^{143}Nd/^{144}Nd_{DM}=0.51310$

$^{87}Rb/^{86}Sr_{DM}=0.0487$ $\quad$ $^{147}Sm/^{144}Nd_{DM}=0.2238$

1.6. $^{40}Ar/^{39}Ar$ mass spectrometry

Pure, hand-picked mineral separates for $^{40}Ar/^{39}Ar$ analysis were packed in aluminium foil and loaded into known positions within a foil cylinder. The flux monitors Hb3gr and MMHb1 were included in the cylinder as standards to monitor neutron flux during irradiation. The samples were irradiated at the Ford reactor, Michigan. The J value for the irradiation, calculated using the flux monitors, was as follows :

$$0.01056 \pm 0.00005.$$

The samples were loaded into an ultra high vacuum laser port and heated overnight to reduce atmospheric blank levels. Argon was extracted from individual mineral grains by firing short pulses of a continuous Spectron SL902CW YAG laser beam (TEMoo, wavelength 1064nm) through a customised petrological microscope. The beam was focussed using a CCD camera, coaxial with the laser beam, to a spot size of about 20 μm on the sample surface. The power of the beam was increased gradually on individual mineral grains until they began to melt. This method prevents grains jumping around the sample chamber when the laser beam impinges. Typical powers of 10-17 W were used, and pulse lengths of between 50 and 200 ms, depending upon the reflectivity of the sample.

The argon was purified using a SAES GP10 getter at 400 °C for 5 minutes, and then allowed into a Mass Analyser Products 215-50 noble gas mass spectrometer via automated valves. Seven masses were analysed; 25, 36, 37, 38, 39, 40 and 41. Peaks between 35 and 41 were scanned 7 times and amounts extrapolated back to the inlet time. This overcomes the problem of argon either being released from or being absorbed onto the mass spectrometer walls. A blank run was made after every sample run and blank corrections to the sample analysis were made by averaging the blank before and the blank after analysis. Mean blank levels, x 10^{-12} ccSTP, were :

^{41}Ar 0.35 ± 0.08

^{40}Ar 1.81 ± 0.28

^{39}Ar	0.38 ± 0.10
^{38}Ar	0.17 ± 0.04
^{37}Ar	1.67 ± 0.18
^{36}Ar	0.19 ± 0.04
^{35}Ar	4.51 ± 0.42

These values are significantly smaller than blanks obtained from furnace step-heating argon machines where the walls of the furnace are also outgassed during heating. The data were corrected for interfering nuclear reactions involving Ca and K; the correction factors used were $(^{39}Ar/^{37}Ar)_{Ca}$=0.000781 ± 0.000053, $(^{36}Ar/^{37}Ar)_{Ca}$ = 0.000205 ± 0.000022 and $(^{40}Ar/^{39}Ar)_{K}$ = 0.031 ± 0.008. Corrections were also applied for mass spectrometer fractionation, ^{37}Ar decay since the time of irradiation, and background levels of Ar (monitored from analysis of blanks).

Appendix 2 - Electron Microprobe Data

Representative probe analyses for metamorphic samples from the Nanga Parbat-Haramosh Massif - Kohistan region. All analyses are rim analyses except where shown. Order of samples : S17; S22; S24; S28; G31; G28; S34; T23; S62; S29; D18; D19; I1; S90; S89; A7; A3; A21; T20; T64; T69; L8; M6; M9; M16; G1; G7; G9; G17; G20.

Abbreviations (where present) : incl. = inclusion in garnet; Hb = hornblende; Diop = diopside; Plag = plagioclase; K-spar = k-feldspar. Indus conf. = Indus confluence; L. Darchan = lower Darchan valley.

S17	Garnet						Hornblende		
Amphibolite	YGA	YGB	YGC	YGD	YGE	YGF	YHD	YHE	YHF
Sassi	1-Core	1-Rim	2-Core	2-Rim	3-Core	3-Rim			
SiO2	38.13	38.15	37.93	37.95	37.99	37.93	42.12	41.81	41.44
TiO2	0.23	0.09	0.21	0.11	0.11	0.12	1.06	0.94	1.06
Al2O3	20.94	21.16	21.00	21.18	21.01	20.93	12.78	12.77	13.02
Cr2O3	0.00	0.00	0.00	0.00	0.00	0.00	0.00	0.00	0.00
FeO	26.97	29.26	27.33	29.42	28.41	28.91	20.57	20.18	20.59
MnO	3.64	1.59	3.31	1.15	1.75	1.64	0.17	0.17	0.17
MgO	1.44	1.65	1.52	1.89	2.09	1.71	6.84	6.70	6.28
CaO	9.69	9.43	9.62	9.29	9.37	9.57	11.40	11.72	11.34
Na2O	-	-	-	-	-	-	1.63	1.37	1.60
K2O	-	-	-	-	-	-	1.01	0.93	1.03
F	-	-	-	-	-	-	0.08	0.13	0.04
Total	**101.04**	**101.33**	**100.92**	**100.99**	**100.73**	**100.81**	**97.71**	**96.79**	**96.63**
Formula Units	12	12	12	12	12	12	23	23	23
Si	3.0139	3.0071	3.0037	2.9990	3.0052	3.0062	6.4401	6.4490	6.4141
Ti	0.0135	0.0052	0.0125	0.0062	0.0062	0.0073	0.1224	0.1089	0.1238
Al	1.9513	1.9658	1.9603	1.9724	1.9595	1.9548	2.3031	2.3217	2.3760
Cr	0.0000	0.0000	0.0000	0.0000	0.0000	0.0000	0.0000	0.0000	0.0000
Fe	1.7832	1.9290	1.8096	1.9444	1.8795	1.9160	2.6298	2.6031	2.6651
Mn	0.2438	0.1063	0.2218	0.0771	0.1170	0.1100	0.0219	0.0221	0.0221
Mg	0.1701	0.1940	0.1792	0.2227	0.2463	0.2015	1.5594	1.5408	1.4496
Ca	0.8206	0.7968	0.8162	0.7863	0.7945	0.8129	1.8682	1.9378	1.8807
Na	-	-	-	-	-	-	0.4838	0.4112	0.4802
K	-	-	-	-	-	-	0.1971	0.1831	0.2039
F	-	-	-	-	-	-	0.0402	0.0614	0.0205
Total	**7.9964**	**8.0042**	**8.0033**	**8.0081**	**8.0082**	**8.0087**	**15.6787**	**15.6583**	**15.6521**

S17	Plagioclase					Biotite			
Amphibolite	YFA	YFB	YFC	YFD	YFE	YBA	YBB	YBH	YBF
Sassi			1-Core	1-Rim		1-Core	1-Rim		
SiO2	63.26	61.46	64.49	64.42	64.01	35.37	35.40	35.46	35.17
TiO2	-	-	-	-	-	2.49	2.66	2.28	2.07
Al2O3	22.42	23.48	21.66	21.72	21.71	15.33	15.58	15.41	15.69
Cr2O3	-	-	-	-	-	0.00	0.00	0.00	0.00
FeO	0.07	0.06	0.03	0.06	0.01	23.60	23.78	22.98	22.62
MnO	-	-	-	-	-	0.11	0.11	0.06	0.11
MgO	-	-	-	-	-	7.76	7.66	8.43	8.55
CaO	4.18	5.45	3.17	3.28	3.31	0.04	0.04	0.03	0.01
Na2O	8.98	8.27	9.64	9.41	9.45	0.11	0.13	0.13	0.13
K2O	0.11	0.10	0.05	0.11	0.08	9.06	9.10	9.07	9.12
F	0.00	0.04	0.00	0.04	0.00	0.24	0.28	0.24	0.16
Total	**99.02**	**98.86**	**99.05**	**99.05**	**98.57**	**94.21**	**94.84**	**94.18**	**93.72**
Formula Units	8	8	8	8	8	22	22	22	22
Si	2.8197	2.7560	2.8650	2.8632	2.8579	5.6018	5.5738	5.5979	5.5705
Ti	-	-	-	-	-	0.2963	0.3155	0.2704	0.2461
Al	1.1781	1.2411	1.1342	1.1376	1.1424	2.8620	2.8917	2.8665	2.9291
Cr	-	-	-	-	-	0.0000	0.0000	0.0000	0.0000
Fe	0.0026	0.0021	0.0010	0.0020	0.0005	3.1253	3.1312	3.0335	2.9960
Mn	-	-	-	-	-	0.0143	0.0142	0.0081	0.0143
Mg	-	-	-	-	-	1.8313	1.7967	1.9834	2.0187
Ca	0.1996	0.2618	0.1507	0.1563	0.1584	0.0072	0.0071	0.0048	0.0024
Na	0.7760	0.7190	0.8305	0.8107	0.8183	0.0346	0.0402	0.0400	0.0400
K	0.0061	0.0054	0.0027	0.0061	0.0047	1.8296	1.8277	1.8261	1.8423
F	0.0000	0.0060	0.0000	0.0059	0.0000	0.1223	0.1414	0.1218	0.0817
Total	**4.9821**	**4.9914**	**4.9843**	**4.9820**	**4.9822**	**15.7508**	**15.7654**	**15.7753**	**15.7640**

S22	Garnet						Hornblende		
Amphibolite	TGC	TGA	TGF	TGE	TGO	TGN	OHC	OHD	OHE
Sassi	1-Core	1-Rim	2-Core	2-Rim	3-Core	3-Rim			
SiO2	38.00	37.61	38.44	38.30	38.37	38.44	41.25	42.10	41.43
TiO2	0.12	0.18	0.21	0.09	0.18	0.14	0.85	0.89	0.58
Al2O3	21.29	21.18	21.38	21.47	21.30	21.34	13.48	13.73	14.42
Cr2O3	-	-	-	-	-	-	0.00	0.00	0.00
FeO	26.12	26.90	26.74	28.50	27.14	28.00	19.36	19.41	19.03
MnO	3.21	2.81	3.25	1.26	3.85	2.23	0.34	0.29	0.29
MgO	1.89	1.72	1.88	2.32	1.89	2.12	7.08	7.23	7.07
CaO	9.93	9.99	10.02	9.49	9.13	9.24	11.79	11.61	9.47
Na2O	-	-	-	-	-	-	1.18	1.43	1.57
K2O	-	-	-	-	-	-	0.86	1.14	0.86
F	-	-	-	-	-	-	-	-	-
Total	**100.56**	**100.39**	**101.92**	**101.43**	**101.86**	**101.51**	**96.19**	**97.83**	**94.72**
Formula Units	12	12	12	12	12	12	23	23	23
Si	3.0029	2.9875	3.0021	2.9992	3.0051	3.0112	6.3685	6.3866	6.4316
Ti	0.0073	0.0105	0.0124	0.0052	0.0103	0.0083	0.0987	0.1011	0.0674
Al	1.9831	1.9829	1.9681	1.9820	1.9665	1.9705	2.4528	2.4542	2.6391
Cr	-	-	-	-	-	-	0.0000	0.0000	0.0000
Fe	1.7265	1.7870	1.7466	1.8668	1.7775	1.8340	2.4993	2.4626	2.4712
Mn	0.2146	0.1890	0.2149	0.0836	0.2555	0.1480	0.0443	0.0376	0.0384
Mg	0.2229	0.2031	0.2186	0.2709	0.2202	0.2477	1.6301	1.6353	1.6359
Ca	0.8405	0.8502	0.8384	0.7965	0.7659	0.7752	1.9499	1.8867	1.5758
Na	-	-	-	-	-	-	0.3544	0.4212	0.4735
K	-	-	-	-	-	-	0.1699	0.2200	0.1696
F	-	-	-	-	-	-	-	-	-
Total	**7.9978**	**8.0102**	**8.0011**	**8.0042**	**8.0010**	**7.9949**	**15.5679**	**15.6053**	**15.5025**

S22	Plagioclase						Biotite		
Amphibolite	TFA	TFB	TFC	TFD	TFE	TFF	OBD	OBE	OBF
Sassi	1-Rim	1-Core	1-Rim	1-Core	1-Rim	1-Core			
SiO2	61.96	64.50	59.34	62.12	60.51	61.75	36.34	36.30	35.99
TiO2	-	-	-	-	-	-	3.18	2.71	2.62
Al2O3	24.18	22.67	23.67	23.85	25.23	24.25	15.64	15.52	15.66
Cr2O3	-	-	-	-	-	-	0.00	0.00	0.00
FeO	0.13	0.06	2.43	0.04	0.10	0.11	21.31	22.55	21.73
MnO	-	-	-	-	-	-	0.17	0.15	0.17
MgO	-	-	-	-	-	-	8.85	9.05	9.33
CaO	5.81	3.94	6.41	5.54	6.97	6.06	0.01	0.01	0.03
Na2O	8.19	9.24	7.69	8.36	7.65	8.11	0.09	0.13	0.11
K2O	0.13	0.19	0.23	0.13	0.15	0.18	9.13	8.72	9.24
F	-	-	-	-	-	-	-	-	-
Total	**100.40**	**100.60**	**99.77**	**100.04**	**100.61**	**100.46**	**94.72**	**95.14**	**94.88**
Formula Units	8	8	8	8	8	8	22	22	22
Si	2.7381	2.8286	2.6815	2.7521	2.6789	2.7302	5.6222	5.6124	5.5806
Ti	-	-	-	-	-	-	0.3697	0.3147	0.3060
Al	1.2595	1.1716	1.2608	1.2456	1.3167	1.2637	2.8526	2.8284	2.8627
Cr	-	-	-	-	-	-	0.0000	0.0000	0.0000
Fe	0.0046	0.0020	0.0917	0.0015	0.0036	0.0041	2.7572	2.9161	2.8177
Mn	-	-	-	-	-	-	0.0220	0.0200	0.0221
Mg	-	-	-	-	-	-	2.0399	2.0847	2.1571
Ca	0.2753	0.1850	0.3104	0.2630	0.3305	0.2871	0.0023	0.0023	0.0047
Na	0.7016	0.7857	0.6738	0.7183	0.6569	0.6952	0.0276	0.0389	0.0332
K	0.0073	0.0107	0.0129	0.0074	0.0087	0.0100	1.8028	1.7201	1.8280
F	-	-	-	-	-	-	-	-	-
Total	**4.9864**	**4.9836**	**5.0311**	**4.9879**	**4.9953**	**4.9903**	**15.4963**	**15.5376**	**15.6121**

S24	Garnet						Plagioclase		
Amphibolite	ZGH	ZGJ	ZGK	ZGM	ZGP	ZGO	ZFH	ZFI	ZFJ
Sassi	1-Core	1-Rim	2-Core	2-Rim	3-Core	3-Rim	1-Core	1-Rim	2-Core
SiO2	38.58	38.50	38.53	38.50	38.19	38.49	60.07	60.13	61.63
TiO2	-	-	-	-	-	-	-	-	-
Al2O3	21.73	21.78	21.59	21.58	21.16	21.27	24.62	25.37	23.64
Cr2O3	-	-	-	-	-	-	-	-	-
FeO	25.82	25.81	25.96	25.07	26.21	26.29	0.14	0.21	0.07
MnO	2.51	1.46	3.81	1.42	3.90	2.40	-	-	-
MgO	2.13	2.31	2.04	2.08	1.88	2.01	-	-	-
CaO	10.97	11.71	9.72	11.65	9.63	10.73	6.45	7.15	5.84
Na2O	-	-	-	-	-	-	7.80	7.57	8.17
K2O	-	-	-	-	-	-	0.38	0.11	0.19
F	-	-	-	-	-	-	0.00	0.04	-
Total	**101.74**	**101.57**	**101.65**	**100.30**	**100.97**	**101.19**	**99.46**	**100.54**	**99.54**
Formula									
Units	12	12	12	12	12	12	8	8	8
Si	3.0015	2.9940	3.0098	3.0213	3.0122	3.0167	2.6922	2.6670	2.7480
Ti	-	-	-	-	-	-	-	-	-
Al	1.9930	1.9959	1.9874	1.9962	1.9674	1.9653	1.3005	1.3265	1.2425
Cr	-	-	-	-	-	-	0.0000	0.0000	0.0000
Fe	1.6800	1.6782	1.6958	1.6451	1.7287	1.7229	0.0052	0.0078	0.0026
Mn	0.1655	0.0964	0.2522	0.0943	0.2606	0.1595	-	-	-
Mg	0.2475	0.2673	0.2372	0.2436	0.2209	0.2352	-	-	-
Ca	0.9142	0.9760	0.8136	0.9798	0.8139	0.9008	0.3096	0.3399	0.2791
Na	-	-	-	-	-	-	0.6780	0.6511	0.7061
K	-	-	-	-	-	-	0.0217	0.0060	0.0108
F	-	-	-	-	-	-	0.0000	0.0061	-
Total	**8.0017**	**8.0078**	**7.9960**	**7.9803**	**8.0037**	**8.0004**	**5.0072**	**4.9983**	**4.9891**

S24				Hornblende			Biotite		
Amphibolite	ZFK	ZFM	ZFN	ZHC	ZHD	ZHE	ZBA	ZBB	ZBC
Sassi	2-Rim	3-Core	3-Rim				1-Core	1- Rim	
SiO2	58.74	60.01	54.20	42.24	41.86	41.53	35.75	38.56	35.70
TiO2	-	-	-	1.00	1.02	1.00	2.88	2.85	3.11
Al2O3	24.92	24.37	24.85	12.85	13.48	13.59	15.69	15.67	15.54
Cr2O3	-	-	-	0.02	0.00	0.00	0.00	0.00	0.00
FeO	1.18	0.04	6.01	18.14	18.12	18.25	21.18	20.42	21.52
MnO	-	-	-	0.25	0.28	0.28	0.17	0.15	0.18
MgO	-	-	-	7.98	7.76	7.40	9.27	8.43	9.42
CaO	7.14	6.76	7.73	11.66	11.62	11.70	0.01	0.03	0.01
Na2O	7.28	7.79	6.20	1.35	1.44	1.44	0.09	0.09	0.15
K2O	0.12	0.09	0.31	0.98	1.19	1.22	9.29	9.77	9.15
F	-	-	-	0.00	0.04	0.00	0.04	0.04	0.00
Total	**99.38**	**99.06**	**99.30**	**96.54**	**96.87**	**96.48**	**94.49**	**96.11**	**94.88**
Formula									
Units	8	8	8	23	23	23	22	22	22
Si	2.6503	2.6971	2.5231	6.4587	6.3911	6.3748	5.5666	5.8412	5.5412
Ti	-	-	-	0.1147	0.1166	0.1151	0.3368	0.3245	0.3625
Al	1.3251	1.2908	1.3635	2.3157	2.4256	2.4587	2.8806	2.7975	2.8434
Cr	0.0000	0.0000	0.0000	0.0019	0.0000	0.0000	0.0000	0.0000	0.0000
Fe	0.0445	0.0015	0.2338	2.3189	2.3136	2.3432	2.7581	2.5863	2.7937
Mn	-	-	-	0.0319	0.0359	0.0360	0.0222	0.0196	0.0241
Mg	-	-	-	1.8199	1.7657	1.6941	2.1525	1.9043	2.1793
Ca	0.3451	0.3256	0.3856	1.9104	1.9016	1.9249	0.0023	0.0046	0.0023
Na	0.6371	0.6790	0.5599	0.3992	0.4249	0.4283	0.0277	0.0267	0.0443
K	0.0068	0.0054	0.0181	0.1909	0.2327	0.2383	1.8452	1.8870	1.8108
F	-	-	-	0.0000	0.0204	0.0000	0.0203	0.0197	0.0000
Total	**5.0089**	**4.9994**	**5.0840**	**15.5813**	**15.6440**	**15.6326**	**15.6445**	**15.4365**	**15.6272**

S28	Garnet		Hornblende		Plagioclase				Zoisite
Calcsilicate	IGA	IGB	IHA	IHD	IFE	IFF	IFG	IFH	ICC
Sassi	1-Core	1-Rim			1-Core	1-Rim	2-Core	2-Rim	
SiO2	38.53	38.58	42.89	43.22	59.34	57.20	46.55	46.30	41.18
TiO2	0.11	0.05	0.84	0.78	-	-	-	-	0.09
Al2O3	21.65	21.76	12.53	11.92	25.61	27.01	26.95	27.24	23.05
Cr2O3	0.02	0.00	0.02	0.07	-	-	-	-	-
FeO	18.01	20.77	18.04	18.02	0.06	0.06	0.20	0.27	8.53
MnO	6.68	3.25	0.40	0.42	-	-	-	-	0.17
MgO	1.29	2.00	8.37	8.54	-	-	-	-	2.74
CaO	15.06	14.45	11.90	11.92	7.40	9.09	17.41	17.78	21.46
Na2O	-	-	0.81	0.88	7.04	6.45	3.44	3.27	0.02
K2O	-	-	1.50	1.22	0.24	0.14	0.21	0.17	0.03
F	-	-	-	-	-	-	-	-	-
Total	**101.35**	**100.86**	**97.30**	**96.99**	**99.75**	**100.02**	**94.80**	**95.09**	**97.27**
Formula Units	12	12	23	23	8	8	8	8	23
Si	3.0016	3.0064	6.5181	6.5802	2.6529	2.5660	2.2839	2.2674	6.0128
Ti	0.0063	0.0031	0.0954	0.0893	-	-	-	-	0.0102
Al	1.9881	1.9990	2.2441	2.1401	1.3495	1.4283	1.5586	1.5727	3.9668
Cr	0.0010	0.0000	0.0019	0.0079	-	-	-	-	-
Fe	1.1794	1.3603	2.3049	2.3060	0.0021	0.0021	0.0080	0.0109	1.0470
Mn	0.4409	0.2142	0.0516	0.0537	-	-	-	-	0.0212
Mg	0.1492	0.2320	1.8961	1.9375	-	-	-	-	0.5961
Ca	1.2575	1.2064	1.9381	1.9451	0.3544	0.4369	0.9151	0.9333	3.3575
Na	-	-	0.2382	0.2601	0.6104	0.5610	0.3273	0.3101	0.0047
K	-	-	0.2911	0.2365	0.0135	0.0081	0.0129	0.0107	0.0063
F	-	-	-	-	-	-	-	-	-
Total	**8.0240**	**8.0214**	**15.5795**	**15.5564**	**4.9842**	**5.0042**	**5.1070**	**5.1067**	**15.0226**

S28			Biotite			Anorthite		Diopside	
Calcsilicate	ICD	ICE	IBA	IBB	IBC	IDB	IDC	IDA	IDB
Sassi	1-Core	1-Rim							
SiO2	36.85	37.26	38.45	37.00	36.98	45.91	46.00	52.44	52.57
TiO2	0.24	0.08	1.21	2.66	2.90	0.02	0.02	0.06	0.07
Al2O3	25.54	25.67	16.49	15.77	16.26	27.85	27.46	0.74	0.74
Cr2O3	-	-	-	-	-	0.00	0.00	0.00	0.00
FeO	7.25	7.68	17.66	17.91	17.55	0.11	0.13	11.31	10.40
MnO	0.17	0.20	0.35	0.34	0.25	0.02	0.03	0.52	0.47
MgO	0.18	0.02	12.05	12.36	11.98	0.00	0.02	11.11	11.57
CaO	21.42	24.79	0.00	0.03	0.00	18.72	18.25	23.92	23.81
Na2O	0.00	0.00	0.04	0.00	0.02	2.88	3.13	0.14	0.14
K2O	0.00	0.00	9.23	8.74	9.54	0.16	0.16	0.00	0.00
F	-	-	-	-	-	-	-	-	-
Total	**91.65**	**95.70**	**95.48**	**95.05**	**95.48**	**95.67**	**95.20**	**100.24**	**99.77**
Formula Units	23	23	22	22	22	8	8	6	6
Si	5.7057	5.5987	5.7716	5.6132	5.5852	1.6782	1.6889	1.9872	1.9913
Ti	0.0283	0.0084	0.1363	0.3035	0.3294	0.0005	0.0005	0.0016	0.0021
Al	4.6615	4.5451	2.9175	2.8204	2.8954	1.1998	1.1882	0.0331	0.0330
Cr	-	-	-	-	-	0.0000	0.0000	0.0000	0.0000
Fe	0.9432	0.9693	2.2275	2.2842	2.2285	0.0034	0.0038	0.3603	0.3310
Mn	0.0225	0.0258	0.0450	0.0434	0.0315	0.0004	0.0009	0.0165	0.0150
Mg	0.0414	0.0036	2.6970	2.7954	2.6961	0.0000	0.0008	0.6276	0.6533
Ca	3.5539	3.9911	0.0000	0.0046	0.0000	0.7332	0.7179	0.9711	0.9663
Na	0.0000	0.0000	0.0102	0.0000	0.0051	0.2039	0.2228	0.0101	0.0100
K	0.0000	0.0000	1.7670	1.6907	1.8386	0.0074	0.0075	0.0000	0.0000
F	-	-	-	-	-	-	-	-	-
Total	**14.9565**	**15.1420**	**15.5721**	**15.5696**	**15.6098**	**3.8268**	**3.8313**	**4.0075**	**4.0020**

G31	Garnet						Biotite		
Pelitic gneiss	HGC	HGD	HGE	HGF	HGG	HGH	HBB	HBC	HBD
Sassi	1-Core	1-Rim	2-Core	2-Rim	3-Core	3-Rim			Incl.
SiO2	39.01	38.21	38.93	38.45	38.60	38.24	36.17	36.97	36.54
TiO2	0.05	0.02	0.03	0.02	0.02	0.02	2.48	2.22	2.39
Al2O3	22.17	21.71	21.94	21.64	21.83	21.66	18.53	19.10	18.74
Cr2O3	0.02	0.05	0.00	0.00	0.03	0.03	-	-	-
FeO	32.20	33.06	32.32	33.35	33.32	33.69	18.76	17.52	18.57
MnO	0.47	0.72	0.45	0.66	0.62	0.71	0.05	0.03	0.03
MgO	6.73	4.20	6.59	4.29	5.09	4.10	9.90	10.49	9.94
CaO	1.19	2.91	1.11	2.86	2.21	2.75	0.01	0.04	0.01
Na2O	-	-	-	-	-	-	0.20	0.25	0.18
K2O	-	-	-	-	-	-	9.10	9.27	9.21
F	-	-	-	-	-	-	0.33	0.33	0.25
Total	**101.84**	**100.88**	**101.37**	**101.27**	**101.72**	**101.20**	**95.53**	**96.22**	**95.86**
Formula									
Units	12	12	12	12	12	12	22	22	22
Si	3.0016	3.0064	3.0111	3.0138	3.0035	3.0057	5.4755	5.5120	5.4965
Ti	0.0030	0.0010	0.0020	0.0010	0.0010	0.0010	0.2822	0.2486	0.2705
Al	2.0107	2.0129	2.0004	1.9991	2.0028	2.0065	3.3058	3.3565	3.3231
Cr	0.0009	0.0028	0.0000	0.0000	0.0018	0.0018	-	-	-
Fe	2.0723	2.1751	2.0910	2.1857	2.1687	2.2150	2.3748	2.1846	2.3358
Mn	0.0305	0.0483	0.0297	0.0441	0.0408	0.0472	0.0059	0.0038	0.0039
Mg	0.7720	0.4922	0.7603	0.5015	0.5899	0.4802	2.2349	2.3312	2.2295
Ca	0.0982	0.2456	0.0918	0.2400	0.1843	0.2312	0.0023	0.0068	0.0023
Na	-	-	-	-	-	-	0.0575	0.0709	0.0517
K	-	-	-	-	-	-	1.7574	1.7634	1.7671
F	-	-	-	-	-	-	0.1571	0.1545	0.1169
Total	**7.9892**	**7.9843**	**7.9863**	**7.9852**	**7.9928**	**7.9886**	**15.6534**	**15.6323**	**15.5973**

G31	Muscovite		Plagioclase		G28	Garnet			
Pelitic gneiss	HMA	HMB	HFA	HFC	Pelitic gneiss	JGH	JGI	JGJ	JGL
Sassi					Sassi	1-Core	1-Rim	2-Core	2-Rim
SiO2	46.92	46.69	63.31	62.16	SiO2	38.64	38.37	38.66	38.60
TiO2	1.31	1.07	0.02	0.02	TiO2	-	-	-	-
Al2O3	33.43	34.38	24.06	23.84	Al2O3	22.15	21.87	22.21	22.02
Cr2O3	-	-	-	-	Cr2O3	-	-	-	-
FeO	1.37	1.30	0.04	0.06	FeO	33.95	33.35	33.92	33.53
MnO	0.00	0.02	-	-	MnO	1.13	1.81	1.19	1.49
MgO	1.11	1.06	0.00	0.00	MgO	5.00	3.03	4.94	3.57
CaO	0.00	0.01	5.37	5.57	CaO	0.83	3.19	0.98	2.66
Na2O	0.89	0.92	8.59	8.43	Na2O	-	-	-	-
K2O	9.98	9.98	0.08	0.06	K2O	-	-	-	-
F	0.04	0.09	0.00	0.04	F	-	-	-	-
Total	**95.05**	**95.52**	**101.47**	**100.19**	**Total**	**101.70**	**101.62**	**101.90**	**101.87**
Formula					Formula				
Units	22	22	8	8	Units	12	12	12	12
Si	6.2580	6.1981	2.7622	2.7513	Si	2.9920	2.9973	2.9889	2.9990
Ti	0.1311	0.1063	0.0006	0.0006	Ti	-	-	-	-
Al	5.2552	5.3793	1.2372	1.2441	Al	2.0217	2.0138	2.0236	2.0162
Cr	-	-	-	-	Cr	-	-	-	-
Fe	0.1531	0.1446	0.0015	0.0020	Fe	2.2634	2.2444	2.2579	2.2439
Mn	0.0000	0.0017	-	-	Mn	0.0740	0.1195	0.0778	0.0980
Mg	0.2207	0.2103	0.0000	0.0000	Mg	0.5771	0.3531	0.5696	0.4140
Ca	0.0000	0.0021	0.2510	0.2640	Ca	0.0686	0.2672	0.0811	0.2213
Na	0.2312	0.2369	0.7269	0.7236	Na	-	-	-	-
K	1.6988	1.6900	0.0046	0.0033	K	-	-	-	-
F	0.0189	0.0375	0.0000	0.0059	F	-	-	-	-
Total	**13.9670**	**14.0068**	**4.9840**	**4.9950**	**Total**	**7.9968**	**7.9953**	**7.9989**	**7.9924**

S34	Garnet					Hb	Anorthite		
Calcsilicate	PGC	PGI	PGE	PGN	PGL	PHA	PFF	PFC	PFA
Sassi		1-Core	1-Rim	2-Core	2-Rim		1-Core	1-Rim	
SiO2	38.59	38.29	38.48	38.32	38.47	41.14	45.65	44.40	45.99
TiO2	0.04	0.05	0.05	0.04	0.05	0.73	0.02	0.02	0.00
Al2O3	21.19	21.37	21.30	21.75	21.69	14.28	34.34	35.50	34.46
Cr2O3	0.02	0.08	0.05	0.00	0.00	-	-	-	-
FeO	23.15	21.66	21.85	22.42	22.16	18.77	0.01	0.13	0.08
MnO	2.22	1.27	2.25	0.60	2.11	0.42	0.03	0.02	0.00
MgO	2.02	1.43	1.50	1.28	1.49	7.09	0.00	0.00	0.00
CaO	13.22	16.47	15.23	16.73	15.34	12.04	18.01	18.02	18.00
Na2O	-	-	-	-	-	0.98	1.28	0.94	1.16
K2O	-	-	-	-	-	1.90	0.02	0.01	0.02
F	-	-	-	-	-	-	-	-	-
Total	**100.45**	**100.62**	**100.71**	**101.14**	**101.31**	**97.35**	**99.36**	**99.04**	**99.71**
Formula									
Units	12	12	12	12	12	23	8	8	8
Si	3.0241	2.9932	3.0081	2.9811	2.9909	6.2956	2.1153	2.0656	2.1217
Ti	0.0021	0.0031	0.0031	0.0021	0.0031	0.0834	0.0006	0.0006	0.0000
Al	1.9574	1.9693	1.9630	1.9943	1.9877	2.5766	1.8756	1.9471	1.8739
Cr	0.0009	0.0050	0.0030	0.0000	0.0000	-	-	-	-
Fe	1.5171	0.0842	0.1490	0.0394	0.1391	2.4026	0.0012	0.0006	0.0032
Mn	0.1470	1.4161	1.4282	1.4585	1.4407	0.0539	0.0005	0.0049	0.0000
Mg	0.2355	0.1661	0.1752	0.1489	0.1722	1.6165	0.0000	0.0000	0.0000
Ca	1.1100	1.3791	1.2758	1.3950	1.2782	1.9734	0.8944	0.8984	0.8900
Na	-	-	-	-	-	0.2898	0.1148	0.0850	0.1037
K	-	-	-	-	-	0.3702	0.0013	0.0006	0.0013
F	-	-	-	-	-	-	-	-	-
Total	**7.9941**	**8.0161**	**8.0054**	**8.0193**	**8.0119**	**15.6620**	**5.0037**	**5.0028**	**4.9938**

S34	Biotite			T23	Garnet		Diop	Anorthite	Plag
Calcsilicate	PBA	PBB	PBC	Calcsilicate	OGU	OGN	OPA	OFH	OFJ
Sassi				Tato	1-Core	1-Rim			
SiO2	35.88	36.58	35.66	SiO2	39.56	39.40	55.76	45.38	61.17
TiO2	1.81	1.89	1.81	TiO2	0.13	0.15	0.02	0.00	0.02
Al2O3	15.45	15.60	15.70	Al2O3	21.24	21.43	0.57	35.32	25.54
Cr2O3	0.00	0.00	0.00	Cr2O3	0.00	0.00	0.00	-	-
FeO	21.14	20.99	22.48	FeO	2.75	3.02	10.00	0.06	0.07
MnO	0.29	0.28	0.37	MnO	0.06	0.08	0.16	-	-
MgO	9.41	9.64	9.36	MgO	0.06	0.18	10.45	-	-
CaO	0.04	0.03	0.16	CaO	36.23	35.82	22.94	18.98	6.70
Na2O	0.06	0.05	0.04	Na2O	-	-	0.07	0.82	7.37
K2O	9.43	8.50	7.16	K2O	-	-	0.00	0.01	0.26
F	-	-	-	F	-	-	-	-	-
Total	**93.51**	**93.56**	**92.74**	**Total**	**100.03**	**100.08**	**99.97**	**100.57**	**101.13**
Formula				Formula					
Units	22	22	22	Units	12	12	6	8	8
Si	5.6440	5.6970	5.6181	Si	3.0017	2.9895	2.0746	2.0817	2.6877
Ti	0.2135	0.2218	0.2147	Ti	0.0076	0.0087	0.0005	0.0000	0.0006
Al	2.8645	2.8644	2.9156	Al	1.8998	1.9164	0.0249	1.9096	1.3227
Cr	0.0000	0.0000	0.0000	Cr	0.0000	0.0000	0.0000	-	-
Fe	2.7810	2.7337	2.9619	Fe	0.1747	0.1916	0.3111	0.0021	0.0025
Mn	0.0387	0.0364	0.0489	Mn	0.0040	0.0050	0.0049	-	-
Mg	2.2060	2.2374	2.1978	Mg	0.0072	0.0198	0.5793	-	-
Ca	0.0072	0.0047	0.0263	Ca	2.9455	2.9122	0.9143	0.9330	0.3153
Na	0.0168	0.0165	0.0113	Na	-	-	0.0048	0.0731	0.6280
K	1.8927	1.6898	1.4394	K	-	-	0.0000	0.0006	0.0146
F	-	-	-	F	-	-	-	-	-
Total	**15.6644**	**15.5017**	**15.4340**	**Total**	**8.0405**	**8.0432**	**3.9144**	**5.0001**	**4.9714**

S62	Garnet						Biotite		
Pelitic gneiss	GGC	GGA	GGD	GGE	GGK	GGL	GBA	GBC	GBE
Sassi	1-Core	1-Rim	2-Core	2-Rim	3-Core	3-Rim			
SiO2	37.95	37.77	38.07	37.77	37.98	37.80	36.33	37.51	35.89
TiO2	0.03	0.03	0.03	0.03	0.03	0.02	2.00	1.68	1.98
Al2O3	20.97	20.99	21.12	21.23	20.96	21.26	18.12	21.34	19.08
Cr2O3	0.02	0.02	0.00	0.00	0.00	0.00	-	-	-
FeO	32.32	31.90	32.74	32.36	33.21	33.41	18.36	15.90	18.39
MnO	1.30	0.23	0.65	0.42	0.94	2.00	0.09	0.09	0.09
MgO	3.17	2.73	3.94	3.78	4.17	3.31	9.89	8.34	9.89
CaO	4.98	6.73	4.28	5.20	3.41	3.08	0.01	0.04	0.01
Na2O	-	-	-	-	-	-	0.21	0.19	0.23
K2O	-	-	-	-	-	-	8.65	8.68	8.65
F	-	-	-	-	-	-	-	-	-
Total	**100.74**	**100.40**	**100.83**	**100.79**	**100.70**	**100.88**	**93.66**	**93.77**	**94.21**
Formula									
Units	12	12	12	12	12	12	22	22	22
Si	3.0112	3.0038	3.0071	2.9864	3.0080	3.0020	5.5654	5.6190	5.4659
Ti	0.0020	0.0020	0.0020	0.0020	0.0020	0.0010	0.2298	0.1893	0.2264
Al	1.9608	1.9678	1.9662	1.9791	1.9569	1.9902	3.2714	3.7674	3.4255
Cr	0.0009	0.0009	0.0000	0.0000	0.0000	0.0000	-	-	-
Fe	2.1446	2.1220	2.1630	2.1399	2.1996	2.2192	2.3524	1.9925	2.3419
Mn	0.0873	0.0153	0.0434	0.0283	0.0627	0.1347	0.0119	0.0117	0.0119
Mg	0.3754	0.3236	0.4633	0.4451	0.4928	0.3919	2.2585	1.8633	2.2461
Ca	0.4230	0.5738	0.3621	0.4409	0.2891	0.2623	0.0023	0.0069	0.0023
Na	-	-	-	-	-	-	0.0633	0.0553	0.0681
K	-	-	-	-	-	-	1.6903	1.6594	1.6808
F	-	-	-	-	-	-	-	-	-
Total	**8.0052**	**8.0092**	**8.0071**	**8.0217**	**8.0111**	**8.0013**	**15.4453**	**15.1648**	**15.4689**

S62	Muscovite		Plagioclase						
Pelitic gneiss	GMB	GMC	GFA	GFB	GFC	GFF	GFG	GFH	GFI
Sassi			1-Core	1-Rim	incl.	2-Core	2-Rim	3-Core	3-Rim
SiO2	45.85	46.18	61.97	60.82	63.00	61.66	61.05	61.74	61.74
TiO2	0.75	0.88	-	-	-	-	-	-	-
Al2O3	34.69	33.92	23.69	23.19	22.16	23.88	24.45	23.15	23.62
Cr2O3	-	-	-	-	-	-	-	-	-
FeO	1.22	1.25	0.11	0.03	0.10	0.07	0.03	0.04	0.04
MnO	0.00	0.02	-	-	-	-	-	-	-
MgO	0.84	1.04	0.00	0.00	0.00	0.00	0.00	0.00	0.00
CaO	0.01	0.01	5.26	5.66	4.63	5.50	6.01	5.25	5.12
Na2O	0.98	0.89	8.43	8.57	9.04	8.43	8.18	8.67	8.54
K2O	9.37	9.28	0.08	0.10	0.12	0.14	0.08	0.10	0.11
F	-	-	-	-	-	-	-	-	-
Total	**93.71**	**93.47**	**99.54**	**98.37**	**99.05**	**99.68**	**99.80**	**98.95**	**99.17**
Formula									
Units	22	22	8	8	8	8	8	8	8
Si	6.1745	6.2306	2.7574	2.7472	2.8148	2.7443	2.7165	2.7664	2.7576
Ti	0.0756	0.0890	-	-	-	-	-	-	-
Al	5.5063	5.3948	1.2427	1.2348	1.1668	1.2526	1.2825	1.2227	1.2435
Cr	-	-	-	-	-	-	-	-	-
Fe	0.1373	0.1407	0.0041	0.0010	0.0036	0.0026	0.0010	0.0015	0.0015
Mn	0.0000	0.0017	-	-	-	-	-	-	-
Mg	0.1685	0.2082	0.0000	0.0000	0.0000	0.0000	0.0000	0.0000	0.0000
Ca	0.0021	0.0021	0.2509	0.2741	0.2215	0.2620	0.2867	0.2519	0.2450
Na	0.2558	0.2338	0.7271	0.7507	0.7828	0.7272	0.7058	0.7533	0.7394
K	1.6092	1.5976	0.0047	0.0054	0.0068	0.0081	0.0047	0.0054	0.0061
F	-	-	-	-	-	-	-	-	-
Total	**13.9293**	**13.8985**	**4.9869**	**5.0132**	**4.9963**	**4.9968**	**4.9972**	**5.0012**	**4.9931**

S29	Garnet				Plagioclase		Musc	Biotite	
Pelitic gneiss	SGA	SGB	SGD	SGE	SFE	SFF	SMA	SBA	SBB
Sassi	1-Core	1-Rim	2-Core	2-Rim	1-Core	1-Rim			
SiO2	37.99	37.78	38.04	38.17	46.40	50.42	46.58	35.62	36.37
TiO2	0.07	0.05	0.02	0.04	0.02	0.02	1.08	2.92	1.13
Al2O3	21.49	21.48	21.26	21.43	30.65	30.61	31.25	18.36	19.73
Cr2O3	0.02	0.00	0.00	0.00	-	-	-	-	-
FeO	29.84	30.30	29.07	29.77	0.10	0.10	1.95	20.13	19.81
MnO	2.39	1.11	3.58	1.73	-	-	0.03	0.32	0.40
MgO	1.08	1.99	1.89	2.06	0.00	0.00	1.36	8.22	8.20
CaO	8.58	7.96	7.09	8.00	17.21	14.44	0.00	0.01	0.06
Na2O	-	-	-	-	2.48	3.43	0.22	0.07	0.09
K2O	-	-	-	-	0.05	0.10	10.63	9.89	9.59
F	-	-	-	-	1.34	0.00	0.09	0.37	0.45
Total	**101.46**	**100.67**	**100.95**	**101.20**	**98.25**	**99.12**	**93.19**	**95.91**	**95.83**
Formula Units	12	12	12	12	8	8	22	22	22
Si	3.0011	2.9947	3.0142	3.0076	2.2097	2.3191	6.3761	5.4476	5.5290
Ti	0.0041	0.0031	0.0010	0.0020	0.0006	0.0006	0.1114	0.3357	0.1292
Al	2.0016	2.0067	1.9852	1.9902	1.7207	1.6593	5.0424	3.3094	3.5354
Cr	0.0009	0.0000	0.0000	0.0000	-	-	-	-	-
Fe	1.9716	2.0084	1.9260	1.9617	0.0039	0.0037	0.2228	2.5754	2.5184
Mn	0.1600	0.0742	0.2405	0.1153	-	-	0.0036	0.0417	0.0513
Mg	0.1276	0.2353	0.2227	0.2424	0.0000	0.0000	0.2769	1.8737	1.8576
Ca	0.7262	0.6761	0.6022	0.6756	0.8784	0.7117	0.0000	0.0023	0.0093
Na	-	-	-	-	0.2286	0.3056	0.0593	0.0215	0.0265
K	-	-	-	-	0.0028	0.0061	1.8569	1.9296	1.8606
F	-	-	-	-	0.2014	0.0000	0.0394	0.1794	0.2147
Total	**7.9931**	**7.9985**	**7.9918**	**7.9948**	**5.2461**	**5.0061**	**13.9888**	**15.7163**	**15.7320**

D18	Garnet			Plag	K-spar	Biotite		Musc	Epidote
Orthogneiss	GGB	GGG	GKB	GKA	GKH	GBC	GBD	GMA	GEE
W. Darchan	1-Core	1-Rim	1-Core	1-Rim					
SiO2	37.93	37.78	63.26	63.71	65.14	35.77	35.85	46.51	37.10
TiO2	0.07	-	-	-	-	2.60	2.92	0.76	0.13
Al2O3	20.99	20.80	22.81	22.88	18.32	16.85	16.28	29.62	23.79
Cr2O3	-	-	-	-	-	-	-	-	-
FeO	18.33	18.43	0.06	0.07	0.03	22.41	22.36	5.20	10.83
MnO	13.36	13.08	-	-	-	0.61	0.55	0.02	0.76
MgO	1.03	1.23	-	-	-	7.41	7.68	1.38	0.07
CaO	9.63	9.87	4.60	4.23	0.01	0.03	0.01	0.01	22.38
Na2O	-	-	8.62	9.00	0.67	0.06	0.09	0.25	0.00
K2O	-	-	0.33	0.24	14.91	9.39	9.25	10.52	0.00
F	-	-	-	-	-	0.04	0.08	0.04	-
Total	**101.34**	**101.19**	**99.75**	**100.19**	**99.48**	**95.22**	**95.12**	**94.40**	**95.06**
Formula Units	12	12	8	8	8	22	22	22	23
Si	3.0029	2.9975	2.8048	2.8100	3.0115	5.5552	5.5730	6.3970	5.6793
Ti	0.0041	-	-	-	-	0.3035	0.3412	0.0786	0.0149
Al	1.9583	1.9454	1.1919	1.1896	0.9982	3.0853	2.9829	4.8018	4.2931
Cr	-	-	-	-	-	-	-	-	-
Fe	1.2138	1.2232	0.0020	0.0025	0.0010	2.9109	2.9068	0.5986	1.3869
Mn	0.8959	0.8789	-	-	-	0.0804	0.0724	0.0018	0.0989
Mg	0.1215	0.1456	-	-	-	1.7158	1.7804	0.2824	0.0153
Ca	0.8171	0.8390	0.2186	0.1997	0.0007	0.0047	0.0023	0.0021	3.6708
Na	-	-	0.7407	0.7699	0.0598	0.0168	0.0281	0.0658	0.0000
K	-	-	0.0189	0.0134	0.8796	1.8614	1.8354	1.8463	0.0000
F	-	-	-	-	-	0.0202	0.0405	0.0193	-
Total	**8.0136**	**8.0296**	**4.9787**	**4.9865**	**4.9588**	**15.5572**	**15.5660**	**14.0986**	**15.1592**

D19	Garnet						Plagioclase		
Pelitic gneiss	MGA	MGB	MGE	MGF	HGF	HGE	MFB	MFC	MFF
E. Darchan	1-Core	1-Rim	2-Core	2-Rim	3-Core	3-Rim	1-Core	1-Rim	2-Core
SiO2	38.37	38.29	38.13	38.18	38.70	38.02	62.92	62.16	62.36
TiO2	0.03	0.03	0.02	0.03	0.02	0.02	-	-	-
Al2O3	21.89	21.74	21.85	21.70	21.72	21.57	22.88	23.44	23.60
Cr2O3	0.00	0.00	0.00	0.00	-	-	-	-	-
FeO	31.73	32.04	32.02	32.07	31.91	32.78	0.06	0.08	0.03
MnO	1.10	1.37	1.24	1.24	1.25	2.23	-	-	-
MgO	5.10	4.50	4.80	4.71	5.04	3.43	-	-	-
CaO	3.21	3.26	3.32	3.26	3.10	3.07	4.18	4.93	4.92
Na2O	-	-	-	-	-	-	9.22	8.86	8.92
K2O	-	-	-	-	-	-	0.14	0.10	0.13
F	-	-	-	-	-	-	-	-	-
Total	**101.43**	**101.23**	**101.38**	**101.19**	**101.74**	**101.12**	**99.40**	**99.57**	**99.96**
Formula									
Units	12	12	12	12	12	12	8	8	8
Si	2.9990	3.0077	2.9910	3.0007	3.0075	3.0034	2.7987	2.7662	2.7644
Ti	0.0020	0.0020	0.0010	0.0020	0.0010	0.0010	-	-	-
Al	2.0165	2.0132	2.0204	2.0103	1.9893	2.0080	1.1997	1.2296	1.2329
Cr	0.0000	0.0000	0.0000	0.0000	-	-	-	-	-
Fe	2.0847	2.1155	2.1114	2.1188	2.0740	2.1657	0.0020	0.0031	0.0010
Mn	0.0730	0.0914	0.0823	0.0824	0.0825	0.1492	-	-	-
Mg	0.5938	0.5272	0.5607	0.5513	0.5843	0.4040	-	-	-
Ca	0.2686	0.2743	0.2786	0.2745	0.2578	0.2600	0.1992	0.2351	0.2336
Na	-	-	-	-	-	-	0.7954	0.7640	0.7668
K	-	-	-	-	-	-	0.0081	0.0054	0.0074
F	-	-	-	-	-	-	-	-	-
Total	**8.0376**	**8.0313**	**8.0454**	**8.0400**	**7.9964**	**7.9913**	**5.0031**	**5.0034**	**5.0061**

D19		Biotite					Muscovite		
Pelitic gneiss	MFG	MBB	MBD	MBE	MBF	MBG	MMB	MMC	MMD
E. Darchan	2-Rim			Incl. Core	Incl. Rim				
SiO2	63.00	36.24	35.59	36.10	49.72	35.37	47.48	47.05	47.16
TiO2	-	1.99	2.24	2.20	1.55	2.04	0.84	0.99	1.05
Al2O3	22.81	18.66	18.51	18.25	14.23	18.08	33.31	33.20	33.56
Cr2O3	-	-	-	-	-	-	-	-	-
FeO	0.14	18.78	19.63	20.69	16.76	19.20	1.35	1.42	1.49
MnO	-	0.17	0.17	0.17	0.19	0.17	0.02	0.02	0.02
MgO	-	9.81	9.40	8.72	6.54	10.21	1.20	1.19	1.18
CaO	4.98	-	-	-	-	-	0.00	0.00	0.00
Na2O	8.23	0.12	0.13	0.16	0.24	0.13	0.83	0.91	0.88
K2O	0.08	8.52	8.82	8.94	6.96	8.62	9.95	9.86	9.79
F	-	-	-	-	-	-	0.04	0.09	0.04
Total	**99.24**	**94.42**	**94.68**	**95.23**	**96.19**	**93.82**	**95.02**	**94.73**	**95.17**
Formula									
Units	8	22	22	22	22	22	22	22	22
Si	2.8029	5.5259	5.4617	5.5236	7.0443	5.4590	6.3229	6.2952	6.2747
Ti	-	0.2284	0.2584	0.2531	0.1653	0.2373	0.0842	0.0996	0.1046
Al	1.1962	3.3544	3.3487	3.2917	2.3761	3.2890	5.2292	5.2364	5.2634
Cr	-	-	-	-	-	-	-	-	-
Fe	0.0052	2.4074	2.5329	2.6609	1.9960	2.4911	0.1498	0.1583	0.1652
Mn	-	0.0218	0.0219	0.0218	0.0222	0.0220	0.0017	0.0017	0.0017
Mg	-	2.2304	2.1495	1.9890	1.3806	2.3489	0.2378	0.2365	0.2350
Ca	0.2371	-	-	-	-	-	0.0000	0.0000	0.0000
Na	0.7101	0.0369	0.0375	0.0485	0.0672	0.0376	0.2153	0.2358	0.2268
K	0.0047	1.6570	1.7277	1.7459	1.2581	1.6983	1.6899	1.6827	1.6616
F	-	-	-	-	-	-	0.0188	0.0380	0.0188
Total	**4.9562**	**15.4697**	**15.5451**	**15.5345**	**14.3098**	**15.5832**	**13.9496**	**13.9842**	**13.9518**

I1	Garnet						Hornblende		Biotite
Amphibolite	EGB	EGA	EGC	EGD	IGA	IGB	EHA	EHB	EBA
L. Darchan	1-Core	1-Rim	1-Core	1-Rim	3-Rim	3-Core			
SiO2	38.53	38.66	38.24	38.77	38.67	38.09	43.62	43.77	37.07
TiO2	0.03	0.05	0.03	0.04	0.05	0.14	1.17	1.19	3.12
Al2O3	21.71	21.78	21.55	21.76	21.84	21.42	12.38	12.92	15.18
Cr2O3	0.00	0.02	0.00	0.02	-	-	0.00	0.00	-
FeO	28.80	28.85	29.21	28.92	29.05	28.64	15.64	15.07	16.70
MnO	2.53	1.83	2.21	1.15	1.17	2.80	0.15	0.14	0.05
MgO	4.13	4.80	4.07	5.47	4.86	3.59	10.52	10.75	12.99
CaO	5.82	5.81	5.97	5.21	5.60	5.84	11.01	10.76	0.00
Na2O	-	-	-	-	-	-	1.38	1.45	0.33
K2O	-	-	-	-	-	-	0.50	0.55	8.90
F	-	-	-	-	-	-	0.13	0.21	0.42
Total	**101.55**	**101.80**	**101.28**	**101.34**	**101.24**	**100.52**	**96.56**	**96.87**	**94.91**
Formula									
Units	12	12	12	12	12	12	23	23	22
Si	2.9998	2.9932	2.9916	3.0018	3.0024	3.0032	6.5478	6.5282	5.6230
Ti	0.0020	0.0030	0.0020	0.0020	0.0030	0.0082	0.1316	0.1329	0.3559
Al	1.9928	1.9880	1.9867	1.9858	1.9984	1.9904	2.1902	2.2718	2.7131
Cr	0.0000	0.0009	0.0000	0.0009	-	-	0.0000	0.0000	-
Fe	1.8750	1.8679	1.9112	1.8723	1.8861	1.8886	1.9633	1.8796	2.1186
Mn	0.1668	0.1203	0.1465	0.0756	0.0768	0.1871	0.0196	0.0176	0.0059
Mg	0.4796	0.5534	0.4742	0.6316	0.5626	0.4220	2.3528	2.3910	2.9376
Ca	0.4855	0.4822	0.5004	0.4324	0.4656	0.4935	1.7709	1.7190	0.0000
Na	-	-	-	-	-	-	0.4008	0.4202	0.0977
K	-	-	-	-	-	-	0.0964	0.1046	1.7218
F	-	-	-	-	-	-	0.0606	0.1001	0.1995
Total	**8.0015**	**8.0089**	**8.0126**	**8.0024**	**7.9949**	**7.9930**	**15.5497**	**15.5806**	**15.8109**

I1				Plagioclase					
Amphibolite	EBB	EBC	EBD	EFB	EFC	IFD	IFC	IFF	IFE
L. Darchan				1-Core	1-Rim	2-Core	2-Rim	3-Core	3-Rim
SiO2	36.64	36.72	37.11	59.63	52.27	56.20	55.56	52.89	52.30
TiO2	3.32	3.13	3.28	-	-	-	-	-	-
Al2O3	15.02	15.12	14.99	24.94	29.57	27.86	28.41	29.90	29.74
Cr2O3	-	-	-	-	-	-	-	-	-
FeO	16.81	17.42	17.20	0.10	0.24	0.04	0.08	0.08	0.15
MnO	0.03	0.05	0.05	-	-	-	-	-	-
MgO	12.86	12.67	12.65	-	-	-	-	-	-
CaO	0.01	0.01	0.03	7.21	12.75	10.13	10.65	12.81	13.32
Na2O	0.35	0.35	0.23	7.32	4.15	5.72	5.54	4.02	4.10
K2O	8.76	8.76	8.92	0.06	0.04	0.04	0.04	0.07	0.00
F	0.46	0.33	0.42	0.00	0.00	-	-	-	-
Total	**94.39**	**94.69**	**95.00**	**99.26**	**99.03**	**99.99**	**100.28**	**99.77**	**99.61**
Formula									
Units	22	22	22	8	8	8	8	8	8
Si	5.5971	5.5975	5.6353	2.6757	2.3931	2.5241	2.4939	2.3989	2.3831
Ti	0.3809	0.3591	0.3745	-	-	-	-	-	-
Al	2.7044	2.7161	2.6825	1.3189	1.5958	1.4749	1.5030	1.5983	1.5974
Cr	-	-	-	-	-	-	-	-	-
Fe	2.1473	2.2203	2.1845	0.0037	0.0091	0.0015	0.0031	0.0032	0.0059
Mn	0.0039	0.0059	0.0059	-	-	-	-	-	-
Mg	2.9273	2.8795	2.8629	-	-	-	-	-	-
Ca	0.0023	0.0023	0.0046	0.3465	0.6254	0.4876	0.5121	0.6227	0.6505
Na	0.1039	0.1042	0.0673	0.6365	0.3685	0.4983	0.4825	0.3535	0.3625
K	1.7079	1.7040	1.7289	0.0033	0.0020	0.0020	0.0020	0.0040	0.0000
F	0.2218	0.1602	0.1998	0.0000	0.0000	-	-	-	-
Total	**15.8317**	**15.7839**	**15.7777**	**4.9846**	**4.9941**	**4.9884**	**4.9966**	**4.9806**	**4.9994**

S90	Garnet						Hornblende		Plag
Amphibolite	VGA	VGB	SGD	SGC	VGC	VGD	VHA	VHB	VFC
Shengus	1-Core	1-Rim	2-Core	2-Rim	3-Core	3-Rim	1-Core	1-Rim	
SiO2	38.14	38.01	38.13	38.37	37.44	38.32	41.72	41.62	58.30
TiO2	0.18	0.07	0.11	0.13	0.91	0.09	1.09	1.36	0.02
Al2O3	21.04	21.37	21.18	21.20	20.80	21.34	13.89	13.30	25.82
Cr2O3	0.00	0.00	0.00	0.00	0.00	0.00	0.00	0.02	-
FeO	22.89	23.29	23.10	22.93	24.34	24.76	18.27	18.87	0.15
MnO	3.37	1.85	3.02	2.86	3.12	2.41	0.25	0.32	-
MgO	1.79	1.94	1.77	1.71	1.77	1.78	7.89	7.81	0.00
CaO	13.11	13.83	13.41	13.61	12.59	12.53	12.16	12.27	8.62
Na2O	-	-	-	-	-	-	1.33	1.32	6.81
K2O	-	-	-	-	-	-	1.69	1.74	0.17
F	-	-	-	-	-	-	0.13	0.08	-
Total	**100.52**	**100.36**	**100.72**	**100.81**	**100.97**	**101.23**	**98.42**	**98.71**	**99.90**
Formula Units	12	12	12	12	12	12	23	23	8
Si	3.0017	2.9876	2.9954	3.0065	2.9529	2.9989	6.3012	6.2957	2.6151
Ti	0.0105	0.0042	0.0063	0.0073	0.0537	0.0052	0.1237	0.1547	0.0006
Al	1.9522	1.9798	1.9611	1.9583	1.9333	1.9687	2.4727	2.3718	1.3650
Cr	0.0000	0.0000	0.0000	0.0000	0.0000	0.0000	0.0000	0.0019	-
Fe	1.5063	1.5311	1.5175	1.5026	1.6055	1.6203	2.3071	2.3867	0.0058
Mn	0.2248	0.1231	0.2011	0.1895	0.2086	0.1596	0.0315	0.0414	-
Mg	0.2100	0.2278	0.2074	0.2002	0.2080	0.2078	1.7757	1.7599	0.0000
Ca	1.1057	1.1644	1.1285	1.1423	1.0643	1.0507	1.9687	1.9892	0.4141
Na	-	-	-	-	-	-	0.3886	0.3867	0.5920
K	-	-	-	-	-	-	0.3263	0.3350	0.0094
F	-	-	-	-	-	-	0.0604	0.0403	-
Total	**8.0112**	**8.0180**	**8.0173**	**8.0067**	**8.0263**	**8.0112**	**15.7559**	**15.7633**	**5.0022**

S90			Biotite		S89	Garnet		Plagioclase	
Amphibolite	VFD	VFE	VBB	VBC	Amphibolite	UGB	UGC	UFB	UFC
Shengus					Shengus	1-Core	1-Rim	2-Core	2-Rim
SiO2	59.85	58.66	36.04	34.99	SiO2	38.32	37.95	52.71	52.54
TiO2	0.02	0.00	3.96	3.92	TiO2	0.09	0.05	0.02	0.02
Al2O3	24.91	25.75	14.82	15.03	Al2O3	21.71	21.49	29.46	29.76
Cr2O3	-	-	0.02	0.02	Cr2O3	0.00	0.00	-	-
FeO	0.08	0.07	21.62	22.25	FeO	26.34	27.69	0.11	0.13
MnO	-	-	0.18	0.21	MnO	1.11	1.58	-	-
MgO	0.00	0.00	9.37	9.00	MgO	3.58	3.01	0.00	0.00
CaO	7.24	8.10	0.03	0.03	CaO	9.79	8.92	12.78	13.04
Na2O	7.43	6.92	0.11	0.13	Na2O	-	-	4.27	4.35
K2O	0.31	0.22	9.46	9.39	K2O	-	-	0.06	0.04
F	-	-	0.12	0.12	F	-	-	-	-
Total	**99.84**	**99.72**	**95.73**	**95.09**	**Total**	**100.94**	**100.69**	**99.41**	**99.89**
Formula Units	8	8	22	22	Formula Units	12	12	8	8
Si	2.6747	2.6300	5.5588	5.4661	Si	2.9868	2.9860	2.4027	2.3876
Ti	0.0006	0.0000	0.4594	0.4603	Ti	0.0052	0.0031	0.0006	0.0006
Al	1.3124	1.3607	2.6936	2.7683	Al	1.9949	1.9928	1.5828	1.5939
Cr	-	-	0.0019	0.0019	Cr	0.0000	0.0000	-	-
Fe	0.0031	0.0026	2.7894	2.9068	Fe	1.7173	1.8221	0.0042	0.0048
Mn	-	-	0.0240	0.0283	Mn	0.0734	0.1053	-	-
Mg	0.0000	0.0000	2.1544	2.0956	Mg	0.4154	0.3530	0.0000	0.0000
Ca	0.3467	0.3891	0.0047	0.0047	Ca	0.8172	0.7519	0.6243	0.6348
Na	0.6438	0.6013	0.0331	0.0395	Na	-	-	0.3773	0.3835
K	0.0175	0.0128	1.8615	1.8717	K	-	-	0.0034	0.0020
F	-	-	0.0604	0.0613	F	-	-	-	-
Total	**4.9988**	**4.9965**	**15.6412**	**15.7045**	**Total**	**8.0102**	**8.0142**	**4.9953**	**5.0074**

A7	Garnet						Plagioclase		
Calcsilicate	EGA	EGB	EGC	EGD	EGF	EGG	EFA	EFC	EFD
Tarshing	1-Core	1-Rim	2-Core	2- Rim	3-Core	3-Rim			
SiO2	38.57	39.68	38.50	38.85	38.29	38.98	59.01	59.54	57.23
TiO2	0.12	0.05	0.11	0.05	0.09	0.11	0.02	0.02	0.02
Al2O3	21.45	22.01	21.29	21.87	21.39	21.48	26.38	25.75	27.15
Cr2O3	0.00	0.02	0.02	0.02	0.02	0.00	-	-	-
FeO	28.14	26.81	26.41	24.84	28.12	26.08	0.07	0.10	0.04
MnO	1.50	1.72	3.93	2.59	0.97	1.84	-	-	-
MgO	1.64	4.64	2.23	4.14	1.47	2.46	-	-	-
CaO	9.63	7.15	8.25	8.31	10.43	10.11	8.65	7.99	9.75
Na2O	-	-	-	-	-	-	6.68	6.85	5.95
K2O	-	-	-	-	-	-	0.04	0.05	0.05
F	-	-	-	-	-	-	0.00	0.00	0.00
Total	**101.05**	**102.08**	**100.74**	**100.67**	**100.78**	**101.06**	**100.85**	**100.31**	**100.19**
Formula									
Units	12	12	12	12	12	12	8	8	8
Si	3.0288	3.0359	3.0314	3.0174	3.0177	3.0379	2.6152	2.6468	2.5609
Ti	0.0072	0.0030	0.0062	0.0031	0.0052	0.0062	0.0006	0.0006	0.0006
Al	1.9850	1.9853	1.9758	2.0019	1.9868	1.9736	1.3779	1.3494	1.4321
Cr	0.0000	0.0009	0.0009	0.0009	0.0009	0.0000	-	-	-
Fe	1.8480	1.7156	1.7393	1.6136	1.8534	1.6999	0.0026	0.0036	0.0015
Mn	0.1000	0.1114	0.2620	0.1703	0.0649	0.1216	-	-	-
Mg	0.1919	0.5296	0.2616	0.4791	0.1729	0.2856	-	-	-
Ca	0.8101	0.5859	0.6964	0.6914	0.8809	0.8440	0.4107	0.3804	0.4674
Na	-	-	-	-	-	-	0.5740	0.5905	0.5166
K	-	-	-	-	-	-	0.0020	0.0026	0.0026
F	-	-	-	-	-	-	0.0000	0.0000	0.0000
Total	**7.9710**	**7.9676**	**7.9736**	**7.9777**	**7.9827**	**7.9688**	**4.9830**	**4.9741**	**4.9817**

A7	Muscovite			Biotite				Zoisite	
Calcsilicate	EMB	EMC	EMD	EBA	EBB	EBD	EBE	EUE	EUD
Tarshing									
SiO2	47.37	46.87	47.25	39.33	37.75	37.60	38.82	39.90	40.34
TiO2	1.12	0.95	0.80	1.26	1.51	1.51	1.42	0.08	0.13
Al2O3	33.18	33.84	33.45	19.07	18.55	18.27	18.32	32.69	32.25
Cr2O3	-	-	-	-	-	-	-	0.02	0.00
FeO	1.12	0.94	1.12	11.79	13.29	13.12	13.31	1.11	1.21
MnO	0.03	0.00	0.02	0.05	0.05	0.08	0.06	0.06	0.03
MgO	1.47	1.18	1.27	12.80	13.74	14.06	13.78	0.02	0.11
CaO	0.01	0.01	0.00	0.56	0.00	0.03	0.01	24.71	23.05
Na2O	0.79	0.87	0.80	0.81	0.25	0.25	0.23	0.00	0.03
K2O	10.14	9.96	10.09	8.64	9.04	8.86	8.93	0.01	0.49
F	0.09	0.13	0.09	0.42	0.54	0.62	0.58	-	-
Total	**95.32**	**94.75**	**94.89**	**94.73**	**94.72**	**94.40**	**95.46**	**98.60**	**97.64**
Formula									
Units	22	22	22	22	22	22	22	23	23
Si	6.2973	6.2582	6.3031	5.7621	5.6031	5.6005	5.6995	7.7285	7.8648
Ti	0.1121	0.0957	0.0806	0.1388	0.1685	0.1691	0.1567	0.0110	0.0195
Al	5.1990	5.3260	5.2604	3.2936	3.2453	3.2079	3.1711	7.4621	7.4117
Cr	-	-	-	-	-	-	-	0.0026	0.0000
Fe	0.1246	0.1048	0.1251	1.4451	1.6502	1.6338	1.6339	0.1799	0.1970
Mn	0.0035	0.0000	0.0017	0.0057	0.0058	0.0097	0.0077	0.0103	0.0052
Mg	0.2904	0.2349	0.2526	2.7959	3.0400	3.1225	3.0167	0.0044	0.0312
Ca	0.0021	0.0021	0.0000	0.0885	0.0000	0.0046	0.0022	5.1280	4.8143
Na	0.2033	0.2264	0.2076	0.2292	0.0723	0.0725	0.0666	0.0000	0.0115
K	1.7205	1.6964	1.7171	1.6149	1.7122	1.6830	1.6732	0.0027	0.1212
F	0.0377	0.0569	0.0378	0.1942	0.2538	0.2943	0.2689	-	-
Total	**13.9905**	**14.0014**	**13.9860**	**15.5680**	**15.7512**	**15.7979**	**15.6965**	**20.5295**	**20.4764**

A3	Garnet						Plagioclase		
Pelitic gneiss	DGB	DGC	DGD	DGE	DGH	DGI	DFA	DFB	DFD
Astor valley	1-Core	1- Rim	2-Core	2-Rim	3-Core	3-Rim	1-Core	1-Rim	1-Core
SiO2	38.59	39.34	38.45	38.08	38.57	37.85	66.46	72.68	66.42
TiO2	0.03	0.03	0.03	0.03	0.02	0.03	0.02	0.02	0.02
Al2O3	21.71	21.00	21.58	21.51	21.47	21.40	21.05	17.40	19.33
Cr2O3	0.00	0.00	0.00	0.00	0.00	0.01	-	-	-
FeO	34.54	34.63	34.97	34.64	34.63	35.28	0.04	0.06	0.03
MnO	0.83	1.08	0.92	0.93	0.90	1.04	-	-	-
MgO	4.51	3.15	4.22	3.84	4.49	3.39	-	-	-
CaO	1.35	1.54	1.20	1.50	1.05	1.67	2.33	1.92	2.09
Na2O	-	-	-	-	-	-	9.92	8.58	9.36
K2O	-	-	-	-	-	-	0.23	0.16	0.16
F	-	-	-	-	-	-	0.00	0.00	0.04
Total	**101.56**	**100.77**	**101.37**	**100.53**	**101.13**	**100.67**	**100.05**	**100.82**	**97.45**
Formula									
Units	12	12	12	12	12	12	8	8	8
Si	3.0192	3.1038	3.0215	3.0193	3.0315	3.0118	2.9140	3.1145	2.9770
Ti	0.0020	0.0020	0.0020	0.0020	0.0010	0.0020	0.0006	0.0006	0.0006
Al	2.0022	1.9533	1.9986	2.0104	1.9891	2.0065	1.0877	0.8789	1.0211
Cr	0.0000	0.0000	0.0000	0.0000	0.0000	0.0009	-	-	-
Fe	2.2601	2.2852	2.2985	2.2969	2.2760	2.3472	0.0015	0.0020	0.0010
Mn	0.0549	0.0724	0.0611	0.0627	0.0601	0.0699	-	-	-
Mg	0.5256	0.3699	0.4943	0.4541	0.5265	0.4016	-	-	-
Ca	0.1133	0.1305	0.1009	0.1276	0.0882	0.1419	0.1093	0.0883	0.1005
Na	-	-	-	-	-	-	0.8435	0.7133	0.8138
K	-	-	-	-	-	-	0.0127	0.0085	0.0089
F	-	-	-	-	-	-	0.0000	0.0000	0.0060
Total	**7.9773**	**7.9171**	**7.9769**	**7.9730**	**7.9724**	**7.9818**	**4.9693**	**4.8061**	**4.9289**

A3		K-feldspar		Muscovite			Biotite		
Pelitic gneiss	DFE	DFH	DFI	DMA	DMB	DMC	DBB	DBE	DBF
Astor valley	1-Rim	2-Core	2-Rim						
SiO2	68.29	65.75	65.95	47.12	46.27	46.66	36.41	36.57	37.15
TiO2	0.02	0.04	0.02	1.79	1.85	1.85	3.84	3.99	3.87
Al2O3	21.50	18.44	18.18	31.99	32.09	32.15	17.35	17.67	17.23
Cr2O3	-	-	-	-	-	-	-	-	-
FeO	0.03	0.04	0.03	1.46	1.53	1.58	19.00	18.42	17.89
MnO	-	-	-	0.02	0.02	0.02	0.03	0.03	0.02
MgO	-	-	-	1.32	1.26	1.31	8.80	8.66	9.06
CaO	2.33	0.03	0.03	0.01	0.00	0.01	0.01	0.00	0.01
Na2O	10.17	1.82	1.99	0.38	0.39	0.37	0.11	0.13	0.12
K2O	0.23	13.87	13.79	10.52	10.38	10.54	9.52	9.54	9.39
F	0.00	0.04	0.00	0.27	0.36	0.41	0.95	0.83	0.87
Total	**102.57**	**100.28**	**100.23**	**94.88**	**94.15**	**94.90**	**96.02**	**95.84**	**95.61**
Formula									
Units	8	8	8	22	22	22	22	22	22
Si	2.9191	3.0070	3.0158	6.3291	6.2751	6.2855	5.5435	5.5507	5.6292
Ti	0.0006	0.0013	0.0006	0.1811	0.1884	0.1872	0.4396	0.4552	0.4405
Al	1.0835	0.9937	0.9799	5.0641	5.1290	5.1039	3.1143	3.1618	3.0780
Cr	-	-	-	-	-	-	-	-	-
Fe	0.0010	0.0016	0.0010	0.1636	0.1731	0.1782	2.4189	2.3386	2.2666
Mn	-	-	-	0.0017	0.0018	0.0017	0.0039	0.0039	0.0019
Mg	-	-	-	0.2646	0.2556	0.2627	1.9967	1.9599	2.0461
Ca	0.1067	0.0014	0.0014	0.0021	0.0000	0.0021	0.0023	0.0000	0.0023
Na	0.8426	0.1611	0.1763	0.1000	0.1014	0.0967	0.0319	0.0369	0.0366
K	0.0124	0.8090	0.8042	1.8026	1.7964	1.8110	1.8482	1.8482	1.8157
F	0.0000	0.0064	0.0000	0.1155	0.1560	0.1735	0.4576	0.3993	0.4192
Total	**4.9659**	**4.9860**	**4.9834**	**14.0244**	**14.0768**	**14.1025**	**15.8569**	**15.7545**	**15.7361**

A21	Garnet						Plagioclase		
Pelitic gneiss	TGA	TGB	TGC	TGD	TGH	TGI	TFF	TFE	TFH
Astor valley	1-Core	1-Rim	2-Core	2-Rim	3-Core	3-Rim	1-Core	1-Rim	2-Core
SiO2	38.34	38.16	38.58	38.43	38.59	38.49	65.06	64.84	65.10
TiO2	0.03	0.02	0.03	0.02	-	-	0.00	0.02	0.02
Al2O3	21.79	21.94	21.87	21.79	21.97	21.71	22.09	22.32	22.25
Cr2O3	0.00	0.02	0.00	0.03	-	-	-	-	-
FeO	33.59	33.17	33.74	32.93	33.43	32.98	0.06	0.13	0.03
MnO	1.84	1.39	1.78	1.40	1.94	1.70	0.02	0.02	0.00
MgO	5.23	4.89	5.43	4.89	5.07	4.73	0.00	0.00	0.00
CaO	0.75	1.88	0.70	2.15	1.02	2.15	3.21	3.18	3.14
Na2O	-	-	-	-	-	-	9.58	9.60	9.58
K2O	-	-	-	-	-	-	0.41	0.34	0.29
F	-	-	-	-	-	-	-	-	-
Total	**101.57**	**101.47**	**102.13**	**101.64**	**102.02**	**101.76**	**100.43**	**100.45**	**100.41**
Formula									
Units	12	12	12	12	12.0000	12.0000	8	8	8
Si	2.9971	2.9856	2.9972	2.9988	3.0011	3.0041	2.8560	2.8464	2.8548
Ti	0.0020	0.0010	0.0020	0.0010	-	-	0.0000	0.0006	0.0006
Al	2.0080	2.0232	2.0030	2.0045	2.0143	1.9972	1.1432	1.1552	1.1501
Cr	0.0000	0.0009	0.0000	0.0018	-	-	-	-	-
Fe	2.1960	2.1703	2.1920	2.1490	2.1746	2.1528	0.0020	0.0046	0.0010
Mn	0.1216	0.0919	0.1169	0.0927	0.1280	0.1126	0.0005	0.0005	0.0000
Mg	0.6094	0.5708	0.6292	0.5687	0.5883	0.5501	0.0000	0.0000	0.0000
Ca	0.0624	0.1573	0.0585	0.1801	0.0851	0.1800	0.1512	0.1498	0.1476
Na	-	-	-	-	-	-	0.8158	0.8175	0.8143
K	-	-	-	-	-	-	0.0228	0.0187	0.0160
F	-	-	-	-	-	-	-	-	-
Total	**7.9965**	**8.0010**	**7.9988**	**7.9966**	**7.9914**	**7.9968**	**4.9915**	**4.9933**	**4.9844**

A21				Muscovite			Biotite		
Pelitic gneiss	TFG	TFL	TFK	TMC	TMB	TMD	TBA	TBC	TBE
Astor valley	2-Rim	3-Core	3-Rim						
SiO2	63.92	64.62	64.87	46.11	46.43	45.88	36.94	36.45	36.47
TiO2	0.02	0.02	0.02	1.63	1.79	1.79	3.75	3.61	3.70
Al2O3	22.25	22.41	22.27	32.19	32.22	32.08	17.26	17.42	18.09
Cr2O3	-	-	-	-	-	-	-	-	-
FeO	0.04	0.01	0.06	1.44	1.41	1.83	17.15	16.50	16.46
MnO	0.00	0.00	0.02	0.02	0.02	0.02	0.05	0.05	0.03
MgO	0.00	0.00	0.00	1.29	1.26	1.43	10.57	10.35	10.25
CaO	3.33	3.46	3.40	0.01	0.01	0.01	0.03	0.01	0.01
Na2O	9.52	9.30	9.48	0.28	0.28	0.27	0.07	0.05	0.07
K2O	0.26	0.45	0.26	10.80	10.91	10.96	9.76	9.79	9.98
F	-	-	-	0.14	0.18	0.18	0.75	0.63	0.84
Total	**99.35**	**100.27**	**100.39**	**93.91**	**94.51**	**94.45**	**96.33**	**94.86**	**95.90**
Formula									
Units	8	8	8	22	22	22	22	22	22
Si	2.8375	2.8416	2.8479	6.2659	6.2728	6.2258	5.5470	5.5417	5.4947
Ti	0.0006	0.0006	0.0006	0.1660	0.1822	0.1828	0.4234	0.4126	0.4192
Al	1.1644	1.1617	1.1526	5.1558	5.1301	5.1314	3.0553	3.1211	3.2130
Cr	-	-	-	-	-	-	-	-	-
Fe	0.0015	0.0005	0.0020	0.1639	0.1598	0.2081	2.1537	2.0980	2.0737
Mn	0.0000	0.0000	0.0005	0.0018	0.0017	0.0018	0.0058	0.0059	0.0039
Mg	0.0000	0.0000	0.0000	0.2617	0.2539	0.2895	2.3663	2.3463	2.3026
Ca	0.1582	0.1630	0.1600	0.0021	0.0021	0.0021	0.0046	0.0023	0.0023
Na	0.8192	0.7933	0.8072	0.0741	0.0736	0.0704	0.0205	0.0155	0.0204
K	0.0149	0.0255	0.0147	1.8716	1.8809	1.8980	1.8700	1.8980	1.9188
F	-	-	-	0.0588	0.0778	0.0780	0.3555	0.3035	0.3982
Total	**4.9965**	**4.9862**	**4.9857**	**14.0217**	**14.0349**	**14.0879**	**15.8021**	**15.7449**	**15.8468**

T20	Garnet						Hornblende		
Calcsilicate	QGA	QGB	QGC	QGD	QGE	QGF	QHB	QHA	QHD
Tato Road	1-Core	1-Rim	2-Core	2-Rim	3-Core	3-Rim	1-Core	1-Rim	2-Core
SiO2	38.43	38.65	38.24	38.61	38.37	38.43	40.79	41.76	41.70
TiO2	0.07	0.11	0.05	0.09	0.11	0.11	0.81	0.84	0.79
Al2O3	21.32	21.57	21.53	21.70	20.93	21.20	12.57	11.64	13.11
Cr2O3	0.08	0.02	0.08	0.00	0.21	0.00	0.14	0.06	0.07
FeO	22.60	20.30	22.57	20.19	19.78	20.04	22.96	23.49	20.10
MnO	3.25	2.21	3.19	2.24	2.72	2.13	0.96	1.07	0.62
MgO	1.35	1.33	1.41	1.31	1.30	1.31	5.35	5.21	7.01
CaO	14.06	17.01	14.02	17.14	16.89	17.19	11.54	11.58	11.69
Na2O	-	-	-	-	-	-	1.08	0.97	1.14
K2O	-	-	-	-	-	-	1.43	1.26	1.70
F	-	-	-	-	-	-	-	-	-
Total	**101.16**	**101.20**	**101.09**	**101.28**	**100.31**	**100.41**	**97.63**	**97.88**	**97.93**
Formula Units	12	12	12	12	12	12	23	23	23
Si	3.0044	2.9984	2.9911	2.9924	3.0086	3.0054	6.3597	6.4937	6.3797
Ti	0.0042	0.0063	0.0031	0.0052	0.0063	0.0063	0.0946	0.0984	0.0914
Al	1.9648	1.9725	1.9846	1.9824	1.9345	1.9542	2.3098	2.1326	2.3637
Cr	0.0049	0.0010	0.0049	0.0000	0.0131	0.0000	0.0178	0.0079	0.0078
Fe	1.4775	1.3171	1.4767	1.3090	1.2973	1.3104	2.9938	3.0547	2.5719
Mn	0.2154	0.1452	0.2114	0.1471	0.1803	0.1413	0.1274	0.1411	0.0797
Mg	0.1577	0.1538	0.1640	0.1515	0.1517	0.1530	1.2445	1.2072	1.5977
Ca	1.1774	1.4139	1.1747	1.4231	1.4189	1.4403	1.9276	1.9297	1.9159
Na	-	-	-	-	-	-	0.3264	0.2929	0.3371
K	-	-	-	-	-	-	0.2854	0.2509	0.3322
F	-	-	-	-	-	-	-	-	-
Total	**8.0063**	**8.0082**	**8.0165**	**8.0107**	**8.0107**	**8.0109**	**15.6870**	**15.6091**	**15.6771**

T20		Plagioclase				Biotite			
Calcsilicate	QHE	QFA	QFB	QFD	QFE	QBA	QBB	QBC	QBD
Tato Road	2-Rim	1-Core	1-Rim	2-Core	2-Rim	Incl. Core	Incl. Rim		
SiO2	41.46	52.39	56.96	56.76	56.36	35.96	36.13	36.03	36.40
TiO2	0.63	0.00	0.02	0.02	0.08	2.69	2.99	2.60	2.08
Al2O3	12.16	21.84	27.45	26.93	26.13	14.98	15.08	15.10	15.02
Cr2O3	0.18	0.00	0.00	0.00	0.00	0.03	0.03	0.10	0.08
FeO	22.62	0.15	0.08	0.07	0.08	21.87	22.09	21.64	21.68
MnO	0.87	0.00	0.00	0.00	0.00	0.43	0.43	0.38	0.35
MgO	5.54	0.05	0.00	0.00	0.02	9.59	9.34	9.91	10.25
CaO	11.66	7.85	9.38	9.12	9.08	0.21	0.04	0.04	0.06
Na2O	1.13	6.33	6.05	6.02	6.17	0.06	0.06	0.07	0.07
K2O	1.42	0.80	0.21	0.19	0.08	7.93	9.14	8.84	8.02
F	-	-	-	-	-	-	-	-	-
Total	**97.67**	**89.41**	**100.16**	**99.11**	**98.00**	**93.85**	**95.43**	**94.78**	**94.06**
Formula Units	23	8	8	8	8	22	22	22	22
Si	6.4435	2.6417	2.5512	2.5661	2.5779	5.6178	5.5903	5.5915	5.6570
Ti	0.0734	0.0000	0.0006	0.0006	0.0025	0.3158	0.3482	0.3038	0.2436
Al	2.2277	1.2979	1.4494	1.4352	1.4090	2.7586	2.7496	2.7615	2.7508
Cr	0.0217	0.0000	0.0000	0.0000	0.0000	0.0039	0.0039	0.0118	0.0098
Fe	2.9397	0.0065	0.0031	0.0026	0.0032	2.8577	2.8582	2.8088	2.8175
Mn	0.1150	0.0000	0.0000	0.0000	0.0000	0.0567	0.0561	0.0503	0.0463
Mg	1.2834	0.0035	0.0000	0.0000	0.0010	2.2336	2.1545	2.2922	2.3752
Ca	1.9417	0.4242	0.4500	0.4415	0.4450	0.0355	0.0070	0.0070	0.0094
Na	0.3410	0.6191	0.5254	0.5278	0.5474	0.0168	0.0167	0.0222	0.0222
K	0.2824	0.0513	0.0121	0.0108	0.0048	1.5807	1.8033	1.7498	1.5891
F	-	-	-	-	-	-	-	-	-
Total	**15.6695**	**5.0442**	**4.9920**	**4.9846**	**4.9908**	**15.4832**	**15.5938**	**15.6034**	**15.5239**

T64	Garnet						Hornblende		Plag
Calcsilicate	XGA	XGB	XGG	XGE	XGK	XGL	XHA	XHB	XFG
Tato Road	1-Core	1-Rim	2-Core	2-Rim	3-Core	3-Rim	1-Core	1-Rim	1-Core
SiO2	38.62	38.94	39.57	38.62	38.52	38.51	41.28	41.49	57.57
TiO2	0.13	0.13	-	-	-	-	0.73	0.78	-
Al2O3	21.44	21.34	21.66	21.50	21.14	21.33	14.09	13.66	26.48
Cr2O3	0.00	0.00	-	-	-	-	0.00	0.02	-
FeO	20.32	20.06	18.85	20.66	20.98	20.83	18.99	18.79	0.13
MnO	2.18	1.93	2.05	2.04	1.90	2.04	0.29	0.31	-
MgO	1.17	1.28	1.09	1.17	1.35	1.30	7.50	7.71	-
CaO	17.06	15.78	16.55	16.73	16.63	16.80	11.87	11.68	8.82
Na2O	-	-	-	-	-	-	1.27	1.23	6.30
K2O	-	-	-	-	-	-	1.98	1.94	0.30
F	-	-	-	-	-	-	0.50	0.50	-
Total	**100.92**	**99.46**	**99.77**	**100.72**	**100.52**	**100.81**	**98.50**	**98.11**	**99.60**
Formula									
Units	12	12	12	12	12	12	23	23	8
Si	3.0051	3.0538	3.0774	3.0108	3.0128	3.0042	6.2842	6.3311	2.5902
Ti	0.0074	0.0074	-	-	-	-	0.0830	0.0894	-
Al	1.9667	1.9723	1.9857	1.9753	1.9493	1.9615	2.5283	2.4571	1.4044
Cr	0.0000	0.0000	-	-	-	-	0.0000	0.0019	-
Fe	1.3223	1.3153	1.2260	1.3466	1.3724	1.3590	2.4172	2.3971	0.0047
Mn	0.1436	0.1285	0.1347	0.1347	0.1260	0.1348	0.0377	0.0398	-
Mg	0.1359	0.1490	0.1263	0.1363	0.1577	0.1510	1.7029	1.7533	-
Ca	1.4228	1.3259	1.3794	1.3977	1.3939	1.4043	1.9362	1.9088	0.4251
Na	-	-	-	-	-	-	0.3734	0.3633	0.5492
K	-	-	-	-	-	-	0.3839	0.3783	0.0169
F	-	-	-	-	-	-	0.2411	0.2424	-
Total	**8.0038**	**7.9522**	**7.9295**	**8.0014**	**8.0121**	**8.0148**	**15.9879**	**15.9625**	**4.9905**

T64				Biotite		Diopside			
Calcsilicate	XFH	XFI	XFK	XBA	XBC	XPA	XPB	XPE	XPF
Tato Road	1-Rim	2-Core	2-Rim			1-Core	1-Rim	2-Core	2-Rim
SiO2	57.47	56.43	56.65	36.95	37.08	52.20	52.11	52.07	51.60
TiO2	-	-	-	3.03	2.12	0.04	0.06	0.04	0.07
Al2O3	26.53	24.95	27.06	14.36	14.59	0.70	0.54	0.37	0.74
Cr2O3	-	-	-	-	-	0.00	0.00	0.02	0.00
FeO	0.17	0.03	0.07	20.27	19.91	12.48	13.06	14.23	15.09
MnO	-	-	-	0.18	0.18	0.31	0.33	0.50	0.36
MgO	-	-	-	10.48	11.23	10.35	9.84	9.01	8.57
CaO	8.93	7.58	9.53	0.04	0.04	23.98	23.53	23.99	23.45
Na2O	6.33	7.02	6.08	0.05	0.05	0.19	0.14	0.12	0.20
K2O	0.27	0.12	0.22	9.38	9.55	0.00	0.00	0.00	0.01
F	-	-	-	0.90	0.89	-	-	-	-
Total	**99.70**	**96.13**	**99.61**	**95.64**	**95.64**	**100.25**	**99.61**	**100.35**	**100.09**
Formula									
Units	8	8	8	22	22	6	6	6	6
Si	2.5849	2.6247	2.5538	5.6984	5.7097	1.9858	1.9981	1.9970	1.9889
Ti	-	-	-	0.3509	0.2450	0.0010	0.0016	0.0010	0.0021
Al	1.4064	1.3676	1.4381	2.6099	2.6473	0.0314	0.0242	0.0167	0.0337
Cr	-	-	-	-	-	0.0000	0.0000	0.0005	0.0000
Fe	0.0063	0.0010	0.0026	2.6141	2.5642	0.3971	0.4188	0.4564	0.4864
Mn	-	-	-	0.0240	0.0240	0.0100	0.0106	0.0161	0.0116
Mg	-	-	-	2.4105	2.5774	0.5871	0.5626	0.5149	0.4927
Ca	0.4305	0.3779	0.4605	0.0070	0.0070	0.9776	0.9668	0.9856	0.9685
Na	0.5517	0.6330	0.5311	0.0163	0.0162	0.0140	0.0104	0.0092	0.0146
K	0.0155	0.0070	0.0128	1.8447	1.8770	0.0000	0.0000	0.0000	0.0005
F	-	-	-	0.4392	0.4352	-	-	-	-
Total	**4.9953**	**5.0112**	**4.9989**	**16.0150**	**16.1030**	**4.0040**	**3.9931**	**3.9974**	**3.9990**

T69	Garnet						Hornblende		K-feldspar
Amphibolite	KGA	KGB	KGC	KGD	KGE	KGF	KHA	KHC	KFA
Tato Road	1-Core	1-Rim	2-Core	2-Core	3-Rim	3-Core			1-Core
SiO2	38.06	38.04	37.76	38.08	38.01	38.08	39.57	39.95	64.27
TiO2	0.20	0.05	0.07	0.09	0.07	0.16	0.97	1.25	0.00
Al2O3	21.04	20.97	21.14	21.12	20.91	21.11	13.63	13.59	18.45
Cr2O3	0.02	0.02	0.00	0.00	0.00	0.02	0.00	0.00	0.00
FeO	21.46	25.33	24.41	23.78	25.04	24.11	24.57	24.02	0.01
MnO	4.37	0.46	1.05	1.64	0.41	1.88	0.32	0.26	0.00
MgO	0.52	0.85	0.47	0.54	0.71	0.78	3.72	4.59	0.00
CaO	14.27	14.14	14.77	14.95	15.29	13.66	11.30	11.54	0.07
Na2O	0.00	0.00	0.00	0.00	0.00	0.00	1.15	1.24	1.26
K2O	0.00	0.00	0.00	0.00	0.00	0.00	1.88	1.91	14.19
F	-	-	-	-	-	-	-	-	-
Total	**99.94**	**99.86**	**99.67**	**100.20**	**100.44**	**99.80**	**97.11**	**98.35**	**98.32**
Formula Units	12	12	12	12	12	12	23	23	8
Si	3.0238	3.0255	3.0109	3.0184	3.0113	3.0275	6.2706	6.2340	2.9967
Ti	0.0117	0.0032	0.0043	0.0053	0.0042	0.0096	0.1151	0.1472	0.0000
Al	1.9704	1.9659	1.9872	1.9735	1.9530	1.9780	2.5470	2.5002	1.0142
Cr	0.0010	0.0010	0.0000	0.0000	0.0000	0.0010	0.0000	0.0000	0.0000
Fe	1.4332	1.6931	1.6362	1.5840	1.6677	1.6109	3.2731	3.1499	0.0005
Mn	0.2938	0.0308	0.0712	0.1098	0.0277	0.1264	0.0431	0.0343	0.0000
Mg	0.0621	0.1012	0.0560	0.0642	0.0835	0.0925	0.8788	1.0684	0.0000
Ca	1.2150	1.2051	1.2622	1.2700	1.2979	1.1639	1.9196	1.9287	0.0037
Na	0.0000	0.0000	0.0000	0.0000	0.0000	0.0000	0.3537	0.3741	0.1139
K	0.0000	0.0000	0.0000	0.0000	0.0000	0.0000	0.3807	0.3796	0.8443
F	-	-	-	-	-	-	-	-	-
Total	**8.0110**	**8.0258**	**8.0280**	**8.0252**	**8.0453**	**8.0098**	**15.7817**	**15.8164**	**4.9751**

T69				Plagioclase			Biotite		
Amphibolite	KFB	KFC	KFD	KFE	KFF	KFH	KBB	KBC	KBD
Tato Road	1-Rim	2-Core	2-Rim	1-Core	1-Rim				
SiO2	64.19	64.41	64.64	60.72	60.19	60.43	34.86	34.68	35.08
TiO2	0.00	0.00	0.00	0.00	0.00	0.00	3.87	3.84	4.13
Al2O3	18.35	18.43	18.37	24.64	24.93	24.61	14.63	14.79	14.60
Cr2O3	0.00	0.00	0.00	0.00	0.00	0.00	0.00	0.00	0.00
FeO	0.01	0.07	0.00	0.13	0.22	0.13	27.57	27.67	26.57
MnO	0.00	0.00	0.00	0.00	0.00	0.00	0.20	0.23	0.18
MgO	0.00	0.00	0.00	0.00	0.00	0.00	5.84	5.36	5.95
CaO	0.06	0.07	0.04	6.32	6.66	6.49	0.01	0.04	0.06
Na2O	1.09	1.03	1.07	7.62	7.43	7.72	0.00	0.06	0.08
K2O	14.73	14.86	14.43	0.46	0.38	0.42	9.34	9.11	8.95
F	-	-	-	-	-	-	-	-	-
Total	**98.48**	**98.94**	**98.62**	**99.93**	**99.87**	**99.87**	**96.46**	**95.92**	**95.71**
Formula Units	8	8	8	8	8	8	22	22	22
Si	2.9963	2.9949	3.0047	2.7048	2.6861	2.6974	5.5184	5.5225	5.5559
Ti	0.0000	0.0000	0.0000	0.0000	0.0000	0.0000	0.4611	0.4593	0.4913
Al	1.0096	1.0098	1.0067	1.2937	1.3113	1.2947	2.7307	2.7754	2.7249
Cr	0.0000	0.0000	0.0000	0.0000	0.0000	0.0000	0.0000	0.0000	0.0000
Fe	0.0005	0.0027	0.0000	0.0047	0.0084	0.0047	3.6681	3.7038	3.5374
Mn	0.0000	0.0000	0.0000	0.0000	0.0000	0.0000	0.0264	0.0307	0.0244
Mg	0.0000	0.0000	0.0000	0.0000	0.0000	0.0000	1.3790	1.2721	1.4035
Ca	0.0030	0.0037	0.0022	0.3017	0.3186	0.3105	0.0023	0.0072	0.0095
Na	0.0984	0.0928	0.0966	0.6583	0.6429	0.6685	0.0000	0.0182	0.0239
K	0.8773	0.8816	0.8559	0.0263	0.0216	0.0236	1.8865	1.8511	1.8086
F	-	-	-	-	-	-	-	-	-
Total	**4.9865**	**4.9873**	**4.9679**	**4.9906**	**4.9903**	**5.0012**	**15.6809**	**15.6487**	**15.5862**

LS	Garnet						Hornblende		Zoisite
Amphibolite	YGE	YGF	YGH	YGI	YGK	YGL	MHB	MHC	MCB
Liachar	1-Rim	1-Core	2-Rim	2-Core	3-Rim	3-Core	1-Core	1-Rim	
SiO2	38.51	38.41	38.37	38.36	38.59	38.97	41.11	40.75	37.17
TiO2	0.04	0.05	0.05	0.04	0.05	0.09	1.06	0.99	0.24
Al2O3	21.42	21.37	21.44	21.47	21.51	21.81	15.15	15.27	26.23
Cr2O3	-	-	-	-	-	-	0.02	0.02	0.00
FeO	23.85	24.76	24.28	24.56	21.32	21.53	13.08	13.38	6.89
MnO	1.45	1.22	1.68	1.27	1.03	0.83	0.11	0.09	0.02
MgO	3.75	4.30	3.62	4.15	4.17	4.51	10.40	10.46	0.24
CaO	10.47	9.62	10.31	9.85	12.45	12.22	11.79	11.93	23.05
Na2O	-	-	-	-	-	-	1.46	1.40	0.00
K2O	-	-	-	-	-	-	2.02	2.02	0.00
F	-	-	-	-	-	-	-	-	0.00
Total	**99.49**	**99.73**	**99.75**	**99.70**	**99.12**	**99.96**	**96.20**	**96.31**	**93.84**
Formula Units	12	12	12	12	12	12	23	23	23
Si	3.0215	3.0094	3.0113	3.0070	3.0160	3.0138	6.2008	6.1540	5.6281
Ti	0.0021	0.0031	0.0031	0.0021	0.0031	0.0052	0.1207	0.1125	0.0277
Al	1.9813	1.9741	1.9833	1.9835	1.9813	1.9884	2.6924	2.7180	4.6802
Cr	-	-	-	-	-	-	0.0019	0.0020	0.0000
Fe	1.5650	1.6223	1.5937	1.6098	1.3937	1.3924	1.6491	1.6893	0.8718
Mn	0.0964	0.0810	0.1116	0.0841	0.0680	0.0542	0.0138	0.0119	0.0020
Mg	0.4386	0.5023	0.4235	0.4854	0.4853	0.5199	2.3379	2.3557	0.0549
Ca	0.8803	0.8079	0.8671	0.8268	1.0424	1.0125	1.9056	1.9303	3.7392
Na	-	-	-	-	-	-	0.4275	0.4092	0.0000
K	-	-	-	-	-	-	0.3894	0.3897	0.0000
F	-	-	-	-	-	-	-	-	0.0000
Total	**7.9852**	**8.0001**	**7.9936**	**7.9987**	**7.9898**	**7.9864**	**15.7391**	**15.7726**	**15.0039**

LS			Biotite			Plagioclase			
Amphibolite	MCD	MCE	MBE	MBG	MBF	YFA	YFB	YFE	YFF
Liachar	1-Core	1-Rim				1-Rim	1-Core	2-Rim	2-Core
SiO2	34.04	37.04	36.63	36.92	36.52	60.25	60.83	59.57	59.70
TiO2	0.20	0.22	3.24	2.59	3.65	-	-	-	-
Al2O3	22.44	24.83	17.04	17.20	17.35	24.31	23.84	25.13	25.02
Cr2O3	0.00	0.00	0.00	0.00	0.00	-	-	-	-
FeO	8.09	6.87	17.93	17.94	17.74	0.23	0.07	0.11	0.03
MnO	0.05	0.03	0.15	0.14	0.17	-	-	-	-
MgO	0.65	0.29	9.98	10.57	9.68	-	-	-	-
CaO	17.96	21.32	0.01	0.01	0.01	5.88	5.62	7.01	6.83
Na2O	0.02	0.00	0.11	0.09	0.09	7.92	7.69	7.60	7.62
K2O	0.00	0.01	9.66	9.57	9.78	0.24	0.75	0.09	0.17
F	0.00	0.00	-	-	-	-	-	-	-
Total	**83.45**	**90.61**	**94.75**	**95.03**	**94.99**	**98.83**	**98.80**	**99.51**	**99.37**
Formula Units	23	23	22	22	22	8	8	8	8
Si	5.7957	5.7808	5.5752	5.5924	5.5422	2.7107	2.7366	2.6685	2.6759
Ti	0.0261	0.0263	0.3707	0.2954	0.4169	-	-	-	-
Al	4.5030	4.5669	3.0565	3.0707	3.1035	1.2894	1.2643	1.3266	1.3220
Cr	0.0000	0.0000	0.0000	0.0000	0.0000	-	-	-	-
Fe	1.1516	0.8967	2.2825	2.2728	2.2515	0.0084	0.0026	0.0042	0.0010
Mn	0.0067	0.0041	0.0198	0.0177	0.0217	-	-	-	-
Mg	0.1644	0.0682	2.2645	2.3868	2.1903	-	-	-	-
Ca	3.2761	3.5652	0.0023	0.0023	0.0023	0.2835	0.2707	0.3362	0.3282
Na	0.0056	0.0000	0.0314	0.0260	0.0261	0.6909	0.6708	0.6597	0.6619
K	0.0000	0.0022	1.8762	1.8505	1.8942	0.0136	0.0430	0.0054	0.0095
F	0.0000	0.0000	-	-	-	-	-	-	-
Total	**14.9292**	**14.9104**	**15.4791**	**15.5146**	**15.4487**	**4.9965**	**4.9880**	**5.0006**	**4.9985**

M6	Garnet		Hornblende		Biotite		Anorthite		Diopside
Calcschist	LGA	LGC	LHB	LHC	LBC	LBD	LFB	LDA	LDC
Tato									
SiO2	37.89	38.02	48.05	45.06	37.42	37.40	47.17	46.84	52.66
TiO2	0.56	0.56	0.79	0.86	1.84	3.08	0.02	0.02	0.02
Al2O3	9.84	9.79	6.94	9.17	14.78	13.38	33.51	33.55	0.35
Cr2O3	0.00	0.00	0.08	0.03	-	-	-	0.00	0.00
FeO	16.02	16.34	15.60	16.39	18.30	16.92	0.20	0.25	11.93
MnO	0.39	0.39	0.37	0.34	0.28	0.15	-	0.02	0.61
MgO	0.07	0.09	12.18	11.18	13.22	13.17	0.00	0.00	10.13
CaO	34.62	34.79	12.38	12.13	0.01	0.71	17.30	17.85	24.79
Na2O	-	-	0.81	0.99	0.09	0.11	1.67	1.41	0.03
K2O	-	-	0.77	1.30	9.62	8.49	0.03	0.02	0.00
F	-	-	0.43	0.68	1.13	1.17	0.00	-	-
Total	**99.39**	**99.98**	**98.40**	**98.13**	**96.69**	**94.58**	**99.90**	**99.96**	**100.52**
Formula									
Units	12	12	23	23	22	22	8	8	6
Si	3.1365	3.1334	7.0982	6.7689	5.6689	5.7424	2.1694	1.6174	1.9977
Ti	0.0348	0.0347	0.0872	0.0968	0.2091	0.3558	0.0006	0.0004	0.0005
Al	0.9605	0.9515	1.2088	1.6233	2.6396	2.4214	1.8162	1.3654	0.0156
Cr	0.0000	0.0000	0.0096	0.0039	-	-	-	0.0000	0.0000
Fe	1.1093	1.1260	1.9266	2.0587	2.3190	2.1721	0.0075	0.0073	0.3785
Mn	0.0272	0.0270	0.0465	0.0433	0.0355	0.0200	-	0.0004	0.0195
Mg	0.0087	0.0109	2.6813	2.5045	2.9847	3.0143	0.0000	0.0000	0.5726
Ca	3.0709	3.0724	1.9590	1.9521	0.0023	0.1174	0.8524	0.6604	1.0078
Na	-	-	0.2305	0.2880	0.0260	0.0315	0.1490	0.0945	0.0025
K	-	-	0.1443	0.2492	1.8590	1.6620	0.0020	0.0010	0.0000
F	-	-	0.1992	0.3220	0.5418	0.5659	0.0000	-	-
Total	**8.3479**	**8.3559**	**15.5912**	**15.9107**	**16.2859**	**16.1028**	**4.9971**	**3.7468**	**3.9947**

M9	Garnet		K-feldspar		Plagioclase		Biotite		Cordierite
Pelitic gneiss	GGA	GGB	GCD	GCE	GCK	GCM	GBA	GBC	GCG
Tato	1-Core	1-Rim					Incl.		
SiO2	38.19	37.31	64.84	65.39	60.71	62.05	34.77	34.91	47.03
TiO2	0.03	0.19	-	-	-	-	1.17	1.76	-
Al2O3	21.35	21.20	18.44	18.35	24.27	23.10	18.85	19.45	35.73
Cr2O3	-	-	-	-	-	-	-	-	-
FeO	33.34	34.17	0.01	0.03	0.01	0.11	24.09	22.63	9.29
MnO	3.37	4.23	-	-	-	-	0.14	0.14	-
MgO	3.42	2.50	-	-	-	-	7.22	6.96	6.26
CaO	1.44	1.06	0.06	0.10	6.03	4.89	-	-	0.01
Na2O	-	-	2.46	2.17	8.04	8.56	0.21	0.22	0.23
K2O	-	-	13.24	13.44	0.17	0.35	8.79	9.17	0.00
F	-	-	-	-	-	-	-	-	-
Total	**101.14**	**100.66**	**99.08**	**99.49**	**99.27**	**99.13**	**95.29**	**95.29**	**98.57**
Formula									
Units	12	12	8	8	8	8	22	22	18
Si	3.0240	2.9971	2.9947	3.0055	2.7173	2.7758	5.4067	5.3948	4.8491
Ti	0.0020	0.0113	-	-	-	-	0.1370	0.2050	-
Al	1.9923	2.0069	1.0040	0.9942	1.2805	1.2178	3.4554	3.5425	4.3422
Cr	-	-	-	-	-	-	-	-	-
Fe	2.2076	2.2953	0.0005	0.0010	0.0005	0.0042	3.1327	2.9244	0.8011
Mn	0.2258	0.2877	-	-	-	0.0000	0.0180	0.0180	-
Mg	0.4034	0.2988	-	-	-	0.0000	1.6722	1.6032	0.9617
Ca	0.1225	0.0908	0.0029	0.0051	0.2891	0.2343	-	-	0.0015
Na	-	-	0.2203	0.1936	0.6981	0.7426	0.0621	0.0665	0.0464
K	-	-	0.7802	0.7883	0.0095	0.0197	1.7439	1.8088	0.0000
F	-	-	-	-	-	-	-	-	-
Total	**7.9776**	**7.9879**	**5.0033**	**4.9880**	**4.9961**	**4.9962**	**15.6310**	**15.5662**	**11.0029**

M16	Garnet						Anorthite		
Calcsilicate	EGA	EGB	EGD	EGE	EGJ	EGK	EPD	EPE	EPF
Fairy Mdws	1-Core	1-Rim	2-Core	2-Rim	3-Core	3-Rim		1-Core	1-Rim
SiO2	38.79	38.35	38.38	38.67	38.51	38.43	47.45	47.96	46.84
TiO2	0.03	0.03	0.02	0.02	0.02	0.03	0.00	0.00	0.00
Al2O3	21.49	21.23	21.44	21.56	21.27	21.30	33.45	32.66	33.40
Cr2O3	-	-	-	-	-	-	-	-	-
FeO	28.35	28.63	27.66	27.48	29.25	29.43	0.11	0.20	0.23
MnO	3.71	5.78	3.95	3.23	4.05	4.53	0.00	0.00	0.00
MgO	3.94	3.39	3.70	3.81	3.89	3.96	-	-	-
CaO	5.72	4.14	5.85	6.86	4.08	3.83	17.79	17.13	18.00
Na2O	-	-	-	-	-	-	1.61	1.86	1.47
K2O	-	-	-	-	-	-	0.02	0.01	0.01
F	-	-	-	-	-	-	-	-	-
Total	**102.03**	**101.55**	**101.00**	**101.63**	**101.07**	**101.51**	**100.43**	**99.82**	**99.95**
Formula									
Units	12	12	12	12	12	12	8	8	8
Si	3.0134	3.0155	3.0109	3.0091	3.0259	3.0136	2.1719	2.2050	2.1580
Ti	0.0020	0.0020	0.0010	0.0010	0.0010	0.0020	0.0000	0.0000	0.0000
Al	1.9676	1.9675	1.9830	1.9771	1.9701	1.9684	1.8049	1.7700	1.8136
Cr	-	-	-	-	-	-	-	-	-
Fe	1.8415	1.8827	1.8145	1.7880	1.9217	1.9303	0.0043	0.0075	0.0086
Mn	0.2439	0.3847	0.2626	0.2128	0.2694	0.3007	0.0000	0.0000	0.0000
Mg	0.4561	0.3970	0.4321	0.4415	0.4559	0.4628	-	-	-
Ca	0.4758	0.3490	0.4921	0.5716	0.3437	0.3219	0.8723	0.8440	0.8888
Na	-	-	-	-	-	-	0.1430	0.1659	0.1313
K	-	-	-	-	-	-	0.0013	0.0006	0.0006
F	-	-	-	-	-	-	-	-	-
Total	**8.0003**	**7.9984**	**7.9962**	**8.0011**	**7.9877**	**7.9997**	**4.9977**	**4.9930**	**5.0009**

M16	Biotite			Plagioclase			Hornblende		
Calcsilicate	EBC	EBD	EBA	EPJ	EPL	EPK	EHA	EHB	EHF
Fairy Mdws					1-Core	1-Rim			
SiO2	37.45	37.65	37.61	58.43	59.08	58.87	43.28	43.07	43.88
TiO2	1.62	1.24	1.60	-	-	-	0.65	0.72	0.64
Al2O3	15.29	15.54	14.94	25.83	25.16	25.63	13.04	12.17	12.36
Cr2O3	-	-	-	-	-	-	-	-	-
FeO	18.92	18.76	18.87	0.15	0.11	0.17	17.06	18.98	17.01
MnO	0.26	0.22	0.25	-	-	-	0.42	0.54	0.34
MgO	12.62	12.18	12.44	-	-	-	9.88	9.25	10.14
CaO	-	-	-	8.81	7.86	8.45	11.38	10.99	11.28
Na2O	0.21	0.23	0.21	6.65	6.98	6.91	1.22	1.32	1.27
K2O	8.82	8.58	8.61	0.24	0.26	0.18	1.10	0.81	0.88
F	-	-	-	-	-	-	-	-	-
Total	**95.19**	**94.40**	**94.53**	**100.11**	**99.45**	**100.21**	**98.03**	**97.85**	**97.80**
Formula									
Units	22	22	22	8	8	8	23	23	23
Si	5.6801	5.7376	5.7348	2.6160	2.6538	2.6302	6.4631	6.4983	6.5500
Ti	0.1844	0.1421	0.1833	-	-	-	0.0735	0.0821	0.0714
Al	2.7335	2.7912	2.6860	1.3628	1.3323	1.3496	2.2946	2.1648	2.1753
Cr	-	-	-	-	-	-	-	-	-
Fe	2.3994	2.3907	2.4057	0.0058	0.0042	0.0063	2.1303	2.3953	2.1230
Mn	0.0335	0.0277	0.0317	-	-	-	0.0527	0.0689	0.0429
Mg	2.8530	2.7666	2.8279	-	-	-	2.2004	2.0809	2.2566
Ca	-	-	-	0.4224	0.3781	0.4043	1.8202	1.7760	1.8035
Na	0.0627	0.0682	0.0631	0.5775	0.6079	0.5986	0.3526	0.3849	0.3674
K	1.7059	1.6682	1.6747	0.0135	0.0149	0.0101	0.2089	0.1558	0.1675
F	-	-	-	-	-	-	-	-	-
Total	**15.6525**	**15.5923**	**15.6072**	**4.9980**	**4.9912**	**4.9991**	**15.5963**	**15.6070**	**15.5576**

G1	Garnet						Plagioclase		
Metasediment	DPD	DPA	DPG	DPH	DPI	DPJ	DFD	DFL	DFE
Parri	1-Core	1-Rim	2-Core	2-Rim	3-Core	3-Rim	1-Core	1-Rim	2-Core
SiO2	37.80	37.68	37.81	37.36	39.01	37.93	56.78	57.52	51.97
TiO2	0.02	0.05	0.02	0.03	0.02	0.02	-	-	-
Al2O3	21.52	21.37	21.34	21.30	21.93	21.14	27.04	26.60	30.16
Cr2O3	0.00	0.03	0.00	0.00	0.00	0.02	-	-	-
FeO	31.08	32.09	31.76	31.24	32.67	31.14	0.04	0.03	0.04
MnO	3.33	2.89	4.00	3.17	4.13	3.08	-	-	-
MgO	3.92	2.76	3.25	2.58	3.27	2.88	-	-	-
CaO	2.25	3.55	2.87	3.77	2.53	3.51	9.37	9.07	13.25
Na2O	-	-	-	-	-	-	6.24	6.48	4.02
K2O	-	-	-	-	-	-	0.07	0.06	0.05
F	-	-	-	-	-	-	-	-	-
Total	**99.92**	**100.42**	**101.05**	**99.45**	**103.56**	**99.72**	**99.61**	**99.76**	**99.56**
Formula									
Units	12	12	12	12	12	12	8	8	8
Si	3.0088	3.0048	2.9993	3.0060	3.0155	3.0348	2.5579	2.5831	2.3694
Ti	0.0010	0.0031	0.0010	0.0020	0.0010	0.0010	-	-	-
Al	2.0194	2.0093	1.9959	2.0204	1.9982	1.9935	1.4357	1.4081	1.6206
Cr	0.0000	0.0019	0.0000	0.0000	0.0000	0.0009	-	-	-
Fe	2.0691	2.1405	2.1074	2.1022	2.1121	2.0835	0.0015	0.0010	0.0016
Mn	0.2247	0.1954	0.2691	0.2158	0.2707	0.2085	-	-	-
Mg	0.4655	0.3278	0.3845	0.3097	0.3772	0.3432	-	-	-
Ca	0.1916	0.3033	0.2443	0.3251	0.2095	0.3010	0.4525	0.4366	0.6474
Na	-	-	-	-	-	-	0.5448	0.5643	0.3558
K	-	-	-	-	-	-	0.0040	0.0033	0.0027
F	-	-	-	-	-	-	-	-	-
Total	**7.9801**	**7.9861**	**8.0015**	**7.9812**	**7.9842**	**7.9664**	**4.9982**	**4.9964**	**4.9994**

G1				Muscovite		Biotite		Zoisite	
Metasediment	DFJ	DFK	DFH	DNB	DNC	DBC	DBD	DCC	DCB
Parri	2-Rim	3-Core	3-Rim					1-Core	1-Rim
SiO2	51.51	53.17	56.35	45.26	46.42	36.35	36.07	39.22	38.78
TiO2	-	-	-	0.49	0.78	2.09	2.55	0.25	0.26
Al2O3	30.24	29.18	26.77	34.16	33.82	18.69	17.98	29.45	29.24
Cr2O3	-	-	-	-	-	-	-	-	-
FeO	0.01	0.07	0.18	1.43	1.71	17.96	18.85	4.36	4.52
MnO	-	-	-	0.02	0.02	0.11	0.09	0.11	0.11
MgO	-	-	-	0.87	1.31	9.79	9.63	0.03	0.03
CaO	13.45	11.94	9.33	0.03	0.00	0.09	0.04	24.56	24.21
Na2O	3.83	4.64	6.18	0.52	0.46	0.18	0.14	0.02	0.02
K2O	0.04	0.06	0.07	10.46	10.58	9.14	9.45	0.01	0.01
F	-	-	-	0.00	0.09	0.25	0.17	-	-
Total	**99.14**	**99.13**	**98.97**	**93.35**	**95.37**	**94.71**	**95.03**	**98.01**	**97.18**
Formula									
Units	8	8	8	22	22	22	22	23	23
Si	2.3592	2.4255	2.5575	6.1696	6.2090	5.5261	5.5026	5.6028	5.5905
Ti	-	-	-	0.0498	0.0789	0.2386	0.2926	0.0263	0.0286
Al	1.6323	1.5690	1.4322	5.4882	5.3330	3.3490	3.2335	4.9594	4.9691
Cr	-	-	-	-	-	-	-	-	-
Fe	0.0005	0.0026	0.0069	0.1628	0.1911	2.2838	2.4047	0.5204	0.5452
Mn	-	-	-	0.0018	0.0017	0.0138	0.0119	0.0133	0.0134
Mg	-	-	-	0.1768	0.2602	2.2185	2.1910	0.0067	0.0068
Ca	0.6600	0.5836	0.4536	0.0043	0.0000	0.0139	0.0070	3.7591	3.7394
Na	0.3401	0.4108	0.5436	0.1362	0.1184	0.0522	0.0423	0.0044	0.0044
K	0.0020	0.0034	0.0041	1.8190	1.8057	1.7731	1.8384	0.0020	0.0020
F	-	-	-	0.0000	0.0378	0.1192	0.0797	-	-
Total	**4.9956**	**4.9968**	**5.0001**	**14.0141**	**14.0454**	**15.5919**	**15.6074**	**14.8944**	**14.8994**

G7	Garnet								Plag
Metasediment	OGE	OGF	OGG	MGE	MGC	MGD	MGG	MGF	OFB
Indus conf.	1-Core	1-Rim	1-Rim	2-Core	2-Rim	2-Rim	3-Core	3-Rim	1-Core
SiO2	37.51	37.18	37.72	37.93	38.00	37.79	37.73	38.00	53.20
TiO2	0.03	0.07	0.02	0.03	0.02	0.02	0.00	0.05	-
Al2O3	21.68	21.66	21.54	21.68	21.62	21.67	21.65	21.72	28.10
Cr2O3	0.00	0.02	0.00	-	-	-	-	-	-
FeO	33.04	28.52	31.70	32.81	31.97	31.77	33.07	29.49	0.22
MnO	3.74	3.86	3.70	3.62	4.18	4.12	3.80	3.99	-
MgO	3.65	2.18	3.00	3.67	2.78	2.74	3.46	2.13	-
CaO	1.77	6.61	2.97	1.91	3.22	3.24	1.83	6.54	10.69
Na2O	-	-	-	-	-	-	-	-	5.06
K2O	-	-	-	-	-	-	-	-	0.13
F	-	-	-	-	-	-	-	-	-
Total	**101.42**	**100.10**	**100.65**	**101.65**	**101.79**	**101.35**	**101.54**	**101.92**	**97.47**
Formula									
Units	12	12	12	12	12	12	12	12	8
Si	2.9797	2.9780	3.0096	2.9889	2.9973	2.9922	2.9827	2.9863	2.4635
Ti	0.0020	0.0042	0.0010	0.0020	0.0010	0.0010	0.0000	0.0030	-
Al	2.0304	2.0453	2.0259	2.0139	2.0103	2.0227	2.0178	2.0114	1.5340
Cr	0.0000	0.0009	0.0000	-	-	-	-	-	-
Fe	2.2061	1.9199	2.1261	2.1622	2.1091	2.1037	2.1867	1.9382	0.0087
Mn	0.2518	0.2616	0.2503	0.2419	0.2794	0.2766	0.2546	0.2654	-
Mg	0.4319	0.2606	0.3573	0.4315	0.3272	0.3237	0.4073	0.2498	-
Ca	0.1509	0.5673	0.2540	0.1614	0.2718	0.2752	0.1548	0.5505	0.5304
Na	-	-	-	-	-	-	-	-	0.4544
K	-	-	-	-	-	-	-	-	0.0076
F	-	-	-	-	-	-	-	-	-
Total	**8.0528**	**8.0378**	**8.0242**	**8.0018**	**7.9961**	**7.9951**	**8.0039**	**8.0046**	**5.0085**

G7				Biotite		Zoisite		Muscovite	
Metasediment	OFC	OFD	OFE	OBC	OBD	OCB	OCG	OMB	OMC
Indus conf.	1-Rim	2-Core	2-Rim						
SiO2	57.03	54.93	54.55	35.84	35.68	39.22	39.25	46.42	46.04
TiO2	-	-	-	2.08	2.69	0.26	0.23	0.75	0.73
Al2O3	26.81	28.49	28.45	18.51	18.69	29.38	29.07	35.03	34.67
Cr2O3	-	-	-	-	-	0.00	0.00	0.00	0.00
FeO	0.28	0.13	0.17	19.13	18.64	4.98	5.30	1.58	1.51
MnO	-	-	-	0.06	0.08	0.13	0.13	0.02	0.02
MgO	-	-	-	9.82	9.63	0.03	0.05	0.76	0.87
CaO	8.48	10.78	10.94	0.03	0.06	24.02	23.90	0.01	0.00
Na2O	6.59	5.43	5.01	0.14	0.18	0.00	0.00	0.70	0.65
K2O	0.21	0.07	0.09	8.95	9.24	0.00	0.00	9.98	9.78
F	-	-	-	-	-	-	-	-	-
Total	**99.49**	**99.94**	**99.28**	**94.71**	**95.05**	**98.02**	**97.93**	**95.25**	**94.27**
Formula									
Units	8	8	8	22	22	23	23	22	22
Si	2.5723	2.4790	2.4764	5.4804	5.4366	5.6079	5.6262	6.1728	6.1796
Ti	-	-	0.0000	0.2394	0.3087	0.0284	0.0243	0.0747	0.0735
Al	1.4255	1.5157	1.5224	3.3355	3.3566	4.9527	4.9111	5.4912	5.4850
Cr	-	-	-	-	-	0.0000	0.0000	0.0000	0.0000
Fe	0.0106	0.0047	0.0064	2.4589	2.3879	0.5958	0.6356	0.1760	0.1698
Mn	-	-	-	0.0079	0.0099	0.0152	0.0152	0.0017	0.0017
Mg	-	-	-	2.2382	2.1870	0.0067	0.0102	0.1512	0.1738
Ca	0.4100	0.5210	0.5323	0.0046	0.0093	3.6808	3.6713	0.0021	0.0000
Na	0.5766	0.4750	0.4407	0.0424	0.0527	0.0000	0.0000	0.1812	0.1680
K	0.0122	0.0040	0.0054	1.7454	1.7960	0.0000	0.0000	1.6930	1.6741
F	-	-	-	-	-	-	-	-	-
Total	**5.0094**	**5.0024**	**4.9854**	**15.5617**	**15.5544**	**14.8875**	**14.8939**	**13.9439**	**13.9255**

G9	Garnet						Plagioclase		
Metasediment	FGD	FGE	FGF	FGG	FGH	FGI	FFA	FFB	FFD
Indus conf.	1-Core	1-Rim	2-Core	2-Rim	3-Core	3-Rim	1-Core	1-Rim	2-Core
SiO2	37.43	37.70	37.75	37.97	37.52	37.37	56.86	56.04	54.43
TiO2	0.02	0.02	0.03	0.09	0.02	0.03	-	-	-
Al2O3	21.62	21.53	21.59	21.41	21.48	21.53	27.26	27.54	28.06
Cr2O3	-	-	-	-	-	-	-	-	-
FeO	31.56	28.73	27.04	26.07	31.37	28.31	0.06	0.13	0.07
MnO	4.74	5.22	5.04	4.78	4.62	5.19	-	-	-
MgO	3.37	2.68	2.17	1.72	3.20	2.34	-	-	-
CaO	1.79	4.56	6.81	8.79	2.50	5.71	9.61	10.19	10.80
Na2O	-	-	-	-	-	-	6.20	5.69	5.44
K2O	-	-	-	-	-	-	0.08	0.07	0.06
F	-	-	-	-	-	-	-	-	-
Total	**100.53**	**100.44**	**100.43**	**100.83**	**100.71**	**100.48**	**100.16**	**99.73**	**98.96**
Formula Units	12	12	12	12	12	12	8	8	8
Si	2.9854	2.9996	2.9973	3.0024	2.9890	2.9787	2.5502	2.5271	2.4815
Ti	0.0010	0.0010	0.0020	0.0052	0.0010	0.0020	-	-	-
Al	2.0323	2.0193	2.0205	1.9956	2.0165	2.0231	1.4410	1.4638	1.5079
Cr	-	-	-	-	-	-	-	-	-
Fe	2.1050	1.9116	1.7953	1.7238	2.0901	1.8872	0.0021	0.0047	0.0026
Mn	0.3200	0.3519	0.3388	0.3198	0.3117	0.3507	-	-	-
Mg	0.4006	0.3176	0.2571	0.2025	0.3796	0.2778	-	-	-
Ca	0.1527	0.3883	0.5789	0.7450	0.2135	0.4876	0.4616	0.4923	0.5275
Na	-	-	-	-	-	-	0.5395	0.4978	0.4811
K	-	-	-	-	-	-	0.0047	0.0040	0.0034
F	-	-	-	-	-	-	-	-	-
Total	**7.9970**	**7.9893**	**7.9899**	**7.9943**	**8.0014**	**8.0071**	**5.0013**	**4.9915**	**5.0066**

G9				Biotite		Muscovite		Zoisite	
Metasediment	FFE	FFF	FFG	FBA	FBC	FMA	FMB	FCA	FCB
Indus conf.	2-Rim	3-Core	3-Rim					1-Core	1-Rim
SiO2	55.35	54.37	54.63	36.47	35.41	46.24	47.19	37.20	38.59
TiO2	-	-	-	3.02	2.73	0.97	1.19	0.19	0.26
Al2O3	28.24	28.31	28.30	17.93	18.15	32.85	33.52	27.11	28.37
Cr2O3	-	-	-	-	-	-	-	-	-
FeO	0.11	0.01	0.06	18.28	19.27	1.96	1.99	6.25	5.87
MnO	-	-	-	0.11	0.12	0.02	0.02	0.19	0.13
MgO	-	-	-	8.93	9.13	1.19	1.14	0.24	0.29
CaO	10.66	10.94	10.93	-	-	-	-	21.59	22.87
Na2O	5.47	5.42	5.38	0.16	0.18	0.50	0.55	0.02	0.03
K2O	0.06	0.08	0.06	9.42	9.53	10.52	10.62	0.05	0.32
F	-	-	-	-	-	-	-	-	-
Total	**99.98**	**99.20**	**99.45**	**94.45**	**94.63**	**94.49**	**96.46**	**92.84**	**96.73**
Formula Units	8	8	8	22	22	22	22	23	23
Si	2.4942	2.4730	2.4780	5.5676	5.4426	6.2509	6.2460	5.6457	5.6204
Ti	-	-	-	0.3467	0.3152	0.0986	0.1189	0.0214	0.0288
Al	1.4997	1.5179	1.5133	3.2271	3.2883	5.2343	5.2291	4.8508	4.8704
Cr	-	-	-	-	-	-	-	-	-
Fe	0.0042	0.0005	0.0021	2.3342	2.4773	0.2216	0.2200	0.7927	0.7150
Mn	-	-	-	0.0139	0.0159	0.0017	0.0017	0.0241	0.0154
Mg	-	-	-	2.0333	2.0908	0.2402	0.2255	0.0548	0.0625
Ca	0.5147	0.5333	0.5313	0.0000	0.0000	0.0000	0.0000	3.5114	3.5692
Na	0.4777	0.4781	0.4730	0.0475	0.0536	0.1321	0.1401	0.0048	0.0091
K	0.0033	0.0047	0.0034	1.8349	1.8677	1.8148	1.7940	0.0087	0.0585
F	-	-	-	-	-	-	-	-	-
Total	**4.9960**	**5.0093**	**5.0033**	**15.4127**	**15.5582**	**14.0067**	**13.9875**	**14.9144**	**14.9493**

G17	Garnet		Hornblende			Biotite			
Basic schist	DGA	DGB	DHA	DHB	DHC	DBA	DBB	DBC	DBD
Shuta	1-Core	1-Rim				1- Core	1-Rim		
SiO2	38.78	38.55	42.12	42.77	42.75	36.45	35.87	37.03	37.06
TiO2	0.04	0.02	0.78	1.00	0.58	2.37	2.13	2.30	2.23
Al2O3	21.41	21.57	15.13	14.56	15.24	17.38	17.19	18.10	17.61
Cr2O3	0.02	0.02	0.05	0.03	0.02	-	-	-	-
FeO	27.31	27.69	16.11	15.88	14.86	16.14	15.89	15.84	15.22
MnO	1.70	3.38	0.14	0.22	0.26	0.08	0.06	0.09	0.09
MgO	4.94	3.25	8.63	8.94	9.45	11.47	11.55	11.70	12.71
CaO	6.86	7.14	11.61	11.34	11.62	0.09	0.16	0.06	0.01
Na2O	-	-	1.35	1.28	1.35	0.16	0.17	0.19	0.19
K2O	-	-	0.82	0.83	0.63	9.25	9.00	9.35	9.37
F	-	-	0.17	0.09	0.09	0.17	0.25	0.17	0.17
Total	**101.06**	**101.62**	**96.98**	**97.03**	**96.90**	**93.63**	**92.34**	**94.88**	**94.72**
Formula									
Units	12	12	23	23	23	22	22	22	22
Si	3.0123	3.0080	6.3330	6.4065	6.3746	5.5687	5.5577	5.5609	5.5634
Ti	0.0020	0.0010	0.0885	0.1128	0.0655	0.2720	0.2485	0.2595	0.2515
Al	1.9604	1.9836	2.6818	2.5710	2.6782	3.1306	3.1397	3.2041	3.1169
Cr	0.0009	0.0009	0.0058	0.0039	0.0019	-	-	-	-
Fe	1.7740	1.8069	2.0255	1.9892	1.8534	2.0618	2.0594	1.9893	1.9106
Mn	0.1120	0.2233	0.0177	0.0274	0.0332	0.0099	0.0081	0.0117	0.0117
Mg	0.5719	0.3775	1.9351	1.9971	2.1009	2.6117	2.6687	2.6185	2.8443
Ca	0.5710	0.5969	1.8711	1.8196	1.8568	0.0140	0.0261	0.0092	0.0023
Na	-	-	0.3932	0.3707	0.3895	0.0464	0.0523	0.0553	0.0549
K	-	-	0.1577	0.1594	0.1197	1.8031	1.7781	1.7923	1.7956
F	-	-	0.0807	0.0403	0.0402	0.0812	0.1241	0.0792	0.0793
Total	**8.0045**	**7.9981**	**15.6090**	**15.5199**	**15.5264**	**15.6184**	**15.6820**	**15.5925**	**15.6461**

G17	Zoisite					Plagioclase			
Basic schist	DCA	DCB	DCC	DCD	DCE	DFA	DFB	DFC	DFD
Shuta			1-Core	1-Rim		1-Core	1-Rim		
SiO2	38.81	38.37	38.51	38.50	38.45	55.15	56.38	55.07	52.72
TiO2	0.13	0.17	0.17	0.15	0.21	-	-	-	-
Al2O3	27.09	26.80	27.02	27.01	26.90	27.94	27.35	28.45	30.10
Cr2O3	-	-	-	-	-	-	-	-	-
FeO	7.69	7.84	7.56	7.83	7.87	0.06	0.10	0.06	0.08
MnO	0.13	0.17	0.16	0.14	0.20	-	-	-	-
MgO	0.03	0.07	0.08	0.07	0.08	-	-	-	-
CaO	23.81	23.34	23.89	23.83	23.98	10.77	9.98	11.02	12.80
Na2O	-	-	-	-	-	5.28	6.01	5.30	4.15
K2O	-	-	-	-	-	0.07	0.09	0.06	0.04
F	-	-	-	-	-	-	-	-	-
Total	**97.69**	**96.76**	**97.39**	**97.53**	**97.69**	**99.27**	**99.91**	**99.96**	**99.90**
Formula									
Units	23	23	23	23	23	8	8	8	8
Si	5.6563	5.6501	5.6335	5.6305	5.6208	2.5003	2.5370	2.4823	2.3897
Ti	0.0144	0.0186	0.0185	0.0165	0.0226	-	-	-	-
Al	4.6534	4.6526	4.6591	4.6555	4.6348	1.4931	1.4509	1.5117	1.6082
Cr	-	-	-	-	-	-	-	-	-
Fe	0.9370	0.9653	0.9251	0.9569	0.9617	0.0021	0.0037	0.0021	0.0032
Mn	0.0154	0.0214	0.0193	0.0174	0.0251	-	-	-	-
Mg	0.0070	0.0142	0.0177	0.0141	0.0177	-	-	-	-
Ca	3.7190	3.6826	3.7450	3.7342	3.7562	0.5233	0.4810	0.5322	0.6216
Na	-	-	-	-	-	0.4641	0.5242	0.4632	0.3644
K	-	-	-	-	-	0.0040	0.0054	0.0033	0.0020
F	-	-	-	-	-	-	-	-	-
Total	**15.0025**	**15.0048**	**15.0182**	**15.0251**	**15.0389**	**4.9869**	**5.0022**	**4.9948**	**4.9893**

G20	Garnet						Plagioclase		
Basic schist	FGS	FGP	FGF	FGE	FGN	FGR	FFD	FFC	FFF
Shuta	1-Core	1-Rim	2-Core	2-Rim	3-Core	3-Rim	1-Core	1-Rim	2-Core
SiO2	38.72	38.51	38.49	38.18	38.99	38.55	58.18	57.08	56.68
TiO2	0.03	-	0.03	0.09	-	-	-	-	-
Al2O3	21.72	21.62	21.32	21.28	21.44	21.58	26.08	26.91	27.40
Cr2O3	-	-	-	-	-	-	-	-	-
FeO	27.13	25.78	27.44	24.95	27.06	24.28	0.10	0.21	0.06
MnO	3.67	6.16	3.43	6.53	2.46	6.71	-	-	-
MgO	4.66	2.70	4.76	2.64	5.29	2.70	-	-	-
CaO	5.99	7.21	6.06	7.98	6.61	8.31	7.98	8.83	9.53
Na2O	0.00	-	-	-	-	-	6.77	6.51	6.00
K2O	0.00	-	-	-	-	-	0.15	0.04	0.08
F	0.00	-	-	-	-	-	-	-	-
Total	**101.93**	**101.98**	**101.53**	**101.65**	**101.85**	**102.13**	**99.42**	**99.58**	**99.88**
Formula									
Units	22	12	12	12	12	12	8	8	8
Si	5.4936	3.0050	2.9962	2.9949	3.0076	3.0005	2.6167	2.5698	2.5472
Ti	0.0037	-	0.0020	0.0051	-	-	-	-	-
Al	3.6322	1.9889	1.9557	1.9672	1.9492	1.9794	1.3829	1.4277	1.4515
Cr	-	-	-	-	-	-	-	-	-
Fe	3.2193	1.6828	1.7865	1.6363	1.7457	1.5805	0.0037	0.0079	0.0021
Mn	0.4409	0.4072	0.2259	0.4336	0.1607	0.4425	-	-	-
Mg	0.9854	0.3138	0.5522	0.3085	0.6079	0.3133	-	-	-
Ca	0.9104	0.6027	0.5051	0.6704	0.5463	0.6933	0.3848	0.4257	0.4591
Na	0.0000	-	-	-	-	-	0.5903	0.5679	0.5227
K	0.0000	-	-	-	-	-	0.0088	0.0020	0.0047
F	0.0000	-	-	-	-	-	-	-	-
Total	**14.6861**	**8.0004**	**8.0236**	**8.0160**	**8.0174**	**8.0095**	**4.9912**	**5.0010**	**4.9906**

G20		Biotite		Zoisite			Hornblende		
Basic schist	FFE	FBD	FBE	FEB	FEA	FED	FEC	FHB	FHA
Shuta	2-Rim			1-Core	1-Rim	1-Core	1-Rim	1-Core	1-Rim
SiO2	55.77	36.59	36.63	38.37	38.55	38.52	38.49	41.24	41.33
TiO2	-	2.68	2.88	0.17	0.17	0.19	0.21	0.78	0.74
Al2O3	27.32	17.13	17.62	26.41	26.31	26.23	26.14	15.09	15.31
Cr2O3	-	-	-	-	-	-	-	0.00	0.02
FeO	0.07	18.67	17.92	8.87	8.86	9.07	9.00	17.68	17.45
MnO	-	0.22	0.17	0.31	0.28	0.25	0.28	0.32	0.37
MgO	-	10.73	10.93	0.03	0.05	0.05	0.08	8.53	8.59
CaO	9.51	0.03	0.03	23.14	23.12	23.51	23.65	11.66	11.30
Na2O	5.86	0.14	0.19	0.02	0.02	-	-	1.48	1.37
K2O	0.05	9.16	8.98	0.00	0.00	-	-	1.00	0.91
F	-	0.08	0.00	-	-	-	-	0.08	0.17
Total	**98.71**	**95.66**	**95.59**	**97.32**	**97.36**	**97.82**	**97.85**	**97.90**	**97.60**
Formula									
Units	8	22	22	23	23	23	23	23	23
Si	2.5366	5.5364	5.5117	5.6492	5.6702	5.6518	5.6478	6.2116	6.2287
Ti	-	0.3045	0.3256	0.0186	0.0186	0.0206	0.0227	0.0884	0.0843
Al	1.4647	3.0558	3.1253	4.5823	4.5611	4.5365	4.5221	2.6796	2.7189
Cr	-	-	0.0000	0.0000	0.0000	0.0000	0.0000	0.0000	0.0019
Fe	0.0026	2.3626	2.2549	1.0922	1.0896	1.1123	1.1041	2.2277	2.1996
Mn	-	0.0275	0.0215	0.0389	0.0350	0.0310	0.0349	0.0413	0.0472
Mg	-	2.4206	2.4519	0.0072	0.0107	0.0107	0.0179	1.9143	1.9305
Ca	0.4636	0.0046	0.0046	3.6501	3.6430	3.6963	3.7190	1.8819	1.8243
Na	0.5172	0.0418	0.0568	0.0047	0.0047	0.0000	0.0000	0.4308	0.3992
K	0.0027	1.7686	1.7229	0.0000	0.0000	0.0000	0.0000	0.1927	0.1754
F	-	0.0394	0.0000	0.0000	0.0000	0.0000	0.0000	0.0400	0.0801
Total	**4.9907**	**15.5752**	**15.4893**	**15.8432**	**15.8329**	**15.8592**	**15.8685**	**15.7115**	**15.6933**

Appendix 3 - Whole-Rock Geochemical Data

X-Ray Fluorescence, Instrumental Neuton Activation and Isotope analyses for whole-rock granite and metamorphic samples from the Nanga Parbat-Haramosh Massif - Kohistan region. Order of samples : undeformed Confluence granites; deformed Confluence granites; undeformed Parri granites; deformed Parri granites; Jutial granite; leucogranite dykes; Iskere quartz-diorite; metamorphics.

Explanation : numbers in brackets refer to samples collected from the same granite sheet. Liachar SZ = Liachar shear zone. * = deformed leucogranite dykes (mainly collected from the western margin of the NPHM at Sassi or Liachar). B = biotite; Ep = epidote; M = muscovite; G = garnet; T = tourmaline; Hb = hornblende; K = kyanite; Si = sillimanite; parentheses indicate subsidiary minerals. A/CNK = alumina index in molar proportions. Isotopic analyses presented in italics are from the VG 54E; all other analyses are from the Finnagan MAT 261; quoted errors are to one sigma. Metamorphic samples M3-Leuc. and M3-Rest. are the leucome and restite portions of the same migmatite sample collected from Tato; samples J13 and J14 are roof pendants to the Jutial granite.

	Uneformed Confluence		(1)	(1)	(1)	(1)	(1)
Sample	**G4**	**G5**	**G10A**	**G10B**	**G10C**	**G10D**	**G10E**
Location	Gigit valley	Indus conf.	Jaglot	Jaglot	Jaglot	Jaglot	Jaglot
Mineralogy	B-Ep	B-M-Ep	B-(M)	B-(M)	B-(M)	B-(M)	B-(M)
XRF							
SiO2	67.98	75.10	72.65	73.50	71.45	73.32	69.43
TiO2	0.42	0.04	0.14	0.09	0.27	0.18	0.34
Al2O3	17.31	14.17	14.82	15.13	15.32	14.85	16.79
Fe2O3	2.86	0.64	1.08	0.68	2.08	1.51	2.26
MnO	0.05	0.04	0.02	0.01	0.04	0.02	0.04
MgO	0.84	0.09	0.24	0.15	0.49	0.31	0.64
CaO	4.52	1.44	1.85	1.99	2.36	1.81	3.22
Na2O	4.95	3.83	3.71	3.86	4.18	3.60	4.71
K20	1.22	4.68	4.58	4.34	3.35	4.66	2.51
P2O5	0.14	0.03	0.02	0.04	0.08	0.06	0.10
LOI	0.40	0.23	0.48	0.58	0.55	0.42	0.54
Total	**100.69**	**100.29**	**99.59**	**100.37**	**100.16**	**100.74**	**100.58**
A/CNK	0.98	1.01	1.03	1.03	1.03	1.04	1.03
Rb	63	116	92	73	83	92	62
Sr	710	283	431	430	404	482	742
Y	7	6	2	2	4	3	6
Zr	118	37	109	59	128	128	129
Nb	7	2	5	3	5	5	5
Ba	279	683	1248	1022	844	1424	748
Pb	15	39	37	34	30	34	23
Th	8	3	7	7	15	15	16
U	1	1	1	0	2	1	3
Sc	5	1	0	2	5	3	1
V	44	8	13	9	25	16	30
Cr	19	5	7	7	20	6	9
Co	4	0	0	0	1	0	3
Ni	5	3	3	2	3	3	3
Cu	11	3	2	3	5	5	5
Zn	62	15	33	20	53	41	63
Ga	19	15	15	14	17	16	20
INAA							
La						28.7	
Ce						47.7	
Nd						16.4	
Sm						2.38	
Eu						0.68	
Tb						0.22	
Yb						0.24	
Lu						0.07	
Th						17.1	
U						2.17	
Ta						0.15	
Hf						3.56	
Isotopes							
87Sr/86Sr			0.705351±10			0.705213±10	0.705013±10
duplicate			0.705410±25				
duplicate							
143Nd/144Nd						0.512670±4	

Sample	(1) G10F	(1) G10G	(1) G10H	(1) G10I	G12	G13	(2) G16
Location	Jaglot	Jaglot	Jaglot	Jaglot	Indus conf.	Indus conf.	Indus conf.
Mineralogy	B-(M)	B-(M)	B-(M)	B-(M)	B	B-(Ep)	B-Ep-(M)
XRF							
SiO2	72.94	73.34	70.85	73.25	71.95	71.90	75.41
TiO2	0.16	0.14	0.30	0.18	0.20	0.23	0.07
Al2O3	14.59	14.74	16.27	14.65	15.06	15.72	14.13
Fe2O3	1.35	1.14	1.97	1.45	1.52	1.46	0.42
MnO	0.02	0.02	0.03	0.02	0.03	0.03	0.01
MgO	0.26	0.25	0.52	0.29	0.37	0.48	0.10
CaO	1.73	1.83	2.94	1.79	2.86	2.96	1.46
Na2O	3.55	3.59	4.46	3.55	4.21	4.68	3.63
K20	4.76	4.61	2.82	4.63	3.26	2.51	4.96
P2O5	0.04	0.04	0.09	0.05	0.06	0.06	0.01
LOI	0.64	0.47	0.35	0.20	0.87	0.18	0.31
Total	**100.04**	**100.17**	**100.60**	**100.06**	**100.38**	**100.21**	**100.51**
A/CNK	1.03	1.03	1.03	1.04	0.96	0.99	1.01
Rb	90	83	63	91	68	44	87
Sr	423	495	677	485	403	524	320
Y	2	2	6	3	4	7	1
Zr	97	95	116	120	120	97	41
Nb	5	4	5	5	5	5	2
Ba	1249	1572	943	1409	757	771	485
Pb	33	36	24	34	26	22	33
Th	14	11	14	12	12	8	3
U	2	2	2	2	1	2	1
Sc	2	2	2	1	3	4	2
V	15	13	31	15	21	20	8
Cr	7	20	9	9	9	7	6
Co	0	0	2	0	0	0	0
Ni	5	3	3	3	2	2	4
Cu	11	3	5	5	21	17	14
Zn	33	31	54	41	38	29	11
Ga	15	16	19	14	17	16	13
INAA							
La		22.4	32.5				
Ce		37.9	55.2				
Nd		12.2	18.3				
Sm		1.94	2.69				
Eu		0.67	0.71				
Tb		0.14	0.27				
Yb		0.21	0.44				
Lu		0.06	0.08				
Th		14.1	16.4				
U		2.28	3.21				
Ta		0.15	0.21				
Hf		2.85	2.99				
Isotopes							
87Sr/86Sr	*0.705124±29*	0.705114±22	0.705013±11				
duplicate							
duplicate							
143Nd/144Nd			0.512664±6				

	(2)	(3)	(3)		Deformed Confluence		
Sample	G18	S6G	S6I	S109	S42	S67	S69
Location	Indus conf.	Indus conf.	Indus conf.	Gilgit Valley	Sassi	Shahbatot	Shahbatot
Mineralogy	B-Ep-(M)	B-M-(Ep)	B-M-(Ep)	B-M-Ep	M-B-(G)	B-Ep	B-(T)
XRF							
SiO2	69.07	72.21	72.45	66.03	72.99	72.96	72.21
TiO2	0.38	0.27	0.28	0.54	0.05	0.11	0.04
Al2O3	16.94	14.88	14.85	15.95	14.79	15.90	16.01
Fe2O3	2.57	1.83	1.81	3.62	1.00	0.88	0.25
MnO	0.05	0.03	0.03	0.04	0.01	0.02	0.01
MgO	0.76	0.58	0.55	1.00	0.44	0.32	0.07
CaO	3.80	2.14	2.09	2.93	1.10	3.25	2.43
Na2O	5.20	4.17	4.12	3.84	2.40	5.20	5.13
K20	1.22	3.65	3.62	4.49	6.52	1.39	2.95
P2O5	0.12	0.10	0.09	0.26	0.09	0.03	0.01
LOI	0.33	0.32	0.26	0.90	0.81	0.15	0.29
Total	100.43	100.18	100.15	99.60	100.19	100.20	99.39
A/CNK	1.01	1.01	1.02	0.97	1.14	0.99	1.00
Rb	47	85	83	116	129	35	47
Sr	551	385	392	510	355	540	544
Y	5	4	3	11	4	1	2
Zr	108	155	152	315	71	12	12
Nb	7	4	5	12	2	2	2
Ba	188	908	946	934	1567	562	1649
Pb	15	20	18	16	32	22	23
Th	5	9	9	13	7	0	1
U	1	1	1	2	1	1	1
Sc	4	4	1	3	3	2	1
V	39	25	27	47	9	11	5
Cr	12	11	16	9	47	17	19
Co	3	1	1	3	0	0	0
Ni	3	4	4	6	9	2	3
Cu	21	38	25	144	3	2	3
Zn	57	49	46	39	13	18	7
Ga	20	17	16	16	12	13	11
INAA							
La							
Ce							
Nd							
Sm							
Eu							
Tb							
Yb							
Lu							
Th							
U							
Ta							
Hf							
Isotopes							
87Sr/86Sr	0.704763±10	0.704804±11				0.708461±9	
duplicate							
duplicate							
143Nd/144Nd	0.512659±7	0.512689±6					

Sample	(4) S75	(4) S76	S78	S81	S95	S96	D14
Location	Shahbatot	Shahbatot	Shahbatot	Shahbatot	L. Darchan	L. Darchan	W. Darchan
Mineralogy	B-M-Ep	B-M-Ep	B-M-Ep	B-(Ep)-(T)	B	B-(M)	B-(M)-(Ep)
XRF							
SiO2	73.13	71.34	74.97	74.19	73.31	74.20	72.29
TiO2	0.04	0.14	0.09	0.10	0.18	0.14	0.04
Al2O3	15.58	16.56	14.36	14.97	15.08	14.77	16.04
Fe2O3	0.31	1.18	0.62	1.03	1.29	0.99	0.38
MnO	0.01	0.02	0.01	0.01	0.04	0.02	0.01
MgO	0.10	0.46	0.32	0.12	0.37	0.26	0.27
CaO	3.32	3.60	1.77	1.23	2.05	1.94	2.25
Na2O	5.51	5.61	4.57	3.54	4.12	4.12	5.34
K20	0.44	0.76	2.59	5.18	3.74	3.86	2.69
P2O5	0.01	0.05	0.01	0.06	0.05	0.04	0.02
LOI	0.34	0.47	0.42	0.35	0.36	0.25	0.30
Total	**98.79**	**100.19**	**99.72**	**100.78**	**100.59**	**100.59**	**99.62**
A/CNK	1.00	1.00	1.06	1.09	1.03	1.02	1.02
Rb	8	19	46	74	80	74	40
Sr	676	670	428	276	355	343	424
Y	1	4	2	3	3	3	1
Zr	3	50	42	25	102	92	38
Nb	1	2	2	2	5	5	2
Ba	131	260	2770	623	826	736	1367
Pb	14	14	29	48	28	28	43
Th	0	2	4	0	8	8	1
U	1	1	1	2	2	2	1
Sc	3	2	2	1	3	3	1
V	5	15	11	6	18	12	6
Cr	6	6	13	23	8	6	12
Co	0	0	0	0	0	0	0
Ni	4	6	6	4	3	3	14
Cu	17	13	59	1	3	2	1
Zn	10	16	9	8	40	29	12
Ga	13	14	9	15	16	15	11
INAA							
La							
Ce							
Nd							
Sm							
Eu							
Tb							
Yb							
Lu							
Th							
U							
Ta							
Hf							
Isotopes							
87Sr/86Sr	0.709687±10	0.708198±10		0.707859±11	0.704876±13		
duplicate	*0.709672±86*						
duplicate							
143Nd/144Nd							

	Undeformed Parri						Def. Parri
Sample	D17	G2	G3	G14	G15	G23	G30
Locality	W. Darchan	Gilgit valley	Gilgit valley	Indus conf.	Indus conf.	Shuta	Sassi
Mineralogy	M	M-B-G	M-G-Ep	M-B-G	M-B-G	M-G-Ep	M-B-G
SiO2	73.65	74.86	75.00	74.72	75.30	74.29	73.56
TiO2	0.06	0.04	0.02	0.03	0.03	0.03	0.36
Al2O3	15.98	14.82	14.50	15.11	14.87	15.02	15.09
Fe2O3	0.64	0.59	0.43	0.63	0.39	0.47	2.72
MnO	0.01	0.09	0.05	0.05	0.04	0.08	0.04
MgO	0.20	0.06	0.03	0.05	0.04	0.04	0.64
CaO	2.47	1.12	0.86	2.03	1.99	1.29	2.27
Na2O	4.71	4.20	4.69	6.09	5.97	4.72	3.19
K20	1.88	4.43	4.09	1.07	0.97	3.94	1.94
P2O5	0.05	0.02	0.02	0.02	0.01	0.02	0.07
LOI	0.48	0.32	0.38	0.42	0.21	0.66	0.82
Total	**100.13**	**100.54**	**100.07**	**100.22**	**99.81**	**100.56**	**100.70**
A/CNK	1.12	1.08	1.06	1.02	1.03	1.04	1.31
Rb	38	197	251	31	26	252	82
Sr	427	97	13	93	97	50	224
Y	2	9	9	7	5	9	13
Zr	23	38	16	49	17	36	222
Nb	3	8	12	6	3	13	11
Ba	690	183	22	0	34	13	869
Pb	26	36	45	25	31	55	46
Th	0	5	6	0	0	2	34
U	1	5	8	2	1	5	2
Sc	3	2	1	3	2	3	4
V	10	3	2	3	5	4	27
Cr	5	4	4	4	10	5	12
Co	0	0	0	0	0	0	5
Ni	3	3	2	2	3	4	9
Cu	1	0	1	2	0	0	30
Zn	10	28	22	24	13	34	45
Ga	14	16	25	17	16	22	15
INAA							
La		6.6					
Ce		12.6					
Nd		7.5					
Sm		1.55					
Eu		0.23					
Tb		0.33					
Yb		0.75					
Lu		0.11					
Th		6.97					
U		4.84					
Ta		1.25					
Hf		2.03					
Isotopes							
87Sr/86Sr	0.708120±9	0.707525±10	0.728323±10	0.705809±10	0.706276±10	0.710762±12	0.740513±11
duplicate							
duplicate							
143Nd/144Nd		0.512763±14	0.512631±26				0.511898±8

Sample	(5) G35	(5) G36	G43	G48	S97	S101	D5
Locality	Sassi	Sassi	Sassi	Sassi	L. Darchan	L. Darchan	W. Darchan
Mineralogy	M-G-(B)	M-G-(B)	M-B-G	M-B-G	M-(B)	M-(B)	M
SiO2	71.94	74.77	71.92	73.98	73.72	74.62	73.79
TiO2	0.05	0.02	0.20	0.13	0.05	0.06	0.05
Al2O3	16.55	15.34	14.91	15.14	15.06	14.35	15.60
Fe2O3	0.32	0.31	1.76	1.21	0.55	0.47	0.74
MnO	0.01	0.12	0.04	0.05	0.01	0.01	0.01
MgO	0.14	0.04	0.38	0.29	0.10	0.12	0.10
CaO	1.70	1.99	1.45	1.44	1.16	0.97	1.65
Na2O	4.15	4.73	3.35	3.67	3.52	3.60	4.59
K20	4.79	3.20	4.85	3.93	5.67	5.59	3.14
P2O5	0.01	0.01	0.13	0.01	0.03	0.01	0.02
LOI	0.96	0.28	0.48	0.71	0.50	0.93	0.68
Total	**100.63**	**100.81**	**99.47**	**100.56**	**100.37**	**100.73**	**100.37**
A/CNK	1.09	1.03	1.11	1.17	1.07	1.04	1.12
Rb	198	122	210	177	213	246	120
Sr	194	165	113	181	259	234	199
Y	9	14	10	22	6	4	4
Zr	20	48	90	80	12	33	34
Nb	24	3	8	21	6	11	7
Ba	588	250	377	497	218	632	45
Pb	82	55	57	94	113	88	70
Th	1	1	11	5	7	2	2
U	4	1	2	8	2	3	4
Sc	5	2	4	8	2	2	3
V	14	0	16	16	6	5	3
Cr	8	14	11	11	10	9	4
Co	0	0	0	0	0	0	0
Ni	4	2	5	4	3	5	3
Cu	2	2	3	2	1	3	0
Zn	5	6	37	17	17	10	27
Ga	25	16	16	23	17	19	21
INAA							
La	2.3		24.1				
Ce	4.7		47.0				
Nd	3.2		19				
Sm	0.89		4.00				
Eu	0.16		0.88				
Tb	0.21		0.46				
Yb	1.50		0.73				
Lu	0.27		0.10				
Th	2.91		13.2				
U	4.37		2.34				
Ta	7.00		0.49				
Hf	1.16		2.86				
Isotopes							
87Sr/86Sr	0.725046±11	*0.708376±46*	0.760320±11	*0.756402±23*	0.735459±11		0.723503±10
duplicate							
duplicate							
143Nd/144Nd			0.511959±12		0.511661±9		

		Jutial Granite					
Sample	S66	J1A	J1B	J1C	J1D	J1E	J1F
Location	Shahbatot	Jutial	Jutial	Jutial	Jutial	Jutial	Jutial
Mineralogy	M-(B)	M-B	M-B	M-B	M-B	M-B	M-B
SiO2	78.14	74.45	74.24	74.00	73.46	74.92	73.81
TiO2	0.04	0.07	0.09	0.10	0.18	0.08	0.10
Al2O3	12.62	14.95	14.78	14.80	14.49	14.55	14.88
Fe2O3	0.52	0.88	0.97	1.00	1.37	0.85	1.02
MnO	0.01	0.01	0.01	0.01	0.01	0.01	0.01
MgO	0.21	0.09	0.09	0.11	0.35	0.09	0.11
CaO	1.26	1.12	1.19	1.23	1.02	1.22	1.20
Na2O	2.96	3.74	3.63	3.51	3.09	3.59	3.51
K2O	4.98	4.93	4.99	4.97	5.90	4.58	5.14
P2O5	0.01	0.06	0.05	0.05	0.04	0.05	0.05
LOI	0.28	0.47	0.52	0.56	0.54	0.56	0.47
Total	**101.03**	**100.77**	**100.56**	**100.35**	**100.45**	**100.50**	**100.31**
A/CNK	1.00	1.10	1.09	1.10	1.09	1.11	1.10
Rb	215	276	316	310	293	253	289
Sr	114	51	69	76	122	61	74
Y	38	19	8	8	8	19	10
Zr	13	41	57	52	37	30	73
Nb	12	13	12	13	12	11	12
Ba	364	98	160	160	564	48	162
Pb	48	75	78	77	72	69	81
Th	9	15	21	19	38	10	22
U	10	18	24	24	9	12	23
Sc	2	4	3	5	4	2	5
V	7	5	5	4	6	4	6
Cr	12	10	7	8	8	9	8
Co	0	0	0	0	0	0	0
Ni	7	4	2	4	5	4	3
Cu	9	1	1	1	2	0	0
Zn	8	25	26	27	33	22	28
Ga	20	21	22	22	18	21	22
INAA							
La			22.8			12.2	28.8
Ce			58.0			28.9	70.4
Nd			32.8			17.9	33
Sm			4.18			2.46	5.32
Eu			0.40			0.34	0.42
Tb			0.50			0.49	0.60
Yb			0.63			1.49	0.57
Lu			0.10			0.24	0.10
Th			24.2			13.3	30
U			45.10			25.10	41.50
Ta			1.21			1.14	1.13
Hf			2.08			1.31	2.13
Isotopes							
87Sr/86Sr	*0.758424±23*	0.887235±10	0.890410±13	0.891988±13	0.874651±12	0.888386±13	0.891712±13
duplicate							
duplicate							
143Nd/144Nd	0.511292±7		0.511297±7				

Sample	J1G	J1H	J1i	J11	J19	J15	Leg dykes S87
Location	Jutial	Jutial	Jutial	Jutial	Jutial	Jutial	Shengus
Mineralogy	M-B	M-B-(T)	M-B	B-(M)-(T)	M-B	B-(M)	B-(M)
SiO2	72.66	74.42	73.72	70.56	73.64	76.39	73.00
TiO2	0.11	0.06	0.08	0.15	0.13	0.08	0.03
Al2O3	15.40	14.91	15.02	14.41	14.50	13.63	15.18
Fe2O3	0.98	0.81	0.95	1.21	0.97	0.64	0.29
MnO	0.02	0.02	0.01	0.01	0.01	0.01	0.01
MgO	0.13	0.07	0.10	0.23	0.20	0.12	0.07
CaO	1.63	1.03	1.23	1.09	1.22	1.31	1.07
Na2O	4.13	3.76	3.68	3.11	3.24	3.58	3.62
K2O	4.69	4.68	4.93	6.26	5.71	4.21	6.61
P2O5	0.05	0.05	0.05	0.03	0.02	0.02	0.08
LOI	0.47	0.38	0.73	1.91	0.32	0.35	0.24
Total	**100.27**	**100.19**	**100.50**	**98.98**	**99.97**	**100.35**	**100.20**
A/CNK	1.04	1.13	1.10	1.04	1.05	1.06	1.01
Rb	270	357	288	309	271	222	283
Sr	106	43	58	110	144	126	85
Y	9	20	20	7	2	4	19
Zr	53	39	46	58	35	33	17
Nb	11	12	13	9	7	5	3
Ba	200	77	107	337	514	332	130
Pb	68	65	79	82	85	65	89
Th	35	12	19	35	15	10	4
U	19	16	22	35	19	7	5
Sc	3	2	3	4	1	1	3
V	3	3	5	7	8	7	5
Cr	5	6	8	10	6	12	18
Co	0	0	0	0	0	0	0
Ni	3	4	4	4	3	4	6
Cu	0	0	1	2	1	1	1
Zn	24	28	29	29	22	21	9
Ga	19	21	22	17	16	15	14
INAA							
La	35		18.6		19.2		
Ce	80.0		47.5		47.5		
Nd	38.9		26.7		25.9		
Sm	5.97		3.67		2.44		
Eu	0.52		0.30		0.65		
Tb	0.61		0.64		0.20		
Yb	0.72		1.64		0.20		
Lu	0.12		0.26		0.04		
Th	40.7		20		22.1		
U	31.00		41.90		46.90		
Ta	1.93		1.37		0.99		
Hf	2.00		1.76		1.03		
Isotopes							
87Sr/86Sr	0.889467±12		0.887690±10	0.884383±13	0.881323±12		0.873616±13
duplicate							
duplicate							
143Nd/144Nd	0.511295±7		0.511270±10		0.511315±9		

Sample	S92	S93	I8	I11	J7 *	J8	J9
Location	Shengus	Shengus	Kutwal	Kutwal	Phuparosh	Phuparosh	Phuparosh
Mineralogy	M-B-T	B-(M)-(T)	M-B-T	G-B-T	M-B	M-T (B)	M-B-T
SiO2	71.93	76.19	74.89	75.19	73.67	74.65	74.51
TiO2	0.07	0.06	0.06	0.04	0.06	0.03	0.04
Al2O3	16.85	13.76	14.46	13.91	15.31	14.69	14.75
Fe2O3	0.98	0.44	1.05	0.74	0.62	0.89	0.80
MnO	0.04	0.01	0.02	0.06	0.01	0.07	0.02
MgO	0.14	0.10	0.12	0.10	0.10	0.07	0.18
CaO	1.02	1.23	0.86	0.59	1.15	0.64	0.67
Na2O	4.26	4.14	3.94	3.82	4.06	4.62	4.09
K2O	4.15	3.93	3.63	4.76	4.76	3.61	4.25
P2O5	0.12	0.07	0.08	0.11	0.08	0.07	0.10
LOI	0.86	0.29	0.61	0.65	0.96	0.71	0.77
Total	**100.41**	**100.22**	**99.72**	**99.97**	**100.78**	**100.04**	**100.19**
A/CNK	1.26	1.03	1.21	1.11	1.10	1.16	1.17
Rb	389	170	296	300	233	332	417
Sr	25	135	17	31	64	12.5	22.6
Y	46	19	32	13	11	10.4	13.9
Zr	70	30	36	26	109	30	26
Nb	18	5	17	7	11	8.1	15.1
Ba	0	167	0	85	54	19	51
Pb	41	65	43	46	73	40	50
Th	14	3	10	5	10	0	4
U	20	7	10	6	20	3	11
Sc	6	4	3	0	3	0	2
V	3	2	3	4	3	0	1
Cr	5	7	4	19	5	40	12
Co	0	0	0	0	0	0	0
Ni	4	4	4	4	5	7	17
Cu	0	0	1	2	2	1	3
Zn	33	14	32	22	18	42	40
Ga	26	14	24	18	22	22	22
INAA							
La							
Ce							
Nd							
Sm							
Eu							
Tb							
Yb							
Lu							
Th							
U							
Ta							
Hf							
Isotopes							
87Sr/86Sr	0.830155±11	*0.755844±20*	0.804849±50	0.808037±12	0.828080±12		
duplicate							
duplicate							
143Nd/144Nd	0.511356±7				0.511383±8		

Sample	J20	G39 *	S47 *	S51 *	S60 *	(6) A9 *	(6) A10 *
Location	S. Jutial	Sassi	Sassi	Sassi	Sassi	Rupal	Rupal
Mineralogy	B	M-G-(B)	B-(T)	M-T	B-(T)	M-T	M-T
SiO2	74.08	74.83	75.19	72.55	75.25	75.25	74.22
TiO2	0.08	0.06	0.05	0.03	0.05	0.05	0.06
Al2O3	14.23	15.32	14.97	15.34	14.49	14.83	14.85
Fe2O3	0.64	0.35	0.37	0.14	0.67	0.89	1.58
MnO	0.01	0.01	0.01	0.00	0.01	0.02	0.03
MgO	0.16	0.10	0.06	0.05	0.07	0.05	0.13
CaO	1.25	1.42	2.14	1.10	1.11	0.94	0.95
Na2O	3.26	4.21	5.71	3.29	4.15	4.42	4.17
K2O	5.44	3.63	1.56	7.11	5.00	2.25	2.39
P2O5	0.06	0.03	0.01	0.01	0.01	0.07	0.13
LOI	0.52	0.70	0.32	0.63	0.38	0.73	0.91
Total	**99.73**	**100.66**	**100.39**	**100.25**	**101.19**	**99.50**	**99.41**
A/CNK	1.05	1.14	1.00	1.01	1.02	1.30	1.33
Rb	203	160	81	367	250	252	224
Sr	188	83	131	71.4	52	11	12
Y	16	40	4	4.9	10	42	55.8
Zr	13	79	9	6	28	42	65
Nb	4	31	6	6.4	13	22	12
Ba	868	116	116	167	122	0	9
Pb	78	80	48	114	67	28	34
Th	121	21	0	9	2	16	18
U	9	19	4	11	12	25	40
Sc	2	5	1	2	1	4	3
V	5	2	3	0	4	5	2
Cr	6	8	10	6	11	10	13
Co	0	0	0	0	0	0	1
Ni	5	4	4	6	2	5	6
Cu	1	4	1	2	11	0	0
Zn	13	7	9	5	9	28	52
Ga	12	27	19	21	22	32	28
INAA							
La							
Ce							
Nd							
Sm							
Eu							
Tb							
Yb							
Lu							
Th							
U							
Ta							
Hf							
Isotopes							
87Sr/86Sr		*0.780721±22*	0.834048±10			1.008309±28	1.007800±12
duplicate							
duplicate							
143Nd/144Nd		0.511279±21					

Sample	(6) A11 *	(6) A14 *	M14	M18	T59 *	T71 *	T74 *
Location	Rupal	Rupal	Fairy Mw's	Fairy Mw's	Liachar SZ	Liachar SZ	Liachar SZ
Mineralogy	M-T	M-T	G-B-T	M-B-T	B-(M)	M-G-B-T	M-T
SiO2	77.21	74.28	73.29	73.62	73.83	76.41	73.79
TiO2	0.09	0.05	0.07	0.09	0.04	0.05	0.05
Al2O3	12.44	14.78	14.44	14.49	14.84	14.30	15.28
Fe2O3	1.65	1.00	1.27	1.14	0.25	0.69	0.44
MnO	0.05	0.02	0.03	0.03	0.01	0.03	0.01
MgO	0.12	0.12	0.21	0.12	0.09	0.21	0.07
CaO	1.34	1.00	0.67	1.20	1.18	1.03	0.94
Na2O	3.35	4.14	3.94	3.58	2.99	3.63	3.78
K2O	2.31	3.56	4.56	4.83	6.81	2.90	5.57
P2O5	0.54	0.13	0.27	0.06	0.01	0.22	0.01
LOI	0.69	0.50	0.22	0.31	0.67	0.88	0.37
Total	**99.80**	**99.58**	**98.98**	**99.47**	**100.72**	**100.34**	**100.31**
A/CNK	1.19	1.18	1.14	1.09	1.03	1.30	1.09
Rb	260	290	320	464	297	115	395
Sr	10	25	36	65	130	136	41
Y	70	22	8	41	2	3	39
Zr	45	28	42	69	15	39	13
Nb	25	6	10	14	3	3	10
Ba	0	0	83	187	598	207	75
Pb	31	43	27	85	94	25	68
Th	24	5	2	14	0	0	4
U	42	18	6	20	8	2	6
Sc	3	2	3	5	2	1	2
V	5	3	6	6	4	2	4
Cr	7	9	10	13	7	8	5
Co	0	0	0	0	0	0	0
Ni	4	4	5	5	4	4	4
Cu	0	0	3	2	0	1	2
Zn	37	30	31	33	7	14	14
Ga	24	21	17	22	14	20	22
INAA							
La							
Ce							
Nd							
Sm							
Eu							
Tb							
Yb							
Lu							
Th							
U							
Ta							
Hf							
Isotopes							
87Sr/86Sr	0.996227±14	1.006964±14		0.881225±12			
duplicate							
duplicate							
143Nd/144Nd				0.511388±5			

Sample	(7) L17E *	(7) L17F *	(7) L17G *	R8 *	Qz-diorite I3	Metamorphics S22	G31
Location	Liachar SZ	Liachar SZ	Liachar SZ	Liachar SZ	Iakere	Sassi	Sassi
Mineralogy	T-(B)	T-(B)	T-(B)	B-T	B	G-Hb-B	K-G-B-M
SiO2	74.74	74.60	73.80	76.46	61.60	46.19	67.09
TiO2	0.02	0.02	0.02	0.04	0.20	3.16	0.82
Al2O3	14.76	15.23	15.34	13.25	22.27	13.83	16.12
Fe2O3	0.22	0.20	0.23	0.31	1.48	16.03	8.10
MnO	0.03	0.05	0.02	0.01	0.02	0.22	0.10
MgO	0.03	0.02	0.04	0.09	0.51	5.42	2.30
CaO	0.89	0.95	0.79	0.62	4.00	9.59	0.59
Na2O	5.26	5.90	4.98	2.67	6.90	1.96	0.73
K2O	3.89	3.22	4.93	6.46	1.92	1.83	3.13
P2O5	0.01	0.01	0.01	0.02	0.07	0.38	0.05
LOI	0.37	0.39	0.21	0.23	0.67	1.45	1.30
Total	**100.22**	**100.59**	**100.38**	**100.16**	**99.63**	**100.06**	**100.33**
A/CNK	1.02	1.02	1.02	1.06	1.07		
Rb	388	318	419	382	127.9	115	129
Sr	14.5	15	21	60	256.3	212	115
Y	77.9	60	48	8	4.8	35	41.3
Zr	40	31	26	8	36	203	237
Nb	17.9	16	34	3	9.7	29.4	14.7
Ba	7	4	6	138	125	244	792
Pb	68	56	66	77	49	16	8
Th	11	9	11	5	12	3	14
U	12	9	10	5	3	1	2
Sc	1	1	2	1	5	38	15
V	3	3	4	3	11	366	121
Cr	8	5	7	14	6	88	158
Co	0	0	0	0	1	66	29
Ni	9	5	5	3	9	62	44
Cu	2	2	0	1	0	98	7
Zn	11	9	8	9	34	138	55
Ga	25	26	26	16	29	19	22
INAA							
La							
Ce							
Nd							
Sm							
Eu							
Tb							
Yb							
Lu							
Th							
U							
Ta							
Hf							
Isotopes							
87Sr/86Sr	1.073848±27	1.065826±13	0.949910±14		0.840913±11	0.735350±13	0.759431±11
duplicate							0.759400±13
duplicate							
143Nd/144Nd					0.511411±6		0.511675±5

					Migmatitc		Roof Pendant
Sample	**S102**	**D7**	**D19**	**D2**	**I6**	**J21**	**J13**
Location	L. Darchan	W. Darchan	E. Darchan	E. Darchan	Iskere	Lower Jutial	Jutial
Mineralogy	Hb-B-G	B-M-Ep	G-B-M	G-Bi-M	B	B	B-(Hb)
SiO2	62.10	67.23	62.12	74.54	68.42	66.84	67.74
TiO2	1.94	0.40	0.65	0.12	0.64	1.03	1.02
Al2O3	14.15	15.87	17.33	14.21	14.86	14.32	14.74
Fe2O3	9.60	3.95	7.89	1.35	4.63	6.97	4.64
MnO	0.12	0.11	0.15	0.03	0.05	0.08	0.05
MgO	1.71	1.37	2.79	0.33	1.49	1.32	0.96
CaO	4.85	3.72	1.79	0.72	1.85	2.84	1.74
Na2O	2.00	4.18	2.63	3.25	3.05	2.74	2.45
K2O	3.61	2.15	3.44	5.27	4.48	2.99	5.81
P2O5	0.26	0.15	0.11	0.18	0.28	0.20	0.33
LOI	0.36	0.55	1.20	0.80	0.56	0.58	0.49
Total	**100.70**	**99.69**	**100.10**	**100.79**	**100.31**	**99.90**	**99.97**
A/CNK							
Rb	131	80.0	175	227	248	206	264
Sr	211	353	181	81.5	152	159	124
Y	47.4	17.6	30.3	17.7	19.0	38.4	24.4
Zr	308	93	155	80	149	304	363
Nb	20.4	6.4	13.4	10.4	18.8	17.4	24.3
Ba	1160	373	634	303	606	795	846
Pb	29	10	22	40	34	28	46
Th	18	6	14	18	30	20	39
U	3	2	2	5	5	11	4
Sc	22	6	16	3	14	18	6
V	96	57	98	11	57	65	45
Cr	30	21	152	16	54	43	50
Co	31	10	31	0	14	22	11
Ni	8	7	59	8	16	12	9
Cu	17	13	25	1	15	14	14
Zn	125	51	97	22	75	95	99
Ga	21	14	23	18	21	21	22
INAA							
La					43		81.6
Ce					101.0		179.0
Nd					50.4		80.3
Sm					11.30		14.30
Eu					0.80		1.06
Tb					0.96		1.29
Yb					2.05		1.90
Lu					0.35		0.30
Th					44.7		42.7
U					5.76		4.51
Ta					1.03		1.66
Hf					5.46		10.99
Isotopes							
87Sr/86Sr	*0.758388±26*	0.704401±10	0.779895±11	0.963919±14	0.839407±12	0.803972±33	0.875653±13
duplicate	*0.758263±56*		0.779877±11	0.962641±12		0.803836±86	*0.875519±51*
duplicate			0.779557±10				
143Nd/144Nd	0.511248±4		0.511294±5		0.511623±4		

Sample	Roof Pendant J14	Migmatitc J6	Migmatitc I9	Migmatitc I10	Migmatitc S91	A13	Migmatitc A3
Location	Jutial	Phuparosh	Kutwal	Kutwal	Shengus	Rupal	Astor valley
Mineralogy	B-M	B	B-M	B-M	Si-B-M	B-(M)	K-G-B-M
SiO2	67.99	75.27	75.48	72.07	69.40	70.10	70.28
TiO2	0.43	0.42	0.41	0.06	0.53	0.69	0.73
Al2O3	14.24	12.72	12.76	14.90	15.55	14.63	15.49
Fe2O3	5.61	2.95	3.22	0.47	4.83	5.05	5.93
MnO	0.04	0.04	0.03	0.01	0.10	0.05	0.09
MgO	2.17	1.10	1.33	0.23	1.51	1.35	1.43
CaO	0.97	2.31	1.25	0.65	0.89	1.47	0.51
Na2O	2.26	3.59	3.23	2.46	2.77	3.31	1.39
K2O	5.65	1.37	2.55	7.24	3.17	4.21	3.71
P2O5	0.07	0.06	0.07	0.20	0.13	0.19	0.13
LOI	0.60	0.35	0.84	0.68	1.38	0.50	0.76
Total	**100.03**	**100.19**	**101.18**	**98.96**	**100.26**	**101.54**	**100.45**
A/CNK							
Rb	455	174	109	151	211	375	375
Sr	88.1	288	152	288	114	129	77.4
Y	14.3	14	10.6	9.3	25.2	21.8	33.1
Zr	109	381	211	13	144	212	206
Nb	13.6	9.5	7.9	2.6	14.1	16.6	16.2
Ba	410	350	418	1347	487	674	594
Pb	55	23	18	57	22	38	23
Th	55	20	9	1	8	41	14
U	14	19	3	2	5	8	4
Sc	12	4	7	1	11	10	11
V	66	44	43	3	74	48	103
Cr	74	77	65	12	61	36	96
Co	18	8	9	0	16	14	17
Ni	37	28	23	10	29	14	35
Cu	5	1	4	6	13	14	11
Zn	99	50	38	16	75	86	115
Ga	21	14	13	12	19	20	20
INAA							
La						60.8	39.8
Ce						133.0	81.7
Nd						58.6	36.1
Sm						10.80	6.78
Eu						1.00	1.39
Tb						1.11	1.03
Yb						1.98	3.56
Lu						0.32	0.57
Th						44.7	16.2
U						7.70	3.51
Ta						1.29	1.34
Hf						7.13	6.15
Isotopes							
87Sr/86Sr	0.878509±37	0.731733±15	0.766134±21	0.768784±44	0.769625±10	0.881931±12	0.838081±12
duplicate			0.766162±11		0.769717±11		
duplicate							
143Nd/144Nd	0.511253±10		0.510999±15			0.511298±4	0.511740±8

Sample	A7	L3	T25	Migmatitic M10	Migmatitic M3-Leuc.	Migmatitic M3-Rest.
Location	Tarshing	Liachar SZ	Liachar SZ	Fairy Mw's	Fairy Mw's	Fairy Mw's
Mineralogy	K-G-B-M	B	B-M	B	B	B
SiO2	62.96	72.28	73.65	60.98	72.84	73.94
TiO2	0.79	0.36	0.31	0.62	0.30	0.48
Al2O3	15.70	13.38	15.28	20.82	14.23	11.99
Fe2O3	7.53	3.79	2.82	7.95	3.39	4.98
MnO	0.23	0.09	0.02	0.05	0.02	0.03
MgO	2.26	1.18	0.61	3.04	1.59	2.31
CaO	3.50	2.56	1.40	0.30	1.94	1.47
Na2O	1.14	2.38	3.59	0.66	2.88	2.10
K2O	2.79	4.12	3.01	4.28	2.87	3.09
P2O5	0.11	0.08	0.10	0.09	0.03	0.06
LOI	2.73	0.59	0.96	1.94	0.77	0.64
Total	**99.74**	**100.80**	**101.76**	**100.73**	**100.87**	**101.08**
A/CNK						
Rb	128	149	291	261	144	186
Sr	231	152	163	39.3	184	131
Y	28.1	13.7	14.1	24.4	8.2	13.8
Zr	152	174	134	114	139	235
Nb	18	9.4	14.6	15.2	5.5	8
Ba	533	1043	171	499	470	446
Pb	23	28	22	10	30	22
Th	16	10	13	20	7	9
U	3	3	9	4	2	2
Sc	13	8	4	19	6	10
V	150	38	20	102	38	79
Cr	126	73	22	142	46	63
Co	23	9	5	33	9	17
Ni	36	14	10	48	21	26
Cu	55	20	0	13	93	22
Zn	121	60	60	54	29	38
Ga	19	15	22	27	14	13
INAA						
La						
Ce						
Nd						
Sm						
Eu						
Tb						
Yb						
Lu						
Th						
U						
Ta						
Hf						
Isotopes						
87Sr/86Sr	0.717080±12	0.786329±12	0.838010±13	0.973111±11	0.843790±12	0.850839±16
duplicate						
duplicate						
143Nd/144Nd		0.511170±8				

Appendix 4 - Normative Granite Compositions

Normative compositions have been derived from *Grannorm* (Harris and Marriner 1980). The values given are the proportions of phases (volume %) which would crystallise from a hydrous melt, taking into account the assignment of potassium to both mica and k-feldspar. In all of the samples, the normative proportions of non-quartzofeldspathic phases is less than 15 % (vol.), and therefore normative values should be accurate to ± 3 %.

Order of samples : Confluence granites; Parri granites; Jutial granite; leucogranite dykes; Iskere quartz-diorite.

vol. %	Confluence granites								
Sample	G4	G5	G10A	G10B	G10C	G10D	G10E	G10F	G10G
Ne	0.0	0.0	0.0	0.0	0.0	0.0	0.0	0.0	0.0
Qtz	25.6	31.7	29.9	30.2	29.9	30.8	26.3	30.7	31.1
Orth	2.2	27.2	26.0	24.3	16.8	25.1	11.3	26.6	25.5
Ab	43.0	32.6	32.0	33.0	36.3	30.8	41.0	30.6	30.8
An	20.8	6.7	8.8	9.2	10.9	8.3	14.9	8.0	8.5
Hb	0.1	0.0	0.0	0.0	0.0	0.0	0.0	0.0	2.8
Bi	7.7	1.4	2.6	1.6	5.2	3.6	6.1	3.1	1.0
Mu	0.0	0.3	0.5	1.4	0.4	1.1	0.1	0.7	1.0
Mag	0.0	0.0	0.0	0.0	0.0	0.0	0.0	0.0	0.0
Haem	0.2	0.1	0.1	0.1	0.2	0.1	0.2	0.1	0.1
Ilm	0.1	0.0	0.0	0.0	0.0	0.0	0.1	0.0	0.0
Ap	0.3	0.0	0.0	0.1	0.2	0.1	0.2	0.1	0.1

vol. %									
Sample	G10H	G10I	G12	G13	G16	G18	S6G	S6I	S109
Ne	0.0	0.0	0.0	0.0	0.0	0.0	0.0	0.0	0.0
Qtz	28.4	31.3	29.1	29.1	31.9	26.9	29.9	30.7	21.6
Orth	13.4	25.3	19.2	12.5	29.2	2.6	18.9	18.8	21.3
Ab	38.6	30.5	36.1	40.3	30.8	45.3	36.0	35.6	33.8
An	13.6	8.2	11.7	13.8	6.8	17.7	9.7	9.5	12.7
Hb	0.0	0.0	2.3	0.0	0.0	0.0	0.0	0.0	0.0
Bi	5.1	3.4	1.4	4.1	1.0	7.1	5.1	5.0	9.7
Mu	0.5	1.0	0.0	0.0	0.2	0.0	0.0	0.0	0.0
Mag	0.0	0.0	0.0	0.0	0.0	0.0	0.0	0.0	0.0
Haem	0.1	0.1	0.1	0.1	0.0	0.2	0.1	0.1	0.3
Ilm	0.1	0.0	0.1	0.0	0.0	0.1	0.1	0.1	0.1
Ap	0.2	0.1	0.1	0.1	0.0	0.2	0.2	0.2	0.5

vol. %									
Sample	S42	S67	S69	S75	S76	S78	S81	S95	S96
Ne	0.0	0.0	0.0	0.0	0.0	0.0	0.0	0.0	0.0
Qtz	32.0	30.6	26.0	32.9	28.5	34.9	31.0	30.8	31.3
Orth	33.2	6.7	17.7	2.1	2.1	12.7	26.9	19.8	21.5
Ab	20.6	44.6	44.1	48.0	48.5	39.4	30.1	35.3	35.2
An	4.7	15.4	11.5	16.1	17.0	8.4	5.5	9.5	9.0
Hb	0.0	0.0	0.0	0.0	0.0	0.0	0.0	0.0	0.0
Bi	3.2	2.6	0.1	0.9	3.6	2.2	2.1	3.5	2.6
Mu	6.0	0.0	0.6	0.0	0.0	2.2	4.4	0.9	0.3
Mag	0.0	0.0	0.0	0.0	0.0	0.0	0.0	0.0	0.0
Haem	0.1	0.0	0.0	0.0	0.0	0.0	0.1	0.1	0.1
Ilm	0.0	0.0	0.0	0.0	0.0	0.0	0.0	0.0	0.0
Ap	0.2	0.1	0.0	0.0	0.1	0.0	0.1	0.1	0.1

vol. %	Parri granites								
Sample	D14	D17	G2	G3	G14	G15	G23	G30	G35
Ne	0.0	0.0	0.0	0.0	0.0	0.0	0.0	0.0	0.0
Qtz	26.3	34.1	30.8	30.1	31.0	32.7	28.9	42.7	25.7
Orth	15.1	5.8	23.3	22.2	5.2	4.5	21.7	1.2	24.7
Ab	45.9	40.7	35.7	40.0	52.3	51.3	40.2	27.4	35.5
An	10.7	11.6	5.2	4.0	9.6	9.4	6.0	10.2	8.0
Hb	0.0	0.0	0.0	0.0	0.0	0.0	0.0	0.0	0.0
Bi	1.6	1.8	1.3	0.9	1.3	0.8	1.0	0.0	1.0
Mu	0.4	6.0	3.5	2.7	0.5	1.2	2.1	14.0	5.0
Mag	0.0	0.0	0.0	0.0	0.0	0.0	0.0	3.7	0.0
Haem	0.0	0.0	0.0	0.0	0.1	0.0	0.0	0.0	0.0
Ilm	0.0	0.0	0.0	0.0	0.0	0.0	0.0	0.4	0.0
Ap	0.0	0.1	0.0	0.0	0.0	0.0	0.0	0.1	0.0

vol. %						Jutial granite			
Sample	G36	G43	G48	S97	S101	J1A	J1B	J1C	J1D
Ne	0.0	0.0	0.0	0.0	0.0	0.0	0.0	0.0	0.0
Qtz	30.5	31.6	34.6	28.9	30.0	31.3	31.5	32.0	30.8
Orth	17.7	23.3	16.6	31.0	31.7	25.0	25.9	25.4	31.3
Ab	40.1	29.2	31.6	30.0	30.6	31.9	31.0	30.1	26.5
An	9.3	6.2	6.8	5.3	4.5	4.9	5.3	5.6	4.6
Hb	0.0	0.0	0.0	0.0	0.0	0.0	0.0	0.0	0.0
Bi	0.9	4.3	3.1	1.2	1.2	1.7	1.9	2.0	3.5
Mu	1.5	5.0	7.1	3.5	1.8	5.0	4.2	4.8	3.1
Mag	0.0	0.0	0.0	0.0	0.0	0.0	0.0	0.0	0.0
Haem	0.0	0.1	0.1	0.0	0.0	0.1	0.1	0.1	0.1
Ilm	0.0	0.0	0.0	0.0	0.0	0.0	0.0	0.0	0.0
Ap	0.0	0.3	0.0	0.1	0.0	0.1	0.1	0.1	0.1

vol. %									Lcg Dykes
Sample	J1E	J1F	J1G	J1H	J1I	J11	J19	J15	S87
Ne	0.0	0.0	0.0	0.0	0.0	0.0	0.0	0.0	0.0
Qtz	33.9	31.2	27.3	32.4	30.9	26.9	30.4	36.5	24.3
Orth	22.9	26.5	26.0	22.7	25.2	36.5	31.7	22.7	38.8
Ab	30.7	30.1	35.4	32.2	31.5	27.3	27.7	30.6	30.6
An	5.5	5.4	7.5	4.6	5.5	5.1	5.7	6.1	4.5
Hb	0.0	0.0	0.0	0.0	0.0	0.0	0.0	0.0	0.0
Bi	1.7	2.0	2.1	1.6	1.9	2.8	2.3	1.5	0.7
Mu	5.1	4.6	1.6	6.3	4.8	1.1	2.1	2.5	0.9
Mag	0.0	0.0	0.0	0.0	0.0	0.0	0.0	0.0	0.0
Haem	0.1	0.1	0.1	0.1	0.1	0.1	0.1	0.1	0.0
Ilm	0.0	0.0	0.0	0.0	0.0	0.0	0.0	0.0	0.0
Ap	0.1	0.1	0.1	0.1	0.1	0.1	0.0	0.0	0.2

vol. % Sample	S92	S93	I8	I11	J7	J8	J9	J20	G39
Ne	0.0	0.0	0.0	0.0	0.0	0.0	0.0	0.0	0.0
Qtz	29.4	34.4	36.7	33.8	29.4	32.8	33.3	31.8	33.3
Orth	14.0	21.8	14.0	23.9	24.1	15.3	18.4	30.4	16.3
Ab	36.8	35.3	34.2	32.8	34.7	39.8	35.2	28.0	36.0
An	4.2	5.4	3.7	2.1	5.0	2.6	2.6	5.6	6.6
Hb	0.0	0.0	0.0	0.0	0.0	0.0	0.0	0.0	0.0
Bi	2.1	1.1	2.2	1.7	1.4	1.8	2.0	1.6	0.9
Mu	13.1	1.8	9.0	5.4	5.3	7.4	8.2	2.4	6.8
Mag	0.0	0.0	0.0	0.0	0.0	0.0	0.0	0.0	0.0
Haem	0.1	0.0	0.1	0.1	0.1	0.1	0.1	0.0	0.0
Ilm	0.0	0.0	0.0	0.0	0.0	0.0	0.0	0.0	0.0
Ap	0.2	0.1	0.1	0.2	0.2	0.1	0.2	0.1	0.1

vol. % Sample	S47	S51	S60	A9	A10	A14	M14	M18	T59
Ne	0.0	0.0	0.0	0.0	0.0	0.0	0.0	0.0	0.0
Qtz	31.3	23.6	29.2	39.6	39.9	35.0	32.6	32.1	27.5
Orth	8.9	42.2	28.9	3.1	2.3	13.8	20.2	25.1	39.7
Ab	48.7	27.9	35.0	38.6	36.7	35.9	34.3	30.9	25.3
An	10.1	5.1	5.2	4.1	3.8	4.0	1.5	5.4	5.5
Hb	0.0	0.0	0.0	0.0	0.0	0.0	0.0	0.0	0.0
Bi	0.8	0.4	1.3	1.6	3.1	2.1	2.9	2.3	0.7
Mu	0.0	0.8	0.4	12.7	13.8	8.8	7.9	4.0	1.3
Mag	0.0	0.0	0.0	0.0	0.0	0.0	0.0	0.0	0.0
Haem	0.0	0.0	0.1	0.1	0.2	0.1	0.1	0.1	0.0
Ilm	0.0	0.0	0.0	0.0	0.0	0.0	0.0	0.0	0.0
Ap	0.0	0.0	0.0	0.1	0.3	0.2	0.5	0.1	0.0

vol. % Sample	T71	T74	L17E	L17F	L17G	R8	Qtz-Diorite I3
Ne	0.0	0.0	0.0	0.0	0.0	0.0	0.0
Qtz	42.8	28.2	27.1	25.7	24.0	34.5	5.8
Orth	6.3	29.7	22.6	18.4	28.5	36.6	5.4
Ab	31.5	32.2	44.7	50.0	42.1	22.6	60.5
An	3.6	4.4	4.1	4.4	3.7	2.8	19.1
Hb	0.0	0.0	0.0	0.0	0.0	0.0	0.0
Bi	1.9	1.0	0.5	0.5	0.5	0.8	4.4
Mu	13.5	4.6	0.9	1.1	1.2	2.5	4.6
Mag	0.0	0.0	0.0	0.0	0.0	0.0	0.0
Haem	0.0	0.0	0.0	0.0	9.0	0.0	0.1
Ilm	0.0	0.0	0.0	0.0	0.0	0.0	0.0
Ap	0.4	0.0	0.0	0.0	9.0	0.0	0.1

Appendix 5 - Representative Thermocalc Output

Mineral equilibria and estimated pressure-temperature conditions with uncertainties for four representative metamorphic samples : G31 (pelitic gneiss, Sassi); S17 (gnt-bio-amphibolite, Sassi); G7 (Kohistan metasediment) and A7 (pelitic gneiss, Tarshing), using the program developed by Powell and Holland (1988).

The activities of the equilibrium endmember phases are entered in an input file for each sample, and a series of runs is made in both temperature-only and pressure-only mode, initially using relatively large P or T windows in order to incorporate all possible reactions. The windows are decreased in size during operation of the program until the optimum statistics are generated on the resulting independent set of reactions. In this work, default uncertainties on endmember activities were used in order to minimise underestimation of this source of error.

Endmember abbreviations : py = pyrope; gr = grossular; alm = almandine; an = anorthite; ab = albite; phl = phlogopite; ann = annite; east = eastonite; naph = Na-phlogopite; mu = muscovite; pa = pargasite; cel = celadonite; ky = kyanite; q = quartz; hb = hornblende; ed = edenite; parg = pargasite; cz = clinozoisite.

Statistical abbreviations : av P; sd; avT; sd; cor fit are average P, average T and their standard errors, correlation coefficient for PT and sigmafit. All pressures are in kbar, temperatures in °C. The final pressure and temperature estimates used are given in Table 4.2.

(1) Sample G-31 : Gnt-ky-2-mica-gneiss, Sassi

(i) Average temperature calculations

An independent set of reactions has been calculated for sd(T) limit = 100°C. Suggested P = 8.5 kbar for x(CO2) = 0.2 and x(H2O) = 0.8.

	py	gr	alm	an	ab	phl	ann
a	0.0056	9.03e-4	0.364	0.419	0.738	0.0483	0.0398
sd(ln a)	0.6095	0.7344	0.07363	0.1013	0.0206	0.3652	0.3904

	east	naph	mu	pa	cel	ky	q	H2O
a	0.0465	0.0020	0.664	0.511	0.0471	1.00	1.00	0.800
sd(ln a)	0.3691	5.0480	0.0206	0.0717	0.367	0	0	

reactions

1) pa + q = ab + ky + H2O
2) gr + 2pa + 3q = 3an + 2ab + 2H2O
3) 7phl + 12ky = 5py + 3east + 4mu
4) py + mu = phl + 2ky + q
5) 3phl + 2pa + 9q = 2py + 2ab + 3cel + 2H2O
6) naph + 9pa + 3cel = 10ab + 3east + 6ky + 10H2O
7) ann + 2pa + 3q = alm + 2ab + mu + 2H2O

calculations

	T(P)	sd	dP/dT	ln_K
1	694	17	0.0708	0.368
2	684	29	0.0284	5.135
3	613	93	-5.5704	-15.606
4	635	98	-0.1028	2.574
5	743	71	-0.1001	-9.728
6	678	65	0.0463	9.190
7	658	30	0.1539	2.539

Diagnostic information

av, sd, fit are result of doubling (first table) /halving (second table) uncertainty on ln a :a ln a is suspect if any are v different from lsq values.e* are ln a residuals normalised to ln a uncertainties : large absolute values, say >2.5, point to suspect info.hat are the diagonal elements of the hat matrix :large values, say >0.47, point to influential data. For 95% confidence, fit (= sd(fit)) should be less than 1.45.

	av	sd	fit
lsq	690	18	1.09

	T	sd	fit	e*	hat
py	690	18	1.07	0.4	0.02
gr	690	18	1.08	-0.3	0.06
alm	690	18	1.07	0.3	0.00
an	690	18	1.09	0.1	0.01
ab	689	19	1.09	-0.0	0.02
phl	690	18	1.08	-0.2	0.01
ann	690	16	0.97	-1.3	0.00
east	690	17	1.04	0.8	0.00
naph	690	18	1.08	0.4	0.00

mu	690	18	1.08	0.1	0.00
pa	687	23	1.08	0.1	0.24
cel	690	14	0.85	-1.8	0.00
ky	690	18	1.09	0	0
q	690	18	1.09	0	0
H2O	690	18	1.09	-0.0	0.00

	T	sd	fit	e*	hat
py	688	18	1.11	0.4	0.02
gr	688	17	1.10	-0.3	0.06
alm	690	18	1.09	0.3	0.00
an	689	18	1.09	0.1	0.01
ab	690	18	1.09	-0.0	0.02
phl	689	18	1.09	-0.2	0.01
ann	690	23	1.39	-1.3	0.00
east	689	19	1.15	0.8	0.00
naph	690	19	1.13	0.4	0.00
mu	690	18	1.09	0.1	0.00
pa	690	16	1.09	0.1	0.24
cel	689	24	1.46	-1.8	0.00
ky	690	18	1.09	0	0
q	690	18	1.09	0	0
H2O	690	18	1.09	-0.0	0.00

P	6.9	7.3	7.7	8.1	8.5	8.9	9.3	9.7	10.1	10.5
av T	660	667	675	682	690	697	704	711	718	725
sd	22	21	20	19	18	18	18	18	19	20
f	1.4	1.3	1.2	1.1	1.1	1.1	1.1	1.1	1.1	1.2

(ii) Average pressure calculations

An independent set of reactions has been calculated for sd(P) limit = 2.0 kbars :

	py	gr	alm	an	ab	phl	ann
east							
a	0.0055	9.03e-4	0.364	0.419	0.738	0.0483	0.0398	0.0465
sd(lna)	0.6095	0.7344	0.0736	0.1013	0.0206	0.3652	0.3904	0.3691

	naph	mu	pa	cel	ky	q	H2O
a	0.00198	0.664	0.511	0.0471	1.00	1.00	0.800
sd(lna)	5.04796	0.02059	0.07172	0.3677	0	0	

reactions
1) 3an = gr + 2ky + q
2) 3an + pa = gr + ab + 3ky + H2O
3) 3an + phl = py + gr + mu
4) 3an + 2phl = py + gr + east + cel
5) 4gr + 3phl + 12ky = py + 12an + 3east
6) 3an + ann = gr + alm + mu
7) 5gr + 3phl + pa + 12ky = 15an + 3east + naph

calculations

	P(T)	sd	dP/dT	ln_K
1	8.7	1.01	0.0161	-4.400
2	8.9	1.19	0.0070	-4.032

3	8.3	1.24	0.0069	-6.974
4	8.7	1.54	0.0038	-9.657
5	9.2	1.07	0.0190	12.290
6	8.1	0.98	0.0136	-2.596
7	9.6	1.53	0.0173	16.331

Diagnostic information

av, sd, fit are result of doubling (first table) /halving (second table) uncertainty on ln a :a ln a is suspect if any are v different from lsq values.e* are ln a residuals normalised to ln a uncertainties :large absolute values, say >2.5, point to suspect info.hat are the diagonal elements of the hat matrix :large values, say >0.47, point to influential data. For 95% confidence, fit (= sd(fit)) should be less than 1.45.

	av	sd	fit		
lsq	9.10	0.76	1.03		
	P	sd	fit	e*	hat
py	9.13	0.74	1.01	0.6	0.01
gr	9.19	0.95	1.03	0.1	0.43
alm	9.12	0.75	1.02	0.3	0.00
an	9.13	0.82	1.03	-0.1	0.07
ab	9.10	0.77	1.03	-0.0	0.01
phl	9.10	0.75	1.02	-0.3	0.00
ann	9.27	0.66	0.89	-1.4	0.04
east	9.02	0.74	1.00	0.6	0.03
naph	9.10	0.75	1.02	0.4	0.00
mu	9.10	0.75	1.03	0.1	0.00
pa	9.13	0.82	1.03	0.1	0.09
cel	8.87	0.62	0.83	-1.6	0.05
ky	9.10	0.76	1.03	0	0
q	9.10	0.76	1.03	0	0
H2O	9.10	0.76	1.03	-0.0	0.00

	P	sd	fit	e*	hat
py	9.04	0.79	1.08	0.6	0.01
gr	9.02	0.56	1.03	0.1	0.43
alm	9.09	0.76	1.04	0.3	0.00
an	9.09	0.74	1.03	-0.1	0.07
ab	9.10	0.76	1.03	-0.0	0.01
phl	9.10	0.76	1.04	-0.3	0.00
ann	8.62	0.95	1.35	-1.4	0.04
east	9.20	0.78	1.08	0.6	0.03
naph	9.10	0.79	1.08	0.4	0.00
mu	9.10	0.76	1.03	0.1	0.00
pa	9.09	0.73	1.03	0.1	0.09
cel	9.52	0.93	1.32	-1.6	0.05
ky	9.10	0.76	1.03	0	0
q	9.10	0.76	1.03	0	0
H2O	9.10	0.76	1.03	-0.0	0.00

T°C	600	625	650	675	700	725	750	775
av P	6.3	6.9	7.6	8.3	9.1	9.9	10.7	11.5
sd	1.30	1.10	0.93	0.81	0.76	0.81	0.93	1.11
f	1.9	1.6	1.3	1.1	1.0	1.1	1.2	1.4

(2) Sample S 17 : Gnt-biotite-amphibolite, Sassi

(i) Average temperature calculations

An independent set of reactions has been calculated for sd(T) limit = 80°C. Suggested P = 9.8 kbar for x(CO2) = 0.2 and x(H2O) = 0.8.

	py	gr	alm	phl	ann	east	an
a	8.90e-4	0.0209	0.237	0.0262	0.109	0.0178	0.259
sd(ln a)	0.7352	0.4723	0.1307	0.4216	0.2462	0.4507	0.1646

	ab	hb	ed	parg	q	H2O
a	0.836	0.0049	5.05e-4	0.0044	1.00	0.800
sd(ln a)	0.0081	0.5191	0.9147	0.6609	0	

reactions
1) 15east + 12hb = 11py + 4gr + 15phl + 12an + 12H2O
2) 7east + 4hb + 4q = 3py + 7phl + 8an + 4H2O
3) 2gr + 3alm + 3east + 6q = 2py + 3ann + 6an
4) 6east + ab + 5hb = 3py + 6phl + 8an + ed + 4H2O
5) 4py + 6ann + 12an + 3parg = 4gr + 6alm + 6east + 3ab + 3hb

calculations

	T(P)	sd	dP/dT	ln_K
1	570	79	-0.3885	-39.251
2	557	75	0.0890	-7.869
3	633	68	0.0247	-4.664
4	539	70	0.1026	-10.345
5	594	76	0.0265	9.087

Diagnostic information

av, sd, fit are result of doubling (first table) /halving (second table) uncertainty on ln a :a ln a is suspect if any are v different from lsq values.e* are ln a residuals normalised to ln a uncertainties :large absolute values, say >2.5, point to suspect info.hat are the diagonal elements of the hat matrix :large values, say >0.38, point to influential data. For 95% confidence, fit (= sd(fit)) should be less than 1.54.

	av	sd	fit
lsq	603	61	1.08

	T	sd	fit	e*	hat
py	572	63	0.96	-0.9	0.28
gr	602	64	1.08	0.0	0.06
alm	599	61	1.06	0.2	0.01
phl	608	58	1.01	0.7	0.01
ann	592	61	1.03	-0.4	0.03
east	602	72	1.08	0.0	0.21
an	611	70	1.07	0.2	0.14
ab	603	61	1.08	-0.0	0.00
hb	617	50	0.86	-1.2	0.03

ed	621	57	0.96	0.9	0.09
parg	598	62	1.06	0.4	0.04
q	603	61	1.08	0	0
H2O	603	61	1.08	0.0	0.00

	T	sd	fit	e*	hat
py	639	55	1.20	-0.9	0.28
gr	604	59	1.08	0.0	0.06
alm	604	62	1.08	0.2	0.01
phl	597	65	1.16	0.7	0.01
ann	607	62	1.10	-0.4	0.03
east	604	56	1.08	0.0	0.21
an	600	58	1.08	0.2	0.14
ab	603	61	1.08	-0.0	0.00
hb	590	70	1.25	-1.2	0.03
ed	582	64	1.21	0.9	0.09
parg	609	61	1.10	0.4	0.04
q	603	61	1.08	0	0
H2O	603	61	1.08	0.0	0.00

P	8.5	8.8	9.1	9.4	9.7	10.0	10.3	10.6	10.9	11.0
av T	558	567	576	585	594	603	612	622	631	634
sd	68	65	63	62	61	61	62	64	66	67
f	1.2	1.1	1.1	1.1	1.1	1.1	1.1	1.1	1.2	1.2

(ii) Average pressure calculations

An independent set of reactions has been calculated for sd(P) limit = 1.5 kbars. Suggested T = 600°C for x(CO2) = 0.2 and x(H2O) = 0.8.

	py	gr	alm	phl	ann	east	an
a	8.90e-4	0.0209	0.237	0.0262	0.109	0.0178	0.259
sd(ln a)	0.7352	0.4723	0.1307	0.4216	0.2462	0.4507	0.1646

	ab	hb	ed	parg	q	H2O
a	0.836	0.00488	5.05e-4	0.00442	1.00	0.800
sd(ln a)	0.0081	0.5191	0.9147	0.6609	0	

reactions
1) 4ann + 11an + 2hb = 5gr + 4alm + 4east + 13q + 2H2O
2) 9ann +36an +12parg = 10py +20gr + 9alm + 9east + 12ab+12H2O
3) 19ann +36an +12parg = 20gr +19alm +10phl +9east +12ab+12H2O
4) 19ann +36an +9ed +3parg = 20gr + 19alm + 19phl + 12ab+12H2O
5) 4ann + 11an + 2parg = 5gr + 4alm + 4east + 2ab + 5q + 2H2O

calculations

	P(T)	sd	dP/dT	ln_K
1	9.4	1.14	0.0116	-6.841
2	10.9	1.46	0.0030	-65.331
3	9.9	1.36	0.0084	-23.712
4	10.1	1.43	0.0099	-0.701
5	10.1	1.24	0.0120	-7.002

Diagnostic information

av, sd, fit are result of doubling (first table) /
halving (second table) uncertainty on ln a :
a ln a is suspect if any are v different from lsq values.
e* are ln a residuals normalised to ln a uncertainties :
large absolute values, say >2.5, point to suspect info.
hat are the diagonal elements of the hat matrix :
large values, say >0.38, point to influential data.
For 95% confidence, fit (= sd(fit)) should be less than 1.54

	av	sd	fit
lsq	9.77	1.12	1.02

	P	sd	fit	e*	hat
py	9.68	1.01	0.92	-0.9	0.01
gr	9.60	1.64	1.02	-0.1	0.42
alm	9.85	1.13	1.01	0.2	0.02
phl	9.86	1.06	0.96	0.7	0.01
ann	10.02	1.15	0.98	-0.4	0.06
east	9.75	1.21	1.02	-0.0	0.12
an	9.44	1.39	1.00	0.2	0.22
ab	9.77	1.12	1.02	-0.0	0.00
hb	10.07	0.93	0.83	-1.1	0.05
ed	9.59	1.01	0.91	0.9	0.03
parg	9.76	1.09	1.00	0.4	0.00
q	9.77	1.12	1.02	0	0
H2O	9.77	1.12	1.02	0.0	0.00

	P	sd	fit	e*	hat
py	9.97	1.32	1.22	-0.9	0.01
gr	9.81	0.92	1.02	-0.1	0.42
alm	9.74	1.11	1.03	0.2	0.02
phl	9.66	1.18	1.09	0.7	0.01
ann	9.68	1.10	1.04	-0.4	0.06
east	9.78	1.05	1.02	-0.0	0.12
an	9.86	1.02	1.03	0.2	0.22
ab	9.77	1.12	1.02	-0.0	0.00
hb	9.48	1.25	1.17	-1.1	0.05
ed	10.01	1.23	1.15	0.9	0.03
parg	9.78	1.15	1.05	0.4	0.00
q	9.77	1.12	1.02	0	0
H2O	9.77	1.12	1.02	0.0	0.00

T°C	500	525	550	575	600	625	650	675	700	725	750
av P	8.7	9.0	9.2	9.5	9.8	10.0	10.3	10.6	10.9	11.1	11.4
sd	1.32	1.23	1.17	1.13	1.12	1.14	1.18	1.26	1.35	1.46	1.58
f	1.4	1.2	1.1	1.1	1.0	1.0	1.0	1.1	1.1	1.2	1.2

(3) Sample G-7 : Gnt-2-mica gneiss; Jaglot

(i) Average temperature calculations

An independent set of reactions has been calculated for sd(T) limit = 100°C. Suggested P = 6.5 kbar for x(CO2) = 0.2 and x(H2O) = 0.8.

	py	gr	alm	cz	mu	pa	cel	an
a	5.98e-4	0.0198	0.196	0.712	0.691	0.484	0.0335	0.751
sd(lna)	0.7547	0.4787	0.1582	0.0249	0.0171	0.0799	0.4004	0.0186

	ab	phl	ann	east	naph	q	H2O
a	0.501	0.0415	0.0542	0.0406	9.87e-4	1.00	0.800
sd(ln a)	0.0749	0.3804	0.3476	0.3825	1.0e+1	0	

reactions
1) 4cz + q = gr + 5an + 2H2O
2) 6cz + ab = 2gr + pa + 6an + 2H2O
3) 3cel + 6an = py + 2gr + 3mu + 6q
4) 24cz + 3cel + 8phl = 9py + 16gr + 11mu + 12H2O
5) 24cz + 11cel + 8east = 9py + 16gr + 19mu + 12H2O
6) alm + 4cz + mu + q = 8an + ann + 2H2O
7) 24cz + pa + 3cel = 7gr + 3mu + 27an + naph + 12H2O

calculations

	T(P)	sd	dP/dT	ln_K
1	565	13	0.0286	-3.990
2	572	25	0.0282	-7.549
3	597	80	0.0164	-4.468
4	573	68	-0.1342	-89.783
5	548	87	-0.1346	-65.401
6	557	9	0.0223	-1.842
7	547	47	0.0285	-24.116

Diagnostic information
av, sd, fit are result of doubling (first table) /halving (second table) uncertainty on ln a :a ln a is suspect if any are v different from lsq values.e* are ln a residuals normalised to ln a uncertainties :large absolute values, say >2.5, point to suspect info.hat are the diagonal elements of the hat matrix :large values, say >0.47, point to influential data. For 95% confidence, fit (= sd(fit)) should be less than 1.45.

	av	sd	fit
lsq	561	6	0.51

	T	sd	fit	e*	hat
py	561	6	0.50	0.2	0.00
gr	561	6	0.47	-0.5	0.03
alm	561	6	0.51	-0.0	0.01
cz	561	6	0.50	0.1	0.09
mu	561	6	0.51	0.0	0.00
pa	562	6	0.49	-0.2	0.08
cel	561	6	0.37	-0.9	0.01
an	561	7	0.50	-0.1	0.17
ab	562	6	0.49	0.2	0.07
phl	561	6	0.50	0.1	0.00

ann	561	6	0.51	0.0	0.05
east	561	6	0.51	0.1	0.00
naph	561	6	0.50	0.3	0.00
q	561	6	0.51	0	0
H2O	561	6	0.51	0.0	0.01

	T	sd	fit	e*	hat
py	561	6	0.52	0.2	0.00
gr	562	5	0.59	-0.5	0.03
alm	561	6	0.51	-0.0	0.01
cz	561	5	0.51	0.1	0.09
mu	561	6	0.51	0.0	0.00
pa	561	5	0.51	-0.2	0.08
cel	562	5	0.69	-0.9	0.01
an	561	5	0.51	-0.1	0.17
ab	561	5	0.51	0.2	0.07
phl	561	6	0.51	0.1	0.00
ann	561	5	0.51	0.0	0.05
east	561	6	0.51	0.1	0.00
naph	561	6	0.54	0.3	0.00
q	561	6	0.51	0	0
H2O	561	6	0.51	0.0	0.01

P	5.0	5.4	5.8	6.2	6.6	7.0	7.4	7.8	8.0
av T	500	516	531	546	561	576	591	607	614
sd	6	5	6	6	6	6	6	6	6
f	1.0	0.8	0.7	0.5	0.5	0.6	0.7	0.9	1.0

(ii) Average pressure calculations

An independent set of reactions has been calculated for sd(P) limit = 2.0 kbars. Suggested T = 575°C for x(CO2) = 0.2 and x(H2O) = 0.8.

	py	gr	alm	cz	mu	pa	cel	an
a	5.98e-4	0.0198	0.196	0.712	0.691	0.484	0.0335	0.751
sd(lna)	0.7547	0.4787	0.1582	0.0249	0.0171	0.0799	0.4004	0.0186

	ab	phl	ann	east	naph	q	H2O
a	0.501	0.0415	0.0542	0.0406	9.87e-4	1.00	0.800
sd(ln a)	0.0749	0.3804	0.3476	0.3825	1.0e+1	0	

reactions
1) 3an + phl = py + gr + mu
2) cel + 3an + east = py + gr + 2mu
3) 3cel + 6an = py + 2gr + 3mu + 6q
4) 2py + 24cz + 3cel = 5gr + 33an + 3phl + 12H2O
5) 3an + ann = gr + alm + mu
6) py + 2pa + 3cel = 2ab + 3east + 9q + 2H2O
7) 3alm + 24cz + pa + 3cel = 4gr + 36an + 3ann + naph + 12H2O

calculations

	P(T)	sd	dP/dT	ln_K
1	6.8	0.99	0.0061	-7.672
2	6.4	1.15	0.0098	-4.624
3	6.1	1.28	0.0163	-4.468

4	6.9	0.37	0.0236	-5.389
5	7.0	0.61	0.0141	-2.148
6	8.0	1.80	0.0135	8.067
7	7.2	0.98	0.0244	-17.673

Diagnostic information
av, sd, fit are result of doubling (first table) /
halving (second table) uncertainty on ln a :
a ln a is suspect if any are v different from lsq values.
e* are ln a residuals normalised to ln a uncertainties :
large absolute values, say >2.5, point to suspect info.
hat are the diagonal elements of the hat matrix :
large values, say >0.47, point to influential data.
For 95% confidence, fit (= sd(fit)) should be less than 1.45

	av	sd	fit
lsq	6.94	0.15	0.55

	P	sd	fit	e*	hat
py	6.95	0.15	0.53	0.4	0.02
gr	6.95	0.15	0.53	-0.4	0.02
alm	6.95	0.15	0.54	0.1	0.03
cz	6.95	0.16	0.55	0.1	0.09
mu	6.94	0.15	0.55	0.0	0.00
pa	6.92	0.15	0.51	-0.3	0.05
cel	6.95	0.15	0.44	-0.8	0.00
an	6.95	0.18	0.55	-0.0	0.18
ab	6.92	0.15	0.51	0.3	0.04
phl	6.94	0.15	0.55	0.0	0.00
ann	6.95	0.16	0.54	-0.2	0.12
east	6.94	0.15	0.55	0.1	0.00
naph	6.94	0.15	0.54	0.3	0.00
q	6.94	0.15	0.55	0	0
H2O	6.94	0.15	0.55	0.0	0.01

	P	sd	fit	e*	hat
py	6.93	0.14	0.59	0.4	0.02
gr	6.92	0.14	0.59	-0.4	0.02
alm	6.94	0.14	0.55	0.1	0.03
cz	6.94	0.14	0.55	0.1	0.09
mu	6.94	0.15	0.55	0.0	0.00
pa	6.95	0.14	0.56	-0.3	0.05
cel	6.93	0.15	0.70	-0.8	0.00
an	6.94	0.14	0.55	-0.0	0.18
ab	6.95	0.14	0.56	0.3	0.04
phl	6.94	0.15	0.55	0.0	0.00
ann	6.93	0.13	0.56	-0.2	0.12
east	6.94	0.15	0.55	0.1	0.00
naph	6.94	0.15	0.58	0.3	0.00
q	6.94	0.15	0.55	0	0
H2O	6.94	0.15	0.55	0.0	0.01

T°C	475	500	525	550	575	600	625	650	675
av P	4.4	5.1	5.7	6.3	6.9	7.6	8.2	8.9	9.5
sd	0.20	0.15	0.14	0.14	0.15	0.15	0.16	0.21	0.26
f	1.5	1.1	0.8	0.5	0.5	0.8	1.0	1.3	1.6

(4) Sample A-7 : Gnt-2-mica-zoisite-gneiss, Tarshing

(1) Average temperature calculations

An independent set of reactions has been calculated for sd(T) limit = 100°C. Suggested P = 8.0 kbar for x(CO2) = 0.2 and x(H2O) = 0.8.

	py	gr	alm	cz	an	ab	phl	ann
a	0.0075	0.0180	0.137	0.938	0.650	0.586	0.109	0.0168
sd(lna)	0.5822	0.4903	0.2112	0.0012	0.0368	0.0513	0.2696	0.4980

	east	naph	mu	pa	cel	q	H2O
a	0.0684	0.0041	0.659	0.480	0.0630	1.00	0.800
sd(ln a)	0.3273	2.4552	0.0213	0.0811	0.3366	0	

reactions

1) 4cz + q = gr + 5an + 2H2O
2) 6cz + ab = 2gr + 6an + pa + 2H2O
3) 24cz + 3phl = py + 8gr + 24an + 3east + 12H2O
4) 2py + 24cz + 3cel = 5gr + 33an + 3phl + 12H2O
5) 2py + 24cz + 3mu = 5gr + 33an + 3east + 12H2O
6) 3an + ann = gr + alm + mu
7) 3naph + 5pa + 3cel = 2py + 8ab + 3east + 8H2O

calculations

	T(P)	sd	dP/dT	ln_K
1	567	13	0.0308	-5.918
2	555	23	0.0312	-10.440
3	568	19	0.0357	-47.243
4	552	14	0.0259	-21.356
5	560	13	0.0271	-29.790
6	569	47	0.0154	-1.045
7	682	99	0.0554	6.367

Diagnostic information

av, sd, fit are result of doubling (first table) /halving (second table) uncertainty on ln a :a ln a is suspect if any are v different from lsq values.e* are ln a residuals normalised to ln a uncertainties :large absolute values, say >2.5, point to suspect info.hat are the diagonal elements of the hat matrix :large values, say >0.47, point to influential data. For 95% confidence, fit (= sd(fit)) should be less than 1.45.

	av	sd	fit
lsq	579	7	1.13

	T	sd	fit	e*	hat
py	580	6	0.98	-1.4	0.00
gr	580	7	1.09	0.8	0.02
alm	580	7	1.11	-0.3	0.00
cz	579	7	1.13	-0.0	0.00
an	583	11	1.11	0.3	0.47
ab	578	8	1.11	-0.3	0.03
phl	579	7	1.07	0.7	0.00
ann	580	7	1.08	0.8	0.01

east	579	7	1.12	0.3	0.00
naph	579	7	1.06	1.0	0.00
mu	579	7	1.13	-0.0	0.00
pa	578	8	1.10	0.4	0.08
cel	579	7	1.03	-1.2	0.00
q	579	7	1.13	0	0
H2O	579	7	1.13	-0.0	0.01

	T	sd	fit	e*	hat
py	579	9	1.37	-1.4	0.00
gr	578	8	1.22	0.8	0.02
alm	579	7	1.13	-0.3	0.00
cz	579	7	1.13	-0.0	0.00
an	578	6	1.13	0.3	0.47
ab	580	7	1.13	-0.3	0.03
phl	579	8	1.16	0.7	0.00
ann	578	8	1.20	0.8	0.01
east	579	7	1.13	0.3	0.00
naph	579	9	1.34	1.0	0.00
mu	579	7	1.13	-0.0	0.00
pa	580	7	1.13	0.4	0.08
cel	580	8	1.28	-1.2	0.00
q	579	7	1.13	0	0
H2O	579	7	1.13	-0.0	0.01

P	6.4	6.8	7.	7.6	8.0	8.4	8.8	9.2	9.6	10.0
av T	523	537	551	565	579	593	607	621	635	649
sd	11	10	9	8	7	7	7	7	7	7
f	1.7	1.6	1.4	1.3	1.1	1.0	0.9	0.8	0.8	0.8

(ii) Average pressure calculations

An independent set of reactions has been calculated for sd(P) limit = 2.0 kbars. Suggested T = 575°C for x(CO2) = 0.2 and x(H2O) = 0.8.

	py	gr	alm	cz	an	ab	phl	ann
a	0.0075	0.0180	0.137	0.938	0.650	0.586	0.109	0.0168
sd(lna)	0.5822	0.4903	0.2112	0.0012	0.0368	0.0513	0.2696	0.4980

	east	naph	mu	pa	cel	q	H2O
a	0.0684	0.00407	0.659	0.480	0.0630	1.00	0.800
sd(ln a)	0.32726	2.45519	0.02126	0.08107	0.33661	0	

reactions
1) 3an + phl = py + gr + mu
2) 3an + 2phl = py + gr + east + cel
3) 6an + 3phl = py + 2gr + 3east + 6q
4) 7py + 24cz + 8mu = 48an + 5phl + 3east + 12H2O
5) 3an + ann = gr + alm + mu
6) 2py + 3gr + 4pa + 3cel = 9an + 4ab + 3phl + 4H2O
7) 6an + 2ann + naph = 2gr + 2alm + east + pa + cel

calculations

	P(T)	sd	dP/dT	ln_K
1	8.7	0.84	0.0085	-5.818
2	9.2	1.09	0.0052	-8.629

3	8.2	1.24	0.0104	-11.737
4	8.5	0.35	0.0207	-0.701
5	8.1	0.73	0.0154	-1.045
6	8.5	0.66	0.0180	20.402
7	9.4	1.36	0.0154	-1.934

Diagnostic information
av, sd, fit are result of doubling (first table) /halving (second table) uncertainty on ln a :a ln a is suspect if any are v different from lsq values.e* are ln a residuals normalised to ln a uncertainties :large absolute values, say >2.5, point to suspect info.hat are the diagonal elements of the hat matrix :large values, say >0.47, point to influential data. For 95% confidence, fit (= sd(fit)) should be less than 1.45.

	av	sd	fit
lsq	7.97	0.21	1.19

	P	sd	fit	e*	hat
py	7.93	0.19	1.03	-1.5	0.03
gr	7.96	0.21	1.16	0.7	0.01
alm	7.96	0.21	1.17	-0.3	0.01
cz	7.97	0.21	1.19	-0.0	0.00
an	7.98	0.33	1.19	-0.0	0.47
ab	8.00	0.21	1.16	-0.4	0.02
phl	7.96	0.20	1.12	0.7	0.01
ann	7.94	0.21	1.14	0.8	0.05
east	7.97	0.21	1.18	0.3	0.00
naph	7.97	0.20	1.13	1.0	0.00
mu	7.97	0.21	1.18	-0.0	0.00
pa	8.02	0.22	1.14	0.5	0.05
cel	7.98	0.19	1.08	-1.2	0.00
q	7.97	0.21	1.19	0	0
H2O	7.97	0.21	1.18	-0.1	0.01

	P	sd	fit	e*	hat
py	8.05	0.25	1.42	-1.5	0.03
gr	8.00	0.22	1.26	0.7	0.01
alm	7.98	0.21	1.19	-0.3	0.01
cz	7.97	0.21	1.19	-0.0	0.00
an	7.97	0.17	1.19	-0.0	0.47
ab	7.96	0.21	1.19	-0.4	0.02
phl	7.98	0.22	1.22	0.7	0.01
ann	8.02	0.22	1.25	0.8	0.05
east	7.97	0.21	1.19	0.3	0.00
naph	7.97	0.25	1.38	1.0	0.00
mu	7.97	0.21	1.19	-0.0	0.00
pa	7.95	0.21	1.20	0.5	0.05
cel	7.96	0.24	1.34	-1.2	0.00
q	7.97	0.21	1.19	0	0
H2O	7.97	0.21	1.19	-0.1	0.01

T°C	475	500	525	550	575	600	625	650	675	700
av P	5.3	6.0	6.6	7.3	8.0	8.6	9.3	10.0	10.7	11.4
sd	0.43	0.37	0.31	0.26	0.21	0.18	0.19	0.19	0.20	0.20
f	2.6	2.2	1.8	1.5	1.2	0.9	0.8	0.7	0.8	1.0

Appendix 6 - Sample Catalogue

Samples S1-S40; T1-T49; R1-R8 and L1-L17 were collected in Spring 1990; all other samples were collected in Autumn 1990.

The term 'leucogranite' has been reserved for those granite dykes and sheets that intrude the NPHM. The grid references apply to US AMS map NI 43-2 (series U502). Granite deformation (def'n) : the indicated granites have been intensely deformed; minor deformation is indicated by a tick mark in parentheses.

Mineral abbreviations : qz = quartz; ksp = k-feldspar; plag = plagioclase; tm = tourmaline; chl = chlorite; bi = biotite; gt = garnet; hb = hornblende; ep = epidote; mu = muscovite; aug = augite; sph = sphene; diop = diopside; act = actinolite; cc = calcite; zo = zoisite; ky = kyanite; sill = sillimanite; tr = tremolite; cord = cordierite; oliv = olivine. Minerals in parentheses are present in subsidiary proportions. The accessory phases zircon, apatite and monazite have been ommitted.

Other abbreviations : L. = lower; U = upper (refer to upstream or downstream part of valley). The orientated samples were collected for microstructural work, and were reorientated prior to thin-sectioning. Th'calc = thermocalc, refering to samples that have successfully yielded P-T measurements.

Sample	Lithology	Location	Grid Ref	Granite def'n	Thin Section	Mineralogy	Orientated	Polished Section	Th'calc	XRF	INAA	Isotopes	Rb/Sr dating	Ar-Ar dating
S1	leucogranite	Shahbatot	6619	√	√	qz; ksp; plag; tm (chl)								
S2	biotite gneiss	Shahbatot	6619				√							
S3	granite	Shahbatot	6522	√	√	qz; ksp; plag; bi	√							
S4	gt amphibolite	Shahbatot	6522		√	gt; bi; hb; ep; ksp; plag; qz	√							
S5	leucogranite	Shahbatot	6619	√	√	qz; ksp; plag; bi (tm)	√							
S6 A	granite	Indus conf.	5519	undef	√	qz; ksp; plag; bi; mu; ep	√							
S6 B	granite	Indus conf.	5519	undef	√	qz; ksp; plag; bi; mu; ep								
S6 C	granite	Indus conf.	5519	undef	√	qz; ksp; plag; bi; mu; ep								
S6 D	granite	Indus conf.	5519	undef	√	qz; ksp; plag; bi; mu; ep								
S6 E	granite	Indus conf.	5519	undef	√	qz; ksp; plag; bi; mu; ep								
S6 F	granite	Indus conf.	5519	undef	√	qz; ksp; plag; bi; mu; ep								
S6 G	granite	Indus conf.	5519	undef	√	qz; ksp; plag; bi; mu; ep				√		Sr & Nd		
S6 H	granite	Indus conf.	5519	undef	√	qz; ksp; plag; bi; mu; ep								
S6 I	granite	Indus conf.	5519	undef	√	qz; ksp; plag; bi; mu; ep				√				
S7	metagabbro	Indus conf.	5519		√	bi; hb; ep; plag; qz	√							
S8	amphibolite	Sassi	6425		√	aug; hb; plag; qz (bi)	√							
S9	biotite gneiss	Sassi	6425				√							
S10	amphibolite	Sassi	6425				√							
S11	amphibolite	Sassi	6425		√	hb; plag; ksp (chl, sph).	√							
S12	granite	Sassi	6425	√	√	qz; ksp; plag (mu)	√							
S13	pelitic gneiss	Sassi	6425		√	gt; bi; mu; plag; qz	√	√						
S14	biotite granite	Sassi	6425				√							
S15	calcsilicate	Sassi	6425		√	bi; diop; plag; act (cc)								
S16	granite	Sassi	6425	√	√	qz; ksp; plag; bi	√							
S17	gt-amphibolite	Sassi	6425		√	gt; bi; hb; plag; qz; sph	√	√	√					
S18	biotite gneiss	Sassi	6425		√	bi; plag; ksp; qz	√							
S19	gt-amphibolite	Sassi	6425		√	gt; hb; plag; qz; sph	√							
S20	granite	Sassi	6425	√	√	bi; plag; ksp; qz								
S21	mylonitic gneiss	Sassi	6425		√	bi; plag; ksp; qz	√							
S22	gt-amphibolite	Sassi	6526		√	gt; bi; hb; plag; ksp; qz; sph	√	√	√	√		Sr	Bi & Hb	
S23	mylonitic gneiss	Sassi	6526		√	bi; mu; plag; qz	√							
S24	gt-amphibolite	Sassi	6526		√	gt; bi; hb; plag; qz; sph	√	√	√					
S25	mylonitic gneiss	Sassi	6526		√	bi; plag; ksp; qz (chl)	√							
S26	pelitic gneiss	Sassi	6526		√	bi; mu; plag; qz	√							
S27	calcsilicate	Sassi	6527		√	bi; diop; plag; ksp; qz; sph	√							

Sample	Lithology	Location	Grid Ref	Granite def'n	Thin Section	Mineralogy	Orientated	Polished Section	Th'calc	XRF	INAA	Isotopes	Rb/Sr dating	Ar-Ar dating
S28	calcsilicate	Sassi	6527		√	gt; hb; diop; bi; zo; plag; qz; sph	√	√	√					
S29	mylonitic gneiss	Sassi	6527		√	gt; bi; mu; plag; qz (chl)	√	√	√					
S30	biotite gneiss	Sassi	6527		√	bi; plag; qz								
S31	pelitic gneiss	Sassi	6527		√	bi; mu; plag; ksp; qz	√							
S32	biotite gneiss	Sassi	6527		√	bi; plag; ksp; qz	√							
S33	gt-amphibolite	Sassi	6527		√	gt; bi; hb; plag; ksp; qz	√	√						
S34	gt-amphibolite	Sassi	6527		√	gt; bi; hb; plag; zo; sph; qz		√	√					
S35	granite	Sassi	6527	√										
S36	granite	Sassi	6527	√	√	plag; ksp; qz (chl)								
S37	granite	Sassi	6527	√	√	plag; ksp; qz (chl)								
S38	gt-amphibolite	Sassi	6527		√	gt; hb; plag; qz; sph								
S39	pelitic gneiss	Sassi	6527		√	gt; bi; mu; plag; qz	√							
S40	pelitic gneiss	Sassi	6527		√	gt; bi; mu; plag; qz	√							
S41	granite	Sassi	6527	√										
S42	granite	Sassi	6527	√	√	ksp; plag; qz; bi; mu				√				
S43	granite	Sassi	6527	√										
S44	granite	Sassi	6527	√	√	ksp; plag; qz; bi								
S45	granite	Sassi	6527	√										
S46	granite	Sassi	6527	√	√	ksp; plag; qz; bi								
S47	granite	Sassi	6527	√	√	ksp; plag; qz; bi				√		Sr		
S48	biotite-gneiss	Sassi	6526				√							
S49	biotite-gneiss	Sassi	6526		√	bi; plag; qz (chl)	√							
S50	calcsilicate	Sassi	6526		√	gt; hb; plag; qz; sph; zo; cc		√						
S51	granite	Sassi	6526	√						√				
S52	pelitic gneiss	Sassi	6526		√	bi; mu; plag; qz	√							
S53	pelitic gneiss	Sassi	6526		√	bi; mu; plag; qz	√							
S54	gt-amphibolite	Sassi	6526		√	gt; bi; hb; plag; qz; sph	√							
S55	biotite-gneiss	Sassi	6526		√	bi; plag; qz	√							
S56	biotite-gneiss	Sassi	6526		√	bi; plag; qz	√							
S57	biotite-gneiss	Sassi	6526		√	gt; bi; plag; qz	√							
S58	calcsilicate	Sassi	6526											
S59	calcsilicate	Sassi	6526		√	diop; hb; mu; plag; qz								
S60	granite	Sassi	6526	√						√				
S61	calcsilicate	Sassi	6526		√	gt; hb; plag; sph; qz; zo		√						
S62	pelitic gneiss	Sassi	6526		√	gt; ky; bi; mu; plag; qz	√	√	√					
S63	pelitic gneiss	Shahbatot	6525				√							

Sample	Lithology	Location	Grid Ref	Granite def'n	Thin Section	Mineralogy	Orientated	Polished Section	Th'calc	XRF	INAA	Isotopes	Rb/Sr dating	Ar-Ar dating
S64	pelitic gneiss	Shahbatot	6525		√	mu; plag; qz	√							
S65	pelitic gneiss	Shahbatot	6525		√	gt; bi; mu; plag; qz; tm	√							
S66	granite	Shahbatot	6524	√	√	ksp; plag; qz (mu)				√		Sr & Nd		
S67	granite	Shahbatot	6522	√	√	ksp; plag; qz; bi				√		Sr		
S68	granite	Shahbatot	6522	√										
S69	granite	Shahbatot	6522	√			√			√				
S70	amphibolite	Shahbatot	6522		√	hb; bi; sph; ep; ksp; plag; qz								
S71	amphibolite	Shahbatot	6522											
S72	marble	Shahbatot	6522		√	cc								
S73	granite	Shahbatot	6522	√										
S74	granite	Shahbatot	6522	√	√	ksp; plag; qz; bi								
S75	granite	Shahbatot	6522	√	√	ksp; plag; qz; bi				√		Sr		
S76	granite	Shahbatot	6522	√	√	ksp; plag; qz; bi				√		Sr		
S77	granite	Shahbatot	6522	√										
S78	granite	Shahbatot	6522	√	√	ksp; plag; qz; bi; mu; ep				√				
S79	granite	Shahbatot	6522	√	√	ksp; plag; qz; bi; mu	√							
S80	granite	Shahbatot	6522	√			√							
S81	granite	Shahbatot	6519	√	√	ksp; plag; qz; bi				√		Sr		
S82	augen gneiss	Shahbatot	6519		√	bi; ksp; plag; qz (sph)	√							
S83	migmatitic gneiss	Shahbatot	6519		√	bi; ksp; plag; qz (mu, chl)								
S84	leucogranite	E. of Shahbatot	6813	undef	√	ksp; plag; qz (mu)								
S85	calcsilicate	E. of Shahbatot	6813		√	gt; diop; hb; ep; qz; mu; sph; cc		√						
S86	pelitic gneiss	E. of Shahbatot	6813		√	gt; bi; mu; plag; qz		√						
S87	leucogranite	E. of Shahbatot	6813	undef	√	ksp; plag; qz; bi (mu)				√		Sr		
S88	gt-amphibolite	Shengus	7612		√	gt; hb; plag; ksp; qz (chl)								
S89	gt-amphibolite	Shengus	7612		√	gt; hb; bi; plag; qz								
S90	gt-amphibolite	Shengus	7612		√	gt; hb; bi; plag; qz (sph)		√	√					
S91	pelitic gneiss	Shengus	8011		√	sill; bi; mu; plag; ksp; qz		√		√		Sr		
S92	leucogranite	Shengus	8011	undef	√	ksp; plag; qz; mu; bi; tm (gt)				√		Sr & Nd	Bi & Mu	Bi & Mu
S93	leucogranite	Shengus	8011	undef	√	ksp; plag; qz; bi (tm, mu)				√		Sr		
S94	pelitic gneiss	Shengus	8011		√	sill; bi; mu; plag; ksp; qz								
S95	granite	L. Darchan	6433	√	√	ksp; plag; qz; bi				√		Sr		
S96	granite	L. Darchan	6433	√	√	ksp; plag; qz; mu; bi				√				
S97	granite	L. Darchan	6433	√	√	ksp; plag; qz; mu				√		Sr & Nd		
S99	granite	L. Darchan	6433	√										
S100	granite	L. Darchan	6433	√										

Sample	Lithology	Location	Grid Ref	Granite def'n	Thin Section	Mineralogy	Orientated	Polished Section	Th'calc	XRF	INAA	Isotopes	Rb/Sr dating	Ar-Ar dating
S101	granite	L. Darchan	6433	√	√	ksp; plag; qz; mu (chl)				√				
S102	gt-amphibolite	L. Darchan	6533		√	gt; hb; bi; plag; qz; sph	√	√		√		Sr & Nd		
S103	biotite gneiss	L. Darchan	6533											
S104	metavolcanic	U. Bagrotte	4549		√	chl; qz; opaques								
S105	metavolcanic	U. Bagrotte	4547		√	hb; plag; chl; qz								
S106	granodiorite	Bagrotte	4340	undef	√	hb; ep; plag; ksp; qz								
S107	granite	Bagrotte	4235	undef										
S108	metavolcanic	L. Bagrotte	3933		√	hb; ep; plag; qz								
S109	granite	L. Bagrotte	3933	undef	√	ksp; plag; qz; mu; bi				√				
G1	pelitic gneiss	Gilgit valley	4625		√	gt; bi; mu; plag; qz; zo		√	√					
G2	granite	Gilgit valley	4625	undef	√	ksp; plag; qz; bi; mu				√	√	Sr & Nd		
G3	granite	Gilgit valley	4821	undef	√	ksp; plag; qz; mu; gt				√		Sr & Nd		
G4	granite	Gilgit valley	5116	undef	√	ksp; plag; qz; bi				√				
G5	granite	Indus conf.	5413	undef	√	ksp; plag; qz; bi; mu				√				
G6	metagabbro	Indus conf.	5413		√	hb; bi; plag; qz; ep								
G7	pelitic gneiss	Indus conf.	5413		√	gt; bi; mu; plag; qz; zo		√	√					
G8	granite	Jaglot	5611	undef										
G9	pelitic gneiss	Jaglot	5611		√	gt; bi; mu; plag; qz; zo		√	√					
G10A	granite	Jaglot	5611	undef	√	ksp; plag; qz; bi; mu				√		Sr		
G10B	granite	Jaglot	5611	undef	√	ksp; plag; qz; bi; mu				√				
G10C	granite	Jaglot	5611	undef	√	ksp; plag; qz; bi; mu				√				
G10D	granite	Jaglot	5611	undef	√	ksp; plag; qz; bi; mu				√	√	Sr & Nd	Bi & Mu	Bi & Mu
G10E	granite	Jaglot	5611	undef	√	ksp; plag; qz; bi; mu				√		Sr		
G10F	granite	Jaglot	5611	undef	√	ksp; plag; qz; bi; mu				√		Sr		
G10G	granite	Jaglot	5611	undef	√	ksp; plag; qz; bi; mu				√	√	Sr		
G10H	granite	Jaglot	5611	undef	√	ksp; plag; qz; bi; mu				√	√	Sr & Nd		
G10I	granite	Jaglot	5611	undef	√	ksp; plag; qz; bi; mu				√				
G11	metagabbro	Indus conf.	5616		√	hb; bi; plag; qz; ep; zo								Bi & Mu
G12	granite	Indus conf.	5616	undef	√	ksp; plag; qz; bi				√				Bi
G13	granite	Indus conf.	5616	undef	√	ksp; plag; qz; bi				√				
G14	granite	Indus conf.	5616	undef	√	ksp; plag; qz; bi; mu				√		Sr	Mu	Bi & Mu
G15	granite	Indus conf.	5518	undef	√	ksp; plag; qz; bi; mu				√		Sr		
G16	granite	Indus conf.	5518	undef	√	ksp; plag; qz; bi				√				
G17	gt-amphibolite	Indus conf.	5622		√	gt; hb; bi; plag; qz; ep		√	√					
G18	granite	Indus conf.	5518	undef	√	ksp; plag; qz; bi				√		Sr & Nd		

Sample	Lithology	Location	Grid Ref'	Granite def'n	Thin Section	Mineralogy	Orientated	Polished Section	Th'calc	XRF	INAA	Isotopes	Rb/Sr dating	Ar-Ar dating
G19	amphibolite	Indus conf.	5622		√	hb; bi; plag; qz; ep								
G20	amphibolite	Indus conf.	5623		√	hb; bi; plag; qz; ep		√	√					
G21	amphibolite	Indus conf.	5623		√	hb; bi; plag; qz								
G22	amphibolite	Indus conf.	5623		√	hb; bi; plag; qz; ep; zo								
G23	granite	Shuta	5623	undef	√	ksp; plag; qz; bi; mu				√		Sr		
G24	pyroxenite	Shuta	5623		√	hb; bi; plag; qz								
G25	pelitic gneiss	Sassi	6527		√	gt; bi; mu; plag; qz	√							
G26	pelitic gneiss	Sassi	6527		√	gt; bi; mu; plag; qz	√	√						
G27	pelitic gneiss	Sassi	6527		√	gt; bi; mu; plag; qz	√	√						
G28	pelitic gneiss	Sassi	6527		√	gt; ky; bi; mu; plag; qz	√	√						
G29	granite	Sassi	6527	√	√	ksp; plag; qz; mu (gt)								
G30	granite	Sassi	6527	√	√	ksp; plag; qz; mu (gt)				√		Sr & Nd		
G31	pelitic gneiss	Sassi	6527		√	gt; ky; bi; mu; plag; ksp; qz	√	√	√	√		Sr & Nd	Mu	
G32	granite	Sassi	6527	√	√	ksp; plag; qz; mu								
G33	granite	Sassi	6527	√										
G34	granite	Sassi	6527	√	√	ksp; plag; qz; bi; gt; tm	√							
G35	granite	Sassi	6527	√	√	ksp; plag; qz; bi; gt; tm	√			√	√	Sr		
G36	granite	Sassi	6527	√	√	ksp; plag; qz; bi; gt; tm	√			√		Sr		
G37	pelitic gneiss	Sassi	6527		√	gt; bi; mu; plag; qz	√							
G38	granite	Sassi	6527	√	√	ksp; plag; qz; mu; bi; gt	√							
G39	granite	Sassi	6527	√	√	ksp; plag; qz; mu; gt				√		Sr & Nd		
G40	granite	Sassi	6527	√	√	ksp; plag; qz; bi; tm								
G41	granite	Sassi	6527	√										
G42	granite	Sassi	6527	√										
G43	granite	Sassi	6527	√	√	ksp; plag; qz; bi; mu	√			√	√	Sr & Nd		
G44	pelitic gneiss	Sassi	6527		√	gt; bi; mu; plag; qz	√	√						
G45	granite	Sassi	6527	√	√	ksp; plag; qz; mu; gt	√							
G46	granite	Sassi	6527	√	√	ksp; plag; qz; mu; bi								
G47	granite	Sassi	6527	√										
G48	granite	Sassi	6527	√	√	ksp; plag; qz; bi; mu	√			√		Sr		
T1	amphibolite	Tato road	5483				√							
T2	amphibolite	Tato road	5483				√							
T3	leucogranite	Tato road	5483	√	√	qz; ksp; plag; bi; mu; tm								
T4	amphibolite	Tato road	5483				√							
T5	amphibolite	Tato road	5483				√							

Sample	Lithology	Location	Grid Ref	Granite def'n	Thin Section	Mineralogy	Orientated	Polished Section	Th'calc	XRF	INAA	Isotopes	Rb/Sr dating	Ar-Ar dating
T6	leucogranite	Tato road	5483	√	√	qz; ksp; plag; mu; tm (bi)	√							
T7	leucogranite	Tato road	5483	√			√							
T8	amphibolite	Tato road	5483		√	hb; bi; plag; qz	√							
T9	leucogranite	Tato road	5483	√	√	qz; ksp; plag; bi								
T10	amphibolite	Tato road	5483		√	hb; bi; plag; ksp; qz	√							
T11	metabasite	Tato road	5483		√	aug; tr; chl; opaques	√							
T12	leucogranite	Tato road	5483	√			√							
T13	leucogranite	Tato road	5483	√	√	qz; ksp; plag; (mu)								
T14	pelitic gneiss	Tato road	5483		√	bi; mu; plag; ksp; qz; tm	√							
T15	pelitic gneiss	Tato road	5483		√	bi; mu; plag; qz; tm	√							
T16	calcsilicate	Tato road	5483		√	bi; diop; act; plag; cc; qz	√							
T17	biotite gneiss	Tato road	5483		√	bi; plag; qz; tm	√							
T18	leucogranite	Tato road	5483	√	√	bi; plag; ksp; qz	√							
T19	calcsilicate	Tato road	5483		√	tr; cc; qz; sph; plag	√							
T20	calcsilicate	Tato road	5483		√	gt; bi; hb; plag; cc; qz; sph	√	√	√					
T21	calcsilicate	Tato road	5483		√	diop; tr; plag; cc; qz	√							
T22	amphibolite	Tato road	5483		√	bi; hb; plag; qz; sph	√							
T23	calcsilicate	Tato road	5483		√	gt; diop; plag; zo; sph; qz		√						
T24	biotite gneiss	Tato road	5483		√	bi; plag; ksp; qz; tm	√							
T25	pelitic gneiss	Tato road	5483		√	bi; mu; ksp; plag; qz	√			√		Sr	Mu	
T26	biotite gneiss	Tato road	5483				√							
T27	amphibolite	Tato road	5483				√							
T28	biotite gneiss	Tato road	5483		√	bi; plag; ksp; qz	√							
T29	leucogranite	Tato road	5483	√			√							
T30	amphibolite	Tato road	5483				√							
T31	biotite gneiss	Tato road	5482		√	bi; plag; ksp; qz (sph, chl)								
T32	biotite gneiss	Tato road	5482				√							
T33	biotite gneiss	Tato road	5482				√							
T34	amphibolite	Tato road	5482		√	gt; bi; hb; plag; qz; sph	√							
T35	leucogranite	Tato road	5482	√	√	ksp; plag; qz; bi (ep, sph)								
T36	biotite gneiss	Tato road	5482											
T37	leucogranite	Tato road	5482	√			√							
T38	flaser-gneiss	Tato road	5480		√	bi; plag; ksp; qz								
T39A	flaser-gneiss	Tato road	5480		√	bi; plag; ksp; qz	√							
T39B	flaser-gneiss	Tato road	5480		√	bi; plag; ksp; qz								
T39C	flaser-gneiss	Tato road	5480		√	bi; plag; ksp; qz								

Sample	Lithology	Location	Grid Ref	Granite def'n	Thin Section	Mineralogy	Orientated	Polished Section	Th'calc	XRF	INAA	Isotopes	Rb/Sr dating	Ar-Ar dating
T39D	flaser-gneiss	Tato road	5480		√	bi; plag; ksp; qz								
T30E	flaser-gneiss	Tato road	5480		√	bi; plag; ksp; qz								
T39F	flaser-gneiss	Tato road	5480		√	bi; plag; ksp; qz								
T39G	flaser-gneiss	Tato road	5480		√	bi; plag; ksp; qz								
T39H	flaser-gneiss	Tato road	5480		√	bi; plag; ksp; qz								
T39I	flaser-gneiss	Tato road	5480		√	bi; plag; ksp; qz								
T40	biotite gneiss	Tato road	5480		√	bi; plag; ksp; qz	√							
T41	biotite gneiss	Tato road	5480		√	bi; plag; ksp; qz								
T42	leucogranite	Tato road	5480	√	√	ksp; plag; qz; tm; bi								
T43	amphibolite	Tato road	5478				√							
T44	biotite gneiss	Tato road	5478				√							
T45	leucogranite	Tato road	5478	√			√							
T46	amphibolite	Tato road	5478				√							
T47	biotite gneiss	Tato road	5478		√	qz; bi; plag; tm	√							
T48	biotite gneiss	Tato village	5477		√	bi; plag; ksp; qz								
T49	leucogranite	Tato village	5477	undef.	√	ksp; plag; qz; tm; bi	√							
T50	metabasite	Tato road	5483		√	aug; hb; bi; plag; ksp	√							
T51	augen-gneiss	Tato road	5483											
T52	leucogranite	Tato road	5483	√	√	ksp; plag; qz; bi; tm								
T53	leucogranite	Tato road	5483	√	√	ksp; plag; qz; mu; tm								
T54	pelitic gneiss	Tato road	5483		√	bi; mu; tm; ksp; plag; qz	√							
T55	pegmatite	Tato road	5483	√	√	ksp; plag; qz; mu								
T56	leucogranite	Tato road	5483	√	√	ksp; plag; qz; bi								
T57	leucogranite	Tato road	5483	√										
T58	amphibolite	Tato road	5483				√							
T59	leucogranite	Tato road	5483	√						√				
T60	biotite gneiss	Tato road	5483		√	gt; bi; plag; qz	√							
T61	biotite gneiss	Tato road	5483		√	bi; plag; qz; tm (chl)	√							
T62	biotite gneiss	Tato road	5483		√	gt; bi; plag; ksp; qz (tm)	√							
T63	biotite gneiss	Tato road	5483		√	gt; bi; plag; qz	√							
T64	calcsilicate	Tato road	5483		√	gt; diop; hb; bi; cc; plag; qz; sph		√	√					
T65	augen-gneiss	Tato road	5483		√	bi; ksp; plag; qz	√							
T66	biotite gneiss	Tato road	5483											
T67	biotite gneiss	Tato road	5483											
T68	leucogranite	Tato road	5483	√										

Sample	Lithology	Location	Grid Ref	Granite def'n	Thin Section	Mineralogy	Orientated	Polished Section	Th'calc	XRF	INAA	Isotopes	Rb/Sr dating	Ar-Ar dating
T69	gt-amphibolite	Tato road	5483		√	gt; hb; bi; plag; ksp; qz; sph	√	√	√					
T70	leucogranite	Tato road	5483	√										
T71	leucogranite	Tato road	5483	√	√	ksp; plag; qz; mu (bi, gt)				√				
T72	leucogranite	Tato road	5483	√										
T73	leucogranite	Tato road	5483	√										
T74	leucogranite	Tato road	5483	√	√	ksp; plag; qz; mu; tm				√				
T75	leucogranite	Tato road	5483	√	√	ksp; plag; qz; mu; tm								
R1	mylonitised lmst	Buldar ridge	5482				√							
R2	pelitic gneiss	Buldar ridge	5482				√							
R3	chert	Buldar ridge	5482				√							
R4	leucogranite	Buldar ridge	5482	√			√							
R5	metabasite	Buldar ridge	5482		√	oliv; tr; opaques (chl)								
R6	leucogranite	Buldar ridge	5482	√	√	ksp; plag; qz; tm; bi								
R7	metabasite	Buldar ridge	5482		√	aug; tr; opaques (chl, ep)	√							
R8	leucogranite	Buldar ridge	5482	√	√	ksp; plag; qz; tm; bi				√				
L1	migmatitic gneiss	L. Liachar	5885		√	bi; qz; ksp; plag; (mu)								
L2	pelitic gneiss	L. Liachar	5885		√	bi; mu; qz; ksp; plag.								
L3	biotite gneiss	L. Liachar	5885		√	gt; bi; qz; plag	√			√		Sr & Nd		
L4	amphibolite	L. Liachar	5885		√	hb; bi; plag; sph; qz	√							
L5	metabasite	L. Liachar	5885		√	oliv; act; bi; chl	√	√						
L6	leucogranite	L. Liachar	5885	√	√	ksp; plag; qz; bi; tm								
L7	biotite gneiss	L. Liachar	5885				√							
L8	gt-amphibolite	Raikhot	5683		√	gt; hb; bi; plag; qz; zo (mu)	√	√	√					
L9	gt-amphibolite	Raikhot	5683		√	gt; hb; qz; zo; sph	√							
L10	pelitic gneiss	Raikhot	5683		√	gt; bi; mu; plag; qz; sph	√	√						
L11	biotite gneiss	U. Liachar	6984		√	gt; bi; qz; plag (mu)	√							
L12	amphibolite	U. Liachar	6984		√	hb; bi; plag; qz; opaques	√							
L13	metabasite	U. Liachar	6984		√	aug; act; chl	√	√						
L14	leucogranite	U. Liachar	6984	√	√	ksp; plag; qz; tm								
L15	leucogranite	U. Liachar	6984	√	√	ksp; plag; qz; tm (bi, mu)								
L16	leucogranite	U. Liachar	6984	√	√	ksp; plag; qz; tm (mu)								
L17A	leucogranite	L. Liachar	5885	√	√	ksp; plag; qz; tm (bi)	√							
L17B	leucogranite	L. Liachar	5885	√	√	ksp; plag; qz; tm (bi)								
L17C	leucogranite	L. Liachar	5885	√	√	ksp; plag; qz; tm (bi)								

Sample	Lithology	Location	Grid Ref	Granite def'n	Thin Section	Mineralogy	Orientated	Polished Section	Th'calc	XRF	INAA	Isotopes	Rb/Sr dating	Ar-Ar dating
L17D	leucogranite	L. Liachar	5885	√	√	ksp; plag; qz; tm (bi)								
L17E	leucogranite	L. Liachar	5885	√	√	ksp; plag; qz; tm (bi)				√		Sr		
L17F	leucogranite	L. Liachar	5885	√	√	ksp; plag; qz; tm (bi)				√		Sr		
L17G	leucogranite	L. Liachar	5885	√	√	ksp; plag; qz; tm (bi)				√		Sr		
L17H	leucogranite	L. Liachar	5885	√	√	ksp; plag; qz; tm (bi)								
L17I	leucogranite	L. Liachar	5885	√	√	ksp; plag; qz; tm (bi)								
M1	migmatitic gneiss	Tato village	5475											
M2	migmatitic gneiss	Tato village	5475											
M3	migmatitic gneiss	Tato village	5475		√	bi; sill, ksp; plag; qz				√		Sr		
M4	migmatitic gneiss	Tato village	5475											
M5	calcsilicate	Tato village	5475		√	gt; diop; plag; qz; cc		√						
M6	calcsilicate	Tato village	5475		√	gt; diop; bi; hb; plag; qz; cc		√	√					
M7	amphibolite	Tato village	5475											
M8	migmatitic gneiss	Tato village	5475											
M9	migmatitic gneiss	Tato village	5475		√	gt; bi; sill; cord; plag; qz; ksp								
M10	migmatitic gneiss	Tato village	5475							√		Sr		
M11	migmatitic gneiss	Tato village	5475											
M12	migmatitic gneiss	Fairy M'dows	6468											
M13	amphibolite	Fairy M'dows	6468											
M14	leucogranite	Fairy M'dows	6468	undef	√	ksp; plag; qz; gt; bi				√				
M15	amphibolite	Fairy M'dows	6468		√	hb; bi; plag; qz								
M16	calcsilicate	Fairy M'dows	6466		√	gt; hb; bi; plag; qz (chl)		√	√					
M17	calcsilicate	Fairy M'dows	6466		√	hb; diop; plag; bi; qz; sph								Bi & Hb
M18	leucogranite	Fairy M'dows	6466	undef	√	ksp; plag; qz; bi; mu; tm				√		Sr & Nd		
A1	biotite gneiss	Astor valley	7578		√	bi; ksp; plag; qz								
A2	biotite gneiss	Astor valley	7578											
A3	pelitic gneiss	Astor valley	7578		√	gt; ky; bi; mu; plag; ksp; qz		√	√	√	√	Sr & Nd	Mu	
A4	pelitic gneiss	Astor valley	7578											
A5	pelitic gneiss	Tarshing	7154											
A6	pelitic gneiss	Tarshing	7154											
A7	pelitic gneiss	Tarshing	7154		√	gt; bi; mu, zo; plag; qz; tm		√	√	√		Sr		
A8	pelitic gneiss	Tarshing	7154											
A9	leucogranite	Rupal	6550	√	√	ksp; plag; qz; mu; tm				√		Sr		
A10	leucogranite	Rupal	6550	√	√	ksp; plag; qz; mu; tm				√		Sr		

Sample	Lithology	Location	Grid Ref	Granite def'n	Thin Section	Mineralogy	Orientated	Polished Section	Th'calc	XRF	INAA	Isotopes	Rb/Sr dating	Ar-Ar dating
A11	leucogranite	Rupal	6550	√	√	ksp; plag; qz; mu; tm				√		Sr		
A12	biotite gneiss	Rupal	6550											
A13	biotite gneiss	Rupal	6550		√	bi; ksp; plag; qz (mu)				√	√	Sr & Nd		
A14	pegmatite	Rupal	6550	√	√	ksp; plag; qz; mu; tm				√		Sr		
A15	biotite gneiss	Rupal	6550											
A16	leucogranite	Rupal	6550											
A17	leucogranite	Rupal	6550											
A18	biotite gneiss	Rupal	6550											
A19	leucogranite	Rupal	6550											
A21	pelitic gneiss	Astor valley	7578		√	gt; ky; bi; mu; plag; ksp; qz		√	√					
A22	pelitic gneiss	Astor valley	7578											
D1	biotite orthogneiss	NE Darchan	6341		√	bi; ksp; plag; qz; an (chl)								
D2	pelitic gneiss	NE Darchan	6341		√	gt; bi; mu; ksp; plag; qz (chl)				√		Sr	Mu	
D3	leucogranite	NE Darchan	6341	√	√	ksp; plag; qz; mu (chl)								
D4	pelitic gneiss	NE Darchan	6341		√	gt; bi; ksp; plag; qz (mu)								
D5	granite	NW Darchan	6245	√	√	ksp; plag; qz; mu (chl)				√		Sr		
D6	biotite gneiss	NW Darchan	6245		√	bi; ep; ksp; plag; qz (hb)	√	√						
D7	biotite gneiss	NW Darchan	6245		√	bi; mu; ep; ksp; plag; qz	√	√		√		Sr	Bi & Mu	
D9	granite	NW Darchan	6245	√										
D10	biotite gneiss	NW Darchan	6245		√	bi; ep; ksp; plag; qz	√							
D11	gt-amphibolite	NW Darchan	6245		√	gt; hb; ep; ksp; plag; qz	√	√						
D12	amphibolite	NW Darchan	6245		√	hb; ep; plag; qz	√							
D14	granite	NW Darchan	6245	√	√	ksp; plag; qz; bi (ep, mu)				√				
D15	granite	NW Darchan	6245	√	√	ksp; plag; qz; bi; mu								
D16	biotite gneiss	NW Darchan	6245		√	bi; ep; ksp; plag; qz	√	√						
D17	granite	NW Darchan	6245	√	√	ksp; plag; qz; mu (ep)				√		Sr	Mu	Bi & Mu
D18	orthogneiss	NW Darchan	6245		√	gt; bi; mu; ksp; plag; qz; ep	√	√	√					Mu
D19	pelitic gneiss	NE Darchan	6441		√	gt; bi; mu; plag; qz	√	√	√	√		Sr & Nd	Bi & Mu	
D20	orthogneiss	NE Darchan	6441		√	bi; ksp; plag; qz (gt, an)	√	√						
D21	biotite gneiss	NE Darchan	6441											
D22	pelitic gneiss	NE Darchan	6441		√	bi; mu; ksp; plag; qz	√							
J1A	Jutial granite	Jutial village	6737	(√)	√	ksp; plag; qz; bi; mu				√		Sr		
J1B	Jutial granite	Jutial village	6737	(√)	√	ksp; plag; qz; bi; mu				√	√	Sr & Nd		
J1C	Jutial granite	Jutial village	6737	(√)	√	ksp; plag; qz; bi; mu				√		Sr		

Sample	Lithology	Location	Grid Ref	Granite def'n	Thin Section	Mineralogy	Orientated	Polished Section	Th'calc	XRF	INAA	Isotopes	Rb/Sr dating	Ar-Ar dating
J1D	Jutial granite	Jutial village	6737	(√)	√	ksp; plag; qz; bi; mu				√		Sr		
J1E	Jutial granite	Jutial village	6737	(√)	√	ksp; plag; qz; bi; mu				√	√	Sr		
J1F	Jutial granite	Jutial village	6737	(√)	√	ksp; plag; qz; bi; mu				√	√	Sr		
J1G	Jutial granite	Jutial village	6737	(√)	√	ksp; plag; qz; bi; mu				√	√	Sr & Nd		
J1H	Jutial granite	Jutial village	6737	(√)	√	ksp; plag; qz; bi; mu (tm)				√				
J1I	Jutial granite	Jutial village	6737	(√)	√	ksp; plag; qz; bi; mu				√	√	Sr & Nd		
J2	pelitic gneiss	Jutial village	6737		√	bi; mu; plag; qz								
J5	leucogranite	Phuparosh	7046	undef	√	ksp; plag; qz; mu; tm								
J6	migmatitic gneiss	Phuparosh	7046		√	bi; ksp; plag; qz				√		Sr		
J7	leucogranite	Phuparosh	7046	√	√	ksp; plag; qz; mu; bi; tm				√		Sr & Nd		
J8	leucogranite	Phuparosh	7046	undef	√	ksp; plag; qz; mu; tm				√				
J9	leucogranite	Phuparosh	7046	undef	√	ksp; plag; qz; mu; tm (bi)				√				
J10	amphibolite	Jutial lake	7248		√	hb; bi; plag; qz; sph (chl)	√							
J11	leucogranite	Jutial lake	7248	√	√	ksp; plag; qz; bi (tm, mu)				√		Sr	Bi & Mu	Bi & Mu
J12	leucogranite	Jutial lake	7248	(√)	√	ksp; plag; qz; bi								
J13	gneiss	Jutial lake	7248		√	bi; hb; mu; plag; qz				√	√	Sr	Bi	Bi & Hb
J14	pelitic gneiss	Jutial lake	7248		√	bi; mu; plag; qz				√		Sr & Nd	Bi	Bi & Mu
J15	Jutial granite	Jutial valley	6737	(√)	√	ksp; plag; qz; bi (tm)				√				
J16	migmatitic gneiss	Jutial valley	6737		√	bi; ksp; plag; qz (zo, chl)								
J17	Jutial granite	Jutial valley	6737	undef	√	ksp; plag; qz; mu (bi, tm)								
J18	migmatitic gneiss	Jutial valley	6737		√	bi; ksp; plag; qz (mu)								
J19	Jutial granite	Jutial valley	6737	(√)	√	ksp; plag; qz; bi; mu (tm)				√	√	Sr & Nd		
J20	leucogranite	L. Jutial	6834	undef	√	ksp; plag; qz; bi (mu, tm)				√				
J21	biotite gneiss	L. Jutial	6834		√	bi; plag; qz				√		Sr	Bi	
I1	gt-amphibolite	Iskere village	7435		√	gt; hb; bi; plag; qz (chl, act)		√	√					
I2	biotite gneiss	Iskere village	7435											
I3	quartz-diorite	Iskere village	7435	undef	√	bi; plag; ksp (qz, mu)				√		Sr & Nd		
I4	quartz-diorite	Iskere village	7435	undef	√	bi; plag; ksp (qz, mu)								
I5	biotite gneiss	Kutwal lake	7934											
I6	migmatitic gneiss	Kutwal lake	7934		√	bi; ksp; plag; qz (chl, mu)				√	√	Sr & Nd	Bi	
I7	leucogranite	Kutwal lake	7934	undef	√	ksp; plag; qz; bi (mu)								
I8	leucogranite	Kutwal lake	7934	undef	√	ksp; plag; qz; mu; bi; tm				√		Sr	Bi & Mu	
I9	pelitic gneiss	U. Kutwal	8435		√	bi; mu; ksp; plag; qz				√		Sr & Nd	Bi & Mu	Bi & Mu
I10	pelitic gneiss	U. Kutwal	8435		√	bi; mu; ksp; plag; qz				√		Sr		
I11	leucogranite	Kutwal	8334	undef	√	ksp; plag; qz; gt; bi; tm				√		Sr		